

2 mis

NASA CR 132848

132848

TRACKING AND DATA RELAY SATELLITE SYSTEM CONFIGURATION AND TRADEOFF STUDY

Volume 5. TDRS Spacecraft Design



HUGHES AIRCRAFT COMPANY
SPACE AND COMMUNICATIONS GROUP

HUGHES AIRCRAFT COMPANY
SPACE AND COMMUNICATIONS GROUP
El Segundo, California

29 September 1972
Part I Final Report

Prepared for
GODDARD SPACE FLIGHT CENTER
Greenbelt, Maryland 20771

NASA-CR-132848) TRACKING AND DATA RELAY
SATELLITE SYSTEM CONFIGURATION AND
TRADEOFF STUDY. VOLUME 5: TDRS
SPACECRAFT DESIGN, PART 1 (Hughes
Aircraft Co.)

W74-10808
Unclas
21940
G3/31
CSSL 22B



Hughes Reference No. B5033 • SCG 20643R

Reproduced by
NATIONAL TECHNICAL
INFORMATION SERVICE
US Department of Commerce
Springfield, VA. 22151

TECHNICAL REPORT STANDARD TITLE PAGE

1. Report No.		2. Government Accession No.		3. Recipient's Catalog No.	
4. Title and Subtitle Tracking and Data Relay Satellite System Configuration and Tradeoff Study			5. Report Date 29 September 1972		
			6. Performing Organization Code		
7. Author(s)			8. Performing Organization Report No. Volume 5 20643R		
9. Performing Organization Name and Address Hughes Aircraft Company, Space and Communications Group NASA Systems Division 1950 E. Imperial Highway El Segundo, California 90009			10. Work Unit No.		
			11. Contract or Grant No. NAS 5-21704		
12. Sponsoring Agency Name and Address National Aeronautics and Space Administration Goddard Space Flight Center Greenbelt, Maryland 20771 G. Clark			13. Type of Report and Period Covered Final Report, Part I 25 January 1972 to 21 August 1972		
			14. Sponsoring Agency Code		
15. Supplementary Notes					
<p>16. Abstract</p> <p>A dual spin stabilized TDR spacecraft design is presented for low data rate (LDR) and medium data rate (MDR) user spacecraft telecommunication relay service. The relay satellite provides command and data return channels for unmanned users together with duplex voice and data communication channels for manned user spacecraft. TDRS/ground links are in the Ku band. Command links are provided at UHF for LDR users and S band for MDR users. Voice communication channels are provided at UHF/VHF for LDR users and at S band for MDR users. The spacecraft is designed for launch on the Delta 2914 with system deployment planned for 1978.</p> <p>This volume contains a description of the overall TDR spacecraft configuration, a detailed description of the spacecraft subsystems, a reliability analysis, and a product effectiveness plan.</p>					
17. Key Words (Selected by Author(s)) TDR spacecraft configuration, reliability, product effectiveness and detailed subsystem description.			18. Distribution Statement		
19. Security Classif. (of this report) Unclassified		20. Security Classif. (of this page) Unclassified		21. No. of Pages	22. Price*

*For sale by the Clearinghouse for Federal Scientific and Technical Information, Springfield, Virginia 22151.

CONTENTS

	<u>Page</u>
1. SUMMARY	1-1
2. INTRODUCTION	
2.1 General Approach	2-1
2.2 Design Objectives	2-1
3. TDR SPACECRAFT BASELINE CONFIGURATION	
3.1 Configuration	3-1
3.2 Design Features	3-4
3.3 Characteristics	3-10
3.3.1 Spacecraft Characteristics Summary	3-10
3.3.2 Power Requirements	3-15
3.3.3 Estimated Spacecraft Mass	3-15
3.3.4 Telemetry and Command Lists	3-15
3.4 Reliability and Product Effectiveness	3-31
3.4.1 Spacecraft Reliability Estimates	3-34
3.4.2 Reliability Program Plan	3-66
3.4.3 Quality Assurance Program Plan	3-90
4. SUBSYSTEM DESIGN	
4.1 Telecommunications Service System	4-1
4.1.1 Requirements	4-1
4.1.2 Repeater Design Description	4-5
4.1.3 Repeater Performance Summary	4-37
4.2 Telemetry and Command Subsystem	4-46
4.2.1 Alternatives Considered	4-46
4.2.2 Design Description	4-46
4.2.3 Performance	4-63
4.2.4 Technology Status	4-64
4.3 Antennas	4-65
4.3.1 Alternatives Considered	4-65
4.3.2 Baseline Description	4-66
4.3.3 Baseline Performance Summary	4-89
4.3.4 Technology Status (Radiation, Inc.) Background Development	4-100
4.4 Attitude and Despin Control	4-102
4.4.1 Design Requirements and Alternatives Considered	4-102
4.4.2 Baseline Design Description	4-107
4.4.3 Component Description	4-126
4.4.4 Despin Control System Performance	4-147
4.4.5 Technology Status	4-152
4.4.6 Reference	4-153

4.5	Reaction Control Subsystem	4-155
	4.5.1 Alternative Considered	4-155
	4.5.2 Baseline Description	4-157
	4.5.3 Baseline Performance	4-165
	4.5.4 Technology Status	4-165
4.6	Electrical Power Subsystem	4-167
	4.6.1 Alternatives Considered	4-167
	4.6.2 Baseline Power Subsystem Description	4-175
	4.6.3 Power Subsystem Performance	4-201
	4.6.4 Technology Status	4-204
4.7	Apogee Motor	4-205
	4.7.1 Alternatives Considered	4-205
	4.7.2 Baseline Description	4-205
	4.7.3 Baseline Performance	4-207
	4.7.4 Technology Status	4-208
4.8	Structure	4-211
	4.8.1 Alternative Considered	4-211
	4.8.2 Baseline Description	4-211
	4.8.3 Performance	4-213
	4.8.4 Technology Status	4-214
4.9	Thermal Control	4-231
	4.9.1 Thermal Design Requirements	4-231
	4.9.2 Design Description	4-231
	4.9.3 Thermal Performance	4-235

APPENDIX. Attitude and Despin Control System

A-1

ILLUSTRATIONS

		<u>Page</u>
2-1	TDRSS Frequency Bands	2-2
3-1	TDR Spacecraft Configuration	3-3
3-2	TDRS Solar Power Output Versus Time	3-17
3-3	TDRSS Communication Subsystem	3-39
3-4	Antenna Positioning	3-41
3-5	TDRSS Telemetry and Command Subsystem Logic Diagram and Mathematical Model	3-43
3-6	TT&C During Launch and Deployment	3-45
3-7	TDRS Attitude Control Subsystem Logic Diagram and Mathematical Model	3-46
3-8	ACS During Launch and Deployment	3-47
3-9	TDRS Power Subsystem Logic Diagram and Mathematical Model	3-48
3-10	TDRSS Harness Logic Diagram and Mathematical Model	3-49
3-11	Thruster Valve Reliability Block Diagram	3-60
3-12	Valve Reliability Flow Diagram	3-60
3-13	TDRS Product Effectiveness Organization	3-66
3-14	Product Effectiveness Functional Relationship	3-66
3-15	Reliability and Quality Assurance Interaction with Subcontractors with Design Responsibility	3-70
3-16	Reliability and Quality Assurance Interaction with Subcontractors without Design Responsibility	3-71
4-1	TDRS Space Link Spectra	4-6
4-2	Forward Ground Link Channels	4-7
4-3	Return Ground Link Channels	4-8
4-4	TDRS Communication Repeater Block Diagram	4-9
4-5	Frequency Synthesizer/Master Oscillator	4-13
4-6	K Band Receiver	4-17
4-7	UHF Transmitter Driver/Power Amplifier	4-20
4-8	UHF Power Amplifier	4-22
4-9	VHF Receiver	4-26
4-10	S Band Transmitter and Receiver	4-28
4-11	S Band Power Amplifier	4-28
4-12	Order Wire Receiver	4-30
4-13	K Band Upconverter	4-30
4-14	K Band Transmitter	4-32
4-15	S Band Transponder	4-36
4-16	Repeater Gain Distribution	4-38
4-17	Tracking, Telemetry, and Command Subsystem	4-48
4-18	Command Format	4-48
4-19	Despun or Spinning Decoder Block Diagram	4-51
4-20	FSK/AM Signal Design	4-53

4-21	Spinning Encoder Block Diagram	4-57
4-22	Attitude Data Processor Time Interval Measurements	4-59
4-23	Despun Encoder Block Diagram	4-61
4-24	TDRS Antenna Subsystem	4-68
4-25	UHF-VHF Antenna for Low Data Rate User Service	4-68
4-26	Dual Frequency VHF/UHF Antenna Layout	4-69
4-27	S Band Order Wire Antenna	4-74
4-28	S Band High Gain Antenna for Medium Data Rate User Service	4-74
4-29	S Band High Gain Antenna Layout	4-75
4-30	Mass Versus Surface Accuracy for Single and Double Mesh 3.8 Meter Antenna	4-78
4-31	Double Mesh Concept Design	4-78
4-32	Deployment Torque Requirements	4-80
4-33	Ku Band Antennas, TDRS/Ground Links	4-80
4-34	Ku Band Antenna Layout	4-85
4-35	VHF Omni Antenna for Telemetry and Command Service	4-88
4-36	Sections Through Deployment Mechanism	4-88
4-37	Two-Axis Antenna Positioner	4-90
4-38	Antenna Positioner Drive Unit	4-90
4-39	Variation of Rib Frequency, Mass, and Tip Deflection for Deployed 3.8 Meter Diameter Antenna	4-98
4-40	Variation of Rib Frequency and Mass Versus Taper Ratio for Deployed 3.8 Meter Diameter Antenna	4-99
4-41	Attitude Control Subsystem Block Diagram	4-108
4-42	Stabilization Time Constants Versus Nutation Angle	4-109
4-43	Despin Control Subsystem Block Diagram	4-110
4-44	Formation of Despin Position Error Signal	4-114
4-45	Rate Error Detection	4-116
4-46	Despin Control Electronics Functional Block Diagram	4-116
4-47	Despin Motor Characteristics	4-118
4-48	Despin Control Model	4-119
4-49	Tracking Loop Open Loop Frequency Response	4-120
4-50	Tracking Loop Root Locus	4-122
4-51	Tracking Loop Open Loop Frequency Response -- Low Gain Mode	4-122
4-52	Tracking Loop Active Nutation Damping	4-123
4-53	Platform Response to Bearing Torque Variations	4-124
4-54	Platform-Response to Sensor Phase Variations	4-124
4-55	LMSC Type 8 Earth Sensor Block Diagram and Signal Processing	4-130
4-56	Sun Sensor Assembly Details	4-132
4-57	Single Sensor Unit Diagram	4-132
4-58	Typical Sensor Output Pulse	4-134
4-59	Sun Sensor Geometry	4-134
4-60	Phase Versus Output Timing	4-134
4-61	Nutation Damper	4-135
4-62	BAPTA	4-137
4-63	Despin Control Electronics	4-140
4-64	Error Measurement Circuit Block Diagram	4-142

4-65	Position Error Measurement Circuit Waveforms	4-142
4-66	Motor Driver Block Diagram	4-144
4-67	Rate Logic Block Diagram	4-146
4-68	Despin Control System Acquisition	4-148
4-69	Steady State Pointing Performance	4-148
4-70	Despin Control System Nutation Damping	4-150
4-71	Despin Control System Apogee Boost	4-151
4-72	RCS Candidate Schematics	4-154
4-73	RCS Baseline Schematic	4-156
4-74	Thruster Family for Use on TDRS (Photo A28658)	4-156
4-75	Propellant Latching Valve	4-160
4-76	Hydrazine Filter	4-162
4-77	Fill/Drain Valve	4-162
4-78	Propellant Tank	4-163
4-79	Pressure Transducer (Photo 20523-147)	4-163
4-80	Bus Voltage Controlled by Battery Voltage Requirements	4-168
4-81	Power System with Battery Discharge Controlled by Switch	4-169
4-82	Power System with Regulated Battery Output Voltage	4-172
4-83	TDRSS Baseline Power Subsystem Block Diagram	4-174
4-84	Solar Cell Array Tradeoff for 5 Years Operation in Synchronous Orbit	4-180
4-85	Solar Input Energy Variation for Typical Orbit	4-183
4-86	Voltage/Current Solar Panel Behavior	4-183
4-87	Normalized Maximum Power Versus Effective Equivalent 1 Mev Electron Fluence	4-186
4-88	Solar Cell Output Degradation (Radiation Effects Only)	4-186
4-89	Battery Cycle Life in Simulated 24 Hour Synchronous Orbit	4-188
4-90	Battery Charge Controller Functional Schematic	4-195
4-91	Battery Discharge Control Block Diagram	4-197
4-92	Tap Limiter Current and Dissipation Characteristics	4-200
4-93	Apogee Motor	4-206
4-94	Beryllium Rib Construction	4-217
4-95	Mass Stations	4-217
4-96	First X Bending of Mast	4-220
4-97	First Y Bending of Mast	4-220
4-98	Second X Bending of Mast	4-221
4-99	Second Y Bending of Mast	4-221
4-100	TDRSS Design Loads - Condition 2: Lateral Loads	4-223
4-101	Math Model Stations	4-226
4-102	Thrust Structure Geometry	4-227
4-103	Spacecraft Moment Diagram	4-227
4-104	Spacecraft Thermal Control Provisions	4-233
4-105	Despun Platform Power/Temperature Performance	4-234
4-106	Steady State Temperature of Outer Ring of TDRSS Despun Platform Versus Heat Flux	4-234
4-107	Motor Bearing Assembly/Structure Thermal Interface	4-236
4-108	Solar Panel Eclipse Response	4-238
4-109	24 Hour Battery Profile for Typical Rib Mounted Pack	4-238

4-110	Rib Temperature Versus Input Wattage	4-240
4-111	Configuration Analyzed for Thermal Distortion of Antenna Support Tubes	4-242
4-112	Tube ΔT Versus Solar Absorptance	4-243
4-113	Tube Deflection Versus Tube ΔT	4-243
4-114	Apogee Motor Propellant Temperature Envelope	4-244
4-115	Barrier/Nozzle Geometry	4-246
4-116	Intelsat IV Apogee Motor Plume Density With Boundary Layer	4-247
4-117	Intelsat IV Apogee Motor With Boundary Layer Constant Mach Lines	4-248
4-118	Intelsat IV Apogee Motor With Boundary Layer Constant Flow Angles	4-249
4-119	Conical Barrier Heating Rates Versus Distance Along Barrier	4-250
4-120	Flat Barrier Heating Rates	4-252
4-121	Maximum Conical Barrier Temperatures	4-252
A-1	Nutation Divergence Due to Spinup of Unbalanced Platform	A-2
A-2	Spacecraft in Flat Spin Condition	A-4
A-3	Motor Torque Boundaries for Flat Spin Recovery	A-6
A-4	Rotor Spin Rate and Nutation Angle During Flat Spin	A-6
A-5	Platform Rates During Flat Spin	A-8
A-6	Motor Torque and Dedamper Torque During Flat Spin	A-9
A-7	S Band Gimbal Control System Block Diagram	A-10
A-8	Equation Concept – Nested Systems of Rigid Bodies	A-24
A-9	General DASFA Spacecraft Configuration	A-28
A-10	Intelsat IV Spacecraft Showing Jet and Accelerometer Locations	A-30
A-11	Results of DASFA Simulation of Intelsat IV Dynamics	A-31
A-12	Flexible Rolled-up Solar Array Application to Spacecraft	A-32
A-13	Comparison Nutation Time Histories for Flexible and Rigid Solar Arrays	A-34
A-14	Spin Stabilized Spacecraft With Rotor Mounted Nutation Damper	A-35
A-15	Time History of Nutation Decay	A-36
A-16	TDRSS Solar Torque Model	A-36
A-17	Torque Versus Speed and Temperature	A-46
A-18	Brushless Motor Assembly Schematic	A-48
A-19	Motor Characteristics	A-50
A-20	Resolver Input and Output Waveforms	A-52
A-21	Marman Type Clamp	A-56
A-22	Geometry Fixture (top) and Material Fixture (bottom) (Photo A24203-CN-A)	A-62
A-23	Sintered Brush Grain Structure	A-62
A-24	Power Brush Wear Performance	A-64
A-25	Signal Brush Wear Performance	A-64
A-26	Wear Performance Versus Vacuum Pressure	A-65
A-27	Slip Ring Internal Pressure Versus Chamber Pressure	A-65
A-28	Wear Data from Life Test Components	A-66

TABLES

		<u>Page</u>
2-1	TDRS General Telecommunications Objectives	2-4
3-1	TDR Spacecraft General Summary	3-11
3-2	Electric Power Summary, Watts	3-16
3-3	Estimated Spacecraft Mass	3-18
3-4	RCS Propellant Requirements	3-20
3-5	TDRSS PCM Telemetry Channel Assignments	3-21
3-6	TDRSS Command Assignments	3-24
3-7	TDRS Major Reliability Program Activities	3-32
3-8	Summary of General Reliability Models	3-35
3-9	Rationale for Use of Hughes Experience Factor	3-36
3-10	Launch and Deployment Reliability Summary	3-38
3-11	Operational Spacecraft Reliability Summary	3-38
3-12	TDRS Communication Subsystem Failure Rate Summary	3-50
3-13	TDRS Telemetry and Tracking Subsystems Failure Rate Summary	3-51
3-14	TDRS ACS Failure Rate Summary	3-52
3-15	TDRS Power Failure Rate Summary	3-52
3-16	TDRS Harness Failure Rate Summary	3-53
3-17	Reaction Control Subsystem Detailed Hughes Failure Rates	3-54
3-18	Reaction Control Subsystem Reliability	3-55
3-19	Launch and Coast/Insertion Reliability Models	3-56
3-20	Mathematical Definition of Terms	3-57
3-21	Successful Conditional States of S(3) Spinup Function	3-57
3-22	Mathematical Definition of Terms in Orbital Operation Reliability Model	3-58
3-23	Successful Conditional States of Attitude Control Propulsion Subsystem	3-59
3-24	Thruster Valve Reliability Math Model	3-62
3-25	Conditional States of Thruster Valve	3-63
3-26	Failure Mode and Effects Analysis – Reaction Control Subsystem	3-64
3-27	Reliability Program Procedural Documents	3-68
3-28	TDRS High Reliability Parts Screening and Burn-in Matrix	3-88
4-1	TDRS Communication Subsystem Requirements	4-1
4-2	TDRS Antenna Parameters	4-3
4-3	UHF EIRP for Low Power Mode – Command Only	4-3
4-4	S Band EIRP	4-4
4-5	K Band EIRP	4-4
4-6	Transmitter Power Required	4-5
4-7	Frequency Synthesizer and Master Oscillator Parameters	4-15

4-8	K Band Receiver Parameters	4-19
4-9	LDR Forward Link UHF Power Summary	4-23
4-10	UHF Transmitter Parameters	4-24
4-11	VHF Receiver Parameters	4-27
4-12	S Band Transmitter Parameters	4-29
4-13	S Band Receiver Parameters	4-29
4-14	S Band Order Wire Receiver Parameters	4-31
4-15	K Band Upconverter Parameters	4-33
4-16	K Band Transmitter Parameters	4-34
4-17	S Band Transponder Parameters	4-35
4-18	Receiver Noise Figures	4-43
4-19	Repeater Mass Summary	4-44
4-20	Repeater Power Summary	4-44
4-20	FM Mode Transmission	4-56
4-21	Telemetry and Command Component Physical Characteristics	4-60
4-22	Telemetry and Command Performance Characteristics	4-63
4-23	UHF/VHF Antenna Mass Budget	4-72
4-24	Required Mesh Tension	4-77
4-25	S Band Antenna Mass Budget	4-82
4-26	Ku Band Antenna Mass Budget	4-84
4-27	VHF-UHF Antenna Performance	4-91
4-28	S Band Order Wire Antenna Performance	4-92
4-29	S Band High Gain Antenna Performance	4-93
4-30	Ku Band Horn Antenna Performance	4-94
4-31	Ku Band Reflector Antenna Performance	4-95
4-32	Telemetry and Command Antenna Performance	4-96
4-33	Results of Rib Analysis	4-97
4-34	Despin Control Design Criteria	4-104
4-35	Despin Control Subsystem Active Nutation Damping	4-125
4-36	Earth Sensor Comparison	4-128
4-37	Sun Sensor Characteristics	4-131
4-38	Nutation Damper Functional Characteristics	4-136
4-39	BAPTA Design Characteristics	4-138
4-40	RCS Requirements	4-164
4-41	Chronological Comparison of Previous Hughes Propulsion Subsystem Components with Proposed RCS	4-166
4-42	TDRSS Electric Power Summary During Eclipse Seasons	4-170
4-43	TDRSS Electric Power Summary During Summer Solstice	4-171
4-44	Power Subsystem Mass Distribution	4-176
4-45	Power Subsystem Design Characteristics	4-176
4-46	Solar Array Design	4-178
4-47	Hughes Solar Panel Degradation History	4-182
4-48	Batteries	4-191
4-49	Power Subsystem Performance	4-202
4-50	Power Electronics Losses, Watts	4-203
4-51	Candidate Motors	4-206
4-52	Apogee Motor Performance and Mass	4-208
4-53	Apogee Motor Requirements	4-209

4-54	Motor Development Status	4-210
4-55	Mass Station Description	4-215
4-56	Nonrigid Joints	4-218
4-57	Modal Characteristics	4-219
4-58	Critical Load Cases	4-222
4-59	Summary of Minimum Margins of Safety	4-224
4-60	Critical Design Loads (Ultimate)	4-225
4-61	Summary of Design Loads for Thrust Cones (Ultimate)	4-228
4-62	Subsystem Temperature Requirements	4-230
4-63	Thermal Dissipation Level, Watts	4-232
4-64	MBA Thermal Performance	4-237
4-65	TDRS/Hercules Baseline Apogee Motor Characteristics	4-245
A-1	Antenna/Vehicle Mass Properties	A-16
A-2	SAD II Digital Simulation Elements	A-26
A-3	Spacecraft Parameters	A-38
A-4	BAPTA Applied Loads, Capacities	A-40
A-5	Bearing Dimensions	A-41
A-6	Significant Bearing Lubrication System Test and Application Experience	A-42
A-7	Resolver Characteristics	A-53
A-8	BAPTA Qualification and Acceptance Tests	A-58
A-9	Slip Ring Test Summary – Dry-Lubricated Tests	A-59
A-10	Slip Ring Assembly Design Characteristics	A-61

1. SUMMARY -

The TDRSS Study Part I baseline TDR spacecraft configuration is presented in this volume. It is designed to provide telecommunication service for low and medium data rate users and to provide voice and data relay for manned user spacecraft. The S band telecommunication subsystem has been designed to meet communication requirements of the Space Shuttle program by the use of a 3.8 meter high gain antenna and by providing an EIRP of 47 dBw. Voice relay at VHF/UHF is also provided as specified.

This study has been directed to utilize a spin stabilized spacecraft design. Recent developments in this field at Hughes have included Intelsat IV, Telesat, and communication satellites for the military services. The technology and applicable components developed on these programs have been used in order to provide a design meeting the mission requirements that can be developed with a high level of confidence. The spacecraft is a Gyrostat design. Both Intelsat IV and TACSAT were Gyrostat designs and all have operated in orbit. TACSAT has been operating for 3.5 years. The Intelsat IV series have accumulated 3 satellite years of operation with four satellites and no satellites have failed. The Gyrostat configuration is a well demonstrated design approach which has proved highly reliable.

The Delta 2914 is the specified launch vehicle for the TDR satellite. Power requirements for the TDRS are approximately 75 percent greater than for Telesat. Mass has been a critical concern for this design, and lightweight subsystem design technology has been required in order to meet the mission design requirements within the mass constraints of the launch vehicle. Mass saving has been principally accomplished by using beryllium structural elements, and by injecting the spacecraft into a 7 degree inclination orbit with a highly efficient apogee injection motor. However, mass saving has not been at the expense of spacecraft reliability. Electronic components in all subsystems have been made redundant to assure a high confidence in mission success with the initial deployment of three satellites.

Propellant for 7 years of spacecraft operations has been included. In the event that the solar cell array has not degraded to the point conservatively predicted and the spacecraft has not failed, the TDRS will continue to function and provide relay service as specified. This will provide a longer time to write off development and deployment costs of the system, and the expected cost effectiveness of the system will be enhanced.

2. INTRODUCTION

2.1 GENERAL APPROACH

The Hughes Tracking and Data Relay Satellite System study is contractually limited to spin stabilized satellite configurations. Part of the study addresses system designs for low and medium data rate users and satellite configurations capable of launch by the Delta 2914 with a nominal payload of 682 kg (1500 pounds).

A 1978 system deployment is planned. This imposes a technology cut off date of approximately 1975 since a low risk operational system cannot be developed without proven design and hardware approaches. At the present time many satellite design disciplines have achieved some degree of design maturity where radical design departures are not expected; therefore, this study has used currently available design and hardware approaches.

In the future, however, technology developments will be continuing and performance improvements, particularly in areas such as power amplifier efficiency, lighter and more efficient solar cells, and lighter deployable antennas and structures, may be expected with a resulting overall improvement in spacecraft performance.

Considerable attention has been devoted during the study to cost effectiveness. The general approach has been to utilize well proven technology for the satellite subsystems and, if compatible with launch vehicle performance limitations, to utilize hardware designed for earlier satellite programs. System performance requirements and the mass limitations of the Delta 2914 launch vehicle have, however, generally led to new designs for most subsystems using available technology. Improvements in system cost effectiveness may perhaps be realized if the study were not restricted to a Delta launch. During Part II of the study the low and medium data rate configuration will be reviewed using other launch vehicles with a goal of achieving a more cost effective design.

2.2 DESIGN OBJECTIVES

The spacecraft configuration for the TDRS Part I study is designed to provide command and data relay capability for low and medium data rate

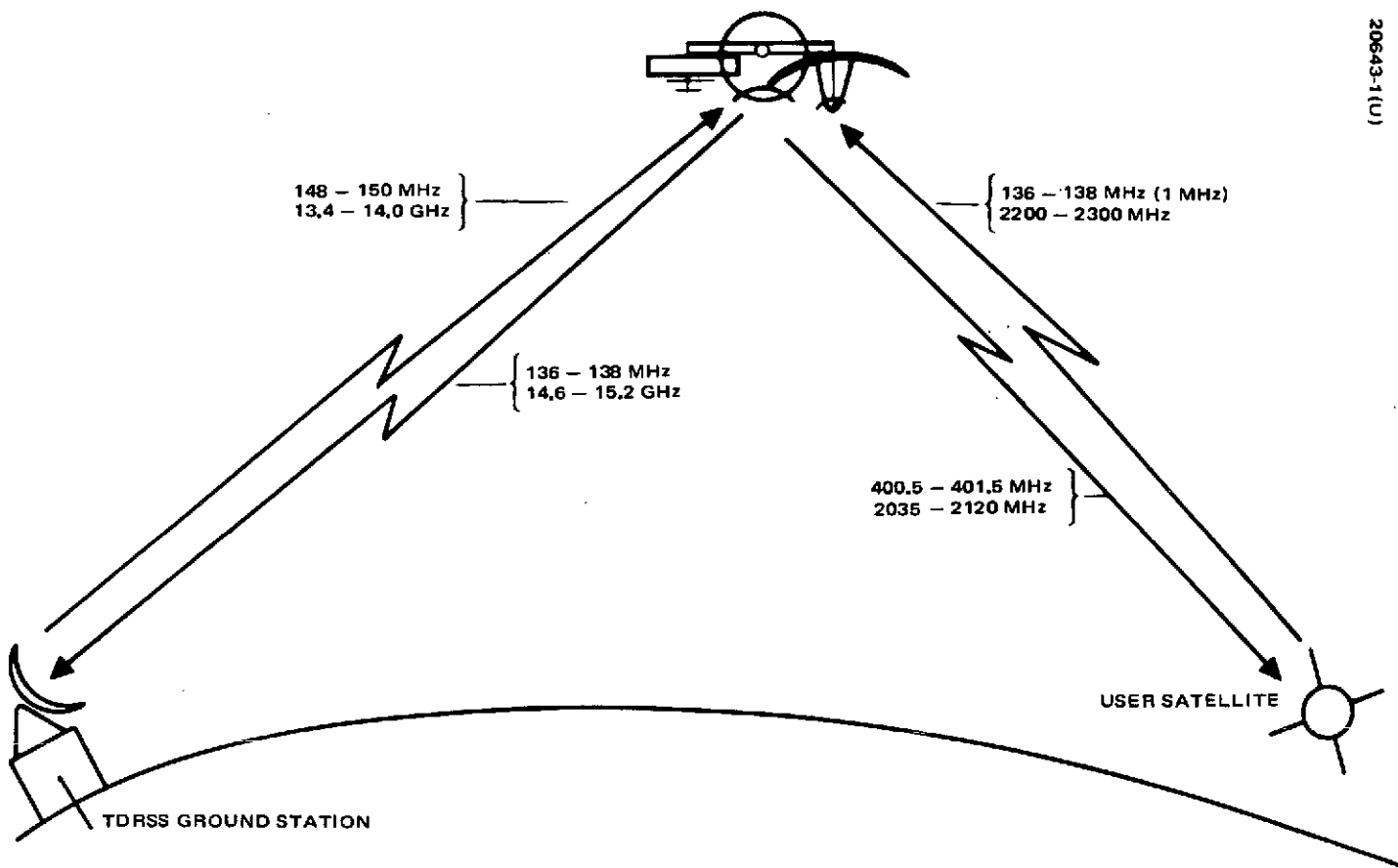


Figure 2-1. TDRSS Frequency Bands

unmanned user spacecraft and voice and data relay capabilities for manned user spacecraft. Low data rate user commands are received at Ku band and are frequency translated to UHF for transmission to the user satellites. The UHF forward link channels utilize broad beam antennas oriented toward earth center. An independent voice channel is also provided in this frequency band that can be used as much as 25 percent of the time. Medium data rate user commands are received at Ku band and frequency translated to S band for transmission to the user satellites. This channel may also be used for voice transmission by increasing power. This mode of operation may be used at least 50 percent of the time. The S band forward link employs a narrow beam 3.82 meter (12.5 foot) diameter parabolical reflector antenna which is pointed at the user satellite by ground command. Data and voice return links are provided at VHF and S band. A broad beam return link is also provided at S band to provide an emergency "order wire" service for manned users. The down link for data and voice is at Ku band and is implemented with a narrow beam return link. A VHF backup service for TDRS telemetry, tracking, and command and an S band transponder for TDRS tracking are also provided. The frequency bands selected for the Phase I TDRSS are shown in Figure 2-1. General requirements for the telecommunications service are listed in Table 2-1.

The TT&C subsystem uses the Ku band links for primary operations. A UHF transponder provides a backup capability in the event that contact cannot be made with the TDRS with the Ku band links. The primary command subsystem uses the 128 bps PCM-FSK/AM format to send the commands. A real time execute capability is desirable to simplify equipment. This requirement is met by providing an execute tone at a different frequency than the 0 and 1 tones employed in the command signals.

It is an objective to provide an efficient assemblage of antennas to perform the TDRS mission. Overall system cost-effectiveness depends largely on meeting the required link performance parameters with a minimum mass spacecraft design. The payload fairing also imposes a design constraint which requires the use of deployable antenna techniques. The design requirement to achieve a highly reliable spacecraft in turn establishes the need to test and check out the antennas and their deployment mechanisms on the ground. A motor drive deployment which can be executed many times is an approach that will develop confidence. Thus the antenna structure must be capable of being deployed and tested in an earth gravity field.

Pointing of the high gain S band and Ku band antennas is most economically accomplished by ground command. In this case of the S band antenna with a beamwidth of approximately 2.5 degrees, open loop pointing with an accuracy of the order 0.5 degree is clearly feasible. The Ku band antenna with a beamwidth of approximately 1 degree, presents a situation which requires in-orbit calibration in order to achieve the required pointing accuracy. This is possible for the TDRS to ground link Ku band antenna as the ground station is fixed and the orbital ephemeris varies slowly for a synchronous orbit satellite.

TABLE 2-1. TDRS GENERAL TELECOMMUNICATIONS OBJECTIVES

Service	Forward Link			Return Link		G/T, dB/K
	Coverage, degrees	Field of View, degrees	EIRP, dBw	Coverage, degrees	Field of View, degrees	
Low data rate user	30	26*	30	30	26	-16*
UHF voice	30	26*	30	30	26	-16*
Medium data rate user	30	1	41	30	1	8**
S band voice	30	1	47	30	1	8**

*At 30 degrees performance degrades approximately 1 dB.

**Specified G/T = 2 dB/K.

Attitude control requirements are to provide a stable platform for antenna pointing. It is not essential to control the despun platform orientation to less than 0.5 degree but it is necessary to measure the orientation of the spin vector and the despun platform azimuth to an accuracy of the order of 0.1 degree. Thus short term dynamic variations in pointing should be restricted by the design to be less than that amount. This requirement leads to a specification for nutation stability and also to a requirement to balance the spinning section. The despun control must be stable and any limit cycle shall not exceed 0.005 degree.

The basic design objectives for the spacecraft "bus" is to provide the required power, thermal control, propulsion, and structures at minimum mass. However, the design of these subsystems should present a low risk to the program. Accordingly, advanced approaches which have been adequately demonstrated are suitable for application to the TDRS.

3. TDR SPACECRAFT BASELINE CONFIGURATION

3.1 CONFIGURATION

The Hughes Gyrostat stabilization concept has been employed to provide a fully stabilized platform for the payload while exploiting the simplicity and long life advantages associated with spinning satellites. The two main elements of the spacecraft are the spinning rotor, comprising approximately 60 percent of the on-station vehicle mass, and the despun earth-oriented platform containing the communication repeater and its antennas. A rotating interface, consisting of conventional ball bearings and slip rings, sustains the relative motion between the two bodies, permits signal transfers to take place, and affords an electrical path over which power from the solar panels and batteries can flow to the repeater payload. The spinning rotor provides a basic gyroscope stability to the spacecraft.

The TDR spacecraft (Figure 3-1) is designed for compatibility with a Delta 2914 launch vehicle. The maximum payload capability into the elliptical transfer orbit is 680.4 kg (1500 pounds). An apogee motor injects the spacecraft into synchronous orbit. Hydrazine propulsion is provided for spin axis attitude control and orbital maneuvers. Power is generated by solar cells, and batteries which provide for peak power demands and eclipse operation.

A despun section houses the communication equipment and some of the telemetry, tracking, and command equipment. Electronic equipment is mounted on a thermally controlled platform. Antennas are mounted off the platform on a mast type support structure. Short backfire type antennas are provided for the low data rate user VHF return link and the UHF forward link. A parabolic reflector antenna is provided for both forward and return link S band service for the medium data rate user. These antennas are folded and stowed within the payload fairing during launch. The TDRS to ground link at Ku band incorporates a high gain parabolic reflector antenna. This antenna is secured to absorb launch loads. Both the S band and Ku band paraboloid antennas are installed on two-axis gimbals, and an S band short backfire antenna is provided for the ground to TDRS and order wire service.

The spinning section supports and houses the propulsion, electrical power, attitude control, and some of the tracking, telemetry, and command equipment. The apogee motor is installed in the central thrust tube. Hydrazine tanks are mounted on ribs extending from the thrust tube to the solar cell

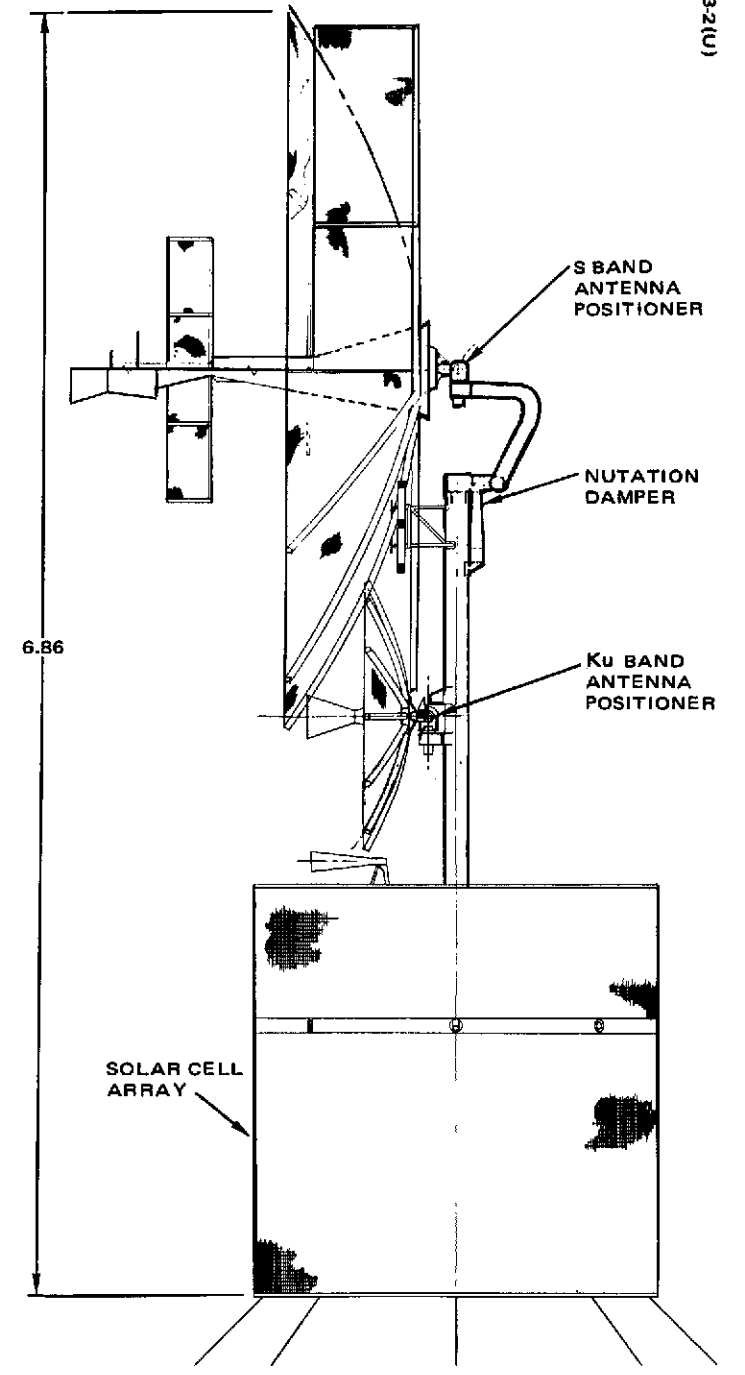
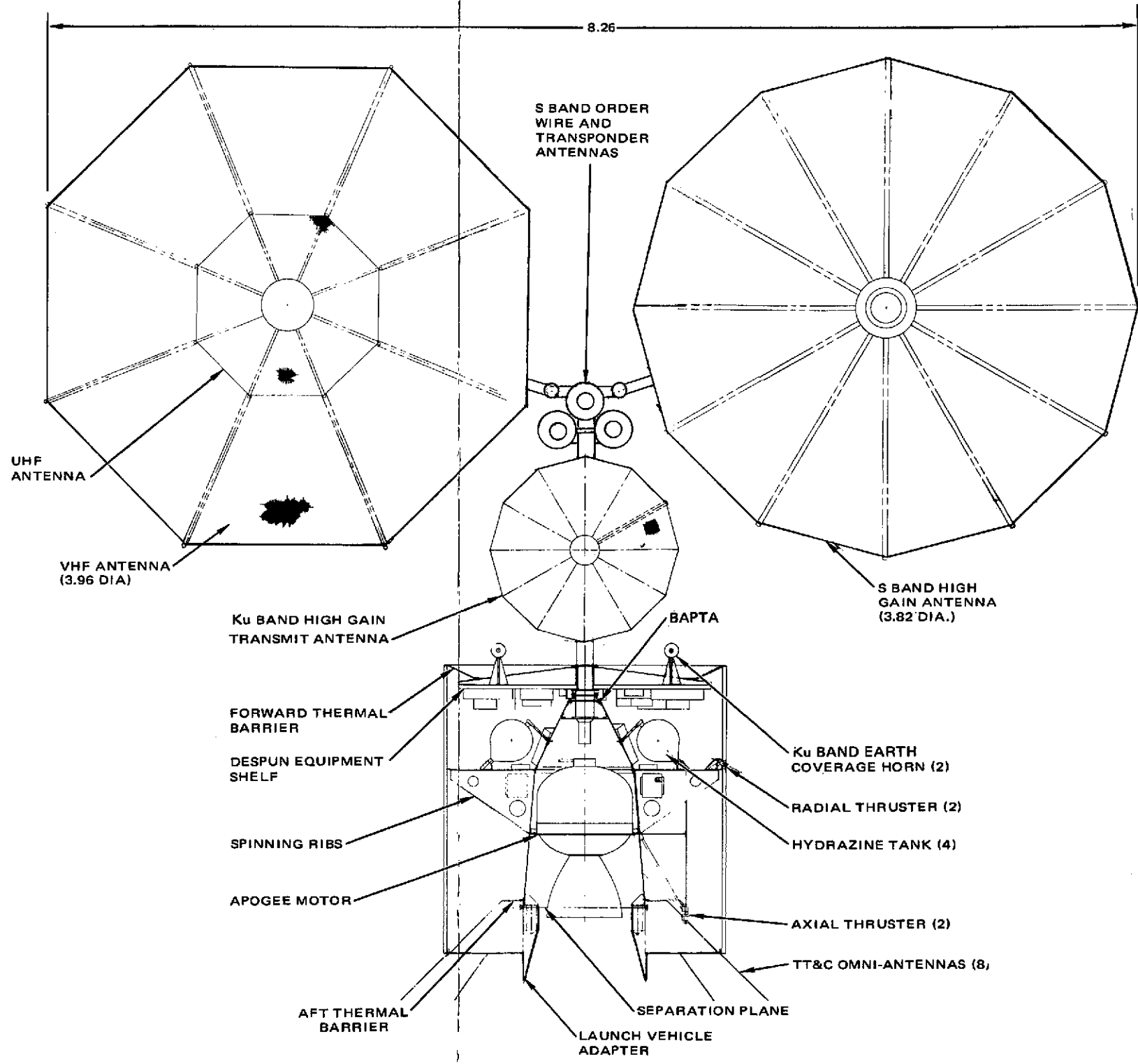
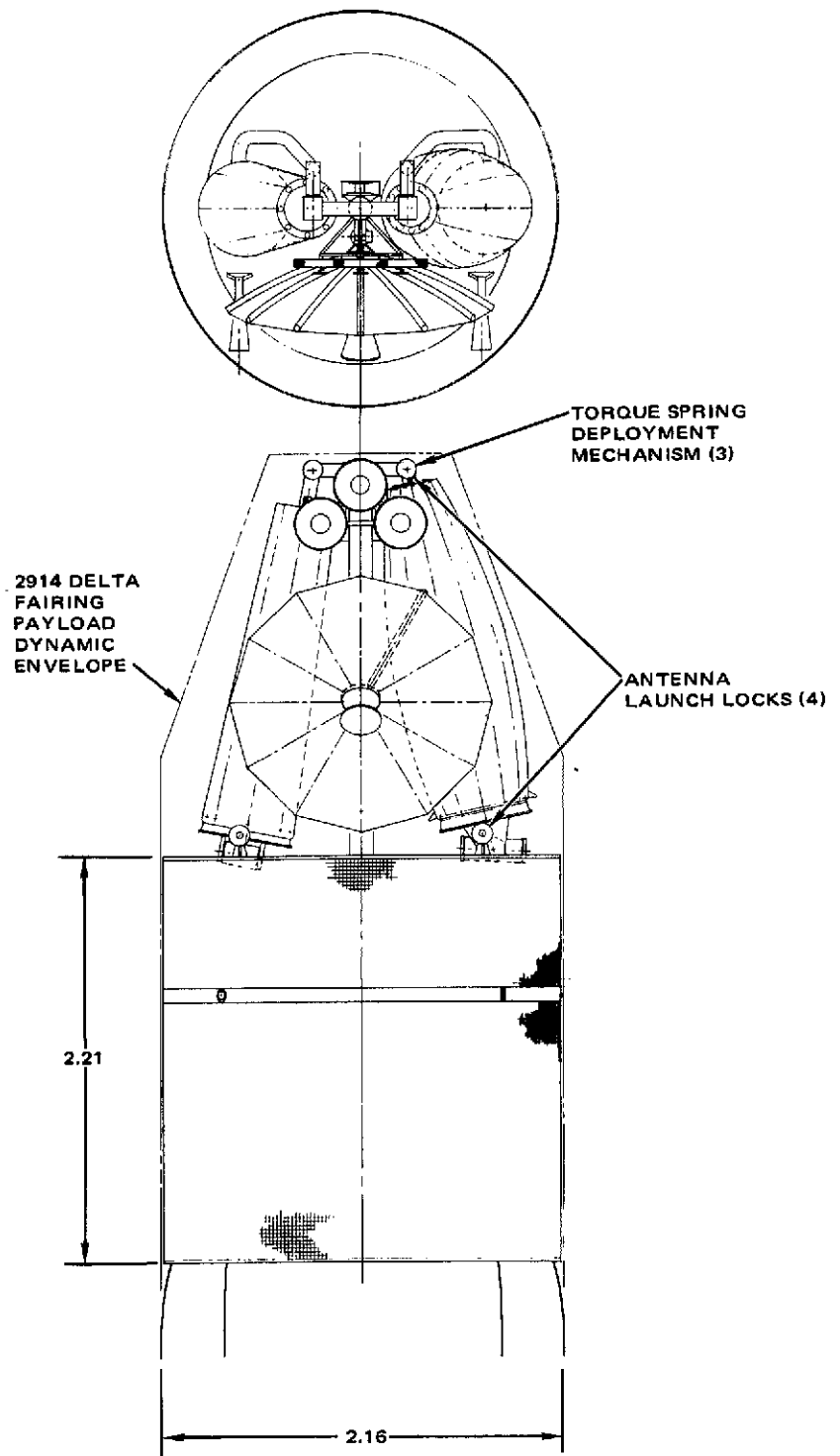
array. Batteries, battery controllers, despin control electronics, and telemetry tracking, and command equipment are mounted on the ribs and small equipment platforms spanning the ribs. The aft end of the spinning section is sealed by means of a thermal barrier which protects the spacecraft equipment during apogee motor firing and minimizes heat loss during orbital operations. Attitude control sensors, the radial control jets, and umbilical connectors are installed in an annular section between sections of the solar cell array. The axial jets are mounted on truss supports and protrude through the aft thermal barrier. The VHF omni antenna is mounted on the aft closure of the solar cell array in the TT&C initial orbital operation.

The spacecraft is attached to the Delta payload attach fitting with a band release clamp. Launch loads are transmitted through a cylindrical thrust tube which supports the apogee motor and the spinning assembly of the spacecraft. A conical structure forward of the apogee motor picks up the despin bearing assembly outer housing. The inner bearing support structure transfers loads to the despin equipment support platform and antenna support structure. A load transfer clamp is installed on the despin bearing assembly to provide a more rigid load path during the early stages of launch. Immediately prior to third stage ignition, the clamp is released and the despin motor activated to provide a stable dual spin configuration during the third stage and apogee injection motor burns (a signal from the launch vehicle third stage sequencer is required). The equipment platform is spun slowly with respect to an inertial reference to minimize attitude perturbations during these burns. The spinning section is spun up by the spin rocket on the Delta third stage. Following firing of the Delta third stage, the spacecraft is separated from the empty stage and then assumes its transfer orbit configuration. Following apogee injection, the spacecraft changes to its operational configuration upon receipt of commands to correct attitude, deploy antennas and turn on equipment.

3.2 DESIGN FEATURES

The spacecraft is designed to achieve the mission with a high reliability by using redundancy for active components. Exceptions occur for items such as the apogee motor, structure, despin bearing assembly, and antennas where it would be prohibitive from mass considerations alone to provide redundancy. In these items, safety factors are employed in their design and assured by test programs. All electronic units are redundant in the TDRS configuration presented.

Spin stabilization is accomplished by rotating the section of the spacecraft containing propulsion and power equipment at 10.47 rad/sec (100 rpm). The angular momentum developed provides a resistance to external torques and minimizes the number of attitude corrections required throughout the mission. The Gryostat principle of stabilization is used in this design of the TDRS. This approach allows large sections of the spacecraft to be despun, thereby accommodating the antennas and communication electronic equipment required for this mission on the stabilized despun platform.



DIMENSIONS IN METERS

Figure 3-1. TDR Spacecraft Configuration

A

B

In order to achieve a benign thermal environment for the communication subsystem and other critical equipment, a thermal control cavity is created inside the spinning solar cell array in which all temperature-sensitive equipment is placed. The aft end of the spacecraft, apogee motor end, is sealed off by an insulating thermal barrier which rotates with the rotor. This barrier has an external surface of stainless steel to protect the spacecraft from the intense heating caused by the apogee motor plume as well as the axial hydrazine jet plume. The forward end of the rotating drum cavity is sealed off by a spinning sunshield. This conical shell structure is covered with silvered quartz mirrors to reject solar input while at the same time radiating the heat generated by the output TWTs and their power supplies. The spin of these primary thermal control surfaces provides a low gradient thermal environment for the communication electronics and primary spacecraft control elements.

The primary load carrying structure is divided into a spun and despun section. The spun section consists of a thrust cone and four equipment carrying ribs fabricated from beryllium. A thin circular magnesium plate is attached to the ribs to provide the shear transfer for torsional loading. The ribs provide the support for the solar panel which is fabricated from two-ply fiberglass facesheets with an aluminum honeycomb core. The despun section consists of a despun shelf which has aluminum facesheets with an aluminum honeycomb core and six beryllium ribs on the forward side. The antenna mast structure is comprised of beryllium tubular elements.

The despin bearing and power transfer assembly (BAPTA) is the structural interface between the spun and despun sections. Its major structural components are also fabricated from beryllium. The bearings selected are 440C CEVM stainless steel angular contact bearings, 60 mm bore, extra light series with a nominal 25 degree contact angle. These bearings are of sufficient size to withstand imposed loads with substantial margin. The bearing lubrication system consists of four sintered nylon reservoirs, two porous ball retainers, the bearing metal parts, and the internal walls of the motor/bearing subassembly. The oil used to lubricate the bearings is per HMS 20-1727, a mixture of Apiezon C and lead naphthanate. The lubricant is vacuum impregnated into the bearing parts prior to assembly.

The despin control system (DCS) controls the orientation of the despun section. Sun or earth sensor information is utilized to establish the inertial attitude of the rotor. A magnet/pipper coil pair located in the bearing and power transfer assembly establishes the relative phase relationship between the rotor and the platform. A brushless, resolver commutated dc torque motor assembly is provided. The motor assembly consists of two redundant motors, segment wound on a common lamination stack and two fully redundant resolvers. Power and signal transfer from spun to despun sections of the satellite is accomplished with a dry lubricated slip ring assembly.

Nutational stability is provided through the passive nutation damper mounted on the despun platform, along with active control through the despin control system and the active nutation control system.

The damper consists of a single degree of freedom magnetic tip mass pendulum supported on a cantilevered beryllium-copper torsion wire. By dimensionally controlling the torsion wire, the natural frequency of the pendulum can be adjusted to spacecraft nutation frequency.

Because of the importance of despin control not only to communication service but also to nutational stability, an automatic rate control logic has been included. If, for any reason, the despin electronics is deprived of inertial reference information, the control logic will automatically switch to a rate hold mode wherein the spacecraft is controlled to maintain the most recent platform-rotor relative rate.

The reaction control subsystem is a four thruster, four tank system, split into completely redundant half systems. The half systems are joined by a normally closed latch type isolation valve. This valve permits common usage of all propellant in the event of a failure to either half system. Two jets, one axial and one radial, are required to maintain both attitude and station. For redundancy, two of each type are carried. Propulsive thrust is by catalytic decomposition of anhydrous hydrazine.

The nominal velocity increment required to circularize the spacecraft orbit at synchronous altitude from the nominal transfer orbit and to remove 20.7 degrees of inclination is 1675 m/sec^2 (5498 fps). The variation will be held within ± 1.0 percent. Maximum thrust of 40,000 Newtons (9000 pounds) and acceleration of 114.77 m/sec (11.5 g) for a 676 kb (1490 pound) spacecraft are imposed to limit the acceleration and static loads on the spacecraft.

The electric power subsystem configuration includes two batteries with active battery discharge control. The batteries are composed of 18 series cells. Battery discharge regulators boost the battery output to a nominal 25.5 volt line. Two battery cells could fail shorted in each battery without affecting system performance.

The battery discharge regulator circuit is of the boost choke type and uses pulsewidth modulation. It has a minimum number of power transistors and requires minimum input line filtering. To reduce power transistor stress and to minimize output filter size, each circuit is two phase, with forced current sharing between phases.

The equivalent battery charge current provided by the solar array to the two batteries is 60 watts. The solar panel output is 364.0 watts at summer solstice and 399 watts 23 days before equinox. The solar cell array uses 0.182 mm (7.2 mil) cells. This choice is based on successful production, test, and delivery of the flexible flight FRUSA solar panels, using 40,000, 0.182 mm (7.2 mil) cells.

The TDRS communication subsystem is completely redundant. Communication is maintained between the earth and TDRS with a Ku band link. UHF and VHF are used to communicate with low data rate users and S band is used to communicate with medium data rate users.

Redundant Ku band receivers are used. Input signals are doubly converted to a low IF frequency where they drive the various transmitters and telemetry within the spacecraft. In addition, the reference frequency pilot tone signal is detected in a phase locked loop which is part of the Ku band receiver. When this loop is locked, the locked reference signal drives the frequency synthesizer to provide a coherent reference for all spacecraft frequency translations. The Ku band receiver also contains sensing circuitry to determine when the phase detector is locked. The Ku band receiver IF amplifiers contain AGC circuits to accommodate the Ku band input signal levels which will vary with weather conditions.

The Ku band transmitter consists of a Ku band upconverter and Ku band TWT amplifiers. The upconverter receives signals from the spacecraft receivers and internal telemetry, amplifies these signals, and shifts them to the Ku band microwave frequency. The traveling wave tube power amplifier provides additional amplification and has a maximum power output of 8 watts.

The UHF transmitter is configured to operate with maximum flexibility in two power modes for transmitting commands to unmanned users and voice to a manned user. The above two signals can be sent simultaneously or either one separately by means of code division multiplexing of voice and commands. The multiplexing of the two signals at baseband in the ground station allows a single RF carrier frequency to be transmitted whether command alone or command plus voice are transmitted.

The total power amplifier consists of ten sections. Any four sections generate 71 watts which result in the required 30 dBw EIRP from the antenna. A push-to-talk feature has been incorporated whereby a subcarrier frequency is sensed when voice has been multiplexed into the channel. This sensing is performed by a discriminator/threshold circuit which activates an additional four sections of the power amplifier, providing 30 dBw EIRP to both command and voice signals. The additional two sections provide redundancy, and by ground command the configuration will be adjusted so that in case of the failure of any section, four will always operate for command and four will be switched on and off by the threshold circuit. A redundant driver stage is provided, and the power amplifier redundancy provided by the two spare sections results in high reliability for the total transmitter with a minimum of complexity.

There are two active VHF receivers. Each receiver has a 2 MHz passband from 136 to 138 MHz which includes both the user telemetry in the 136 to 137 MHz band and, at times, a voice signal in the 137 to 138 MHz band. The total UHF signal is resolved into two components by the VHF antenna corresponding to orthogonal senses of linear polarization. These

two VHF signal components are the separate inputs to the two active receivers which use different frequency synthesizer outputs in their mixers, thus translating the two components to separate frequency channels. There is a redundant receiver for each antenna output.

The S band transmitter and receiver are capable of transmitting and receiving at any frequency within the designated bands. Thus a "bent-pipe" capability is provided. The instantaneous transmit and receive bandwidths are limited to 10 MHz; however, these bands may be placed at any frequency within the specified frequency range in 1 MHz steps. A transistor preamplifier is used to maintain a low receiver noise temperature. A noise figure of 3.9 dB is expected for the receiver. The power amplifiers for the S band transmitter are solid state, providing an output power of 23.5 watts. This is reduced by the line losses to 12.5 watts at the antenna yielding the required 47 dBw EIRP.

The order wire S band receiver is designed as a reception link which provides continuous coverage over the entire earth area and offers the opportunity for any user to signal the earth station through the TDRS of his desire to use the main S band link. The order wire receiver uses an earth coverage antenna at a frequency of 2220 MHz. The noise figure and antenna gain of this receiver allow approximately 1 kHz of data to be transmitted by the user to the ground station via the TDRS.

The VHF/UHF short backfire antenna uses a tandem cavity arrangement. The stowage concept and the mechanical deployment system are essentially those in the S band reflector. The primary VHF reflective surface consists of a 1.27 cm (0.5 inch) grid chromel R wire mesh supported by eight aluminum ribs of 3.82 cm (1.5 inch) diameter. The number of ribs is governed by the deployed frequency and the geometric area loss between a polygon and a circle of 3.97 meter (13 feet) diameter. A secondary mesh surface (fence) is supported by ribs hinged at the tips of the main ribs. The UHF antenna is similarly configured and employs 1.9 cm (0.75 inch) diameter primary ribs. A central cone/cylinder assembly stacks the backfire reflectors and supports their dipole feeds. The mechanical deployment system is housed in the bottom cone section. Both reflector surfaces are unfurled by the same torque spring/motor drive mechanism which is capable of earth gravity antenna deployment.

The high gain S band antenna is a deployable rib mesh design of 3.82 meters (12.5 feet) diameter and an f/D of 0.4. Its surface contour is shaped by 12 aluminum ribs of 3.82 cm (1.5 inch) diameter with tapering wall thickness between 0.15 and 0.30 mm (0.006 and 0.012 inch). The surface contour precision of 0.15 cm (0.060 inch) rms is accomplished by use of the double mesh technique. The reflective (front) mesh is 0.2 cm (0.08 inch) open (gold-plated chromel R knit mesh), and its contour between ribs is adjusted

by tension ties to a back mesh of 1.27 cm (0.5 inch) grid size. A redundant torque spring and motor drive system unfurls the antenna reflector in orbit as well as in earth gravity.

The Ku band transmit antenna is configured with 12 ribs. The double mesh technique is utilized to achieve a surface contour of 0.25 mm (0.010 inch) rms accuracy. The front mesh openings are 0.15 cm (0.06 inch) in size. The subreflector is constructed as a shaped honeycomb sandwich with fiber-glass facesheets and 0.025 mm aluminum foil for RF reflectivity. The reflector is locked to the antenna support mast during launch and gimballed in orbit on a two-axis position drive.

The Ku band reflector and the high gain S band antenna are pointed by ground command by use of two-axis gimbal mechanisms. Antenna locks avoid excessive gimbal drive loading in the launch environment. The VHF/UHF antenna, order wire S band antenna, and Ku band receive horns are mounted to the TDRS despun platform via a support mast. The T&C omni antenna whips attach to the TDRS spin assembly.

Spacecraft commanding is performed through two cross-strapped command systems. Redundant decoders are located on both the spun and despun portions of the spacecraft. A total of 127 commands are used for controlling the state of the rotor, while 127 commands programmed for the despun platform are almost all associated with selecting between multiple operating modes of the communication system.

A command transmission consists of a Ku band or VHF carrier modulated by a sequence of tones at three discrete frequencies, designated 1, 0, and execute. The tones are amplitude modulated with a 128 per second clock. The demodulated FSK/AM output of the Ku band receiver and the VHF command receiver drive both the despun and spinning decoders. Either of the redundant decoders on the despun and spinning side provide up to 128 pulse command outputs. The selection of the executing decoder is by unique decoder address. Command verification is provided by telemetry readout of the command register before sending the execution tone.

The command system is capable of executing jet firing commands in phase with the spin of the satellite. This is performed at the ground station by synchronizing the execute tones with sun or earth pulses received via real time telemetry.

The repetitive command mode is also used for antenna pointing. Slewing is accomplished at a rate of 24 steps per second. Tracking commands are transmitted as required to maintain the antenna pointing at the user satellite.

Squib and solenoid drivers actuate pyrotechnic and jet firing functions in the satellite. The squib drivers fire the apogee motor and BAPTA release

squibs on the spinning side and the antenna deployment squibs on the despun side. The solenoid drivers actuate the axial and radial jet valves.

Telemetry information from the spacecraft is provided by a PCM system. Redundant spun and despun encoders are coupled through the rotary interface by the rotary transformer. A real time FM telemetry mode also is provided to transmit analog pulses from the attitude and despin sensors as well as the (analog) output of two rotor mounted accelerometers.

The PCM mode is used for all attitude, thermal, power, and status information, including command verification. In the PCM mode, the spinning encoder receives, processes, and formats data originating on the spinning portion of the satellite. The output, which is connected across the spinning/despun via slip rings, is an 8 kHz biphasic waveform from which a despun encoder recovers the nonreturn to zero (NRZ-L) bit stream and derives a coherent clock. The despun encoder gathers and processes data originating in the despun compartment. It alternates its bit stream word-by-word with the spinning encoder bit stream, then converts the composite NRZ-L bit stream to a Manchester code format. The converted stream is used for phase modulating the Ku band section of the telecommunications service system on the despun side and the backup VHF transmitter on the spinning side.

The FM real time mode is used for transmitting attitude data (sun sensor pulses, earth sensors pulses, platform index pulses, and command execute pulses). The occurrence of a pulse coherently switches the frequency of an IRIG channel 13 subcarrier oscillator from its pilot tone to a different frequency, depending on the kind of pulse present. The output is connected via a slip ring to the despun encoder, the output of which phase modulates the telemetry transmitter of the primary telecommunication service system at the Ku band frequency or the backup telemetry transmitter and command receiver at VHF. The VHF transponder system will be compatible with the GRARR operational requirements to provide data for orbit determination during this phase. Once the spacecraft is on station, the VHF transponder system will be used as a backup to the Ku band system in providing TDRSS TT&C links to the ground station.

3.3 CHARACTERISTICS

3.3.1 Spacecraft Characteristics Summary

A list of spacecraft design characteristics is presented in Table 3-1. The spacecraft geometrical characteristics were shown on the configuration drawing, Figure 3-1, presented in Section 3.1.

TABLE 3-1. TDR SPACECRAFT GENERAL SUMMARY

GENERAL	
Orbit	Synchronous, 7 deg initial inclination
Launch vehicle	Delta 2914
Payload fairing	Standard 2.44 m fairing (8 ft)
Design lifetime	5 yr
Reliability	0.710 at 5 yr
Station change maneuver	2 maneuvers, 4.5 deg/day
CONFIGURATION	
Stabilization	Hughes Gyrostat
Despun section subsystems	Antennas
Spinning section subsystems	Repeaters Portion of TT&C Electrical power Propulsion Attitude control Portion of TT&C
STRUCTURE	
Nominal dimensions, meters	Uses aluminum and beryllium
<ul style="list-style-type: none"> • Height x width (antennas deployed) • Diameter (rotor) 	6.86 x 8.26 m 2.16 m
Mass, end of 5 yr (dry)	347 kg
THERMAL CONTROL	Thermal control cavity inside spinning solar cell array - passive design
TELECOMMUNICATION SUBSYSTEM	
Low data rate user command	30 dBw EIRP, 400.5 to 401.5 MHz
UHF voice	30 dBw EIRP, 400.5 to 401.5 MHz
Medium data rate user command	41 dBw EIRP, 2035 to 2120 MHz
S band voice	47 dBw EIRP, 2035 to 2120 MHz
Ku band return link	51 dBw EIRP, 13.4 to 14.0 GHz
Low data rate receive sensitivity	-16 dB/K
Medium data rate receive sensitivity	8 dB/K
Order wire receiver sensitivity	-13 dB/K
Ku band forward link sensitivity	-15 dB/K

Table 3-1. (continued)

TELEMETRY SUBSYSTEM	
PCM mode	
• Word length	8 bits
• Frame length	64 words
• Analog	48 words
• Digital words	16
• Bit rate	1000 bits/sec
• Code type output	Manchester
FM mode (attitude data)	
• Subcarrier frequency	14.5 kHz
• Data type	Real time pulses
• Modulation	FM
• Data transmitted	1) Sun pulses 2) North earth pulses 3) South earth pulses 4) Execute receipt
COMMAND SUBSYSTEM	
Tones	1, 0, and execute
Input signal	FSK/AM
Bit rate	128 bits/sec
Command capacity,	256 maximum
Command verification via	Telemetry
Command execution	Real time
Execution synchronization	Sun or earth pulses
Maximum command rate	Approximately 4 per second
ANTENNA SUBSYSTEM	
Low data rate service antennas (VHF and UHF)	Short backfire type, 12 dB
Medium data rate service antenna	Paraboloid reflector type, 36 dB
TDRS to ground link, Ku band	Paraboloid reflector type, 44 dB
Ground to TDRS link, Ku band	Two horns, 16 dB
VHF backup T&C link	Turnstile omni, -13 dB over 97% of sphere
Order wire service	Short backfire type, 13dB
S band transponder	Two short backfire type

Table 3-1. (continued)

ATTITUDE CONTROL SUBSYSTEM	
Stabilization type	Gyrostat type dual spin
Nutation control	Magnetic damper and despin control dynamics
Despin control	Earth center finding with earth sensors
Control accuracy	0.5 deg
Power and signal transfer	Dry lubricated, silver slip rings
Despin motor	Two, independent, brushless dc, resolver commutated
REACTION CONTROL SUBSYSTEM	
Propellant	Hydrazine
Thrusters	Two 22N radial, two 4.5 N axial thrusters
ELECTRICAL POWER SUBSYSTEM	
Sunlit power	(26.5 v)
• Equinox, EOL	404 watts
• 23 days before equinox (EOL)	399 watts
• Summer solstice (EOL)	364 watts
• Maximum power required	438 watts (requires augmentation by batteries)
• Maximum bus voltage	30 volts (clamped by bus limiters)
Solar cells	
• Number	33,048
• Type	2 x 2 cm, silicon N/P, 10 ohm-cm
• Thickness	0.18 mm (7.2 mil)
• Cover glass	0.15 mm (6 mil)
Eclipse power	350 w average (< 60% DOD)
Batteries	
• Number	Two
• Type	Nickel-cadmium
• Capacity	16 amp-hr
• Maximum DOD	<60%
• Augmentation DOD	4.5%
• Charge rate	c/15
• Trickle charge rate	c/60
• Minimum bus voltage	24.5 v

Table 3-1. (continued)

Electronics	
Battery charge controller operation	Automatic or ground commanded
Battery discharge controller operation	Automatic
Battery reconditioning	On ground command (optional)
Tap limiters; operating voltage	29 to 29.5 v
Bus limiters; operating voltage	29.5 to 30 v
APOGEE INJECTION MOTOR	
Type	Solid propellant, $I_{sp} = 302$ sec
Velocity of injection	1670 m/s for 680 kg separation mass

3.3.2 Power Requirements

Electrical power requirements follow directly from the EIRP specifications and supporting equipment required for the mission. A summary of power requirements is shown in Table 3-2. All links are continuous except for the VHF and S band voice links, which are designed for partial usage. The UHF voice service shares the channel with low data rate user command service. When voice communications are used the output power of the UHF forward link transmitter is doubled, resulting in a power requirement which exceeds the capability of the solar cell array and requires some power output from the batteries. It is permissible to use the UHF voice channel service 25 percent of the time in sunlight and eclipse. During the S band voice service, the power required does not exceed the capability of the solar cell array, and battery augmentation is not required as was the case during UHF voice operations. It is necessary to discontinue battery charging during the S band voice relay; consequently the S band voice service can only be used 50 percent of the time during periods of solar eclipse. A larger usage of voice channels is allowable during the noneclipse season. If the UHF voice service is used, then time must be allowed for recharging the batteries. The profile of power available from the solar cell array is shown over the spacecraft lifetime in Figure 3-2. During the early period of the spacecraft life time, more power is available and continuous voice transmission would be possible except during the eclipse seasons.

3.3.3 Estimated Spacecraft Mass

The estimated mass of the spacecraft and its components is presented in Table 3-3. The estimates are based on flight proven equipment where applicable, and on comparison with developed equipment when design requirements force development of new equipment. Structural weights have been estimated from the size, loads, and characteristics of the selected materials. A contingency of 25.6 kg has been identified during the spacecraft definition study. This is approximately 8 percent of the total hardware mass and 14 percent of hardware items requiring essentially new design and development (except for the apogee injection motor). Hydrazine propellant requirements are shown in Table 3-4 for the various attitude correction and velocity maneuvers required throughout the mission.

3.3.4 Telemetry and Command Lists

Lists of telemetry and command requirements are presented in Tables 3-5 and 3-6. A total capability of 62 words is provided for telemetry divided equally between the spun and despun section of the spacecraft. Each

TABLE 3-2. ELECTRIC POWER SUMMARY, WATTS

	Command Mode	Intermittent S Band Voice	Intermittent UHF/VHF Voice	Command Mode	Intermittent S Band Voice	UHF/VHF Voice
	Solar Power		Solar and Battery Power 25.5 v	Battery Power in Solar Eclipse 25.5 v		
	27.5 v	27.5 v				
Maximum Operating Time, Percent	100	50	25	100	50	25
Frequency synthesizer	8.0	8.0	7.4	7.4	7.4	7.4
K band equipment	36.0	36.0	33.5	33.5	33.5	33.5
UHF/VHF equipment						
Command and data	157.8	157.8	146.1	146.1	146.1	146.1
Voice	--	--	142.0	--	--	142.0
S band equipment						
Command data	24.0	--	22.2	22.2	--	22.2
Voice	--	96.3	--	--	89.5	--
Telemetry equipment	15.6	15.6	14.5	14.5	14.5	14.5
Antenna position control	6.0	6.0	6.0	6.0	6.0	6.0
Despin control	19.7	19.7	18.3	18.3	18.3	18.3
Thermal control	5.6	5.6	4.6	4.6	4.6	4.6
Power electronics	18.0	11.0	20.0	40.0	45.0	50.0
Battery charging	60.0	--	--	--	--	--
Distribution losses	8.0	8.0	9.0	7.0	8.0	9.0
Reserve power	40.3	35.0	--	--	--	--
Power required or available	399.0*	399.0	416.4	292.2	359.5	453.6

*Power available: 23 days before autumnal equinox 399 watts, summer solstice 364 watts.

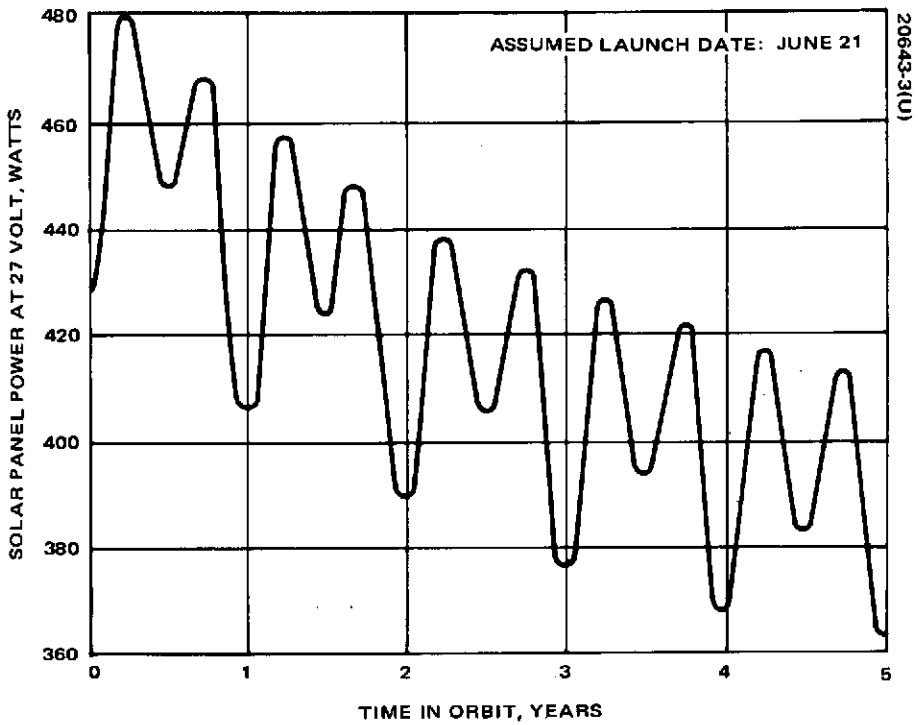


Figure 3-2. TDRS Solar Power Output Versus Time

TABLE 3-3. ESTIMATED SPACECRAFT MASS

Subsystem/Item	Quantity	Mass, kg	Basis
REPEATER SUBSYSTEM			
		<u>55.1</u>	
Receiver Ku band	2	2.6	Design estimate
Transmitter, Ku band	2	4.1	Design estimate
Up converter, Ku band	2	0.8	Design estimate
Receiver, MDR, S band	2	1.4	Design estimate
Receiver, OW S band	2	1.9	Design estimate
Transmitter, S band	2	7.3	Design estimate
Transponder, S band	2	7.6	Design estimate
Receiver, LDR, VHF	2	4.0	Design estimate
Transmitter, UHF	2	17.2	Design estimate
Frequency synthesizer	2	8.2	Design estimate
TELEMETRY AND COMMAND SUBSYSTEM			
		<u>18.1</u>	
Despun decoder	2	2.7	HS 312
Despun encoder	2	3.2	HS 312
Despun squib driver	1	0.5	HS 312
Dual transponder	2	3.1	HS 333
Diplexer	1	0.5	Design estimate
Spin decoder	2	2.7	HS 312
Spin encoder	2	4.0	HS 312
Squib and solenoid driver	1	0.9	HS 320
Latching valve/heater driver	1	0.5	HS 312
ANTENNA SUBSYSTEM			
		<u>36.6</u>	
Parabolic reflector, Ku band	1	1.4	Design estimate
Horn, Ku band	2	0.5	Design estimate
Parabolic reflector, S band	1	8.3	Design estimate
VHF/UHF backfire type	1	7.9	Design estimate
Order wire, backfire type		0.5	Design estimate
VHF turnstile array	8	1.0	ATS
Antenna positioner	2	8.4	HS 318
Positioner controllers	2	1.8	HS 318
Coax and waveguide		6.8	Design estimate
ATTITUDE CONTROL SUBSYSTEM			
		<u>23.5</u>	
BAPTA	1	15.0	Design estimate
Earth sensors	3	2.2	HS 312
Sun sensor	1	0.1	HS 312
Despin control electronics	2	3.6	HS 312
Accelerometers	2	0.3	HS 312
Nutation damper	1	2.3	HS 312 scaled
REACTION CONTROL SUBSYSTEM			
		<u>11.4</u>	
Tanks	4	6.0	HS 333
Thrusters	4	1.7	HS 333/312
Miscellaneous		2.7	HS 333
Pressurant		1.0	Calc

Table 3-3. (Continued)

Subsystem/Item	Quantity	Mass, kg	Basis
ELECTRICAL POWER SUBSYSTEM		<u>61.5</u>	
Solar cell array		20.0	Design estimate
Batteries	2	28.6	HS 312
Battery discharge controllers	2	9.1	HS 318
Battery charge controllers	2	0.9	HS 312
Voltage limiters	6	2.7	HS 308
Current sensor	1	0.2	HS 318
WIRE HARNESS		<u>11.5</u>	Design estimate
APOGEE MOTOR, BURNED OUT		<u>25.5</u>	Design estimate (Hercules)
STRUCTURE		<u>68.2</u>	
Thrust cone assembly		19.5	Design estimate
Substrate		23.7	Design estimate
Despun compartment		10.0	Design estimate
Antenna support		8.2	Design estimate
RCS tank and thruster support		4.5	Design estimate
Balance weights		2.3	Design estimate
THERMAL CONTROL		<u>10.0</u>	
Forward sun shield		2.0	Design estimate
Aft barrier		2.9	Design estimate
RCS tank wrap		0.6	HS 333
RCS lines, valves, heaters		0.5	HS 312
Thruster heat shield		0.1	HS 312
Apogee blanket		0.7	Design estimate
Paint		1.5	Design estimate
Despun sun shield		0.7	Design estimate
Despun mast blanket		1.0	Design estimate
CONTINGENCY		<u>25.6</u>	
FINAL MASS IN ORBIT		<u>347</u>	
HYDRAZINE PROPELLANT		<u>38</u>	
INITIAL MASS IN ORBIT		<u>385</u>	
APOGEE MOTOR EXPENDABLES		<u>293</u>	
SEPARATION MASS		<u>678</u>	

TABLE 3-4. RCS PROPELLANT REQUIREMENTS

Operational Requirement	Magnitude	Propellant, kg
Preapogee motor orientation	13.2 deg	2.0
Postapogee motor orientation	12.1 deg	1.6
Solar torque compensation	—	8.5
Injection trim	55.5 m/s	10.9
Stationkeeping, east-west	15.0 m/s	3.6
Station change	51.3 m/s	10.3
Jet misalignment effects	—	0.7
Total propellant required	—	37.6

section of the spacecraft is provided with a capability of 127 commands for a total spacecraft command capability of 254 commands. The assignments listed are for planning purposes only and are not expected to be final.

TABLE 3-5. TDRSS PCM TELEMETRY CHANNEL ASSIGNMENTS

Frame Word	Spinning	Despun
0	Frame sync	
1		Frame sync
2	Decoder 1 command verify ⁽¹⁾	
3		Decoder 1 command verify ⁽¹⁾
4	Decoder 2 command verify ⁽¹⁾	
5		Decoder 2 command verify ⁽¹⁾
6	Status word 6 Execute Separation/spin up Time of day Parallel relay	
7		Status word 7 Execute Encoder identifier
8	Status word 8 Sun/earth select Despin electronics Bypass relays	
9		Status word 9 Frequency synthesizer status
10	Attitude determination	
11		Status word 11 Frequency synthesizer status
12	Attitude determination	
13		Status word 13 Communications status

Table 3-5. (continued)

Frame Word	Spinning	Despun
14	Attitude determination	
15		Status word 15 Communications status
16	Telemetry calibration	
17		Telemetry calibration
18	Bus Current	
19		Bus voltage
20	Bus voltage	
21		Spare
22	Battery A voltage	
23		Antenna azimuth C/D ***
24	Battery B voltage	
25		Antenna elevation C/D ***
26	Battery pack 1 temperature	
27		BAPTA hub temperature 1/2*
28	Battery pack 2 temperature	
29		UHF command transmitter temperature A/B*
30	Charge/discharge A current	
31		UHF voice transmitter temperature A/B*
32	Charge/discharge B current	Aft shelf temperature (B)*
33		S band transmitter temperature A/B*
34	Battery pack 1 temperature	
35		Platform temperature 1/2*
36	Battery Pack 2 temperature	
37		Auxiliary battery voltage
38	Radial jet 1/2 temperature*	
39		K band transmitter temperature A/B*

Table 3-5. (continued)

Frame Word	Spinning	Despun
40	Axial jet 1/2 temperature*	
41		Heater bank A current
42	Spare	
43		Heater bank B current
44	Fuel tank 1/2 temperature*	
45		Heater bank C current
46	Hydrazine 1 pressure	
47		Heater bank D current
48	Hydrazine 2 pressure	
49		Spare
50	Motor torque command**	
51		Spare
52	BAPTA temperature 1/2*	
53		Spare
54	Despin position torque command**	
55		Spare
56	Solar panel temperature 1	
57		Spare
58	Solar panel temperature 2	
59		Spare
60	Apogee motor temperature 1/2*	
61		Spare
62	Sunshield temperature 1/2*	
63		Spare

* No. 1 or A input on encoder 1; No. 2 or B input on encoder 2.

** Both torque command signals are connected to each encoder via OR circuits, since only one despin control electronics unit is on at a time.

*** Antenna C (west) on encoder 1; antenna D (east) on encoder 2. Digital output increase when antenna steers toward north or west.

TABLE 3-6. TDRSS COMMAND ASSIGNMENTS

Despun

COMMUNICATIONS

1. Frequency synthesizer A on
2. Frequency synthesizer B on
3. Frequency synthesizers off
4. Frequency synthesizer A output step for S band transmit L. O.
5. Frequency synthesizer B output step for S band transmit L. O.
6. Frequency synthesizer A output step for S band receive L. O.
7. Frequency synthesizer output step for S band receiver L. O.
8. K band receiver A on
9. K band receiver B on
10. K band receivers off
11. K band transmitter A on
12. K band transmitter B on
13. K band transmitters off
14. UHF command transmitter A on
15. UHF command transmitter B on
16. UHF command transmitters off
17. UHF power amplifier 1A on
18. UHF power amplifier 1A off
19. UHF power amplifier 2A on
20. UHF power amplifier 2A off
21. UHF power amplifier 3A on
22. UHF power amplifier 3A off
23. UHF power amplifier 4A on
24. UHF power amplifier 4A off
25. UHF power amplifier 5A on
26. UHF power amplifier 5A off
27. UHF power amplifier 6A on
28. UHF power amplifier 6A off
29. UHF power amplifier 7A on

Table 3-6. (continued)

- | | |
|-----|------------------------------|
| 30. | UHF power amplifier 7A off |
| 31. | UHF power amplifier 8 A on |
| 32. | UHF power amplifier 8. A off |
| 33. | UHF power amplifier 9 A on |
| 34. | UHF power amplifier 9 A off |
| 35. | UHF power amplifier 10 A on |
| 36. | UHF power amplifier 10 A off |
| 37. | UHF power amplifier 1B on |
| 38. | UHF power amplifier 1B off |
| 39. | UHF power amplifier 2B on |
| 40. | UHF power amplifier 2B off |
| 41. | UHF power amplifier 3B on |
| 42. | UHF power amplifier 3B off |
| 43. | UHF power amplifier 4B on |
| 44. | UHF power amplifier 4B off |
| 45. | UHF power amplifier 5B on |
| 46. | UHF power amplifier 5B off |
| 47. | UHF power amplifier 6B on |
| 48. | UHF power amplifier 6B off |
| 49. | UHF power amplifier 7B on |
| 50. | UHF power amplifier 7B off |
| 51. | UHF power amplifier 8 B on |
| 52. | UHF power amplifier 8 B off |
| 53. | UHF power amplifier 9 B on |
| 54. | UHF power amplifier 9 B off |
| 55. | UHF power amplifier 10 B on |
| 56. | UHF power amplifier 10 B off |
| 57. | UHF voice transmitter A on |
| 58. | UHF voice transmitter B on |
| 59. | UHF voice transmitters off |
| 60. | VHF horizontal receiver A on |
| 61. | VHF horizontal receiver B on |

Table 3-6 (continued)

62.	VHF horizontal receivers off
63.	VHF vertical receiver A on
64.	VHF vertical receiver B on
65.	VHF vertical receivers off
66.	S band transmitter A on
67.	S band transmitter B on
68.	S band transmitters off
69.	S band power amplifier 1A on
70.	S band power amplifier 1A and 1B off
71.	S band power amplifier 2A on
72.	S band power amplifier 2A and 2B off
73.	S band power amplifier 3A on
74.	S band power amplifier 3A and 3B off
75.	S band power amplifier 4A on
76.	S band power amplifier 4A off
77.	S band power amplifier 1B on
78.	S band power amplifier 2B on
79.	S band power amplifier 3B on
80.	S band power amplifier 4B on
81.	S band receiver A on
82.	S band receiver B on
83.	S band receivers off
84.	Order wire receiver A on
88.	Order wire receiver B on
89.	Order wire receivers off
90.	S band transponder A on
91.	S band transponder B on
92.	S band transponder A and B off
TT&C	
93.	Telemetry encoder A on
94.	Telemetry encoder B on
95.	Telemetry encoders off

Table 3-6 (continued)

DEPLOYMENT MECHANISMS

- 96. Fire VHF/UHF antenna squib I
- 97. Fire VHF/UHF antenna squib II
- 98. Fire VHF/UHF antenna squib III
- 99. Fire S band antenna squib I
- 100. Fire S band antenna squib II
- 101. Fire S band antenna squib III
- 102. Fire K band antenna squib
- 103. Fire nutation damper squib
- 104. S band antenna positioner motors on
- 105. Ku band antenna positioner motors on
- 106. Antenna positioner power off
- 107. Step S band antenna azimuth east
- 108. Step S band antenna azimuth west
- 109. Step S band antenna elevation north
- 110. Step S band antenna elevation south
- 111. Step Ku band antenna azimuth east
- 112. Step Ku band antenna azimuth west
- 113. Step Ku band antenna elevation north
- 114. Step Ku band antenna elevation south

POWER SUBSYSTEM

- 115. Voltage limiters off
- 116. Voltage limiter 1 on
- 117. Voltage limiter 2 on

SPARES

- 118-127.

Table 3-6. (continued)

Spinning	
REACTION CONTROL SUBSYSTEM AND APOGEE MOTOR	
1.	Axial jet 1
2.	Axial jet 2
3.	Axial jets 1 and 2
4.	Radial jet 1
5.	Radial jet 2
6.	Latching valve 1 open
7.	Latching valve 1 close
8.	Latching valve 2 open
9.	Latching valve 2 close
10.	Latching valve 3 open
11.	Latching valve 3 close
12.	Apogee motor squib 1 (decoder 1)
13.	Apogee motor squib 2 (decoder 2)
14.	Apogee motor heaters on
15.	Apogee motor heater 1 off
16.	Apogee motor heater 2 off
17.	Apogee motor heater 3 off
18.	Apogee motor heater 4 off
19.	Spinup jet heaters off
20.	Spinup jet heaters on
21.	Radial jet heater off
22.	Radial jet heater on
POWER SUBSYSTEM	
23.	Battery A charge on
24.	Battery B charge on
25.	Battery A and B charge off
26.	Trickle charge on
27.	Trickle charge battery A off

Table 3-6. (continued)

28. Trickle charge battery B off
29. Reconditioning discharge battery A on
30. Reconditioning discharge battery B on
31. Reconditioning charge batteries A and B off
32. Set charge temperature limit 1
33. Set charge temperature limit 2
34. Set charge temperature limit 3
35. Set charge temperature limit 4
36. Thermal charge limit set override
37. Voltage limiters off
38. Voltage limiter 1 on
39. Voltage limiter 2 on
40. Voltage limiter 3 on
41. Voltage limiter 4 on

DESPIN ELECTRONICS

42. BAPTA heater 1 on
43. BAPTA heater 2 on
44. Despin control electronics 1 on 2 off
45. Despin control electronics 2 on 1 off
46. Motor drive 1 on
47. Motor drive 2 on
48. Motor drive 1 off
49. Motor drive 2 off
50. Pseudo earth pulse select
51. Sun despin reference select
52. N earth sensor mode
53. S earth sensor mode
54. Pseudo psi despin reference
55. Time correction step west
56. Time correction step east

Table 3-6. (continued)

58.	Torque bias step negative
59.	Torque bias step positive
60.	Spinup sequencer enable
61.	Spinup sequencer off
TT&C	
62.	Telemetry encoder 1 PCM mode
63.	Telemetry encoder 2 PCM mode
64.	Telemetry encoder 1 on
65.	Telemetry encoder 1 off
66.	Telemetry encoder 2 on
67.	Telemetry encoder 2 off
68.	Telemetry encoder 1 FM mode
69.	Telemetry encoder 2 FM mode
70.	Telemetry transmitter A on
71.	Telemetry transmitter B on
72.	Telemetry transmitter A and B off
SPARES	
73 to 128	

3.4 RELIABILITY AND PRODUCT EFFECTIVENESS

The TDRS integrated product effectiveness program assures maximum program effectiveness through coordinated activities of the four product effectiveness technical disciplines, as performed during the study phase, Table 3-7, and to receive further effort during the subsequent phases. These four disciplines are reliability, quality assurance, components and materials, and manufacturing quality assurance. The direct access of the TDRS Product Effectiveness Manager to the highest levels of Hughes management assures top management concern and backing for the product effectiveness program. The integrated product effectiveness organization approach was instituted in 1961 when it became apparent that separate functions resulted in inefficiencies through duplication of efforts and, in some cases, conflict of responsibilities. The following discussion briefly presents the four areas and their assigned responsibilities.

Reliability tasks are:

- 1) Program plan - A TDRS Reliability Program Plan is prepared; when approved by GSFC, this plan describes the effort to be performed.
- 2) Supplier control - Reliability requirements based on the Reliability Program Plan are prepared for each subcontract. Compliance by suppliers is monitored by reliability engineers.
- 3) Reliability engineering:
 - a) Review and sign off all equipment and test specifications.
 - b) Prepare reliability predictions and estimates based on functional block diagrams and mathematical models for each subsystem and the overall system.
 - c) Perform failure mode, effects, and criticality analysis for each functional element and make design change recommendations to engineering.
 - d) Participate in design reviews with reliability inputs and as a review team member.
 - e) Organize and act as chairman of failure review board to investigate, analyze, and assign corrective action resulting from reported failures.
 - f) Issue procedures to standardize design practices.
 - g) Chair the Parts, Materials, and Processes Board.
 - h) Establish and maintain equipment logs.
 - i) Evaluate test plans, monitor tests, and utilize test data in assessing equipment reliability.

TABLE 3-7. TDRS MAJOR RELIABILITY PROGRAM ACTIVITIES

	<u>Applicable Product Effectiveness Plan Sections</u>
Preferred Design Practices	Section 3.4.2.2 of the Reliability Plan.
Mission and Program Goals	Table 3-11 of Section 3.4.1.3 establishes the program reliability goal of 0.717 for the 5 year mission.
Definition of TDRS Terms	Section 3.4.2.12 of Product Effectiveness Plans
Criteria for Acceptability of New Technology	Section 3.4.2.2 of PE Plans
Criteria for Acceptability of New Technology	Section 3.4.2.2 of PE Plans
Criteria for Use of Redundancy	Section 3.4.2.5 of PE Plans
Functions to be Accomplished to Achieve Operational Status in Orbit	Table 3-10 of the PE Plans establishes the functions to be accomplished to achieve operational status in orbit.
Review Evolving Design Concepts	Section 3.4.2.3 of the PE Plans
Tradeoff Studies	Section 3.4.2.3 of the PE Plans
Failure Mode Analyses	Table 3-26 and Section 3.4.2.4 of the PE Plans
Reliability Program Elements During Phase C	Section 3.4.2 of the PE Plans

Quality assurance tasks are:

- 1) Program plan - A TDRS Quality Assurance Plan is prepared; when approved by GSFC, this plan will describe the effort to be performed.
- 2) Quality engineering:
 - a) Prepare Project Instructions and Procedures to Manufacturing Quality Control.
 - b) Maintain budget control and direct and coordinate the Manufacturing Quality Control Program.
 - c) Perform GSFC and DCAS liaison for quality activities.
 - d) Prepare quality requirements inputs for subcontractor RFPs and review proposals.
 - e) Monitor subcontractor quality performance.

Components and materials tasks are:

- 1) Participate as a member of TDRS Parts, Materials, and Processes Control Board and maintain the TDRS Approved Parts, Materials, and Processes List.
- 2) Perform subcontractor/supplier liaison for parts, materials, and processes.
- 3) Support Materiel organization during procurement activities.
- 4) Support design engineering through responses to Components and Materials Engineering Requests (CMERs) and application review of hardware designs and signoff drawings.
- 5) Qualify all unqualified TDRS parts and materials.
- 6) Develop, specify, and evaluate any new processes.

Manufacturing Quality Assurance tasks are:

- 1) Prepare inspection procedures and hardware flow plans.
- 2) Perform all inspection operations including receiving, fabrication, test, packaging, shipping, and field support.
- 3) Initiate trouble and failure reports for MQA tests.
- 4) Calibrate all AGE, BTE, and standard test equipment.

- 5) Evaluate, audit, monitor, and source inspect subcontractors and suppliers.
- 6) Certify personnel and equipments for TDRS fabrication and test.
- 7) Maintain records and data for hardware log books.
- 8) Establish and chair internal and customer Material Review Boards.

3.4.1 Spacecraft Reliability Estimates

3.4.1.1 Assumptions and Models

Assumptions. The following general assumptions apply to the TDRS reliability analysis:

- All parts exhibit constant failure rate.
- Parts within a block on logic diagrams fail independently. Failure of any part in a block causes loss of the equipment represented by the block (exceptions are noted on logic diagrams).
- All functions represented by blocks in a logic diagram fail independently.
- Subsystem logic diagrams are for the initial operations and orbital life phases.
- Average ambient temperature is 298K. Integrated circuit junction temperatures are 308K and on the average, parts are derated to 20 percent of their rated stress or less. (These assumptions are equivalent to assuming part application within the preferred region of the derating curves).
- Hughes unit failure rates reflect Hughes orbital experience through January 24, 1972.
- Wearout failures are not reflected in predicted reliability.

Models. Table 3-8 summarizes the general reliability models used for the reliability analyses. A unique model is used for the reaction control subsystem and is described in subsection 3.4.1.3.

3.4.1.2 Failures Rates

Hughes failure rates are based upon more than 2 billion part hours in space, with only five electronic part failures. As these failure rates reflect Hughes design techniques, parts programs, and manufacturing processes, they provide the most accurate estimate of achievable TDRS reliability levels.

TABLE 3-8. SUMMARY OF GENERAL RELIABILITY MODELS

<u>Description</u>	<u>Model</u>
Series - no redundancy	$R(t) = e^{-\lambda t}$
Active redundancy, c units required out of n	$R(t) = \sum_{k=c}^n \binom{n}{k} (e^{-\lambda t})^k (1 - e^{-\lambda t})^{n-k}$
Standby redundancy, n units, one required. Dormant failure rate $\neq 0$	$R(t) = e^{-\lambda t} \sum_{k=1}^n \frac{(1 - e^{-\mu t})^{k-1} \Gamma\left(\frac{\lambda}{\mu} + k - 1\right)}{\Gamma(k) \Gamma(\lambda/\mu)}$
where	
λ = operational failure rate	
μ = standby failure rate	
$\Gamma(n)$ = gamma function equal to $(n-1)!$ if argument is integer	

Basic Failure Rates. Hughes Space and Communications Group Document PEH 06-0203 establishes the basic failure rates for space systems. These failure rates are established for an average temperature of 298K, and an average stress of 20 percent. The basic failure rates reflect the top quality level and laboratory environment from that document. The dormant failure rates for the power-on condition are based upon the same document using failure rates at zero stress. Power-off failure rates were based upon comparison by component specialists of the physical difference in effect of power on and power off. Power-off failure rates apply to all standby redundant spacecraft equipment.

When detailed design indicates the actual temperature and stress, the failure rates are adjusted in accordance with the curves of PEH 06-0201. These curves have been utilized as the basis for the establishment of parts derating requirements on Hughes space programs.

E Factor. Experience with Hughes satellites in space indicates that the basic set of failure rates are conservative for Hughes designs. Therefore, the electronic part failure rates at the unit level are adjusted by an experience factor, E. This factor reflects the actual experience in space utilizing Hughes designs, the Hughes parts program, and Hughes manufacturing. Thus, the E-factor takes into account many factors that cannot be included in a standard handbook. These factors are summarized in Table 3-9.

The E-factor is determined as follows:

- 1) From the operational satellite block diagrams, parts counts are determined for each satellite unit. The operating and nonoperating times for all units are determined under both operating and nonoperating conditions.
- 2) Using the basic failure rates described in the preceding, the expected number of failures is determined equal to

$$\sum_i \lambda_i t_i.$$

- 3) From telemetry data, the number of actual failures, f , is determined.

TABLE 3-9. RATIONALE FOR USE OF HUGHES EXPERIENCE FACTOR

The Hughes experience factor:

- Reflects reliability of equipment which has experienced system and environmental prelaunch testing.
- Includes failures due to equipment interfaces.
- Includes failures due to causes other than pure random catastrophic part failures such as manufacturing defects, design errors, etc.
- Reflects actual Hughes engineering practices such as component application and circuit tolerances.
- Reflects Hughes practices in part screening and vendor controls.
- Reflects the actual environment experienced by equipment in the operational orbit.

4) The experience, E, factor is then calculated as

$$E = \frac{\text{actual failures}}{\text{expected failures}}$$

If μ_i represents the true failure rate of the i^{th} part, then the expected value of f is

$$E(f) = \sum_i \mu_i t_i$$

Hence, E represents an unbiased estimate of the ratio of true to basic black box failure rates.

It should be noted that an advantage in the application of the E-factor is that it is not necessary to isolate a failure to a single part, since only the total number of failures is important. Of the 14 electronic part failures which have occurred to date, 3 have been identified to single parts.

Conservatism is introduced into the E-factor due to two factors. First, significant improvement has occurred in many electronic parts since launch of the early satellites. Second, the current E-factor is based upon satellite data to 24 January 1972. The current E-factor is 0.60, and therefore gives an improvement over the basic failure rates derived from PEH 06-0201.

3.4.1.3 Subsystem Reliability Modeling

Launch and Deployment. The probability of the spacecraft being properly deployed on the desired station is 0.944, based on the estimates of subsystem performance summarized in Table 3-10.

Operational Spacecraft. A reliability summary for the operational phase is given in Table 3-11. The reliability model life for the spacecraft subsystems is shown in Figures 3-3 through 3-10, with corresponding failure rates given in Tables 3-12 through 3-16. The modeling of the reaction control subsystem is much more complicated than the general models described in subsection 3.4.1.1, and is discussed in detail.

TABLE 3-10. LAUNCH AND DEPLOYMENT
RELIABILITY SUMMARY

Subsystem	Reliability Estimate	Estimate Basis
Apogee kick stage	0.996	192 flight tests of X-259 and BE-3
TT&C	0.9999	Subsystem analysis
Separation and deployment	0.998	Subsystem analysis
ACS and RCS	0.9999	Subsystem analysis
Launch booster	0.95	GSFC/Delta Symposium document September 1971
Total	<u>0.944</u>	

TABLE 3-11. OPERATIONAL SPACECRAFT
RELIABILITY SUMMARY

<u>Subsystem</u>	<u>5 Year Reliability Estimate</u>
Communication and antenna positioning	0.889
Telemetry and command	0.900
ACS	0.955
Power	0.975
Harness	0.990
RCS	<u>0.972</u>
Total	0.717

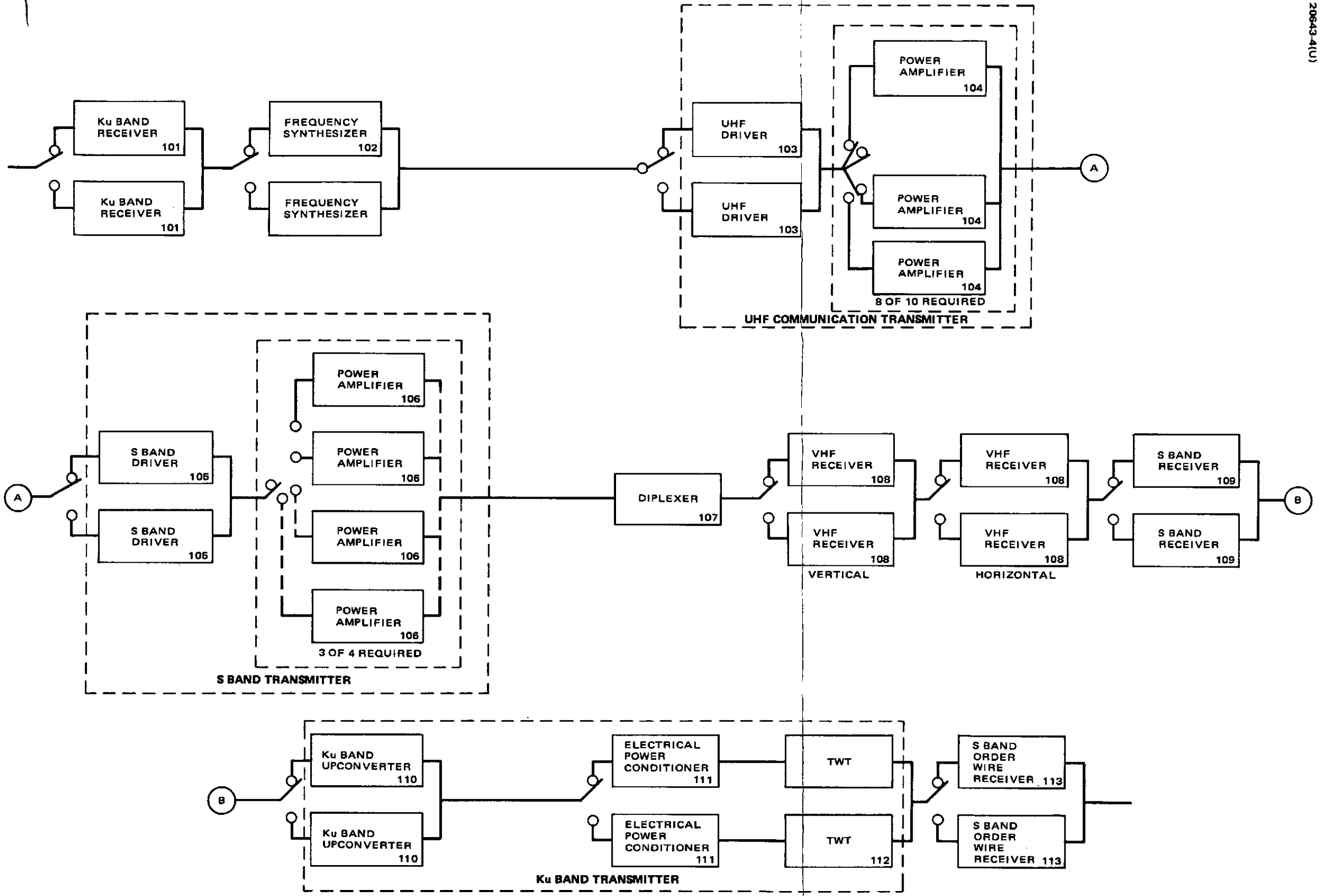
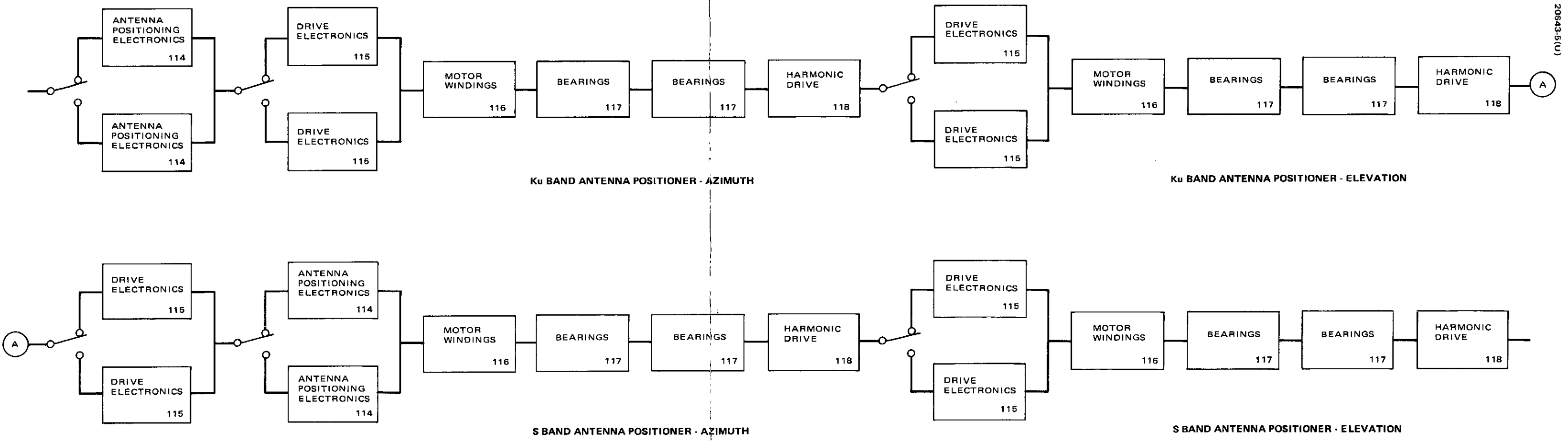


Figure 3-3. TDRSS Communication Subsystem

A

B



20643-5(U)

Figure 3-4. Antenna Positioning

A

B

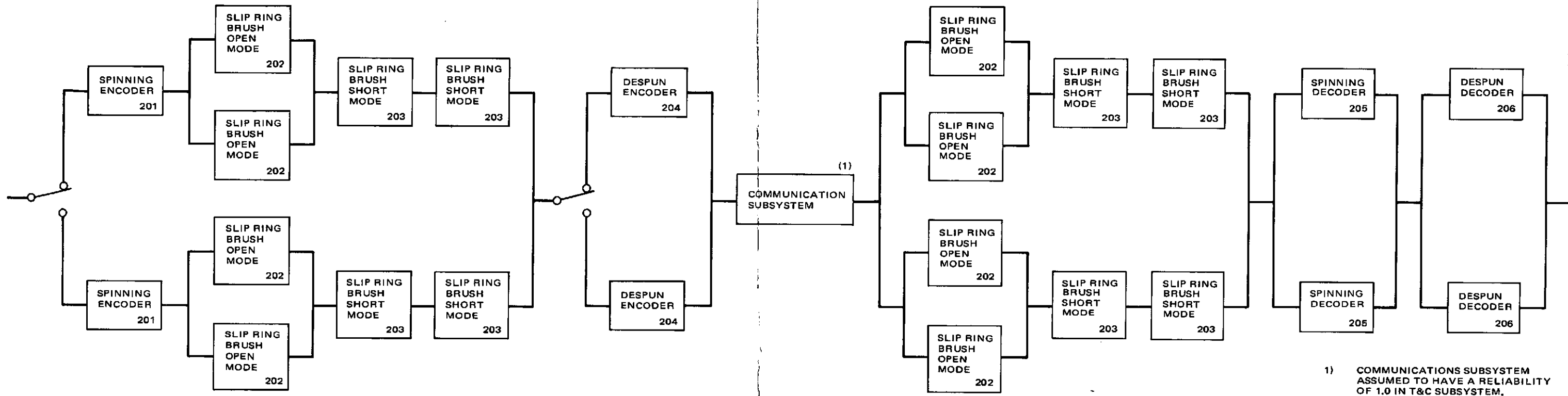


Figure 3-5. TDRSS Telemetry and Command Subsystem Logic Diagram and Mathematical Model

1) COMMUNICATIONS SUBSYSTEM ASSUMED TO HAVE A RELIABILITY OF 1.0 IN T&C SUBSYSTEM.

A

B

20643-6(U)

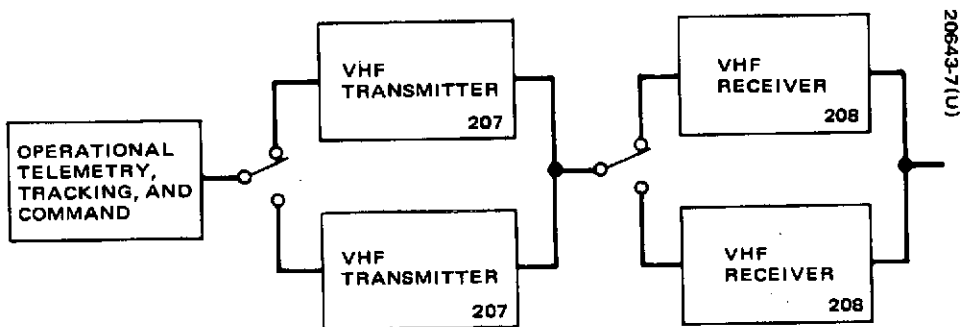
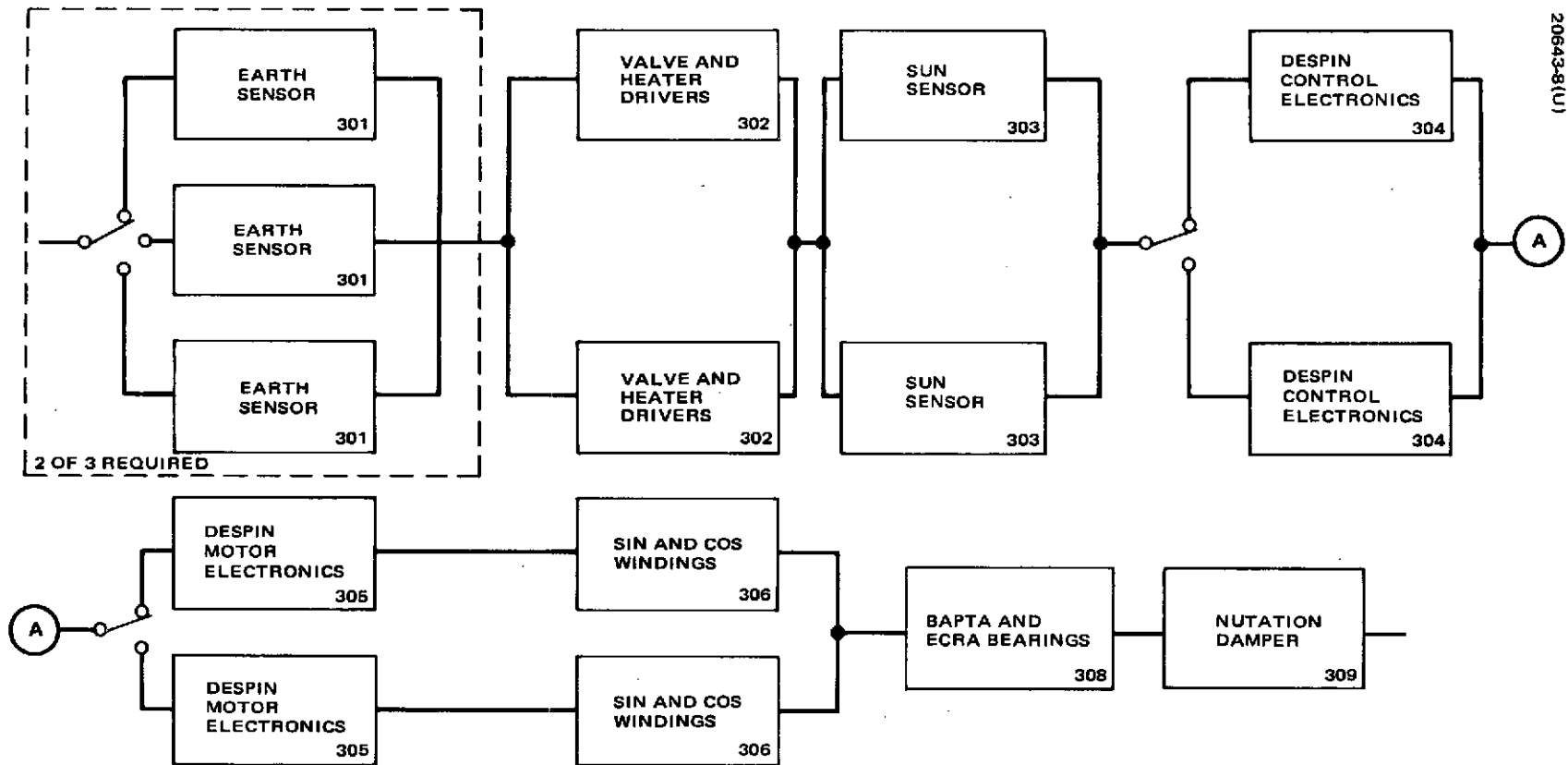


Figure 3-6. TT&C During Launch and Deployment

3-46



20643-8(U)

Figure 3-7. TDRS Attitude Control Subsystem Logic Diagram and Mathematical Model

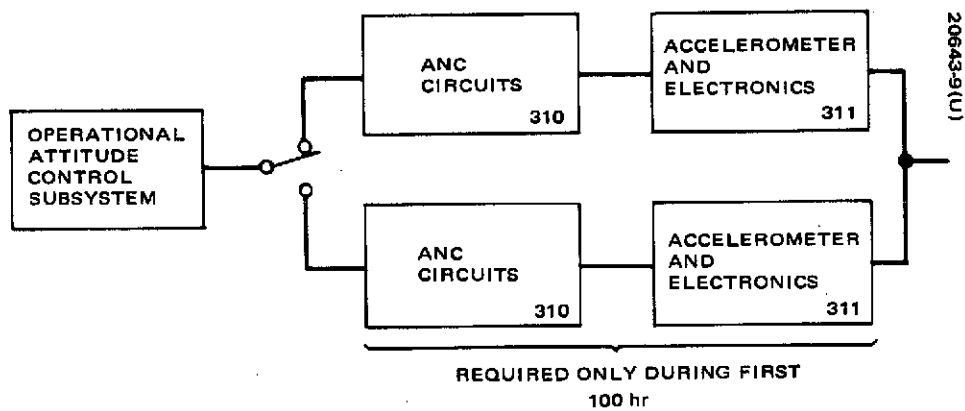


Figure 3-8. ACS During Launch and Deployment

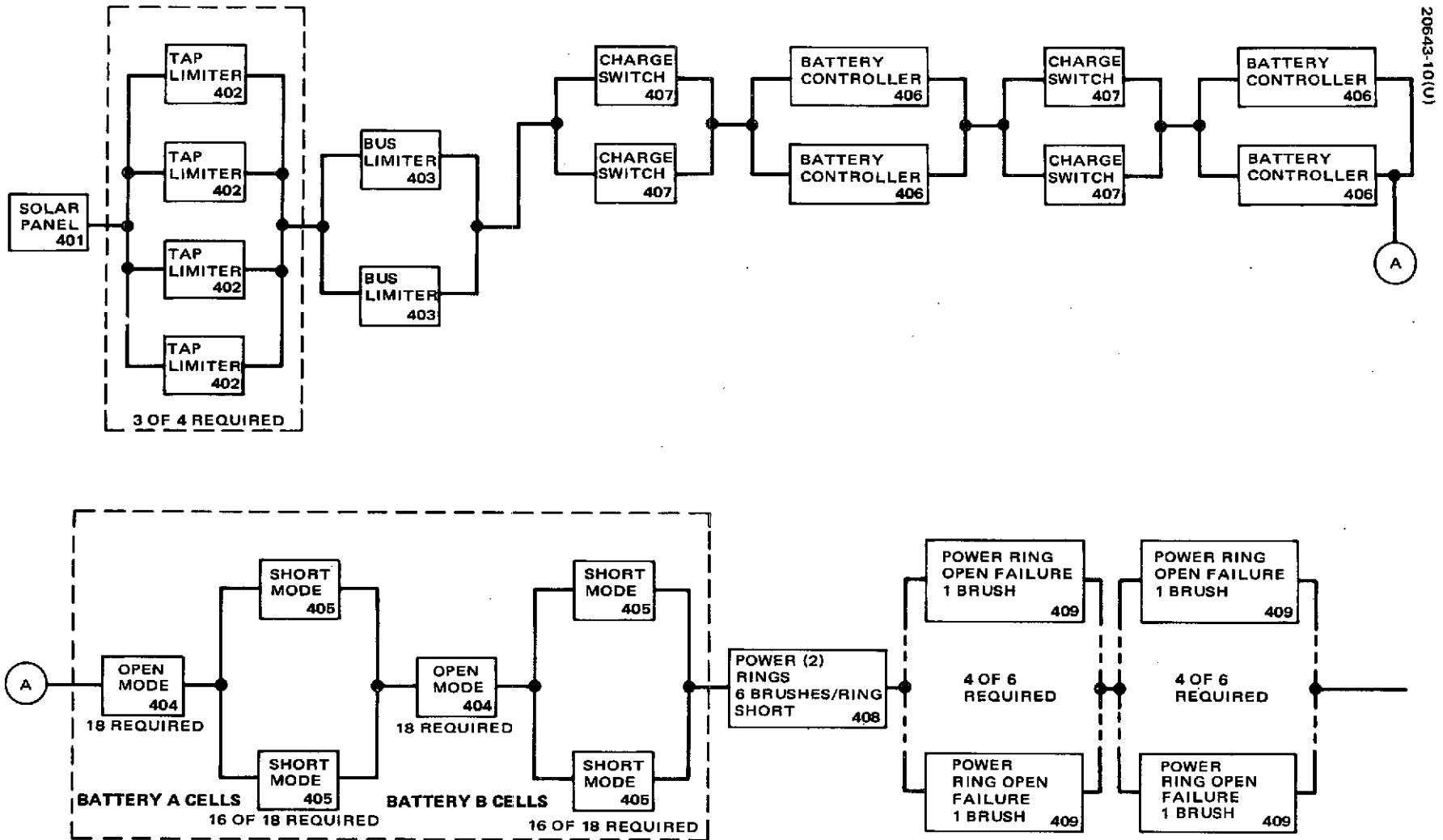


Figure 3-9. TDRS Power Subsystem Logic Diagram and Mathematical Model

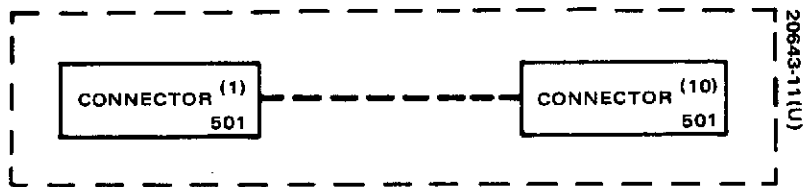


Figure 3-10. TDRSS Harness Logic Diagram and Mathematical Model

TABLE 3-12. TDRS COMMUNICATION SUBSYSTEM FAILURE RATE SUMMARY

Block No.	Item	No.	No. Required	Method of Redundancy	Duty Cycle	Reliability of Failure Rates/10 ⁹			Source
						On	Adjusted for Duty Cycle	Off	
101	Ku band receiver	2	1	Standby	1.0	3142	3142	2365	Parts count
102	Frequency synthesizer	2	1	Standby	1.0	6286	6286	4491	Parts count
103	UHF driver	2	1	Standby	1.0/0.25	780	780	505	Parts count
104	Power amplifier	10	8	Standby	1.0/0.25	530	530	426	Parts count
105	S band driver	2	1	Standby	1.0	1037	1037	657	Parts count
106	Power amplifier	4	3	Standby	1.0	113	113	97	Parts count
107	Diplexer	1	1	None	1.0	2	2	2	Parts count
108	VHF receiver	4	2	Standby	1.0	1880	1880	1462	Parts count
109	S band receiver	2	1	Standby	1.0	1914	1914	1537	Parts count
110	Ku band upconverter	2	1	Standby	1.0	1074	1074	964	Parts count
111	EPC	2	1	Standby	1.0	374	374	235	Parts count
112	TWT	2	1	Standby	1.0	500	500	250	Parts count
113	S band order wire receiver	2	1	Standby	1.0	1102	1102	794	Parts count
114	Antenna position electronics	4	2	Standby	0.01	2005	1788	1603	Classified program
115	Drive electronic	8	4	Standby	0.01	637	351	290	Classified program
116	Motor winding	4	4	None	0.01	14	4	3	HS 318 program
117	Bearings	8	8	None	0.01	70	21	14	HS 318 program
118	Harmonic drive	4	4	None	0.01	94	27	19	HS 318 program

TABLE 3-13. TDRS TELEMETRY AND TRACKING SUBSYSTEMS FAILURE RATE SUMMARY

Block No.	Item	No.	No. Required	Method of Redundancy	Duty Cycle	Reliability or Failure Rates/10 ⁹		
						On	Off	Source
201	Spinning encoder	2	1	Standby	1.0	6500	3500	Intelsat IV and modified design
202	Slip ring brush open mode	8	2	Active	1.0	265	-	Intelsat
203	Slip ring brush short mode	8	8	None	1.0	3		Intelsat
204	Despun encoder	2	1	Standby	1.0	4157	1799	Intelsat
203	Spinning decoder	2	1	Active	1.0	2750	-	Intelsat IV
206	Despun decoder	2	1	Active	1.0	3515	-	Intelsat IV
207	VHF transmitter	2	1	Standby	1 week after launch	4404	1468	Vendor prediction
208	VHF receiver	2	1	Standby	1 week after launch	1880	1462	Parts Count

TABLE 3-14. TDRS ACS FAILURE RATE SUMMARY

Block No.	Item	No.	No. Required	Method of Redundancy	Duty Cycle, Percent	Reliability or Failure Rates/10 ⁹			Source
						On	Adjusted for Duty Cycle	Off	
301	Earth sensor	3	2	Standby	100	1627	1143	660	Intelsat IV
302	Valve driver & heater	2	1	Active	1	1600	808	800	Eng. estimate
303	Sun sensor	2	1	Active	100	18	18	18	Intelsat IV
304	DCE	2	1	Standby	100	5478	5478	2693	Fleet Sat Com
305	DME	2	1	Standby	100	808	808	388	Fleet Sat Com
306	Motor windings	2	1	Standby	100	22	22	2	Fleet Sat Com
308	Bapta and ECRA bearing	1	1	None	100	44	44	NA	HS-312, -318
309	Nutation damper	1	1	None	100	9	9	NA	Fleet Sat Com
310	ANC circuits	2	1	Standby	100 for first 100 hours	321	321	154	Fleet Sat Com
311	Accelerometer and electronics	2	1	Standby	100 for first 100 hours	268	268	206	Intelsat IV

TABLE 3-15. TDRS POWER FAILURE RATE SUMMARY

Block No.	Item	No.	No. Required	Method of Redundancy	Duty Cycle	Reliability or Failure Rates/10 ⁹			Source
						On	Adjusted for Duty Cycle	Off	
401	Solar panel	1	1	Internal	1.0	~1.0	-	-	Engineering part count estimate
402	Tap limiter	4	3	Active	1.0	214	214	-	Engineering part count estimate
403	Bus limiter	2	1	Active	1.0	214	214	-	Engineering part count estimate
404	Battery cell open mode	18	18	None	1.0	8	8	-	Data from operational satellite
405	Battery cell short mode	18	16	Active	1.0	412	412	-	
406	Battery controller	4	2	Active	0.15	626	412	374	Similar to HS-318 design
407	Charge switch	4	2	Active	1.0	90	90	-	Similar to HS-318 design
408	Two power rings short	2	2	None	100	32	32	NA	Hughes experience
409	Power ring open	12	8	Active	100	265	265	NA	Hughes experience

TABLE 3-16. TDRS HARNESS FAILURE RATE SUMMARY

Block No.	Item	No.	No. Required	Method of Redundancy	Duty Cycle	Reliability or Failure Rates/10 ⁹			Source
						On	Adjusted for Duty Cycle	Off	
501	Connector	10	10	None	1.0	24			Preliminary parts count

Reaction Control Subsystem

Reliability Analyses and Mathematical Models. The total mission was divided into three distinct phases, each typified by unique environmental conditions, duration, and space vehicle equipment requirements. Detailed analyses for each mission phase utilizing the failure rates shown in Table 3-17 are presented in subsequent paragraphs. Unless otherwise noted, subscripts used with all terms correspond with numbers shown in Table 3-17. The reliability predictions are summarized in Table 3-18.

Launch Phase. Launch phase reliability, $R_{5,L}$ is defined as the probability all equipment in the propulsion subsystem required for orbital operation (but not required for spinup) survives launch. The launch phase reliability model is defined in Table 3-19.

Coast/Insertion Phase. Successful performance of the propulsion subsystem during the coast/insertion phase occurs if space vehicle spinup to within 10 percent of the desired spin rate is accomplished, and the complete propulsion subsystem performs as required during transfer orbit and survives AKM insertion into synchronous orbit.

For this analysis it was conservatively assumed that both spinup thrusters must fire for spinup to occur within the mission constraints. The spacecraft will spinup if only one spinup thruster fires, but the time required for spinup would nearly double. Predicted spinup reliability, $R_{5,S}$ is the product of the following three probabilities, modeled as shown in Tables 3-19 and 3-20:

- S(1) is the probability that no loss of propellant or pressurant due to failure of tanks, pressure transducer, or manifolding.
- S(2) is the probability that neither acceleration G switch closes prematurely, neither spinup latching valve shifts position (opens) during launch, both spinup thrusters fire as required, and both RCS latching valves close following spinup.
- S(3) is the probability that the remainder of the system is in a condition such that the two spinup (tangential) thrusters can and do fire and shut off at the proper time. The multiple conditional states of S(3) are defined in Table 3-21.

TABLE 3-17. REACTION CONTROL SUBSYSTEM DETAILED
HUGHES FAILURE RATES*

x No.	Description	Failure Rates, Failures per 10 ⁹ hours				
		y = 1 Spinup	Launch/Transfer		Orbital	
			y = 2 Attitude	y = 3 Spin	y = 4 Attitude	y = 5 Spin
1	TCA valve fails closed	424.45	26.01	4.92	31.32	3.27
2	TCA valve fails open (common)	380.09	21.92	1.83	25.98	0.26
3	TCA valve fails open (primary)	652.48	51.76	18.06	58.56	15.43
4	TCA valve fails open (secondary)	857.71	63.59	19.05	72.59	15.58
5	TCA valve drive fails to open valve - (no output)	78.2	78.2	78.2	40.94	40.6
6	TCA fuel filter clogged	20.0	20.0	20.0	20.0	20.0
7	Thruster fails to generate thrust	143.5	8.28	0.69	9.81	0.1
8	Latching valve fails closed	495.1	9.52	2.38	3.67	1.23
9	Latching valve fails open	712.8	13.7	3.43	5.31	1.27
10	Latching valve driver fails to open valve	264.4	264.4	264.4	128.2	128.1
11	Latching valve driver fails to close valve	264.4	264.4	264.4	128.2	128.1
12	Tanks (4) and central manifold fails	320.0	320.0	320.0	160.0	160.0
13	1/2 RCS manifolding leaks	4.0	4.0	4.0	2.0	2.0
14	1/2 RCS manifolding bursts	2.0	2.0	2.0	1.0	1.0
15	Spinup manifolding leaks	12.0	12.0	12.0	6.0	6.0
16	Spinup manifolding bursts	6.0	6.0	6.0	3.0	3.0

*Valve failure rates derived from both hourly and cycling dependent failure modes.

TABLE 3-18. REACTION CONTROL SUBSYSTEM RELIABILITY

Term	Mission Phase	Reliability
$R_{5,L}$	Launch	0.99998
$R_{5,I}$	Coast/insertion	0.9996
$R_{5,0(t)}$	Orbital operation	0.972

Successful operation of the propulsion subsystem during the transfer orbit is defined as completion of initial orbit adjust maneuvers, without any failures. The predicted transfer orbit reliability $R_{5,T}$ is modeled as shown in Table 3-19.

Overall coast and insertion phase reliability $R_{5,I}$ is therefore given by

$$R_{5,I} = R_{5,S} R_{5,T}$$

Orbital Operation Phase. The propulsion subsystem is considered successful during the orbital operation phase if:

- 1) No loss of propellant from the tanks or manifolding occurs
- 2) At least one radial, one axial, and one tangential thruster can be used
- 3) The crossover latching valve can be used as required to equalize the propellant in the tanks at any time during the mission

Predicted orbital reliability, $R_{5,0}$ of the propulsion subsystem is the product of two basic probabilities described below and defined mathematically in Table 3-22.

- P_A is the probability that there is no loss of propellant from the tanks and central manifolding, that the RCS and spinup manifolding does not burst during orbital operation, and that the spinup TCA function and that the crossover latching valve functions as required
- P_B is the probability that the remainder of the subsystem is in a condition such that at least one radial and one precession thruster can be used as described in Table 3-23.

TABLE 3-19. LAUNCH AND COAST/INSERTION RELIABILITY MODELS

LAUNCH PHASE	
$R_{5,L}$	$= R_{3,2}^4 [\exp (-\lambda_{G18,3}(80t_B + 8t_C))]$
$\lambda_{G18,2}$	= series failure rate of equipment required for orbital operation (ambient orbital environment)
$R_{3,2}$	= thruster valve reliability
t_B	= launch vehicle burn time = 700 seconds
t_C	= launch vehicle coast time = 750 seconds
COAST INSERTION PHASE	
<u>Spinup Operation</u>	
R_{5S}	$= S(1) S(2) S(3)$
$S(1)$	$= \exp (-\lambda_{G12,i} t_{\text{launch}})$
$S(2)$	$= R_{7,1}^2 R_{8,1}^2 R_{2,1}^2 P_6^2 P_7^2 R_{G10}^2$
$S(3)$	$= P_a (P_b + P_c)$
$G_{12,1}$	$= \lambda_{12} + 2(\lambda_{13} + \lambda_{14}) + \lambda_{15} + \lambda_{16}$
$R_{7,1}$	= probability of latching valve not shifting position during launch
$R_{8,1}$	= probability of G switch not terminating spinup prematurely
R_{G10}	= probability of RCS latching valve closing
$R_{2,1}$	= probability of TCA valve opening as required for spinup
t_{launch}	= equivalent launch time = $80t_B + 8t_C$
R_i	$= \exp (-\lambda_i t_{\text{launch}})$
<u>Transfer Orbit</u>	
$R_{5,T}$	$= R_{1,2}^4 R_{2,2}^4 R_{3,3}^2 [\exp (-\lambda_{G19}(80t_{AB} + 8t_T))]$
λ_{G19}	= series failure rate of entire subsystem less thrust valves
$R_{1,2}$	= probability of RCS-TCA valve closing
$R_{2,2}$	= probability of RCS-TCA valve opening
$R_{3,3}$	= probability of spinup TCA valve surviving transfer orbit
t_{AB}	= AKM burn time = 36 sec
t_T	= duration of coast and insertion phase = 87.1 hours

TABLE 3-20. MATHEMATICAL DEFINITION OF TERMS

<u>Term</u>	<u>Formula for R_{5S} Terms</u>
P_a	$1 - (1 - R_{6,1})^2$
P_b	$R_{G9}^2 (R_{7,1}^2 P_{G9}^2 + 2R_{7,1} R_{G9} Q_{7,1} + Q_{7,1}^2)$ $(P_{G10}^2 + Q_{G10} R_{1,1}^2 (P_{G10} + 1))$
P_c	$2P_{G9} Q_{G9} (R_{7,1} P_{G9} + Q_{7,1})$ $(R_{G10} + Q_{G10} R_{1,1}^2)$
R_{G9}	$R_8 R_{10}$
R_{G10}	$R_9 R_{11}$
$R_{1,1}$	probability of TCA valve closing after spinup
$R_{6,1}$	probability that separation switch functions as required
Q_x	$1 - R_x$
R_x	$\exp(-\lambda_{x,3} t_{\text{launch}})^j$

TABLE 3-21. SUCCESSFUL CONDITIONAL STATES OF S(3) SPINUP FUNCTION

i	Event E _i Condition of Initial Command Circuits	P(E _i)	ST E _i = Conditional states of acceptable system operation given that Event E _i has occurred	P(ST E _i)
1	Either separation switches functions along with its respective signal ring and redundant pair of brushes	P_a	Both spinup latching valves open and at least one of two RCS latching valves open during launch, and either both spinup latching valves close or both spinup latching valves close or both spinup TCA valves close at completion of spinup. or Either RCS latching valves and associated spinup latching valve fails closed while the remaining spinup latching valve opens, and either spinup latching valve closes or both spinup TCA valves close at completion of spinup.	P_b $+P_c$

TABLE 3-22. MATHEMATICAL DEFINITION OF TERMS IN ORBITAL OPERATION RELIABILITY MODEL

Term	Formula for Terms
$R_{5,0}$	$P_A P_B$
P_A	$R_{16} P_{12} P_{14}^2 P_{G9,5} P_{G10,5} \left[R_{1,5}^2 R_{2,5}^2 (1 - Q_{G9,5}^2) + 2 R_{1,5} R_{2,5} Q_{2,5} P_{G8,5} \right]$
P_B	$P_{AA} \left[P_{aa} (P_{bb} + P_{cc} + P_{dd}) + P_{ee} (P_{ff} + P_{gg}) + P_{hh} + P_{BB} P_{jj} P_{kk} + P_{ll} \right]$
P_{AA}	$P_{G9,4}^2 P_{13,4} \left[P_{G10,1}^2 + P_{G11,4} R_{1,1}^2 (1 - P_{G10,1}^2) \right]$
P_{BB}	$2 P_{G9,4} P_{13,4} P_{G10,1} P_{16,4} \left[P_{13,4} Q_{G10,1} (1 - P_{15,4} R_{1,1}^2) \right]$
P_{aa}	$R_{2,4}^4$
P_{bb}	$R_{G8,4}^4 (R_{1,4}^4 + 4 R_{1,4}^2 Q_{1,4} P_{G10,4})$
P_{cc}	$4 R_{G8,4}^3 Q_{G8,4} (R_{1,4}^4 + 2 R_{1,4}^2 Q_{1,4} P_{G10,4})$
P_{dd}	$4 R_{G8,4}^2 Q_{8,4}^2 (R_{1,4}^4 + R_{1,4}^2 Q_{1,4} P_{G10,4})$
P_{ee}	$4 R_{2,4}^3 Q_{2,4}$
P_{ff}	$R_{1,4}^3 (2 P_{G8,4}^2 - P_{G8,4}^3)$
P_{gg}	$P_{G8,4}^2 P_{G10,4} R_{1,4}^2 Q_{1,4}$
P_{hh}	$4 R_{2,4}^2 R_{1,4}^2 P_{G8,4}^2 Q_{2,4}^2$
P_{jj}	$R_{2,4}^2 R_{1,4}^2 P_{G8,4}^2$
P_{kk}	$R_{7,1} Q_{7,1} P_{G9,4} P_{G10,4}$
P_{ll}	$R_{7,1} Q_{7,1} P_{G9,4} P_{G10,4}$
$R_{G8,y}$	$R_{6,y} R_{7,y}$
$R_{G10,y}$	$R_{9,y} R_{11,y}$
R_{G11}	$R_{15,y} R_{16,y}$
$R_{1,4}$	Probability TCA valve closes (does not fail open)
$R_{2,4}$	Probability TCA valve opens (does not fail closed)
$Q_{x,y}$	$1 - R_{x,y}$ or $1 - P_{x,y}$; $Q_{x,y}^* = 1 - R_{x,y}^*$
$R_{x,y}$	$\exp(-\lambda_{x,y} t)$

TABLE 3-23. SUCCESSFUL CONDITIONAL STATES OF ATTITUDE CONTROL PROPULSION SUBSYSTEM*

f	Event E _i	P(E _i)	ST E _i = Conditional states of operation system operation given that event E _i has occurred.	P(ST E _i)
AA	Neither half of RCS manifold develops any tasks, either both spinup latching valves close or both spinup TCA valves close and the spinup manifold does not develop a leak or burst, both RCS latching valves open on command.	P _{AA}	All four RCS TCA valves open and all four thrusters fire and either all four RCS TCA valves close or one set (both TCAs on one side) of RCS TCA valves closed and at least one RCS TCA valve in the other set fails to close but the associated RCS latching valve closes on command. or Any one of the four RCS thrusters fails to fire, and all four RCS TCA valves close or the two RCS RCA valves in the good set close and at least one RCS TCA valve in the bad set fails to close but the associated RCS latching valve closes on command. or Any two RCS thrusters (one radial, one precession) fail to fire and all four RCS TCA valves close or, given both failed thrusters are in the same set, at least one RCS TCA valve fails to close but associated RCS latching valve closes on command. or Any one of the four RCS TCA valves fails to open and at least one radial and one precession thruster fire and the three remaining RCS TCA valves close. or One set of RCS thrusters fires and their respective TCA valves close and the remaining RCS TCA valve fails to close but associated RCS latching valve closes on command. or Any one axial and one precession TCA valves fail to open and the remaining two RCS TCAs function properly.	[P _{aa} (P _{bb} + P _{cc} + P _{dd}) + P _{ee} (P _{ff} + P _{gg}) + P _{hh}]
BB	At least one spinup latching valve fails to close and the spinup manifold does not burst, but at least one spinup TCA valve fails to close or the spinup manifold develops a leak or either half of RCS manifold develops a leak and the spinup latching valve on the good side closes, and the associated RCS latching valve opens on command.	P _{BB}	The two RCS TCAs on the good side function properly and the RCS latching valve on the side allowing system leakage can be closed on command. or The RCS latching valve on the side allowing system leak closes on command and the other RCS latching valve does open on command.	P _{jj} (P _{kk} + P _{ll})

*Math model: $P_B = P_{AA} [P_{aa} (P_{bb} + P_{cc} + P_{dd}) + P_{ee} (P_{ff} + P_{gg}) + P_{hh}] + P_{BB} P_{jj} [P_{kk} + P_{ll}]$

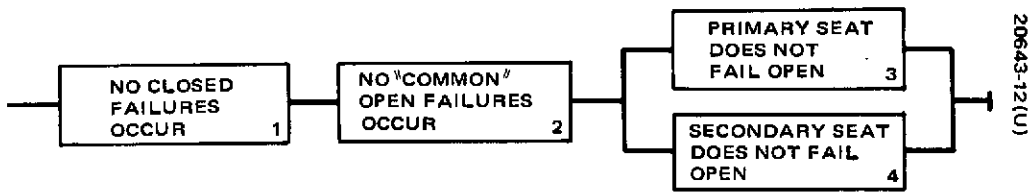


Figure 3-11. Thruster Valve Reliability Block Diagram

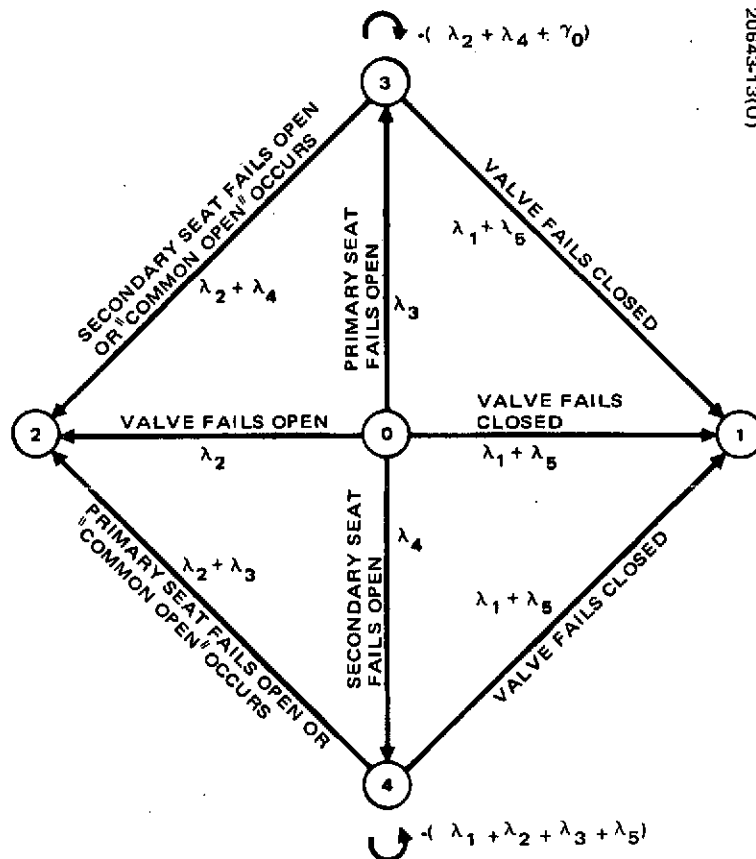


Figure 3-12. Valve Reliability Flow Diagram

Because of the complex nature of the thruster valves, a separate analysis was performed to determine valve reliability. The thruster valve and associated driver can be represented by the reliability block diagram (Figure 3-11) where each block represents nonoccurrence of a particular failure mode. Figure 3-12 depicts the transition from one state to another. Thruster valve reliability and probability of failure (open or closed) is given by the mathematical models in Table 3-24, which mathematically define the states of the valve and associated solenoid drivers as defined in Table 3-25.

The following assumptions apply to this analysis:

- 1) Failure of a tank or manifold during launch is charged to the spinup portion of the coast/insertion phase.
- 2) Failure of the RCS tanks or manifolds after the initial spinup is charged to the RCS subsystem.
- 3) Failures of RCS heaters have no mission effect.
- 4) Based on calculations and engineering judgment, the probability of at least one redundant separation switch actuating on release, $R_{6,1}$, is at least 0.99998.
- 5) Based on calculations and engineering judgment, the probability of the latching valve not shifting position during launch, $R_{7,1}$, is at least 0.999999.
- 6) It is further assumed that the probability of the G switch assembly not terminating the spinup prematurely, $R_{8,1}$, is at least 0.999996.
- 7) Based on engineering judgment, the probability of the G switch functioning properly, $R_{9,1}$, is assumed to be 0.9998.
- 8) Leakage of the fill and vent valve can be neglected (the valve has a redundant seal and is capped).
- 9) Valve failures in the open and closed mode are mutually exclusive events.
- 10) The failure rate associated with propellant leakage to space from the pressure transducer or any of the latching valves is included in the central and RCS manifolding leak mode failure rates.
- 11) All failure rates are constant with time (cycles).

TABLE 3-24. THRUSTER VALVE RELIABILITY MATH MODEL

Thruster Valve Reliability

$$R_{\text{valve}} = e^{-\gamma_1 t} + e^{-\gamma_2 t} - e^{-\gamma_0 t}$$

Probability that valve fails in open mode

$$Q_{1,4}^* = \frac{\lambda_2 + \lambda_4}{\gamma_1} (1 - e^{-\gamma_1 t}) + \frac{\lambda_2 + \lambda_3}{\gamma_2} (1 - e^{-\gamma_2 t}) - \frac{\gamma_0 - \gamma_3}{\gamma_0} (1 - e^{-\gamma_0 t})$$

$$R_{1,4}^* = 1 - Q_{1,4}^*$$

Probability that valve fails in closed mode

$$Q_{1,4} = \frac{\gamma_3}{\gamma_1} (1 - e^{-\gamma_1 t}) + \frac{\gamma_3}{\gamma_2} (1 - e^{-\gamma_2 t}) - \frac{\gamma_3}{\gamma_0} (1 - e^{-\gamma_0 t})$$

$$R_{1,4} = 1 - Q_{1,4}^*$$

where

$$\gamma_0 = \lambda_1 + \lambda_2 + \lambda_3 + \lambda_4 + \lambda_5$$

$$\gamma_1 = \gamma_0 - \lambda_3$$

$$\gamma_2 = \gamma_0 - \lambda_4$$

$$\gamma_3 = \lambda_1 + \lambda_5$$

and λ_1 through λ_5 are defined in Table 3-17 for $y = 4$

TABLE 3-25. CONDITIONAL STATES OF THRUSTER VALVE

<u>State</u>	<u>Condition of Valve</u>
0	No failures have occurred.
1	Valve has failed closed (driver failure) and/or either or both seats have failed closed.
2	Valve has failed open (both seats are open or leaking).
3	Primary seat has failed open or is leaking. No other failures have occurred.
4	Secondary seat has failed open or is leaking. No other failures have occurred.

- 12) An open failure in one of the RCS thruster valves associated with a particular RCS latching valve precludes use of the other thruster valve associated with that RCS latching valve.
- 13) Valve failure rates (failures/second) are derived from cycling failure rates (failures/cycle), seconds of mission operation, and total cycles required.

Rationale for Redundancy and FMEA. RCS design employs extensive redundancy to protect against known failure modes. TCA valve design incorporates dual seats to protect against valve opens. Redundant axial and radial TCAs are provided. Spinup TCAs are redundant in that spinup can be accomplished with one jet but will take twice as long. Latching valves isolate each pair of axial and radial thrusters to protect against propellant loss if a valve should fail open. Similarly, two latching valves isolate spinup TCAs, manifolding, and reservoirs from the rest of the subsystem. A fifth latching valve connects the two halves of the central manifolding on the liquid side which assures recovery from a flat spin if no opens occur.

The preliminary subsystem FMEA, Table 3-26, indicates that RCS design minimizes single-point mission catastrophic failures. The only such failure mode identified is a leak in the spinup reservoirs during the launch phase. The probability of this event occurring is minimized by burst and proof pressure testing to preclude use of faulty devices.

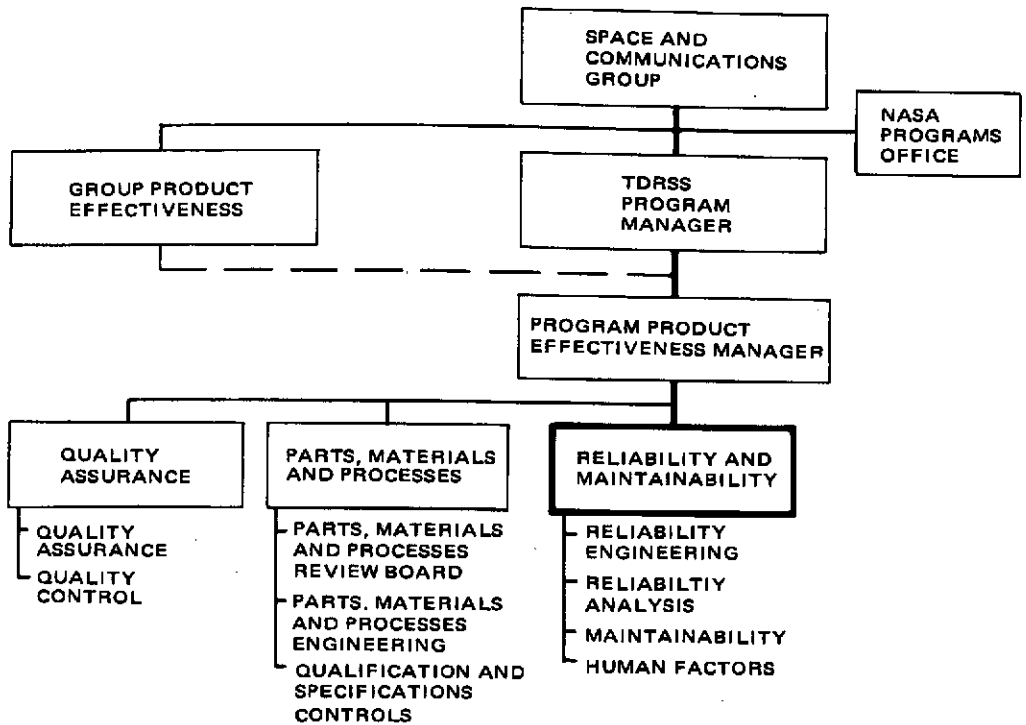
TABLE 3-26. FAILURE MODE AND EFFECTS ANALYSIS -
REACTION CONTROL SUBSYSTEM

Line Number	Control Item Name and Number Name and Reference Designator or Part Number	Control Item Function; Input (IN ₁) Output (OUT ₁)	Failure Mode and Cause; Mode ₁ Cause ₁	Phase or Activity	Failure Effect on		Failure Detection Method(s)	Probability of Failure or Failure Rate ($\lambda \times 10^9$)	Failure Class	Corrective Action Available or Recommended
					Next Higher Indentured Equipment or Control Items	End Item				
	Propulsion tank	Hydraulic storage	Leak - Faulty tank	Orbit	Loss of propellant	Partial mission loss	Loss of RCS functions		I	Burst and proof pressure test prevents use of autotanks and reservoirs.
	Reservoir	Spinup hydrazine storage	Major leak or rupture - faulty reservoir Minor leak		Loss of spinup or spin control Potential loss of spinup with loss of spin control function	Mission loss Potential mission loss		I II		
	Transducer	Transforms hydrazine pressure to electrical signal	Loss of response to pressure Leak - faulty pressure capsule and housing		Loss of hydrazine quantity indication Loss of propellant	No effect Partial mission loss		III I	Transducer is burst tested. Would require both capsule and housing to fail.	
	Spinup TCA valve	Spinup thrust generation	Failed closed		Slower spinup with one spinup valve	No effect - redundant	Slow spinup response isolation is accomplished by selective actuation of spinup valves.	III	Valves have been life tested to 20,000 cycles with no wear or damage. Cleanliness demonstration is required in tests.	
		Provides radial thrust	Failed open		RCS latching valve is closed isolating spinup valve	No effect	Excessive spinup	III	No single failure results in continuous power to solenoid	
	Radial TCA valve	Provides radial spacecraft position control	Failed closed Failed open		No effect - redundant RCS latching valve is closed isolating failure	No effect No effect	Slow radial responses selective radial valve actuation Abnormal radial spacecraft response	III III	Longer pulsing periods are required for radial positioning with one valve rather than two.	

Table 3-26 (continued)

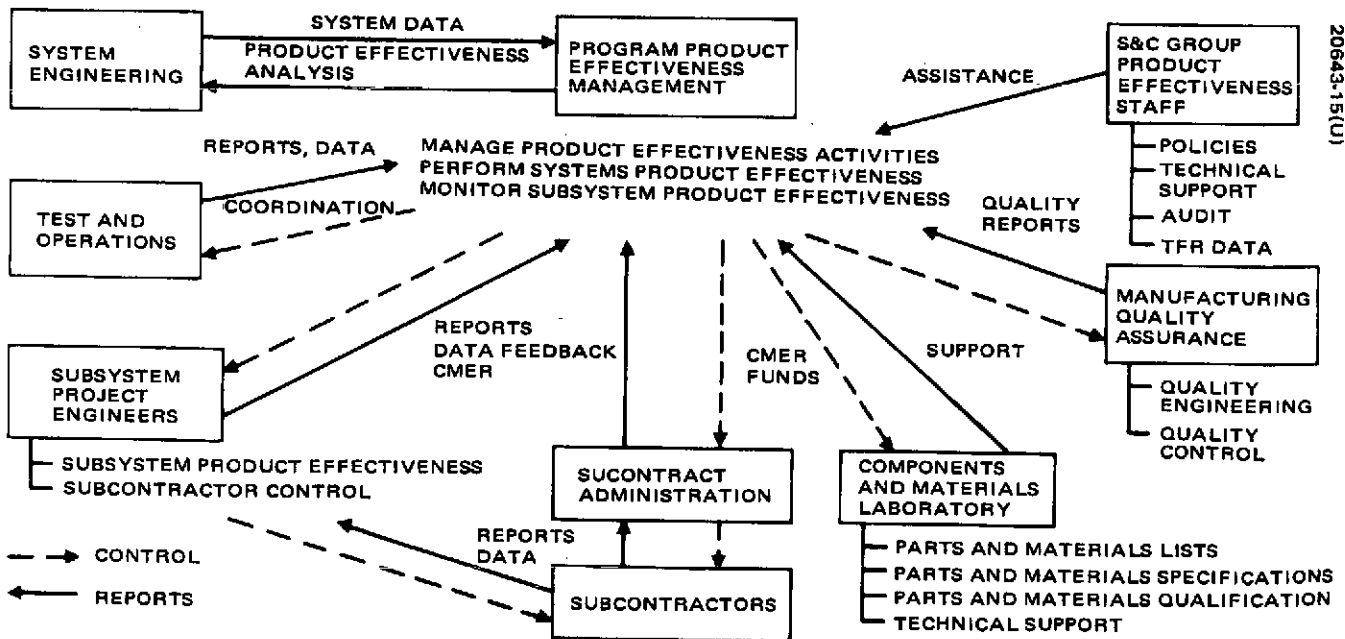
Line Number	Control Item Name and Number Name and Reference Designator or Part Number	Control Item Function: Input (IN ₁) Output (OUT ₁)	Failure Mode and Cause Mode ₁ Cause ₁	Phase or Activity	Failure Effect on		Failure Detection Method(s)	Probability of Failure or Failure Rate (λ x 10 ³)	Failure Class	Corrective Action Available or Recommended
					Next Higher Indentured Equipment or Control Items	End Item				
	Axial TCA valve	Provides axial position control	Failed closed		Redundant axial valve is actuated	No effect	Slow axial response selective axial drive		III	Longer pulsing periods are required for axial positioning with one valve rather than two.
			Failed open		RCS latching valve is closed isolating failure	No effect				
	RCS manifold 1/2 section	Provides hydrazine feed for one set of radial and axial valves	Failed open		Loss of hydrazine	No effect	Selective actuation of valves		III	Close one RCS line valve isolating open valve
	Fill and drain valve	Provides fill and drain valve for ground operations	Leak		Loss of hydrazine RCS latching valve and spinup latching valve are closed isolating failure	No effect	Selective actuation valves		III	Isolate leak with selected valves
	Spinup latching valve	Traps propellant in lines to initiate spinup, and protect system in event of spinup TCA or manifold leak	Failure to open	Spinup or orbit	No effect	No effect - redundant valves			III	
			Failure to close		Loss of leak protection	No effect on spinup partial loss of RCS in the event of spinup TCA or manifold leak RCS latching valve on that side must close		III		
	RCS latching valve	Provide leak protection in the event of RCS TCA or manifold leak	Failure to open	Spinup or orbit	Use of 1/2 RCS TCAs would require supplying propellant through spinup manifold	No effect			III	
			Failure to close	LOA	Loss of leak protection	No effect			III	
	Crossover latching valve	Prevents propellant transfer in tank sets in the event of a flat spin	Failure to open		Balancing propellant in tank sets would require use of spinup manifold	No effect			III	
			Failure to close		Loss of protection in the event of a flat spin	No effect unless spacecraft goes into a flat spin			III	

3-65



20643-14(U)

Figure 3-13. TDRS Product Effectiveness Organization



20643-15(U)

Figure 3-14. Product Effectiveness Functional Relationship

3.4.2 Reliability Program Plan

This plan describes the Hughes Aircraft Company Reliability Program for TDRS, and is compatible with NASA specification NHB 5300.4(1A).

3.4.2.1 Program Organization and Management

Organization. A Product Effectiveness Manager is appointed to be responsible for Reliability, Quality Assurance, Materials and Processes, and Contamination Control. He reports directly to the Program Manager and also to the Group Manager of Product Effectiveness. A Reliability Manager reports to the Program Product Effectiveness Manager. He is responsible for assuring that reliability, maintainability and human factors are employed in unit, subsystem, and system design. He is further responsible for assuring that reliability tasks are satisfactorily completed on schedule and within budget. The organizational relationships are shown in Figure 3-13. Figure 3-14 shows the functional relationships and information and control flow between Program Product Effectiveness Management and the design and supporting organizations.

Reliability Program Plan. The following sections of this program plan discuss the reliability activities to be accomplished. Each activity is divided into several tasks. Since a system of internal Hughes Space and Communications Group procedures are available which cover almost all aspects of a total reliability program (Table 3-27), only a brief discussion of the approach to each task is presented in this plan; details and implementation procedures are contained in the Hughes Space and Communications Group internal documents.

Reliability Program Control. In addition to meeting contractual technical requirements and schedule milestones, a prime function of the Program Reliability Manager will be to monitor and control the expenditure of pertinent funds. Once participating organizations budgets have been established and work authorizations distributed, funding will be monitored through use of weekly accounting tabulations.

Policies and procedures which are not covered in standard Hughes documentation and those which require modification to comply with program requirements will be generated by the Program Reliability Manager. These will be disseminated to cognizant organizations within Hughes prior to the scheduled need for their implementation. Dissemination of such information will be accomplished through the use of program instructions, interdepartment correspondence, and bulletins issued by the Program Reliability Manager. Authorization to participating organizations to proceed with work will be distributed by Work Authorization Directives (WADs) which are a standard Hughes internal form and are controlled by a defined company procedure.

Reliability Indoctrination and Training. Hughes conducts periodic training courses in Reliability for management, engineering, manufacturing, and other line and staff personnel whose activities could affect the end product reliability. Therefore no general reliability training programs will be required as a result of the TDRS program. TDRS program training and

TABLE 3-27. RELIABILITY PROGRAM PROCEDURAL DOCUMENTS
Space and Communications Group Product Effectiveness Handbook

Document Number	Title	Description of Contents
PEH 06-0201	Parts Stress Derating	Establishes parts stress derating policy and derating curves.
PEH 06-0203	Approved Failure Rates and Procedures for Use	Contains Hughes approved failure rates and procedures for use in reliability analyses of spacecraft equipment.
PEH 06-0204	Failure Mode and Effects Analysis	Describes procedures and format for conducting FMEAs.
PEH 06-0205	Trouble and Failure Reporting and Corrective Action System	Describes requirements and responsibilities for reporting, analysis, corrective action, and closeout of troubles and failures occurring during performance and/or test of equipment designed and produced by SCG and its subcontractors and suppliers.
PEH 06-0301	Subcontractor Reliability Program Requirements	Reliability program requirements specification for SCG subcontractors.
PEH 06-0304	Subcontractor Data Management	Describes procedures for disseminating Product Effectiveness data requirements to and receiving data from SCG subcontractors.
PEH 06-0305	Approved Failure Rates and Parts Derating Policy for Subcontractors	Delineates Hughes parts derating and failure rate requirements contained in documents 06-0201 and 06-0203 for use by subcontractors.
PEH 06-0306	Subcontractor Parts, Materials, and Processes Program Requirements	Parts, materials, and processes program requirements specifications for SCG subcontractors.
PEH 06-0307	Materials and Processes Requirements for Space System Subcontractors	Outlines requirements for subcontractor use of materials and processes in design and fabrication of hardware for use in space systems and defines requirements for submittal of data and obtaining approval.
PEH 06-0401	Parts, materials, and Processes Engineering Requirements	Establishes SCG requirements and controls for parts, materials and processes engineering internal to Hughes.
SCG Management Directives Manual	Statement of Responsibilities, Space and Communications Group Product Effectiveness	Establishes Product Effectiveness Management authority

indoctrination activities will be implemented when required to establish and maintain lines of communication between the Program Reliability Manager and other program office personnel, engineering, manufacturing, and support organizations and subcontractors.

Subcontractor and Supplier Control. Subcontractor and supplier surveillance will be performed at the particular facility by participating in design reviews and reliability audits, and at Hughes by reviewing status reports and checking accuracy of reliability estimates, failure mode analyses, and other required documentation. Test data will be analyzed, and failure

reports with resultant corrective actions will be followed-up to assure a closed-loop system. Subcontractor and supplier selection is preceded by a facility survey; control will continue until delivery of the equipment. Pertinent reliability activities fall into the two general categories discussed below. Figures 3-15 and 3-16 show the Reliability (and Quality Assurance) interaction with subcontractors and suppliers.

Preprocurement Survey. Procedures for evaluating and selecting subcontractors and suppliers include examination of facilities; study of methods, processes, and procedures in use; evaluation of the capabilities of responsible personnel; and consideration of past achievements in implementation of reliability programs. Hughes policy and procedures relating to preprocurement survey and evaluation of subcontractors and suppliers will be employed. The value engineering concept will be applied to assure true value in terms of equipment function considering quality, reliability, delivery, and cost. Subcontractors and suppliers will be encouraged to work with Hughes personnel toward improving total value of the product.

Surveillance and Performance Evaluation. Surveillance and evaluation of the performance of suppliers and subcontractors will be governed by Hughes policies and procedures. As applicable, Hughes Space and Communications Group Product Effectiveness Handbook documents and relevant Quality Assurance documentation will be imposed. Purchase orders and subcontracts will be monitored to assure adherence to these requirements.

Requirements for reports, documents, or other required data pertaining to items or services being requested, will be stipulated in a Subcontractor Data Requirements List, supplemented with Data Preparation Instructions, attached to the Statement of Work. All such supplier and subcontractor generated information submitted to Hughes will be received by Hughes Materiel, who will effect internal distribution.

Requests for corrective action to be performed by a supplier or subcontractor will be initiated by the requesting or monitoring organization through Materiel. Corrective action requests that may affect price, delivery, or performance will be documented and must be approved by the Hughes TDRSS Product Effectiveness Manager and will be coordinated through Materiel.

The reliability engineer assigned to each subcontractor or supplier will work with their reliability organization and will be in attendance at the subcontractor's or supplier's facility when required to resolve problems. He will review design specifications and procedures, and will recommend rejection and/or rework of equipment where reliability is considered to be compromised.

In the event a subcontractor's or supplier's performance becomes unacceptable to those Hughes personnel concerned, notification of the available facts will be made to Materiel. Appropriate steps will then be taken by Materiel to reevaluate the subcontractor or supplier by reviewing the procurement to determine corrective action.

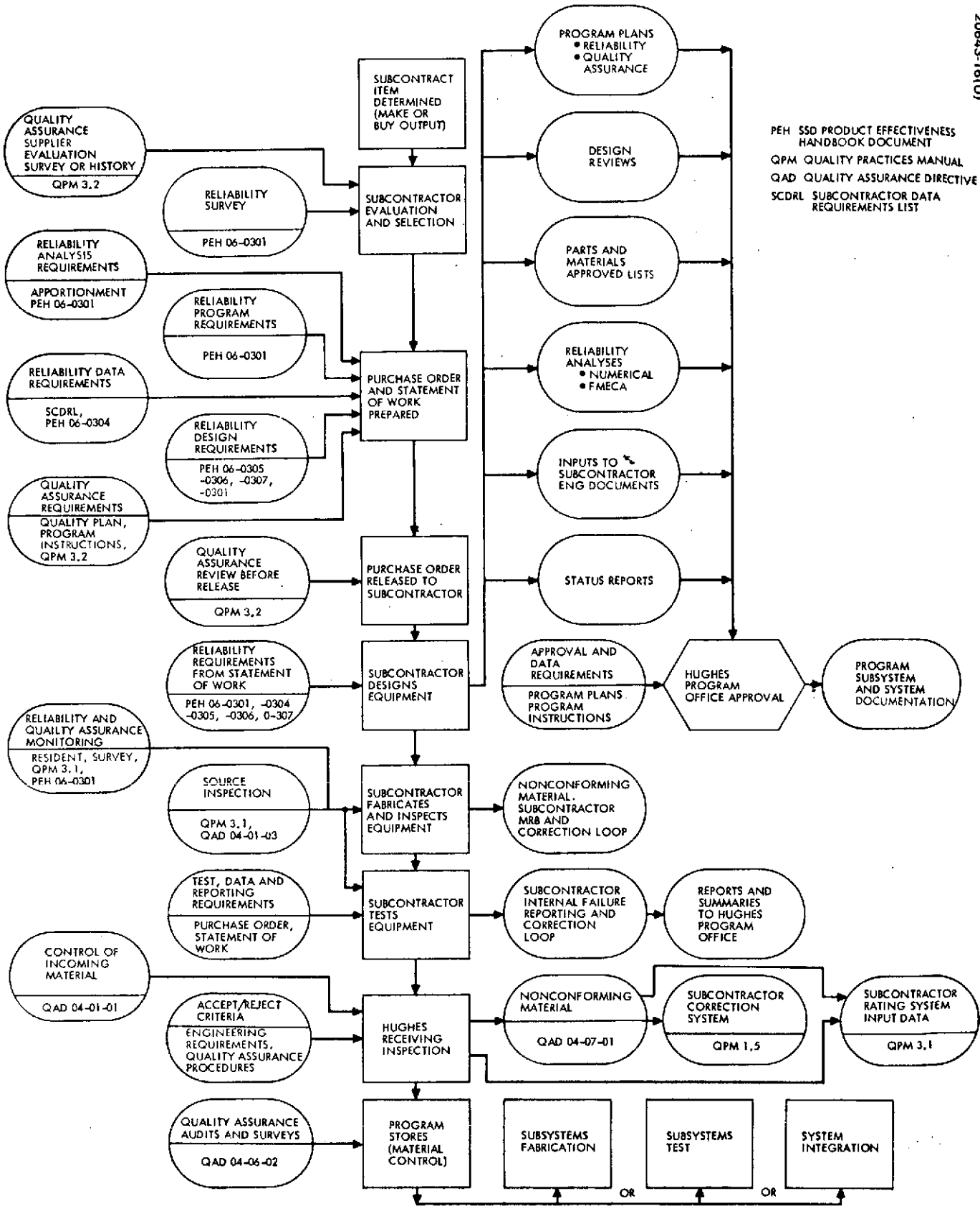
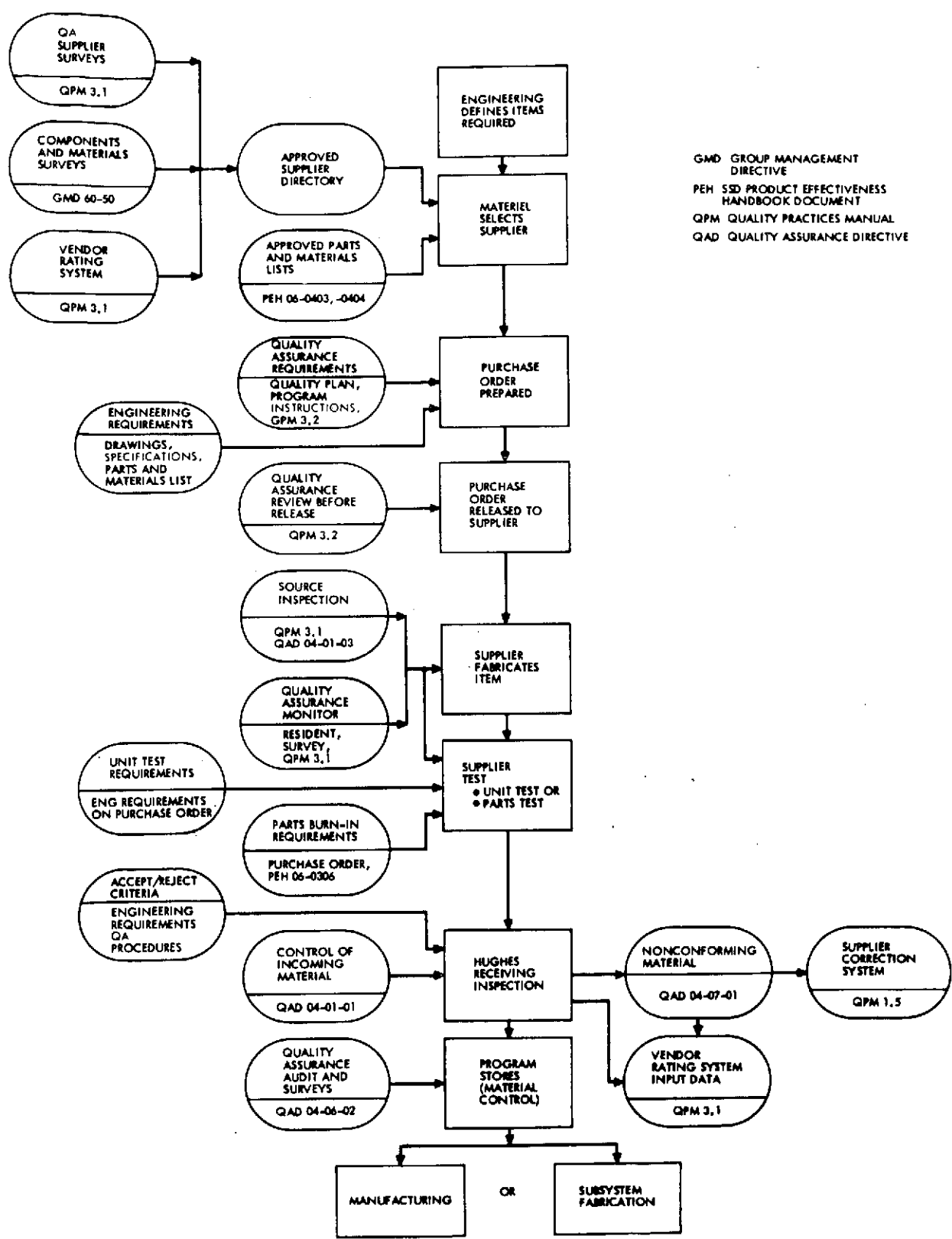


Figure 3-15. Reliability and Quality Assurance Interaction With Subcontractors With Design Responsibility



GMD GROUP MANAGEMENT DIRECTIVE
 PEH S&D PRODUCT EFFECTIVENESS HANDBOOK DOCUMENT
 QPM QUALITY PRACTICES MANUAL
 QAD QUALITY ASSURANCE DIRECTIVE

Figure 3-16. Reliability and Quality Assurance Interaction With Subcontractors Without Design Responsibility

Government Furnished Property (GFP). The approach to consideration of the reliability effect of GFP on the spacecraft is described within the pertinent task discussions contained in this program plan. Tasks which are concerned with GFP are reliability estimation, failure reporting and corrective action, and progress reporting. Essentially, GFP will receive equal consideration with other program hardware (from a reliability standpoint) except that numerical reliability data will be furnished by GSFC and GSFC will be expeditiously notified of problems which occur.

3.4.2.2 Reliability Engineering During Design

Specifications Review. Engineering documentation governing design, procurement, test, and integration will be subject to review by Reliability Engineering. Such documentation primarily includes system, subsystem, and equipment specifications. The object of these reviews will be to assure inclusion of numerical reliability criteria; authorized parts, materials, and processes; nonallowable failure modes; derating requirements; failure reporting and correction procedures; and other appropriate aspects of the reliability program.

Anomalies will be promptly brought to the attention of the responsible engineering activity for resolution. If necessary, resolution will be obtained through the Program Product Effectiveness Manager and Supervisory channels.

The maintenance of these specifications will be provided through the application of specification and configuration management disciplines to prevent changes detrimental to overall system reliability objectives, and to provide for complete accountability of configured end items.

Preferred Design Practices. The Product Effectiveness Handbook document PEH 06-0201 contains the derating policy and procedures to be used on the TDRS program for electronic parts. This document will be disseminated by the TDRS PPEM to the responsible engineering activities. A parallel document, Product Effectiveness Handbook document PEH 06-0305, will be appended to statements of work for subcontractors with applicable design responsibility.

The failure rates and derating curves are based on the Hughes Approved Parts List. Preferred, acceptable, and approval required usage areas are defined for the specific electrical/electronic part types. These are enveloped by multiplicative factors of the part failure rate, using electrical stress and temperature as the criteria. Reliability Engineers will compare the usage envelope of each part against the stress applied, to verify that the parts are adequately derated. Use of these curves and adherence to the specified policy by designers is mandatory and all engineering activities will be so notified through a TDRS Program Instruction. Any parts usage requests in the "approval required" region must be submitted in writing to the TDRS PPEM for review and approval. Usage of parts will be reviewed with the cognizant REA to assure validity for the application. Proper derating will be assured through stress analyses and approved derating

agreements. The structures subsystem design will be based on the Intelsat IV, HS 308, and HS 318 spacecrafts configurations.

The primary structural materials selected are aluminum and beryllium. To provide a minimum mass structure, beryllium will be used in key areas to achieve a significant mass saving. Hughes has gathered considerable experience over the past 7 years, in the use of beryllium in primary load carrying structures.

Material strength and other mechanical and physical properties will be selected from MIL-HDBK-5 or other procuring agency approved sources. Allowable material strengths used in the design will reflect the effects of load, temperature, and time associated with the design environment. Allowable yield and ultimate properties are as follows:

- 1) For single load path structures, the minimum guaranteed values ("A" values in MIL-HDBK-5, Metallic Materials and Elements for Flight Vehicle Structures, current edition) were used.
- 2) For multiple load path structures, the 90 percent probability values ("B" values in MIL-HDBK-5, Metallic Materials and Elements for Flight Vehicle Structures, current edition) were used.

These values are consistent with the overall spacecraft reliability requirements.

The margin of safety is defined as: $MS = 1/R - 1$, where R is the ratio of applied load to the allowable load. The allowable load used in these calculations is the design ultimate load which contains a safety factor of 1.25 over the predicted (limit).

The preferred design loads are:

- 1) Condition 1 is used to represent loads during the Delta 2914 POGO flight event. It consists of a -18.0 g axial load combined with a \pm nonuniform lateral load distribution in which the spacecraft adapter experiences lateral loads equivalent to a uniform 1 g.
- 2) Condition 2 is used to design for nonuniform loading of the type that occurs during liftoff and maximum α_q . This type of loading is characterized by relatively high g lateral loads on the appendages at the top of the spacecraft, with much lower loading in the region of the adapter. Condition 2 has the following characteristics:
 - Lateral loads on the spacecraft vary as the fundamental spacecraft mode with the tip acceleration being 25.0 g's (with a reduction to 3 g's at the spacecraft cg).
 - The axial load is -4.5 g's and +1.5 g's.

- 3) Condition 3 represents the third stage motor burnout condition. It results in -16.2 g axial acceleration coincident with a lateral load of 0.5 g. In addition, a centrifugal radially directed spin loading of $0.344R$ g's exists where R equals the radius in inches to the cg of the component in question.

Loads due to MECO are encompassed by the POGO and liftoff events. This is also true in the case for second-stage burn. The apogee motor load condition is encompassed by condition 3.

Maintainability and Human Factors. Attention to the maintainability and maintenance concepts for the TDRS subsystems will be a requirement in achieving on-schedule performance, sustaining operational reliability, and controlling support system and logistics costs. Program Instructions will be issued to authorize and direct performance of these activities.

Maintainability activity on TDRSS will be controlled by the decision to use as much existing space proven hardware as possible. During the analysis process, the maintenance tasks will be reviewed, and those having impact on the testing and preparation of the subsystems for launch or those having impact on the mission success will be evaluated to develop the best method for accomplishment. Maintainability engineers will work directly with designers and will participate in design reviews as required.

Acceptability of Off the Shelf Hardware. Off the shelf hardware will be accepted on the TDRS program if that hardware has a history of satisfactory performance on satellite programs. Off the shelf hardware acceptance criteria will be evaluated based on the following requirements:

- 1) Subcontractor/part vendor history of past performance
- 2) Completion of hardware environmental tests
- 3) Hughes Aircraft Company high reliability 908XXX electronic parts are used
- 4) All failure reports and Quality Assurance discrepancy reports are properly closed with the required corrective action
- 5) Materials and processes have been qualified for space use

Acceptability of New Technology for TDRS. New technology items, such as electronic units, electronic parts, electrochemical and mechanical items, materials and processes, will be used on the TDRSS program only if existing items will not meet the program requirements. To determine if an

item will be classified as new technology, the following criteria needs to exist:

- 1) The item has an inherent weakness and redesign is required.
- 2) The item is difficult to manufacture or control because of inherent design limitations or complexity and the manufacturing process will be changed.
- 3) The item may be difficult to apply because its use consumes most of its design margins.
- 4) The item represents new design or new fabrication techniques which involve state of the art technology and which are not a direct extension of extant design or fabrication techniques.

Critical Item List. New technology items, as determined by the criteria established above, will be listed as TDRSS program critical items.

Control of the critical items will be achieved via the critical items list maintained by Program Reliability, which will identify the items and specify schedules and organizations responsible for execution of required analyses or tests. Responsibility for actual test performance rests with the responsible engineering organization for each critical item. Control methods, as well as the list, will be subject to review and evaluation by Systems Engineering and the Program Manager. Acceptability for use on the TDRSS program will be determined by the status of the testing of the new technology items.

Program Reliability Engineers will be responsible for monitoring and reporting on the critical item effort. Through the use of Program Instructions they will effect the distribution of critical items lists and status information to the following affected personnel: design, purchasing, manufacturing, inspection, test, handling personnel, and those subcontractors/suppliers who supply these items.

Program Reliability Engineers will also monitor the flow of critical item information within Hughes, to suppliers and subcontractors, and with the procuring agency and in union with System Engineering will identify and coordinate special testing to be performed on reliability critical items.

Periodic Reviews. Periodic reviews at PDR, CDR, and FCA, of the Critical Item List and the effectiveness of the critical item controls/tests will be held at Hughes with NASA/GSFC in attendance. Test/inspection data, failure reports, and other data will be presented to establish history of the critical items.

Additions and Deletions. Hughes will determine at the periodic reviews if additions and/or deletions to the Critical Item List are warranted. The classification of an item as critical may be cancelled when:

- 1) Assurance has been obtained that the original reasons for selection are no longer applicable and there are no new basis for such classification, because of
 - Item redesign
 - Increased or revised manufacturing or procurement controls
- 2) Elimination of the item from use on the program

Cancellation will be considered complete only when approval signatures have been obtained from the Responsible Engineer, System Engineering, Program Reliability Manager, and a designated NASA/GSFC representative.

Critical Item Form. The Critical Item Control Form is the procedural method of logging acceptabilities information. Each critical item constitutes a special case which requires unique handling and resolution. Thus, each potential problem must be clearly defined and evaluated so that optimum control and followup action can be administered. The Critical Item Control form lists the following information on each critical item:

- 1) Identification, including nomenclature, control item number and part number
- 2) Manufacturer
- 3) Responsible Engineering Activity (REA) Manager and Engineer, and their organization codes
- 4) Criteria used to categorize the item as critical
- 5) Reliability impact on the system
- 6) Corrective action
- 7) Critical test parameters
- 8) Tests to be performed including the test requirements, subcontractor/supplier development tests, functional tests, design assurance tests, and any special requirements associated with specific product evaluation
- 9) Schedule of investigation, control, and corrective action, plus any special remarks which may clarify objectives or timing of the action or which may relate to interpretation of the seriousness of priority of enumerated items.

The responsible engineers will be required to provide status inputs to the Program Reliability Manager on each critical item in test. This information will be provided in a timely manner, so that visibility can be maintained.

Design Reviews. Design reviews will provide a progressive evaluation of the hardware capability to meet design requirements and concepts. Assurance will be obtained that factors affecting function, reliability, and potential reliability degradations have been considered, and that accumulated past experience in malfunction analysis, data retention files, checklists, procedures, specifications, and failure mode and effects analyses are used.

The reviews will be performed in accordance with the Hughes Master Phasing Schedule. In addition, each subsystem will be reviewed as a Hughes Divisional or subcontractor requirement. Design reviews will be conducted in accordance with Hughes Space and Communications Group Engineering Procedure 9-1. If there are any changes to an engineering release, and in the opinion of any of the committee members a design review of the change is required, it will be scheduled and budgeted as one of the change activity requirements.

Design reviews will be held with subcontractors who have equipment design and development responsibility. These reviews will follow the same procedures as imposed at Hughes. Subcontractor design review requirements are established in Space and Communications Group document 06-0301.

The responsible participants and their assigned functions for the design reviews will be issued in a Program Instruction by the Program Product Effectiveness Manager. The responsibilities will be sustained through the complete implementation of design review cycles for each subsystem and will thereby provide continuity. The responsible engineer, presenting engineer, and committee members will be appointed in accordance with the Program Instruction for a limited tenure as required to complete each of the required subsystem reviews. Reliability Engineering will be responsible for the administration of design reviews, providing technical inputs to the reviews, and following up on action items to assure implementation prior to closeout. A Reliability representative will be on all design review committees.

A design review will not be considered complete until the committee members agree that the design under review will meet its requirements upon satisfactory resolution of any action items. Review minutes will be prepared, signed by the principal participants to indicate concurrence with the conclusions, and disseminated to concerned personnel. Reliability signature on design review proceedings will indicate concurrence that all required reliability tasks were satisfactorily accomplished except as noted in the proceedings.

3.4.2.3 Reliability Prediction and Trade Studies

Mathematical Models and Reliability Prediction. Early in the design phase, mathematical models of the spacecraft and its subsystems will be developed from block diagrams depicting the functional relationships of the equipment. These mathematical models will be updated as required to reflect the evolving design. They will be used in the conduct of tradeoff analyses to determine the design approach in evaluating the need for equipment redundancy with respect to the system design life, and to evaluate the effect of potential design changes.

Reliability predictions are an integral part of the design and development process. They will be used in design tradeoff studies, in the determination of potential problem areas, as an indication of the reliability progress of the design, and to obtain numerical requirements for inclusion in design specifications. Development of reliability math models and diagrams will reflect the probability of achieving the TDR satellite mission over the expected lifetime.

Early reliability predictions will use the parts count method and will assume constant ambient temperatures (298K) and electrical stress ratios (20 percent) for application of part failure rates for electronic equipment. As design details become firmer, failure rates and reliability predictions will be updated to reflect data obtained from thermal analyses, design, and test activities, which define design temperatures and stress levels in terms of analytical and actual environments. In each prediction, consideration will be given to actual redundancy, possible failure modes of parts and assemblies, and effects of failures on the spacecraft and observatory.

Failure Rates. Failure rates of parts used on Hughes spacecraft are adjusted to reflect the appropriate environmental and application factors associated with space usage of the parts and have been compiled into an approved list in Hughes Product Effectiveness Handbook document PEH 06-0203. The failure rates are adjusted by application of the derating curves as described above.

Allocation. The system reliability requirement will be allocated to each subsystem and among the comprising assemblies and subassemblies. Mission requirements will be examined to determine operational duty cycles; quantities of parts and circuits will determine complexity of the units.

Tradeoff Studies. Hughes designers emphasize the use of proven reliable standard designs. When a nonstandard design approach is taken, analytic validation is required.

System reliability analyses performed during the study phase are an integral part of the overall systems analysis activity to assure that reliability was appropriately considered in system design and that allocation of resources such as mass, cost, and schedules is accomplished in an optimum fashion. System analysis inputs to the reliability analyses included data required to support the system reliability analyses described in Section 3.4.1.3.

Design Concepts Review. A spacecraft level reliability versus weight optimization program is utilized during the study effort to verify that spacecraft weight was optimally allocated to redundancy. This analysis is documented in Section 3.4.1.3. This optimization program will be rerun if major design changes occur and prior to PDR and CDR to assure that redundancy continues to be allocated in an optimum fashion. Results of these analyses will be documented by internal memorandums and in the design reviews.

3.4.2.4 Failure Mode, Effect, and Criticality Analyses (FMECAs)

FMECA Approach. FMECAs shall be conducted for the subsystems of the TDRSS spacecraft.

The primary objectives of the FMECAs shall be to:

- 1) Identify all assemblies of the spacecraft; stipulate those requiring redesign to meet requirements
- 2) List all significant failure modes of each assembly and their effects on the spacecraft's performance
- 3) List the causes of each potential failure
- 4) Identify all parameters contributing to these causes
- 5) Determine the criticality of all significant failure modes on the spacecraft's success
- 6) List the most critical failure modes in order of priority of study

In order to effect design improvement without costly changes to the TDR satellite, the FMECA analyses shall be initiated early in the design phase. The corrective actions recommended as a result of these analyses shall be included in the design reviews and in monthly progress reports. Design changes that have been implemented as a result of FMECA recommendations or other reasons that affect the analyses shall be reflected in appropriate FMECA updates.

While accomplishment of suitable FMECAs is the responsibility of the PPEM, FMECAs shall be conducted as a joint activity of responsible TDRSS reliability, spacecraft, subsystem, unit, and part engineers. At the spacecraft level, the analyses shall be supported by TDRSS Systems Engineering. Emphasis shall be on potential subsystem failure modes and their effects on other subsystems. The effects of GFE experiment failure and the interfacing equipment failures on subsystems shall also be examined. The responsible engineering activities shall conduct unit and subsystem FMECAs in participation with TDRSS Reliability Engineers.

The TDRS PPEM shall coordinate with the responsible engineering activities to assure that the above analyses are conducted in a timely manner and in accordance with the requirements described herein. In addition to the requirements herein, the specific instructions for preparation of the FMECA forms contained in SCG PE Handbook document PEH 06-0204 are imposed.

FMECA Report Contents. Each TDRS FMECA analysis shall be compiled into a separate report with the following standardized contents:

- 1) Cover-Page - shall identify TDRS spacecraft program number, control item name and number, terminology FMECA, date of issue, originator's name, and TDRS report identification number with any revision identification, if applicable.
- 2) Introduction - shall describe scope of the analysis, indenture level(s) of the control item(s) analyzed with traceability to the end item, master index issue used, and equipment's intended use.
- 3) Functional Description - shall provide reference to TDRS drawings, schematics, and other information sources used in preparation of the FMECA report, a complete description of the equipment functional requirements and interface requirements, and applicable block diagrams and schematics.
- 4) Method of Analysis - shall discuss assumptions, basis for probability of failure calculations, any deviations from standard FMECA forms or procedures, any special codings applied, definitions of unique terms, and any pertinent factors that may influence the FMECA, such as stress analyses, redundancy analyses, derating, operating times, environmental conditions, failure rates, model and predictions, etc.
- 5) Conclusions and Recommendations - shall summarize the FMECA reliability, if applicable, system safety and maintainability, and conclusions and recommendations concerning areas requiring redesign or other corrective action. Actual changes incorporated in the design as a result of the FMECA will be identified and ECRs ECOs, and SCNs referenced. Reasons for no action will also be discussed. Pending actions will be cited and a followup report prepared, if applicable.
- 6) FMECA Forms - which may include any one type, or combinations of, FMECA.

3.4.2.5 Redundancy Analyses

The need for TDRSS equipment redundancy shall be determined by review and evaluation of the initial reliability predictions and FMECAs. Hughes past experience with similar or identical items shall be considered during this analysis. When a potential need for redundancy has been identified and redesign of a unit is not practical, the addition of redundant units shall be

evaluated. At this point, the reliability of the subsystem and the TDRS spacecraft shall be recalculated, and the reliability improvement shall be evaluated against such factors as weight, maintainability, etc. System Engineering, with the cognizant Reliability Engineer and the responsible engineering activity, shall perform this tradeoff analysis. Subsequent to implementing the configuration change, the spacecraft and subsystem math model and block diagrams shall be updated by Reliability Engineers. Recommendations for changes occurring after release of drawings shall be processed by initiation of Engineering Change Requests (ECRs).

3.4.2.6 Support to TDRS Design Engineering

The TDRS unit, subsystem, and spacecraft design shall be monitored constantly through reliability estimates, functional block diagram analysis, reliability mathematical models, failure modes, effects and criticality analyses, and the formal design reviews. TDRS Reliability Engineers assigned to each subsystem shall iterate the results of each of these disciplines to the TDRS Design Engineers through internal documentation and formal design review data package inputs. Through this iterative feedback process shall evolve the TDRS spacecraft design containing the optimum of redundancy to meet TDRS reliability and performance requirements as identified in the specification.

In addition to the above design support activities, TDRS Components and Materials Engineers shall review designs for parts application and parts stress/derating, supplying the TDRS design engineers with the latest application information based on vendor and Hughes performance and test data.

During the design phase, whenever alternate approaches are possible, TDRS Reliability Engineers shall be required to participate in tradeoff studies to determine the optimum design. Internal documentation shall present a comparison of the possibilities and the recommended approach from the reliability considerations. If as a result of these studies, there are meaningful reliability benefits to be gained within the scope of stated design objectives, these shall become mandatory design features.

3.4.2.7 Failure Reporting and Corrective Action

The TDRS program shall utilize the Hughes Space and Communications Group failure reporting, analysis, and corrective action procedure as described in PE Handbook document PEH 06-0205A. The procedure has been developed to assure product reliability through experience feedback and review and shall be implemented on all equipment items in the TDRS program from the first specified functional test at the lowest functional level of assembly. A trouble and failure reporting (TFR) Program Instruction shall be prepared by the TDRS PPEM to supplement the aforementioned procedure as required by the TDRS program.

TDRS subcontractors shall similarly comply with the failure reporting and corrective action requirements of the Hughes PE Handbook document PEH 06-0301, stipulated in their statement of work.

The TDRS PPEM shall chair the Failure Review Board (FRB) and shall be responsible for assuring correct failure analysis, assigning corrective action requirements, as well as monitoring the implementation and assuring the adequacy of the corrections.

Failure analyses shall be performed on all major and critical failures and on all minor failures for which the cause and corrective action is not obvious (major, critical, and minor classifications are defined in the Hughes TFR procedure).

The TDRS PPEM is responsible for assuring that corrective action is timely and adequate. When the failure analysis has been completed, the responsible engineer assigned by the TDRS PPEM shall propose corrective action to prevent recurrence. Follow-up of the corrective action shall be by the responsible TDRS Reliability Engineer with the knowledge of the OSO PPEM.

Control of TFRs. The TDRS PPEM shall collect TFRs, distribute copies, and summarize data in accordance with program requirements. Control points shall be established in each TDRS organization having engineering, manufacturing, test, and/or operation responsibility to assure accurate completion and distribution of TFRs. The TDRS PPEM has overall responsibility for TFR accountability.

Failure Review Board (FRB). Failure Review Board meetings shall be held regularly to review all outstanding failure reports, assure corrective action, and review closeout status. The Board shall review the timeliness, accuracy, and completeness of failure reports. It shall assure that the exact cause of failure is determined, that proper analyses are being conducted, and that corrective action is being taken consistent with TDRSS program requirements. The TDRSS PPEM or his designee shall act as chairman. Other members shall include the cognizant responsible TDRS engineering activity, Systems Engineering, Reliability Engineering, Quality Engineering, and a NASA/GSFC representative. Test Engineers, Design Engineers, and Components and Materials Specialists shall participate as required to adequately review the failures under consideration.

3.4.2.8 Standardization of Design Practices

TDRSS Subcontractor specifications, standards, and drawing practices shall be reviewed by Hughes specialists in the areas of components and materials, reliability engineering, and engineering design to assure that each is compatible with TDRSS reliability program requirements. The TDRS PPEM shall be responsible for this review. Procurement specifications and/or work statements shall define and specify the level of drawings required.

Hughes standard design practices, and parts, materials, and processes specifications and procedures shall be reviewed by the TDRS PPEM to assure their conformance with TDRSS program requirements to the extent described herein.

3.4.2.9 Equipment Logs

Equipment logs shall be maintained for each control item beginning with the first functional testing of that item and ending with the integration of that control item on the spacecraft. Beginning with TDRS spacecraft integration and assembly, a TDRS spacecraft equipment log shall be maintained. Should a control item be required to be removed from the spacecraft, a copy of the spacecraft equipment log covering the period of time that control item was on the spacecraft shall be included with the control item equipment log.

Log entries shall be in chronological order and shall account for all periods of time. The entries in these logs shall in no way subvert information from QCHRs. The equipment logs shall be available for NASA/GSFC review, and shall be delivered to NASA/GSFC when the TDRS spacecraft is shipped to the launch site. A separate log shall be maintained during the launch operations phase. Entries shall be consistent with requirements of paragraph 3.10 of NHB 5300.4(1A) and shall include the following data:

- Nomenclature, part number, and serial number of the unit or subsystem
- Date and time of the event
- Brief description of event
- Description of unusual occurrence, operational or handling problems, or other pertinent situations
- Failure report number or Quality Control History Record that documents the details of inspection or test discrepancies
- Cumulative operating time or cycles if appropriate

Hughes shall similarly be responsible for assuring the maintenance and delivery of the experiment log books covering the period that the experiments are at Hughes.

3.4.2.10 Documentation and Reporting

TDRS reliability activities will be documented in data summary reports, analysis reports, and contractually required documentation. Copies of all documentation, except engineering notebooks, shall be maintained in a program central file and shall be available for review by NASA/GSFC.

Summaries of the TDRS reliability program status shall be submitted in the monthly program progress report. Included in the monthly reports shall be schedule conformance, organizational changes, current status of and revisions to numerical reliability, summary of reliability program task status, failure reporting and corrective action summaries, design review action item summary, and descriptions of any problems or

significant information regarding other aspects of the reliability program and its implementation.

3.4.2.11 Testing and Reliability Evaluation

The TDRS Reliability program element includes the tasks of test plan and procedure approval, test monitoring, failure mode prediction analysis, and reliability assurance relating to unit/subsystem and spacecraft levels of test. The purpose of the test program shall be to substantiate the design and to demonstrate that the TDRSS spacecraft shall survive all handling and assembly operations, prelaunch, launch, and orbital conditions in the space environment.

TDRS Reliability Engineering will furnish inputs to and review and approve test plans and procedures for use in the testing of equipment under environmental conditions. Review and approval of the test plans and procedures shall be concerned with assuring inclusion of appropriate performance limits on all parameters measured, data acquisition procedures (e. g. , operating time/cycles), provisions for failure reporting, analysis, and correction; verification of key performance parameters; and definitions of success and failure, for which applicable criteria concerning failure modes predicted by analysis shall be established to define critical environments, levels of severity, and duration of exposure. These criteria shall specify in particular those environments and levels considered to be critical (induce failures or overstress parts).

TDRS testing and test data shall be evaluated by TDRS Reliability Engineers. The results of these tests shall be compared with analytical prediction. If the results of these tests are applicable and statistically significant, they shall be used in the analytical prediction.

3.4.2.12 TDRS Definition of Terms

- 1) Assembly – A functional subdivision of a unit consisting of parts or subassemblies that perform functions necessary for the operation of the unit as a whole. Examples: regulator assembly, power amplifier assembly, gyro assembly, etc.
- 2) Component – An element of a unit, assembly, or subassembly not normally subject to further subdivision or disassembly without destruction of designed use; synonymous with "part."
- 3) Control Item – An end item or significant portion thereof identified for purposes of Hughes management and control. A control item usually is a separate item of installation and replacement and is capable of individual testing.
- 4) Degradation – The deterioration of quality or ability to perform within established limits.

- 50
- 5) Failure Analysis – The study of a specific failure to determine the circumstances causing the failure and to arrive at a course of corrective action that shall prevent its recurrence.
 - 6) Failure Criticality Analysis – The study of the potential failures that might occur in any part of a space system in relation to other parts of the system to determine the severity of the effect of each failure in terms of a probable resultant safety hazard, unacceptable degradation of performance, or loss of mission of a space system.
 - 7) Failure Effect Analysis – Study of the potential failures that might occur in any part of a space system to determine the probable effect of each on all other parts of the system and on probable mission success.
 - 8) Failure Mode Analysis – The study of a space system and working interrelationships of the parts thereof under various anticipated conditions of operation (normal and abnormal) to determine probable locations and mechanisms by which failures will occur.
 - 9) Functional Test – A test performed to demonstrate that the article operates as required.
 - 10) Malfunction – Any operation of equipment outside the limits of specified requirements.
 - 11) Part – An element of a unit, assembly, or subassembly not normally subject to further subdivision or disassembly without destruction of designed use; synonymous with "component."
 - 12) Spacecraft – The TDRS.
 - 13) Subassembly – An assembly within a larger assembly. Examples: wired printed circuit boards, modules, etc.
 - 14) Subsystem – A self-contained combination of parts and/or assemblies and/or components performing a function or functions necessary to the operation of the TDRS.
 - 15) Test Performance – The actual performance of a specified test, as well as the documentation of the required data and events, in accordance with the applicable test plan/specifications/procedures.
 - 16) Test Verification – The observation of all portions of a test being performed to assure that the data and events are complete, accurate, and in compliance with the applicable test plans/specifications/procedures.

- 17) Unit – A functional subdivision of a system, generally a self-contained combination of assemblies performing a function necessary for the system's operation. Examples: power supply, transmitter, gyro package, etc.

3.4.2.13 Parts, Materials, and Processes

The TDRSS PPEM shall be responsible for overall planning and technical direction of the parts, materials, and processes program. His responsibility shall include assuring coordination among the TDRS responsible engineering activities, including the REA, the Components and Materials Laboratory, Procurement, and Product Effectiveness (including Quality Assurance) so that program activities shall be carried out and continuity provided through the procurement, design, and manufacturing phases.

Organization and Responsibilities. Reporting directly to the TDRS PPEM shall be a TDRS parts, materials, and processes (PMP) coordinator provided from the Components and Materials Laboratory. He shall provide support and visibility to the program on the status of parts, materials, and processes activities, and the necessary interface with the Hughes Components and Materials Laboratory. The responsibilities of the TDRS PMP coordinator include the following:

- 1) Communicate the TDRS PMP requirements and philosophy to suppliers, support organizations, and the Hughes Components and Materials Laboratory.
- 2) Coordinate and monitor the procurement of parts and materials to assure that procurement problems are resolved.
- 3) Establish direct working interfaces between the parts and materials organizations and design organizations.
- 4) Act as a control point for resolution of policy, problems, and corrective action decisions affecting parts and materials used on the TDRSS program.
- 5) Maintain status awareness of part and material selection.
- 6) Maintain directive documentation relating to TDRS parts and materials.
- 7) Prepare and maintain reports affecting the TDRS PMP program status.

The Hughes Components and Materials Laboratory (CML) shall receive direction from the PPEM. Areas of additional CML support to the TDRSS program include the following:

- 1) Parts and materials application engineering support to the responsible engineering activities

- 2) Support to the TDRS Parts, Materials, and Processes Review Board
- 3) Laboratory investigations to develop new materials and processes
- 4) Preparation and revision of PMP specifications
- 5) Qualification of new parts, materials, and suppliers
- 6) Part correlation sample analysis and failure analysis
- 7) Evaluation of test specimens and special testing as requested by the responsible engineering activities
- 8) Parts, materials, and process applications engineering review and signoff of each production level drawing

Policy and Procedural Documentation and Specifications. Hughes PMP program policies and procedures are described in two Product Effectiveness Handbook documents: PEH 06-0401 for Hughes and PEH 06-0306 for TDRSS subcontractors. Included in these documents are requirements for screening parts, inspection and testing of parts, burn-in, failure analysis, and parts and materials handling and storage. Parts derating requirements are also included through reference to Product Effectiveness Handbook document PEH 06-0201 for Hughes and PEH 06-0305 for subcontractors.

Parts Screening, Testing, and Burn-In. General requirements for quality conformance tests and burn-in are listed in Product Effectiveness Handbook document PEH 06-0401. Since both burn-in time and quality conformance tests vary by individual part type, detail requirements must be obtained from the applicable Hughes 908XXX series part specifications. Table 3-28 summarizes the high reliability parts screening and burn-in requirements by generic part category. A description of the nondestructive tests to be conducted follows:

- 1) 100 percent visual inspection - Visual inspection is required on parts as one method of removing possible defectives. Opaque components are examined externally, and parts with glass or other transparent packages are examined externally and internally before painting. All opaque semiconductors, integrated circuits, and hybrid circuits are examined internally by Hughes Quality Source Inspectors prior to the final sealing of the package. Acceptance criteria are specified for each part type. Rejected parts are removed.

TABLE 3-28. TDRS HIGH RELIABILITY PARTS SCREENING AND BURN-IN MATRIX

Type of Device ⁽¹⁾	Internal Visual Inspection	High Temperature Storage	Temperature Cycling	Acceleration	Vibration	Seal Tests (Gross and Fine)	X-Ray	Correlation Samples	Noise Test	Minimum Burn-In Typical Test Conditions
Semiconductors ⁽²⁾	X	X	X	X		X	X	X		7 days, rated power ⁽³⁾
Integrated Circuits ⁽²⁾	X	X	X	X		X	X	X		7 days, rated power
Hybrid Circuits ⁽²⁾	X	X	X	X		X	X	X		7 days, rated power
Resistors										
Metal Film			X			X	X			4 days, rated power 498K
Carbon Film									X	4 days, twice rated power, 398K
Power Wirewound			X				X			4 days rated power, 398K, 90 minutes on, 30 minutes off
Precision Wirewound			X				X			4 days rated power, 498K
Capacitors										
Solid Tantalum			X			X	X			4 days, 1.3 to 1.5 times rated voltage, 358K (WEIBULL Plot)
Ceramic NPO			X				X			4 days, 2.0 times rated voltage, 498K
Ceramic K1200			X				X			4 days, 2.0 times rated voltage, 358K
Glass			X			X				2 days, 1500 volts, 398K
Wound Metalized			X				X			4 days, 1.4 times rated voltage, 498K
Magnetic Devices			X				X ⁽⁴⁾			7 days, rated excitation current
Crystals	X		X		X	X				Temperature aged, 30 days 358K
Relays			X		X	X				(5)5000 Cycle operating life

- Notes: (1) All parts also receive visual inspection and temperature cycling.
 (2) Visual inspection before sealing; high temperature storage and acceleration before seal tests and X-ray.
 (3) For some devices this will be an intermittent test of power applied 900 seconds on followed by 300 seconds.
 (4) As appropriate to determine potential defects.
 (5) Determined by cycle time.

- 2) X-ray Inspection - X-ray inspection is required on parts with internal construction that will allow meaningful X-ray examination. Inspection is made with the assistance of image magnification through photographic enlargement, projection, or examination through a microscope. Acceptance criteria for each part type are specified. X-ray specimens must be correlatable to the film image to allow identification of each part to its X-ray image. Rejected parts are segregated from accepted parts.
- 3) Temperature Cycling - Temperature cycling is specified as a prescreening test for detection of mechanical construction defects in parts. A minimum of five complete cycles is specified, with the maximum and minimum storage temperature of the part as the cycling extremes. A minimum of 1800 seconds per cycle at each extreme is specified, with 900 seconds at room temperature between cycles.
- 4) High Temperature Storage - A minimum of 2 days storage at the maximum specified storage temperature of the part is required for semiconductors and microcircuit devices. This procedure has proven to be a great value in stabilizing parametric characteristics.
- 5) Seal Test - A fine and gross leak test is required of hermetically sealed components.
- 6) Acceleration - $294,200 \text{ m/sec}^2$ acceleration in a direction perpendicular to the bond surface is required on semiconductors, except large stud-mounted packages that require $98,070 \text{ m/sec}^2$. This test has proven to be particularly valuable for assuring adequate bonding.
- 7) Noise - Carbon composition resistors are measured for noise, using Method 308 of MIL-STD-202. This test segregates parts and lots with abnormal behavior. Part and lot acceptance criteria are specified.
- 8) Burn-In - After the above prescreening tests, as specified in the applicable procurement specification or source control drawing, parts are placed on burn-in for the minimum period specified. The critical electrical parameters are recorded at specified intervals and data are examined for instability of parameters. Lot rejection criteria, i. e. , percent defective allowable (PDA), are specified for each generic part type. Hughes may elect to extend the burn-in period to further assure stability of parameters and reliability of the parts.

Parts, Materials, and Processes Control Board. A TDRS Parts, Materials, and Processes Control Board shall be established to effect standardization with minimum usage of nonstandard parts, materials, and processes.

The Board shall prepare and maintain the Hughes TDRS Authorized Parts, Materials, and Processes Lists for use by the designers in selecting parts to be used in the spacecraft equipment. Actions and recommendations by the Board shall include the following:

- 1) Obtain agreement with NASA/GSFC and accomplish all necessary coordination on parts and materials to be designated for use in the configuration of the spacecraft equipment.
- 2) Approve refinements and/or revisions to parts and material specifications, describing items selected.
- 3) Exchange information concerning parts and materials, performance requirements, availability, and deficiencies.
- 4) Consider adequacy of suppliers.
- 5) Request the preparation of specifications for procurement purposes.
- 6) Monitor suppliers.
- 7) Assure compatibility of new parts qualification with parts procurement and hardware fabrication needs.

3.4.3 Quality Assurance Program Plan

The provisions herein constitute the basic Quality Assurance Program for Hughes Aircraft Company divisions delivering prototype, flight, and flight spares for spacecraft under NASA Contract. The content and format of this plan are based on NHB 5300.4(1B) "Quality Program Provisions for Aeronautical and Space System Contractors," as modified herein. The Quality Assurance Program complements the reliability and safety functions without duplication of effort. The operations and work of Hughes and of its subcontractors are subject to continuous evaluation, review, and inspection by the cognizant Customer Quality Representative. Reasonable facilities and assistance are provided to support the performance of his duties. Quality program documentation requiring submittal to GSFC, as specified in the contract, will be submitted by the Program Office. Quality program documents, such as process and quality control procedures developed specifically for this contract shall be identified with the program. Other documents, general in nature but applicable to the program, will be obtained in

specifications and drawings developed for the program. Quality procedures applicable to the program will be available for GSFC review.

3.4.3.1 Quality Program Management and Planning

Hughes maintains an effective and timely Quality Program planned and developed in conjunction with all other Hughes functions necessary to satisfy the contract requirements. This program demonstrates recognition of the quality aspects of the contract and an organized approach to achieve them. The program ensures that quality requirements are satisfied throughout all phases of contract performance, including design, manufacture, inspection, test, checkout, packaging, shipping, storage, and flight preparations. The program provides for prompt detection of actual or potential deficiencies, system incompatibility, marginal quality, and trends or conditions which could result in unsatisfactory quality. It also provides for effective corrective action. Objective evidence of quality conformance, including records of inspection and test will be available to the Customer Quality Representative.

Organization. The Hughes Quality Organization is structured in a manner that provides for direct unimpeded access to management and also for responsiveness to the requirements of a specific program. Hughes Management Directives instruct the Quality Assurance Organization in their responsibilities for assuring that the S&CG, divisional, and contractual requirements are fulfilled.

Training. Training and instruction to improve the skills of key personnel is accomplished by each Quality Assurance and Manufacturing Section. Training programs are coordinated with the Personnel Development Section of Industrial Relations. Routine training and retraining is required when new processes or assembly techniques are introduced and when inspection and test results or internal audit reports indicate the possibility of deterioration in job performance.

Certification of Personnel. Hughes personnel responsible for controlling special processes are certified as required by Government and/or Hughes specifications. Certification of personnel for processes such as welding, soldering, radiography, magnetic particle, and dye penetrant includes training followed by a testing procedure. Personnel unable to meet the certification requirements are not permitted to perform the operations involved. These personnel are provided additional training prior to retesting. Inspection personnel need not be as proficient as the actual operator; their certification assures a familiarity with the requirements that must be met in order that the process is properly accomplished.

Recertification of Personnel. Results of inspections and quality audits are used as indicators of the need for additional training and recertification prior to the normal certification period expiration.

Records. Records are maintained of all individuals certified. Each person certified is given a dated card or badge as evidence of his certification, which is carried on his person while performing his duties.

Quality Information. Data collection is used to indicate trends in processing, planning, screening, and receiving inspection. Statistical charts are used where they provide effective control over the articles being produced, such as process areas.

Quality Status Reporting. Status reports will be presented to the cognizant GSFC installation on a periodic basis as established in the contract.

Quality Program Audits. Audits of the adequacy of quality procedures, inspections, tests, process controls, and certification are performed on a random unscheduled basis by impartial quality supervisors or quality engineers. The audits include notification of required corrective action, and follow-up to assess results. The results of audits are covered by a report to appropriate management. Action is taken by management to ensure effective correction of the reported deficiencies. Reports remain active until corrective action has been completed.

Quality Program Plan. This Quality Program Plan will be maintained throughout the life of this program. It defines the program requirements and will be revised as necessary to reflect program changes. Implementation of this Quality Plan will not be limited to those procedures listed where more detail or internal control is necessary. Hardware flow plans will be developed for major subsystems to assure adequate quality control. These plans depict key inspection operations with acceptance-rejection criteria. A separate Quality Plan or a plan with separate parts will be prepared for locations where any difference in operations from this plan may be required.

3.4.3.2 Design and Development Controls

Technical Documents. The Engineering Data Department develops Engineering Procedures (EPs). These procedures implement appropriate Company engineering policies and practices and provide group-wide uniformity.

Quality Assurance participates in Design Reviews, operates the Quality Change Control Group and the Quality Data Center, screens planning, and has a member on the Engineering Change Control Board. These participating quality activities prevent document deficiencies from being incorporated into the product. Engineering Data Control, has the responsibility for the review and checking of engineering documents prior to release. Quality assures through the previously mentioned activities that engineering is following standard Company practices and procedures. Engineering Change Requests (ECR) are generated to document and correct any deficiencies.

Quality Support to Design Reviews. Quality Assurance participates in Design Reviews at the control item level. Design review activities include evaluation of documented quality requirements, incorporation of processes, and consideration of inspection-type characteristics.

To assure that quality requirements specific to program needs are assessed, a specific detailed check sheet is used for each Design Review meeting. These checklists include items such as: new materials are approved, units can be adequately inspected, new training required, new inspection equipment required, equipment is manufacturable/maintainable/interchangeable, clarity of information, etc.

Change Control. The Engineering Data Control Department controls the release of and change to engineering requirements in accordance with appropriate EPs and the Configuration Management Plan. Released engineering is distributed to Document Control Centers, where it is readily available to manufacturing, test, and inspection personnel. Upon receipt of the released engineering, the following actions occur:

Planning documents are written by the Manufacturing Department to reflect the released engineering. All planning documents are submitted to the Quality Assurance planning screener, who verifies the proper incorporation of drawing and quality requirements.

Those engineering releases that affect procured hardware are reflected in the procurement documents. All procurement documents are submitted to the Quality Assurance procurement document screener, who verifies the proper incorporation of quality requirements.

Quality Assurance Engineering reviews all released engineering for effect on quality procedures and flow plans. Those affected documents are revised as required.

The Quality Assurance Change Control Group also receives a copy of each item of released engineering by direct distribution from the Engineering Data Control Point. All changes are reviewed, and a change verification copy of the document is forwarded to the cognizant Quality Assurance Group, who verifies the proper incorporation of the change at the required point of effectivity. The verified copies are returned to the Quality Assurance Change Control Group and retained on file for use by program configuration management.

To ensure that each item of prototype, flight, and flight spares hardware conforms to its "as designed" configuration, the Configuration Control System (CCS) is used. This system provides a shorthand method for identifying the total configuration of each complex item of hardware. It provides for a tabular listing on the CCS form of each pertinent drawing, with its respective change status, affecting the hardware as well as the drawing number and latest release engineering change status on each major subassembly of the item. The CCS is then assigned the number of the starting effectivity point. This CCS number is then appended through use of a standard coding that provides for scattered effectivities and multiple changes. CCS files are maintained by Quality Assurance in the responsible hardware manufacturing area. When final inspection is performed on an item prior to entry into bonded stores, verification of its correct configuration to latest design requirements is made.

A duplicate file is maintained in the spacecraft buildup and shipping area. Control items delivered to the area for installation on the spacecraft and again just prior to shipment have their CCS number checked against the CCS file to again verify that they are of the proper configuration. Copies of all CCS changes are sent to Quality Assurance supervision in the hardware manufacturing areas and the spacecraft area. Completed items that do not have the change incorporated will be documented as discrepant. Discrepancies will be resolved.

3. 4. 3. 3 Identification and Data Retrieval

EPs are developed by the Engineering Data Department, defining engineering policies, practices, and responsibilities throughout the S&CG.

Identification Methods. EPs in the EP-2-X series define the system controls, criteria, and assignments for identification. Parts, materials, and items are also identified and controlled by one or more of the following methods:

- 1) Date codes when age control is necessary
- 2) Lot numbers or work order numbers when items are produced or processed in homogeneous groups
- 3) Serial numbers when individual control or data is required
- 4) Other identification such as tags, labels, paint dots, or containers as approved.

Documentation. Technical documents detail method and location for identification. Hughes Process documents (HPs) (series HP8-X) define the method of applying the identification. Quality Assurance assures that the identification is located, applied, and maintained as specified in applicable technical documents.

Identification Control. A traceability documentation system is maintained/monitored by Quality Assurance. The system permits, at any point during the manufacturing cycle, the tracing of assemblies, items, or parts back to their procurement or manufacturing document and forward to like items within a level of process or assembly.

All prototype and flight parts, materials, and items manufactured or purchased specifically for TDRSS will be identified in accordance with Section 4. 4. 2 and will reflect its program identifications, end-item use, and inspection status.

Traceability and identification are required on prototype and flight program parts and high reliability parts and materials. Traceability and identification are maintained up to and including the subsystem level. While

traceability is not applicable to common stock items, this in no way implies any reduction in the inspections/tests required for acceptance.

Identification List. EPs describe the use, scheduling, identification, format, content, and processing of the Master Index (MI). The MI is a listing of this equipment, end items, and other control items required.

Retrieval of Records. All records pertaining to procured articles and material, fabrication, processing, inspection, and test activity are related to the items assigned identification and are readily retrievable.

3. 4. 3. 4 Procurement Controls

Hughes assumes the responsibility for the adequacy and quality of materials, articles, and services procured for this program.

Selection of Contractor Procurement Sources. Procurement will be from sources on the Company's master list of qualified suppliers in the Supplier Directory or Unique Suppliers Lists per Hughes Aircraft Quality Practice Manual (QPM).

Quality Engineering participates during supplier survey operations, and source selection.

Surveys, conducted in accordance with Hughes Supplier Control System are required for those suppliers not already approved. Suppliers may be resurveyed when conditions arise that may invalidate a previous survey, such as deficiencies in materials received. Survey reports are maintained and available to the Customer upon request. Quality Control maintains records necessary for establishing and maintaining a quality history for each subcontractor and supplier in accordance with Hughes standard evaluation and rating procedure.

Preprocurement evaluations are conducted on potential suppliers of complex or critical items by Quality Control when directed by the Materiel Department.

Commercial equipment not designed/fabricated specifically for this program need not be procured from suppliers listed in the Supplier Directory or Unique Suppliers Lists provided they are thoroughly inspected/tested upon receipt to applicable technical documents.

Procurement Documents. All purchase orders issued are screened by Quality Control to assure compliance with the requirements listed below, and that the supplier is listed in the Supplier Directory or Unique Suppliers Lists.

Work Authorization and Delegation (WAD) documents used for intracompany suppliers are screened to assure inclusion of applicable Quality Program requirements.

Procurement documents contain provisions for the following:

- 1) Subcontracts for systems, subsystems, and related services will contain all or applicable requirements of this Quality Program Plan. Purchase Orders for materials, parts, and related services will include the appropriate Hughes Quality Attachment (Q-4 series) in accordance with QPM.
- 2) Latest applicable revision of the drawings, engineering order, specifications inspection/test instructions, reliability and quality requirements, and special inspection and/or test equipment if required.
- 3) The following detailed Quality Plan requirements are also included in procurement documents, as necessary.
 - a) Suppliers having design cognizance will be required to obtain Hughes TDRS Program Office approval of any design change made after their product has passed qualification test. The supplier will appropriately identify any item in this category.
 - b) Purchased raw materials will be accompanied by a physical and/or chemical report of analyses on tests conducted to assure conformance to the specifications.
 - c) The supplier will be notified that he is responsible for maintaining records of the test conducted on his raw materials showing their acceptability, and these records must be made available to the Hughes or the cognizant Government Source Inspector upon request.
 - d) Necessary identification, special preservation, and packaging to preserve the quality of procured articles will be required.
 - e) Manufacture date and the date when useful life will be expended for items having definite characteristics of quality degradation or drift with age and/or use will be required.
 - f) Parts or material will be identified with part number or designators.
 - g) There will be special requirements concerning product qualification and characteristics to be inspected/tested by the supplier.
 - h) Inspection/test records that are required to verify compliance with purchase order requirements will be identified.

- i) All articles rejected by Hughes and subsequently resubmitted by the supplier will be identified as being resubmitted either on the articles or on the supplier's shipping document. The supplier must reference the Hughes rejection document and supply information as to the corrective action taken.
- j) Hughes Quality Attachment Q-1 for Hughes Source Inspection for those items or suppliers selected by the Quality Assurance Project Engineer and purchase order screener based on supplier's current performance or past history.
- k) If Government Source Inspection is required at the supplier's plant, Hughes Quality Attachment Q-12A will be specified which includes the following statement: "All work on this order is subject to inspection and test by the Government at any time and place. The Government Quality Representative who has been delegated NASA Quality Assurance functions shall be notified immediately upon receipt of this order. The Government representative shall also be notified 48 hours in advance of the time articles or materials are ready for inspection or test.
- l) If Government source inspection is not required, the following statement will be included: "The Government reserves the right to inspect any or all of the work included in this order at the supplier's plant. "
- m) Subcontracts under which hand-soldering will be performed will invoke the requirements of NHB 5300.4(3A) and visual inspection magnification of at least seven power (7X).
- n) Equipment records will be prepared and maintained for each component (blackbox), subsystem, and system to document its history. These records will be initiated at the start of assembly and remain at the supplier's facility for the period specified in the contract. The records will contain history on the following:
 - (1) Configuration and traceability
 - (2) Fabrication and assembly history
 - (3) Test and inspection records
 - (4) Cumulative operating time and cycles

An End Item Data Package will be shipped with each end item. The package will include those items specified in the procurement/document package.

Contractor Quality Assurance Personnel at Source. Hughes will utilize source inspection or require objective evidence that the supplier complies in detail with applicable requirements if the following exists:

- 1) Articles are at a level of assembly that precludes inspection at Hughes
- 2) Verification tests at Hughes are destructive in nature.
- 3) Special test equipment or environment required is available only at the supplier's.
- 4) Past performance or quality history have been marginal.
- 5) Qualification testing will be performed by the supplier.
- 6) Items are designated for direct shipment from source to a Government facility or using site.

Government Source Inspection. Government source inspection for those items specified by the procuring GSFC installation or its resident Government inspection agency at Hughes, shall be required on Hughes procurement documents. The applicable attachment is Q-12A.

Receiving Inspection System. Receiving inspection is performed on all incoming parts and materials to ensure the following:

- 1) Inspection and tests performed by the supplier were in accordance with purchase requirements. Inspection and test data have accompanied the item as required.
- 2) Items/material or records indicate evidence of source inspection, as required.
- 3) Those characteristics not Hughes source inspected will be verified in accordance with applicable drawings, specifications, Hughes processes, or vendor catalogs. The degree and quantity of inspections performed will be consistent with the critical nature of the article or from records of previous inspections and the quality history of the article. Where sampling is used, it will conform to the requirements of Section 4.12 of this document.
- 4) Periodic disassembly will be performed when detailed verification of characteristics is required.
- 5) Article and materials are identified and related records are complete.

- 6) Receiving Inspection has the necessary inspection and test equipment, drawings, specifications, catalogs, Hughes Process Specifications, etc. , available in order to perform its operation upon receipt of the item. Where the cost of certain inspection or test equipment is prohibitive, Hughes will verify the item's quality at the supplier's facility.
- 7) The incoming items having shelf life characteristics will bear the manufacturing and expiration dates. The useful life will be specified in the Aerospace Group Shelf Life Manual. Items subject to cycle deterioration will have a record of previous cycles expended and the useful cycles remaining.
- 8) When engineering or procurement documents require test specimens to be supplied with purchased items, these specimens will receive chemical and physical test. (Chemical tests are with regard to the molecular/atomic species comprising the material and physical tests and include the thermal conductivity, density, thermal coefficients of expansion, etc. Mechanical (physical) tests are those pertaining to the material responsiveness to mechanical loads.)
- 9) Raw materials are periodically chemically and physically analyzed on a random basis and when specified in engineering requirements.
- 10) Quality status is maintained during the receiving operations. Physical separation and identification of items in the following categories are maintained:
 - a) Materials or articles awaiting inspection or test results.
 - b) Conforming materials or articles
 - c) Rejected material or articles
- 11) Articles and materials and their records indicate acceptance or nonconformance when released from receiving inspection and test.
- 12) Articles and material released from receiving inspection and tests are adequately protected for subsequent handling, storage, or use.

Receiving Records. Receiving Inspection and Test maintains records for articles and material to indicate, as a minimum, date of receipt, accomplishment of applicable requirements (items 1 through 12 above), results of inspection and tests performed, instructions utilized, acceptance or rejection with associated records, and copies of pertinent supplier documents received.

Supplier Rating System. A supplier rating system is maintained that is based on inspection/test results of purchased materials or services. Suppliers may be resurveyed when conditions arise that may invalidate a previous survey, such as deficiencies in materials received, or when requested by Material Control or Hughes Quality Assurance Management.

Coordination of Contractor-Supplier Inspection and Tests. Hughes Receiving Quality organizations maintain coordination of inspections and tests with suppliers' inspection and tests for compatibility on received end items.

Nonconformance Information Feedback. A deficiency feedback system to suppliers of material that is found defective during any phase of inspection, test, assembly, or use is maintained.

4. SUBSYSTEM DESIGN

4.1 TELECOMMUNICATIONS SERVICE SYSTEM

4.1.1 Requirements

The requirements for the telecommunications service system are presented in Section 3.1 of Volume 4. The general requirements as they apply to the TDRS communication subsystem summarized in Table 4-1. In addition to these, two other transmitter requirements have been derived in the analysis of Volume 4: 1) to allow voice communication at S band with a manned spacecraft which has an omnidirectional antenna, a TDRS EIRP of 47 dBw is required and 2) the ground link requires a saturation EIRP at K band of 51 dBw.

TABLE 4-1. TDRS COMMUNICATION SUBSYSTEM REQUIREMENTS

LOW DATA RATE SERVICE	
Forward link	
1) User command EIRP	30 dBw
2) Voice EIRP	30 dBw
Return link	
1) G/T	-16 dB/K within conical coverage of 26 degrees
2) Linear amplification	
3) Separation of orthogonal linear polarized signal	
MEDIUM DATA RATE SERVICE	
Forward link EIRP at S band	41 dBw
Return link G/T at S band	2 dB/K
GENERAL	
1) Repeater shall be of the frequency translation type	
2) Coherent frequency translations	
3) Order wire capability	
4) S Band ranging transponder	

The telecommunications system design has been described and discussed in subsections 3.4 of Volume 4, where each transmitter and receiver is discussed separately. The material presented here is for completeness of this volume. The TDRS repeater has been designed not only to satisfy all of the statement of work requirements, but also to allow two way voice and/or data communication with the Space Shuttle. The communication subsystem interfaces with the ground station at K band and with the users, both in the VHF/UHF bands and at S band. The K band interface to the ground station has four individual uplink channels and five individual downlink channels.

The LDR service employs both UHF and VHF bands at 400.5 to 401.5 and 136 to 138 MHz. The TDRS VHF/UHF subsystem transmits voice and commands at UHF. The reception from the user occurs at VHF. Up to 20 users' signals are simultaneously amplified through the VHF receiver. Further, the VHF antenna resolves the incoming signals into vertical and horizontal components which are amplified separately.

The TDRS MDR service, an S band system, transmits within the 2035 to 2120 MHz band. A single user is serviced by the S band transmitter and receiver. The receiver operates in the 2200 to 2300 MHz band. Both the transmitter and receiver may be tuned in 1 MHz steps, and each has a .10 MHz bandwidth. Thus, the S band system is capable of operating at any frequency within the assigned frequency bands and in effect provides a "bent-pipe" type of system. In addition to the S band transmitter and receiver for data transmission and reception, there is an S band "order-wire" receiver. The order wire receiver uses an earth coverage antenna and is capable of receiving from any user in near-earth orbit. The purpose of the order wire receiver is to provide an "always available" channel from a manned spacecraft through the TDRS to the ground station, for requesting MDR service.

Voice capability is provided by either of two transmitters: The UHF and the S band transmitter. Each is utilized on a push-to-talk basis to conserve TDRS battery power. Only one voice channel is used at a time.

A telemetry and command channel is provided by the main K band communication subsystem links. Backup telemetry and command service is provided by VHF links. The two VHF telemetry receivers are on continuously, while only one of the K band receivers is on at a given time.

Although the communication subsystem includes the antennas, their design is greatly influenced by deployment techniques and storage requirements. The details of antenna design are discussed in subsection 3.4.3. The following discussion primarily treats the repeater electronic design.

EIRP is the sum of RF power and antenna gain; thus, antennas must be selected before transmitters can be designed. The selection of the MDR S band antennas and return ground link K band antenna is discussed above in subsections 2.3.3.2 and 2.3.3.3. The S band order-wire antenna size was chosen to provide broad coverage but sufficient gain without severely impacting the weight and mechanical design of the spacecraft. The VHF antenna

size was chosen to provide the required coverage and G/T and to fit into the volume available for storage. The UHF antenna size was chosen to provide the required coverage for forward link command and voice. The two redundant K band receiving horns were chosen to allow broad northern hemisphere coverage and uplink reliability with low mass. The antenna parameters are summarized in Table 4-2.

Preliminary calculations determined the transmission losses, and the EIRP requirement and antenna gains of Table 4-2, together with these losses, determined the required transmitter power amplifier output. The determination of these power levels is summarized in Tables 4-3 through 4-5 for the UHF, S band, and K band transmitters, respectively. The required power of Table 4-3 must be doubled when both voice and command are transmitted. The RF power requirements are summarized in Table 4-6.

TABLE 4-2. TDRS ANTENNA PARAMETERS

Link	Antenna Frequency, MHz	Antenna Diameter, meters	Minimum Antenna Gain, dB
LDR forward	UHF	1.43	12.5
LDR return	VHF	3.82	11.8
MDR forward	S band	3.82	36.0
MDR return	S band	3.82	36.6
Order wire	S band	0.267	13.1
TDRS/ground	K band	1.43	44.0
Ground/TDRS	K band	Horns	18.5

TABLE 4-3. UHF EIRP FOR LOW POWER MODE - COMMAND ONLY

Antenna gain	12.5 dB
Cable (20 feet) and connectors loss	-0.44 dB
Hybrid loss	-0.16 dB
Low pass filter loss	-0.4 dB
Required RF power (summer output)	18.5 dBw (71 watts)
EIRP	30.0 dBw

TABLE 4-4. S BAND EIRP

	Low Power	High Power
Antenna gain, dB	36.0	36.0
Cable loss, dB	-1.2	-1.2
Diplexer loss, dB	-0.8	-0.8
Isolator loss, dB	-0.2	-0.2
Summer loss, dB	--	-0.25
Switch loss, dB	-0.2	--
RF power, minimum, dBw	<u>8.0</u>	<u>13.7</u>
EIRP, dBw	41.4	47.0

TABLE 4-5. K BAND EIRP

Antenna gain	44.0 dB
Waveguide loss	-1.0 dB
Rotary joints loss	-0.5 dB
Switch loss	-0.2 dB
Filter loss	-0.3 dB
Transmitter power	<u>9.0 dBw</u>
	51.0 dBw

The frequency spectra requirements for each link are shown in Figures 4-1 through 4-3. Ground link frequency selections within the allocated bands were somewhat arbitrary, but simplicity of the repeater, and particularly of the frequency synthesizer, was a primary objective. Note that the MDR forward link and return link occupy fixed frequency positions in the K band spectrum. However, the TDRS shifts these spectra

TABLE 4-6. TRANSMITTER POWER REQUIRED

<u>Transmitter</u>	<u>Required Power Amplifier Output, watts</u>
UHF	
Low power mode	71
High power mode	142
S band	
Low power mode	6.3
High power mode	23.5
K band saturation power	8
S band transponder	3.2

appropriately in order to match the user requirements and to provide the bent pipe operation for the medium data rate user. Further, the earth station may transmit at any frequency within the provided 10 MHz bandwidth. Thus, any frequency in the allocated S band may be used.

The order wire receiver provides the capability for any user to request the S band link usage.

The S band transponder provides frequency translation of an S band ranging signal to an S band downlink frequency within an 8 MHz bandwidth.

4.1.2 Repeater Design Description

4.1.2.1 Baseline Configuration

The TDRS communication subsystem repeater configuration is shown in Figure 4-4. The principal units are outlined with dashed lines. Input and output frequencies are in megahertz, and gain values shown on various modules are in decibels.

The ground-to-TDRS links are transmitted and received at K band. The uplink or forward link contains command data on 13,526.75 MHz, a pilot tone beacon on 13,530 MHz, low data rate information on 13,532.5 MHz, and medium data rate information on 13,545 MHz carriers. The receiver antennas are low gain horns. The K band receiver

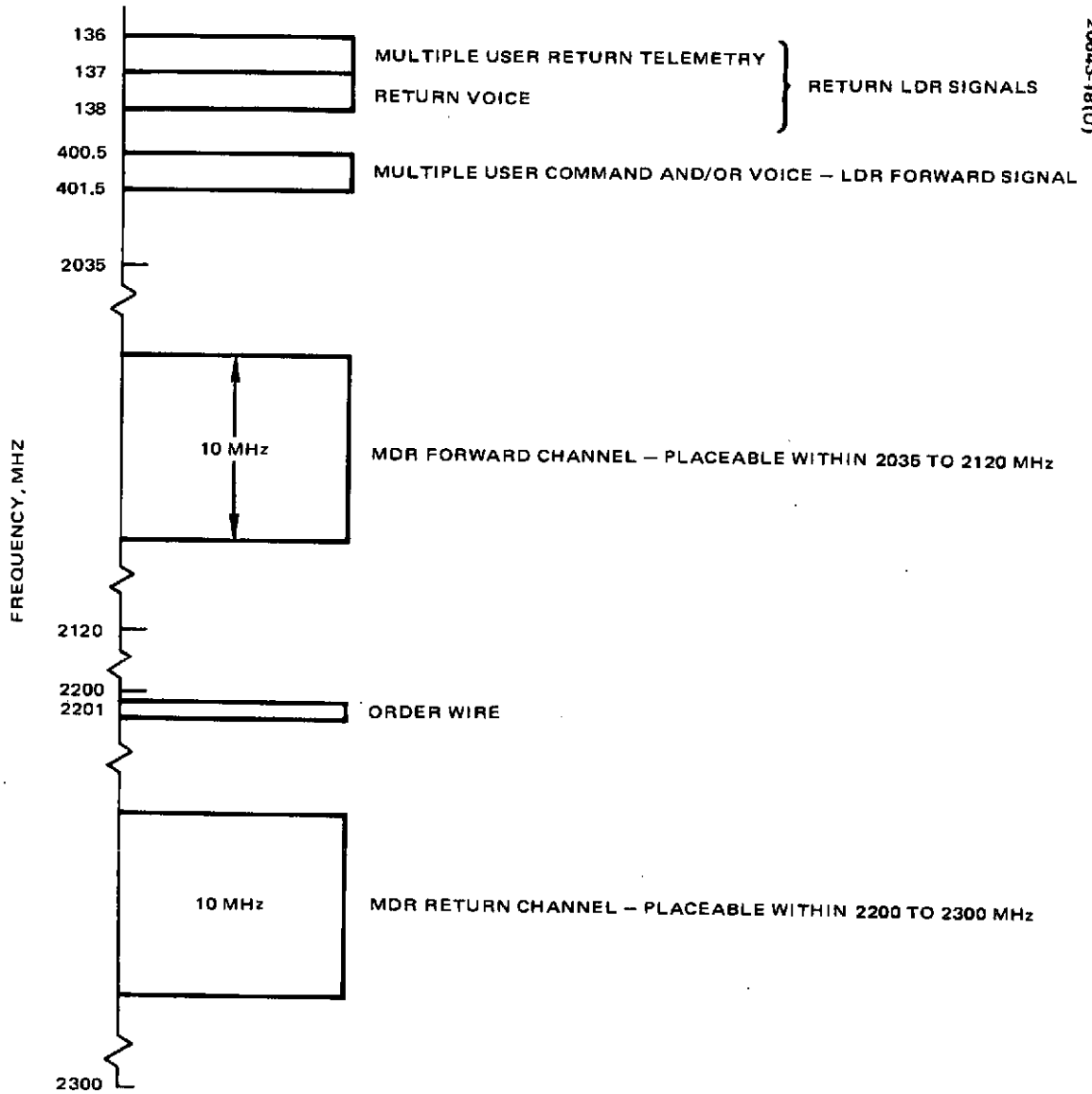
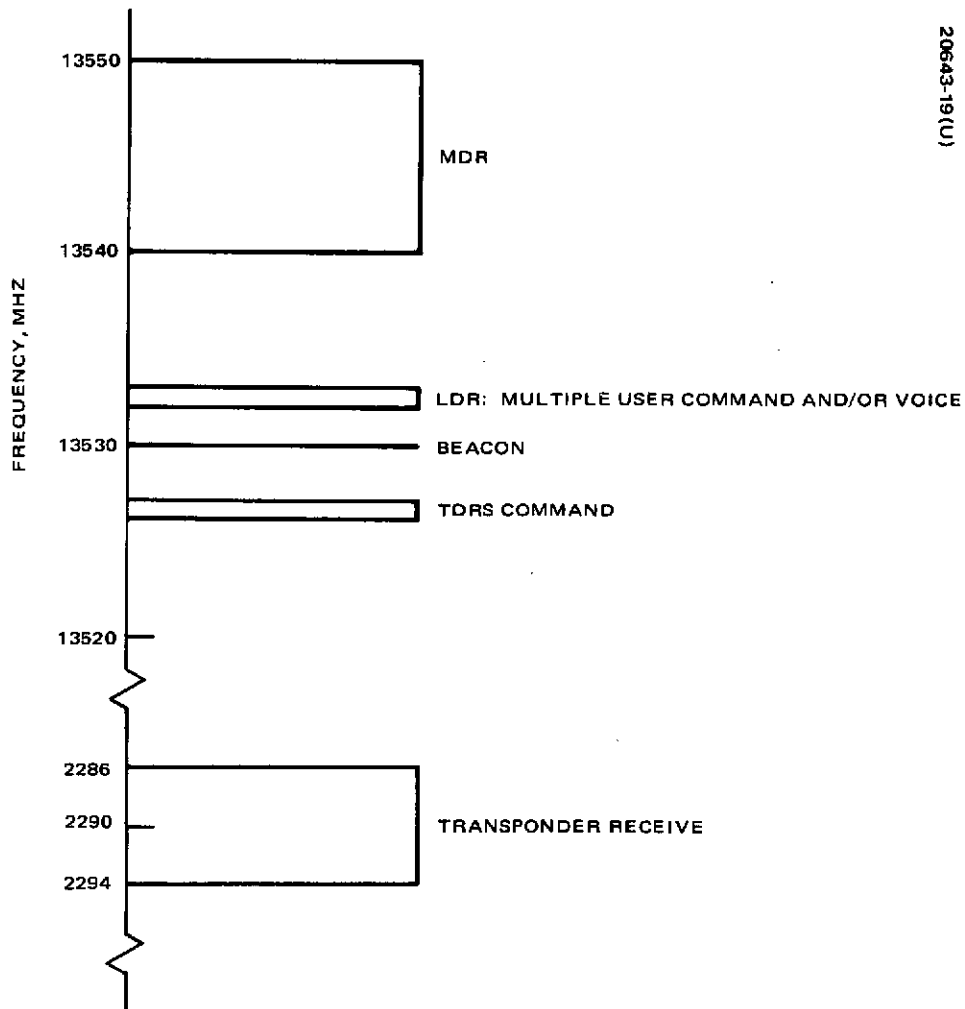


Figure 4-1. TDRS Space Link Spectra



20643-19(U)

Figure 4-2. Forward Ground Link Channels

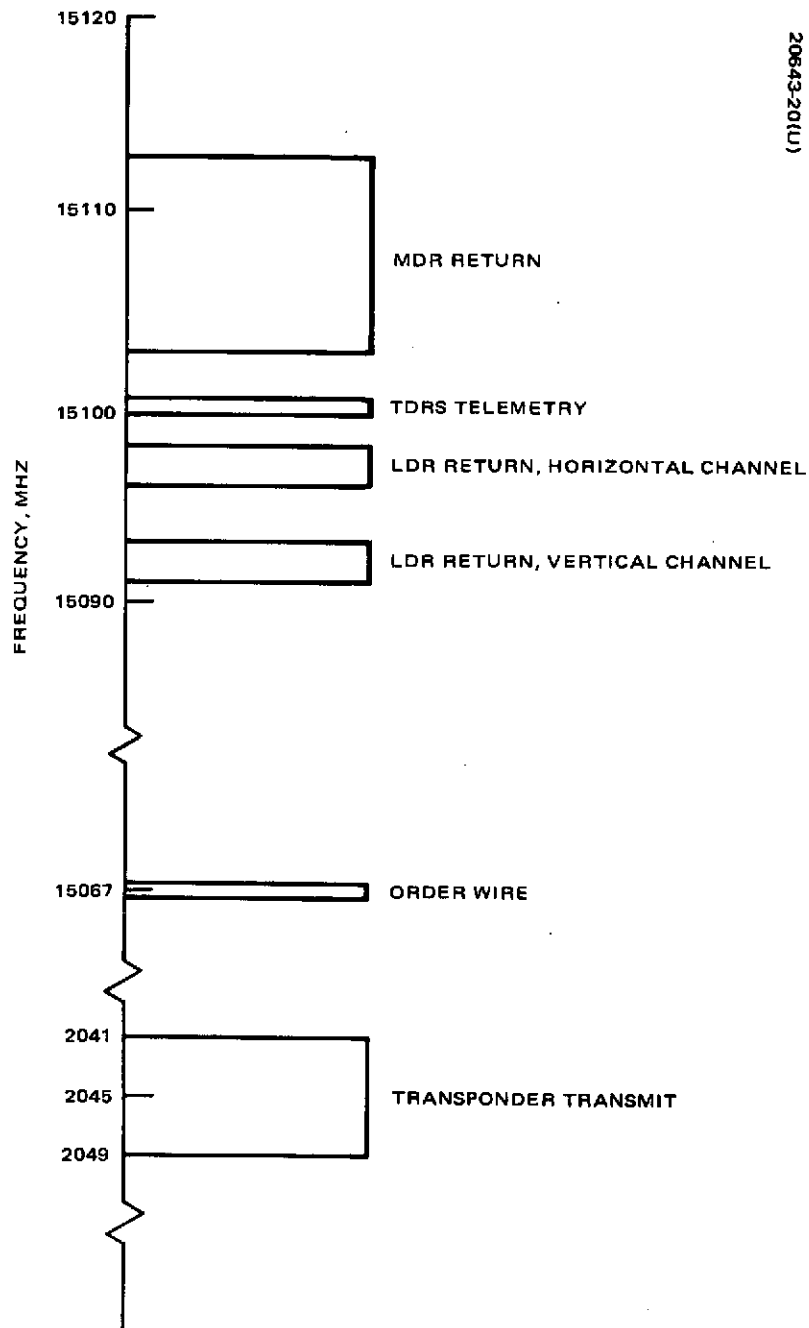


Figure 4-3. Return Ground Link Channels

Page intentionally left blank

shifts all channels to a low IF through a double conversion mixing process. These signals are distributed to the repeater transmitters via a power divider. Every active element is completely redundant in every unit of the repeater.

The output of the six-way power divider supplies the UHF transmitters, the S band transmitter, and the command subsystem. One additional signal, the reference pilot tone signal, is received by the K band receiver which phase locks its local oscillator to this reference. The local oscillator signal then drives the frequency synthesizer to provide coherent translation of all frequencies within the communication subsystem.

The received signals from the VHF receivers, the S band receivers, and the S band order wire receivers are each shifted to a unique IF frequency before being summed in the ten-way power summer. The output of the power summer provides the input to the K band transmitters. These signals are linearly processed and transmitted via TWT amplifier to the earth station.

The VHF telemetry receivers are both continuously on during the life of the TDRS. This allows two redundant channels for command and control of the spacecraft in addition to a K band receiver.

In addition to the signals coming from the various receivers on the TDRS, the telemetry and command signals are also routed through the K band transmitters. Receiver characteristics are those of current state of the art equipment except for the K band receiver which has only a nominal noise figure, as sufficient power is available at the ground station.

An S band transponder is provided to receive and return to earth a ranging signal having an 8 MHz bandwidth. This is accomplished using solid state microwave amplifiers. The output power is 8 dBw.

Detailed descriptions of the unit designs are given in the following paragraphs along with parameter summaries for each unit.

4.1.2.2 Frequency Synthesizer, Master Oscillator

The frequency synthesizer provides the necessary conversion frequencies for each of the receivers and transmitters in the TDRS communication subsystem. This requires a total of 12 frequencies to be derived from a stable crystal oscillator reference source. The primary reference source is a 20 MHz voltage controlled oscillator that is phase locked to an incoming pilot tone through the K band receiver. When phase locked to the pilot tone, the reference oscillator becomes a coherent frequency reference source. A secondary or standby reference source is also provided for use when the primary reference source is not phase locked to the incoming pilot tone. The secondary reference source is a quartz crystal master oscillator, temperature controlled to maintain the required stability. The 12 output frequencies are generated by several solid state multiplier chains. Two S band outputs are programmable in 1 MHz steps to provide repeater

flexibility of user spacecraft interface frequencies. This flexibility is accomplished by using a phase locked loop containing a programmable frequency divider that is controllable by command logic. The 20 MHz reference sources are redundant and cross strapped with redundant frequency synthesizers.

A simplified block diagram of the frequency synthesizer is shown in Figure 4-5. The 20 MHz stable source is amplified and then split into two paths. The signal is used to drive a harmonic comb generator as well as inputs for a frequency divider and four-way power splitter. The comb generator consists of a step diode multiplier producing a set of harmonic related spectrum lines. This spectrum is filtered to provide four frequencies which are multiplied, mixed, amplified, and filtered to generate nine of the ten fixed frequency outputs of the frequency synthesizer. The output of the four-way power splitter is used as 1) an offset frequency to mix with the 40 MHz spectrum line to generate the 45 MHz fixed frequency output, 2) the reference frequency for the two phase lock loops after being divided to a lower frequency of 125 kHz, and 3) the inputs to both phase lock loop circuits to produce the S band transmit and receive selectable conversion frequencies and the tenth fixed frequency at 245 MHz.

All of the frequency synthesizer circuitry is straightforward in design. Extensive use of MSI circuits will be made. Frequency divider IC breadboards developed for other space programs are directly applicable for this unit. Compact VCXO modules for the phase lock loop oscillators as required in the frequency synthesizer have been space qualified. Wherever practical, monolithic crystal filters will be used to minimize circuit element mass, such as in the lower IF channel filters.

The dual regulator used for the frequency synthesizer, typical of those used throughout the repeater, is a series dissipative regulator. This regulator design has exhibited excellent in-orbit performance and reliability on the ATS and Intelsat IV satellites. The regulators are designed with discrete component construction; however, the design is adaptable to hybrid microcircuit techniques. All TDRS regulators will have the same basic circuit topology with only small differences in command buffer logic.

In summary, the frequency synthesizer provides 12 different output frequencies that are coherent with the ground transmit frequencies when phase locked to the K band pilot tone frequency. A quartz crystal master oscillator source is used when the phase locked coherent source is inoperative. Two of the 12 output frequencies are S band transmit and receive conversion frequencies that are programmable in 1 MHz steps. The total dc power required of the frequency synthesizer is 7.3 watts at a 24.5 volt bus. The mass of the master oscillator and two frequency synthesizers is 8.23 kg. These parameters are summarized in Table 4-7.

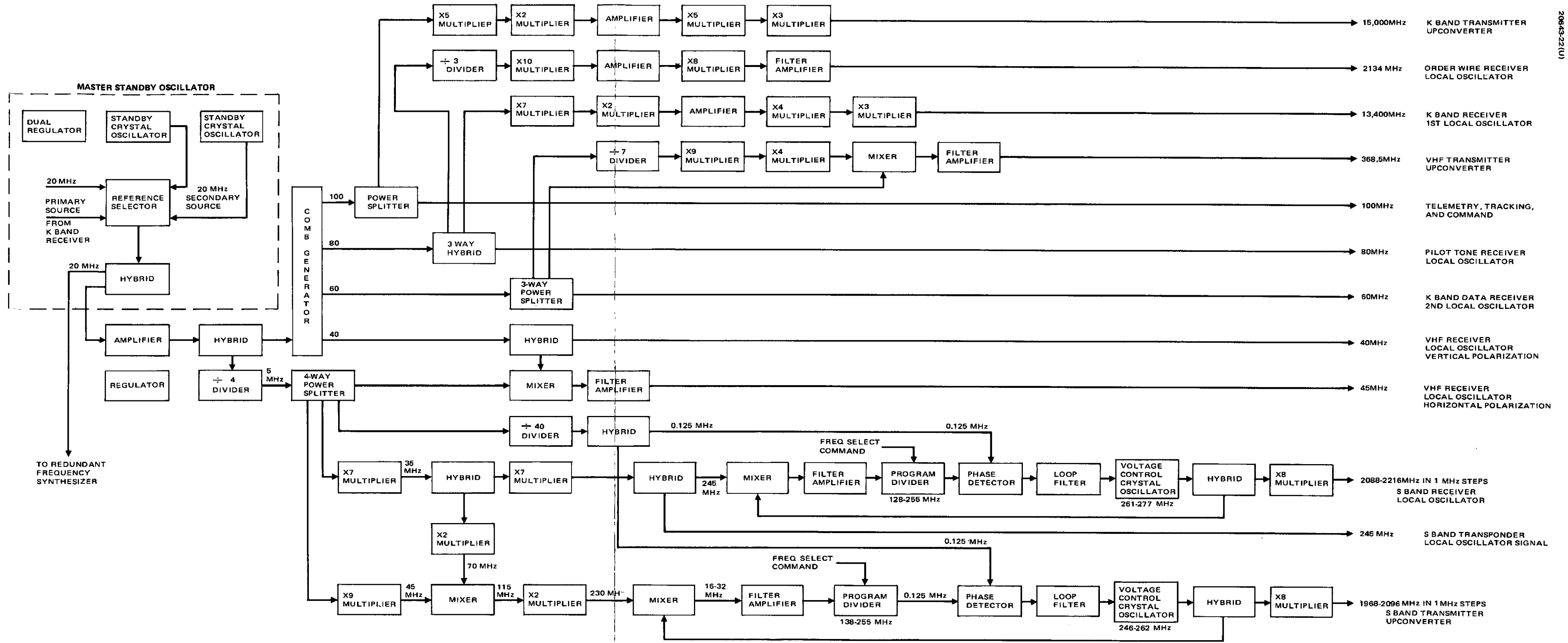


Figure 4-5. Frequency Synthesizer/Master Oscillator

B

C

A

TABLE 4-7. FREQUENCY SYNTHESIZER AND MASTER OSCILLATOR PARAMETERS

Input reference frequency	20 MHz
Output frequencies	15,000 MHz
	2,134 MHz
	13,400 MHz
	368.5 MHz
	100 MHz
	80 MHz
	60 MHz
	40 MHz
	45 MHz
	Stepped 2088 to 2216 MHz
	Stepped 1968 to 2096 MHz
	245 MHz
Input power (at 24.5 volt dc bus)	7.3 watts
Mass (including redundancy)	8.23 kg.

4.1.2.3 K Band Receiver

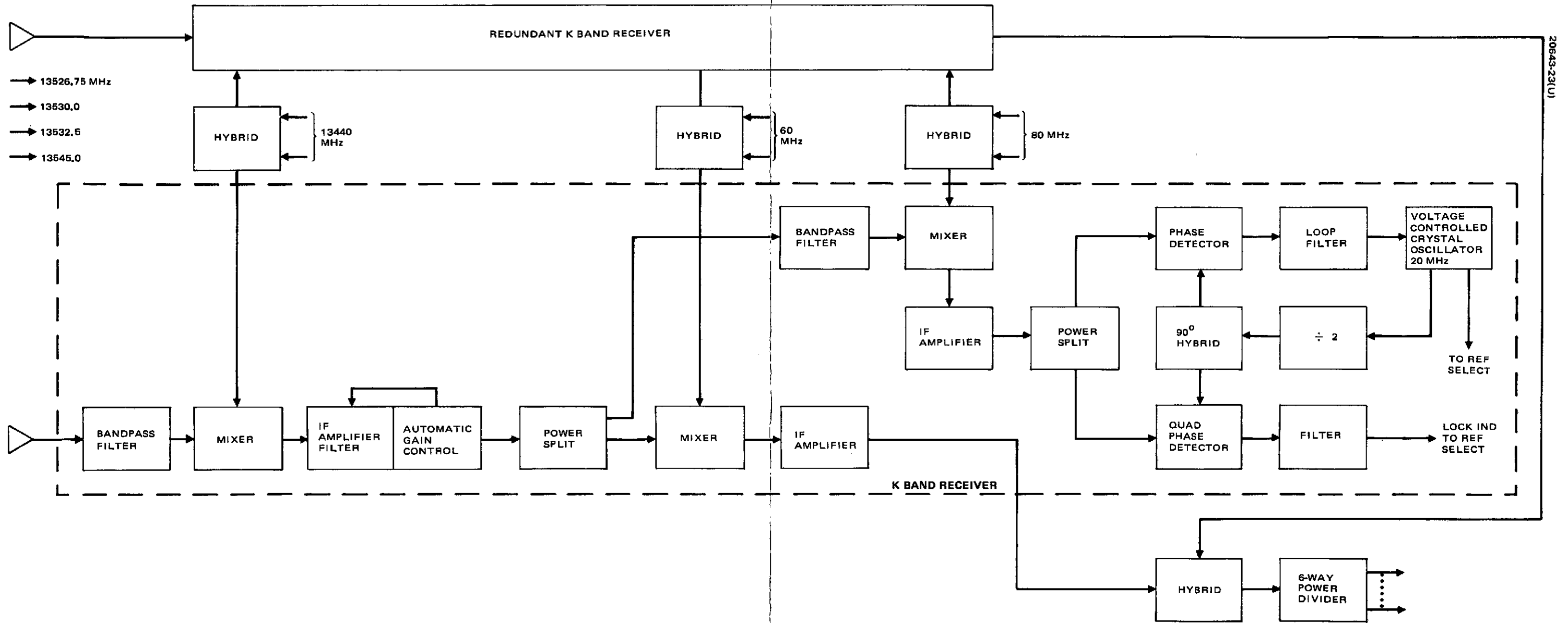
The TDRS K band receiver is designed to satisfy the ground forward link requirements. The forward link contains four channels providing low data rate, medium data rate, beacon, and TDRS command services. The receive frequency band is from 13,526.75 to 13,550.0 MHz. The K band receiver inputs are double-converted to low intermediate frequencies and distributed to various transmitters where they are frequency translated to the proper user link frequencies. A phase lock loop is used in the receiver to establish a stable reference source for the repeater frequency synthesizer. A VCXO is locked to the received beacon pilot tone having a 1 kHz bandwidth. The VCXO becomes the reference source driving the frequency synthesizer when phase locked and provides a coherent signal having the stability of the beacon pilot tone. The receiver also contains a sensor to determine when

the phase detector is locked so that a standby high Q quartz crystal oscillator may be substituted for the synthesizer reference when the loop is not locked, such as during initial acquisition.

The K band receiver block diagram is shown in Figure 4-6. Each redundant receiver is connected to its own horn antenna. The input bandpass filter and mixer provide an overall receiver noise figure of 9 dB or a noise temperature of 2000 K. The first IF amplifier is automatic gain controlled to accommodate the dynamic range of the input signal levels. This IF amplifier provides 50 dB gain over the IF range of 86.75 to 105 MHz. The beacon channel intermediate frequency is selected by a bandpass filter and converted to a 10 MHz reference signal for the VCXO phase lock loop. A quadrature phase detected output provides the lock indication signal needed to operate the reference selector switch in the master oscillator unit. The other three channels are mixed and amplified in a common mixer amplifier module and distributed throughout the repeater through a six-way power divider.

The input filter is a waveguide cavity filter with a 24 MHz 1 dB bandwidth and adequate image frequency rejection at the mixer. The mixer is a balanced mixer with waveguide input and has a 6 dB conversion loss. The local oscillator signals are derived in the frequency synthesizer unit. A 3 dB hybrid combines the two redundant LO frequencies and distributes them to the redundant K band receivers. The first IF amplifier is a multistage broadband transistor amplifier having an overall gain of 50 dB with an LC filter of 24 MHz bandwidth. The amplifier has an AGC circuit providing relatively constant drive to the second mixers over the expected receive signal dynamic range. A 3 dB hybrid splits the output of the first IF to the pilot tone phase lock loop and the command and data mixer amplifier circuits. A narrowband filter selects the pilot tone frequency for conversion to a second IF through a balanced mixer and multistage transistor amplifier having about 50 dB of gain. This provides the stable reference signal for the phase detector of the phase locked loop. The phase locked loop using integrated circuits controls a voltage controlled crystal oscillator to provide a 20 MHz reference signal having a stability equal to that of the received pilot tone frequency. The other output port of the hybrid connects the TDRS command, LDR, and MDR channels to a balanced mixer amplifier where they are converted to IF frequencies between 26 and 50 MHz. The amplifier is a multistage transistor amplifier having 30 dB gain and 24 MHz bandwidth. A 3 dB hybrid combines the redundant receiver outputs to a six-way power divider. This provides three redundant pairs of signals distributed to the TT&C, the LDR UHF transmitter, and the MDR S band transmitter units.

The K band receiver is designed to operate with the predicted input signal levels with high reliability using conventional receiver design techniques. An overall gain of approximately 65 dB is required. The redundant receivers including dual regulators will have a mass of 2.64 kg. The dc power required for each K band receiver is 1.76 watts at 24.5 volt bus voltage. The K band receiver parameters are listed in Table 4-8.



20643-23(U)

Figure 4-6. K Band Receiver

A

B

PRECEDING PAGE BLANK NOT FILMED

TABLE 4-8. K BAND RECEIVER PARAMETERS

Noise figure (noise temperature)	9 dB (2000°K)
Input frequency	13, 526. 35 to 13, 550 MHz
Output frequencies	
VCXO reference	20 MHz
TT&C IF	26. 75 MHz
LDR IF	32. 5 MHz
MDR IF	45 MHz
RF input levels	
Telemetry and beacon	-120 dBw
LDR	-104. 5 dBw
MDR	-101. 3 dBw
Bandwidth	24 MHz
Overall gain	65 dB
Input power (24. 5 volt bus)	1. 76 watts
Mass (including redundancy)	2. 64 kg

4. 1. 2. 4 UHF Transmitter

The UHF transmitter is designed to operate with maximum flexibility in two power modes for transmitting commands to unmanned users and voice to a manned user. The two LDR signals can be sent simultaneously or individually. Code division multiplexing of voice and commands is accomplished by digital multiplexing of the two signals at baseband or IF in the ground station allowing a single RF carrier frequency to be transmitted. Thus, only one common passband and power amplifier is required on the TDRS. However, when both signals are in the UHF forward link channel, the transmitter power is divided equally between the signals, and so more transmitter power is required to maintain link margins equivalent to the case where each signal has its own frequency channel. Doubling the EIRP when both command and voice signals are transmitted effectively provides the 30 dBw EIRP per signal required for the single carrier CDM low data rate channel. The UHF transmitter comprises an upconverter, driver, and

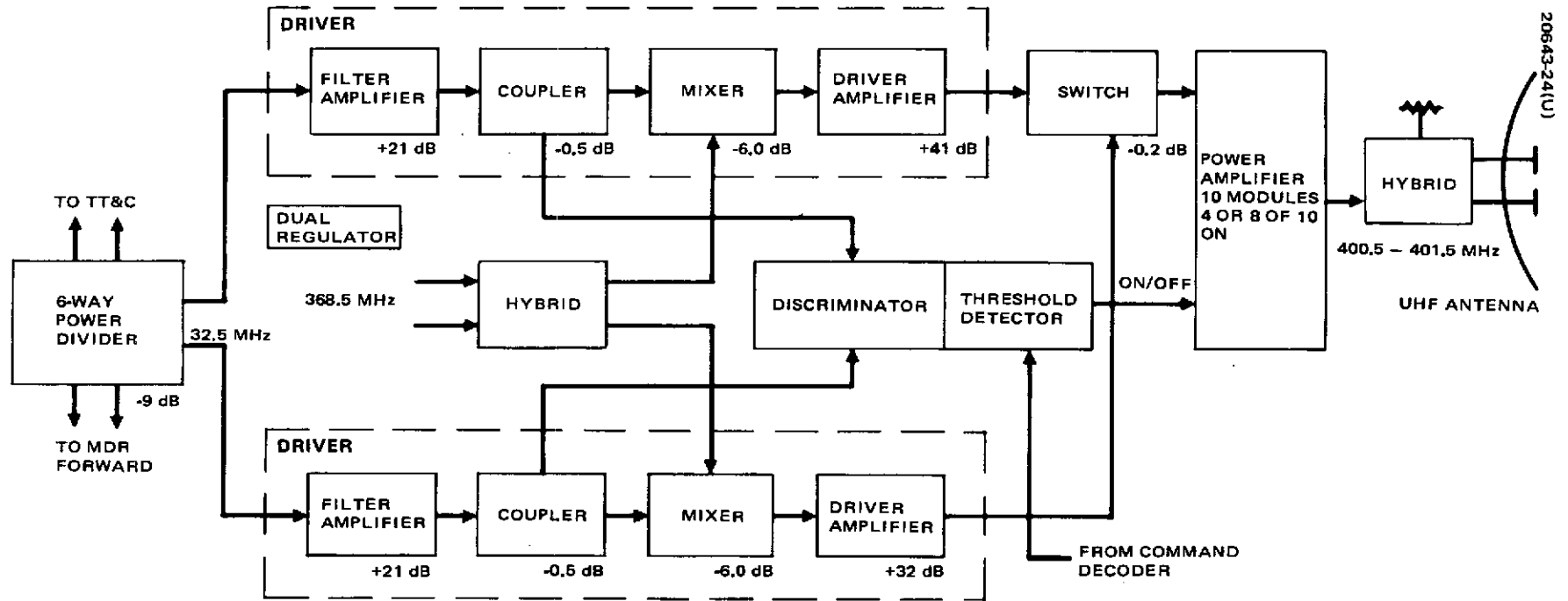


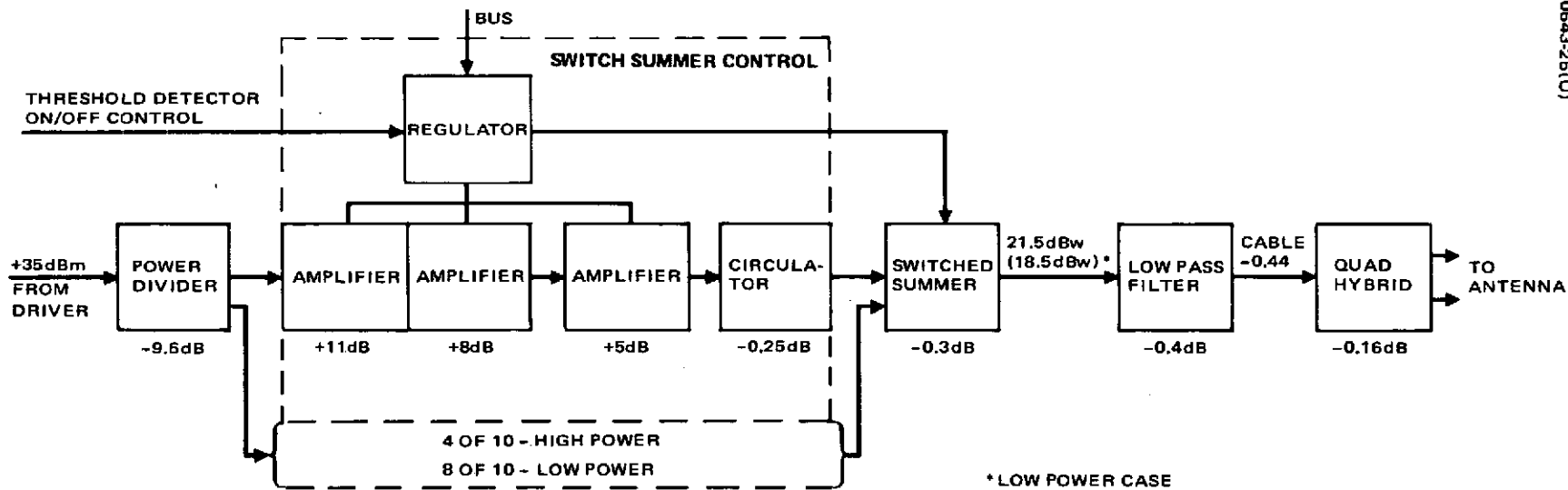
Figure 4-7. UHF Transmitter Driver/Power Amplifier

power amplifier. Figure 4-7 shows the essential modules of the transmitter. This configuration was selected after trade studies of alternate designs for translating the command and voice signals to the UHF power levels required. One alternate, more complex approach processed the command and voice data signals through separate upconverters and power amplifiers which in turn were redundant. Savings in mass and power were prime considerations leading to the selected design. Reliability also improved slightly as a result of the reduced complexity when command and voice signals were combined and redundancy of power amplifiers was reconfigured.

The input to the transmitter driver is a 32.5 MHz low data rate signal at approximately -20 dBm as distributed from the six-way power divider. An input filter amplifier, consisting of an LC bandpass filter of 1 MHz 1 dB bandwidth characteristics, and a multistage transistor amplifier process the signal to a level of approximately 0 dBm at the upconverter mixer input. After upconversion to 401 MHz, the signal is further amplified in a multistage transistor amplifier to provide a +35 dBm signal at the power amplifier input. A coupler preceding the mixer samples the subcarrier and connects it to a discriminator/threshold circuit where the presence of the voice data is sensed. The output of the voice sensing circuit activates additional power amplifier modules by controlling their regulators and the output summer, thus increasing the output power automatically when the voice channel is activated.

The power amplifier design is shown in more detail in Figure 4-8. Although the power amplifier output is considered to be at the summer output, the diagram includes the low pass filter and hybrid as shown with a final output to the vertical and horizontal elements of the UHF circular polarized antenna.

The power amplifier modules are paralleled by power dividing the input and summing the output. The input divider consists of a corporate hybrid ten-way splitter. The summer is a switched Wilkinson summer as used in TACSAT, consisting of quarter wavelength lines with characteristic impedance given by $\sqrt{N} Z_0$, where N is the number of summing ports for which the summer design is optimized. When an amplifier is not being used, the quarterwave line is short circuited by a commandable RF relay switch, thus reflecting an open circuit at the summing point. A switched Wilkinson summer used to combine the eight power amplifiers would have approximately 0.25 dB total insertion loss if optimized to sum eight inputs. When only four inputs are summed, when optimized for eight, an excess summer loss of 0.35 dB results. To obtain equal summer losses for both the high and low power modes, the summer is designed to be optimized for five inputs; the total summer loss will then be 0.3 dB when eight amplifiers are summed, and 0.3 dB when four amplifiers are summed. This will result in the desired 3 dB change in EIRP when converting from the low power to high power mode. The power doubling by doubling the number of amplifiers is thus accomplished using a summer optimized for five inputs. This summer design requires only 0.5 watt more than RF output from each amplifier than a switched summer optimized for eight inputs during the high power configuration.



* LOW POWER CASE

Figure 4-8. UHF Power Amplifier

Each amplifier module is capable of delivering about 20 watts at 401 MHz. This is provided by three cascaded transistor amplifiers. The final power stage uses high Q tuned circuits and a ferrite circulator to provide the high power input to the switched summer at high efficiency. High reliability with a minimum of complexity is achieved by selecting four of ten or eight of ten power amplifier modules to be summed and combined depending upon the mode or commands. The specific power amplifiers to be operated may be determined automatically by the threshold detector or directly through the command decoder and ground command link.

The UHF transmitter output is lowpass filtered to prevent spurious radiation from entering the TDRS receivers. The quadrature hybrid network is part of the RF circuitry associated with the antenna to assure proper element phasing to create circular polarized radiation. The lowpass filter is a coaxial cavity type similar to UHF filters used on TACSAT.

The UHF transmitter is one of the largest power consumers of the communication repeater subsystem and is designed with emphasis on maximum efficiency. The values in Table 4-9 summarize the RF losses, amplifier output, amplifier efficiency, and dc power required to provide a 30 dBm EIRP. The RF losses include the quadrature hybrid (0.16 dB), line losses (0.44 dB), and filter (0.4 dB). The power amplifier output is considered to be at the summer output. The amplifier efficiency shown is the overall efficiency required to provide the necessary output and represents the ratio of dc to RF with allowance for end of life and space environmental degradation of 2.5 percent. The transmitter dc power includes the power amplifier and upconverter driver.

TABLE 4-9. LDR FORWARD LINK UHF POWER SUMMARY

LDR Mode	EIRP, dBw	Antenna Gain, dB	RF Losses	P. A. * Output, dBw	P. A. * Output, watts	η Amp, %	Power Amp dc power 25.5 v bus, watts	Transmitter dc power 25.5 v bus, watts
Voice and Command	33	12.5	1.4	21.5	141.4	51	278	280
Voice or Command	30	12.5	1.4	18.5	70.7	51	139	141

*Summer output.

The UHF transmitter parameters are summarized in Table 4-10. The high power mode is implemented when both voice and data links are transmitted simultaneously; otherwise, the low power mode is used. The output power level is that required at the antenna terminals to provide an EIRP of 30 dBm. The total mass including all elements from the driver input to the antenna terminals is 17.2 kg. The total RF gain from the driver input to the antenna terminals is 67 to 70 dB.

TABLE 4-10. UHF TRANSMITTER PARAMETERS

Output power at the antenna terminal	
High power mode/two links	112 watts
Low power mode/one link	56 watts
Output center frequency	401.0 MHz
Bandwidth	1.0 MHz
Input dc power	
High power mode	280 watts at 25.5 v bus
Low power mode	141 watts at 25.5 v bus
Input center frequency	32.5 MHz
Gain	
High power mode	70 dB
Low power mode	67 dB
Total mass of equipment	17.2 kg

4.1.2.5 VHF Receivers

There are two active VHF receivers. Each receiver has a 2 MHz passband from 136 to 138 MHz, which includes both the user telemetry in the 136 to 137 MHz band and, at times, a voice signal in the 137 to 138 MHz band. The total VHF signal is resolved into two components by the VHF antenna corresponding to orthogonal senses of linear polarization. These two VHF signal components are processed as separate inputs to two active receivers which use different frequency synthesizer outputs in their mixers, thus translating the two components to separate frequency channels: 91 to 93 MHz and 96 to 98 MHz. There is a redundant receiver for each antenna polarization output. Both AGC and step attenuators are provided in each receiver. The AGC maintains a nominal level at the step attenuator input, while the step attenuator provides the ability to change the power mix in the K band transmitter, modifying the transmitted spectrum in accordance with the TDRS communication traffic. The vertical and horizontal polarization components are frequency translated in the TDRS repeater independently and transmitted to earth on separate K band channels.

The receiver input power level, predicted to be between -84 to -96 dBm, is received by the VHF antenna and processed by a conventional receiver having a noise figure of 3.9 dB at the bandpass filter input. The receiver design configuration is shown in the block diagram of Figure 4-9. The 2 MHz BPF is a coaxial filter with a center frequency of 137 MHz. The filter is required to provide 60 dB of rejection at the transmitter frequency and 60 dB of rejection at the image frequency. After filtering, the signal is switched to either of the redundant receivers by an RF switch. A low noise transistor preamplifier and balanced mixer provide the input noise figure of 3.9 dB and adequate gain to drive the mixer. The local oscillator signals, 45 and 40 MHz, for the vertical and horizontal channel receivers respectively, are mixed with the input to form an IF of 92 and 97 MHz with a noise bandwidth of 2 MHz. A multiple stage transistor IF amplifier with 40 dB gain brings the signal level to -33 dBm. This amplifier has an AGC circuit designed to maintain the output at this level over the dynamic range of the input signals. The output level of the receiver is then controlled by a step attenuator which can be varied between 0 and 12 dB. This effectively controls the drive level to the K band upconverter and TWT power amplifier transmitter.

The VHF receiver design contains standard components and materials and has circuit designs previously used in space communication repeaters. The dual regulators are similar to those of the K band receiver and provide power to the primary and redundant channel sets. The dc power required of both VHF receivers, vertical and horizontal, operating simultaneously is 2.1 watts at a 25.5 volt bus. The net gain input to output is about 58 dB with ± 6 dB controllable by the step attenuator. The mass allowed for all VHF receivers is 4.0 kg. The VHF receiver parameters are listed in Table 4-11.

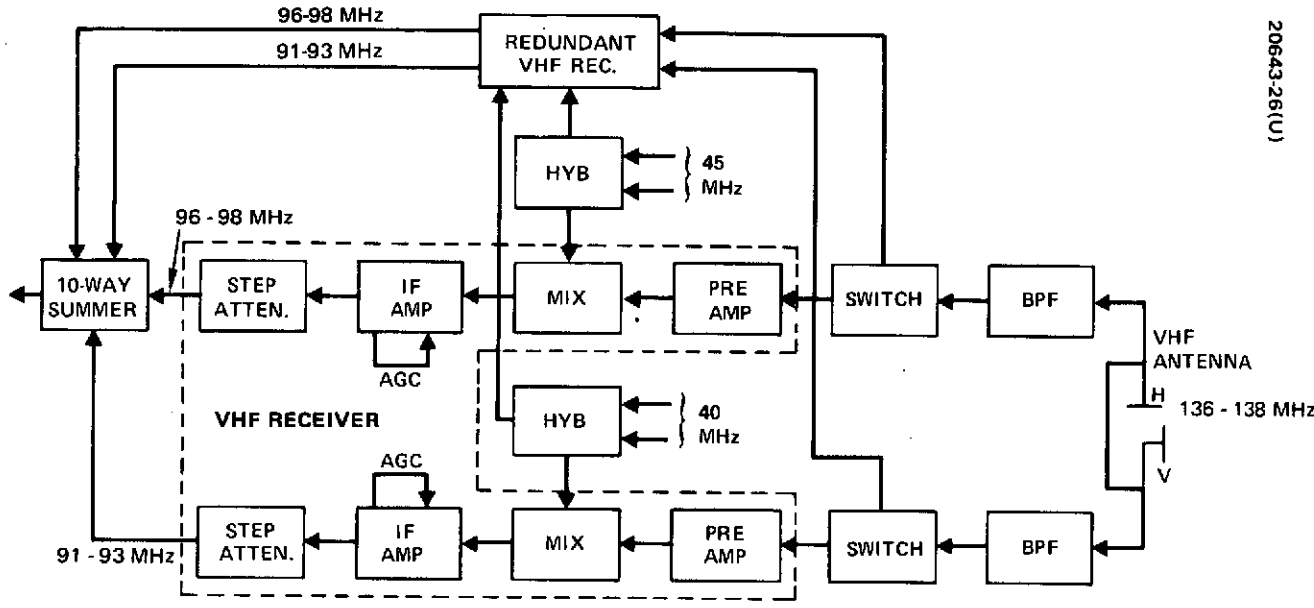


Figure 4-9. VHF Receiver

TABLE 4-11. VHF RECEIVER PARAMETERS

Noise figure (noise temperature)	3.9 dB (420° K)
Input band	136 to 138 MHz
Output band	91 to 93 MHz, 96 to 98 MHz
Bandwidth	2 MHz
Input power	2.1 watts
Gain	58 ± 6 dB
Mass (two receivers)	4 kg
Reliability for 5 years	0.9894

4.1.2.6 S Band Transmitter Power Amplifier and Receiver

The S band transmitter and receiver are designed to transmit and receive over a broad range of frequencies to accommodate many potential user channels. The transmit band covers 85 MHz, and the receive band covers 100 MHz. The instantaneous bandwidth is 10 MHz for both transmit and receive; however, the channel center frequency may be selected anywhere within the specified band in 1 MHz steps. The transmitter provides 41 dBm EIRP for a low power mode and 47 dBm EIRP for a high power mode. The receiver is designed to have a low noise temperature (420° K) by implementing a low noise transistor preamplifier.

The design configuration is illustrated by the block diagram of Figure 4-10. The diplexer requires a transmit filter with rejection at the receive frequency of 75 dB and a receive filter with rejection at the transmit frequency of 80 dB. The input to the transmitter is a 45 MHz IF signal from the six-way power divider at -15 dBm. A transistor amplifier and LC filter provide the necessary power and select the medium data rate IF plus or minus 5 MHz. This spectrum is mixed with a stepped local oscillator signal generated in the frequency synthesizer to provide the transmit channel output within 2035 to 2120 MHz. A multistage transistor driver amplifier provides +21 dBm into the hybrid network which connects the redundant units to the power amplifier. The power amplifier design is illustrated in more detail in Figure 4-11. Two transistor amplifiers are used to raise the drive level at the final power amplifier input to about 6.3 watts. This output is switched directly to the antenna through the filter and diplexer to provide the low power mode EIRP of 41 dBw. A group of three power transistors is combined to provide the high power mode output of 24 watts at the summer output. The high or low power mode is selected by commands operating the RF switches shown in the diagram. There are four final power amplifiers combined by the hybrid divider and switched Wilkinson summer. Only three of the four operate simultaneously providing high reliability.

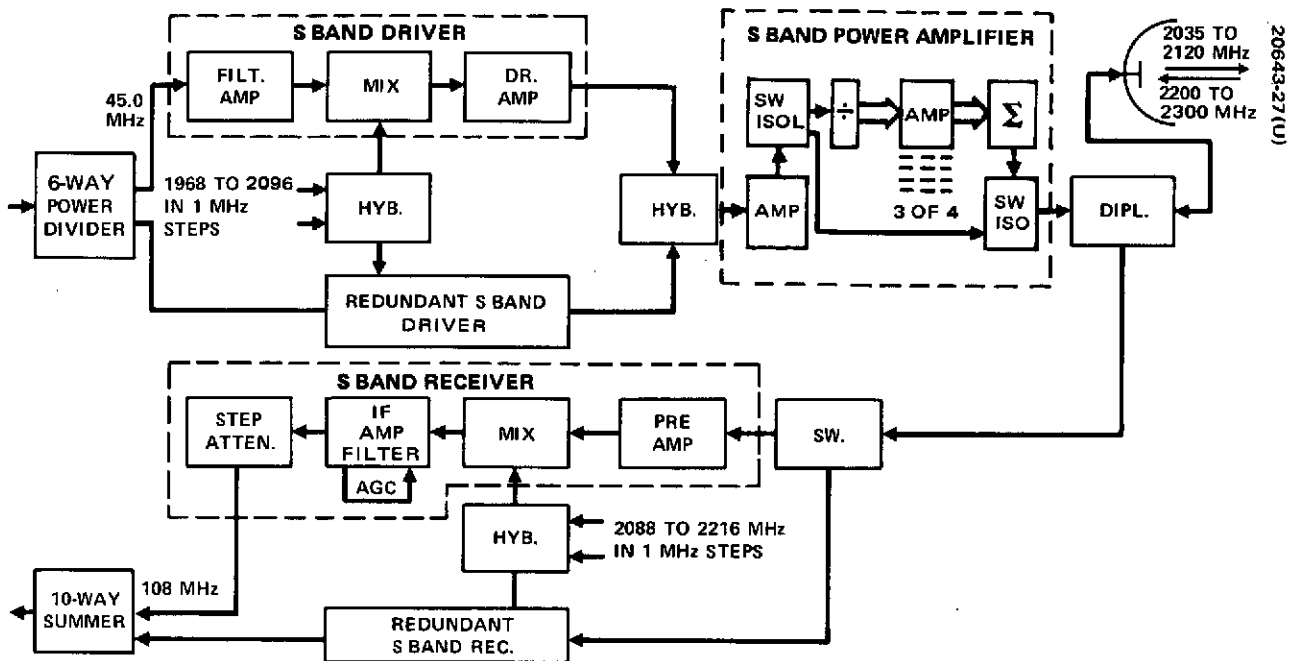


Figure 4-10. S Band Transmitter and Receiver

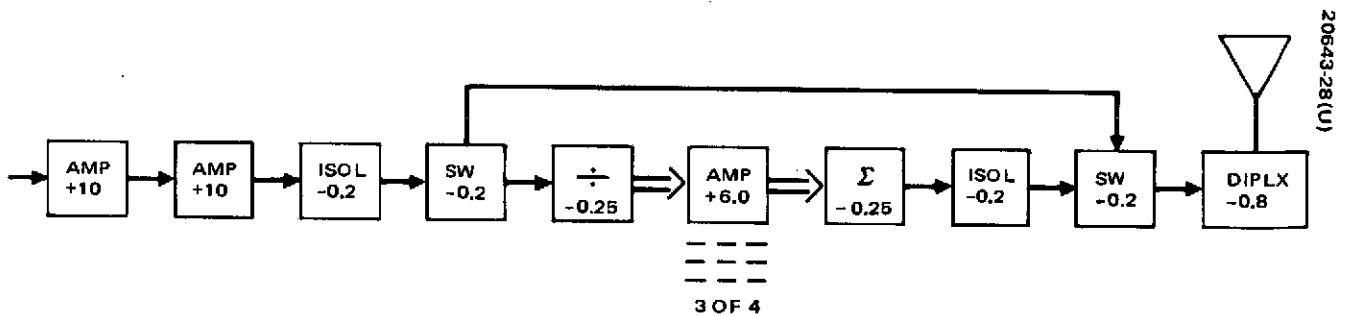


Figure 4-11. S Band Power Amplifier

The S band receiver processes the 10 MHz bandwidth medium data rate signals and puts out an IF centered at 108 MHz at about -27 dBm. The input to the receiver is first switched to either redundant receiver preamplifier. The preamplifier is a low noise multistage transistor amplifier having an overall gain of 30 dB. The S band receiver noise temperature is 420°K. After mixing with a stepped local oscillator signal from the frequency synthesizer, the signal is further amplified by a transistor amplifier with AGC. This provides a constant level input for the step attenuator over a wide range of received signal levels. The step attenuator adjusts the output IF level and hence the K band transmitter drive over a 6 dB range.

The transmitter portion requires 1.5 watts of dc power at a 24.5 volt bus. The S band power amplifier portion requires 18.5 watts in the low power mode and 86.5 watts in the high power mode. The total transmitter power is then 20 or 88 watts depending on the mode selected. The receiver power required is 0.9 watt. The transmitter and receiver parameters are summarized in Tables 4-12 and 4-13 respectively.

TABLE 4-12. S BAND TRANSMITTER PARAMETERS

Power output (at antenna)	3.2/12.5 watts
Input frequency	45 MHz
Output frequency	2035 to 2120 MHz
Bandwidth	10 MHz
Input power	20/88 watt
Gain	50 dB/56 dB
Mass (including redundancy)	7.3 kg

TABLE 4-13. S BAND RECEIVER PARAMETERS

Noise figure (noise temperature)	3.9 dB (420°K)
Input frequency range	2200 to 2300 MHz
Output frequency	108 MHz
Bandwidth	10 MHz
Input power	0.9 watt
Gain	63 ± 3 dB
Mass (including redundancy)	1.4 kg

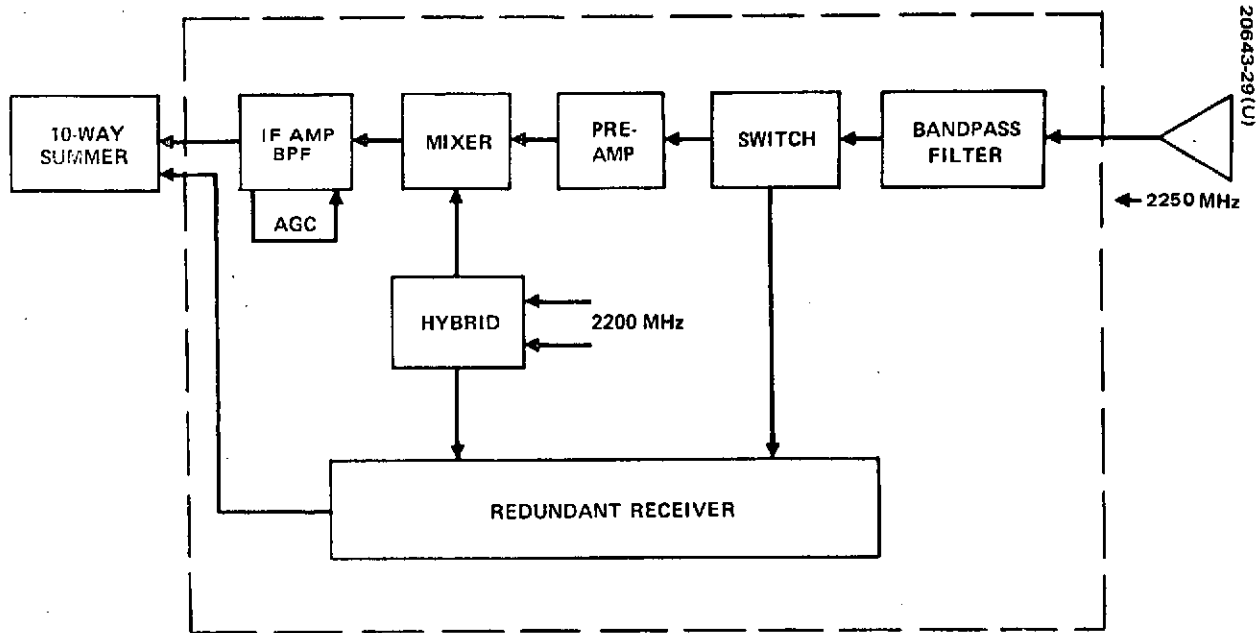


Figure 4-12. Order Wire Receiver

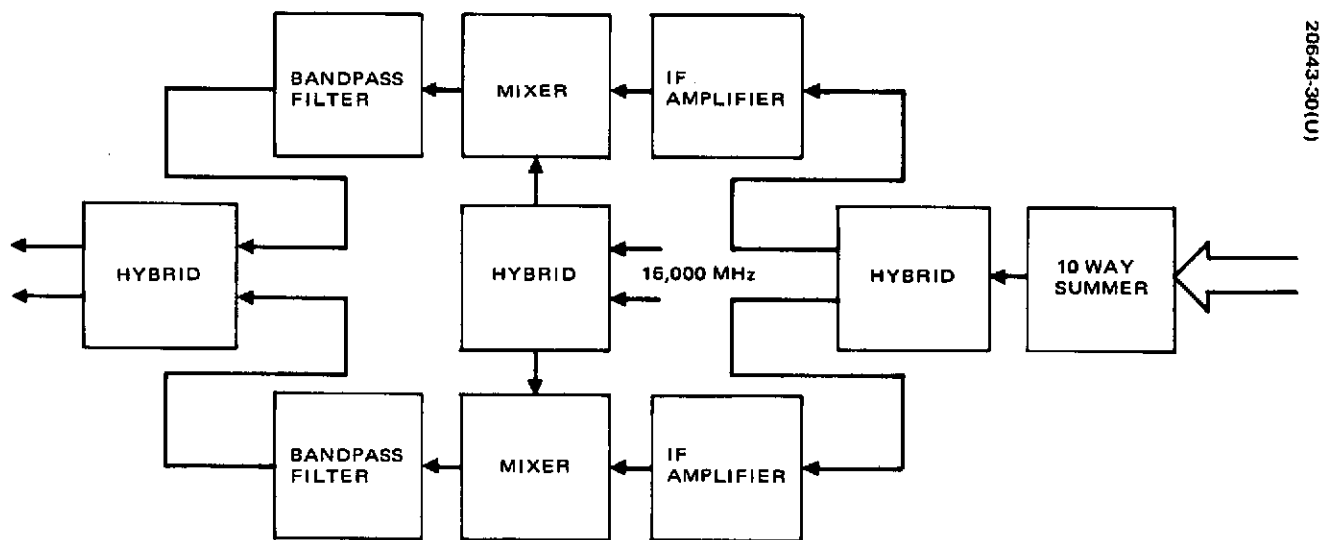


Figure 4-13. K Band Upconverter

4.1.2.7 Order Wire Receiver

The order wire receiver provides continuous service to offer the opportunity for any user to signal the earth station of its desire to use the main S band link through the TDRS. The order wire receiver is designed with a low noise preamplifier using a tunnel diode to provide a 3.9 dB noise figure or 420 K noise temperature at the bandpass filter input. A four-section coaxial filter similar to the S band receiver duplex filter precedes the tunnel diode amplifier. Sufficient gain is provided to drive the mixer with a -130 dBw signal level. After mixing, the 67 MHz IF signal is amplified with a multistage transistor IF amplifier with AGC control to maintain a level of -100 dBw at the ten-way summer. An LC bandpass filter establishes the 10 MHz receiver bandwidth at the IF amplifier output. A block diagram of the order wire receiver is shown in Figure 4-12. The S band order wire receiver parameters are summarized in Table 4-14.

4.1.2.8 K Band Upconverter

The output of the ten-way summer is upconverted and amplified at K band for transmission over the return ground link. The upconverter translates five IF channels to five K band channels for final amplification through a TWT. There are redundant amplifier-mixer modules in the upconverter, and dc power is provided by a dual regulator as in the other subsystem units. The redundant modules are hybrid coupled at the input and output to provide reliable performance.

The main parts of the upconverter are the linear IF amplifier and mixer/filter modules as shown in the block diagram of Figure 4-13. The IF amplifier is a multistage linear broadband transistor amplifier having

TABLE 4-14. S BAND ORDER WIRE RECEIVER PARAMETERS

Noise figure (noise temperature)	3.9 dB (420 K)
Input frequency	2201 MHz
Bandwidth	1 MHz
Input power (24.5 v bus)	0.93 watts
Gain overall	67 dB
Mass (including redundancy)	1.9 kg
Reliability	0.9752

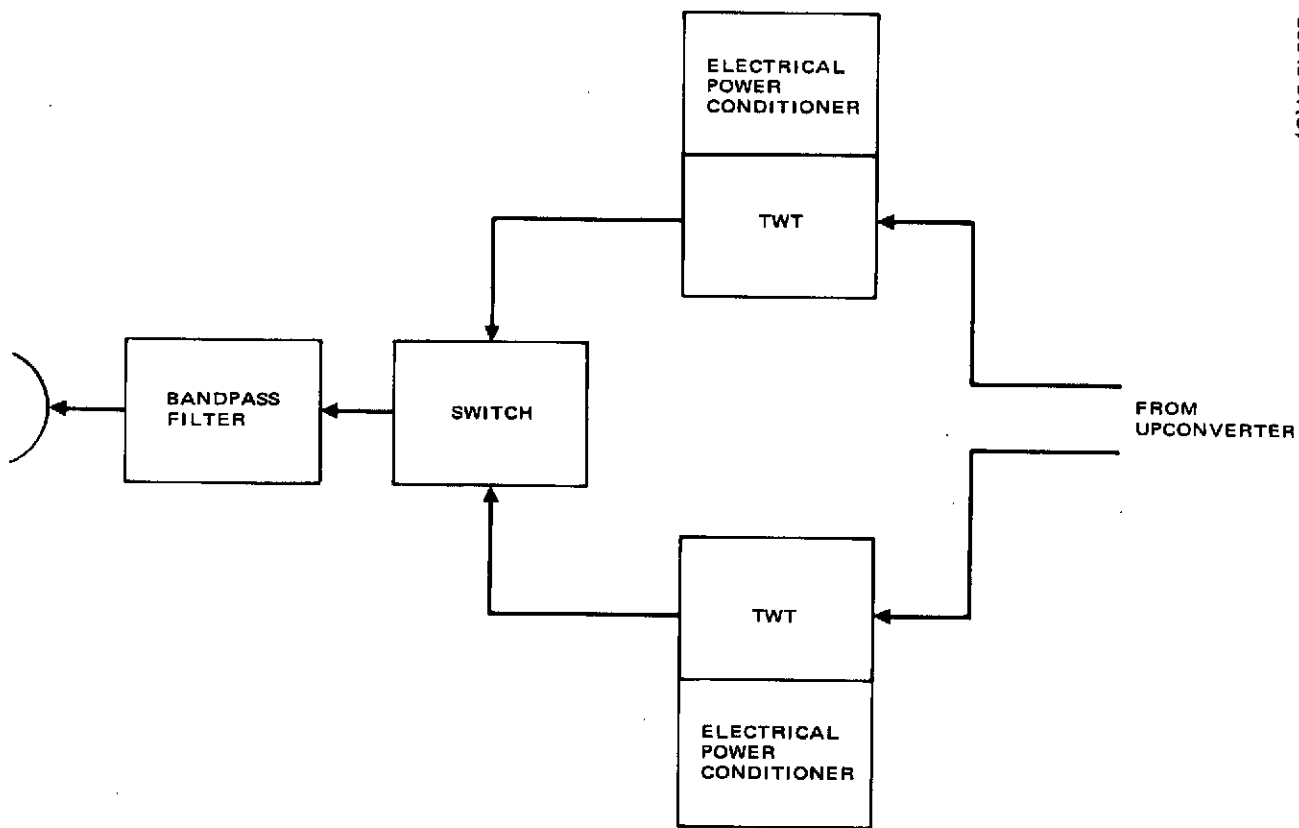


Figure 4-14. K Band Transmitter

35 dB gain. The IF level at the mixer input is a function of the channel frequency. Medium data rate signals are between -40 to -50 dBw, low data rate signals are about -50 to -60 dBw, and order wire/telemetry signals are about -80 dBw. The mixer has a waveguide output connector and a conversion loss of 0.6 dB. The output bandpass filter is a waveguide filter with a 63 MHz bandwidth between the 1 dB points.

The K band upconverter uses 0.8 watts of dc power at 24.5 volts. Its mass is predicted to be 1.1 kg. Overall gain of the upconverter is predicted to be 21.8 dB. The upconverter parameters are summarized in Table 4-15.

4.1.2.9 K Band Transmitter

The K band transmitter consists of two TWTs and two electronic power conditioners to provide redundant operation. The TWT input consists of five K band signals from the K band upconverter. These signals include LDR and MDR signals, the TDRS telemetry signals, plus the order wire signals. Each of the five signals processed through the K band transmitter is at a level well below the saturation level of the TWT. When all signals are present, the TWT operates 5 dB below its rated saturated power output, 8 watts. This maintains the necessary linearity of the return link channels.

The K band transmitter block diagram is shown in Figure 4-14. The hybrid network used to cross-strap the TWTA (TWT plus EPC) is part of the upconverter unit and therefore is not shown. The output bandpass filter provides the necessary rejection of out of band noise and spurious signals, while passing the 63 MHz band of signals comprising the five return link channels. The TWTA characteristics are listed in Table 4-16. This tube

TABLE 4-15. K BAND UPCONVERTER PARAMETERS

Power output	-30 to -70 dBw
Input frequency	50 to 113 MHz
Output frequency	15,050 to 13,115 MHz
Bandwidth	63 MHz
Input dc Power (24.5 v bus)	0.8 watts
Gain overall	21.8 dB
Mass (includes redundancy)	1.1 kg

TABLE 4-16. K BAND TRANSMITTER PARAMETERS

Frequency	15,050 to 15,113 MHz
Δf (bandwidth)	63 MHz
Saturated power	8 w (maximum)
TWT small signal gain	50 dB
TWT efficiency (overall)	32 percent
Noise figure	33 dB
Instantaneous gain slope	0.02 dB/MHz
Mass	0.7 kg
Size	1-1/2 x 1-1/2 x 10 in.
TWT connectors	W/G (WR 62)
Wearout life	10 years
EPC efficiency	80 percent
EPC size	8.5 x 6 x 2 in.
EPC mass	1.1 kg
TOTAL transmitter weight	4.1 kg

is a scaled version of existing space qualified TWTs and similar to current space development tubes. The high efficiency is achieved by operating the TWT at a higher voltage; 8 percent over that which corresponds to maximum gain. There may be an excessive (0.5 dB) gain slope when operating at the maximum efficiency point. If this becomes intolerable, then a dual pitch helix slow wave structure may be incorporated in the design. This is a proven technique used in a number of present X to K band TWTs. The cathode life of 10 years is well within the state of the art. The 32 percent efficiency requires 25 watts of input power to operate the 8 watt TWT.

The TWT power supply is an electronic power conditioner containing filament and high voltage outputs required by the TWT. The TWT voltages are provided by a filament inverter and a high voltage dc-dc converter. The dc-dc converter provides outputs to the TWT anode, collector, and cathode. A shunt boost regulator supplies the dc input required by the filament inverter and high voltage converter. The filament inverter consists of two switching transistors operating push pull in a common base

mode with a center tapped linear power transformer as collector load. The high voltage converter consists of three high voltage dc outputs in series to supply anode, collector, and cathode voltages. Because of the low current required, the anode voltage output is derived from half-wave rectification followed by an LC filter. A voltage doubler circuit provides the collector voltage. The cathode voltage requires low ripple voltages, usually less than 1.0 volt with no harmonic exceeding 25 mv rms. The regulator output voltage is adjusted to yield the correct cathode voltage at full load. Typical cathode regulation is ± 0.5 percent for line, load, and temperature, and a total of 1 percent with line drift superimposed.

The TWT EPC weight is 1.2 kg and is packaged in a box 8.5 by 6 by 2 inches. The redundancy provided for high reliability requires two EPC units per spacecraft. The efficiency of the EPC unit is about 80 percent and therefore requires about 31 watts of dc input power at a 24.5 volt bus to provide the 25 watts of power to operate the TWT. The transmitter parameters are summarized in Table 4-16. The total mass includes waveguide transmission lines and connectors plus redundancy features.

4.1.2.10 S Band Transponder

The S band transponder provides for ground link ranging by translating received frequencies in 2206 to 2214 MHz to transmit frequencies in 2071 to 2079 MHz in a single conversion. The input signal contains ranging data within an 8 MHz bandwidth at a received signal level of -120 dBw. A redundant transponder is provided for reliable operation. A block diagram of the S band transponder is shown in Figure 4-15.

The input bandpass filter has a 24 MHz bandwidth and is a four-section coaxial type filter with about 0.5 dB insertion loss. The transistor amplifier after the redundancy switch has 42 dB gain and provides a low (420° K) receiver noise temperature. The amplified signal is wired with 245 Mhz from the frequency synthesizer to convert to the 2075 transmit frequency. The transmit frequency is amplified by 43 dB in a solid state multistage amplifier with an AGC circuit to maintain an even drive level to the transmit power amplifier. The final power output is about 6.3 watts. The output filter has a narrow, 8 MHz, bandwidth and requires a large size cylindrical cavity two-section filter design. The S band transponder parameters are summarized in Table 4-17.

TABLE 4-17. S BAND TRANSPONDER PARAMETERS

Input frequency	2200 MHz
Output frequency	2065 MHz
Output power	6.3 watts
Bandwidth	8 MHz
Input power (24.5 v bus)	21 watts
Mass (including redundancy)	7.6 kg

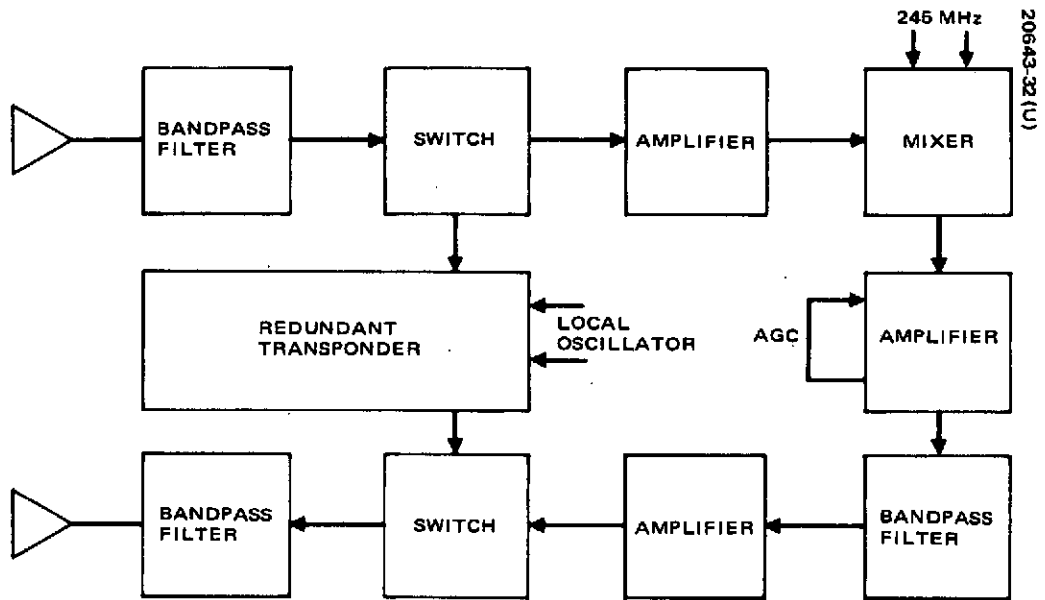


Figure 4-15. S Band Transponder

4.1.3 Repeater Performance Summary

The repeater performance is summarized with a discussion of the gain distribution, receiver noise figures, and noise temperatures at the receiver input. The mass, and power are tabulated for each unit of the repeater to show the relative contribution of each to the whole subsystem.

4.1.3.1 Repeater Gain Distribution

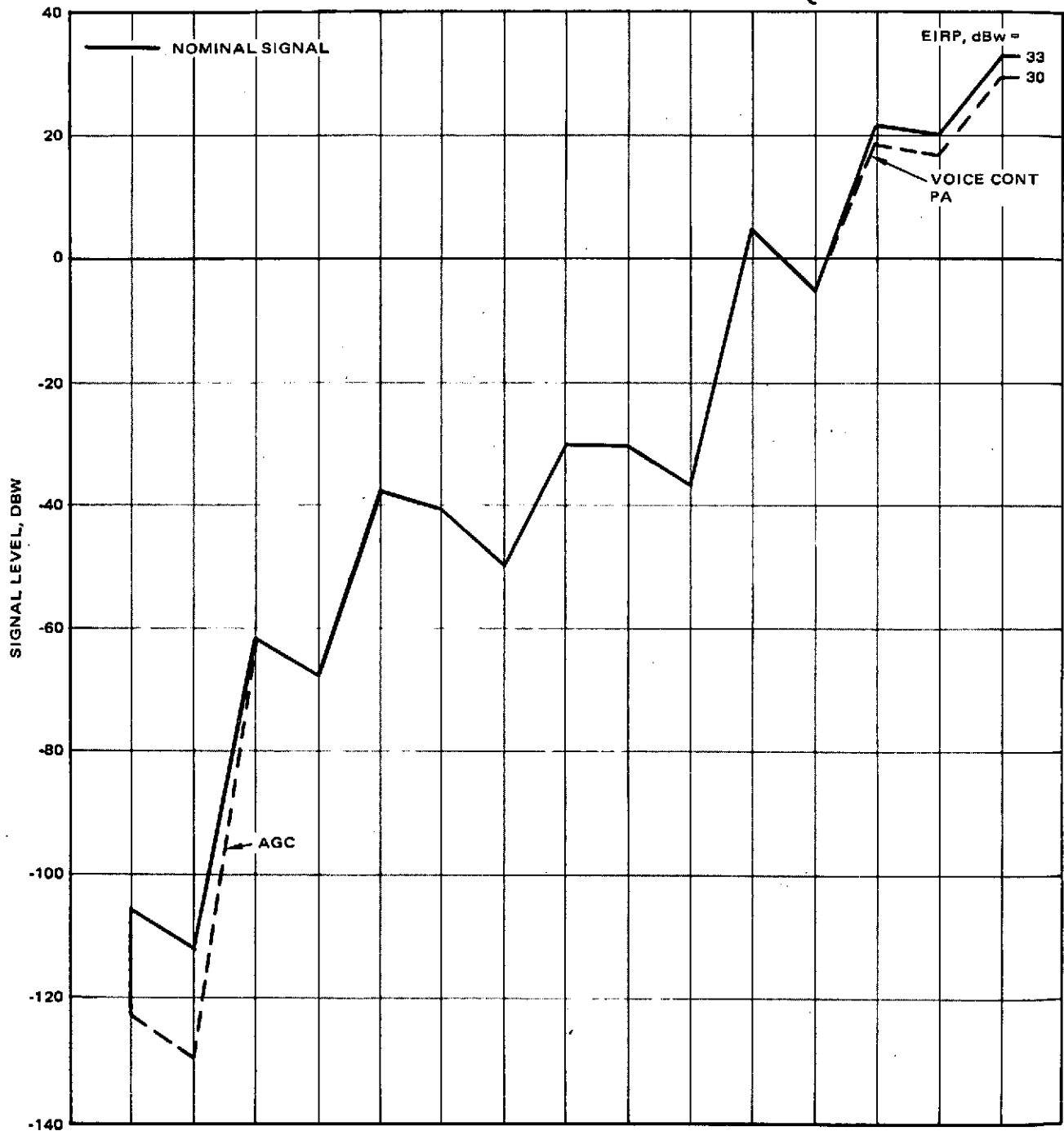
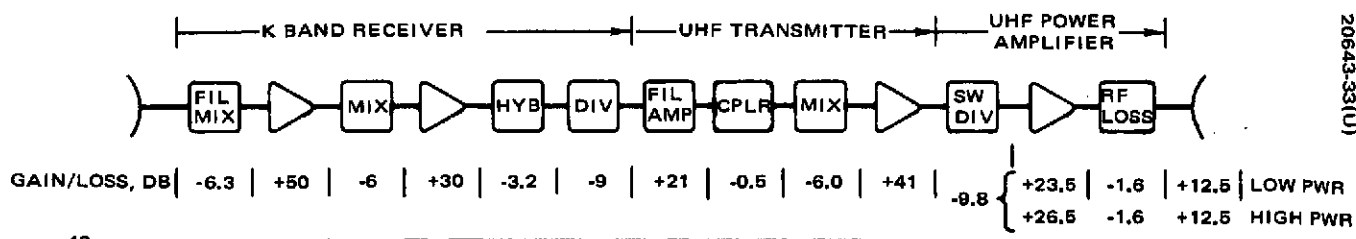
The gain distribution throughout each data channel is designed to compensate for the losses incurred by the hybrid coupling and switching of redundant circuits as well as channel distribution and combining losses. Consideration was given to the dynamic range of received signals and various output power mode requirements. Figure 4-16 shows the various gain distribution steps through each data channel. The forward link gain/loss values are shown below the appropriate unit modules with signal flow shown from left to right. The return link gain/loss values are similarly shown below appropriate modules; however signal flow is from right to left.

The low data rate signals are received at K band and transmitted on UHF. The K band receiver has an AGC amplifier that operates over the input signal dynamic range variations caused principally by the weather propagation margin. The UHF output is controlled by the threshold detection of the low data rate voice signal, applying greater power to the antenna when both voice and command signals are to be transmitted simultaneously. The medium data rate forward link signal processing is similar to the low data rate; however, the bandwidth is broader and the output is transmitted on an S band carrier. The S band power amplifiers are command controlled to provide a 47 dBw EIRP or 41 dBw EIRP by commands from the earth station.

The return link receivers all have AGC amplifiers and stepped attenuators to control the drive levels applied to the TWT amplifier for subsequent transmission to earth. The higher level drive is shown by a dotted line on the gain distribution curves. The solid lines represent the nominal levels to be expected throughout each channel. With all step attenuators at minimum attenuation, the K band TWT will be operated at about a 5 dB backoff point, assuring the linearity needed for the return link data transmission.

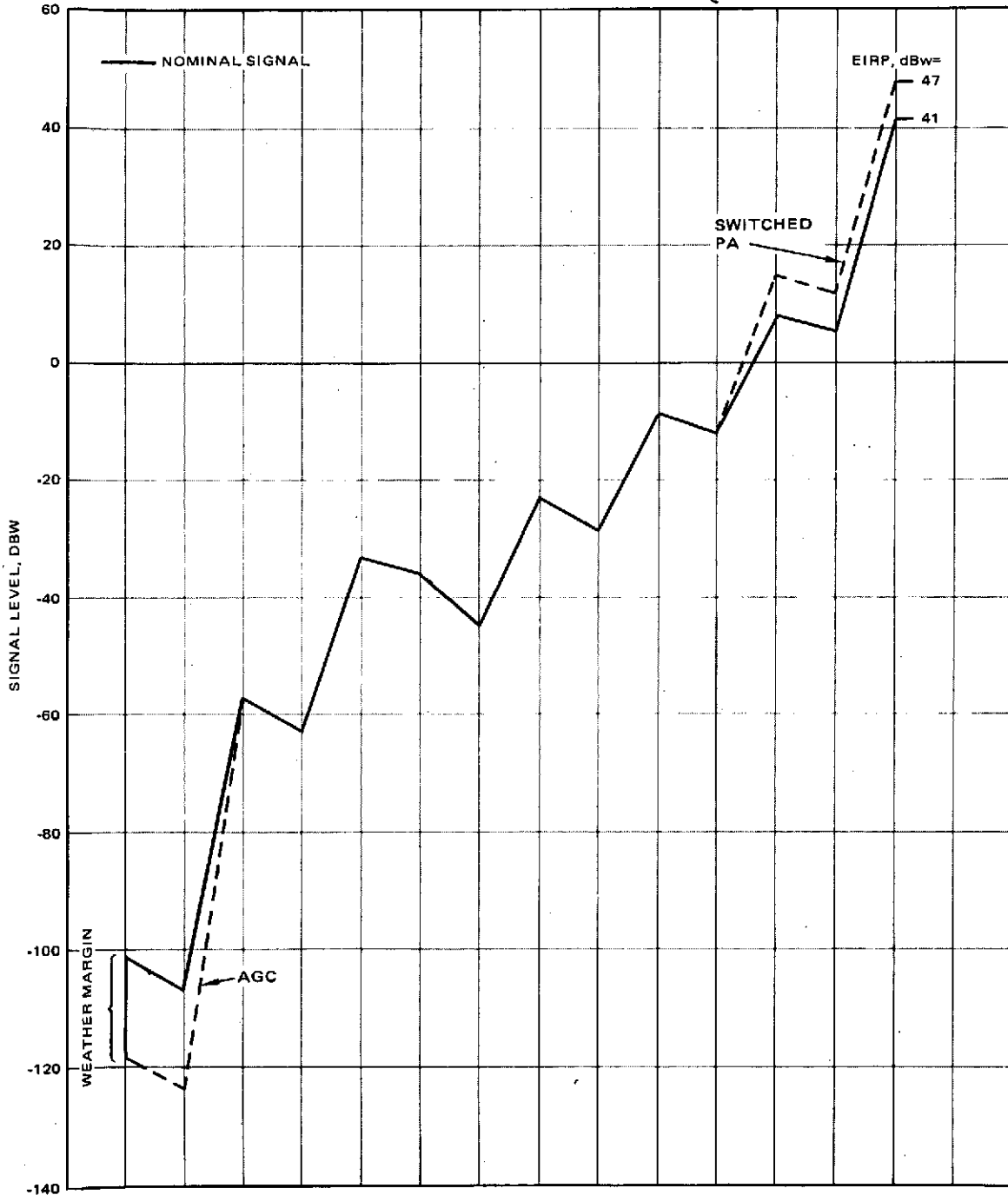
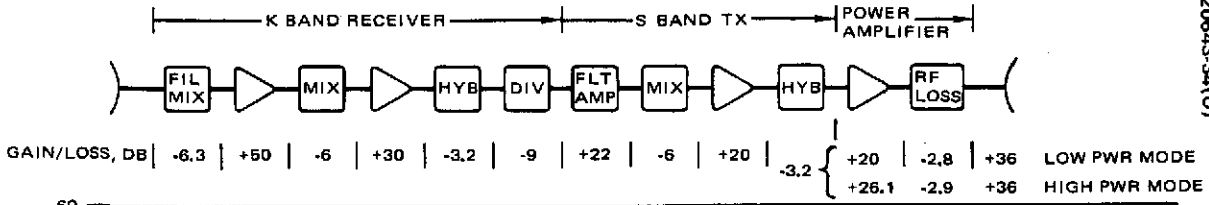
4.1.3.2 Receiver Noise Temperatures

The low noise receivers provide the performance required for the TDRS ground and user links. They represent state of the art amplifier designs except for the K band receiver, which is nominal and did not use a low noise preamplifier. The values listed in Table 4-18 represent the receiver noise figures at the bandpass filter inputs in all cases.



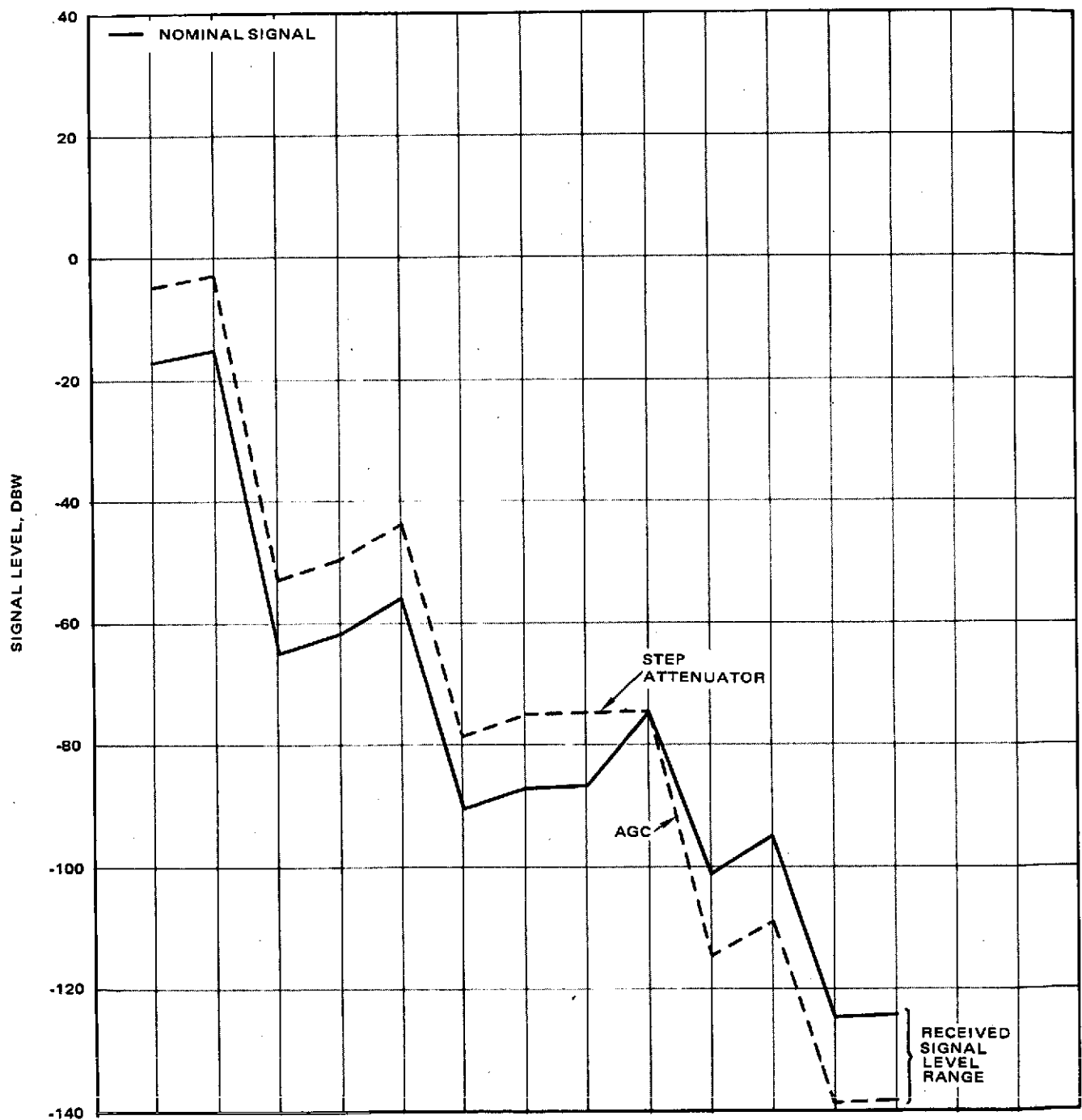
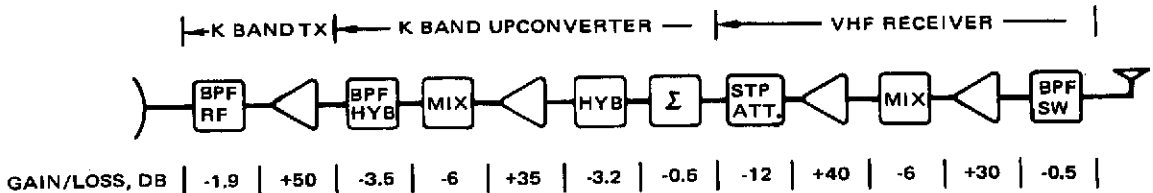
a) Low Data Rate Forward Link

Figure 4-16. Repeater Gain Distribution



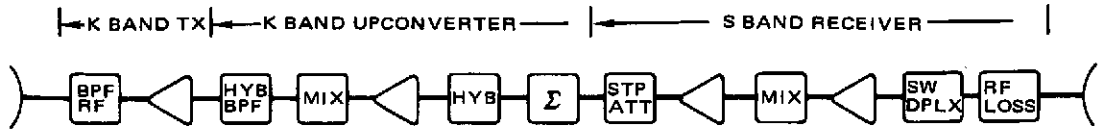
b) Medium Data Rate Forward Link

Figure 4-16 (Continued). Repeater Gain Distribution

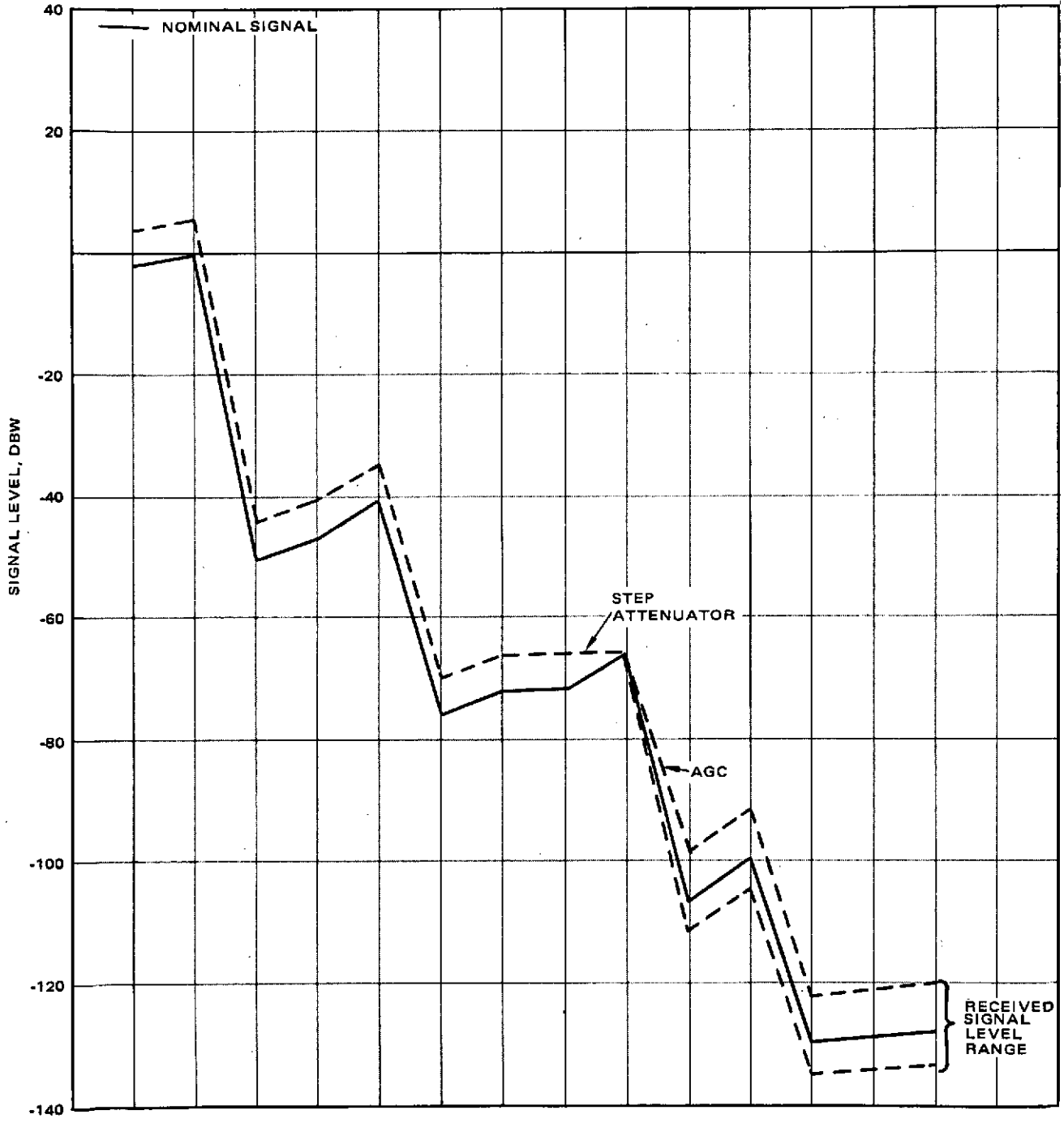


c) Low Data Rate Return Link

Figure 4-16 (Continued). Repeater Gain Distribution

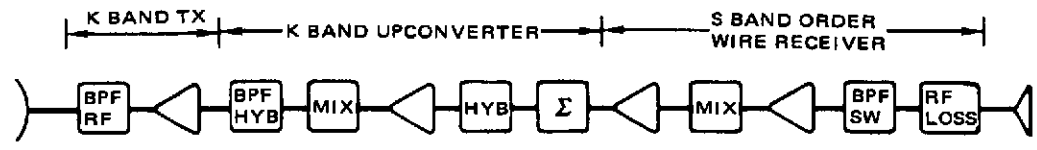


GAIN/LOSS, DB	-1.9	+50	-3.5	-6	+35	-3.2	-0.5	+6	+45	-6	+30	-1.0	-1.2
---------------	------	-----	------	----	-----	------	------	----	-----	----	-----	------	------

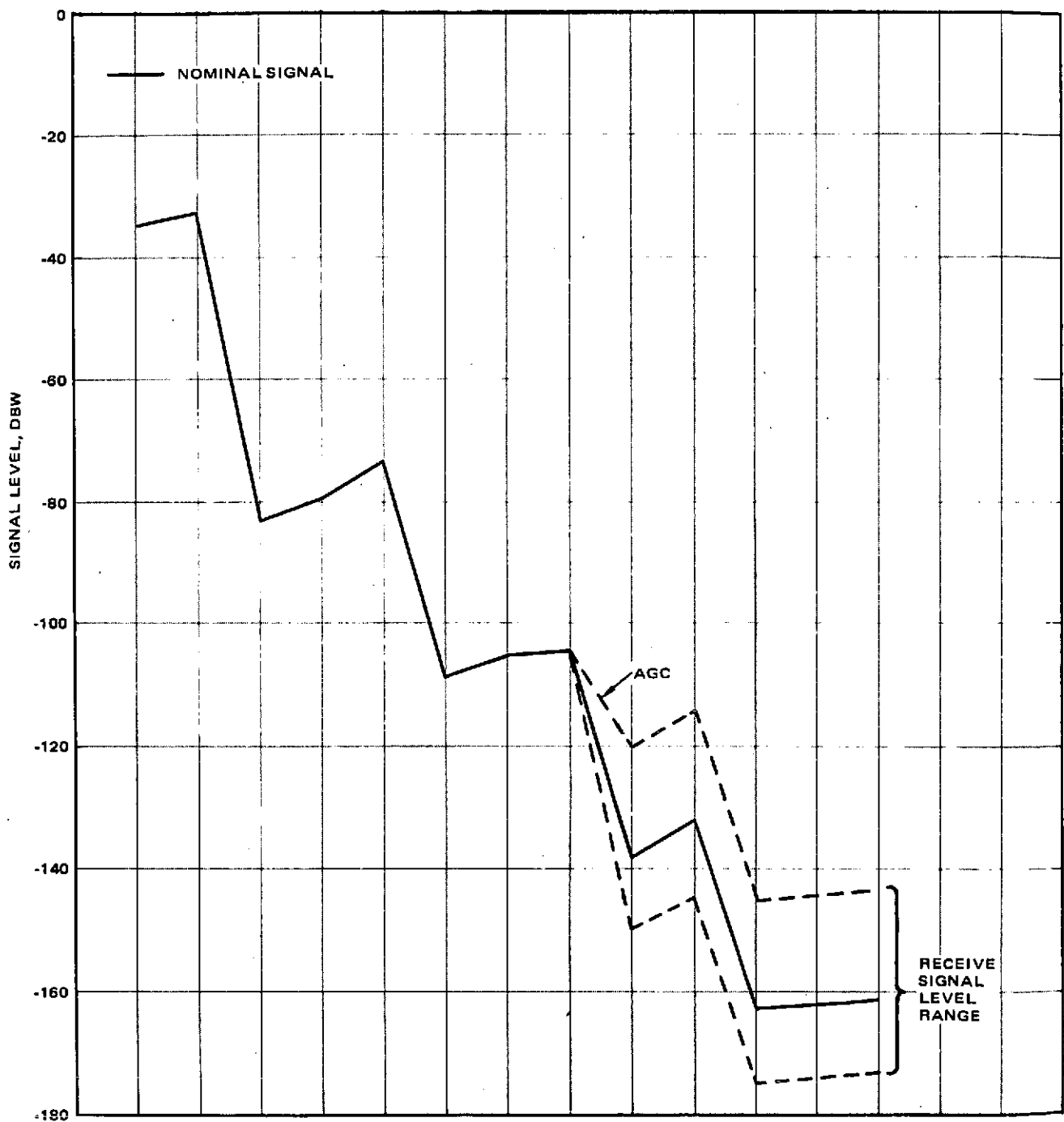


d) Medium Data Rate Return Link

Figure 4-16 (Continued). Repeater Gain Distribution



GAIN/LOSS, DP | -1.9 | +50 | -3.5 | -6 | +35 | -3.2 | -0.5 | +45 | -6 | +30 | -0.7 | -1.0 |



e) Order Wire

Figure 4-16 (Continued). Repeater Gain Distribution

TABLE 4-18. RECEIVER NOISE FIGURES

Receiver Band	Noise Figure, dB	Noise Temperature, K
VHF	3.9	420
S band	3.9	420
K band	9.0	2000

4.1.3.3 Mass and Power Summary

Table 4-19 lists the masses of the repeater components, which total 55.1 kg. There are six power modes possible corresponding to high or low UHF transmitter power and the S band transmitter high, low, or off. However, it has been tacitly assumed that for TDRS design, operation of both transmitters in their high power modes should not be considered. This is because the high power modes are for voice transmission and only one or the other system will be used, not both simultaneously. Further, the case where the S band transmitter is off and the UHF power is low presents little useful design information. A power summary for the other four modes is presented in Table 4-20.

4.1.3.4 Technology Status

The TDRS communication subsystem design utilizes the techniques applied to many of the previously successful satellite communication programs at Hughes. Advanced development circuit designs and packaging techniques are also applicable to TDRS and will be used to minimize the mass and power consumption while maintaining the reliability and performance requirements. The most critical units satisfying the subsystem design criteria are the large power users and those most sensitive to the subsystem performance.

The K band TWTA is a critical design unit because it will require a new TWT tailor-made to the gain, bandwidth, power, and efficiency requirements of TDRS. Although new tube development is required, the technical risk involved is minimal because the requirements can be met by using a scaled version of present space qualified TWT amplifiers. The efficiency of the TWT and associated electronic power conditioner is a major parameter which will be given special emphasis during design development to assure that the most advanced techniques consistent with high reliability are utilized.

The UHF and S band power amplifier units are designed to provide the required power outputs with the best efficiency performance available. Previous space program design techniques are applied to the TDRS solid state power amplifiers to achieve the desired high efficiencies. Recent

TABLE 4-19. REPEATER MASS SUMMARY

	<u>Mass, kg</u>
K band receivers	2.6
K band transmitters	4.1
K band upconverter	0.8
Frequency synthesizers	8.2
S band transmitters	7.3
S band receivers	1.4
S band order wire receivers	1.9
S band transponder	7.6
UHF transmitters	17.2
VHF receivers	4.0
Total	<u>55.1</u>

TABLE 4-20. REPEATER POWER SUMMARY

	Unit Power	Telecommunication Mode			
		UHF High		UHF Low	
		S Band Low	S Band Off	S Band High	S Band Low
K band receiver	1.8	1.8	1.8	1.8	1.8
K band transmitter	31	31	31	31	31
K band upconverter	0.8	0.8	0.8	0.8	0.8
Frequency synthesizer	7.3	7.3	7.3	7.3	7.3
S band receiver	0.9	0.9	--	0.9	0.9
Order wire S band receiver	0.9	0.9	0.9	0.9	0.9
S band transmitter	21 or 88	21	--	88	20
S band transponder	21	21	21	21	21
UHF transmitter	141 or 280	280	280	141	141
VHF receiver	2.1	2.1	2.1	2.1	2.1

development design and packaging concepts are also implemented in the TDRS design as well as use of the most advanced components available for space applications.

The receiver noise temperatures are one of the most sensitive design parameters influencing overall system performance. The TDRS receivers used in the spacecraft user links are designed to have the best noise temperature practical within the state of the art. This requires the use of low noise solid state preamplifiers which are similar to or identical to those on existing space vehicles. Adequate K band receiver noise temperature is achievable without low noise preamplification using conventional microwave front-end components.

The remaining subsystem units will contain circuit designs already space qualified and will also contain many of the new packaging concepts being applied to present space communication subsystem unit designs. The technology status of all design aspects of the TDRS communication subsystem is within the state of the art using space qualified components for the most part. Where new development is required, there is very little technical risk involved.

4.2 TELEMETRY AND COMMAND SUBSYSTEM

4.2.1 Alternatives Considered

Before configuring the baseline subsystem for telemetry and command, several alternative configurations were considered. Principal among these tradeoffs were the following.

4.2.1.1 Centralized Versus Master-Remote Concepts

To meet the telemetry and command requirements of the TDR satellite, Hughes considered the use of a centralized system where all telemetry or command functions are centralized units such as the ones used on Intelsat IV satellites. Also considered was the use of a master-remote system where the telemetry and command functions are dispersed throughout the satellite by the use of remote units such as the ones used on the OSO satellite. Cost and weight were the factors considered in this trade but the overriding consideration was weight. The master-remote concept for telemetry and command can be weight effective for satellites above a certain minimum size and complexity; below this size the centralized concept proves to be more weight effective. The size of the TDS satellite is such that a centralized concept is more weight effective. This approach is also more cost effective and was chosen for the baseline configuration.

4.2.1.2 Real Time Execute Versus Automatic Execute for the Commands

In compliance with the Statement of Work, Hughes has provided a standard GSFC AM-FSK command format, except that it includes a real time execution capability which necessitates the use of a third execute tone. This is the system used on other satellite systems such as ATS and Intelsat IV because it greatly reduces the complexity and weight of the satellite versus an automatic execute system. With the real time system the requirement for a complex onboard attitude control and antenna pointing processor is eliminated. For these reasons real time execution was adopted.

4.2.2 Design Description

The primary telemetry and command requirements are to provide telemetry data and command control of the spacecraft using the GSFC standard telemetry and command formats. These requirements must be satisfied via either the primary telecommunication service system at the Ku band frequency or the backup telemetry transmitter and command receiver at VHF. The VHF transponder system will be compatible with the GRARR operational requirements to provide data for orbit determination during launch and injection phase. Once the spacecraft is on station, the VHF transponder system will be used as a backup to the Ku band system in providing TDRS telemetry and command links to the ground station. The telemetry subsystem must provide data for the determination of performance, status, operational mode, attitude, and antenna pointing of the TDRS. The command subsystem must provide control of the spacecraft for selection of

redundant units, operational mode changes, stationkeeping, and orientation of the spacecraft and the antenna. Figure 4-17 is a schematic diagram of the telemetry and command subsystem.

4.2.2.1 Command Subsystem

The units of the command subsystem, as shown in Figure 4-17, are fully redundant and cross-strapped so that either unit of every pair could fail completely without impairing the satellite's ability to receive and execute all commands. A command transmission consists of a microwave carrier modulated by a sequence of tones at three discrete frequencies, designated 1, 0, and execute. The tones are amplitude modulated at 128 Hz. The demodulated output of the Ku band receiver and the VHF command receiver drive both the despun and spinning decoders. Either of the redundant decoders on the despun and spinning side provide up to 128 pulse command outputs. The selection of the executing decoder is by unique decoder address. Command verification is provided by telemetry readout of the command register before sending the execution tone.

The command subsystem is capable of executing jet firing commands in phase with the spin of the satellite. This is performed at the ground station by synchronizing the execute tones with sun or earth pulses, received via real time telemetry. The repetitive command mode is used for antenna pointing and jet firings. Slewing is accomplished at a rate of 24 steps per second. Tracking commands are transmitted as required to maintain the antenna beam on the user satellite.

Signal and Word Format. The demodulated command from a receiver output consists of a sequence of 1, 0, and execute tone pulses; these are arranged as shown in Figure 4-18. For convenience, the 1 and 0 pulses will be referred to as bits, as they do, in fact, convey binary information to the decoder logic circuitry.

The introduction portion of the command word consists of at least sixteen 0 bits followed by one 1 bit. During this time a receiver is selected and the decoder registers and logic are reset. The decoder is then able to process the remainder of the command word. The next 8 bits comprise the address portion of the command word. The first 6 provide the coding for digital addresses. The address words are separated by a minimum Hamming distance of 2, so that a single error in the transmission or reception of a decoder address will not result in the successful addressing of a wrong decoder. The last two bits are both 1s, which ensures that the introduction sequence will never be repeated within the command word.

The command itself consists of 8 bits. The 8 command bits are entered into a storage register for verification via telemetry. Once a command word is entered into storage, further processing of data bits is inhibited and an introduction format must be sent to clear the register. Upon receipt of the execute tone, a coincident pulse will occur on the decoder output line corresponding to the stored command. Execute tone pulses can be

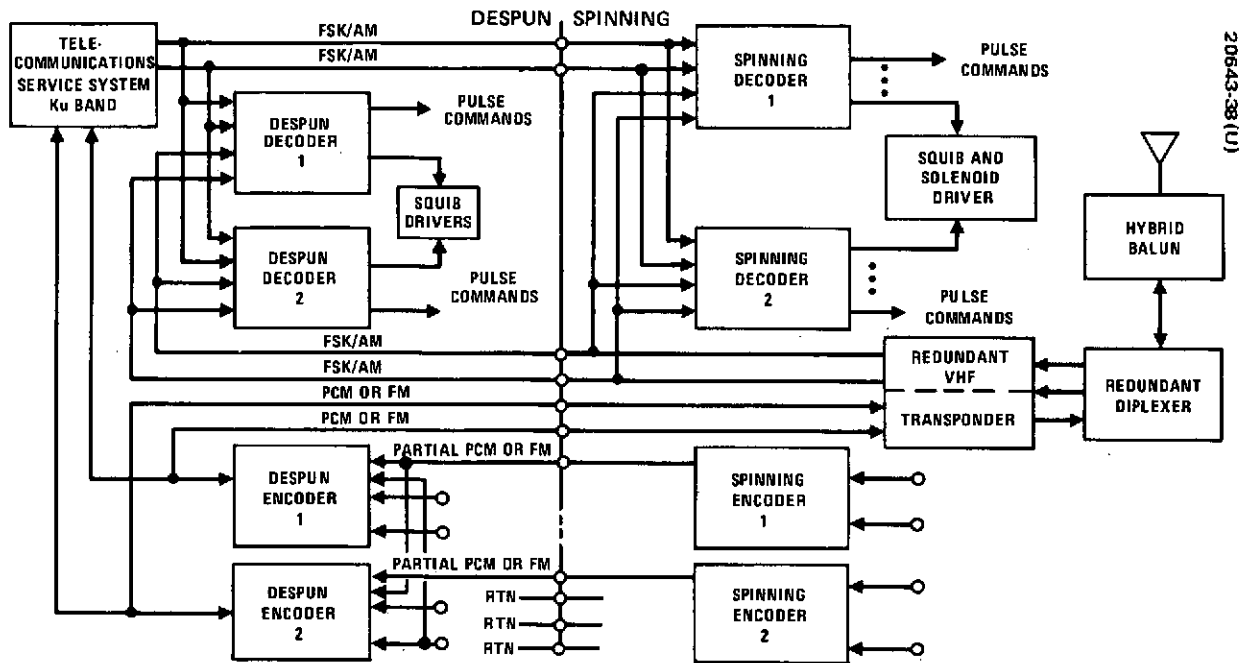


Figure 4-17. Tracking Telemetry and Command Subsystem

COMMAND GENERATOR CONTROL	FUNCTION PERFORMED	TONE	CODE	DURATION
ACTUATE XMIT				
	INTRODUCTION (CLEAR)	0	16 BITS	} 258 ms
		1	1 BIT	
		DECODER ADDRESS		
	1	2 BITS		
	COMMAND	0 AND 1	8 BITS	
READ DECODER REGISTERS	COMMAND VERIFICATION VIA TELEMETRY			
ACTUATE EXECUTE				
	COMMAND EXECUTE	EXECUTE TONE	AS REQUIRED	} VARIABLE TIME (40 ms FOR STANDARD SINGLE COMMAND)
ACTUATE CLEAR				
	CLEAR THE DECODER REGISTERS	0	16 BITS	} 133 ms
		1	1 BIT	

Figure 4-18. Command Format

sent for as long or as frequently as required. After the command has been executed (or if necessary at any time during the commanding sequence), the commanding ground station resets and clears the decoder by repeating the introduction. As shown in Figure 4-18, the time necessary for introduction, addressing, and entering a command into the register is 258 ms. This means that the minimum time required before executing a command is 258 ms (even when bypassing the telemetry verification step).

Command Decoders. The despun and spinning decoders differ from each other in only the following particulars:

- 1) Despun decoders are implemented with more command outputs from the output matrix than from the spinning output matrix.
- 2) Despun decoders each contain a TWT sequencer.
- 3) Spinning decoders each contain a spinup sequencer.

In all other aspects, including method of operation, the despun and spinning decoders are identical. Both types, therefore, will be described with reference to the block diagram of Figure 4-19.

There are two receiver sequencers. Each feeds a set of 1, 0, and execute tone filters (six different frequencies). This arrangement provides positive identification of the command link (VHF or Ku) being used for a given command, as each sequencer drives only one set. Cross-strapping is achieved by connecting the two corresponding tone filter outputs together at the input to their respective detector circuits.

The receiver sequencers sample the two VHF and the two Ku receiver outputs to select one which has a suitable output signal. The signal at the receiver output is shown in Figure 4-20. Tone filters are two-stage, stagger tuned, passive, bandpass filters with -3 dB bandwidths of approximately 1200 Hz. The output of the first stage of each filter goes to the AM detector where the two signals are summed and the composite signal is full-wave rectified and fed to a clock pulse generator which contains a narrow bandpass filter tuned to the 128 Hz bit rate. The output of the 128 Hz bandpass filter is the demodulated AM, an 128 Hz sine wave with an amplitude proportional to the signal strength of the received AM-FSK signal. The 128 Hz sine wave is fed to a hard limiting circuit in the squelch circuit. The squelch circuit puts out a signal to enable the decoder processing when the input signal exceeds a preset threshold level. The 128 Hz sine wave is also fed to the clock pulse generator which generates the clock signals which drive the remainder of the demodulator.

When power is turned on, the decoder is initialized by the power turnon reset circuit as follows: 1) the command register is cleared to all 0s (an illegal command), 2) the count register's count is set to zero, 3) the address check logic is reset, and 4) the full count logic is set to zero. Whenever an 0 or 1 tone pulse is detected, the clock pulse generator will

provide a clock pulse (CP) to the introduction sequence monitor which checks the pattern of the incoming data. Upon receipt of eight or more 0s followed by a 1, it initializes the decoder in the same manner as the power turn on reset.

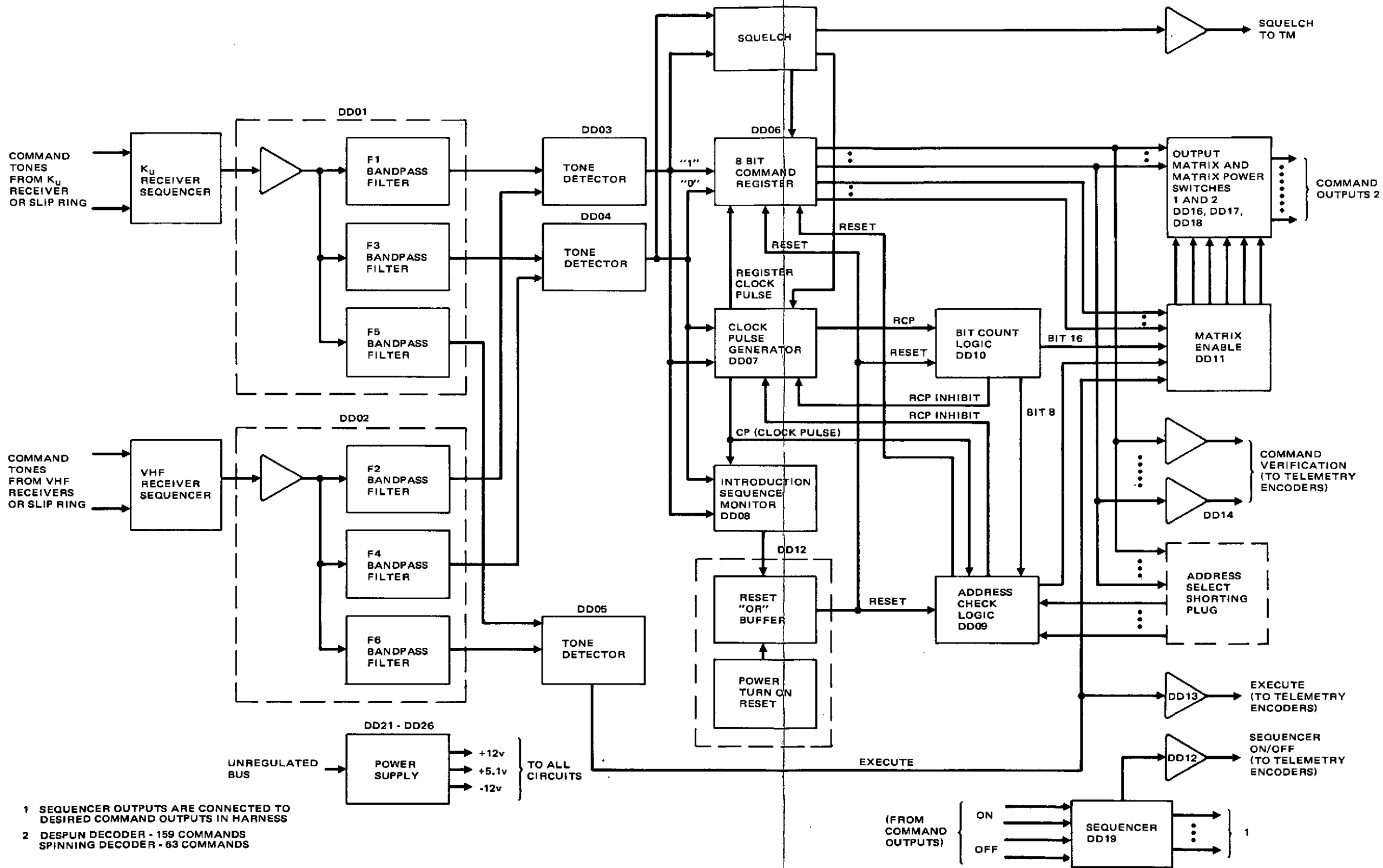
The command register is an 8 bit register. It receives 1s and 0s from the demodulator and RCPs (register clock pulses) from the clock pulse generator. Its output goes to the address check logic, output matrix, and to the telemetry buffers for parallel entry of its contents into redundant telemetry encoders.

The bit count logic provides a pulse to the address check logic when it has counted eight RCPs and a pulse to the full count logic when it has counted 16 RCPs. When the address check logic receives its pulse from the bit count logic, it checks the output of the command register (which now contains the address) and 1) if the address checks correctly, an enable signal is sent to the matrix enable or 2) if the address does not check, it inhibits further RCPs and clears the command register. Each decoder has an address plug which permits changing its address any time prior to launch. When the bit count logic has counted 16 RCPs, it inhibits further RCPs to prevent false clocking of the command register and also sends an enable signal to the matrix enable.

Use of two series matrix power switches prevents a single component failure in the matrix power switching circuitry from generating a false command. When both matrix power switches are enabled, an execute signal from the execute tone detector closes both power switches, causing a command pulse to occur on the output selected by the command portion of the command word. The command pulse is coincident with and lasts as long as the execute tone pulse.

Each despun decoder contains a TWT sequencer which, when turned on by command, times for a specified period, then generates a sequence of eight command-type output pulses spaced at 105 seconds, generates a second sequence of six pulses, and finally shuts itself off (it may also be commanded off, and thereby reset, at anytime during its cycle). The command-type outputs that each TWT sequencer generates appear on separate lines. Each line, in turn, is wired directly to selected command matrix output lines to execute those selected.

Squib and Solenoid Drivers. The squib and solenoid drivers actuate pyrotechnic and jet firing functions in the satellite. The squib drivers fire the apogee motor and bearing and power transfer assembly (BAPTA) release squibs, and the solenoid drivers actuate the axial, radial, and spinup jet valves and the latching valve in the spinup jet line. There are four squib drivers and ten solenoid drivers which are capable of firing three squibs and driving eight pairs of solenoids. All of the squib drivers apply power to their respective squibs after specified delay times. The BAPTA clamp release squib drivers are commanded by redundant separation switches. The apogee



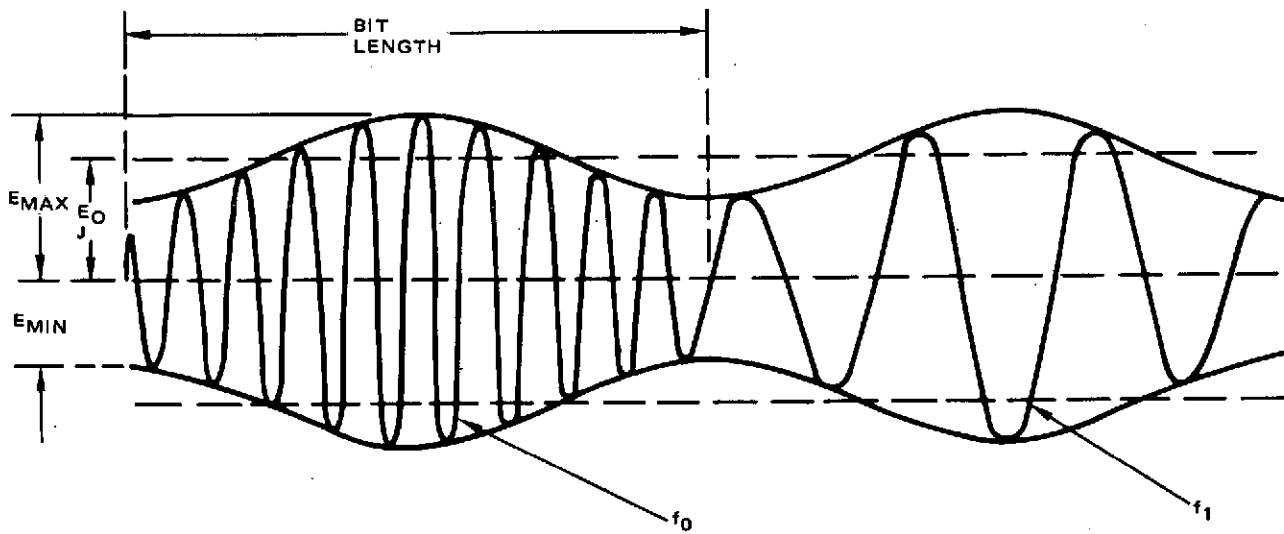
- 1 SEQUENCER OUTPUTS ARE CONNECTED TO DESIRED COMMAND OUTPUTS IN HARNESS
- 2 DESPUN DECODER - 159 COMMANDS
SPINNING DECODER - 63 COMMANDS

Figure 4-19. Despun or Spinning Decoder Block Diagram

A

B

20643-41 (U)



$$\text{MODULATION INDEX, } m = \frac{E_{\text{MAX}} - E_{\text{MIN}}}{2E_0} = 0.50 \pm 0.05$$

Figure 4-20. FSK/AM Signal Design

motor squib drivers are each commanded redundantly by the spinning decoders. After mating of the spacecraft to the adapter, until actuation of the separation switches, all squib driver power inputs are directly connected to ground.

4.2.2.2 Telemetry Subsystem

The encoder units of the telemetry subsystem, as shown in Figure 4-17, are fully redundant and cross-strapped so that either unit or every pair could fail completely without impairing the satellite's ability to transmit all telemetry data. Normally one encoder unit or the despun pair operates with one unit of the spinning pair. Two modes of data processing are used: PCM and FM real time.

The PCM mode is used for all attitude, thermal, power, and status information, including command verification. In the PCM mode, the spinning encoder receives, processes, and formats data originating on the spinning portion of the satellite. The output, which is connected across the spinning/despun via slip rings, is an 8 kHz biphasic waveform from which a despun encoder recovers the nonreturn to zero (NRZ-L) bit stream and derives a coherent clock. The despun encoder gathers and processes data originating in the despun compartment. It alternates its bit stream word-by-word with the spinning encoder bit stream, then converts the composite NRZ-L bit stream to a Manchester code format. The converted stream is used for phase modulating a Ku band carrier within the telecommunications repeater on the despun side and modulates the backup VHF transmitter on the spinning side.

The FM real time mode is used for real time attitude pulses (sun sensor pulses, earth sensors pulses, platform index pulses, and command execute pulses). The occurrence of a pulse coherently switches the frequency of an IRIG channel 13 subcarrier oscillator from its pilot tone to a different frequency, depending on the kind of pulse present. The output is connected via a slip ring to the despun encoder, the output of which phase modulates the Ku and VHF telemetry transmitters.

Spinning Encoder. In the PCM mode a spinning encoder conditions, multiplexes, and encodes the telemetry data originating on the spinning section of the satellite into a PCM bit stream. In the FM real time mode, the composite of real time pulses coherently switches the frequency of the SCO. All sequenced operations within the spinning encoder, including multiplexing, analog-to-digital conversion, attitude sensor pulse interval digitizing, and digital formatting, are timed by a 1.024 MHz crystal oscillator and countdown chain. The operation of the spinning encoder is described below with reference to the block diagram shown in Figure 4-21.

Multiplexers provide analog and digital gating circuits to time multiplex the telemetry inputs. The telemetry inputs consist of bilevel and analog data with a normalized range of 0.00 to 5.12 volts. Both analog and digital signals are multiplexed with the same type of circuitry, the digital signals being treated as analog signals up to the output stage of the digital multiplexer, which converts them to standard logic levels. The analog multiplexer

output is fed to a successive approximation type analog-to-digital converter which encodes each analog input into a serial 8-bit NRZ-L word, providing resolution of better than 0.5 percent of full scale. The outputs of the analog-to-digital converter and digital multiplexer are combined at a data node to form the partial PCM bit stream.

The attitude data processor performs a sequence of ten time interval measurements (Figure 4-22), to facilitate the accurate and rapid determination of satellite attitude. Each measurement equals the number of cycles of a 32 kHz reference frequency, derived from the 1.024 MHz crystal oscillator, counted during the time of the interval being measured. The count is telemetered along with a 4 bit code identifying which measurement it represents. The inherent measurement resolution is $\pm 1/2$ period of the 32 kHz reference, or approximately 16 microseconds. Measurement T2, from the occurrence of a sun or earth pulse to the start of the next telemetry frame, is of particular significance. It allows a suitably equipped ground station to synthesize a pulse train at the spin rate and at a known phase with respect to the generation of pulses on board the satellite. Such a pulse train (which can also be derived from the FM mode telemetry) is required for synchronous pulsing of the spacecraft jets.

The biphasic modulator converts the NRZ bit stream to a coherent biphasic format, in effect adding an easily recoverable clock for use by the despun decoder. It also adds a double amplitude pulse once each frame to which the despun decoder synchronizes its frame timing.

When the encoder is in the FM real time mode, it accepts and processes various real time pulses and transmits their occurrences as discrete changes in SCO frequency. The frequency transmitted and the duration of transmission correspond to the particular group that includes the occurring pulse (Table 4-20). All of the tone frequencies are within the IRIG channel 13 band. If two pulses in different groups should occur simultaneously, priority gating of the pulses permits the occurrence of only one pulse to be transmitted. The highest frequency group takes precedence. The most critical telemetry data are the attitude determination and execute pulses needed for spacecraft control. Except for a shared power supply and rotary transformer driver, the circuitry in the PCM path is entirely separate from that in the FM path to provide significant extra redundancy for these data.

Despun Encoder. In the PCM mode, a despun encoder conditions, multiplexes, and encodes the telemetry data originating in the despun compartment into a PCM bit stream, which it synchronizes and merges with the partial PCM from its associated spinning encoder. In the FM mode, a despun encoder switches the spinning encoder FM output to the telemetry transmitter. A comparison of block diagrams shows that the despun encoder (Figure 4-23) is identical in most respects to the PCM portion of the spinning encoder. In order to merge its PCM words with those of the spinning encoder, the despun encoder must derive its bit clock from the spinning encoder bit stream and synchronize the start of its telemetry frame with the spinning encoder double amplitude frame sync pulse. These tasks are performed,

TABLE 4-20. FM MODE TRANSMISSION

Pulse	Frequency, kHz	Duration, ms	Remarks
Group 1			
Psi (ψ)	15.059	5	
Psi (ψ_2)	15.059	5	
Group 2			
North enter earth	14.222	10	
North leave earth	14.222	20 (exception)	For identification on ground
South enter earth	14.222	10	
South leave earth	14.222	10	
Platform index	14.222	10 to 120	Variable with spin speed
Group 3			
Command execute	13.838	Variable time	= execute duration (40 ms for standard single pulse)
Pilot Tone	13.474		Transmitted when no pulse is present

respectively, by the clock and data detector circuit and the sync detector circuit. If the clock detector is unable to derive a bit clock, either because the spinning encoder has failed or has been commanded off, the clock selector will switch the despun encoder to its internal 1.024 MHz crystal oscillator so that despun telemetry may continue to be transmitted. The formatting logic performs the required merging of the partial PCM from the spinning encoder with despun encoder PCM. The combined NRZ-L bit stream is then coded into an NRZ-M waveform which biphas modulates the 32 kHz subcarrier output.

4.2.2.3 Component Physical Characteristics

Weight, power, and size data for selected components for the telemetry subsystem are listed in Table 4-21.

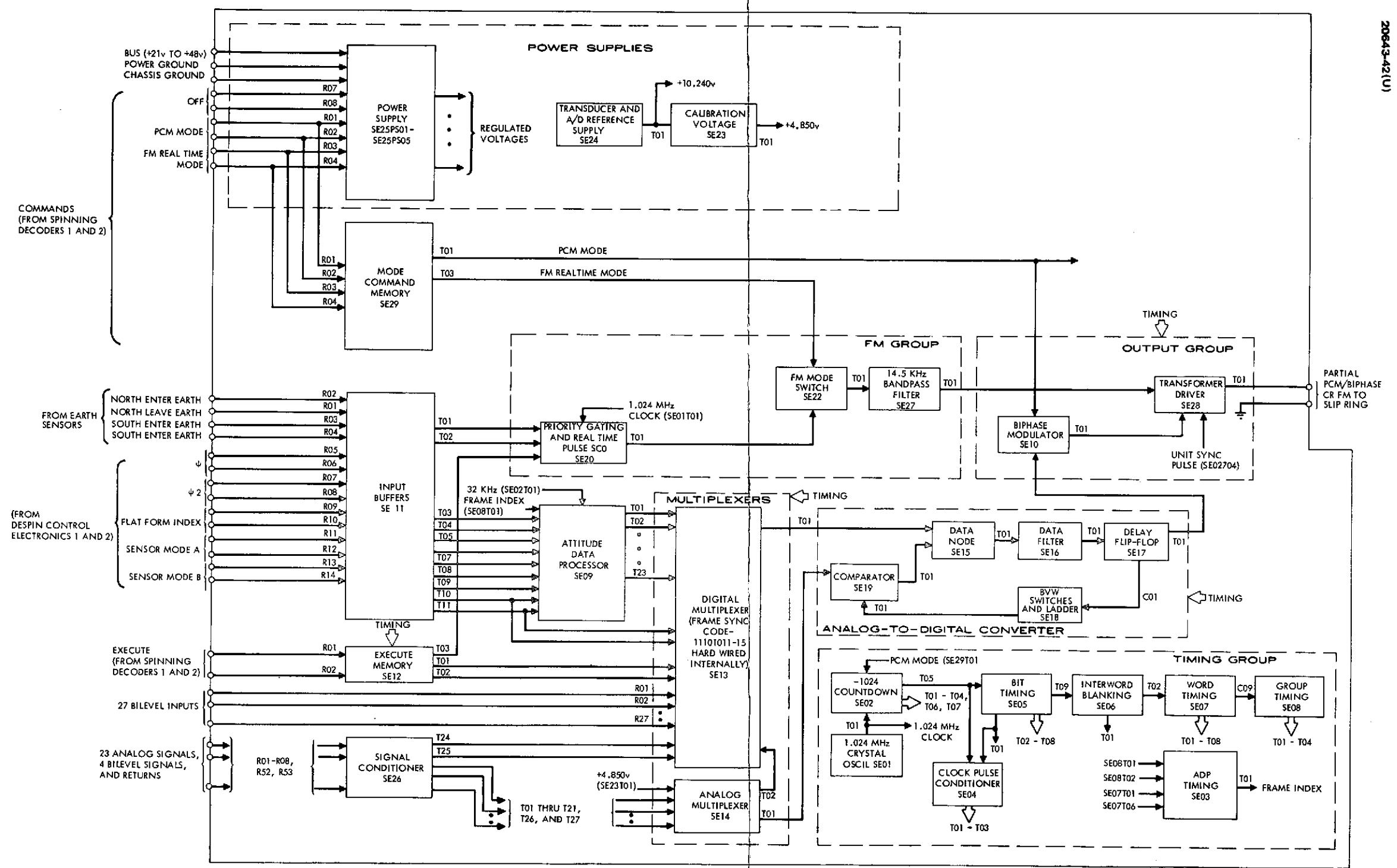


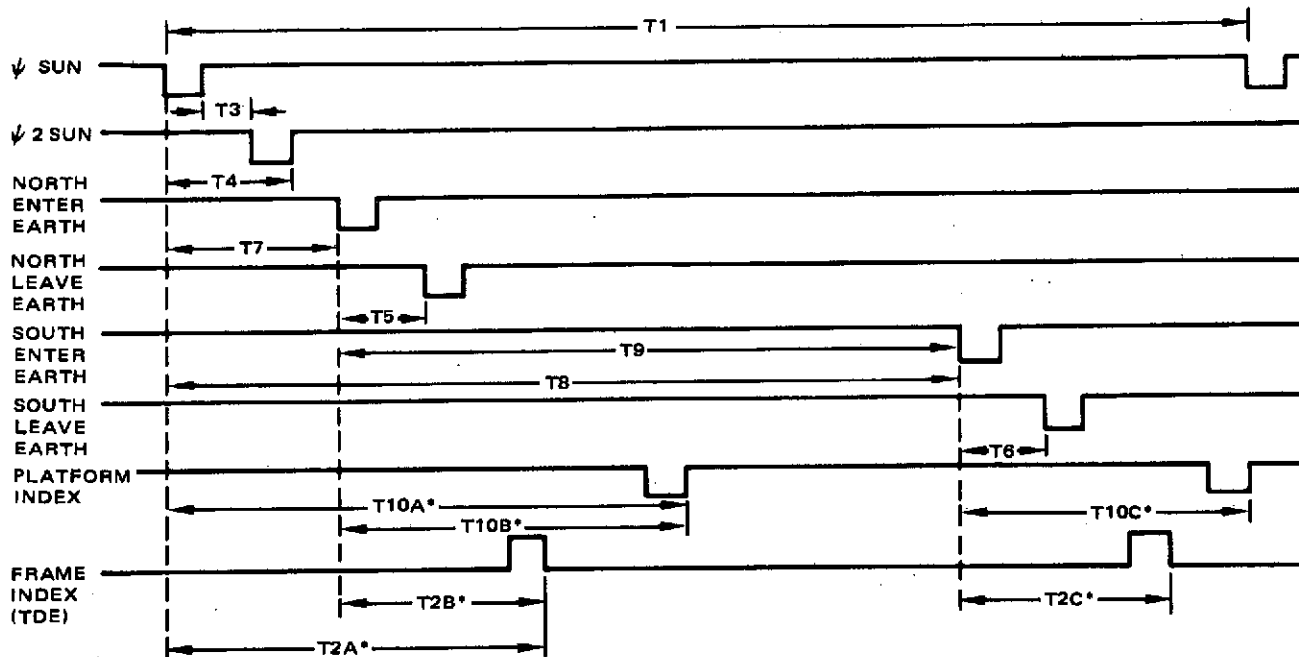
Figure 4-21. Spinning Encoder Block Diagram

A

B

PRECEDING PAGE BLANK NOT FILMED

20843-43(U)



*THESE MEASUREMENTS ARE TAKEN RELATIVE TO THE SPECIFIC SENSOR IN USE AT THE TIME; THUS, A DENOTES THE MEASUREMENT TAKEN WHEN IN SUN MODE, B WHEN IN NORTH EARTH MODE, C WHEN IN SOUTH EARTH MODE.

Figure 4-22. Attitude Data Processor Time Interval Measurement

TABLE 4-21. TELEMETRY AND COMMAND COMPONENT PHYSICAL CHARACTERISTICS

Unit	Number per Spacecraft	Mass per Spacecraft kg	28 Volt Bus		Size, cm			Program Identification
			Power Per Unit, watts	Spacecraft Standby Power, watts	Width	Length	Height	
Despun								
Decoder	2	2.7	0.9/1.8 ⁽³⁾	1.8	14.7	22.6 ⁽¹⁾	6.9	HS 312
Encoder	2	3.2	4.0		14.7	22.6 ⁽¹⁾	6.9	HS 312 M. C.
Squib driver	1	0.5	--	--	14.7	15.2	3.6	
Dual transponder	1	3.1	21/9.6 ⁽²⁾	9.6	18.5	43.2	5.1	
Diplexer	1	0.5	--	--	8.9	19.1	10.0	HS 333
Spun								
Decoder	2	2.7	0.9/1.8 ⁽²⁾	1.8	14.7	31.0 ⁽¹⁾	6.9	HS 312
Encoder	2	4.0	5.0	5.0	14.7	31.0 ⁽¹⁾	6.9	HS 312 Mod
Solenoid and squib driver	1	0.9	--	--	14.7	34.3	3.6	HS 320
Latching valve - heater driver	1	0.5	--	--	6.6	8.9	7.4	--

Notes:

(1) Stackable units

(2) High power/low power

(3) Standby/execute

FOLDOUT FRAME

FOLDOUT FRAME

20643-44(U)

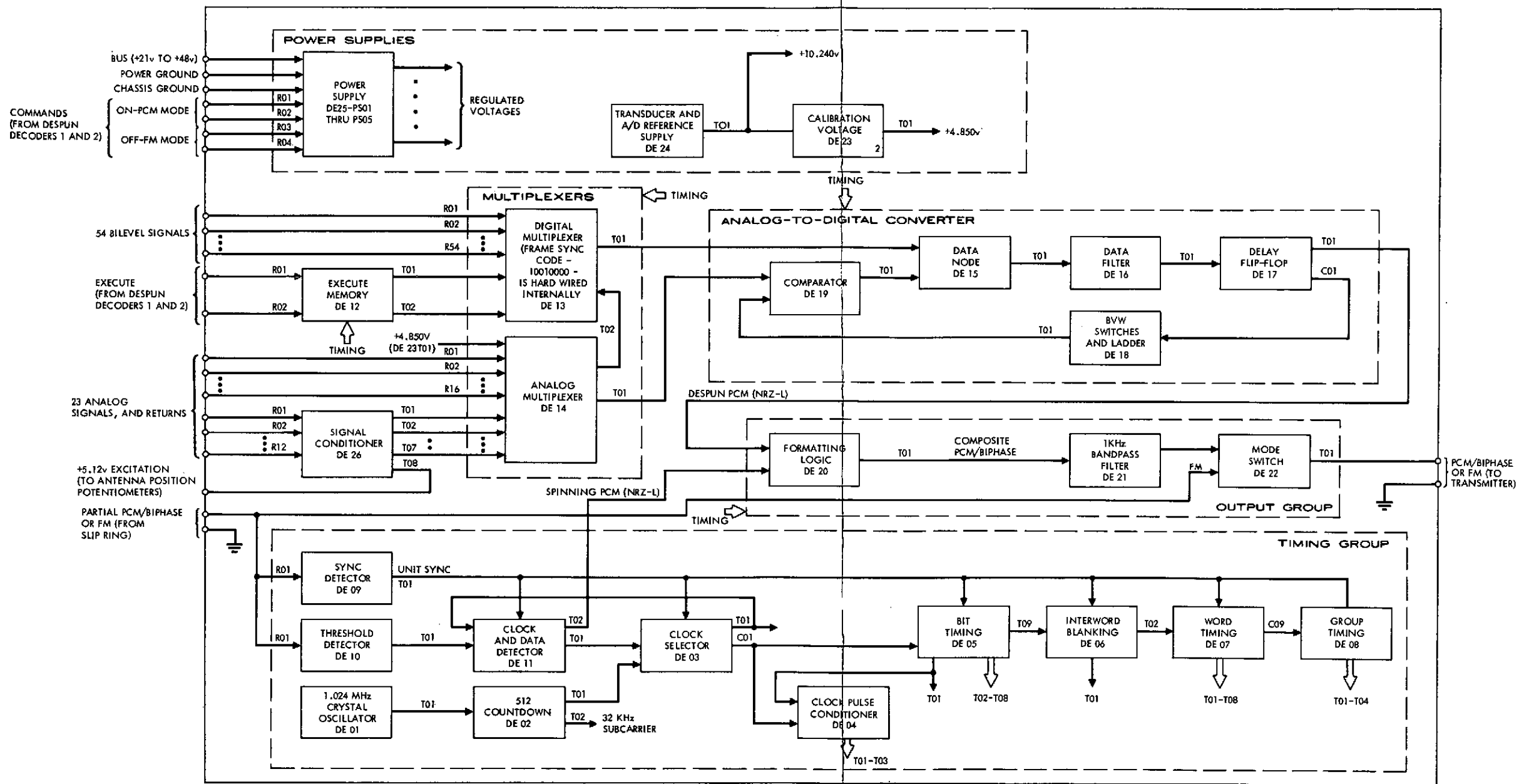


Figure 4-23. Despun Encoder Block Diagram

(Handwritten mark)

A

TABLE 4-22. TELEMETRY AND COMMAND PERFORMANCE CHARACTERISTICS

<u>Parameter</u>	<u>Characteristics</u>
TELEMETRY - INTELSAT IV TYPE	
PCM Mode	
Word length	8 bits
Frame length	64 words
Analog	48 words
Digital words	16
Bit rate	1000 bits/sec
Code type output	Manchester
FM Mode (attitude data)	
Subcarrier frequency	14.5 kHz
Data type	Real time pulses
Modulation	FM
Data transmitted	1) Sun pulses 2) North earth pulses 3) South earth pulses 4) Execute receipt
COMMAND - INTELSAT IV TYPE, MODIFIED	
Tones	1, 0, and execute
Input signal	FSK/AM
Bit rate	128 bits/sec
Command capacity,	255 maximum
Command verification via	Telemetry
Command execution	Real time
Execution synchronization	Sun or earth pulses
Maximum command rate	Approximately 4 per second

4.2.3 Performance

Telemetry and command performance characteristics are listed in Table 4-22. The command capacity may be divided as required between the spinning and despun sections of the spacecraft.

4. 2. 4 Technology Status

The Hughes configuration implementation for telemetry and command units was based primarily upon the use of technology approximating that used on the Intelsat IV program. This technology is now more than 3 years old. Although the system concept may not change significantly for the next few years, the availability and choice of parts will create some design problems. Also use of large scale integration techniques to implement more recent digital systems of this type (OSO for example) has proven effective both in cost and weight and is therefore being considered for all future systems at Hughes. In the event a production is scheduled in the future for telemetry and command units, it is suggested that consideration be given to the latest fabrication techniques to make the design more effective in cost, reliability, and weight.

4.3 ANTENNAS

4.3.1 Alternatives Considered

The frequency bands selected for low data rate user service are 400.5 to 401.5 MHz for the forward link and 136 to 137 MHz for the return link. The antenna design for this service was selected following a trade study which considered array paraboloid reflector and backfire type antennas.

Array elements considered were log periodic dipole radiators, helices, slot radiators, dipoles, and short backfire radiators. The number of elements in an array varies from three to nine depending on the gain of the individual elements of the array. The gain of an end fire type radiator such as the log periodic radiator is of the order of 10 dB and only three of these need be assembled to obtain a gain comparable to that obtained with nine of the simple dipole radiators. The dimensions of each of the arrays were adjusted to optimize the array gain over a 26 degree field of view. Array antennas were heavier, and more complex folding mechanisms are required to stow them in the available column within the payload fairing than other antenna types considered.

Paraboloid reflector type antennas with reflectors ranging from 3.66 to 5.48 meters (12 to 18 feet) were considered. Dual frequency feeds were utilized consisting of an efficient cup dipole at the focal point for the VHF feed and a small yagi array placed forward of the focal point for the UHF feed. The yagi array used for the UHF feed has a narrower beam than the cup dipole feed and tends to under illuminate the reflector thus broadening the UHF radiation patterns. The UHF pattern is also broadened by defocusing the UHF feed. However, the dual feed paraboloid reflector antenna, while mechanically attractive, was rejected because the gain and beamwidth would not be maintained over the frequency range required for the forward and return links.

The backfire radiator consists of a leaky cavity resonator formed by two reflectors of different diameters separated by a multiple of a half wavelength. The large reflector intercepts most of the energy radiated by the feed which may be located approximately a quarter wavelength from either reflector. The small reflector acts as a forward scattering obstacle for the feed radiation and forms the leaky cavity wall. The backfire radiator is a narrowband device but has a relatively high aperture efficiency intermediate between that of a planar array and that of a parabolic reflector. The electrical characteristics of backfire radiators of various dimensions were obtained from the measured data of L. R. Dod (References 1 and 2) and H. W. Ehrenspeck (Reference 3). A tandem arrangement of short backfire

type antennas was selected as the optimum choice from the standpoint of weight, size, and mechanical complexity of the various configurations considered.

Paraboloid reflector type antennas were selected for the medium data rate user service operating at S band. Configurations incorporating both 1.83 and 3.82 meter diameter antennas were considered. The 3.82 meter diameter antenna was selected to achieve compatibility with manned user spacecraft requirements.

A broad beam S band antenna for "order wire" service is also provided for MDR user emergency service requests. This antenna is of the backfire type.

A paraboloid reflector type antenna was selected for the TDRS-ground link operating at Ku band. Beam steering is required to compensate for altitude errors, orbital position, and the daily north-south movement caused by orbit inclination. Horns with northern hemisphere coverage were selected for the ground - TDRS link to avoid the occasional loss of contact resulting from inaccurate tracking of the high gain dish. Thus command and control of the TDR spacecraft is maintained in a reliable manner, and the use of the backup VHF telemetry and command links is not expected to be required once the TDR spacecraft are on station.

4.3.2 Baseline Description

The baseline antenna subsystem consists of eight antennas as shown in Figure 4-24. They are deployable VHF band backfire antenna for the low data rate user return link, the deployable UHF band backfire antenna for the low data rate user forward link, the deployable S band high gain parabolic reflector antenna for both forward and return links of the medium data rate user, the Ku band parabolic reflector for the telemetry space to ground link, two Ku band earth coverage horns for the command ground to space link, the S band backfire antenna for the order wire function, and the telemetry and command VHF omni antennas.

A lightweight rib-mesh antenna design has been selected for use in the S band, Ku band, and VHF/UHF antennas. The open mesh approach achieves low mass and minimizes thermal effects on surface tolerances. A mechanical deployment system is used which provides uniform, controlled rib and mesh unfurling and allows gravity testing without adding special fixturing. Radiation, Incorporated is presently on contract to the Air Force and NASA (AAFE NAS 1-11444) to design, analyze, fabricate, and test 3.82 meter diameter models.

The antenna design details have been generated by Radiation, Incorporated in response to a set of design requirements and configurational constraints specified by Hughes for its TDR satellite. This cooperative effort

has provided in-depth information on the antenna subsystem thus ensuring confidence in the spacecraft system design.

4.3.2.1 VHF/UHF Antennas

The VHF/UHF deployable medium gain antenna is made up of two stacked short backfire antennas as shown in Figure 4-25. The short backfire antenna consists of two plane reflectors spaced approximately a half wavelength apart with a feed placed between them. The area of the VHF antenna reflector is much larger than that of the UHF antenna. Both antenna reflectors are cupped to form a cavity. The feed is a crossed dipole centered between the two reflectors. The back reflector of the UHF antenna is 1.9 wavelengths in diameter, and the front reflector is 0.6 wavelengths in diameter for maximum gain. The back reflector of the VHF antenna is 1.7 wavelengths diameter to fit within the available stowage volume. Its front reflector is slightly larger than 0.6 wavelength in diameter to maximize the gain of the UHF antenna.

The coaxial cable feed lines are 0.635 cm Alumispline by Times Wire and Cable Company. Stripline hybrids and baluns are located at the base of the antenna post to generate the two orthogonal senses of linear polarization at VHF and the two orthogonal senses of circular polarization at UHF. The cables for the UHF antenna are routed down inside the VHF center post feed support.

The primary VHF reflective surface consists of a 1.27 cm grid Chromel-R wire mesh supported by 8, 3.82 cm diameter, tubular aluminum ribs as shown in Figure 4-26. Since the reflective surface is flat in the deployed condition, the surface accuracy has little dependency on the number of ribs used. The governing parameters affecting the number of ribs are deployed frequency, weight, gravity effects on the mesh panels, and the surface area loss due to the noncircular shape of the perimeter. With the choice of eight ribs, the geometric area loss between an octagon and a circle is approximately 10 percent. Further area loss due to a scalloping effect of the mesh gores between the ribs is eliminated by utilizing several intercostal wires at the outer edge of ribs and stepped increases in the circumferential mesh tension as the mesh progresses toward the outer boundary.

The secondary mesh surface, or "fence", is shaped and supported by secondary ribs hinged at the outer tip of each primary rib. The tendency of the mesh of this surface to scallop at the base and the tip of the secondary ribs is controlled by multiple intercostal wires and stepped tension values as described above.

The mesh is constructed from five-strands of 17.8 micron Chromel-R wire knitted into a flexible wire screen. The mesh is knitted with 1.27 cm openings for the VHF antenna and 0.635 cm openings for the UHF antenna. The mesh is plated and tensioned in a similar manner as described for the S band antenna.

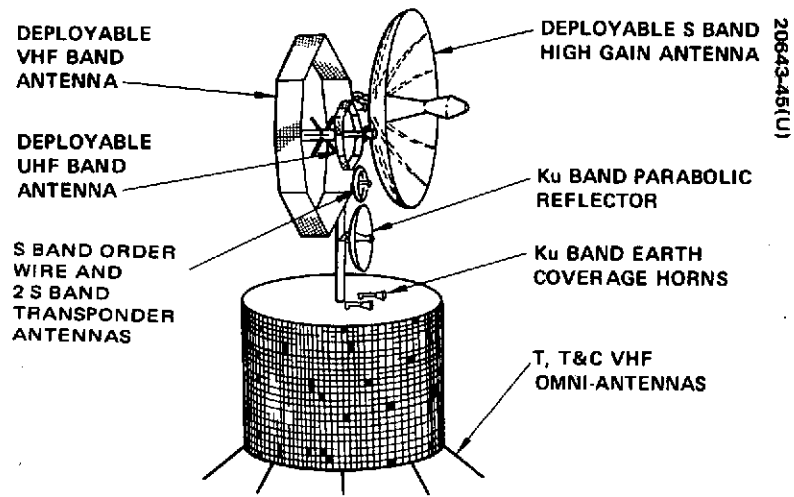


Figure 4-24. TDRS Antenna Subsystem

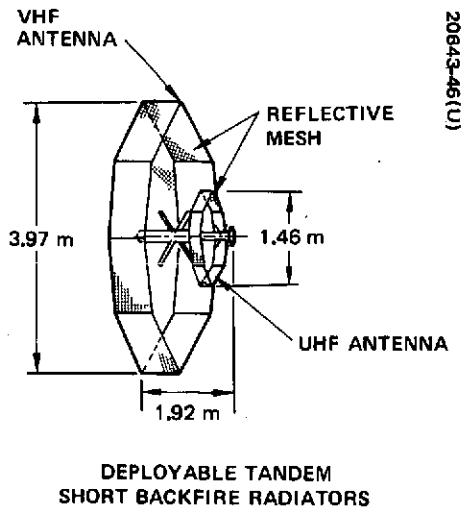
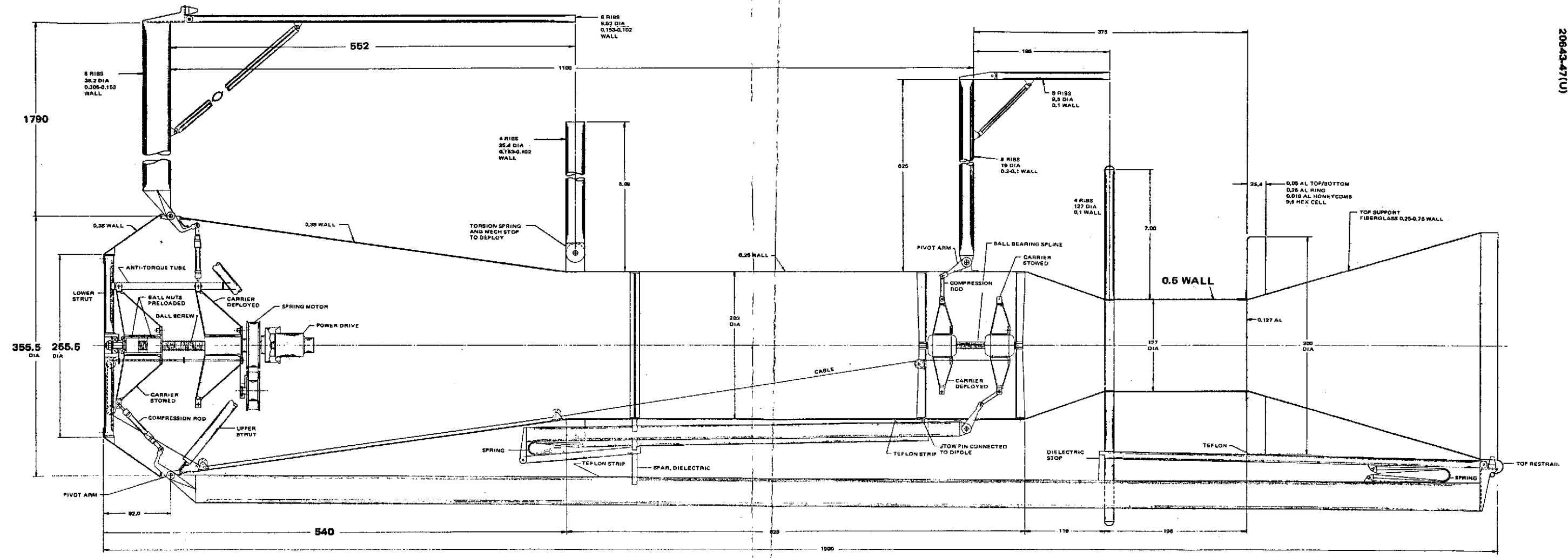


Figure 4-25. UHF-VHF Antenna for Low Data Rate User Service



DIMENSIONS IN MILLIMETERS

Figure 4-26. Dual Frequency VHF/UHF Antenna Layout

A

B

PRECEDING PAGE BLANK NOT FILMED

The VHF primary rib diameter of 3.82 cm was based on consideration of deployed resonant frequency, launch stress, gravity deflections, and mass. The ribs vary in wall thickness from 305 to 152 microns at the tips. The secondary ribs are made from 0.954 cm diameter aluminum tubes and have a tapered wall thickness from 152 to 102 micrometers at their tips. The ribs are constructed from 6061 T6 aluminum alloy for strength and are highly polished ($\alpha_s = 0.18-0.2$) for thermal requirements. The rib pivot arms are the same design described for the S band antenna.

The UHF antenna primary ribs are constructed from 1.91 cm diameter tubes with the wall thickness tapering from 204 microns at the root to 102 microns at the tip. The secondary ribs are 0.954 cm in diameter and have a constant wall thickness of 102 microns. The rib pivot arms are of the same design used in the VHF antenna. The ribs are highly polished to provide the necessary thermal control.

A cone/cylinder provides the central support for stacking the dual antenna cavities. This central structure consists of five portions: three cones and two cylinders. Each section is manufactured from 6061 T6 aluminum sheet which is rolled and welded along a vertical seam. Three final members are constructed from these pieces making a hub, lower cone/cylinder, and an upper cone/cylinder. These three sections are assembled by screws which allow the structure to be disassembled for access to each deployment system, RF feed lines, and microwave components within the cone. The center structure is topped off with a dielectric structure extending up to the top of the folded ribs. The function of this member is to provide an attachment structure for attaching the antenna to the spacecraft and also provides a base to restrain the ribs in the stowed condition. The structure loads are primarily reacted at the antenna base and tip through tiedown locks to spacecraft structure.

The mechanism used to deploy the VHF antenna ribs is identical to that described for the S band antenna. A second mechanism used to deploy the UHF ribs has a kinematic action identical to the VHF deployment system with the exception that it uses a cable drive to move the UHF carrier along a recirculating ball spline from the stowed position to the deployed location. The cable is connected to the carrier of the VHF antenna so as to synchronize the two deployment actions and to use the deployment energy from the VHF MDS for the UHF deployment. The deployment cable has a built-in delay which allows the VHF ribs to partially deploy before the UHF ribs are rotated from their stowed positions. The VHF rib will be deployed approximately 0.436 radians at the start of the UHF rib rotation. As the VHF ribs are moving away from the stowed UHF ribs the "fence" portion (secondary ribs) of both antennas start to unfold. This action continues until the deploying springs pop through from a bent leaf spring shape to a straight rigid column having an elliptical cross section. With the secondary ribs now fixed in position relative to the primary ribs, the VHF ribs continue to unfold reaching the 0.436 radian position at which time the UHF starts to move away from the center support. At this time, both sets of ribs are moving with the VHF ribs pulling further away from the UHF secondary rib tips.

The VHF dipoles are located out of line with the folded ribs by one diameter (2.54 cm). A pin attached to the tip of the dipole extends over and underneath the stowed UHF antenna rib. With the rib in its stowed position it preloads the dipole against an adjustable stop on the center cone. The UHF primary and secondary ribs are also restrained and preloaded by a set of stacked restraint spars which are released as the VHF rib starts its deployment. These same spars serve to preload and stiffen the longer VHF ribs. The VHF secondary ribs are also preloaded on dielectric stops located on the secondary rib tips. Finally the VHF primary ribs are restrained at their tips by a preloaded cable which is wrapped around the eight rib tips. Table 4-23 itemizes the mass for the combined UHF/VHF antenna.

TABLE 4-23. UHF/VHF ANTENNA MASS BUDGET

<u>Item</u>	<u>Mass, kilograms</u>
Center structure	1.27
Hub	0.36
VHF	4.22
Primary ribs	1.04
Secondary ribs	0.05
Dipoles	0.09
Pivot arms	0.72
MDS	0.96
Cable	0.18
Midrestraint	0.18
Mesh	0.18
Intercostals	0.09
Restraint	0.64
Deploying springs	0.09
UHF	1.40
Primary ribs	0.18
Secondary ribs	0.05
Dipole	0.05
Pivot arms	0.36
MDS	0.59
Mesh	0.09
Deploying springs	0.04
Intercostals	0.04
Adhesives, fasteners, and miscellaneous hardware	<u>0.68</u>
Total	7.93

Cutting of the upper restraint cable allows the cable to be released and snapped out of position by the eight leaf springs and starts the deployment sequence. The spring motor in the VHF deployment system starts the carrier moving via the ball-screw rotation, which in turn starts the ribs to deploy. As the ribs rotate away from the center support, both the UHF and VHF secondary ribs start to deploy. To assure that the secondary rib tips do not tangle in the mesh, a shaped teflon slide strip is located along the primary rib surface in the exact area where the secondary ribs slide along the surface. When the VHF ribs have deployed 0.436 radians, both sets of secondary ribs have completely deployed and their deployment springs have snapped through into stable load bearing columns. At the 0.436 radian position, the UHF ribs start their deployment, allowing the VHF dipoles to release and start deploying. A teflon slide strip is provided along the back of the UHF ribs for the VHF dipole pins to slide on throughout their deployment. The double deployment continues until both sets of ribs reach their mechanical stops and the carriers pass through their overcenter conditions.

4.3.2.2 S Band Antennas

The S band order wire antenna shown in Figure 4-27 is electrically identical to the UHF antenna except scaled to S band. The reflectors are made from perforated sheet metal for low cost and light weight. Single sense circular polarization is generated by slot fed crossed dipoles.

The S band high gain antenna consists of a 3.82 meter diameter, deployable, parabolic reflector and coaxial cavity feed all mounted on a two-axis positioner for beam pointing as shown in Figure 4-28. The parabolic reflector is a rigid rib and mesh device with a focal-length-to-diameter ratio of 0.4. The feed consists of a round coaxial cavity fed by a polarizing network consisting of a quadrature hybrid and two baluns feeding four probes mounted in the cavity. The quadrature hybrid provides operation with the two orthogonal senses of circular polarization.

Figure 4-29 illustrates the 3.82 meter diameter S band antenna reflector in its stowed configuration. An aluminum feed support cone forms the central structure to which all components are attached. The antenna ties to primary spacecraft structure at its base and tip in this stowed position. This support concept differs from a base mounted cantilever support which was used in previous antenna designs by Radiation, Incorporated. The two-point attachment offers appreciable weight savings.

The parabolic reflector is formed by 12 rigid ribs of 3.82 cm thin wall aluminum tubes which support and contour the elastic mesh surface. The number of ribs was based on a tradeoff study of surface tolerance, mass and deployed dynamic performance. Analyses indicate the deployed resonance exceeds the 4 Hz requirement with 12 ribs, and the use of fewer than 12 ribs was not considered practical because of gravity effects in positioning the reflective mesh. With fewer than 12 ribs the mesh gore span between adjacent ribs becomes so large that gravity deflection of the mesh becomes

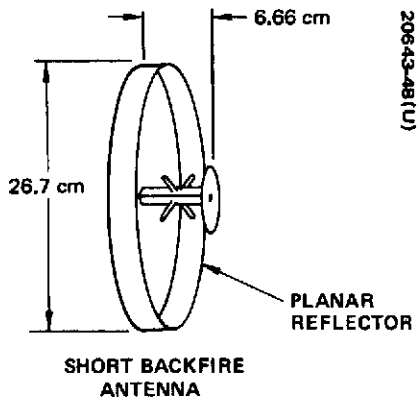


Figure 4-27. S Band
Order Wire/
Transponder Antenna

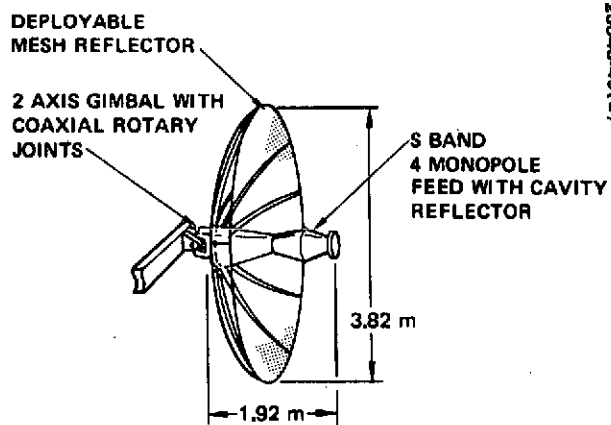


Figure 4-28. S Band High Gain
Antenna for Medium Data Rate
User Service

PRECEDING PAGE BLANK NOT FILMED

significant and makes the setting of the reflector surface a difficult task. The rib walls are uniformly tapered from the 305 micron thickness midsection to 204 microns at the rib root and 152 microns at the rib tip. This tapering matches the rib strength to the moment profile of the rib loading in the maximum stress condition that occurs in the restrained stowed condition.

The double mesh design was selected for the S band antenna. Figure 4-30 illustrates the reasons for this choice. This figure shows antenna mass as a function of the surface accuracy for single and double mesh designs. The surface accuracy of the single mesh design is directly dependent on the number of ribs while the surface accuracy of the double mesh is mass independent since the surface accuracy is achieved through use of ties between the two mesh layers. The surface accuracy requirement of 0.153 cm rms total error dictates the use of a double mesh design for minimum mass.

The reflective mesh is constructed from five-strand bundles of 17.8 micron Chromel-R wire knitted into a wire screen. The front mesh is knitted with openings of 2 mm. This size opening was selected to ensure satisfactory RF reflectivity. The back mesh is knitted with 1.27 cm openings. This size opening is sufficient to allow the back mesh to be utilized as a secondary drawing surface for contouring the front mesh while minimizing the antenna weight. After knitting, the mesh is plated with electroless nickel and gold coatings, respectively. The nickel/gold plating provides the necessary properties for electrical reflectivity and is also compatible with the thermal control design of the antenna. The finished mesh is a low spring rate, elastic material. The use of this "soft" mesh with the rigid ribs results in a rib-dominated reflector surface which is relatively unaffected by changing mesh forces and orbital thermal variations throughout the antenna life. The mesh is attached to the ribs in a tensioned state of predetermined levels which are sufficient to ensure the mesh will remain in a flat, unwrinkled condition throughout the orbital life. Based on mechanical tests of various mesh samples at Radiation, Incorporated, circumferential tension and radial tension loads are employed as listed in Table 4-24. A series of creep tests were performed on specimens of gold plated Chromel-R knitted wire mesh consisting of 14 strands of 0.00127 cm diameter wires spaced at 0.159 cm nominal pitch. A nominal 7.6 by 15.3 cm loaded mesh specimen was attached to the test frame which provides a means of independently imposing strain in two orthogonal directions and measuring the corresponding changes in load, that would occur over a 16 hour period. The test

TABLE 4-24. REQUIRED MESH TENSION

Item	Hoop Tension, Newtons/cm	Radial Tension, Newtons/cm
Front mesh	0.035	0.0175
Back mesh	0.021	0.00526

C 23

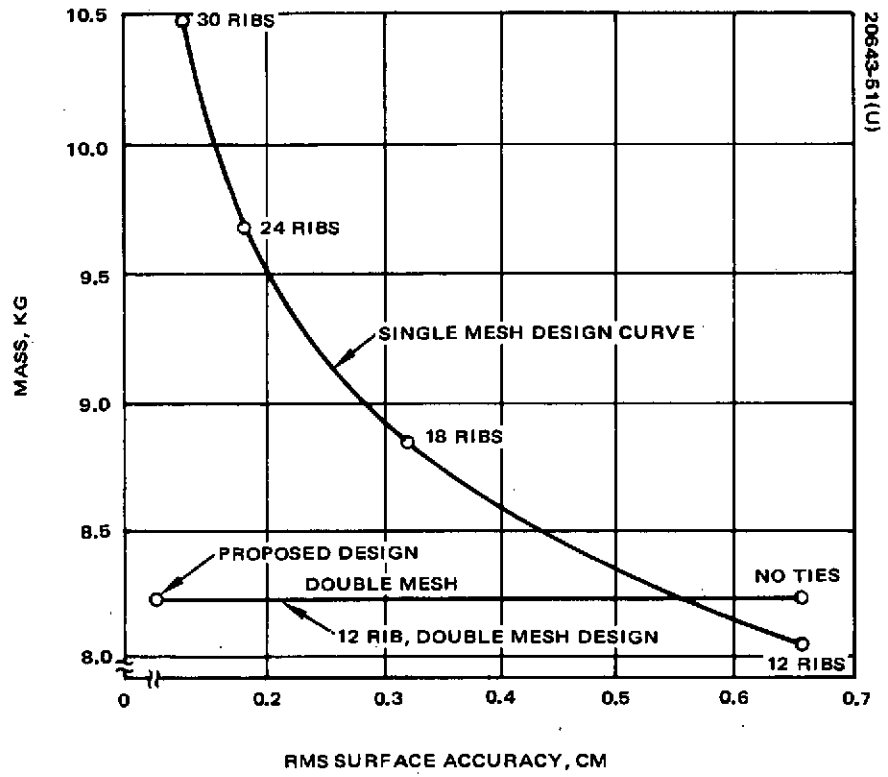


Figure 4-30. Mass Versus Surface Accuracy for Single and Double Mesh 3.8 Meter Antenna

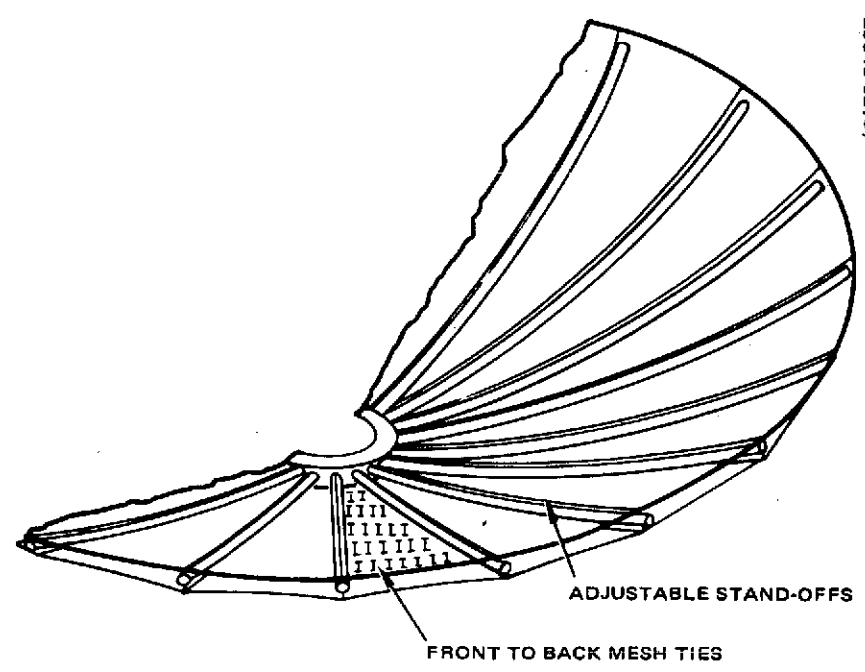


Figure 4-31. Double Mesh Concept Design

specimen frame dimensions were held constant during the test after a prescribed level of load was established. Some small changes in frame dimensions resulted from different temperatures at the start and end of the test. The changes in mesh preload due to creep were found to be negligible at both room temperature and 366 K. The small difference in load was found to coincide with the change in frame temperature.

Another mesh sample was stretched in the form of the antenna gore and was measured after several hundred kiloseconds at ambient temperature with no measurable creep effects.

The double mesh technique essentially eliminates systematic surface error by reversing the front mesh bulge and pulling the front mesh to the back mesh as illustrated in Figure 4-31. The back mesh is separated from the front mesh by the rib diameter, and both meshes are tied by simple tension wires. By properly tensioning these tie wires, the reflector surface can be contoured to a precision parabolic shape. A surface accuracy of 0.176 mm rms has been achieved on a 3.8 meter diameter reflector by Radiation, Incorporated. This accomplishment compares with 1.52 mm surface contour accuracy which is required for the TDRS S band antenna.

The antenna mass is projected as 8.27 kg as shown in Table 4-23. This projection is based on a limited amount of member sizing and factoring from previous deployable antenna programs. The AAFE antenna design by comparison is currently estimated to weigh 10.57 kg. In this application, however, the antenna is cantilevered from its base and it has also a larger central nub.

Deployment of the reflector from the stowed to the fully deployed position is precisely controlled to eliminate the transfer of any deployment energy to the spacecraft. The controlled deployment also prevents impact loading of the rib structures and mesh, thereby assuring that 1) the preset parabolic surface is not distorted by the deployment action and 2) no mesh loading conditions result that exceed the mesh strength limits. Figure 4-28 also illustrates the stowed and deployed positions of the deployment mechanism. The deployment mechanism utilizes redundant energy drive systems to rotate a ball-screw within a recirculating ball nut. The resultant linear motion of the ball nut serves to rotate each rib from the stowed to deployed position through the individual linkages to each rib. The primary drive of this system is a constant torque spring motor. The spring motor also provides a preload on the mechanism in the stowed condition. The spring motor provides sufficient energy to deploy the antenna in any orientation under gravity conditions. In a zero gravity condition, the spring motor capability exceeds the deployment energy requirements (Figure 4-32). The backup drive system consists of two miniature torque motors driven through a gear system. The torque motors normally function as dynamic brakes, controlling the deployment rate and requiring no electrical power. If required to deliver power, the motors can increase the torque to the ball-screw by as much as a factor of four.

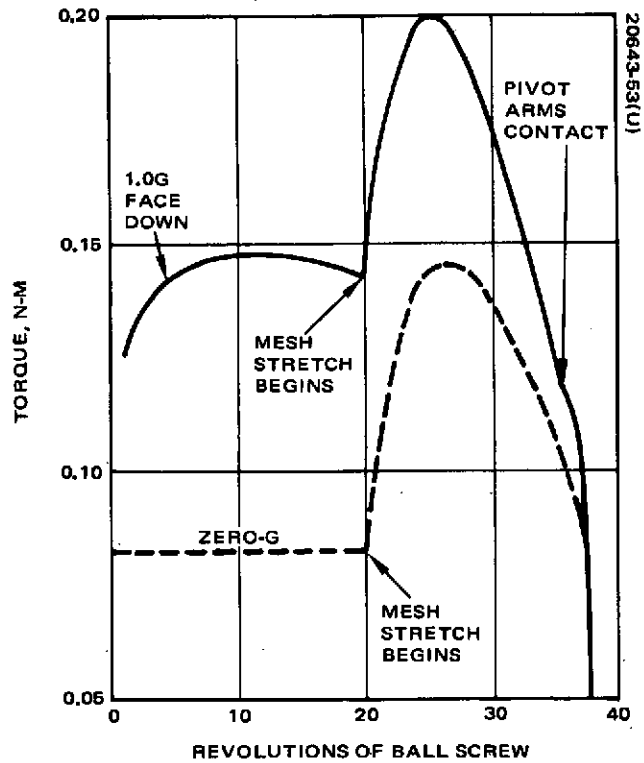


Figure 4-32. Deployment Torque Requirements

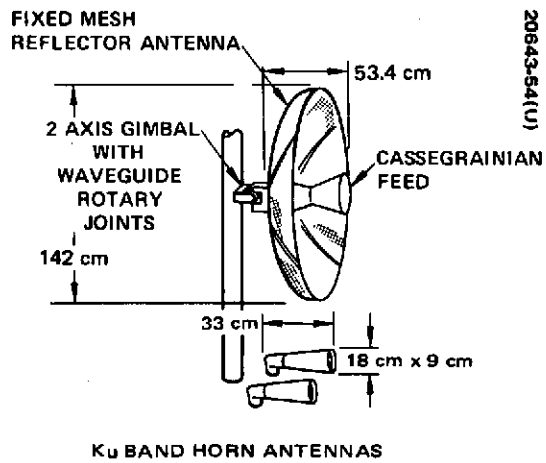


Figure 4-33. Ku Band Antennas, TDRS/Ground Links

Latching in the deployed condition is accomplished by driving the ball nut carrier and linkages through an overcenter condition (relative to the pivot arms). In this condition the mesh tension forces, rib loads, spring motor, and pivot arm preload, all force the carrier against a mechanical stop. Any external loads that tend to restow the antenna only serve to further increase the loading of the ball nut carrier against the mechanical stop. This toggle action eliminates the requirement for additional latching devices in the deployed condition and thereby improves reliability. A secondary advantage of the toggle latching is convenience during ground testing and handling. A reverse torque can be applied to the ball-screw to back drive the mechanism through the latching toggle action. The antenna can thus be remotely stowed during ground testing by reversing the current to the electric motors.

All rib and linkage bearings are designed with simple parallel redundancy. This design greatly reduces the probability of any bearing exhibiting undesirable friction changes. In the event of a high friction condition, the deployment system is designed to transfer the full deployment force to the lagging member and overcome the increased friction. All moving, sliding, and rolling joints can be lubricated with appropriate solid dry film lubrication systems for maximum reliability under worst-case environmental conditions. The estimated mass of the S band antenna is listed in Table 4-25.

The reflector ribs are restrained in the stowed configuration at both the midsection and the tips. This restraint system design forces the stowed antenna to act as a single structural element which achieves a high stowed resonant frequency with minimum launch stress. To maintain structural efficiency, the stowed rib tips are restrained by a moment-resisting joint with a preload maintained by a tensioned cable around the rib tips. At deployment initiation, a redundant set of guillotine cable cutters severs the cable. The severed cable is instantly cleared from the ribs and held captive by 12 leaf springs located directly above the rib tips. The rib midsections are restrained to the feed support cone by a spar supported hoop constructed of high modulus ($E = 55 \text{ GN/m}^2$) fiberglass reinforced epoxy. In the stowed condition, each rib midsection is restrained to the hoop by a ball end stem mated into a socket on the dielectric hoop. Preloading of this ball joint is accomplished by deflecting the rib tips into their restraint after the rib midsections have made contact with the dielectric hoop. Deployment is complete approximately 90 seconds after release when the ribs come to rest against their stops and the mechanical linkages toggle and preload each rib against its stop by a predetermined amount. This preloading develops a moment resisting joint, and effectively eliminates any joint looseness, maintains a high deployed natural frequency, and ensures surface repeatability.

4.3.2.3 Ku Band Antennas

The Ku band high gain parabolic/reflector antenna (Figure 4-33) consists of a 1.42 meter diameter rigid rib and mesh reflector and a

TABLE 4-25. S BAND ANTENNA MASS BUDGET

<u>Item</u>	<u>Mass, kilograms</u>
Feed support system	1.51
Cone	0.98
Hub	0.36
Radome cone	0.04
Upper cone	0.13
Rib assembly	2.83
Ribs	1.63
Pivot arms	0.72
Standoffs	0.13
Midpoint restraint pins	0.13
Rib tips	0.22
Mesh gore assemblies	0.81
Front gore assembly	0.50
Back gore assembly	0.18
Intercostal wire	0.09
Tie wires	0.04
Mechanical deployment system (MDS)	0.95
Restraint system	0.75
Hoop and spar	0.27
Top restraint ring	0.18
Rib tip cones	0.04
Fasteners	0.04
Pyrotechnics and cable	0.22
Thermal control	0.15
Rib insulation	0.05
Cone/hub insulation	0.10
RF feed and microwave components	1.31
Feed	0.30
Cable	0.55
Baluns and hybrid	0.23
Connectors	0.23
Total mass	8.3

multimode-horn feed with a cassegrainian subreflector all mounted on a two-axis positioner for beam positioning. A shaped reflector and multimode feed was chosen for high antenna efficiency. Large amplitude taper across typical reflector antennas is significantly reduced by distorting the shape of the subreflector away from a hyperboloid. Phase error thereby occurring is corrected by slight distortions on the main reflector. Aperture efficiency improvements from 70 to 80 percent have resulted by employing this technique. A corrugated horn gives rise to the two modes needed to make the feed pattern symmetrical with very low sidelobes. The polarizer that generates a single sense of circular polarization consists of a waveguide orthomode tee for good impedance match and a multiple iris phase shifter for good polarization ellipticity.

Two receive Ku band antennas will each cover the northern hemisphere with CP beams. The approximate beamwidth requirements are 9 by 18 degrees. The corresponding on-axis gain estimate is 22.7 dB. An array of two fin-loaded pyramidal horn antennas is presently considered to be the most simple and proven approach toward satisfying the CP beam coverage requirements over the 13.4 to 14.2 GHz transmit and 14.4 to 15.35 GHz receive bands. The fin-loading at the horn aperture equalizes the E and H plane beamwidths, thereby providing CP over the full field of view, as well as at the beam peak. Each antenna assembly type utilizes a four-iris square guide polarizer and an orthomode tee. For simplicity, the unused orthogonal arm of the orthomode tee has been shorted out. Where the CP and VSWR requirements are stringent, it may be necessary to load this unused orthogonal arm.

Figure 4-34 illustrates the high gain Ku band antenna design. A set of 12 tubular aluminum ribs is used with the double mesh technique as described in the previous section to form the reflective surface. This rigid rib and mesh design weighs approximately one-third that of a solid reflector of sandwich construction.

The mesh material is the same type as that for the S band dish except the front mesh openings are 0.152 cm in size. The mesh surface tolerance is held to better than 0.0254 cm rms through use of the double mesh concept and adjustable rib standoffs. The smaller antenna diameter and the rigid antenna construction should allow accomplishment of surface accuracy.

The supporting ribs are 3.18 cm in diameter with a tapered wall of 0.0102 cm at the rib root to 0.0152 cm at the top. The ribs are made from 6061 T6 drawn aluminum tubing. The thermal control will consist of wrapping the ribs with multilayer (superinsulation) blankets. Each rib is supported in a boxed ring used as the hub. The hub is bonded to the feed support to become a rigid structure. It also serves as the interface flange to mount the antenna to the spacecraft. The support cone is made from aluminum sheet metal rolled and welded along a vertical seam. The final product is etched to a 0.0152 cm thickness. Thermal control consists of multilayer blankets.

The subreflector is supported by a dielectric cone made from high modulus fiberglass and epoxy. The subreflector is made in a sandwich form using aluminum honeycomb core and thin wall skins of fiberglass covered with 0.00254 cm aluminum foil. Type 1160 aluminum foil is used for high conductivity and elongation properties.

The Ku band feed for the 140 cm reflector uses a multimode horn feed and a shaped 23 cm subreflector to produce an overall antenna efficiency of 68 percent. The main reflector is also shaped for good phase efficiency. The feed horn and microwave components are made from aluminum plate which has been etched to a waffle pattern to maintain good stiffness to mass ratios. The entire assembly is dip brazed together without any flanges to reduce mass in this area. This assembly is bonded in the support cone before the radome and subreflector are bonded into place. After alignment, the subreflector is bonded to give a single assembly. The radome is coated with an RF transparent space qualified white paint for thermal control while the back of the subreflector is covered with multilayer blankets.

The mass of the total system is 1.39 kg as detailed in Table 4-26.

4.3.2.4 VHF Telemetry and Command Antenna

The telemetry and command VHF antenna shown in Figure 4-35 is a multiple whip design that provides adequate radiation pattern coverage around the entire satellite. This antenna consists of eight whip antennas fed

TABLE 4-26. Ku BAND ANTENNA MASS BUDGET

<u>Item</u>	<u>Mass, kilograms</u>
Front mesh	0.21
Back mesh	0.06
Standoffs and ties	0.06
Ribs	0.31
Rib insulation	0.05
Subreflector	0.07
Support cone	0.34
Horn, polarizer, waveguide	0.22
Cone thermal blankets	<u>0.07</u>
Total mass	1.39

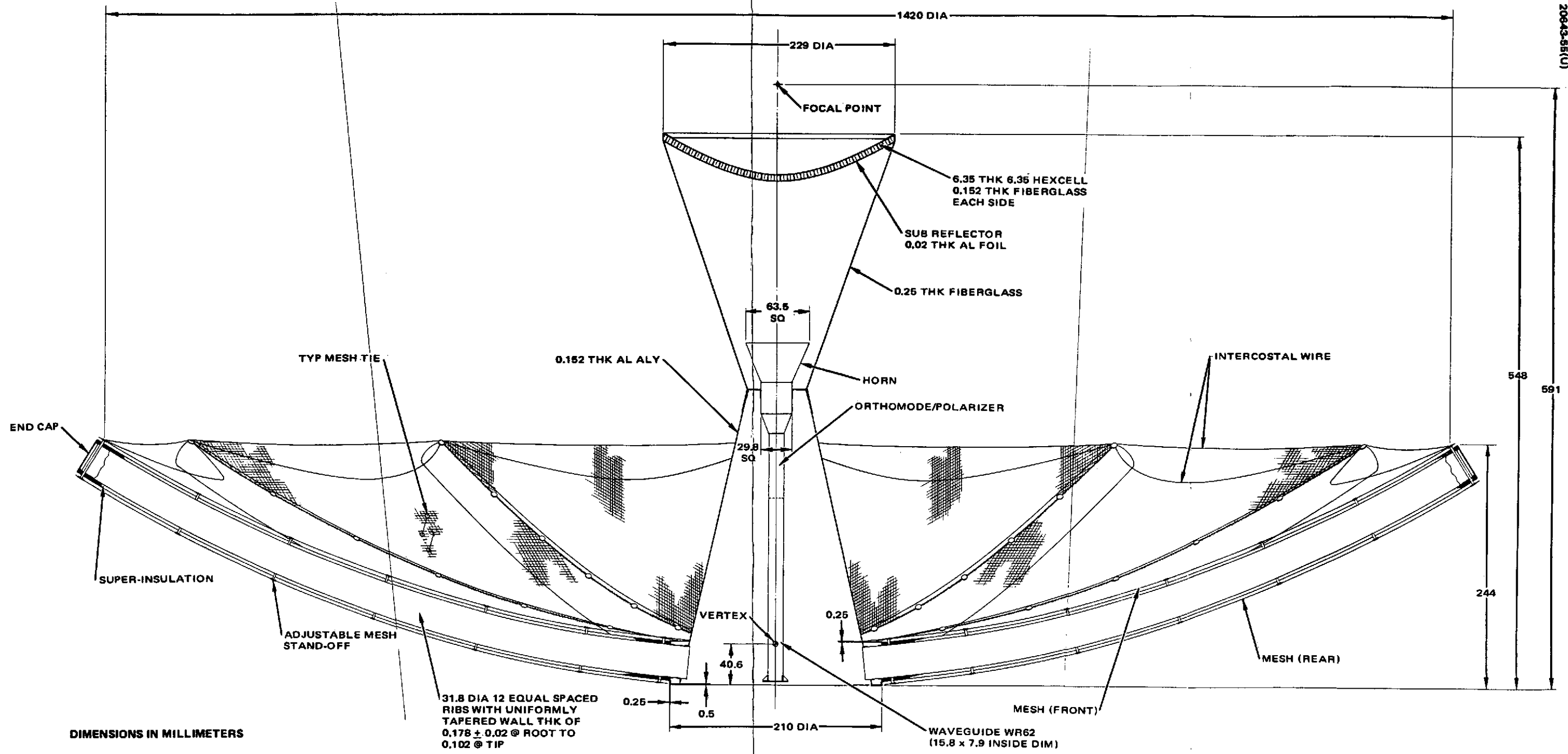


Figure 4-34. Ku Band Antenna Layout

A

B

PRECEDING PAGE BLANK NOT FILMED

by a hybrid balun. The eight whips are attached to the edge of the solar panel and are equally spaced. Each whip is tilted away from the spin axis at a physical angle of 60 degrees and is driven 45-electrical-degrees out of phase with adjacent whips for best radiation coverage. The phase sequence is in opposite directions for the two terminals of the hybrid balun that attaches to the diplexers. The overall radiation pattern is determined by the pattern of the individual whips combined with the pattern of the currents excited on the solar panel by the whips. The resulting radiation pattern of the antenna system is elliptically polarized.

4.3.2.5 Antenna Deployment Mechanisms

Three deployment and two antenna tracking mechanisms are used in the TDRS design. These are described in the following sections.

Deployment Mechanisms. Deployment devices are used for rotation of the S band and VHF/UHF antenna support braces away from the central antenna mast, and a 90 degree azimuth rotation of the VHF/UHF antenna system. These devices are spring loaded hinge joints of identical design which is patterned after the flight proven Hughes Flexible Rolled-Up Solar Array (FRUSA) deployment mechanism. A redundant set of torque springs overcomes inertial forces, bearing friction, RF cable bending, and latch actuation. Kinetic energy contained in the antenna system at latching will be absorbed by elastic structure deflection without relying on elaborate escape-ment or damping arrangements. Figure 4-36 shows the FRUSA deployment hinge assembly. Simplicity of design and operation was the major design goal of the deployment mechanism. The deployment mechanism function is to swing the antenna out from its stowed position and lock it in the flight position when the pyrotechnic launch lock devices are released. The hinge is a simple tongue and clevis joint with ball bearings to ensure low friction. Bearing lubrication is by burnished-in molydisulfide, with additional MoS₂ in the Duroid 5813 ball retainers. Deployment energy is furnished by two symmetrically mounted spiral springs concentric with the hinge pin, wound at assembly to provide a margin adequate to tolerate variations in bearing friction and cable stiffness due to wide ranges in expected temperature at operation. Residual energy at the end of the stroke is absorbed by bending of structure as a consequence of employing a hard stop at the hinge. A door latch type device locks the hinge in flight position. The mechanism performed flawlessly during unit and system tests and in flight.

Tracking Mechanisms. Motorized two-axis drives are used for the high gain S band antenna and the Ku band reflector positioning in azimuth and elevation. The selected position control elements are direct digital in operation and incorporate power off magnetic holding to permit power conservation by requiring spacecraft power only when the antenna is in motion. This magnetic detent is effective for each single step of the motor; therefore no accuracy anomalies occur when power is removed.

The drive mechanism (Figure 4-37) is a two-axis positioner (elevation over azimuth) that moves its assigned load through ± 16 degrees in

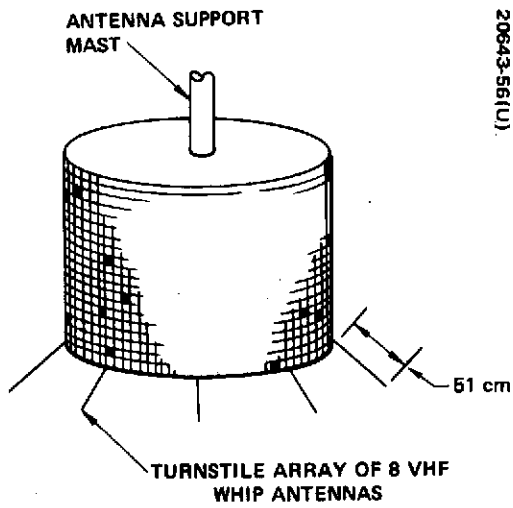
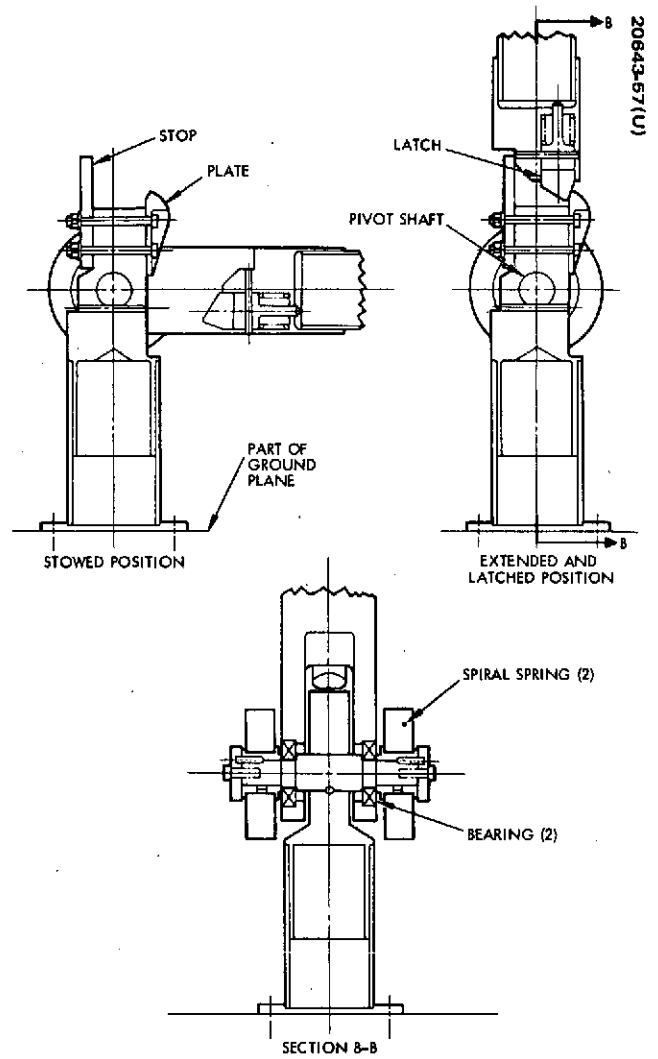


Figure 4-35. VHF Omni Antenna for Telemetry and Command Service

20643-56(U)



20643-57(U)

Figure 4-36. Sections Through Deployment Mechanism

azimuth and elevation. The two axes are driven by identical motor drive assemblies and are joined by a gimbal structure resulting in an elevation over azimuth configuration. The gimbal assembly is supported in each axis by the preloaded angular contact ball bearings of the motor drive assembly and by an outboard radial deep groove bearing. The bearing size is determined for launch load imparted to the mechanism and bearing spacing is chosen sufficient to minimize error due to bearing runout. Dry film lubrication is used throughout the mechanisms for temperature range compatibility and to avoid the need for sealing the moving elements. The lubrication technique has been proven on previous Hughes programs and is amenable to the accuracy requirements and the torque capability of the drivers. The S band antenna positioner employs coaxial rotary joints for low RF loss (total of 0.2 dB). The Ku band drive mechanism has rotary waveguide RF power transmission across its axes.

The drive mechanism is powered by a permanent magnet, bifilar-wound, phase switched stepper motor producing 200 steps per revolution 1.75 degrees per step. The motor provides ample torque at stepping rates beyond the maximum required for this application and provides positive magnetic holding torque when power is removed. The transmission selected is a high ratio harmonic drive with a reduction of 144:1 resulting in a nominal gimbal movement of 0.0125 degree for each pulse to the stepper motor. The antenna positioner drive unit is shown in Figure 4-38.

4.3.3 Baseline Performance Summary

4.3.3.1 Electrical Performance

The major performance factors of the baseline antennas and their loss budgets are summarized in Table 4-27 through 4-32. It is noted that the VHF antenna for the low data rate return link is approximately 1 dB down from the ideal gain for this antenna. This arises from mass and size restrictions imposed by the integration of this antenna into the spacecraft. The UHF antenna is gain limited by its field of view requirements as is also the S band order wire antenna. The S band high gain antenna was specified by link requirements to be at least 3.8 meters in diameter. The Ku band antennas were designed to specified gain requirements.

4.3.3.2 Mechanical Performance

Design loads and structural strength requirements for the antenna result from the launch environment, ground handling, on-orbit deployment, and qualification testing. The latter loading presents generally the critical design condition.

Based on previous Hughes experience, a quasi-static ultimate load factor of $\pm 294 \text{ m/sec}^2$ and a random vibration excitation of 147 m/sec^2 rms were selected for use in the TDRS antenna subsystem design. A safety factor of 1.25 is included in these ultimate load levels. At limit load (ultimate load = 1.25 x limit load) the structure is not allowed to exhibit yielding.

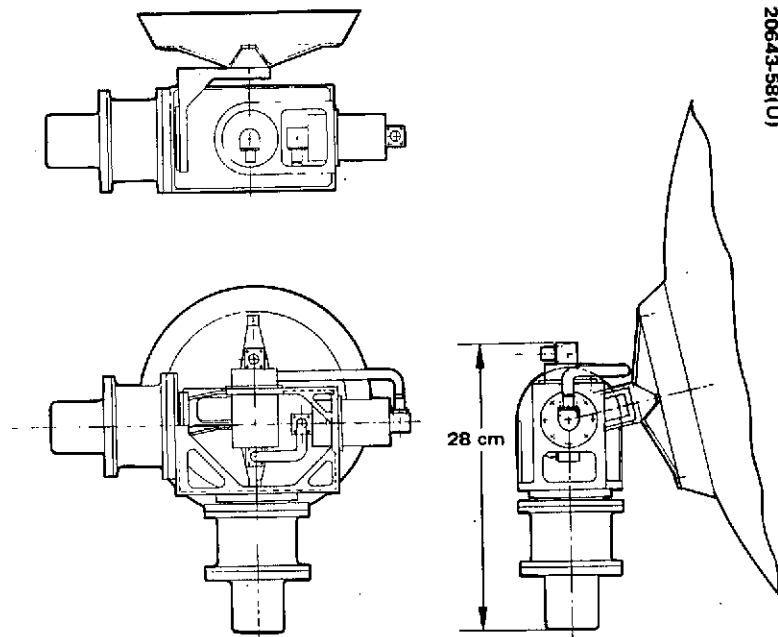


Figure 4-37. Two-Axis Antenna Positioner

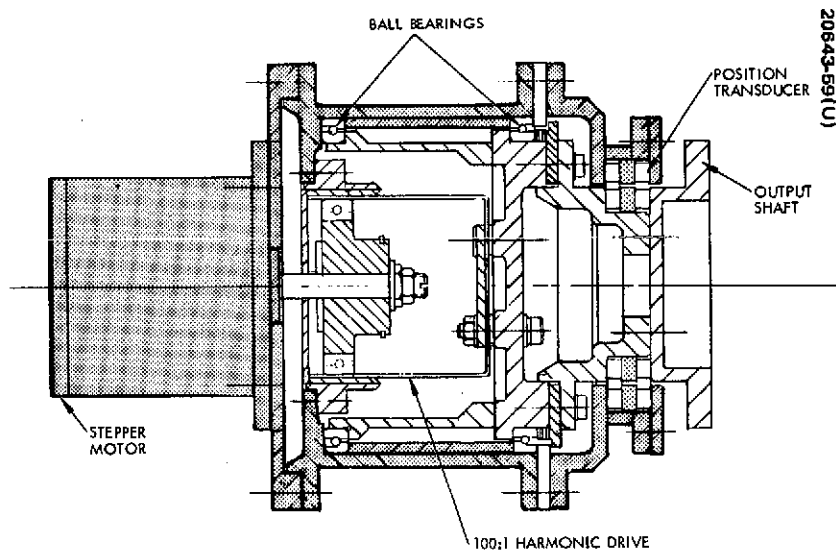


Figure 4-38. Antenna Positioner Drive Unit

TABLE 4-27. VHF-UHF ANTENNA PERFORMANCE

Frequency band, MHz	136 to 138	400.5 to 401.5
Aperture diameter, meters	3.9	1.3
Aperture gain*, dB	14.0	15.0
Reflector surface loss, dB	0.01	0.02
Reflector mesh I ² R loss, dB	0.02	0.08
cm rms	(0.635 cm)	(0.317 cm)
Hybrid loss, dB	0	0.16
Coaxial cable loss, dB	0.03	0.09
VXWR loss (1.3:1), dB	0.08	0.08
Total loss, dB	0.14	0.43
Antenna peak gain, dB	13.86	14.57
Antenna FOV gain (±13 deg) dB	11.86	12.50
Antenna FOV gain (±15 deg) dB	11.21	11.82
Polarization sense	(Horizontal)	(Circular)
Polarization sense		
	Vertical	

*L. R. Dod, Backfire Yagi Antenna Measurements.

TABLE 4-28. S BAND ORDER WIRE ANTENNA PERFORMANCE

Frequency band	2200 to 2290 MHz
Aperture diameter	26.7 cm
Aperture gain*	15.0 dB
Reflector surface loss	0.01 dB
Reflector I^2R loss	0.01 dB
Hybrid loss	0.16 dB
Coaxial cable loss	0.01 dB
VSWR loss (2.0:1)	0.50 dB
Total losses	0.69 dB
Antenna peak gain	14.3 dB
Antenna FOV gain (± 15 deg)	11.4 dB
Polarization sense	Circular

*L. R. Dod, "Backfire Yagi Antenna Measurements."

TABLE 4-29. S BAND HIGH GAIN ANTENNA PERFORMANCE

Frequency, MHz	2070	2250
Aperture area gain ($4\pi A/\lambda^2$), dB	38.45	39.06
Spillover and amplitude taper losses	1.35 dB	
Phase loss	0.09 dB	
Blockage loss	0.10 dB	
Reflector cross-polarization loss	0.10 dB	
Reflector surface loss (0.15 cm rms)	0.11 dB	
Reflector mesh I^2R loss	0.05 dB	
Hybrid losses	0.20 dB	
Coaxial cable loss	0.35 dB	
VSWR loss (1.4:1)	0.12 dB	
Total losses, dB	2.47	2.47
Antenna peak gain, dB	35.98	36.59
Polarization sense*	Circular	Circular

*Sense of polarization for forward and return links are orthogonal.

TABLE 4-30. Ku BAND HORN ANTENNA PERFORMANCE

Frequency	13.7 GHz
Aperture area gain ($4 \pi A/\lambda^2$)	25.1 dB
Amplitude taper and phase losses	1.93 dB
Horn I^2R loss	0.03 dB
Polarizer and transition I^2R loss	0.30 dB
Waveguide loss	0.25 dB
VSWR loss (1.3:1)	0.08 dB
Total losses	2.59 dB
Antenna peak gain	22.5 dB
Antenna earth-edge gain ($\pm 9.1^\circ$)	18.5 dB
Polarization sense	Circular

TABLE 4-31. Ku BAND REFLECTOR ANTENNA PERFORMANCE

Frequency	14.9 GHz
Aperture area gain ($4\pi A/\lambda^2$)	46.94 dB
Spillover and amplitude taper losses	0.86 dB
Phase loss	0.05 dB
Blockage loss	0.30 dB
Reflector cross-polarization loss	0.02 dB
Reflector surface loss (0.02 cm rms)	0.10 dB
Reflector mesh I^2R loss	0.15 dB
Horn I^2R loss	0.02 dB
Polarizer and transition I^2R loss	0.30 dB
Waveguide loss	0.04 dB
VSWR loss (1.3:1)	0.08 dB
Total losses	1.92 dB
Antenna peak gain	45.02 dB
Polarization sense	Circular

TABLE 4-32. TELEMETRY AND COMMAND ANTENNA PERFORMANCE

Telemetry frequency band	136 to 138 MHz
Array gain over 95 percent of sphere (for matched polarization)*	-4.0 dB
Hybrid balun I ² R loss	2.0 dB
Antenna gain over 95 percent of sphere (for matched polarization)	-6.0 dB
Command frequency band	148 to 154 MHz
Array gain over 97 percent of sphere (for circular polarization)	-11.0 dB
Hybrid balun I ² R loss	2.0 dB
Antenna gain over 97 percent of sphere (for circular polarization)	-13.0 dB

*Polarization combining at the ground station constitutes matched polarization.

Preliminary stress analyses were conducted for critical antenna elements to ensure adequate member sizing against failure during launch and/or deployment and to establish confidence in the antenna weight predictions.

A 50 Hz minimum antenna resonance frequency in launch configuration is accepted to limit structure deflections, maintain clearance within the payload envelope, and avoid coupling with the lower frequencies of excitations introduced by the launch vehicle. In the orbit flight configuration, a minimum frequency of 4 Hz is specified so that resonance coupling at the spacecraft spin rate of about 1.7 Hz is prevented.

S Band High Gain Antenna. The design is very similar to the AAFE antenna which has a predicted mass of 10.6 kg, and a stowed fundamental cantilever frequency of 51 Hz. If the AAFE antenna were simply supported on both ends, its fundamental frequency would be 140 Hz. Therefore, the TDRS antenna structure may be reduced and will weigh less.

The ribs have a wall thickness of 0.0152 cm at the root and tip and are 0.0228 cm at the midpoint. This size rib was selected based upon a rib parametric analysis as briefly summarized in Figures 4-39 and 4-40

and upon preload stress analysis. This rib has a deployed fundamental resonance of 5.0 Hz. Previous analysis and test correlation of an antenna revealed that the deployed antenna fundamental lateral and torsional frequencies can be calculated within 4 percent when using only a one rib model. That is, the mesh spring load resistance is so low that it can be neglected when calculating these frequencies.

The MDS was previously analyzed and found to have a fundamental resonance near 100 Hz. It was stress analyzed for 40 g response in the lateral and longitudinal axes and has positive margins. It was also stress analyzed for deployment loads when the antenna is deployed in the face down or face side positions. Margins of safety are all positive.

UHF Antenna. The above remarks also pertain to the UHF antenna. Dynamic performance will be similar although the geometry is not entirely the same. In those areas where the support cone is necked down, the wall was thickened to maintain the required stiffness.

Ku Band High Gain Antenna. The fundamental resonance of this antenna is 54 Hz. Stress level for a 30 g loading is only 39 MN/m².

A parametric rib analysis was performed to enable selection of an optimum rib. Diameters were varied from 31.8 to 12.7 mm and thicknesses were varied from 0.406 to 0.102 mm. Tapered diameter ribs were also analyzed. The lightest mass design consistent with the requirements was selected from a computer printout of 1600 cases. Table 4-33 illustrates some of the more ideal candidates. From these results, a 31.8 mm constant diameter rib with root $t_r = 0.152$ and tip thickness $t_t = 0.12$ mm was selected. Twelve of these ribs have a mass of only 0.261 kg.

TABLE 4-33. RESULTS OF RIB ANALYSIS

D_r , mm	D_t , mm	t_r , mm	t_t , mm	f, Hz	W, kg/12 ribs
28.6	28.6	0.407	0.102	67	0.467
28.6	28.6	0.356	0.102	68	0.420
28.6	28.6	0.203	0.102	52	0.281
29.2	29.2	0.203	0.102	60	0.312
29.2	29.2	0.152	0.102	54	0.261
25.4	25.4	0.407	0.102	57	0.414
29.2	12.7	0.254	0.102	56	0.270
29.2	25.4	0.203	0.102	58	0.284

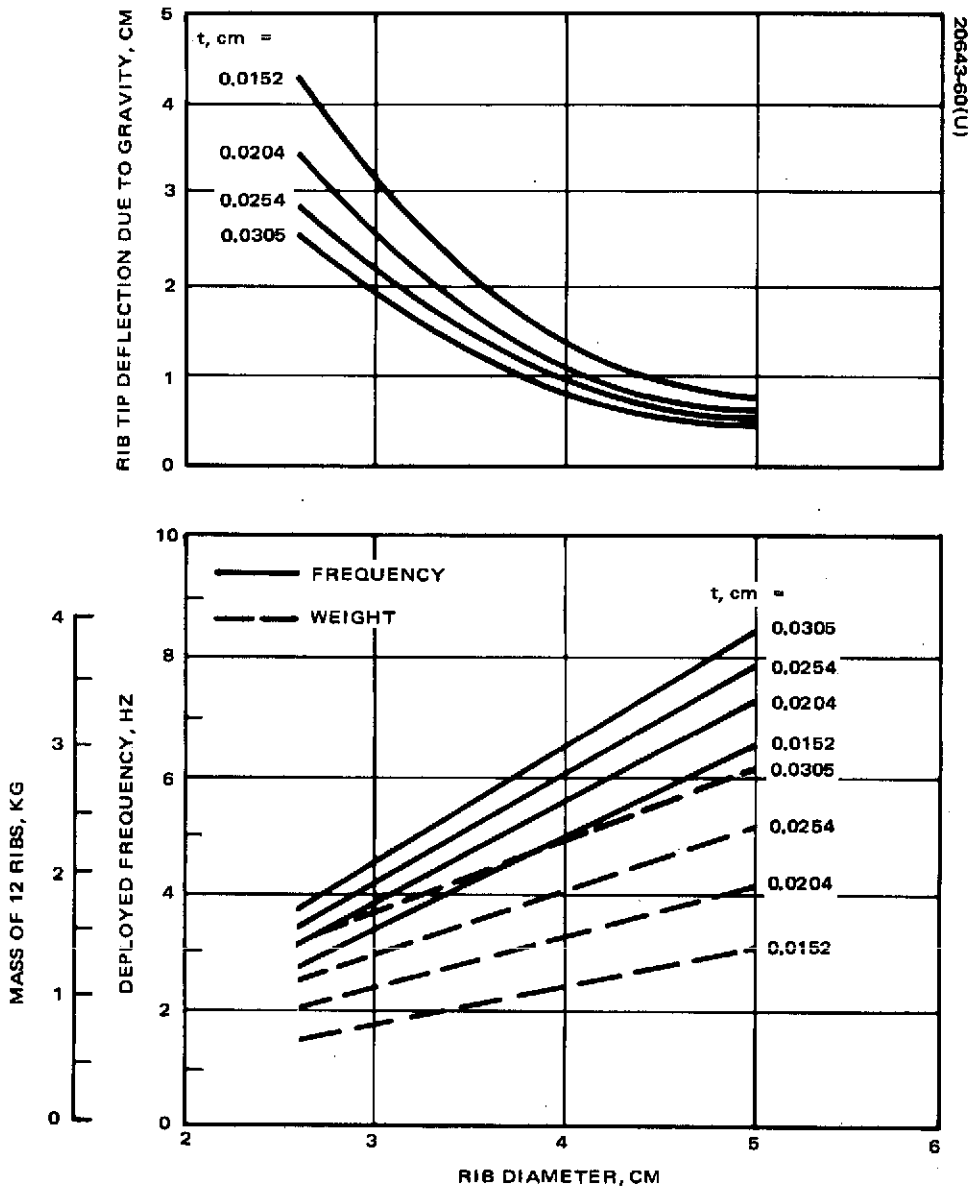


Figure 4-39. Variation of Rib Frequency, Mass, and Tip Deflection for Deployed 3.8 Meter Diameter Antenna

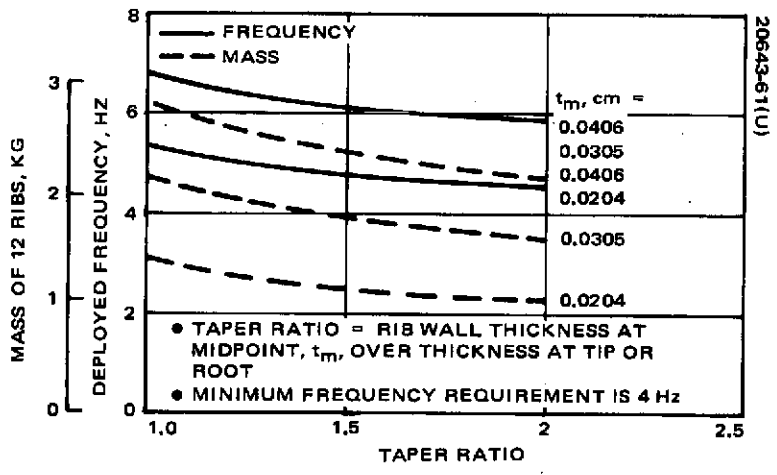


Figure 4-40. Variation of Rib Frequency and Mass Versus Taper Ratio for Deployed 3.8 Meter Diameter Antenna

4.3.3.3 Thermal Performance

The rib and mesh antenna design with insulated deployment hub and feed support cone is capable of maintaining a high surface accuracy with low thermal pointing errors. The high thermal surface accuracy of the rib-dominated antenna is achieved through thermally controlling the antenna ribs. Though large temperature variations occur in the mesh itself, the mesh spring constant is low such that these effects are not transmitted significantly into the rigid ribs. Further, the mesh pretention ratio is such that no wrinkling of the mesh occurs due to orbital temperature excursions.

The temperature variations that affect the antenna performance include hub temperature gradients, diametral rib gradients, feed support cone gradients, and rib and feed support cone average temperatures. These variations are induced by changes in the solar incidence angle and shadow patterns. Hub distortions are potentially the major contributor to the thermal surface error, defocus, and mispointing because of their amplification by the rib length to give large rib tip movements. The hub gradients are effectively controlled by the incorporation of a multilayer insulation blanket around the hub and feed support cone. The diametral rib gradients are directly proportional to the rib solar absorptivity, α_s , and inversely to the diametral thermal conductance. The gradient is therefore reduced by reducing the rib α_s and increasing the wall thickness and thermal conductivity. The feed support cone diametral heat transfer is predominately by radiation: therefore, the gradients are reduced by incorporating a high infrared emittance interior surface and a multilayer insulation blanket around the exterior.

The dual frequency backfire antenna system operates at such a low frequency (~ 400 MHz) that the thermal design requirements will be easily met with a lightweight polished aluminum rib design. The anticipated total reflector surface error of the 3.8 meter diameter S band antenna is well within the performance budget of 1.52 mm. The Ku band antenna system operating at the higher frequency will require a highly accurate surface. The proposed basic thermal design was proven adequate for Ku band for a 3.8 meter diameter antenna. A thermally induced surface distortion of 0.203 mm was predicted for the 3.8 meter reflector. Since the rib thermal distortion is proportional to the square of the rib length, no difficulties are anticipated in meeting the thermal surface accuracy requirements for this 1.42 meter antenna.

4.3.4 Technology Status (Radiation, Inc.) Background Development

The first of these programs, Study of Deployable Directive Antennas for Space Communications, consisted of an extensive trade study of a broad range deployable antenna concept. The study resulted in the selection of the "rib-dominated," rib-and-mesh concept as the most promising candidate for further evaluation and development. The term "rib-dominated" is used to emphasize the role of the ribs as the dominating element (as contrasted to "mesh" control) in the achievement and control of reflector surface accuracy.

The funded Deployable Antenna Evaluation and Test Model program continued the development of the rib-and-mesh design. This program included extensive developmental tests to determine the mechanical and thermal properties of the antenna elements, e. g., the mesh, ribs, release mechanism, deployment mechanism, lubrication, etc., and the design and manufacture of the high surface accuracy 3.8 meter diameter prototype model. This model was subjected to an extensive series of tests to evaluate deployment reliability and repeatability, reflector surface accuracy under solar-vacuum conditions, dynamic behavior in the stowed and deployed conditions, and RF performance. Analysis programs to predict the RF, thermal, dynamic, and surface distortion behavior for the antenna were conducted simultaneously with the test programs. Correlation between predicted and measured test behavior was excellent in all areas.

The third program in the series was the Telecommunications Antenna (TCA). The TCA program resulted in the development of the "double mesh" concept. This concept utilizes a second mesh which is attached to the back of the ribs and used as a drawing surface for contouring the front reflector mesh. The second mesh is tied to the front mesh by tensioned wires. By properly tensioning these tie wires, the reflector surface can be contoured to a precision parabolic shape. Also included were adjustable standoffs in the ribs to which the mesh surfaces were attached. The concept was demonstrated on a sector of 3.8 meter diameter reflector. A surface accuracy of 0.18 mm rms was achieved. The success of this concept has resulted in increased design flexibility, since the reflector surface accuracy is no longer dependent upon the number of ribs used. This allows the achievement of a highly accurate reflector surface while maintaining a low mass.

These programs have resulted in the development of simple, low mass, reliable, deployable space antenna and feed designs for a wide range of applications. Perhaps more important, the programs have allowed the development of a dedicated team of engineers and technicians who possess an understanding of the deployable, rib-and-mesh antenna behavior under the launch and space environment conditions, in the development of cost effective processes and techniques for the manufacture of such antennas, and in the development of correlated analytical techniques for prediction of antenna behavior under all environmental extremes.

4.4 ATTITUDE AND DESPIN CONTROL

4.4.1 Design Requirements and Alternatives Considered

The TDRS spacecraft design considered in this study belongs to the class of Hughes Gyrostat systems which utilizes the attitude stabilization concept first presented by A. J. Iorillo in Reference 1. Previous spacecraft that have successfully used this stabilization technique include TACSAT I and Intelsat IV. For a Gyrostat configuration, gyroscopic stiffness is developed by the spinning rotor, and attitude stability is achieved by both passive energy dissipation from the nutation damper mounted on the despun platform and by active nutation damping through the despin control subsystem. Thus the Gyrostat configuration requires only continuous active control of the vehicle orientation about a single reference axis, i. e. control of the platform azimuth orientation, with periodic corrections to the spin axis orientation resulting from the effects of environmental disturbances.

Spin axis attitude control functions include:

- 1) Establishment of a desired inertial spin axis attitude and maintenance of the attitude in the presence of external disturbances and orbital variations
- 2) Provision for telemetry information in order to accurately determine the spin axis orientation by ground analysis of the telemetered data
- 3) Provision for dynamic stabilization of the desired spin axis attitude

The despin control functions include:

- 1) Control of the azimuth orientation of the despun platform to the required accuracy
- 2) Provision for platform rate stability in the event of loss of an inertial despin reference
- 3) Provision for dynamic stabilization of nutation.

4.4.1.1 Spin Axis Orientation

The design criteria involved in spin axis orientation control are summarized:

- 1) Attitude control subsystem must provide vehicle asymptotic nutational stability, with residual nutation consistent with antenna pointing accuracy requirements.
- 2) Nutation transients that occur in normal operation (such as those due to attitude correction maneuvers) must be rapidly damped.

- 3) Vehicle must be autonomously stable in failure modes involving large nutation angles.
- 4) Spin axis control requirements
 - North-south error allocation: ≤ 0.0019 radian
 - Orientation determination: ≤ 0.00035 radian
 - System nutation damping time constant: ≤ 300 seconds

Two stabilization principles are available for satisfying these requirements: The first is the energy sink criterion which states that a Gyrostat configuration with energy dissipation on the rotor may be made nutationally stable by providing sufficient energy dissipation on the despun portion. The second principle is that a Gyrostat configuration with an asymmetrical platform may also be stabilized nutationally using only torques applied by the despun motor. The energy sink analysis provides a means for estimating accurately the nutation damping or dedamping time constant associated with any passive dissipative device. Because the separate effects on system stability are only very weakly coupled, the total system nutation damping time constant may be calculated using a principle of superposition.

4.4.1.2 Despin Control

The despin control functions as a closed loop, autonomously operating control system which orients the payload antenna toward the earth while the rotor spins about an axis normal to the orbit plane. Table 4-34 summarizes the basic despin control system design criteria.

The motor torque requirement is established by both the desired margin over bearing friction torque and the torque necessary to overcome dynamic interaction torques which can arise during recovery from a temporary loss of despin control. The presence of a substantial cross product of inertia after deployment of the antenna payload leads to an interaction between spacecraft nutation and the despin control system. By proper design of the control loop dynamics this coupling can be used to augment the primary attitude stabilization which is provided by the nutation damper.

The ability to recover automatically from a flat spin condition resulting from loss of despin control has been accommodated by incorporation of two features in the design of the despin subsystem:

- 1) The initial state of the despin subsystem is to be on when the bus voltage exceeds a certain minimum with both motor drivers active. For the flat spin condition with zero relative rate between platform and rotor, rate loop logic will command full saturation torque to both motors in the direction opposing friction.

TABLE 4-34. DESPIN CONTROL DESIGN CRITERIA

East-west error allocation	≤ 0.0031 radian (3σ)
Design life	> 7 years
Torque required per motor	≥ 2.712 Newton meter (Stall) ≤ 0.814 Newton meter (at 10.47 radians/second)
Nutation coupling	Stable coupling for all modes
Required modes of operation	Earth tracking Earth acquisition Rate command Ground override Rate hold
Initialization state	Select center earth sensor Both motor drivers on Zero commanded rate Low gain mode

- 2) The available motor torque for zero relative rate is sufficient to overcome the opposing dynamic torques due to residual rotor asymmetry and the effects of dedampers.

In addition to the normal earth pointing mode and acquisition mode, a ground control mode of inertial platform rate for transfer orbit operation and a ground override control mode for backup despin control is desirable. Furthermore if earth sensor pulses are temporarily absent, the despin system must maintain the platform rate at a small enough value to maintain linear operation of the nutation damper to ensure nutational stability.

Two concepts for despin control were evaluated. The first uses spinning sun or earth sensors along with a spinning/despun shaft-angle encoder as a despin reference. This is a modified version of the approach successfully used on the Intelsat IV spacecraft. The second and alternate system considered is a beacon tracker which utilizes a ground transmitted pilot signal. This is the despin technique being employed for the Canadian

Domestic Communication Satellite. While the error signal derived from the beacon system is continuous and has very low noise content, the beacon system was not selected for the following reasons:

- 1) The mass of the beacon system is significantly greater (approximately 9 kg) due to the necessary waveguide, brackets, and RF detection electronics.
- 2) The beacon signal would be critical to mission performance and would therefore present a reliability risk in the event of a ground station outage.
- 3) Acquisition of the pilot signal on a spacecraft with a large despun section would require auxiliary earth or sun sensors. Accordingly, it is more economical to use the earth or sun sensors as the primary reference for spacecraft applications where only moderate pointing accuracy is required.

The choice of a spinning sun sensor or spinning earth sensor as the despun reference is influenced by the desire to minimize electronic complexity. The sun sensor is attractive for its inherent reliability, but substantial additional electronics is required to use as a despun reference (spin-synchronous pulse generator and time of day delay logic). The earth sensor contains its own internal electronics but requires no additional processing. The equivalent parts count for the proposed earth sensor is approximately one third of that for the required sun mode electronics. Although the earth sensor has higher pulse-pulse jitter, its performance is quite adequate for the mission requirements. Substantial redundancy is provided with three units selectable by command. The conventional spinning sensor approach has been adopted based on experience gained on both the Intelsat IV and TACSAT programs which show that the accuracy requirements can be met, and since no additional constraints are placed on platform layout or communications design.

Earth leading edge detection, while requiring only a single pulse for error processing, has two disadvantages which make it unsatisfactory for use in TDRS. Both involve additional feedback paths within the control system which tend to create additional undesirable design constraints. Rotor phase (and hence sensor phase) variations result from rotor response to torque commands to the platform. With the rotor spin inertia smaller than the platform inertia for TDRS, this would have a significant effect on pointing jitter and loop stability. The second disadvantage is an additional nutation coupling path through geometric coupling. As the spacecraft nutates, the earth sensor scans a different path across the earth, resulting in a time varying phase error of the earth leading edge pulse (at nutation frequency). This effect can be either stabilizing or destabilizing to nutation, depending on sensor attitude. Use of earth center finding error detection eliminates both effects.

Both single loop (position only) and dual loop (position and rate) were considered for the normal on-station operation. A continuous rate loop eliminates a lower gain crossover (thus improving system stability margins) and provides additional damping of nutation via platform cross products of inertia. However, the implementation of a rate loop having a suitably stable (noise-free) output for continuous use requires increased complexity in both the mechanical and electronic design. All the performance requirements can be met with adequate margin by use of position loop shaping alone. Thus, a rate loop is needed only for acquisition. The proposed deadband-type rate loop and all-analog position loop is functionally equivalent to the space-proven TACSAT despin system design.

Integral or nonintegral shaping can be used in the position loop. In principle, integral shaping is somewhat more complex and yields smaller gain margins, although the resultant sensitivity to friction variations is much less. The electronic complexity of integral versus nonintegral is approximately the same using the all-analog approach. By implementing the integrator along with one of the lead terms as a proportional-plus-integrator stage, the potential problem of integrator windup is circumvented. The computed stability margins are adequate with the integral approach. In the configuration proposed, therefore, the integral shaping provides the desired insensitivity to friction variations without unduly compromising the remaining aspects of system performance.

Analog electronics are generally simpler while digital electronics provide more design flexibility and are inherently more accurate with sufficient quantization. Based on in-orbit experience with both types of systems, the analog approach is preferred for maximum reliability and design/test simplicity. Digital processing is used on as needed; e. g. , in processing small rate errors for reliable platform acquisition with a small torque to inertia ratio.

The motor drive circuitry can be configured either as a voltage drive (which is effectively a speed control) or as a current drive (which is effectively a torque control). The voltage drive is an open-loop circuit, while current drive utilizes negative feedback to deliver a desired torque independent of speed and armature resistance variations (due to temperature changes). Voltage drive is potentially attractive (in spite of the speed and temperature dependence) when controlling a smaller inertia. Then, the voltage drive gives speed control of the load inertia which can be utilized for acquisition and extra damping. For a large despun platform such as TDRS, however, this effect is negligible and the current drive is preferred to minimize parameter sensitivity.

Either a brush-type or a brushless-type torque motor may be used. Each has flown successfully; TACSAT uses a brush motor and Intelsat IV uses a brushless motor. The brush-type requires fewer electronic parts by using mechanical commutation. The brushless motor derives commutation by a resolver that generates sine and cosine drive components. Modulation and demodulation across the resolver are necessary for the brushless motor.

The brushless motor does eliminate the brush wearout failure mode. This feature plus the successful experience with brushless drive electronics resulted in the choice of a brushless approach.

4.4.2 Baseline Design Description

4.4.2.1 Attitude Control

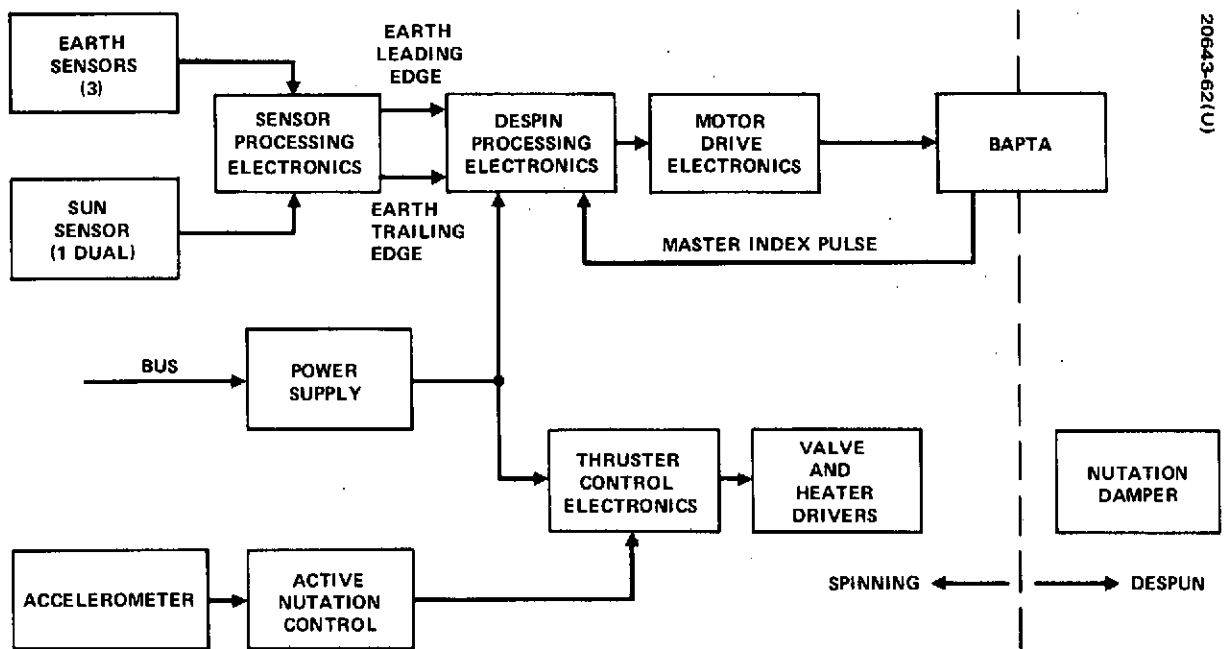
A functional block diagram of the attitude control subsystem is given in Figure 4-41. It involves all components that determine and establish the spin axis orientation in inertial space and assure the spacecraft attitude stability. Determination and control of the spin axis attitude is similar to that used for TACSAT and Intelsat IV, using rotor mounted sun and earth sensors. The sun sensor provides pulse pairs for measurement of the angle between the sun line of sight and the spacecraft spin axis, while the earth sensors provide earth chord width information for attitude measurements. Corrections to the attitude are made using ground commanded pulsing of the jets.

Sensor information for attitude determination is processed by the Hughes ATDET computer program currently used for on-orbit control of TACSAT I. This program models disturbance torques, sensor biases, and attitude commands and produces a least squares fit of attitude to the data. Intelsat IV has demonstrated the adequacy of this system for apogee boost accuracy, while the accuracy for on-orbit control has been demonstrated both by TACSAT I and Intelsat IV. The processing algorithm used permits on-orbit calibration of the sensors and updating of solar torque estimates.

Studies performed for Intelsat IV show that in the orbit normal attitude, during transfer orbit, attitude may be determined to 0.0035 radian (3σ) accuracy. TACSAT experience indicates that an on-orbit accuracy of 0.0005 radian (3σ) after calibration of sensor biases is achievable.

The TDRS attitude stabilization design incorporates despin control damping of nutation along with using the passive, platform mounted, eddy current nutation damper. The stability of the spin axis attitude is illustrated in Figure 4-42. The figure summarizes the nutation damping time constants for the individual elements of the attitude control subsystem as a function of nutation angle. Together these elements provide both redundancy and substantial performance margin.

In addition to the techniques for stabilizing the nutation by action of internal elements, an active nutation control (ANC) loop using reaction jets has been incorporated to stabilize nutation in a failure mode or to reduce transient nutation during the apogee motor firing and antenna deployment phases of the mission. The active nutation control system (ANC) is essentially the same as that used on Intelsat IV. It is provided as a backup during



20643-62(U)

Figure 4-41. Attitude Control Subsystem Block Diagram

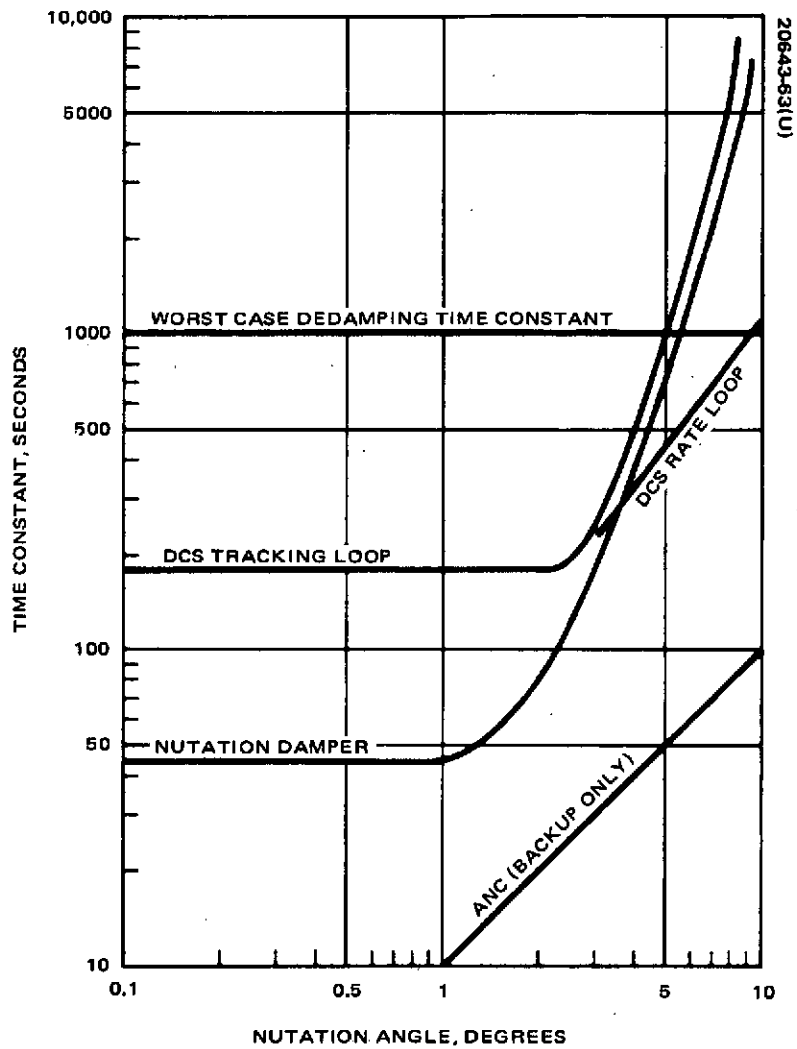


Figure 4-42. Stabilization Time Constants Versus Nutation Angle

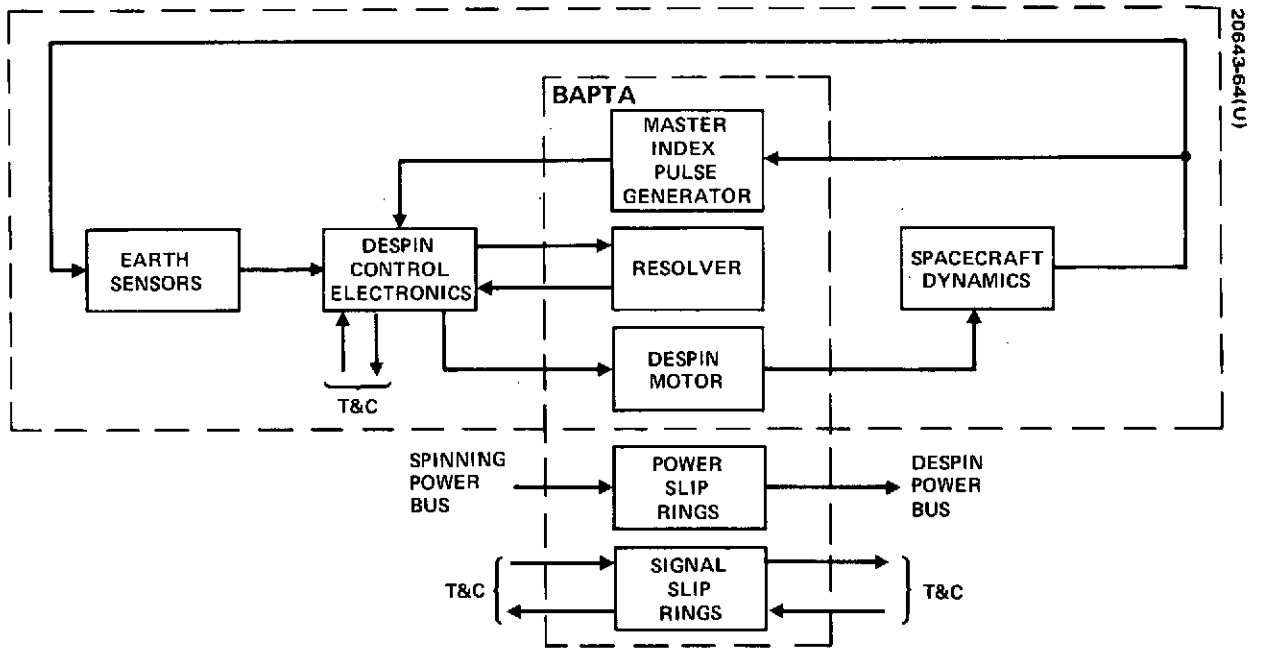


Figure 4-43. Despin Control Subsystem Block Diagram

transfer orbit and as an extra margin of nutational stability during this critical portion of the mission. The methodology of actively controlling nutation is the following:

- 1) An accelerometer detects the presence of nutation and establishes the phase and amplitude of the motion with respect to a rotor-fixed coordinate system.
- 2) The accelerometer output signal is threshold detected, amplified, and converted to a jet command.
- 3) The axial jet fires once per nutation cycle for some fraction of the cycle which results in the application of a transverse torque in opposition to the nutation motion.

The sensor that provides the desired turn-on and turn-off signals is a single axis, force rebalance type accelerometer. The sensor provides a sinusoidal signal at rotor nutation frequency and an amplitude proportional to the nutation angle.

The signal conditioning unit (ANDE) monitors the accelerometer sinusoidal voltage (a lead filter rejects the dc component due to spin axis tilt and accelerometer misalignment), compares the negative portion of the filtered signal to a preset threshold level, and sends control pulses to activate the axial jet solenoid driver when the threshold voltage is exceeded. The duration of the jet command is directly proportional to the time interval during which the acceleration exceeds the threshold value.

On the Intelsat IV spacecraft, while the ANC system has not been required to maintain nutation stability during normal mission operation, the design implementation has been verified in orbit. Following the apogee motor burn on the F-4 spacecraft, the ANC system was observed in operation reducing the 1 degree nutation transient to threshold, 0.4 degree. On the first two spacecraft, the ANC operation was not observed, but the accelerometer signals received shortly after thrust termination strongly suggest that the nutation was actively reduced to threshold.

4.4.2.2 Despin Control

A simplified block diagram of the despin control subsystem (DCS) is given in Figure 4-43. The DCS is composed of three major elements:

- 1) Earth Sensors - Three independent earth sensors are mounted on the spinning rotor and are used to supply rotor phase information relative to the earth center to the despin control subsystem. For on-station operation only a single earth sensor is required for despin control. Use of three elevation orientations allows selection of the sensor to be used by ground command well in advance of sun or moon interference and provides adequate redundancy.

- 2) Bearing and Power Transfer Assembly – The bearing and power transfer assembly (BAPTA) provides electrical and mechanical interconnection between the spinning and despun sections of the satellite. The BAPTA consists of a bearing assembly, a motor drive assembly, and a slip ring assembly for signal and power transfer between the spun and despun sections of the spacecraft.
- 3) Despin Control Electronics – The despin control electronics (DCE) processes the inertial rotor phase information from the ground selected earth sensor and the relative platform phase information from the MIP (sampled once every rotor spin revolution) and generates continuous control torque commands to the BAPTA torque motor. It contains both rate and tracking loop control logic to ensure automatic despin of the platform and acquisition of the earth. The DCE contains the loss of sensor detection logic to provide platform rate stability in the event of loss of an earth sensor, and accepts ground commands for platform rate control and failure mode ground despin control.

The detailed design of each element in the attitude control subsystem is given in 4.4.3.

Operational Modes. There are four basic operating modes for the despin control subsystem:

- 1) Normal earth tracking (low gain and high gain)
- 2) Controlled inertial platform rate
- 3) Pseudo earth control
- 4) Rate hold mode

In the normal tracking mode the despin system aligns the despun antenna boresight to the center of the earth as sensed by the selected spinning earth sensors. Because of the wide variation in platform inertia due to antenna deployment, a low gain tracking mode has been implemented for initial orbital operation of the despin subsystem. When the DCE is turned on, a control loop gain lower by a factor of 2.5 below normal gain is activated. This gain provides good stability margins for the control system during transfer orbit and after antenna deployment. Once initial orbit is achieved and the antennas are deployed, a ground command to change to the higher gain mode is required.

The rate control mode uses an inner rate loop to ensure automatic despin and acquisition during initial rotor spinup and following apogee boost. A three level ground commandable ± 0.21 or -0.42 rad/sec rate bias is included in the DCE for controlling the platform rate prior to apogee boost in order to average the effects of platform cg offset. The magnitude of the maximum

commandable rate torque is scaled so as to override the tracking loop and generate the desired platform rate.

In pseudo earth mode the tracking and rate loops operate using ground transmitted leading and trailing edge pulses, which are locked in frequency to the rotor spin rate. The required spin synchronous pulse train is obtained by use of the sun sensor pulses which are available on real time FM telemetry. An additional sun pulse delayed by 0.244 radian of spin phase from the telemetry sun pulse is created. This pulse train is then sent through the normal command channel to the despun control electronics. By controlling the phase of the retransmitted pulses with respect to the original sun pulse, the azimuth orientation of the payload antenna can be controlled.

In the event of loss of earth sensor pulses, automatic onboard logic will supply a once per revolution pulse to the rate control logic. The pulse frequency is based on a fixed clock rate (internal to the DCE) set to the nominal spin speed. Therefore, in event of a sensor loss, a slight platform rate will develop due to deviations in actual spin speed from the nominal. By ground commanding an alternate sensor, automatic despun and reacquisition will occur.

Signal Processing. Determination of the platform orientation is accomplished by means of an earth center-finding technique, similar to that used successfully in the TACSAT despun control system. The derivation of the pointing error signal is illustrated in Figure 4-44. The earth leading edge pulse from the selected earth sensor initiates a fixed rate integration within the error detector. At the occurrence of the MIP, the slope of the ramp is reversed. The earth trailing edge pulse from the sensor stops the ramp. If the MIP, which is aligned mechanically to the antenna boresight, occurs halfway between the leading and trailing edge pulses, the error is zero. Deviation of the MIP occurrence from the center earth position will result in a nonzero output of the error integrator as sampled at the earth trailing edge pulse. This sampled error (obtained once every rotor spin revolution) is directly proportional to the inertial angular east-west error of the despun platform. At the occurrence of the trailing edge pulse the sensed error is held constant for the entire spin revolution and the integrator is reset to zero. This process is repeated at the occurrence of each earth leading edge pulse.

The linear range of the error detection is 0.122 radian for north earth and south earth oriented sensors and ± 0.140 radian for the center earth sensor. For errors beyond the linear range (as in the case when the platform is rotating), the sensed error is held at plus or minus the saturation value by the DCE. By use of an electronically generated delayed MIP, which is π radians away from the actual MIP, the pointing error characteristic (as is shown in Figure 4-44) can be achieved. This ensures the correct platform direction of rotation during acquisition for shortest acquisition time.

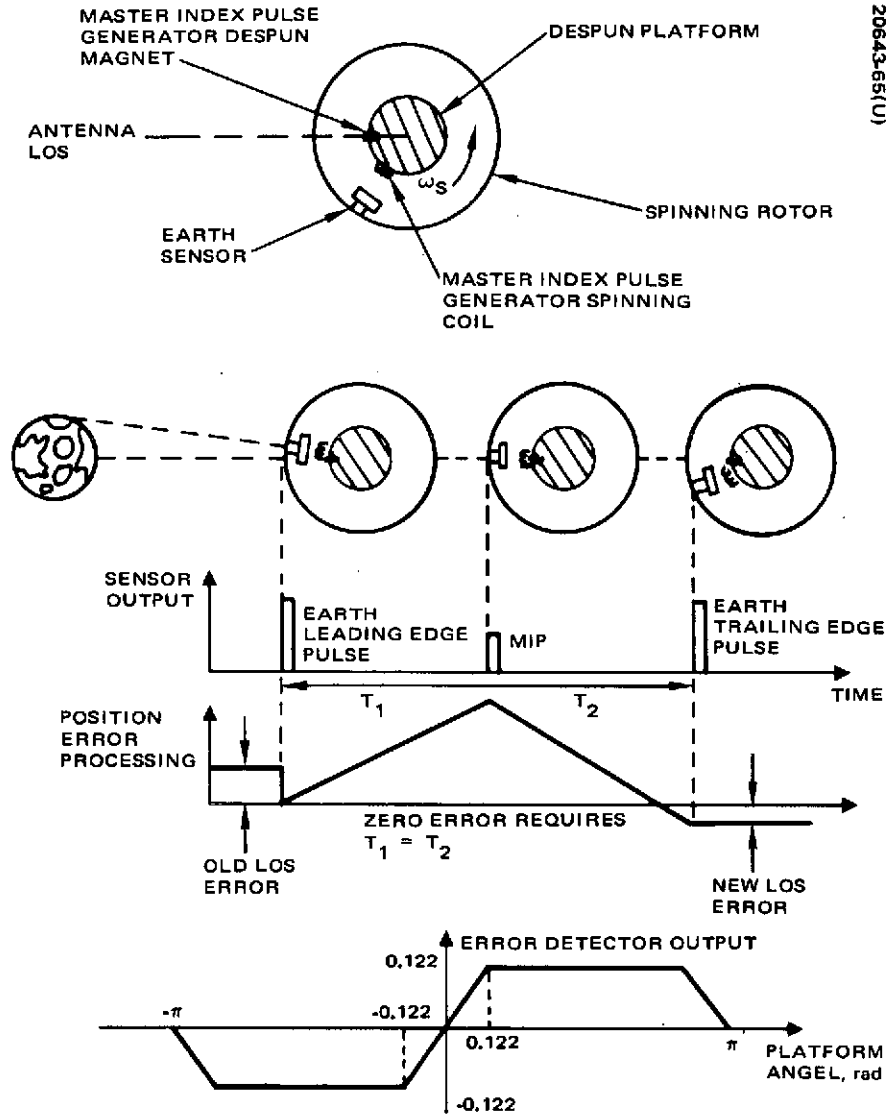


Figure 4-44. Formation of Despinned Position Error Signal

Determination of inertial platform rate (as is shown in Figure 4-45) is similar to the technique used for Intelsat IV and is accomplished by measuring the change in platform position over one rotor spin revolution. The rate logic utilizes the earth leading edge and MIP pulses along with a fixed frequency clock, to form, digitally, this first-back-difference of position. At the occurrence of the earth leading edge pulse an upcounter is set to zero and proceeds to then count from the leading edge pulse to the MIP, using a crystal controlled oscillator as the basic count clock. At the occurrence of the MIP the number occurring in the upcounter is transferred to a downcounter and the downcounter is allowed to count from the next leading edge pulse to MIP. At the occurrence of each MIP the number contained in the downcounter represents the change in platform position over one sample. Thus, for a given spin speed the sensed rate can be determined from

$$\theta_{\text{Platform}} = \frac{\Delta\theta_P \text{ (radians)/sample}}{T \text{ spin seconds/sample}}$$

(spin period = 0.6 second at 10.47 rad/sec)

Note that only the earth leading edge pulse and MIP are used in the rate error processing; thus the chordwidth variation does not effect normal rate loop operation.

The operation of the tracking loop is illustrated in the block diagram, Figure 4-46. The sampled and held output of the position error detector is used to drive an analog shaping network whose dynamics have been selected to provide stable closed loop pointing control and meet the despin system requirements. The resulting output of the shaping network is a torque command to the BAPTA.

The rate control loop is implemented as a bilevel deadband bang-bang controller. The two level staircase prevents an undesirable limit cycle while providing rate loop nutation damping for large nutation angles, which would cause nonlinear tracking loop operation. During normal on-station operation the tracking loop supplies all necessary pointing control and the rate loop is effectively deactivated, since the platform rates are well below the deadband value. The platform rate error is compared to one of four fixed ground commanded levels at the input to the rate torque command logic. A nonzero rate command results in rate loop torques which override tracking loop torques, such that the resulting platform rate is the commanded value plus or minus the small deadband value of the rate torque characteristic. The commanded rate mode is used during apogee boost to average out transverse torques due to platform cg offset. The rate error processing accounts for all possible conditions of platform rate, pulse sequencing, etc. In particular, the rate sensing logic recognizes either the absence of MIPs, or MIPs at a very low rate, as a command for full negative motor torque. This logic provides the necessary torque command function for autonomous flat spin recovery.

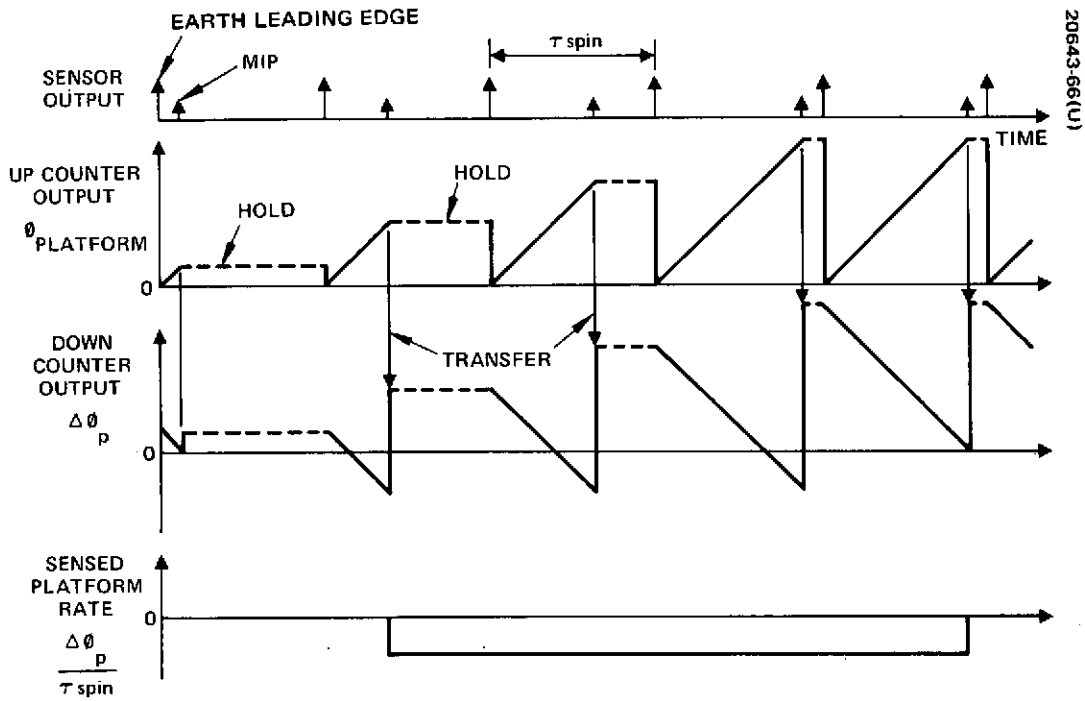


Figure 4-45. Rate Error Detection

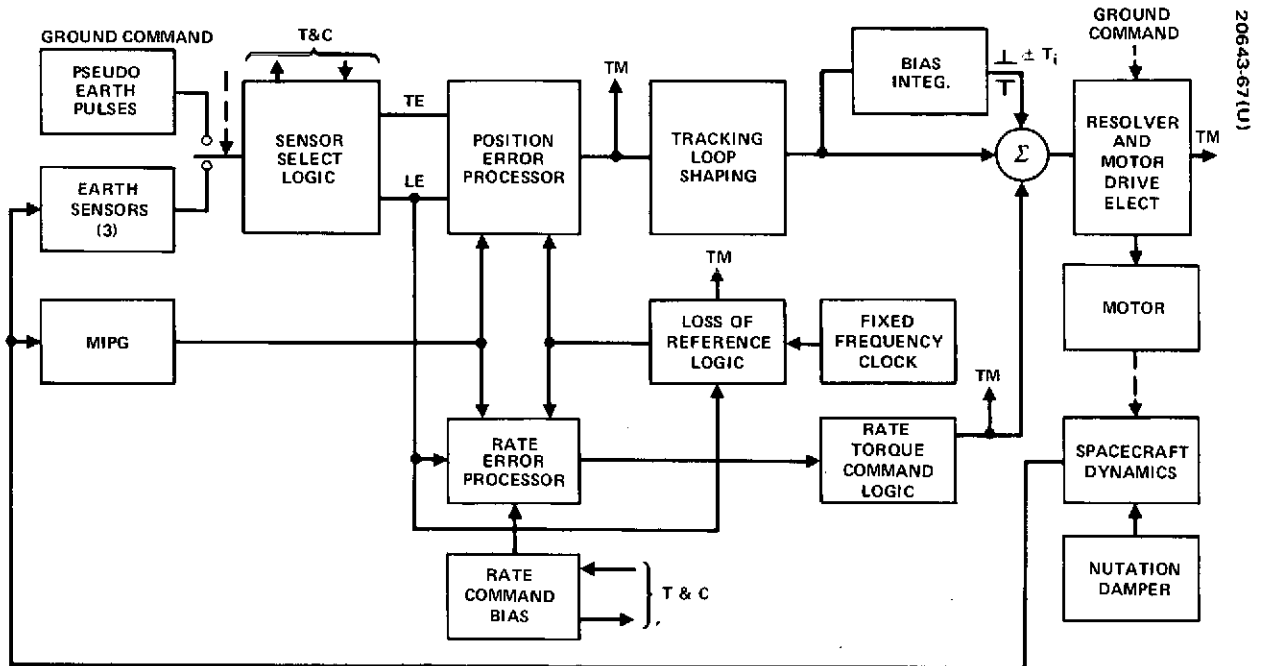


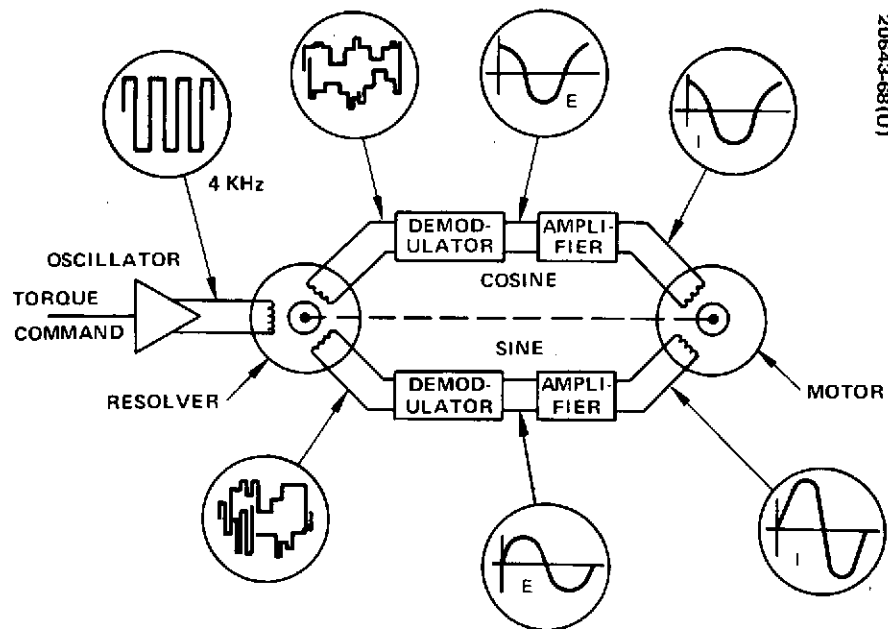
Figure 4-46. Despin Control Electronics Functional Block Diagram

The motor used in the despin control subsystem is essentially a two-phase, 16 pole, ac motor which requires in-phase sine and cosine driving voltages to generate the required rotating magnetic field. To operate as a dc motor, these sine and cosine voltages must be artificially generated. As is shown in Figure 4-47, this is accomplished using a resolver in the BAPTA which is essentially a transformer having both the primary and secondary windings on a stator element and with a transformer core rotor designed to provide a sinusoidal variation in the magnetic coupling between the windings as a function of the shaft rotation angle. A precise phase relation is maintained between the motor rotor and resolver by keying them to a common shaft. The resolver is excited by a 4 kHz carrier from the DCE. The sine and cosine resolver outputs are then synchronously demodulated to remove the carrier and amplified to drive the respective motor windings. The BAPTA motor has two sine and two cosine windings. One sine/cosine pair are driven by the motor driver circuits in a single despin control electronics unit. However the DCE motor driver inputs are cross-strapped so that each DCE can drive either or both of the motor driver/motor pairs.

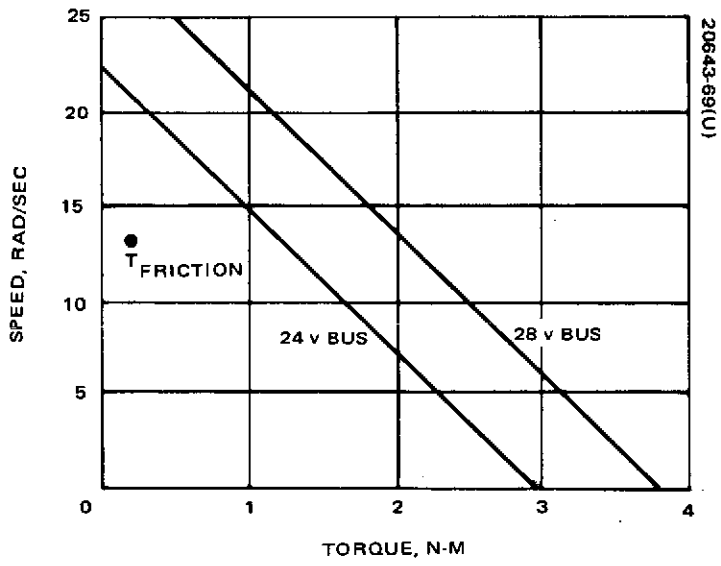
The available motor torque with a single motor driver active is shown in Figure 4-47. Under stall conditions (i. e. zero relative rotor/stator rate) the maximum torque is ≥ 2.98 Newton meters. As the relative rate increases a back electromagnetic force (EMF) is developed in the motor stator windings; therefore, the torque is limited by the maximum available driving voltage which is 19 volts at the motor winding under worst case end of life conditions (24 volt bus). At 10.4 rad/sec and at the expected BAPTA temperature of 294 K, the nominal friction level is 0.20 Newton meter. This implies a torque margin ratio of 7-1/2:1 for the low bus voltages for each motor.

When the DCE receives power, it turns on with several of the internal stages in preferred states. The DCE last utilized (ground command selected) is activated in the low gain mode. Both motor drivers are active and the ground mode logic is off. The rate bias is zero and center earth sensor is selected as the despin reference. This initialization logic is in part determined by the system requirement to recover automatically from a flat spin condition due to battery failure upon exit from eclipse. It should be noted that the initialization logic described is compatible with normal spacecraft operation.

Design Analysis. The analytical model used in the analysis of the DCS is shown in Figure 4-48. In the tracking mode of operation, inertial platform error is sampled and held once every rotor spin revolution. LOS error is processed by an analog shaping network and a control torque is developed to drive the BAPTA motor. The commanded torque is summed with a ground commandable bias and a rate loop torque (acquisition only) to form net commanded torque. Commanded torque is applied to the motor through a proportional and an integral path. The net torque (friction plus motor) controls the vehicle dynamics in azimuth to maintain earth lock. Thus, in the steady state condition, the net commanded motor torque will be equal and opposite to bearing friction torque.

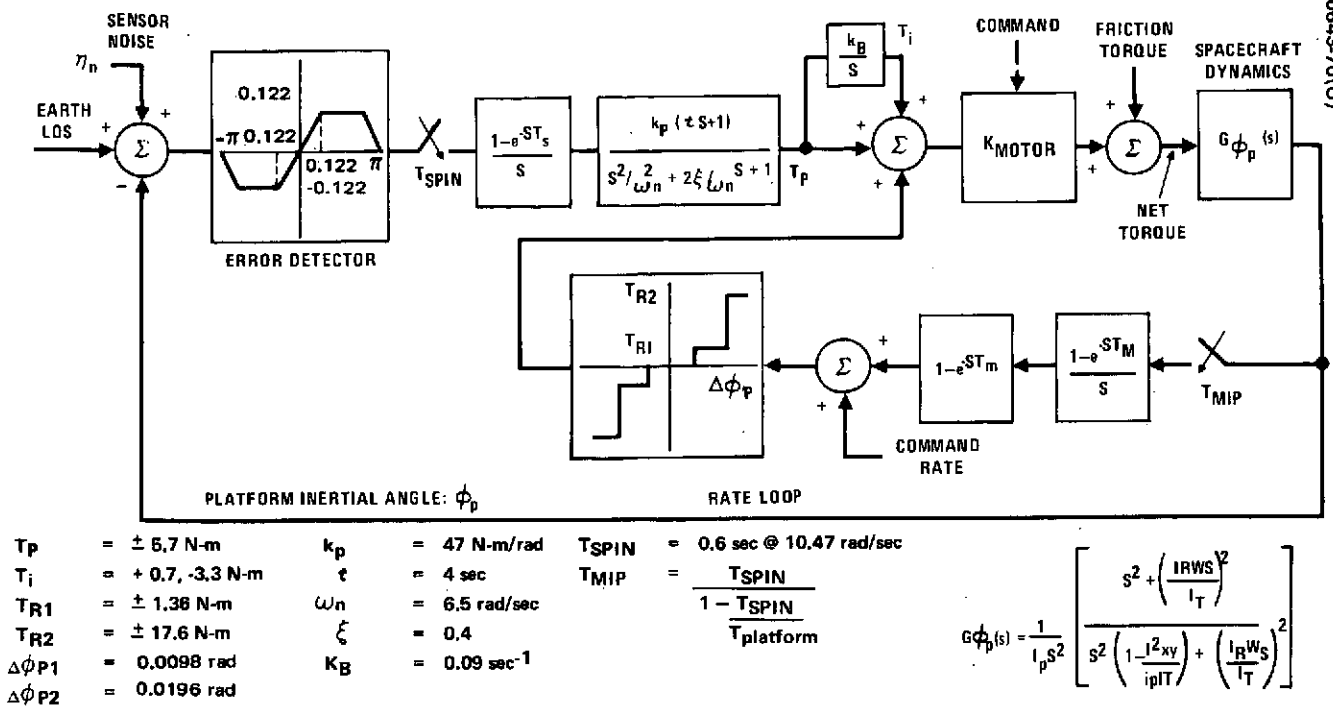


a) Motor Drive System



b) Speed Versus Torque

Figure 4-47. Despin Motor Characteristics



- T_p = ± 5.7 N-m
- T_i = $+ 0.7, -3.3$ N-m
- T_{R1} = ± 1.38 N-m
- T_{R2} = ± 17.6 N-m
- $\Delta\phi_{P1}$ = 0.0098 rad
- $\Delta\phi_{P2}$ = 0.0196 rad

- k_p = 47 N-m/rad
- τ = 4 sec
- ω_n = 6.5 rad/sec
- ζ = 0.4
- K_B = 0.09 sec⁻¹

$T_{SPIN} = 0.6 \text{ sec @ } 10.47 \text{ rad/sec}$
 $T_{MIP} = \frac{T_{SPIN}}{1 - T_{SPIN}}$
 $T_{platform}$

$$G_{\phi_p}(s) = \frac{1}{I_p s^2} \left[\frac{s^2 + \left(\frac{IRWS}{I_T}\right)^2}{s^2 \left(\frac{1 - I_{xy}^2}{I_p I_T} \right) + \left(\frac{I_B W_S}{I_T}\right)^2} \right]$$

Figure 4-48. Despin Control Model

Inertial platform rate is determined by sampling the platform position once per rotor spin cycle and comparing the present sample with the last sample (i.e., a first-back-difference of position). Any error between the two samples indicates a change in platform position over a fixed time, or a nonzero platform rate. The derived platform rate is used to drive a two-level bang-bang controller, with an inner deadband of ± 0.0098 delta radian (or 0.0163 rad/sec), used to remove effectively rate loop dynamics from the normal tracking mode operation. For sensed platform rates outside the deadband but less than ± 0.0196 delta radian, a rate torque of 1.356 Newton meter is commanded. Beyond ± 0.0196 delta radian, full motor torque is commanded which will override any level of commanded tracking loop torque. As noted previously, the bilevel characteristic provides for damping of large nutation angles by the rate loop to a range where the tracking loop exhibits a linear response (0.017 to 0.034 radian), along with ensuring the platform will despin for acquisition. The inner level of 1.356 Newton meters eliminates a potential platform limit cycle response.

The effect of utilizing one or two motor drivers is modeled as twice the dynamic range for motor torque. This model has been implemented on an analog computer simulation with three-axis vehicle dynamics. The simulation has been utilized extensively to evaluate the effects of system nonlinearities, to verify performance predictions based on frequency domain analyses, and to generate performance prediction data (see 4.4.6).

$$G_{OL}(Z) = \left[\frac{(1-e^{-sT})}{I_p s^3} \left[\frac{s + \omega_B}{s} \right] \left[\frac{K_p (\tau s + 1)}{s^2 / \omega_n^2 + 2\zeta / \omega_n s + 1} \right] \right]$$

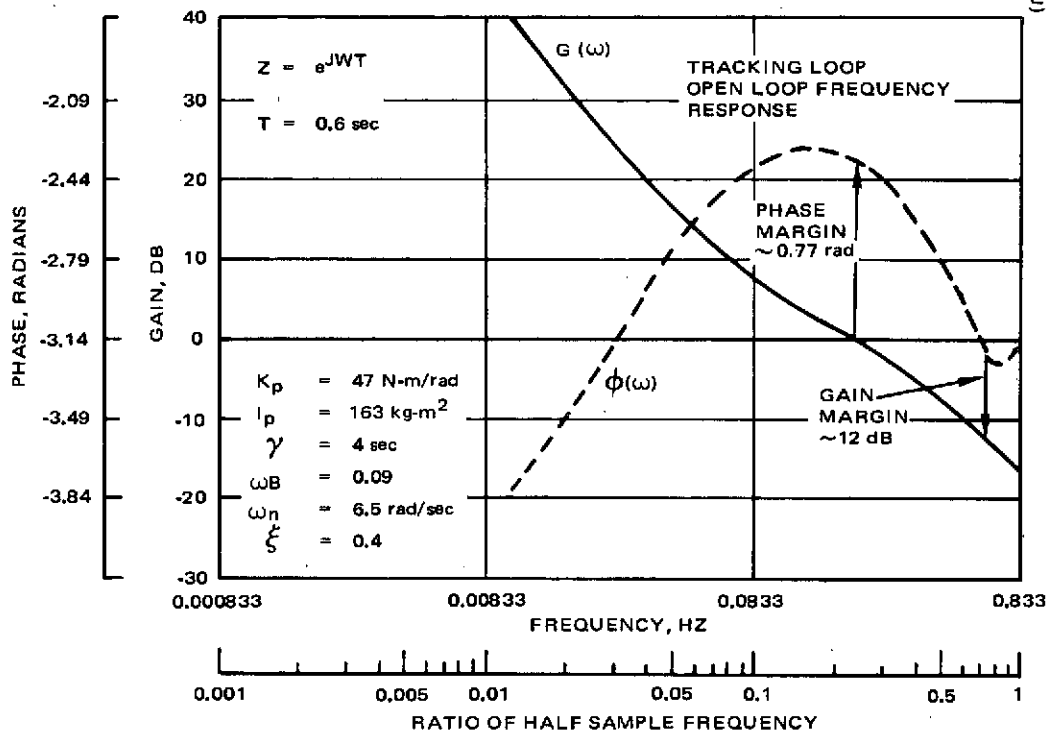


Figure 4-49. Tracking Loop Open Loop Frequency Response

There are a number of considerations determining the tracking loop control dynamics. These include:

- 1) Adequate stability margins for east-west pointing
- 2) Reduction of pointing error due to sensor noise and small friction variations to an acceptable level
- 3) Stable coupling with the nutation dynamics over the mission profile
- 4) Adequate loop stability for the stowed antenna condition

Based on frequency-domain analyses, a lead/quadratic lag followed by lead/integral shaping network was selected. The dc gain and integrator gain were chosen as high as possible to minimize sensitivity to friction torque, while avoiding excessive gain to sensor noise. A gain-phase frequency response plot of the on-station tracking loop open loop transfer function is given in Figure 4-49 with frequency ratio as the independent variable. For a sampled data system, the principal independent variable is the ratio of the input frequency to that of the half-sample frequency. As seen in the figure, the system gain margin is 12 dB, while the phase margin is 0.77 radian. These stability margins are sufficient to accommodate all modes of operation and parameter variations over the mission. The corresponding sampled data root locus is shown in Figure 4-50. The loci of

constant damping ratio and the gain variation numbers show that the response is adequately damped. Figure 4-51 shows the open loop frequency characteristics of the system during transfer orbit (the low gain mode) and for the condition following apogee boost when the antennas have been deployed, but the command to go to the high gain control mode has not been sent. In either case the system exhibits good stability margins.

The quadratic term in the shaping transfer function and the other shaping elements have been adjusted to obtain the desired phase shift characteristics at nutation frequency. The interaction of the despin control system and spacecraft nutation in the presence of a platform cross-product of inertia has been extensively studied at Hughes. The active nutation time constant of the despin control system is given by the following relation:

$$\frac{\xi}{r} = \frac{-A \sin \phi}{2[1 + A^2 + 2A \cos \phi]}$$

where

ϕ = open loop phase shift of control loop at nutation frequency, ω_n

A = open loop gain at nutation frequency, ω_n

$r = I_{yz}^2 / (I_{\text{Platform}} I_{\text{Transverse}})$ is a dimensionless inertia parameter

and

$$\xi = \frac{2}{\tau_{\text{DCS}} \omega_n}$$

where

ω_n = inertial nutation frequency

τ_{DCS} = nutation time constant due to DCS coupling

A plot of the normalized damping parameter for the proposed design for various inertia ratios is shown in Figure 4-52. The system has been optimized for the on/station condition, after antenna deployment. Table 4-35 is a summary of the DCS nutation damping effectiveness over the mission for both the track and rate mode. The substantially weaker coupling during transfer orbit is due to the smaller cross-product of inertia. However, for on-station operation the coupling is approximately equivalent to the performance of a passive damper.

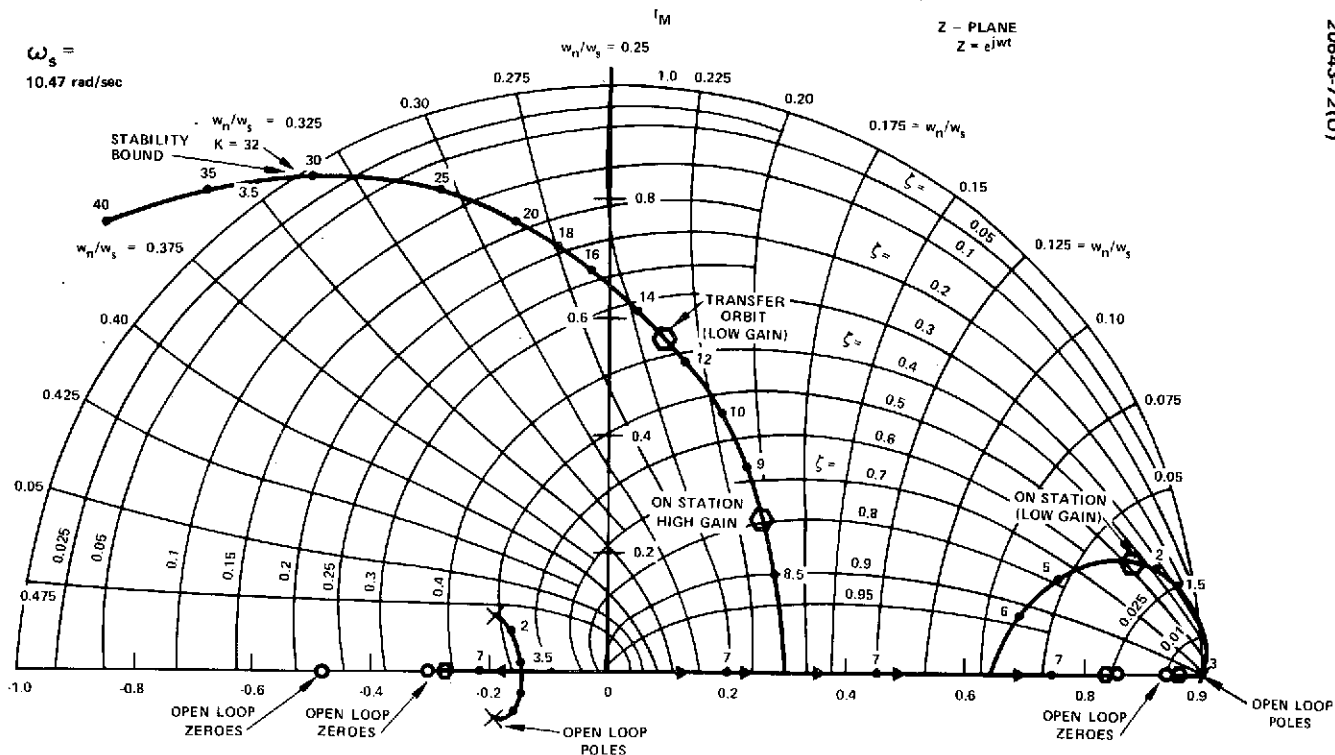


Figure 4-50. Tracking Loop Root Locus

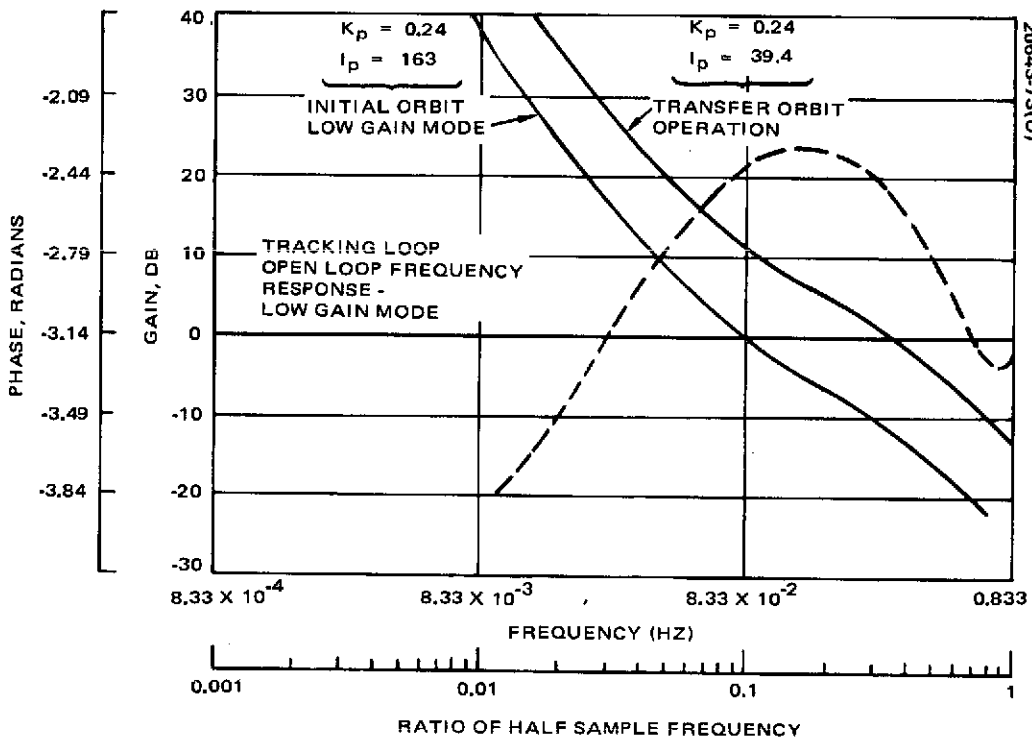


Figure 4-51. Tracking Loop Open Loop Frequency Response - Low Gain Mode

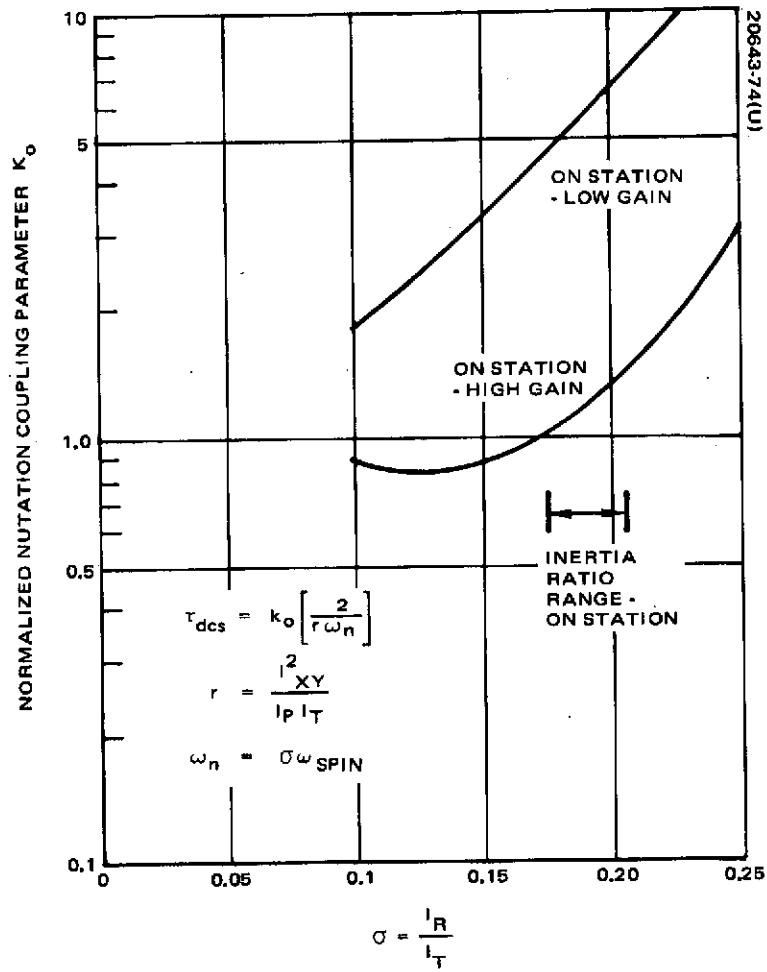


Figure 4-52. Tracking Loop Active Nutation Damping

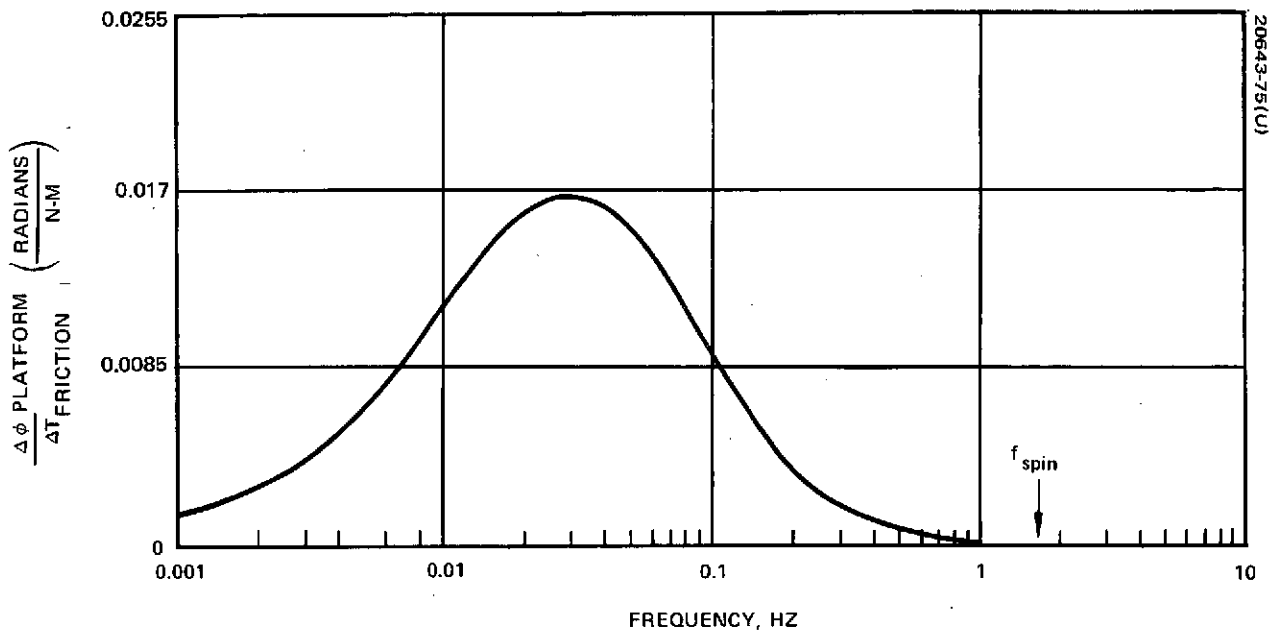


Figure 4-53. Platform Response to Bearing Torque Variations

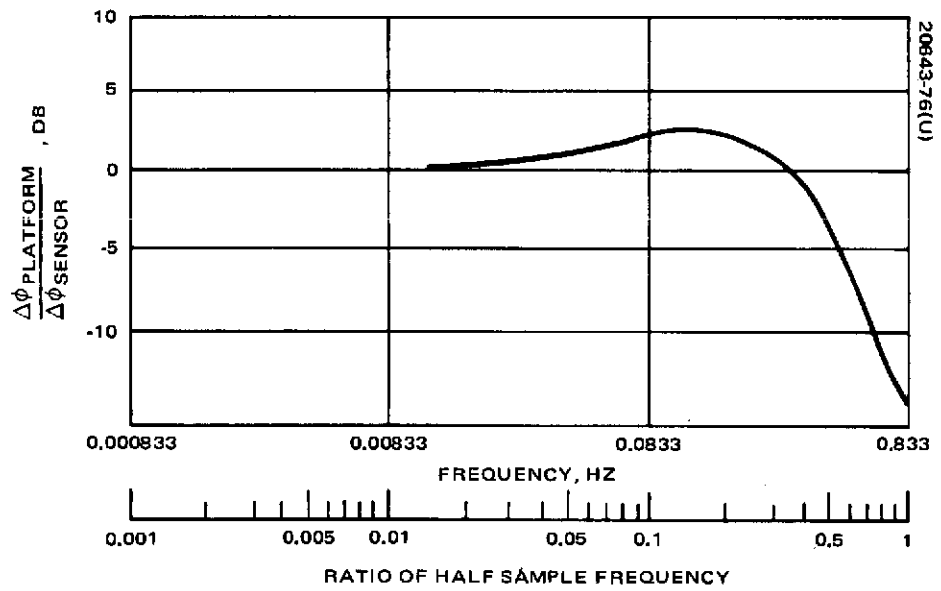


Figure 4-54. Platform Response to Sensor Phase Variations

TABLE 4-35. DESPIN CONTROL SUBSYSTEM
ACTIVE NUTATION DAMPING

Condition	Rate Loop, seconds	Tracking Loop, seconds
Transfer orbit*	$\sim 10^5$	10^4
After antenna deployment	350 100**	170
End of life	300 80**	148

*Despin control subsystem is weakly coupled during transfer orbit due to small platform cross product and higher inertia ratio.

**Two motor drivers active

Figure 4-53 shows the transmission of bearing friction variations to platform pointing error as a function of frequency for the tracking loop. As is seen in the figure the most sensitive region occurs for variations on the order of 30 seconds where the system transmission factor is 0.017 rad/Newton meter. This is a sufficiently low transmission factor, so that even relatively large friction variations would not cause loss of lock (maximum offset 0.12 radian before losing lock). For lower frequencies the feedforward integrator effectively nulls pointing errors due to friction, while at higher frequencies the effect of inertia filtering dominates. On-station platform motion due to low level (~ 0.014 Newton meter rms) friction torque is negligible (~ 0.00023 radian). This is a conservative estimate of expected torque noise based on in-orbit Intelsat IV data and ground test data.

The principal disturbance to platform pointing is the random error on the earth sensor leading and trailing edge pulses. The MIP pulse jitter is an order of magnitude smaller and negligible by comparison.

Figure 4-54 shows the closed loop transfer function from sensor noise to platform pointing as a function of frequency for the proposed design. For a linear system, the noise transmission ratio (rms out/rms in) is simply the area under the square of the transfer function. The ratio for the tracking loop transfer function was found to be 0.8.

The net transmission ratio, however, must also take into account an attenuation inherent in the LOS error processing. As discussed in a previous section, the azimuth error is determined by integrating at a constant slope up at the occurrence of the leading edge earth pulse and down at the occurrence of the MIP, until the occurrence of the earth trailing edge pulse. Any

platform error will result in a change in MIP phasing with respect to the earth center. Analytically the error signal is

$$\phi_{\text{Platform Error}} = \int_{T_{\text{LE}}}^{T_{\text{MIP}}} S_o dt - \int_{T_{\text{MIP}}}^{T_{\text{TE}}} S_o dt$$

where S_o is a constant in degrees/second. With $T_{\text{LE}} \triangleq 0$,

$$\begin{aligned} \phi_{\text{Error}} &= S_o [T_{\text{MIP}} - 0] - S_o [T_{\text{TE}} - T_{\text{MIP}}] \\ &= S_o [2T_{\text{MIP}} - T_{\text{TE}}] \end{aligned}$$

if

$$T_{\text{MIP}} = T_{\text{TE}}/2 \text{ (i. e., the MIP is exactly between the earth pulses)}$$

then $\phi_{\text{error}} \equiv 0$. If the MIP is off-center by one unit, the result of the up-down ramp will be a two-unit error. Thus, a scale factor of 0.5 is necessary in the subsequent electronics to form actual error.

For random, uncorrelated errors on both the leading and trailing edge pulses, the error in the LOS processor output voltage is $\sqrt{2}$ times the rms (or the 3σ) noise on each of the two inputs pulses. However, with the scale factor reduction of 0.5, the net result in terms of input noise to the system transfer function is $\sqrt{2}/2$ or 0.707 of the sensor pulse jitter.

Combining the two attenuation factors, the net transmission from sensor pulse jitter to platform jitter is 0.57. For the worst-case sensor noise of 0.0017 radians (3σ), the platform pointing would then be 0.0010 radian (3σ). These predictions, based on a simplified continuous data mode, have been verified using the analog simulation, as discussed below. The indicated performance is well within the allocation of 0.0026 radian for platform jitter.

4.4.3 Component Description

The following section discusses the design of the individual elements involved in the attitude and despin control subsystem.

4.4.3.1 Earth Sensors

The given requirements call for three earth sensors oriented in-line in azimuth and spaced in elevation such that the sun or moon cannot interfere with more than one sensor each at any time. The elevation orientations used in Intelsat IV, 0 and ± 0.108 radian from the plane normal to the spin axis, provide suitable separation of sensors. The sun passes through the scan path of each sensor twice per year and the moon passes through 27 times per year. All of these periods are predictable from ephemeris data and sensor switching can be accomplished well in advance of requirements. Switching of sensors would be utilized where necessary to avoid sun and moon interferences rather than require circuitry to inhibit the production of output pulses from scanning these sources. Such circuitry can minimize the number of times switching is required, but does not eliminate significant errors produced by scanning these sources when they near an earth edge. Without sun and moon discrimination circuits, the sensors are not damaged by sun exposure but will produce output pulses when scanning the sun and the moon when it is very bright. The 0 radian oriented sensor is used only for despun and the offset sensors are used for despun and attitude determination. Despun will be accomplished by centerfinding using the space-earth (lead edge) and earth-space (trail edge) crossing pulses (or an earth-width pulse).

Known bias is allowable and < 0.0017 radian bias uncertainty is acceptable. Noise < 0.0017 radian at each earth edge crossing is desired. Satellite rotor spin rate would be 10.47 ± 2.09 radians per second. Proven technology, low weight and power, and high reliability have been emphasized. A satellite lifetime of 5 to 7 years is specified.

Barnes Engineering Company and Lockheed Missiles and Space Company (LMSC) are the major producers of this type of earth sensor. Foreign sources (e.g., Sodern of France) and designs that have not been developed were not considered. One Barnes and one LMSC sensor were considered acceptable for this application. Table 4-36 provides a comparison of parameters for these sensors.

Barnes has built three models of spinning earth sensors: The 13-205 (Tiros), the 13-210 (Hughes TACSAT and Intelsat IV), and the 13-211 (for the European Aeros satellite). The 13-205 is an old unit with wideband wavelength sensitivity and without the required accuracy. The 13-211 earth sensor is similar to the 13-210 (see below) but employs fixed thresholding of the differentiated pulse and other simplifications in circuits (and decreased capability) which result in a smaller, lower weight and power unit. The present unit is designed for 1.05 rad/sec spin rate. Bias errors of the order of 0.01 radian can result from use of the fixed threshold. Extensive modification would be required to meet the noise and bias requirements. The result would be very similar to the 13-210 sensor. The 13-211 is therefore not considered to be an acceptable sensor for this application. The 13-210 sensor with some modifications would be an acceptable unit for this application.

TABLE 4-36. EARTH SENSOR COMPARISON

Parameter: Requirement		LMSC Type 8	Barnes 13-210
Maximum error:			
Noise, radian 3σ	0.017*	0.017	0.017
Bias, radian	0.017	0.017	0.017
Output:			
Rectangular lead and trail edge or earth chord pulse		5 volt chord pulse	15 volt lead and trail edge pulses
Mass, KG:	Minimum	0.64	0.82
Dimensions, meters:	Minimum	0.076 x 0.076 x 0.152	0.076 x 0.076 x 0.178
Power, watts:	Minimum	1.2 maximum at 21 to 31 volts	1.2 maximum at 23 to 31 volts
Reliability for 0.158 gigaseconds (5 years):	Maximum	0.928	0.927
Sun discrimination:	Not required	No	No
Moon discrimination:	Not required	No	Yes
Temperature capability:	266° to 325°K**	255 to 333K	255 to 323K
Vibration exposure:			
226 m/sec ² rms random**		142 m/sec ² rms random 20 to 2000 Hz	226 m/sec ² rms random 20 to 2000 Hz
294 m/sec ² sine		74 m/sec ² sine	294 m/sec ² sine
Aperture, diameter - meters:	Not specified	0.038	0.0286
Spectral band, microns:	In a spectral band which results in an essentially uniform earth	14.1 to 15.8	14.5 to 15.5 (will be modified to 14 to 16)
Field of view, radians:	Not specified	0.021 x 0.021	0.026 to 0.026
Detector:	Not specified	Servo Corporation thermistor bolometer	Barnes thermistor bolometer
Development status:	Proven technology	Qualified, 20 flight units built	Qualified, 16 flown
Cost:	Minimum	Roughly equal	
Schedule:	Minimum	Qualification - 0.105 gigaseconds; 3 flight units in 0.132 gigaseconds	Qualification - 0.105 gigaseconds; 3 flight units in 0.132 gigaseconds
Modifications required:	Minimum	Adjust electronics bandpass for 10.47 rad/sec	1. Adjust electronics bandpass for 10.47 rad/sec. 2. Change detector. 3. Increase spectral filter bandwidth.

*At each earth edge crossing.

**Assumes same as Intelsat IV.

Modifications would consist of 1) tailoring the electronic bandpass to the 10.47 rad/sec rate, 2) incorporation of a different type of thermistor bolometer detector to improve long-term noise level and stability, and 3) increasing the spectral bandwidth to 2 micron from the present 1 micron width. These modifications may be incorporated on other programs in the near future.

The 13-210 sensor was developed and qualified by Barnes for the TACSAT program. Three of four units on board that satellite are operational and in use after 3-1/2 years in synchronous orbit. The same sensor with minimal change was qualified for Intelsat IV, and 12 have been launched and are operating on four of those satellites (the first being launched in January 1971). This sensor includes moon discrimination circuitry which precludes moon-produced outputs. With the exception of the moon circuitry and providing separate lead edge and trail edge output pulses, the circuitry is similar to that of the LMSC Type 8 sensor described in more detail below. Basically an earth radiance pulse is amplified and shaped, differentiated, and threshold detected to produce a rectangular pulse at the leading edge and the trailing edge earth crossings. The threshold levels are automatically adjusted to a percentage of the pulse peak to compensate for earth radiance variations. The moon discrimination circuitry incorporates a delay following each threshold which allows an output pulse to be produced only if the source producing the signal exceeds the moon in angular width. The differentiated pulses resulting from scanning the moon are too narrow to produce output pulses. The 13-210 sensor mass is 0.82 kg.

LMSC has produced three basic styles of spinning sensors. Two produce only the differentiated output pulse without thresholding. These include units flown on the TRW Intelsat III and the DSCS II programs. Thresholding and production of a rectangular type of fast rise time pulse is desired for this application. The third style, designated the Type 8, incorporates the variable thresholds and produces a rectangular pulse of length corresponding to the length of earth chord scanned. The Type 8 sensor has been qualified in 1970 and about 20 flight units have been produced for LMSC programs. Although no confirmation of flight history or data are generally available, it appears reasonable to assume the unit has been flown. The circuit functions are essentially the same as the Barnes Model 13-210 used on Intelsat IV. The only change to the Type 8 sensor required for the TDRS application is modification of the electronic frequency response characteristics for the 10.47 rad/sec rate. The larger aperture and wider spectral band as shown in Table 4-36 comparison chart are advantageous in reducing noise error by collecting a larger input radiance. No change is required in the optics or detector. Although the vibration level to which the unit has been qualified is low (74 m/sec² sine and 142 m/sec² rms random) there appears to be no reason the present design would not withstand significantly higher levels.

Figure 4-55 shows a block diagram and signal processing of the sensor. The radiance of the warm earth is detected against the cold space background. The thermistor bolometer detector consists of an active

20643-76X(U)

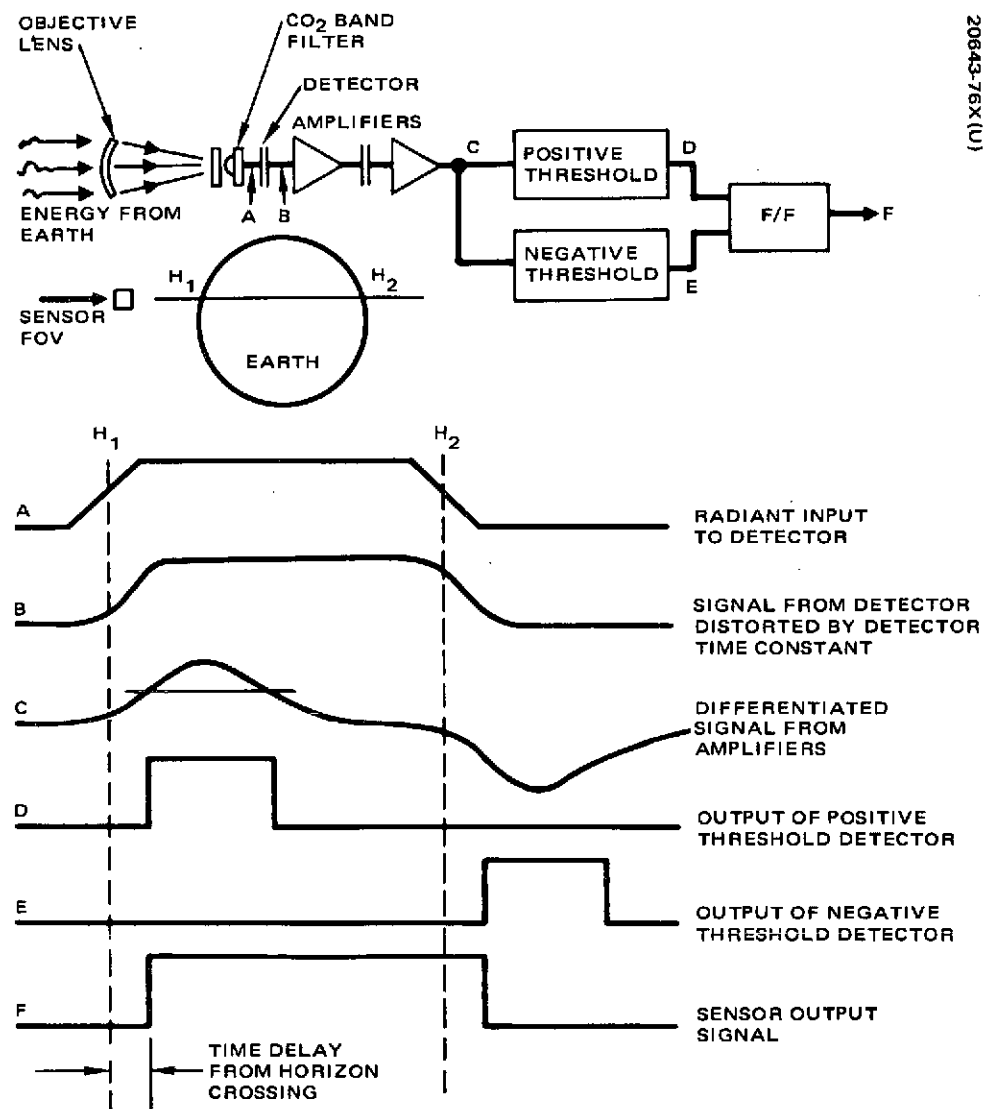


Figure 4-55. LMSC Type 8 Earth Sensor Block Diagram and Signal Processing

thermistor flake immersed on a hemispherical germanium immersion lens and a compensating thermistor flake in the same package. The two thermistors are connected into a bridge network to which bias voltage is applied. The radiant energy is collected by a germanium objective lens, passes through a CO₂ bandspectral filter centered at 15 microns, and is focused on the active thermistor flake by the immersion lens. The change in resistance of the active thermistor flake produced by heat absorption when viewing the earth produces an offset voltage from the bridge. This signal is amplified, shaped, and differentiated to produce analog-type pulses of opposite polarity at the leading and trailing earth edge crossings. A 5 volt amplitude rectangular output pulse is produced when the differentiator pulses trigger threshold circuits. The output pulse is started by the leading edge pulse and stopped by the trailing edge pulse. The threshold levels are variable and are set automatically at a percentage of peak of the differentiator pulses. This technique compensates for variations in earth radiance and almost eliminates error associated with fixed threshold levels due to such radiance variations.

4.4.3.2 Sun Sensor

The highly reliable sun sensor assembly provides redundant pulse pairs for determination of the spacecraft spin axis attitude relative to the sun within 0.0035 radian. Identical assemblies have successfully flown on ATS, TACSAT, and Intelsat IV. The sensor is mounted to the spinning portion of the vehicle so that when the spacecraft spin axis is within 0.61 radian of normal to the sunline, each sensor of the assembly produces one pulse per revolution. The angular relationship between a pair of sensors, ψ and ψ_2 , is used as a measure of the polar sun angle between the sunline of sight and vehicle spin axis. The time relationship between the ψ and ψ_2 pulses is used to compute this angle. Sensor manufacturing and testing techniques have been developed during many Hughes spacecraft programs, making sensor fabrication and testing routine. All sensor parts and materials as presently used in the existing design are adequate for survival and reliable operation in the TDRS environments. The sun sensor provides accurate synchronization reference pulses used for attitude determination. Characteristics are listed in Table 4-37.

TABLE 4-37. SUN SENSOR CHARACTERISTICS

Field of view	0.61 radian from $\phi = 1.57$ radians
Accuracy	0.0035 radian spin azimuth reference 0.0035 radian sun angle measurement
Power	None
Mass	0.11 kg assembly
Redundancy	Redundant ψ and ψ_2 pairs
Reliability	0.9999 per ψ and ψ_2 pairs (5 years)

20643-77(U)

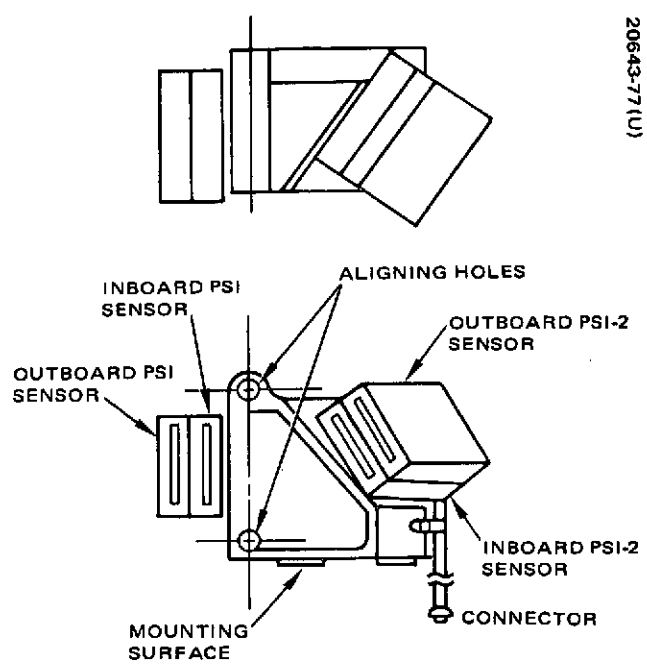
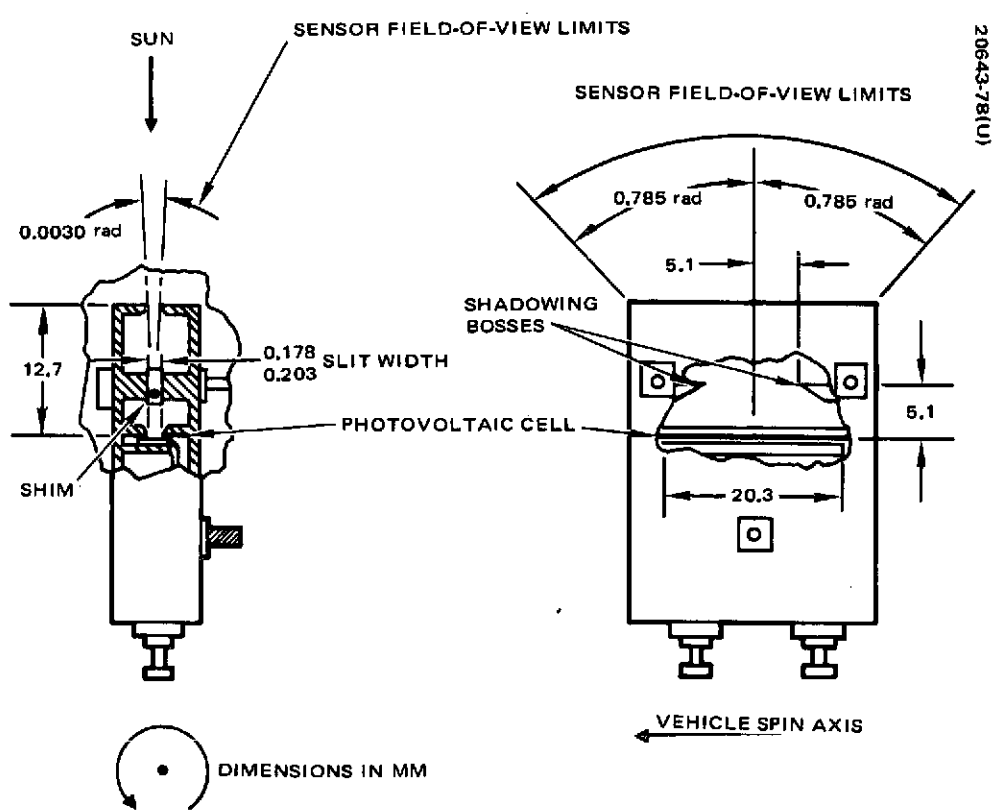


Figure 4-56. Sun Sensor Assembly Details



20643-78(U)

Figure 4-57. Single Sensor Unit Diagram

A sun sensor assembly (Figures 4-56 and 4-57) consists of four identical sensor units (redundant pairs) mounted on a precision bracket. Each pair of sensors provides two fan shaped fields of view (0.003×1.57 radians) whose planes are 0.61 radian from each other. The plane of the field of view of one sensor (ϕ) is oriented parallel to the spin axis. The other sensor viewing plane, ψ_2 , is inclined 0.61 radian to the spin axis and rotated 0.61 radian in azimuth from the ψ plane. As the sunlight enters the sensor field of view, an n/p silicon photovoltaic cell is illuminated. A voltage pulse is generated when the sun passes through the field of view plane. The electrical output signal from the sensor is a function of the input energy from the sun which falls on the cell, the 1 kilohm load resistor and the diode loading effect of the unilluminated area of the cell. The field of view of each cell is ± 0.79 radian from the normal to the cell surface for specified output amplitudes.

The sensors are located on the rotating portion of the spacecraft so that the sensors produce one pulse per revolution when the spacecraft spin axis is within ± 0.61 radian of normal to the sunline. The width of the field of view of each sensor element in conjunction with the 0.0093 radian angular size of the sun results in nominal pulsewidth of approximately 0.0218 radian at the 100 mv thresholding level. Due to the 0.61 radian inclination of the ψ_2 sensor, its nominal pulse width is $0.0218/\cos 0.61 = 0.0267$ radian. A typical output pulse is shown in Figure 4-58. The angular relationship between the ψ and ψ_2 sensors is used to measure ϕ , the polar angle between the sunline and vehicle spin axis. The formula that relates the angle ϕ to the time of occurrence of the ψ and ψ_2 pulses is given in Figure 4-59. The pulse-time relationship of the ψ and ψ_2 pulses as a function of the spacecraft attitude to the sunline is shown in Figure 4-60. The nominal attitude accuracy of the sensor is ± 0.009 radian without calibration. With both prelaunch and in-flight calibration, and by smoothing the data over a number of measurements, the sun angle uncertainty is reduced to approximately ± 0.035 radian.

4.4.3.3 Nutation Damper

The proposed nutation damper is a scaled down version of the unit employed on the Intelsat IV program. Figure 4-61 illustrates the damper and its essential design features. This eddy current damper comprises a single axis permanent magnet pendulum subassembly suspended from a torsion rod, an aluminum alloy conducting vane for eddy current dissipation, and a supporting framework structure. Eddy currents generated in the vane by the moving magnetic tip provide the energy losses. The torsion rod provides the torque to restore the pendulum to the equilibrium position. The damper functional characteristics are listed in Table 4-38.

The torsion rod is machined from beryllium-copper wire stock. this material has been employed successfully in eddy current nutation damper designs for the Intelsat IV. The torsion rod element concept was conceived at Hughes following the demonstrated inability of commercially available flexural pivots to survive the dynamic loading environment of launch

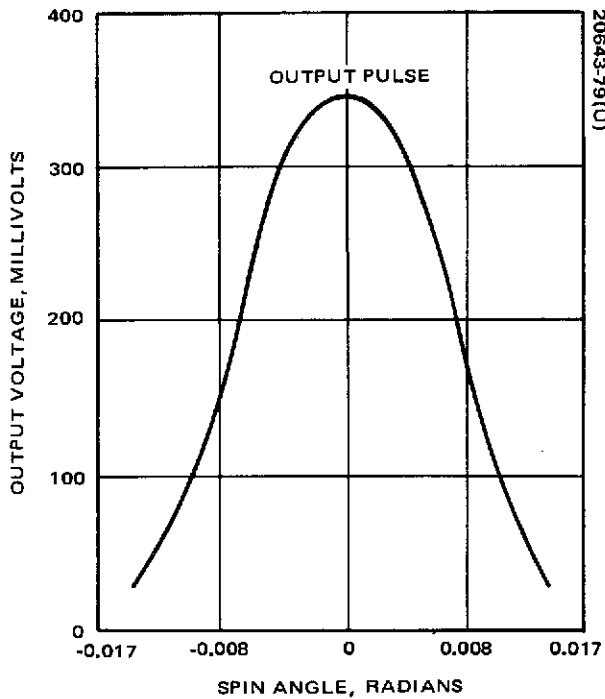


Figure 4-58. Typical Sensor Output Pulse

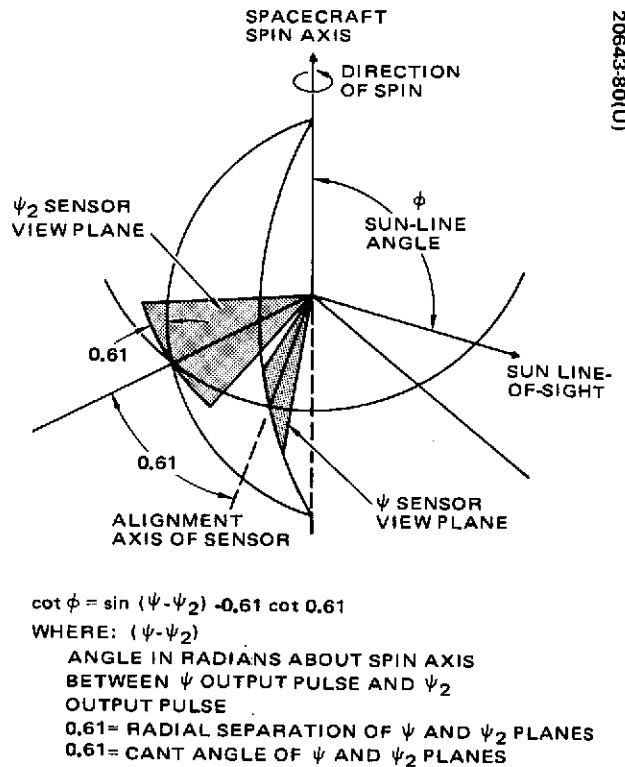


Figure 4-59. Sun Sensor Geometry

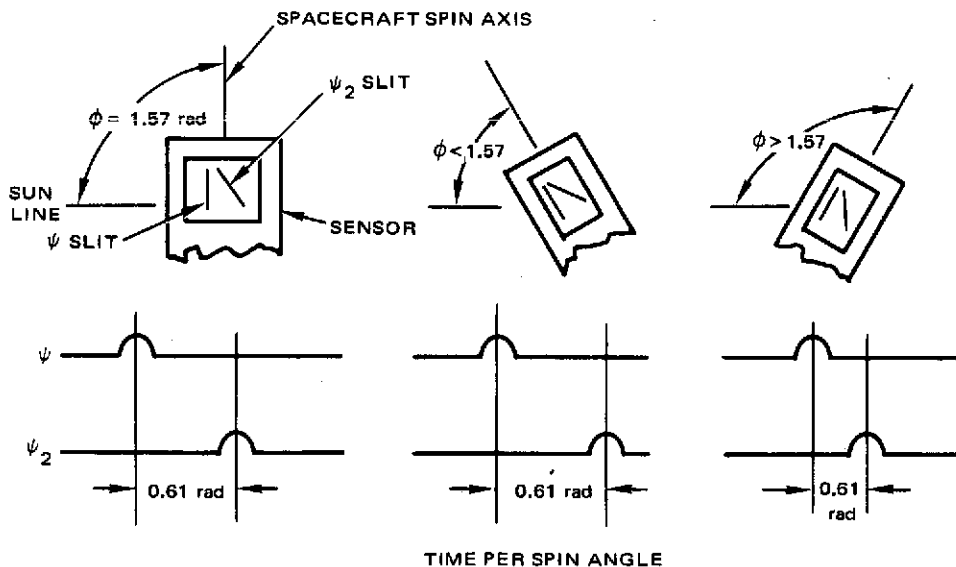
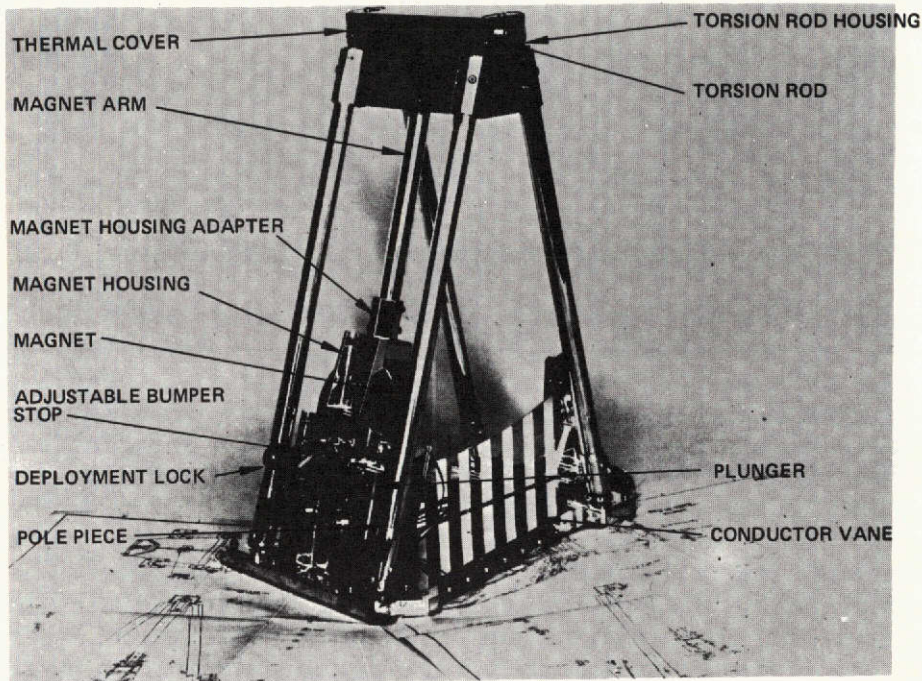


Figure 4-60. Phase Versus Output Timing



20643-82(U)

Figure 4-61. Nutation Damper

This page is reproduced at the back of the report by a different reproduction method to provide better detail.

TABLE 4-38. NUTATION DAMPER FUNCTIONAL CHARACTERISTICS

Natural frequency (ω_n) = 2.10 rads/sec
Damping ratio: $\zeta_{77^\circ\text{F}} = 0.130$, $\zeta_{0^\circ\text{F}} = 0.156$, $\zeta_{150^\circ\text{F}} = 0.124$
Torsion-wire stiffness = 0.374 Newton meter/radian
Pendulum inertia = 0.082 kg/m ²
Angular damping coefficient = 0.046 Newton meter sec/rad
Unit mass = 2.3 kg
Unit envelope = 0.414 high x 0.198 wide x 0.343 long (meters)
Damper mounting surface location = spacecraft station 3.43

simulating vibration tests. The ability of the damper to provide very precise control of spacecraft pointing is due to the unique design combination of torsion rod, bonded solid lubricated journal bearings, and pendulum-rotor-journals. One end of the torsion rod is fixed to damper structure; the other is attached to the pendulum rotor. The pendulum rotor/torsion rod subassembly is suspended via large radial clearance journal bearings. In a 9.8 m/sec² field, pendulum rotor journals contact lubricated bearing bores. However, in a zero m/sec² environment, and in the absence of external accelerations, the torsion rod acts to lift the pendulum rotor journals off the bearing bore surfaces, thus eliminating coulomb friction and allowing energy dissipation to continue as spacecraft nutation angles approach zero. The damper magnetic tip mass employs a cast Alnico VB permanent horseshoe magnet and two vanadium permendur pole pieces. The pendulum arm stiffness and the journal/bearing radial clearance preclude contact between magnet pole pieces and conducting vane during worst case mission lateral accelerations and thermal gradients.

The damper pendulum subassembly is caged during spacecraft launch by means of a pyrotechnic lock mechanism attached to the damper structure. This precaution is taken to preclude excessive dynamic loading and possible damage to the torsion rod and pendulum rotor bearing lubricated surfaces. Following spacecraft separation and prior to spinup, the damper pendulum is uncaged and the damper passive energy dissipation commences. During spacecraft apogee boost, the uncaged damper may experience full pendulum excursion to soft spring loaded stops. The axial thrust load presents no problem for the damper suspension system, as the torsion rod deflects in bending to allow rotor journals to contact bearing bores which carry the load.

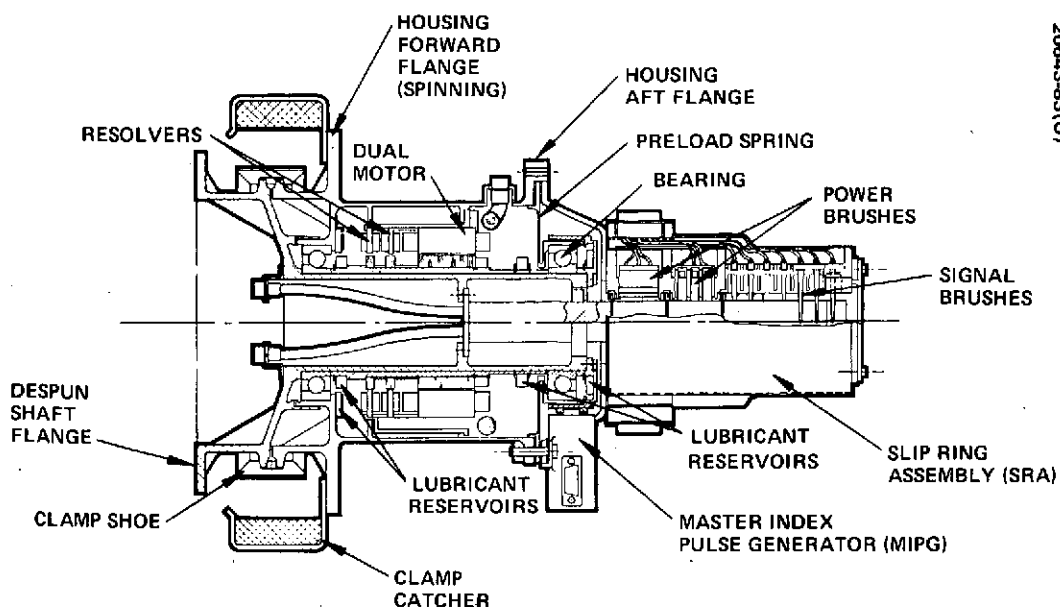


Figure 4-62. BAPTA

4.4.3.4 Bearing and Power Transfer Assembly (BAPTA)

The BAPTA provides all mechanical and electrical interfaces between the spun and despun sections of the satellite. The assembly, shown in cross-sectional view in Figure 4-62 consists of five major components:

- Bearings and BAPTA structure, which support the despun platform and antenna during orbital operations
- Brushless torque motor, which despins and controls pointing of the antenna in response to torque commands from the despun control electronics (DCE)
- Master index pulse generator (MIPG), which provides one pulse per revolution (from each of two redundant coils) to the DCE for relative angle (antenna pointing) information
- Slip ring assembly (SRA), which provides electrical power and signal transfer across the rotating joint
- Launch lock clamp, which provides a rigid structural interface between the spun and despun sections of the satellite during launch and prevents excessive loading of the bearings.

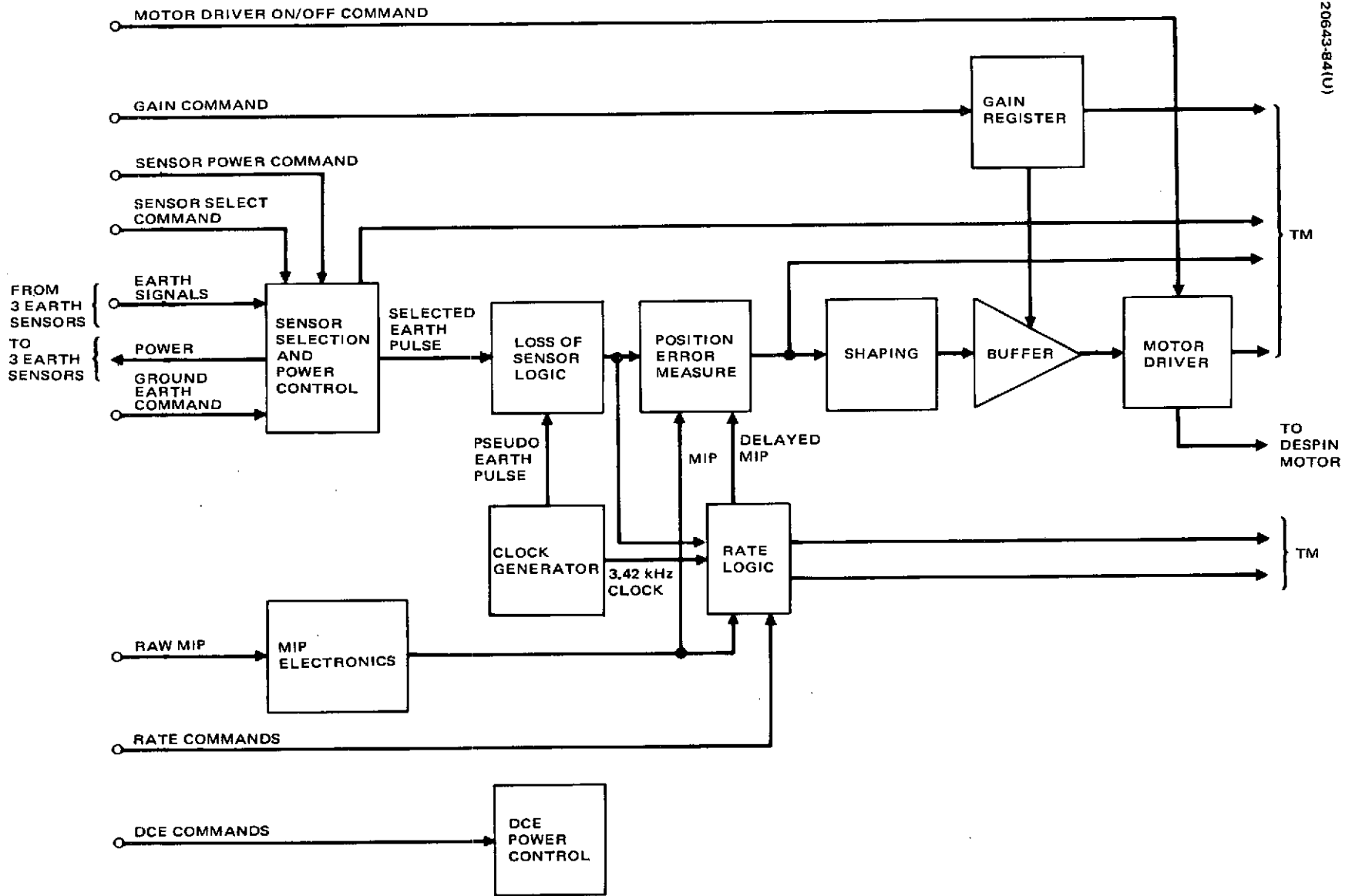
BAPTA design characteristics are summarized in Table 4-39. A detailed description of the BAPTA design is contained in Appendix A-5.

TABLE 4-39. BAPTA DESIGN CHARACTERISTICS

Mass (including launch lock clamp)	<15 kg
Overall length	<0.419 mm
Operating spin speed range	10.47 ±2.09 rad/sec
Operating temperature range	277 to 305K
Maximum temperature gradient, shaft to housing	266 K
Reliability for 0.22 gigasecond (7 year) operation	>0.99
Bearings	
Type	Angular contact, extra light series
Bore	60 mm
O. D.	95 mm
Ball diameter	0.01032 meter
Number of balls	19
Ball grade	5
Bearing tolerances	ABEC Class 9
Retainer material	Cotton phenolic
Retainer type	Outer race riding
Lubricant	HMS 20-1727 (95% Apiezon C, 5% lead naphthanate)
Friction torque	
Nominal (294 K, 10.47 rad/sec)	0.20 Newton meter
Maximum (277 K, 12.56 rad/sec)	<0.34 Newton meter
Torque Available	
Stall, single motor, 24 volts applied	3.8 Newton meters
12.56 rad/sec, single motor, 19 volts applied	>1.02 Newton meters

Table 4-39. (continued)

Motor	
Type	Brushless dc, resolver commutated
Number of motors	2, independent
Torque constant (at motor)	0.84 Newton meter/amp ($\pm 10\%$)
Back EMF (at motor)	0.84 volt/rad/sec ($\pm 10\%$)
Winding resistance (at phase)	5.4 ohms ($\pm 10\%$)
MIPG	
Number of coils	2, independent
Number of output pulses	1 per coil per revolution
Output voltage	>3 volts, 0 to peak, 0.47 rad/sec
Zero crossing slope	>114.6 volts/radian, rad/sec
Slip Ring Assembly	
Brush material	85% Ag, 3% C, 12% MoS ₂
Ring materials	Coin silver
Lubrication	Dry (MoS ₂ contained in brush)
Power section:	
Number of rings	2 (1 positive, 1 negative)
Number of brushes/ring	6 (3 wear tracks, 2 brushes per track)
Current capacity (steady state)	21.6 amperes/ring
Brush type, preload	Cartridge, 80 grams
Signal section:	
Number of rings	12
Number of brushes/ring	2 (1 wear track, 2 brushes per track)
Current capacity (steady state)	100 ma/ring
Brush type, preload	Cantilever spring, 25 grams
Noise level, maximum	<10 mv, peak to peak



20643-84(U)

4-140

Figure 4-63. Despin Control Electronics

4. 4. 3. 5 Despin Control Electronics

The despin control electronics uses information derived from earth sensor signals and the master index pulse (MIP) signal to control the despin motor torque by controlling motor current. Figure 4-63 is a block diagram of the DCE.

When the platform rate is zero and pointing at the earth, the position error controls motor current. The position error processing circuitry receives the selected pulse from one of the three earth sensors or the ground command substitute, the master index pulse (MIP) from the MIP electronics, and the delayed MIP pulse (which occurs 283 ms after the MIP pulse) from the rate logic. The analog position error measurement circuit generates a bipolar proportional error signal based on the position of the MIP within the earth pulse. Outside this linear range, the position error signal is saturated. The position error signal is proportional to the time position of the MIP between LE and TE.

Appropriate shaping of the position error signal is provided by the shaping circuit and the limiting integrator. The shaped position error signal is used as the torque command input to the motor driver. A simple, proportional power amplifier was chosen for the brushless dc motor drive in keeping with the design goal of minimum complexity.

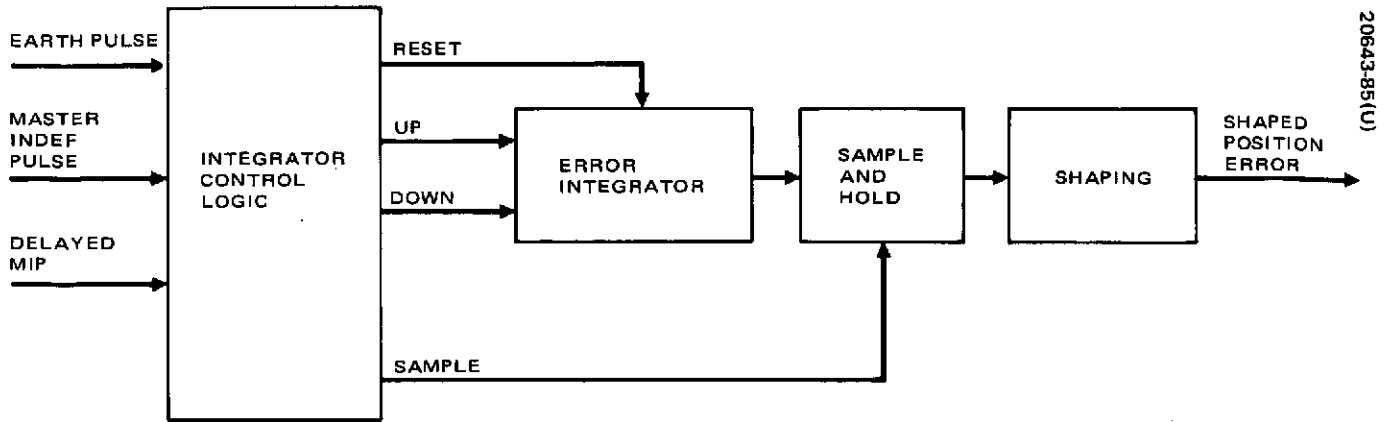


Figure 4-64. Error Measurement Circuit Block Diagram

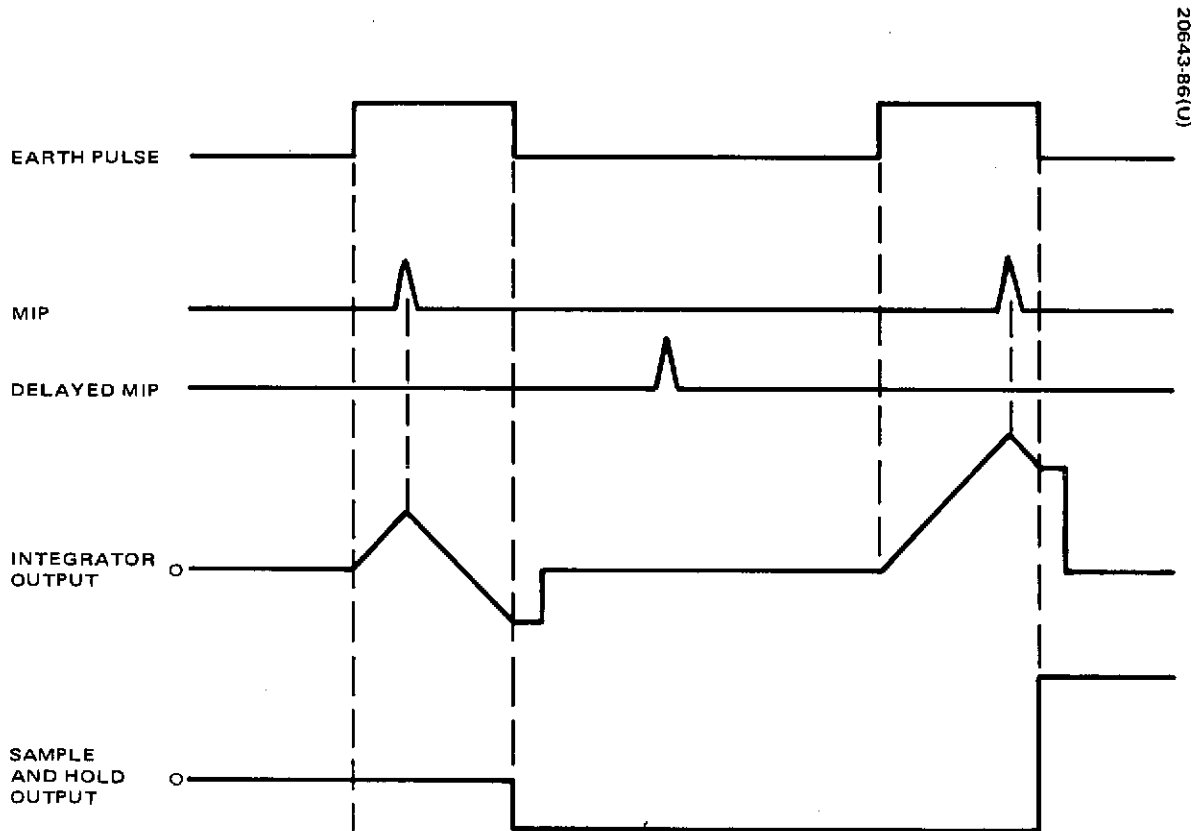


Figure 4-65. Position Error Measurement Circuit Waveforms

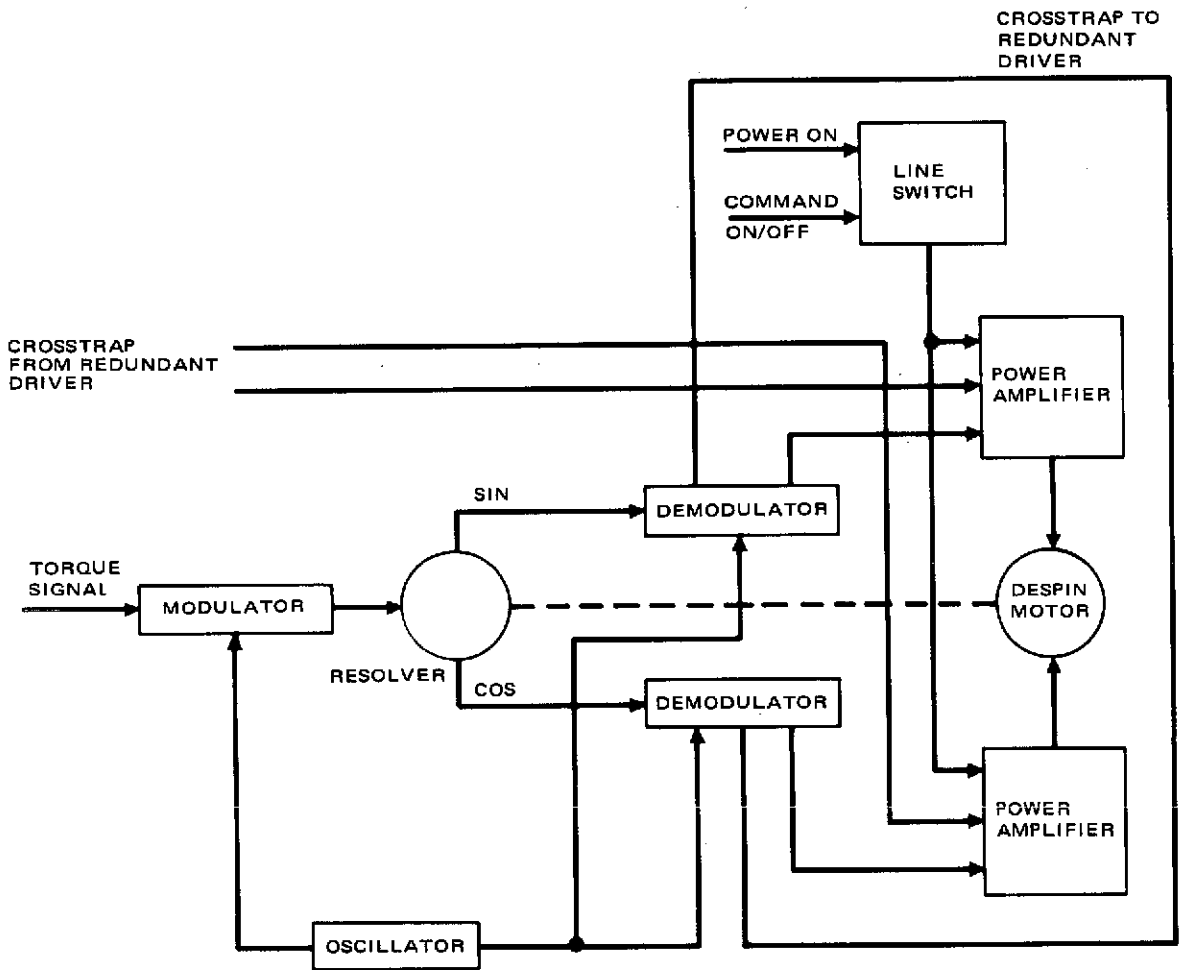
Once each rotor revolution, the position error measurement circuit determines the time position of the MIP pulse within the earth pulse as an analog voltage. The voltage is stored between measurements and shaped with active filters to provide a shaped position error signal.

Figure 4-64 is a block diagram of the position error processing with waveforms. The block diagram shows the integrator control logic receiving the earth pulse and the MIP and delayed MIP. When the time interval between the delayed MIP and the MIP overlaps the earth pulse, the error integrator output will have a positive slope. When the time interval from the MIP to the delayed MIP overlaps the earth pulse, the error integrator slope will be negative. After the earth pulse, the resulting integrator voltage is sampled and held and the integrator is reset to zero. This results in a position measurement characteristic as shown in Figure 4-65. Error reversal at a point opposite the null ensures that the platform will always return to null by the shortest path. The shaping transfer function which processes the error signal consists of a dominant, low frequency zero term and two higher frequency poles. Proportional plus limited integral shaping is also provided to null steady state friction torque. The shaping is realized using active RC networks. Two loop gain settings are selectable by ground command. Power turn on resets the low gain setting.

The motor driver will be compatible with a dc brushless motor-resolver combination. The configuration, which is similar to that used on HS 312 and HS 333, is shown in the block diagram in Figure 4-66. The torque signal into the motor driver is modulated onto a square wave and used to drive the resolver. The carrier is generated by the oscillator. The resolver mounted on the motor shaft produces sine and cosine outputs as a function of the motor rotor to stator angle. These outputs are synchronously demodulated and become inputs to the power amplifiers. The power amplifier is a simple proportional design in keeping with the minimum complexity goal. Current sensing is used to provide true current command drive to the motor independent of speed and for telemetry. The driver will deliver sufficient current to the motor to provide full stall torque capability required for flat spin recovery.

Either or both motor drivers can be selected by ground command. Restoration of bus power after an outage will cause both drivers to turn on. The motor driver cross-trapping is configured such that a single demodulator output may drive its own power amplifier, the redundant unit power amplifier, or both. The motor driver line switch provides current limiting to protect the motor from demagnetization.

When the platform is spinning, the motor current is controlled by the rate logic. The rate logic uses a digital measurement technique to determine the first back difference of platform position resulting in a delta angle measurement. Because the rotor rate is close to constant, this delta angle is interpreted as platform rate.



20643-87(U)

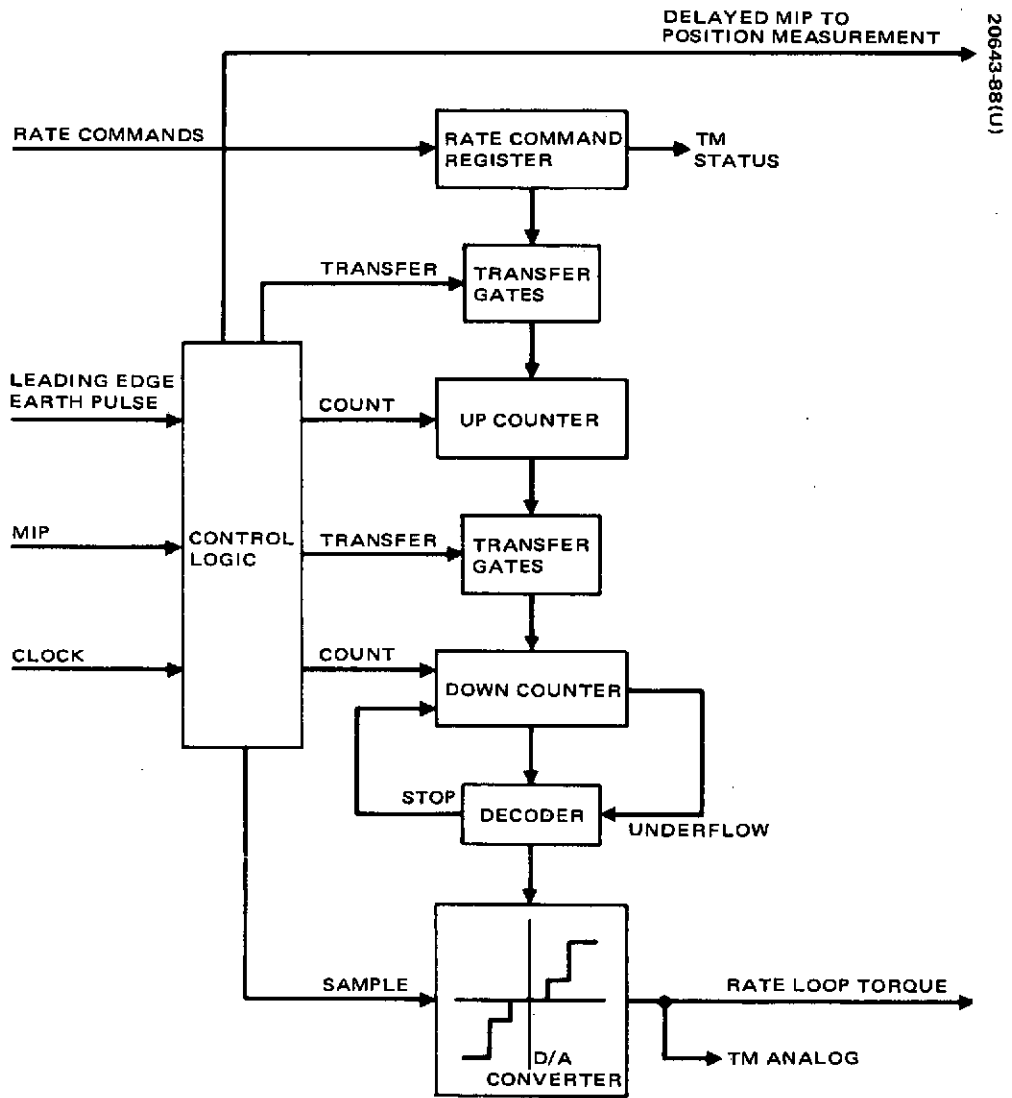
Figure 4-66. Motor Driver Block Diagram

The rate logic configuration shown in the block diagram in Figure 4-67 is similar to that used on Intelsat IV. The control logic receives the earth pulse, the MIP pulse, and the DCE clock. At the occurrence of the earth pulse, the upcounter is loaded with the minus 0.0195 rad/sec. Thus for a commanded rate of zero, the initial upcounter value is -0.0195 rad/sec. The upcounter is allowed to count from the earth pulse to the MIP. (When the MIP is within about 1.4 radians of the earth pulse, the delayed MIP is used instead of the MIP to avoid bad measurements due to MIP earth pulse crossover.) A crystal controlled oscillator provides the basic count clock. The number in the upcounter is now transferred to the downcounter and the downcounter is allowed to count from the next earth pulse to MIP. The number in the downcounter now represents the first back difference or platform rate minus the initial 0.0195 rad/sec offset. Underflow from the downcounter is detected and three bits are decoded as follows: If there is no underflow, then the platform rate is more negative than -0.0195 rad/sec and full spinup torque is applied. With underflow, the three bits are decoded to determine if the rate is between -0.0195 and 0.0098 where 1.356 Newton meter of spinup torque is applied or between -0.0098 and 0.0098 where no torque is applied or between +0.0098 and 0.0195 where 1.356 Newton meter of despin torque is applied. If the decoder determines the rate to be greater than +0.0195 rad/sec, then the downcounter is stopped and full despin torque is applied.

The upcounter and downcounter are operated simultaneously so that a rate sample is available once each rotation. Two special cases occur when the MIP rate is outside the dynamic range of the dual counter technique; that is, when the MIP rate is greater than twice or less than half of the earth pulse rate. When no MIP or delayed MIP occurs between LE pulses, the control logic causes zero to be transferred into the downcounter. This ensures underflow and a detected rate of greater than -0.195 rad/sec so full despin torque is applied. When four or more MIPs plus delayed MIPs occur between LE pulses, the control logic commands a D/A sample right after the LE pulse. This results in no underflow so full spinup torque is applied.

The design provides for commanded rate operation. Flip flops are used to store the rate command of zero or any of three nonzero rates. Power turn-on will reset the rate command to zero. Command rate status is telemetered. At the occurrence of the earth pulse, the upcounter is loaded with the negative of the commanded rate. Thus, the platform rate will be controlled to a value that compensates for this offset resulting in the desired platform rate.

The loss of sensor logic uses a simple two bit counter which counts the 1.66 Hz pseudo-earth signal and is reset by the selected earth pulse. If three pseudo-earth signals are counted without an earth pulse, then it is assumed that the sensor signals are not useful and the pseudo-earth pulse is substituted for the selected sensor signal. Reoccurrence of the sensor pulse restores the normal operation.



20643-98(U)

Figure 4-67. Rate Logic Block Diagram

There are two redundant DCE units, only one of which is turned on at a time. Magnetic latching relays will remember the selected unit despite power loss. The selected DCE unit is cross-strapped to drive either or both motor drivers. After separation, both motor drivers will come on when the power bus comes up. Both can also be commanded on together and commanded off individually.

4.4.4 Despin Control System Performance

The despin system analog simulation has been used to verify approximate analyses used for preliminary design and to generate representative performance data. The results discussed below show the performance of the proposed design for the following conditions:

- 1) Acquisition for east-west pointing
- 2) Steady state pointing in the presence of principal disturbances
- 3) Nutation damping due to inertia cross-coupling (track mode and rate mode)
- 4) Rate mode operation and apogee motor fire response

Figure 4-68 shows the platform acquisition from an initial rate of 0.63 rad/sec. The net torque is initially negative to decelerate the platform to the rate loop deadband of 0.035 rad/sec. Once the rate is reduced to the deadband level, the platform position starts to drift toward null in a direction determined by the polarity of the saturated position loop torque. Eventually the platform LOS drifts into the tracking loop field of view; then the tracking loop shaping provides the necessary damping to capture. An initial offset due to friction is nulled within 30 seconds by the tracking loop integrator. Note that during the acquisition cycle, the integrator is saturated at its limited value of +0.68 Newton meter. This does not adversely affect acquisition because of the parallel type integrator implementation and the greater torque dynamic range of the nonintegral portion of the tracking loop. The example includes acquisition runs with a single motor driver active and for both motor drivers on, which is the normal operational mode for acquisition and apogee boost. Reliable acquisition has been verified over a range of mass properties, spin speed, and initial conditions.

4.4.4.1 On-Station Pointing

The principal disturbance for on-station pointing is sensor noise. MIP noise and small random fluctuations in friction torque have a second order disturbing effect. Figure 4-69 shows the system response to sensor jitter of 0.0017 radian (3σ), or 0.0012 radian (3σ) at the input to the system due to the LOS error processor attenuation. The pointing error is generally below 0.00087 radian with infrequent peaks as high as 0.00105 radian. At very small values of spacecraft nutation, the noise from the earth sensors will randomly obscure the nutation frequency component of the tracking loop

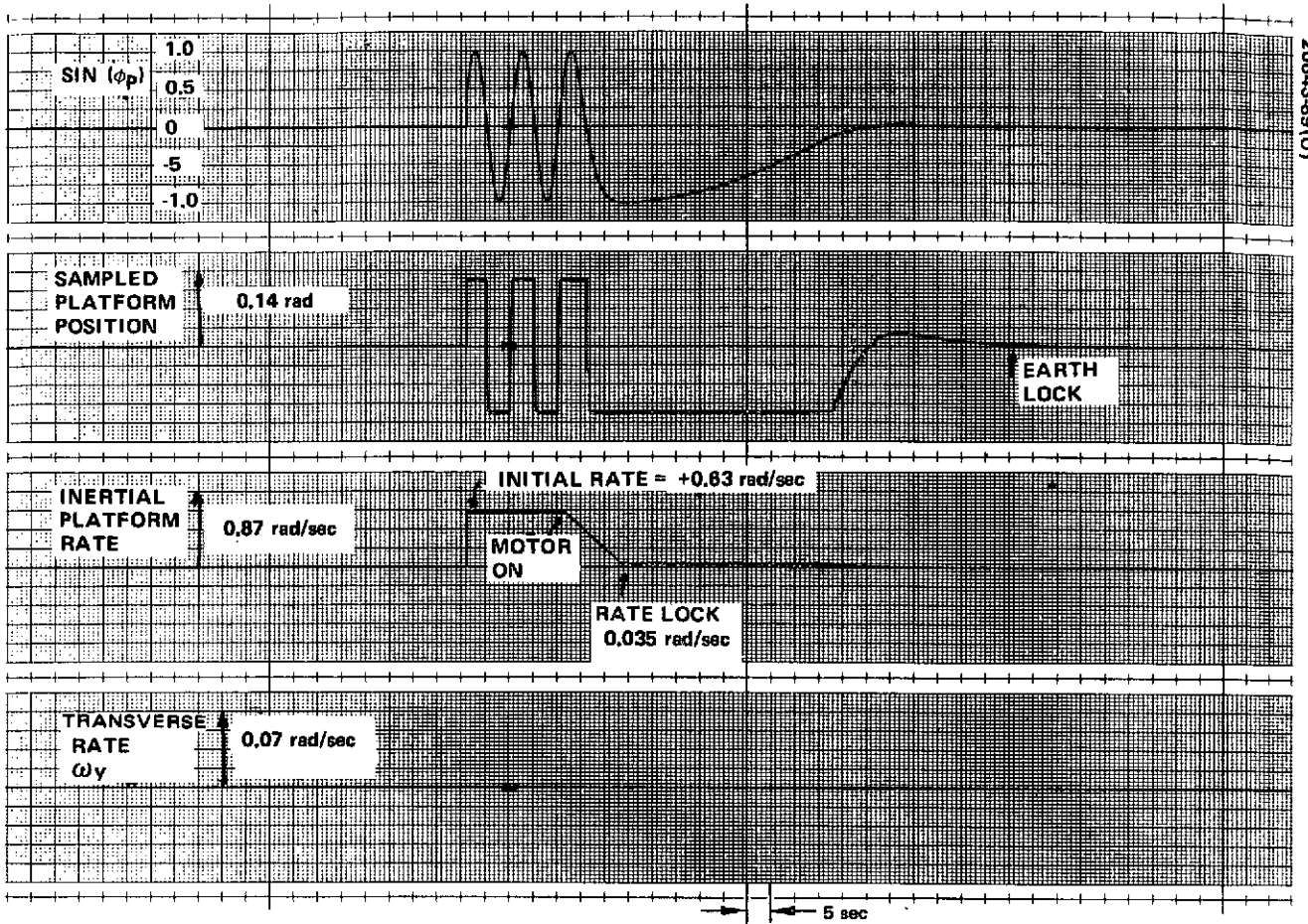


Figure 4-68. Despin Control System Acquisition

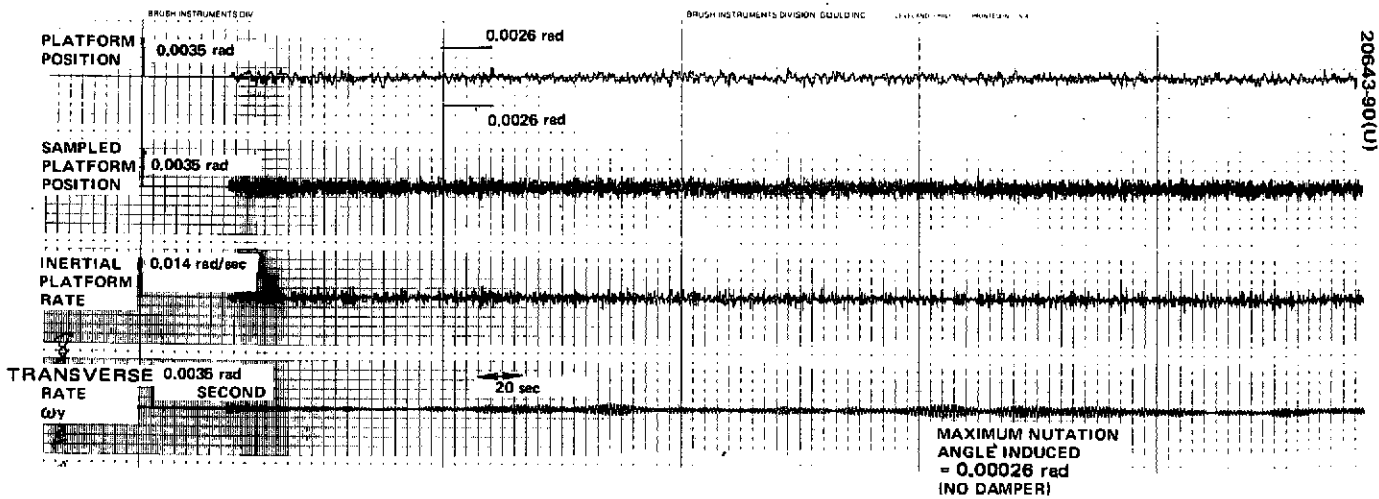


Figure 4-69. Steady State Pointing Performance

error signal; consequently, nutation will sometimes be augmented and sometimes be decremented by random despin torque variations. In the presence of nutation damping, this will result in a steady state randomly varying nutation angle. As can be seen in the figure the maximum level of nutation caused by the worst case earth sensor jitter is 0.00026 radian.

4.4.4.2 Nutation Damping

Figure 4-70 shows the stabilizing effect of the despin system for an initial nutation of 0.087 radian with a single motor driver on. This is a very large nutation and would be expected to occur only in the process of recovery from the flat spin condition (see Appendix A.1). During the initial phase of the damping, the rate loop dominates, leading to a linear decay in nutation angle of approximately 0.00017 rad/sec, or an equivalent time constant at 0.087 radian of 300 seconds. Once the nutation is reduced to the level at which the tracking loop can operate in a linear mode, it is driven toward zero exponentially with a time constant of approximately 175 seconds. The rate and position loops acting together, therefore, provide a substantial backup to the passive nutation damper out to relatively large nutation angles.

4.4.4.3 Rate Mode Operation and Apogee Motor Fire Response

During transfer orbit and prior to apogee boost, the platform will be rotated at several rpm (e.g., .21 to .42 rad/sec) by ground command. Because of the large variation in earth chord width in transfer orbit and the vehicle geometry in AMF attitude, the tracking loop inertial reference may, at times, not be usable. The rate loop will then be the main control mode. By summing the sensed platform rate with a ground command bias, the rate loop will hold the platform to the commanded rate. During periods of no sensor pulses, nominal frequency pulses are supplied on board by the loss of reference logic. The onboard pulses permit normal operation of both the position and rate loops.

Prior to firing of the apogee boost engine for synchronous orbit injection, the platform will be rotated so that during AKM fire, the transverse torques due to platform cg offset will average to zero. After injection, the commanded rate will be removed and a normal acquisition sequence will occur. A simulation of the apogee boost sequence is shown in Figure 4-71. From initial condition of earth lock, with both motor drivers on, a -0.42 rad/sec platform rate is commanded. Rate lock at the desired rate is accomplished in 6 seconds. For the simulation, a 1.356 Newton meter step in bearing friction torque for 35 seconds simulates the effect of firing the AKM. Note that the system maintains rate control during AMF. After injection, the platform retains the commanded rate. When the command is removed, a normal automatic acquisition sequence occurs, with position lock in 140 seconds. Nutation induced during the boost by a simulated dedamper is stabilized by the DCS coupling.

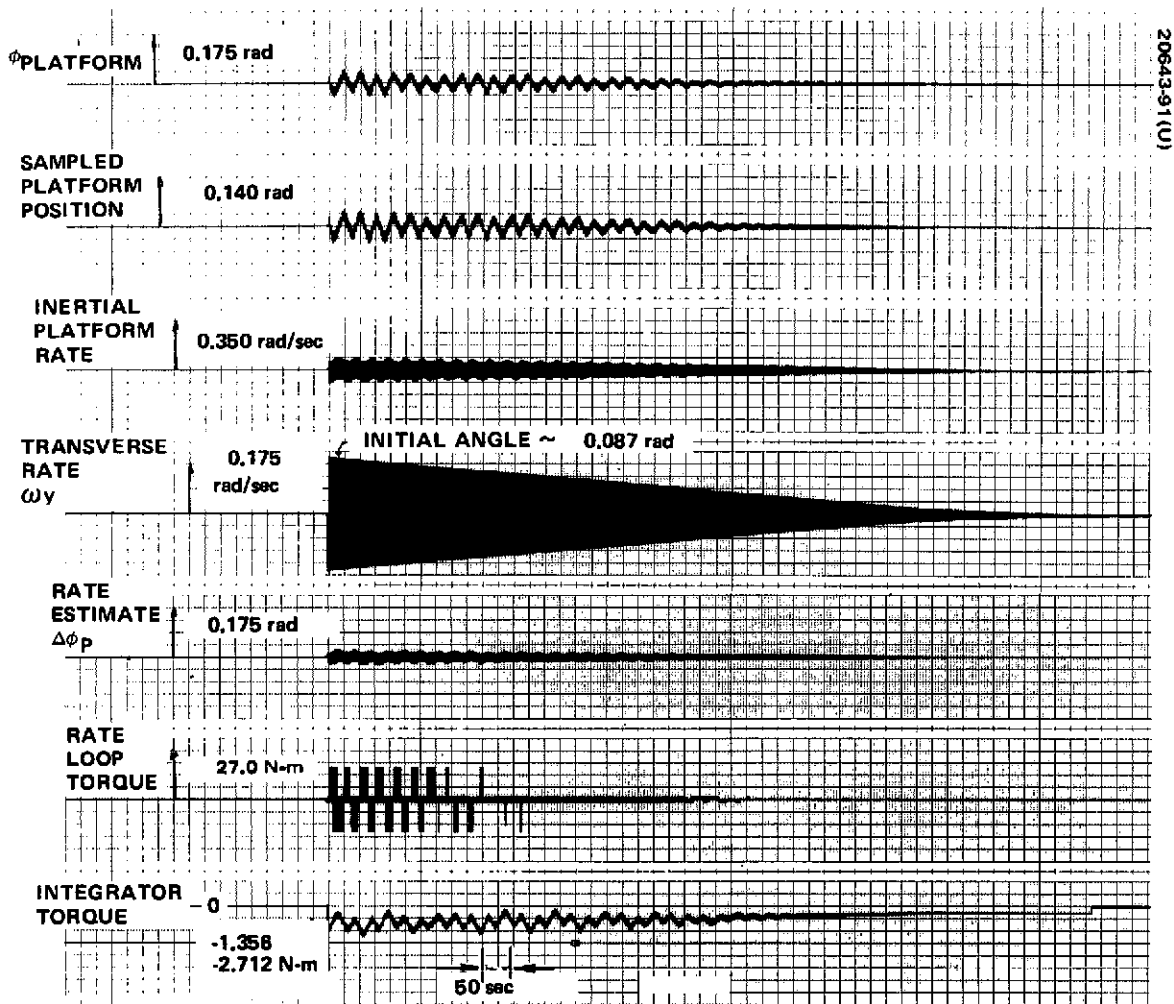


Figure 4-70. Despin Control System Nutation Damping

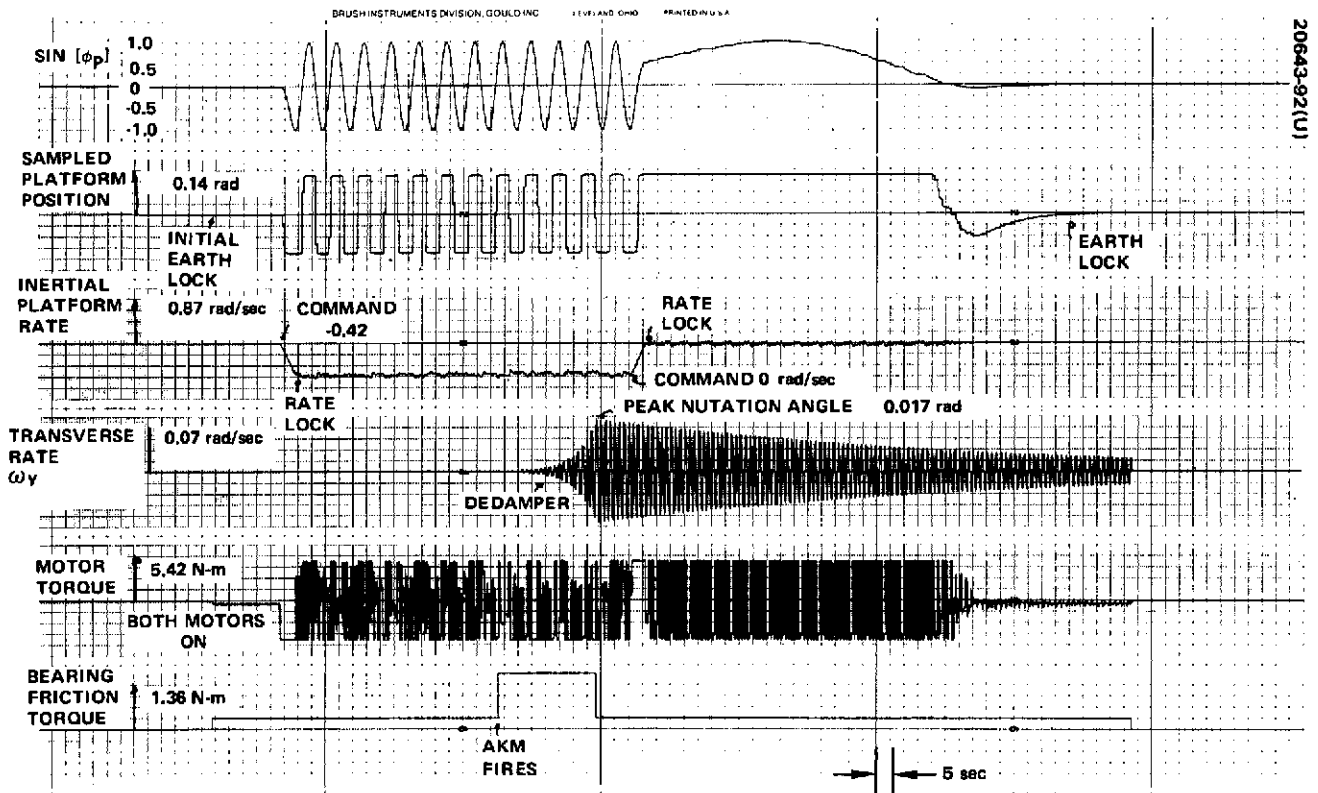


Figure 4-71. Despin Control System Apogee Boost

4.4.5 Technology Status

The design and implementation of the TDRS attitude and despin control subsystem is based on proven technology from such programs as TACSAT I, Intelsat IV, and the Canadian Domestic Communications Satellite, Anik I, which is presently under development. The basic gyrostatic stabilization technique was proven with the flight of TACSAT I and continued to prove successful on all Intelsat IV flights. All mechanical elements of the TDRS subsystem involve flight proven hardware. Control techniques and analytical performance predictions have been verified from observation of the in-orbit behavior of both TACSAT I and Intelsat IV spacecraft. The following summarizes the technology status of the various elements of the subsystem.

4.4.5.1 Bearing and Power Transfer Assembly

The BAPTA design selected is the result of extensive background and years of experience in design, fabrication, test, and orbital operation of despin assemblies for TACSAT, Intelsat IV, and Anik I communications satellites. The TDRS subsystem design represents the best available technology applicable to highly reliable despin assemblies, where each detail has evolved through several generations of analysis and test. This wealth of background experience provides high confidence in meeting the BAPTA functional requirements with minimum risk of development difficulties.

4.4.5.2 Earth Sensors

The proposed earth sensor for TDRS subsystem has been flown on the TRW Intelsat III and DSCS II programs and, therefore, represents flight proven hardware. The circuit functions are similar to the sensor flown on Intelsat IV.

4.4.5.3 Sun Sensor

The proposed sun sensor has been flown successfully on ATS, TACSAT and Intelsat IV. More than 30 of these units have been built and tested; no failures have occurred in any sensor of this type flown on Hughes satellites.

4.4.5.4 Nutation Damper

The TDRS subsystem nutation damper represents a scaled version of the damper successfully flown on Intelsat IV. In-orbit studies of its nutation damping characteristics have been done and found to be in agreement with analytical predictions.

4.4.5.5 Active Nutation Control

The ability to actively control nutation using reaction jets and a rotor mounted accelerometer was developed and proven for Intelsat IV. The ANC performance has been verified during in-orbit testing.

4.4.5.6 Despin Control Electronics

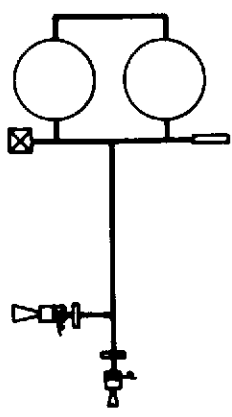
The control techniques and electronic hardware involved in the despin control subsystem are derived from the flight proven hardware of TACSAT I and Intelsat IV. The basic elements and their derivation are as follows:

Position error detection	TACSAT
Control shaping	TACSAT
Rate control loop	Intelsat IV
Motor drive	Intelsat IV

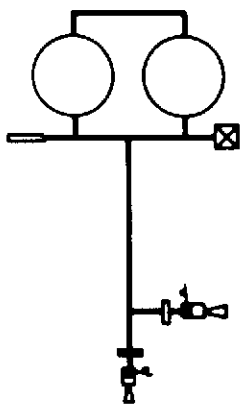
The hardware fabrication and assembly techniques are the same as those used on TACSAT and Intelsat IV and being used on Anik I.

4.4.6 References

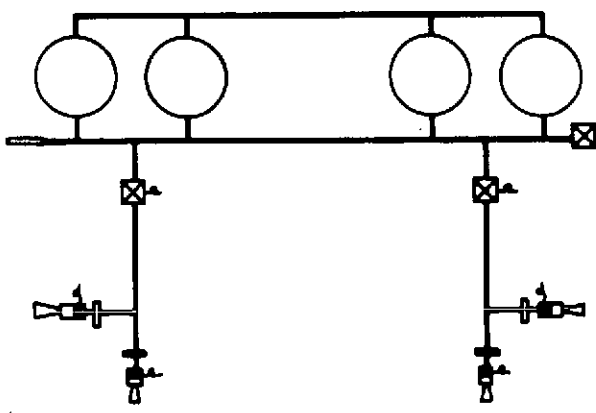
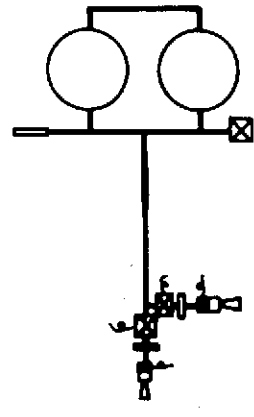
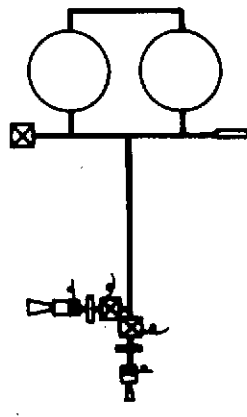
- 1) A. J. Iorillo, "Nutation Damping Dynamics of Axisymmetric Rotor Stabilized Satellites," ASME Winter Meeting, Chicago, Illinois, November 1965.
- 2) "Gyrostat Attitude Dynamics," TACSAT System Design Report, Volume I, Section 6, Contract Data Requirement No. 8047, Contract AF04(695)-1047, May 1969.
- 3) J. T. Neer and J. O. Salvatore, "Fuel Slosh Energy Dissipation on a Spinning Body," Hughes Aircraft Company Report SCG 20047R, February 1972.
- 4) J. R. Velman, "Simulation Results for a Dual Spin Spacecraft," Proceedings of the Symposium on Attitude Stabilization of Dual Spin Spacecraft, August 1-2, 1967, Aerospace Corporation Report, TR-0158, (3307-01) 16, November 1967, Page 11.



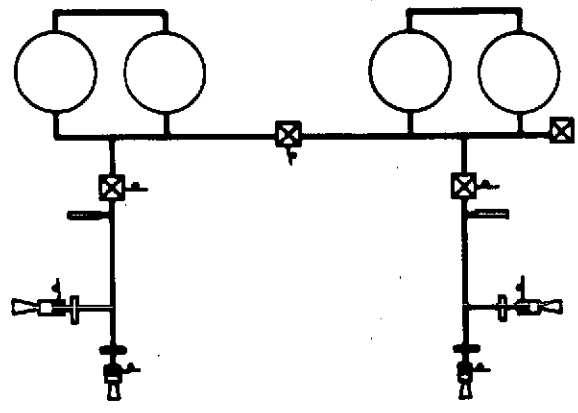
CONFIGURATION 1



CONFIGURATION 2



CONFIGURATION 3



CONFIGURATION 4

-  FILL VALVE
-  LATCH VALVE
-  PRESSURE TRANSDUCER
-  FILTER
-  PROPELLANT VALVE THRUSTER

Figure 4-72. RCS Candidate Schematics

4.5 REACTION CONTROL SUBSYSTEM

4.5.1 Alternatives Considered

There is currently no practical alternative to the baseline hydrazine monopropellant and catalytic thrusters, primarily due to the mission requirements of total ΔV , total pulses, and impulse repeatability. A common thruster size for both the axial and radial positions is not possible. The fine torque quantization and repeatability required to compensate for the solar torque disturbances and to maintain pointing errors within acceptable limits dictates an axial thruster in the 4.45 Newton (1 pound) thrust range. With the radial thruster used to perform station changes, the total number of pulses exceeds the current qualification of the 4.45 Newton thruster. The larger 22.25 Newton (5 pound) size was therefore selected for the radial thrusters.

Several alternate feed system schematics were considered. They are listed below and shown in Figure 4-72:

- Configuration 1. Separate half systems without latch valves
- Configuration 2. Separate half systems with one latch valve backing up each propellant valve
- Configuration 3. All four tanks manifolded together with a latch valve used to isolate each pair of thrusters
- Configuration 4. Separate half systems connected by a normally closed latch valve, and latch valves also used to isolate each pair of thrusters.

Configuration 1 offers complete redundancy except for propellant. The TDRSS mission has a significant amount of propellant assigned for its 7 year life needs, particularly attitude control and the station changes. Thus, a single propellant valve failure can be catastrophic. Configuration 2 protects the subsystem from a single valve failure, but introduces four new valves and would require careful propellant management and dedication of each thruster to a particular task in the event of a valve failure. Configuration 3 permits common access to all of the propellant. Thus, if a propellant valve fails open it can be isolated, and if it fails closed it's redundant counterpart can perform the remainder of the mission without the complication of trapped propellant. Configuration 4 differs from Configuration 3 with the addition of the normally closed latch valve used to isolate the two pairs of propellant tanks which it greatly enhances flat spin recovery by not allowing propellant movement between the pitch and yaw planes except under controlled conditions.

An alternative to Configuration 4 would be to provide latching valves for each propellant valve. The most likely failure of a propellant valve is a slow leak due to a particle lodged in the valve seat. The single latching valve provided by this configuration protects against this type of failure and avoids significant loss of propellant due to slow leakage. The latching valve

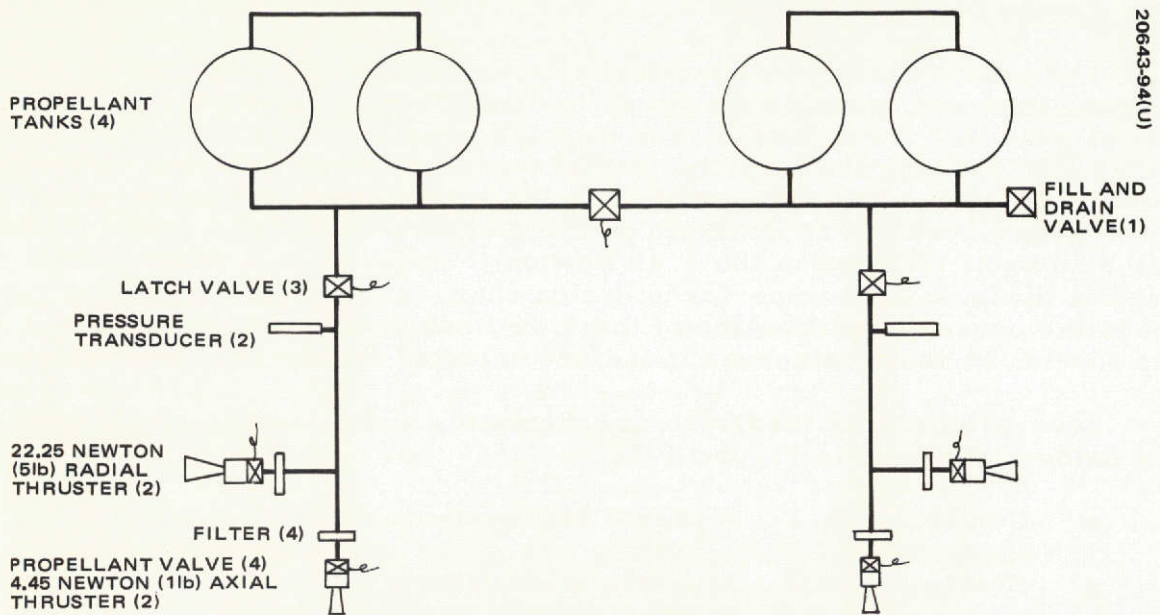


Figure 4-73. RCS Baseline Schematic

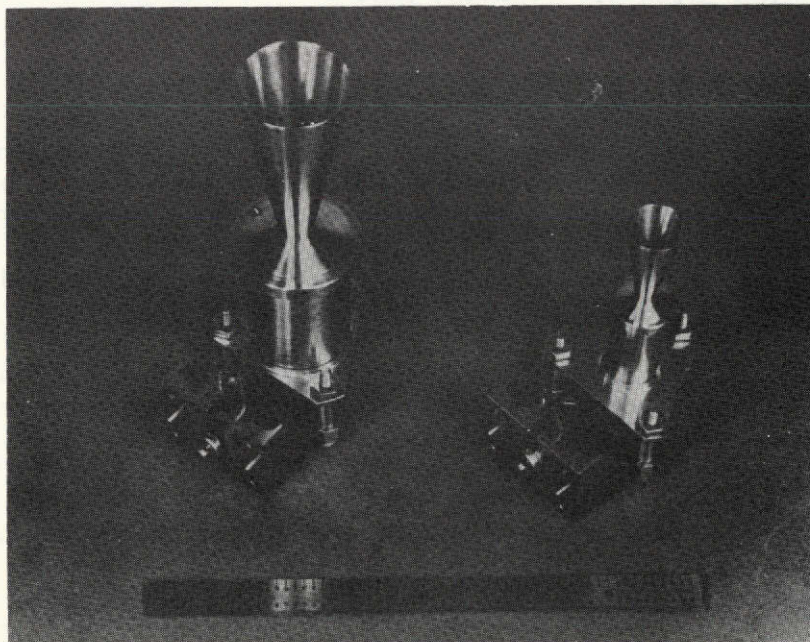


Figure 4-74. Thruster Family for Use on TDRS (Photo A28658)

This page is reproduced at the back of the report by a different reproduction method to provide better detail.

can be opened to permit use of operable thrusters, and the amount of leakage sustained during the attitude control or velocity maneuver is expected to be insignificant. An open failure due to an electrical fault is not expected as the valve drivers are designed so that no single failure will drive a valve open. Even if this should occur, then the mission can be completed using the thrusters in the other half of the subsystem.

Configuration 4 is selected for the baseline design because it provides protection against expected types of failures at minimum cost and mass.

4.5.2 Baseline Description

As shown in Figure 4-73 and previously explained, there are two 4.45 Newton axial thrusters and two 22.25 Newton radial thrusters. Each thruster has its own etched disc type filter and each half system has its own pressure transducer. The Hughes thrusters are shown in Figure 4-74.

4.5.2.1 4.45 Newton (1.0 lbf) Thruster

The Hughes 4.45 Newton thruster recently successfully completed qualification for use on the Canadian Domestic Satellite being built by Hughes for Telesat of Canada. The thruster assembly consists of two major components - the Hydraulic Research and Manufacturing Co. propellant valve and the Hughes Thrust Chamber.

The propellant valve was originally qualified for use on the Intelsat IV and HS 318 programs. It features series redundant seats operated by a torque motor and has proven to be a highly reliable valve with a demonstrated absence of operational or leakage problems.

The Hughes Thrust Chamber utilizes Shell 405 (grade ABSG) catalyst, contained in a chamber of L-605 alloy, to decompose hydrazine. The unit features a novel injection concept which results in performance superior to other existing concepts. The propellant is introduced into the thrust chamber through a single feed tube and is distributed over the cross-sectional area of the catalyst bed by internal flow passages with less included volume than other designs in use in the industry. This injection scheme results in more repeatable and predictable performance, smoother operation, and the capability for high temperature restarts of the thruster without fear of damage from the thermal decomposition of confined volumes of hydrazines.

The unit has successfully completed qualification testing and is now in production. The first four production units are scheduled for flight in November 1972. Two engine assemblies were tested during thruster qualification. The first unit was subjected to acceptance testing, vibration, and a life test which consumed 68 kg (150 pounds) of propellant and consisted of 500 runs totaling over 20,000 pulses and 30,000 seconds steady state at ambient temperature. This thruster surpassed the design goals appreciably. Unit 2 was subjected to an acceptance test, sine and random vibration, and margin tests which consisted of pulse and steady state performance at various duty cycles, temperature conditions, and inlet pressures between 0.103 and 2.42

megaNewtons/m² (15 and 350 psi). All qualification testing was performed under vacuum conditions. Following successful completion of the qualification program, a series of margin limit tests was performed to determine the effect of operating the thruster at inlet pressure conditions above and below the specification design limits.

As a result of the increasing interest in three-axis control and other control schemes requiring small granularity corrections, Hughes has conducted a series of tests to investigate the suitability of the 4.45 Newton thruster for such use. The results to date have been most encouraging. Over 3000 cold starts at 298 K (78°F) thruster and propellant temperature have been conducted on unit S/N 007 with no appreciable change in thruster performance characteristics.

4.5.2.2 22.25 Newton (5.0 lbf) Thruster

Hughes has also recently completed qualification of a 22.25 Newton thruster for use on the Intelsat IV program (spacecraft F-7 and F-8). Except for the obvious dimensional differences, it is very similar in design to the 4.45 Newton thruster. It uses the same highly reliable propellant valve.

The qualification program for this thruster included three units, each of which consumed over 229 kg (503 lbm) of hydrazine, accumulated over 286 starts. Included in the testing of each of the three units were over 31,000 pulses and over 6 hours of steady state operation. The demonstrated advantage of this thruster over competing designs from other manufacturers include more repeatable and predictable operation, smoother operation, and the capability for safely conducting high temperature restarts.

The 22.25 Newton thruster proposed for this program is a modification of the unit qualified for Intelsat IV. The injector has been redesigned as a result of a highly successful IR & D program. The redesigned thruster has completed extensive development testing and its complete requalification will be finished prior to the start of the TDRS program.

The modified unit utilizes the same materials of construction and design features as the previous unit, except that the injector has been redesigned. The injector and head end of the chamber are now machined from one piece of metal. This integral injector further reduces liquid volume downstream of the propellant valve and more uniformly distributes the injected fuel over the cross-sectional area of the catalyst bed. This results in better pulse quality, more rapid impulse tail-off on shutdown, and higher specific impulse (I_p) in the pulsing mode. Another significant advantage of this newly developed design is a substantial reduction in the roughness of operation, which will materially improve the life expectancy of the unit.

4.5.2.3 Propellant Isolation Valve (Latching Valve)

The valve selected for this application will be a latching solenoid valve developed and qualified by Carleton Control Corporation under contract to Hughes for use in the Intelsat IV and HS 318 satellites.

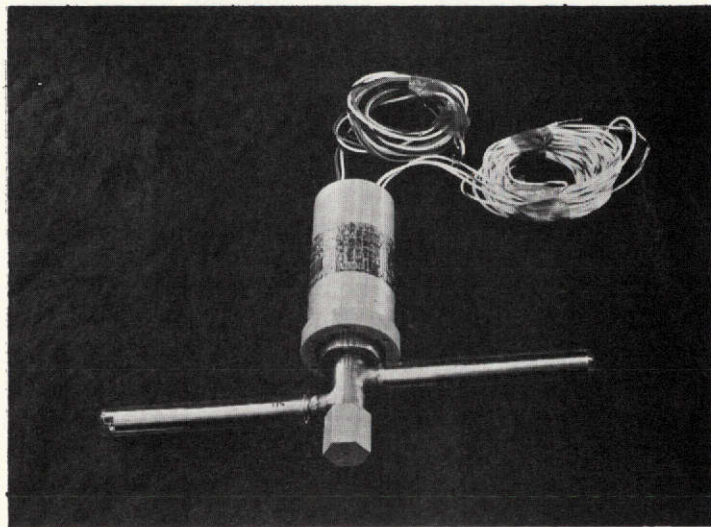
This isolation latching valve (Figure 4-75), employs a soft teflon seat. The valve poppet is held either in the open or closed position without electrical power by a Belleville spring. Pulsing the closing coil pulls the armature, fastened to the poppet, to the closed position. After removal of power, the valve remains held in the closed position by the Belleville spring. Pulsing the opening coil pulls the armature to the open position, reversing the Belleville spring, which holds the valve open after power is removed. Only 20 ms pulses are required to actuate the valve, although it has been designed and qualified to withstand continuous power for 120 seconds over the temperature range of 278 to 333 K (40° to 140°F). The valve is equipped with a single pole, double throw microswitch actuated by the armature so that valve position can be determined by either ground support equipment or by telemetry if desired. It has been qualified for 1000 opening and closing cycles and has demonstrated over 50,000 cycles successfully with less than 0.288 mm³/sec leakage of helium through the valve at 207 megaNewton/m² (300 psia). It also has a burst pressure exceeding the required value of four times the system pressure. The only difficulties encountered during the use of this valve were related to improper cleanliness standards. No difficulties have been encountered when using the rigorous Hughes cleanliness procedures.

External leakage is kept to a minimum by use of an all welded valve assembly using a metal bellows as a seal. The bellows is welded into the valve body and to the poppet and stem, sealing the propellant within the valve and away from the solenoid assembly. The bellows also pressure balances the valve poppet against both inlet and outlet pressure differentials. All components exposed to propellant are made from stainless steel or teflon.

4.5.2.4 Liquid Filter

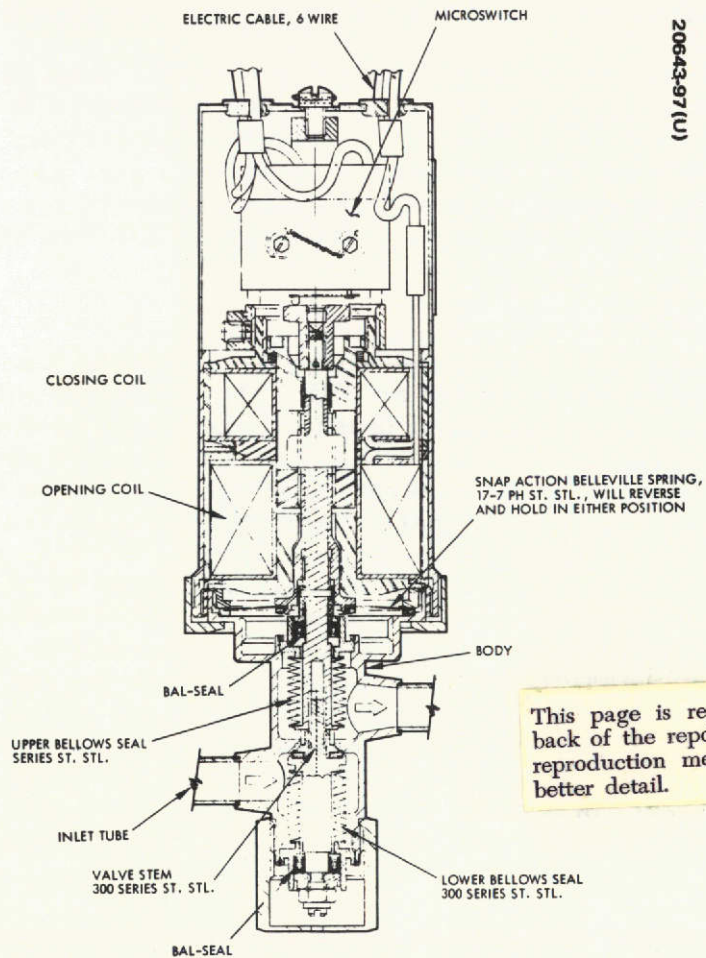
The filter proposed is an edge filter developed by Vacco Industries and qualified for the HS 312, HS 318 and HS 333 propulsion subsystems. This edge filter (Figure 4-76) consists of multiple chem milled discs stacked to form the filter element. By chem milling the washer-like discs, radial flow passages of controlled size are generated. Hughes believes that this filter configuration is the only concept that is both effective and free of particle generating elements. In addition to the Intelsat IV, HS 318, and HS 333 satellites, the filter concept was successfully employed in the helium filter on the Surveyor vernier propulsion subsystem. Prior to adaption of this filter design in the helium system on Surveyor, attempts to qualify wire mesh to filters were unsuccessful, since squib firing shock caused the wire mesh to generate metal fragments which adversely affected the performance of down stream components. Hughes again experienced difficulty with wire mesh filters in the early Intelsat Hydraulic Research valves. It was found that these screen filters not only were ineffective for the intended filtering application, but also could not be cleaned and, in fact, were a source of particle generation.

The Vacco filter proposed is sized and qualified to have a capacity equal to 1000 times the total particulate content of 20.4 kg (45 pounds) of hydrazine verified free of particulates to the degree specified by CS 31023-400.



20643-96 (U)

a) Assembled Configuration (Photo A27887)



20643-97 (U)

This page is reproduced at the back of the report by a different reproduction method to provide better detail.

b) Cross Section View

Figure 4-75. Propellant Latching Valve

4.5.2.5 Fill and Drain Valves

The fill and drain valve concept (Figure 4-77) was initially designed by Hughes Aircraft Company in 1965 for use on the Surveyor program, and initial qualification testing was completed in 1966. In 1968, the Surveyor valve was modified and requalified to the additional requirements of the HS 310 program. The same valve has been used for the HS 312 and HS 318 programs.

The valve is a manually operated shutoff valve using a tungsten carbide ball forced into the valve body seat to seal the flow passage. The ball is retained in a stem assembly and is moved axially on and off the seat when the retainer nut is rotated on the valve body. Due to the small ball size and the large axial loads developed by the retainer nut, very low torque loadings are required to provide high seat loading and a leak tight seal.

To provide seal redundancy and to seal propellant around the stem when the valve is open, an O-ring is used on the stem sealing on the inside of the valve body. A cap is provided to cover the MS 24385 inlet port when the valve is in the closed position. After system loading and before flight, an aluminum closure cap, using a K-seal at its base as an added redundant seal, is added over the complete valve.

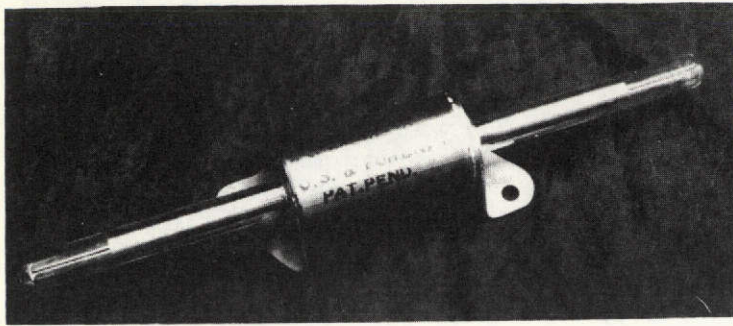
Over 90 of these type valves have been fabricated and tested for spacecraft without a single measurement out of specification. In addition, over 40 of these valves have been used in space and have performed flawlessly.

4.5.2.6 Propellant Tank

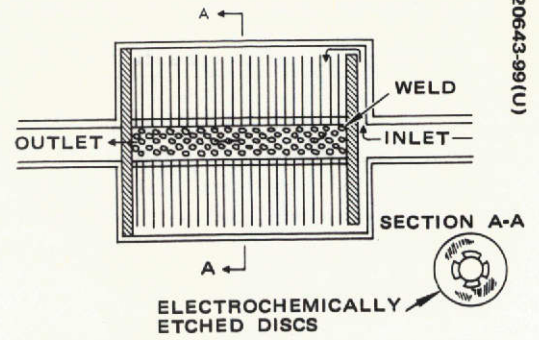
The propellant tank was originally designed and qualified for HS 333. It consists of a 32.5 cm sphere integrated with an 1.5 radian (86°) cone as shown in Figure 4-78. It is fabricated from 6Al-4V titanium by Sargent Industries. Design operating pressure is 2.86 mega Newtons/m² (400 psig) and burst pressure is 11.15 mega Newtons/m² (1600 psig). Total volume is 0.018 m³ (1100 in³) minimum per tank. The cone is located down and away from the satellite spin axis. Thus, 100 percent expulsion efficiency is possible with only two ports, since the fluid port is at the low point in the tank during both static ground servicing and in the in-flight spinning mode.

4.5.2.7 Pressure Transducer

The pressure transducer is a potentiometer of the design used on Syncom, Early Bird, Intelsat II, ATS, HS 308, HS 318, and HS 333. The potentiometer slide wire is actuated by pressure displacement of a welded pressure capsule referenced against vacuum. The transducer is shown in Figure 4-79.

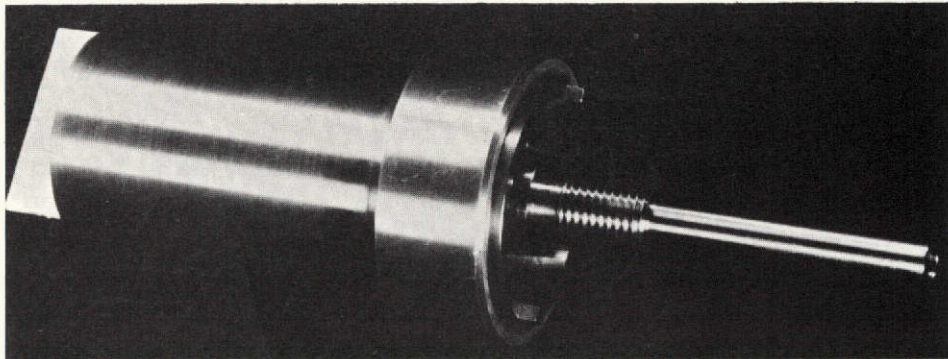


a) Assembled Configuration
(Photo A27890)

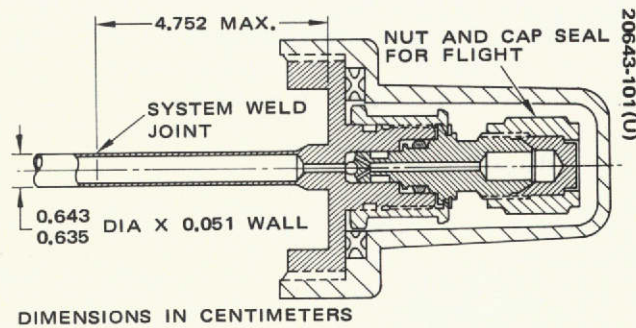


b) Cross Section View

Figure 4-76. Hydrazine Filter



a) Assembled Valve (Photo ES29087)



DIMENSIONS IN CENTIMETERS

b) Cross Section View

Figure 4-77. Fill/Drain Valve

This page is reproduced at the back of the report by a different reproduction method to provide better detail.

20643-102(U)

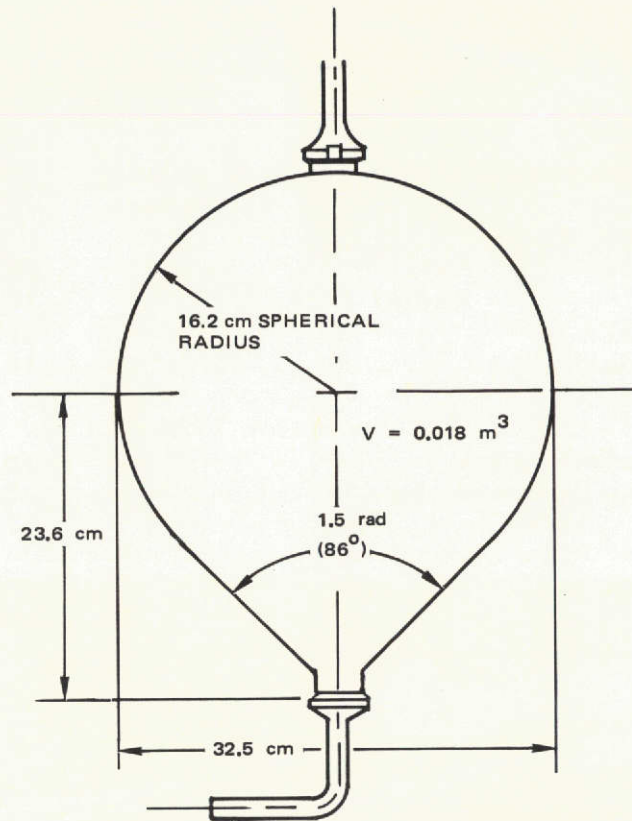
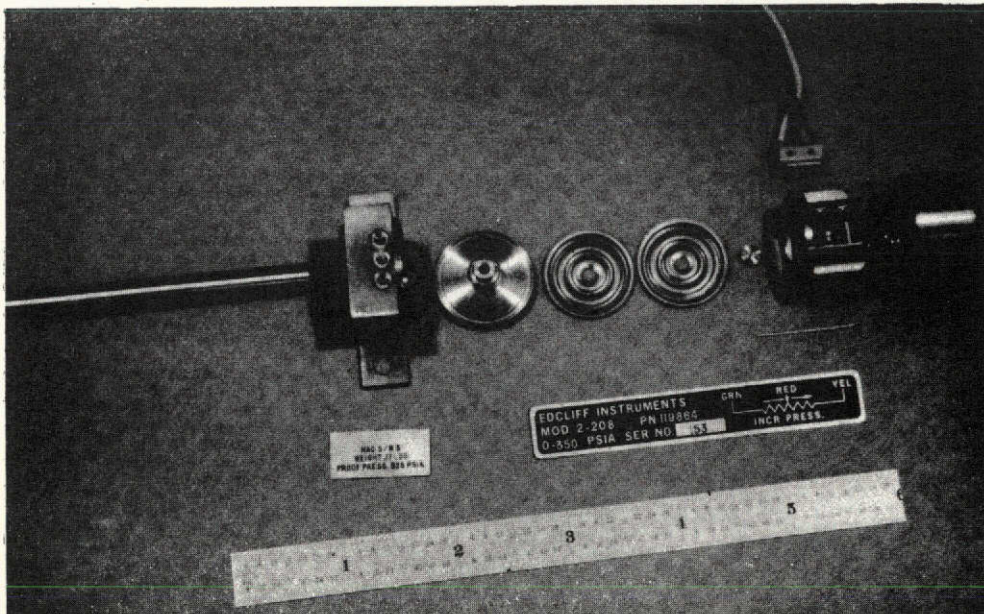


Figure 4-78. Propellant Tank



20643-103(U)

Figure 4-79. Pressure Transducer

This page is reproduced at the back of the report by a different reproduction method to provide better detail.

TABLE 4-40. RCS REQUIREMENTS

Performance		
ΔV		168.25 m/sec (552 fps)
Cumulative impulse predictability for	<10 pulses	20%
	>10 pulses	10%
Burn time:	Steady state	None
	Pulse	Axial 70,000
		Radial 30,000
Cold starts:	Axial	1250
	Radial	30
Physical		
Mass:	Subsystem dry	10.4 kg (23.0 lb)
	Propellant and gas	38.6 kg (82.0 lb)
Environmental		
Temperature range		278 to 333 K (40 to 140° F)

4.5.3 Baseline Performance

The ΔV and fuel budget provide for the following maneuvers and attitude corrections:

- 1) 130 degree precession for alignment of the apogee motor prior to firing
- 2) 120 degree precession for spacecraft operational positioning after firing
- 3) 7 years of solar torque correction assuming 80 percent antenna porosity
- 4) 2 percent margin for jet misalignment compensation
- 5) Injection trim for booster and apogee motor errors
- 6) Two 4.5 degree per day station changes
- 7) 7 years of east-west stationkeeping

The remaining RCS requirements are summarized in Table 4-40. The cumulative impulse predictability, based on spacecraft pointing requirements and verified during previous thruster qualifications, is 20 percent for the first 10 pulses and 10 percent for the remaining pulses in longer trains. The spacecraft attitude granularity requirement dictated a 4.45 Newton thrust range for the axial thruster while the requirement for 0.035 revolution per day station change capability introduced too many pulses for a 4.45 Newton radial thruster. The resulting total number of pulses and cold starts for the 4.45 Newton axial thrusters and 22.25 Newton radial thrusters are shown.

The subsystem total mass is 47.8 kg (105.0 pounds) of which the hardware totals 10.45 kg. A temperature range of 278 to 333 K (40 to 140°F) has been set to be compatible with the hydrazine. The vibration and acceleration levels are assumed the same as the Canadian Domestic Satellite (HS 333) requirements.

4.5.4 Technology Status

Every component included in the RCS has been qualified for flight use on at least one other program. Table 4-41 presents a comparison of the components recommended for use on TDRS with the components used on previous Hughes propulsion subsystems.

TABLE 4-41. CHRONOLOGICAL COMPARISON OF PREVIOUS HUGHES PROPULSION SUBSYSTEM COMPONENTS WITH PROPOSED RCS

	Subsystem Supplier	Propellant	Thruster	Propellant Valve	Fill and Drain Valve	Latching Valve	Relief Valve	Filter	Pressure Transducer	Tanks	Thermal Control	Lines
HS-301 (Syncom)	Kidde	H ₂ O ₂	Kidde	Kidde	Kidde	None	Kidde	None	Edcliff	Kidde (1060-A1)	None	1060-A1, all welded
HS-303 (Early Bird)	Kidde	H ₂ O ₂	Kidde	Kidde	Kidde	None	Kidde	None	Edcliff	Kidde (1060-A1)	None	1060-A1, all welded
HS-306 (ATS, A, B, and C)	Kidde	H ₂ O ₂	Kidde	Kidde	Kidde	None	Kidde	None	Edcliff	Kidde (1060-A1)	None	1060-A1, all welded
At this time it became Hughes' policy to design, fabricate, assemble, and test the propulsion system at Hughes rather than to subcontract.												
Surveyor	Hughes	MMH/ N ₂ O ₄	RMD	RMD	Hughes	None	Carleton	VACCO	Bournes	FanSteel 6-4 Ti	Active and Passive	1060-A1 AN flare joints
HS-306 (ATS D and E) modified at Hughes	Kidde/ Hughes	N ₂ H ₄	Hamilton Standard	Kidde	Kidde	None	None	None	Edcliff	Kidde 1060-A1	None	1060-A1, all welded
HS-308 (TACSAT)	Kidde	H ₂ O ₂	Kidde	Kidde	Kidde	None	Kidde	None	Edcliff	Kidde 1060-A1	None	1060-A1, all welded
HS-312 (Intelsat IV) (Spacecraft 1, 2, 3, 4, 5, and 6)	Hughes	N ₂ H ₄	Hamilton Standard	Hydraulic Research	Hughes	Carleton	None	VACCO	Genisco/ Edcliff	FanSteel 6-4 Ti	Active and Passive	6-4 Ti, all welded
At this time it became Hughes' policy (if economically and technically desirable) to design and fabricate the thrusters smaller than 10 pounds level at Hughes rather than subcontract to a supplier.												
HS-312 (Intelsat IV) (Spacecraft 7 and 8)	Hughes	N ₂ H ₄	Hughes 5 lbf	Hydraulic Research	Hughes	Carleton	None	VACCO	Genisco	FanSteel 6-4 Ti	Active and Passive	6-4 Ti, all welded
HS-310 (in-house development)	Hughes	N ₂ H ₄	Hughes	Hydraulic Research	Hughes	None	None	VACCO	Edcliff	FanSteel 6-4 Ti	Active and Passive	6-4 Ti, all welded
HS-318 (Basic Bus)	Hughes	N ₂ H ₄	Hamilton Standard	Hydraulic Research	Hughes	Carleton	None	VACCO	Edcliff	FanSteel 6-4 Ti	Active and Passive	6-4 Ti, all welded
HS-333 (Anik)	Hughes	N ₂ H ₄	Hughes 1 lbf	Hydraulic Research	Hughes	None	None	VACCO	Edcliff	Sargent Ind.	Active and Passive	6-4 Ti, all welded
TDRS	Hughes	N ₂ H ₄	Hughes 1 & 5 lbf	Hydraulic Research	Hughes	Carleton	None	VACCO	Edcliff	Sargent Ind.	Active and Passive	6-4 Ti, all welded

4.6 ELECTRICAL POWER SUBSYSTEM

4.6.1 Alternatives Considered

Two major alternatives were considered in the selection of the configuration of the electrical power subsystem for the baseline TDRS spacecraft design. The first design alternative was use of a regulated or an unregulated bus; the second was use of a single or a multiple battery configuration. The significant results of these trade studies are presented. The trade studies were based on the power requirements shown in Tables 4-42 and 4-43.

4.6.1.1 Regulated Versus Unregulated Bus

Several schemes for integrating solar cell array for normal power and storage batteries for eclipse power are considered. The bus is provided with overvoltage protection in all cases, and the principal questions are concerned with subsystem weight and solar cell array size required.

Direct Energy Transfer Power System With Battery Floating Across Bus. Figure 4-80 is a schematic of this design concept. The bus voltage can vary in this power subsystem from 24.8 to 34.8 volts, a range slightly wider than with battery discharge regulators, where the variation is 24.5 to 30 volts. This power subsystem configuration is attractive for shorter missions where battery reconditioning is not a requirement. This is especially true in low earth orbit applications where any excess capability of solar panels could be used for battery charging. In such a power system, the loss of battery cells must be detected to prevent overcharging, which requires sensing battery cell voltages, or charge current as a function of cell voltages, and battery temperature.

Power Subsystem With Battery Discharge Controlled by Switch. The battery charge current is supplied above bus voltage by either a battery charge array and battery charge control circuit, or by a battery charger that is powered from the bus as shown in Figure 4-81. The battery discharges directly onto the bus through a battery discharge control switch. A mechanical switch can be replaced by a semiconductor switch with approximately a 1.4 volt drop through the circuit.

In the first configuration the battery charge array is dedicated and can only partially support spacecraft loads when charging is not required. In this arrangement during peak load demand, the battery could be paralleled with the solar panel. With a considerably higher battery voltage capability, the battery would assume most of the load. This would result in many relatively deep battery cycles. It is better to provide sufficient solar panel capability to handle full load at not less than 26.5 volts.

In the second configuration the battery boost charger steps up the line voltage for battery charging. Use of a boost charger results in a solar array of increased size. Solar array mass increases to 25 kg, and the boost charger to 2 kg with a total power system mass of 61 kg.

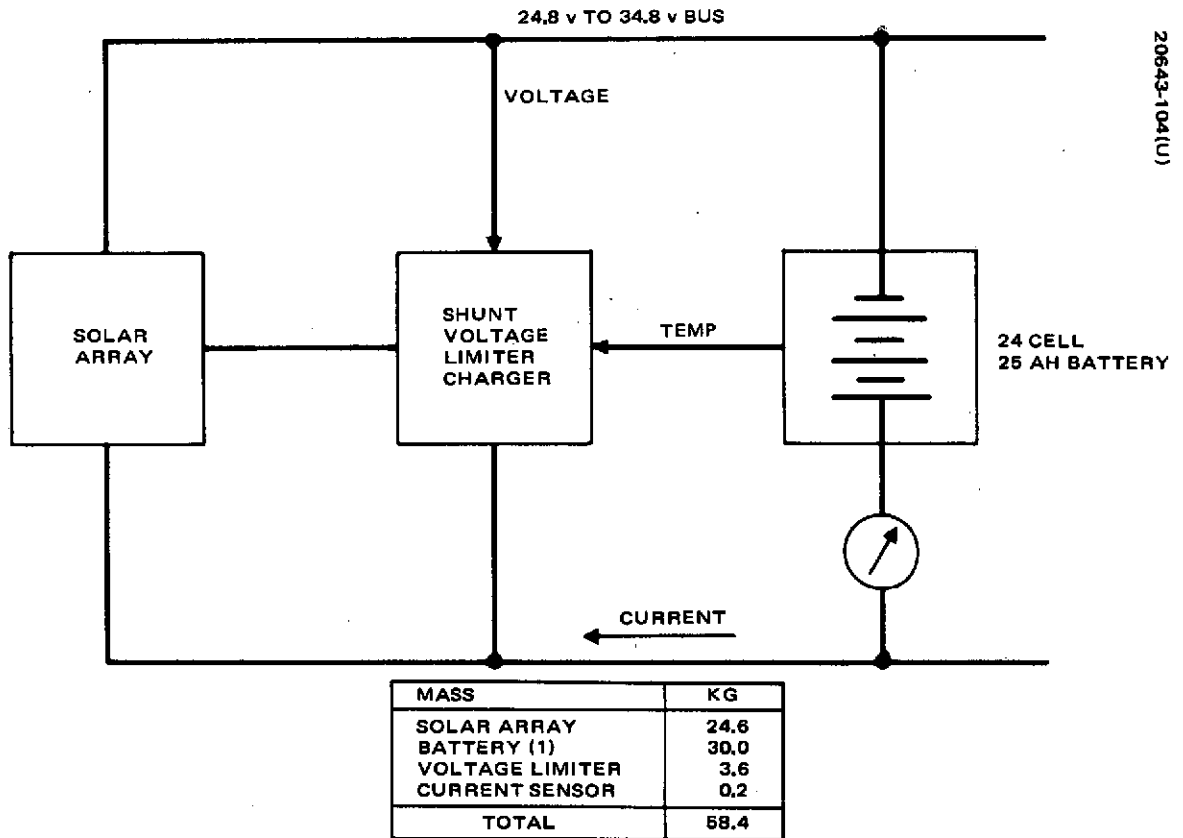
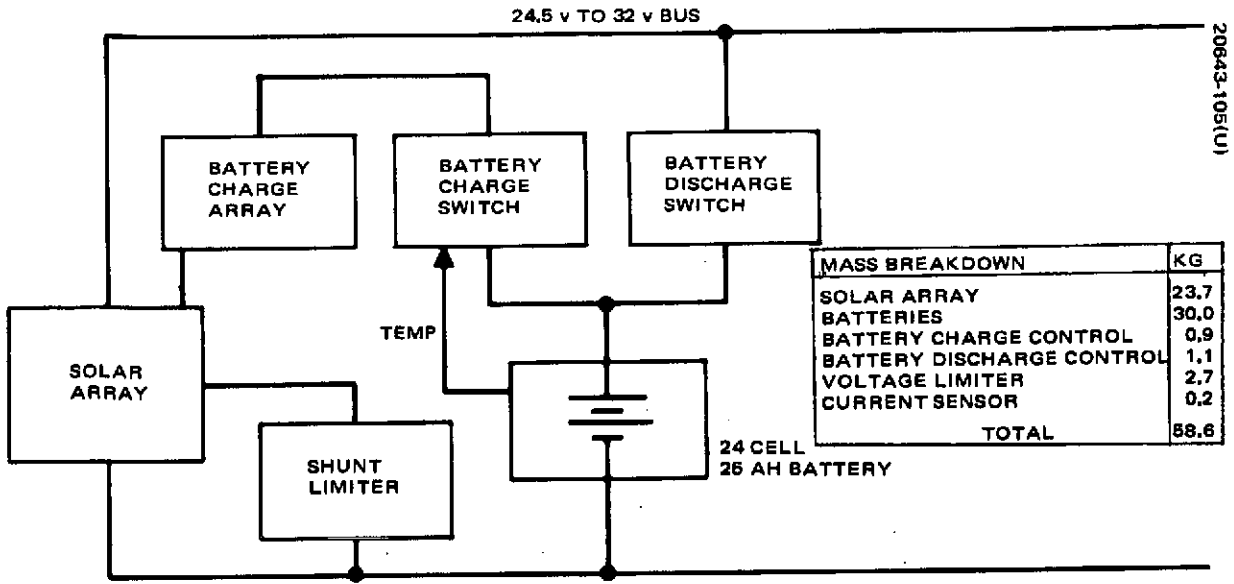
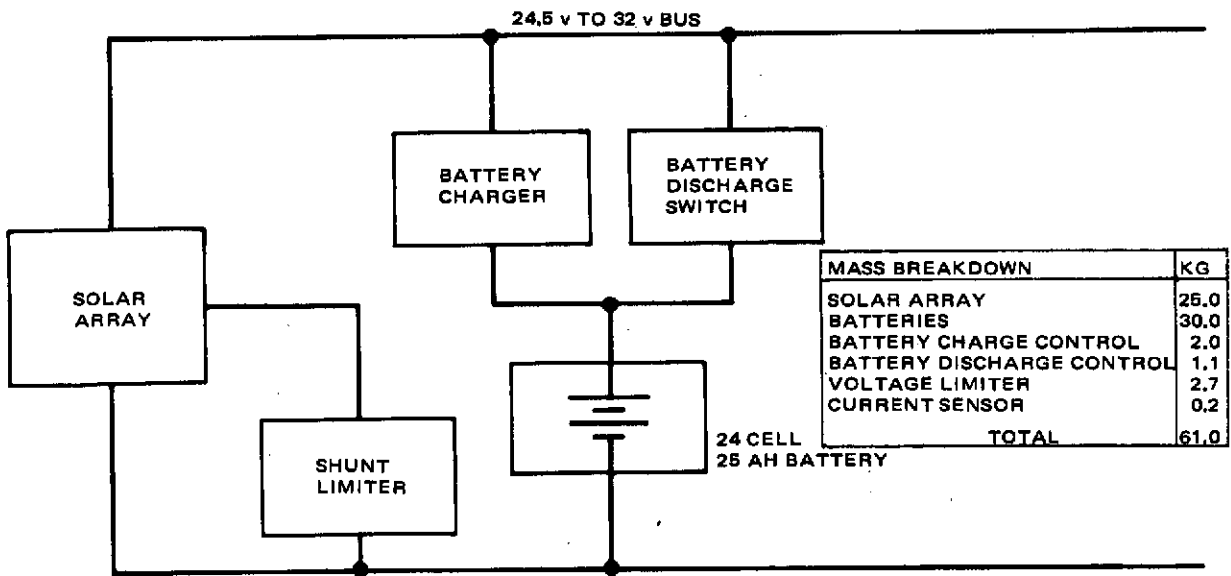


Figure 4-80. Bus Voltage Controlled by Battery Voltage Requirements



a) Single Battery Charged Through Charge Array



b) Single Battery Charged by Boost Add-on Charger

Figure 4-81. Configuration With Battery Discharge Controlled by Switch

TABLE 4-42. TDRSS ELECTRIC POWER SUMMARY DURING ECLIPSE SEASONS

Mode	Command	Intermittent S Band Voice	Intermittent UHF Voice	Command	Intermittent S Band Voice	Intermittent UHF Voice
Illumination	Sunlight			None		
Power Source	Solar at 27.5 Volts	Solar at 27.5 Volts	Solar and Battery at 25.5 Volts	Battery at 25.5 Volts	Battery at 25.5 Volts	Battery at 25.5 Volts
Percent Operating Time	50 to 75*	50*	25*	50 to 75*	50*	25*
Frequency Synthesizer	8.0	8.0	7.4	7.4	7.4	7.4
K band equipment	36.0	36.0	33.5	33.5	33.5	33.5
UHF/VHF equipment						
Command and data	157.8	157.8	146.1	146.1	146.1	146.1
Voice	--	--	142.0	--	--	142.0
S band equipment						
Command data	24.0	--	22.2	22.2	--	22.2
Voice	--	96.3	--	--	89.5	--
Telemetry Equipment	15.6	15.6	14.5	14.5	14.5	14.5
Antenna position control	6.0	6.0	6.0	6.0	6.0	6.0
Despin control	19.7	19.7	18.3	18.3	18.3	18.3
Thermal control	5.6	5.6	4.6	4.6	4.6	4.6
Power electronics	18.0	11.0	20.0	40.0	45.0	50.0
Battery charging	60.0	--	--	--	--	--
Distribution losses	8.0	8.0	9.0	7.0	8.0	9.0
Reserve power	40.3	35.0	--	--	--	--
Power available or required	399.0	399.0	416.4	292.2	359.5	453.6

*Either the UHF or the S band voice transmitter operates but not both simultaneously.

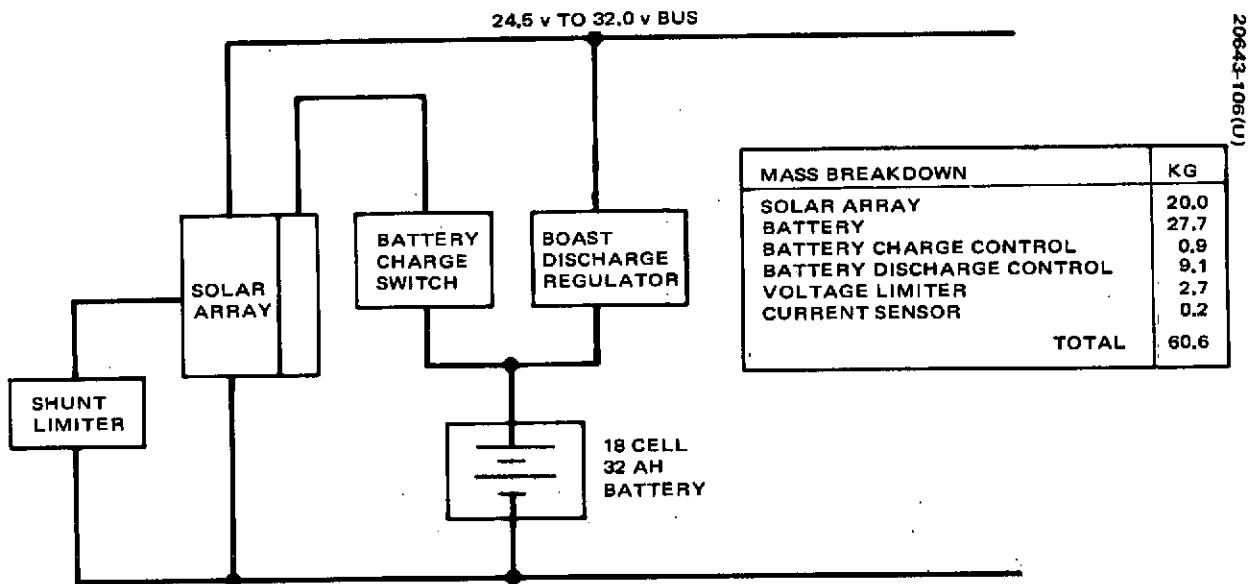
TABLE 4-43. TDRSS ELECTRIC POWER SUMMARY
DURING SUMMER SOLSTICE

Mode	Command	Intermittent S Band Voice	Intermittent UHF/VHF Voice
Power Source	Solar at 27.5 Volts	Solar at 27.5 Volts	Solar and Battery at 25.5 Volts
Percent Operating Time	50 to 75*	50*	25*
Frequency Synthesizer	8.0	8.0	7.4
K band equipment	36.0	36.0	33.5
UHF/VHF equipment			
Command and data	157.8	157.8	146.1
Voice	-	-	142.0
S band equipment			
Command data	24.0	-	22.2
Voice	-	96.3	-
Telemetry equipment	15.6	15.6	14.5
Antenna position control	6.0	6.0	6.0
Despin control	19.7	19.7	18.3
Thermal control	5.6	5.6	4.6
Power electronics	14.8	11.0	30.0
Battery charging	37.5	-	-
Distribution losses	8.0	8.0	9.0
Reserve power	31.0	-	-
Power available or required	364.0	364.0	433.6

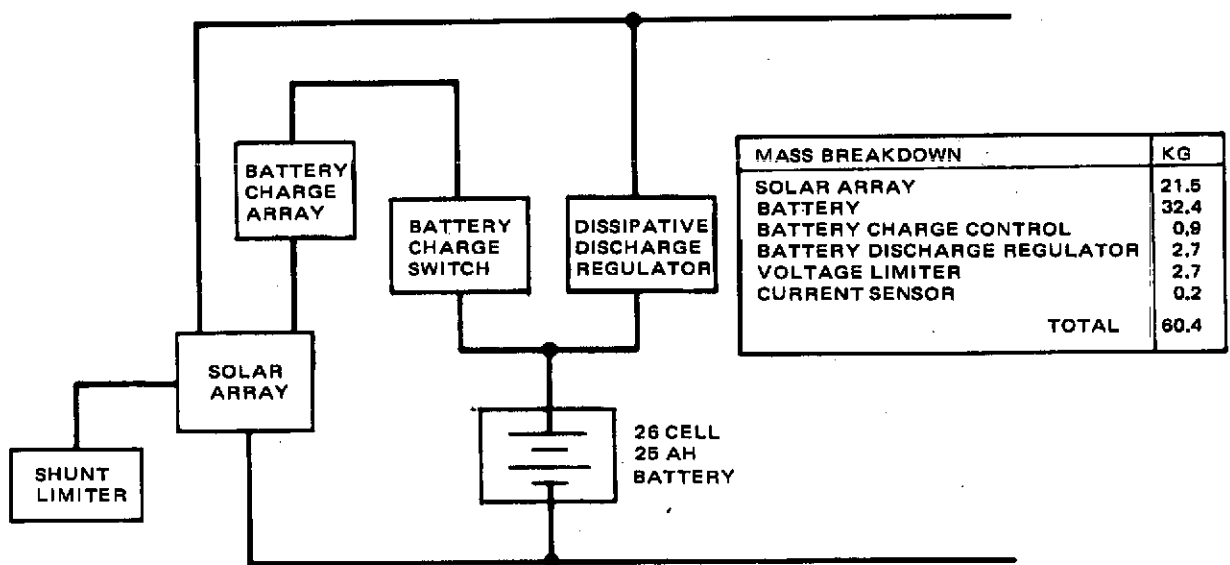
*Either the UHF or the S band voice transmitter operates but not both simultaneously.

This system maintains a closer bus voltage regulation than the direct energy transfer system where the battery was floating across the bus. Load sharing between solar panel and battery can occur at an undefined voltage between 25 and 32 volts. With a fully charged battery, the load sharing will be at the higher voltage and the battery will assume a larger share of the load. Transfer from battery power to solar power may be a problem. A circuit is required to sense the solar array power capability and the load current demand to remove the battery from the load bus when not required. This complex system has no weight advantage.

Power System With Regulated Battery Output Voltage. Two possible configurations are shown in Figure 4-82.



a) Battery Voltage During Discharge Boosted and Regulated



b) Battery Voltage is Higher Than Regulated Bus Voltage

Figure 4-82. Configuration With Regulated Battery Output Voltage

In the first configuration shown a boost add-on discharge regulator is used. Operating redundancy is required in the battery charge-discharge circuits to assure reliability. Battery cells of 32 amp-hr capacity will be used and must be packaged into groups of three, four, or five cells to assure proper heat dissipation.

In the second configuration the battery discharge voltage is stepped down to a regulated level. Any kind of discharge regulator includes switching transistors with a voltage drop of 1.4 volt in a Darlington circuit and additional 0.3 volt drop throughout the circuit. Thus the minimum number of battery cells must be increased to 26 to maintain 25 volt minimum discharge voltage.

Using active battery discharge circuits a minimum of 27 cells would be needed to assure less than 90 percent switching time in the semiconductors. Active circuits utilize battery energy more efficiently by stepping down the battery voltage. Therefore, they require smaller size batteries than is the case with dissipative type circuits. Battery weight is expected to be comparable for the two cases.

Passive discharge regulators, weigh less than active regulators; on the other hand battery size is minimized with active discharge regulators. The combined weight of battery and regulator will be approximately equal in either case. The battery stored energy, however, will be less with active discharge circuits and the battery will require less battery charge power. Therefore, the solar array size is minimized if active battery discharge circuits are used.

A configuration similar to type a) of Figure 4-82 is selected for the TDRS. This configuration is weight competitive with the simpler alternative configurations and because the charge strings of the solar cell array are identical to and can be paralleled with those of the main array a simpler and minimum size solar cell array is possible.

4. 6. 1. 2 Single Battery Versus Multiple Battery

Arguments for single battery configurations are as follows:

- 1) Reliability of one battery only is higher than two batteries in parallel where both have to operate for mission success.
- 2) No battery discharge regulator is needed which results in weight saving.
- 3) Output can be directly connected to the line through a discharge switch.
- 4) Simpler electronics reduce cost and increase system reliability, provided no special battery cell protection is considered against cell open circuit failures.

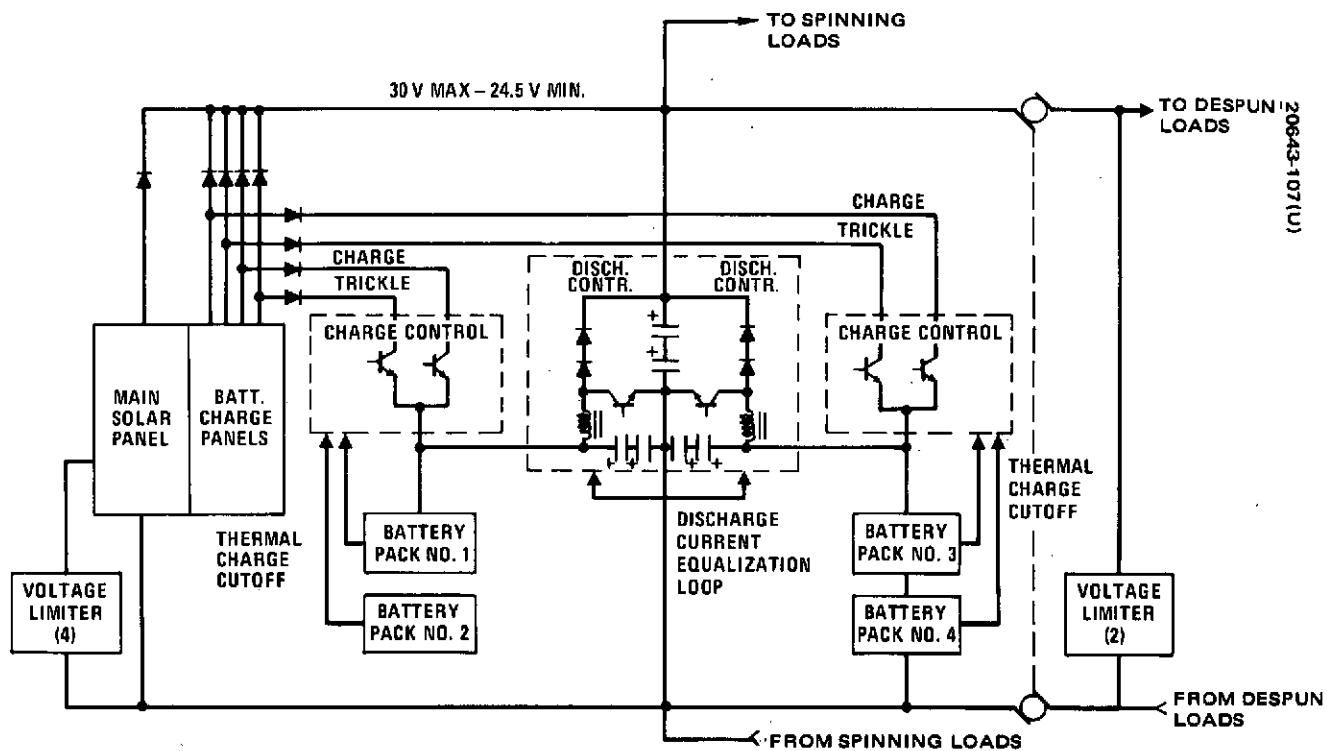


Figure 4-83. TDRSS Baseline Power Subsystem Block Diagram

Cy

Arguments against single battery configurations are as follows:

- 1) With a single battery, battery failure may be catastrophic for the spacecraft. Two battery configurations permit emergency operation in eclipse after one of the batteries fails. Loss of one battery does not satisfy the definition of mission success if the other battery cannot support full service, but the spacecraft can be powered down and will remain ready for full service for the remaining 99 percent of the time when the spacecraft is in sunlight.
- 2) Capacity loss in a battery is not easily detectable and by the time the voltage fades rapidly, it may be too late to switch to emergency mode of operation.
- 3) Battery reconditioning is hazardous with a one-battery system. Battery fading is a distinct possibility and reconditioning could help to extend the useful battery life.

Since the disadvantages of a single battery configuration outweigh the advantages, a two-battery configuration is selected. The two-battery configuration overcomes the disadvantages of a single battery configuration without incurring excessive weight or cost penalties.

4.6.2 Baseline Power Subsystem Description

The electrical power subsystem supports operation of all payload and spacecraft subsystems. It is designed to provide payload power continuously for a minimum of 5 years. The payload includes a continuously operating communications repeater for command and data relay for both low and medium data rate users. In addition, a voice relay will be provided to orbiting manned spacecraft. With the user spacecraft in an approximately 6000 second orbit, either an S band forward voice link can be operational up to a maximum of 50 percent of the time or a UHF forward link 25 percent of the time. The TDRSS requirement on voice channel utilization has been set at 25 percent. Voice operation on the return links is unrestricted in terms of power utilization. Tables 4-42 and 4-43 show the power requirement for the different operating modes for both the sunlit and eclipse portion of the orbit. These power requirements include approximately a 5 percent margin which is reserved for future growth.

The basic configuration of the power subsystem is shown in Figure 4-83. The power subsystem has two batteries with 18 cells each. Each battery is composed of two battery packs. The cells are 57,600 amp-sec (16 amp-hr) in size. The battery output is boosted by a boost discharge regulator to 25.5 volt nominal regulated voltage. Both batteries are required for complete mission success. Each battery is equipped with redundant discharge circuits for reliability. To provide high reliability, two cells in each battery are permitted to fail shorted without loss of the battery. Power system operation with battery power augmentation during UHF voice

TABLE 4-44. POWER SUBSYSTEM MASS DISTRIBUTION

	<u>Kilograms</u>
Solar array, excluding substrate	20.0
Batteries (two)	28.6
Battery discharge controllers (two)	9.1
Battery charge controllers (two)	0.9
Voltage limiters (six)	2.7
Current sensors	0.2
Total	<u>61.5</u>

TABLE 4-45. POWER SUBSYSTEM DESIGN CHARACTERISTICS

Solar Cell Array	
Length:	2.21 meters
Diameter:	2.16 meters
Cells:	2 x 2 cm x 0.18 mm (7.2 mil) 10 ohm-cm
Covers:	2 x 2 cm x 0.15 mm (6.0 mil)
Batteries	
Number	2 with 18 cells each
Capacity	57,600 amp-sec (16 amp-hr)
Discharge cycles	
Eclipse	450 (<60 percent D. O. D.)
Augmentation	7000 maximum (<4.5 percent D. O. D.)
Battery Controller	
Current sharing tolerance	5 percent
Rated output current	10 amperes
Battery input potential	18 to 24 volts
Voltage Limiter, Maximum bus potential	30 volts

communication will result in very shallow battery discharges. The battery control electronics incorporates capability for battery reconditioning.

The solar array will automatically charge the batteries. During battery charging, the solar array voltage will be 27.5 volts or higher. The batteries are charged at C/15 rate. Between eclipse periods, the batteries are trickle-charged. The trickle charge rate selected is C/60. The equivalent battery charge current provided by the solar array to the two batteries is 60 watts. The solar panel output is 364.0 watts at summer solstice and 399 watts 23 days before equinox.

Bus voltage limiters maintain solar panel output voltage below 30 volts independently of load after emerging from eclipse and provide a minimum heat dissipation on the despun platform during launch and orbit acquisition and also during powered down operation. Two types of limiters are used. The tap limiters shunt out selectable sections of the solar array and function primarily to hold the bus voltage below 29.5 volts under full load and post-eclipse periods and to dump surplus panel power in the panel itself for thermal control purposes. The bus limiters shunt the complete bus and function to limit bus to ≤ 30 volts and to provide heat for the despun shelf to keep its temperature within an acceptable limit under light load conditions.

Redundancy is employed in functional components of this subsystem, as well as piece parts, to ensure high reliability for a 5 year mission. A weight saving is accomplished by allowing 60 percent battery depth of discharge. Completely redundant battery discharge circuits are used. Since the probability of a battery open circuit failure is considered negligible, only protection against battery cell short circuit or cell fading is provided. The battery discharge regulator is designed for satisfactory operation even with two shorted cells in a battery. This regulator will operate from a minimum battery voltage of 17 volts at end of discharge.

The selected configuration is a compromise between requirements for minimum weight and high reliability. The power subsystem hardware selected is similar or identical to that used in other Hughes spacecraft, and therefore represents a minimum development risk. The power subsystem weight is listed in Table 4-44, and design characteristics are listed in Table 4-45.

4.6.2.1 Solar Cell Array Design

The solar array design was optimized to achieve the required power output at minimum weight. It provides end-of-life power of 364 watts at summer solstice and 399 watts 23 days before equinox. The design voltage is 26.5 volts. The solar array utilizes design techniques, fabrication methods, and materials previously employed by Hughes which have been confirmed by in-orbit data from TACSAT, ATS, and Intelsat IV, and FRUSA Programs.

TABLE 4-46. SOLAR ARRAY DESIGN

Number of panels:	1
Size	
Diameter	2.16 meters
Length	2.21 meters
Mass	20 kg, excluding substrate
Solar cells	2 x 2 cm 0.18 mm, (7.2 mil) thick
Base resistivity	10 ohm-cm
Solar cell cover	0.15 mm (6 mil) thick
Nominal cell voltage (near maximum power)	0.425 volt
Nominal cell current (near maximum power)	0.122 ampere
Temperature	Function of location and season
Radiation degradation	
Current	0.902
Voltage	0.942
Fabrication loss	
Voltage	1.00
Current	0.98
Ripple	0.98
Effective illuminated area in current	0.318
Curvature edge defects, current	0.962
Solar angle	± 0.554 radian
Seasonal intensity	
Summer solstice, current	0.888
Autumnal equinox, current	0.993
1.99 Ms (23 days) before autumnal equinox, current	0.969
Transmission loss, current	0.98
Diode drop	0.8
Panel harness drop	0.3 volt

The solar cells are 2 x 2 cm, 10 ohm-cm base resistivity, n/p type and are 0.18 mm (7.2 mil) thick cell with 0.15 mm (6 mil) coverglass. The array is 2.16 meter (85 inches) in diameter at the substrate and 2.21 meters (87 inches) long, with a mass of 20.1 kg excluding the substrate. A total of 486 cell strings are in parallel and each string is 68 cells long, resulting in a total of 33,048 cells. The solar array design factors are shown in Table 4-46. These design factors were developed over the entire family of spinning synchronous orbit solar panels and verified by flight data.

In order to achieve the most efficient solar cell array design a parametric weight optimization was completed. Cell thickness, base resistivity and cover thicknesses were optimized to provide minimum system weight for end-of-life conditions. Actual procured cell performance was used where production experience existed. Cell suppliers projections were used for other cell types.*

The analysis used Hughes computer routines for cover thickness optimization. The optimization consists of altering cell characteristics, and compensating with greater or less panel area to maintain the same end-of-life power. All weight elements are included, such as cells, covers, cell array accessories, substrate, and spacecraft-related weight. The spacecraft-related weight includes incremented weight of thermal barriers, ribs, cone, shelf, harnesses, propellant lines, etc.

The results of the optimization are shown in Figure 4-84. The lightest weight system was the 0.15 mm (6 mil) thick, 10 ohm-cm cell with 0.15 mm (6 mil) cover. Although most recent conventional solar panels have been built with 0.25 to 0.35 mm (10 to 14 mil) cells, choice of the 0.18 mm (7.2 mil) cell based on the FRUSA design is reasonable. This is based on the successful production test, and delivery of the FRUSA** solar panels using 40,000 0.18 mm (7.2 mil) average thickness cells and on competitive solar cell price quotations from solar cell manufacturers.

Solar array design factors are discussed below.

Coverslide Degradation. In spite of the existence of an ultraviolet filter to protect the coverslide adhesive from discoloration, some degradation in light transmission occurs. This is due to ultraviolet irradiation from sources such as the sun and appears in the coverslide coatings as well as in the adhesive. Degradation factor of 0.98 is assumed.

Configuration and Geometrical Effects. The effects of cylindrical geometry and fabrication losses must be considered in the design. Corrections for the effects of geometry on current require a $1/\pi$ projection of the array surface. Calculations of projected solar panel area assume that a

*"Performance of Very Thin Silicon Solar Cells," E. L. Ralph, March 1967, Figure 2.

**Flexible Rolled Up Solar Array - an Air Force experiment for space testing.

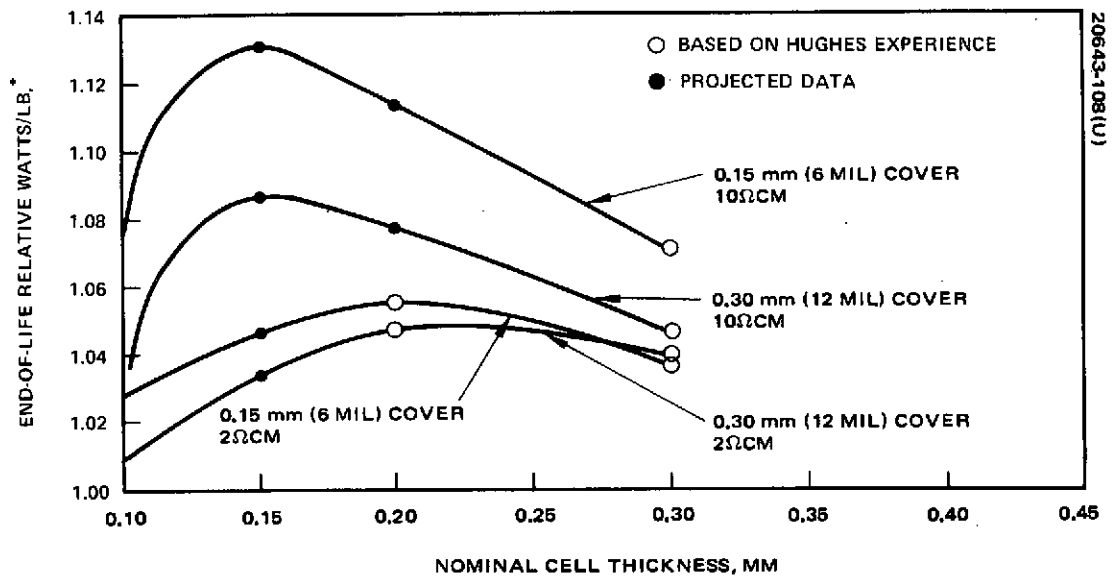


Figure 4-84. Solar Cell Array Tradeoff for 5 Years Operation in Synchronous Orbit

solar cell performs directly as a function of the cosine of the incident angle. This is not precisely the case because of cell mismatch and edge loss effects so an angle of incidence effect factor of 0.962 must be included.

Fabrication Effect. Fabrication and assembly losses result from the interconnection of the solar cells into the series parallel arrays, and are expected to degrade the current by a factor of 0.98 based on actual performance measurements obtained on the Intelsat IV and Telsat programs.

Orbital Effects. In synchronous orbit solar intensity varies from 135.1 mw/cm² at summer solstice to 144.3 mw/cm² at winter solstice (Figures 4-85 and 4-86). Since the axis of the satellite is parallel to the axis of the earth, the satellite experiences a maximum 23.5 degree inclination at the solstice condition. The worst orbital condition, therefore, is summer solstice where the intensity is lowest and the angle of inclination the greatest. Corrections for intensity are made by multiplying the cell output at air mass zero by the ratio of the intensities (0.968). To correct the cell output for the angle of inclination, the current is multiplied by the cosine of the angle of inclination. The resulting correction factors for several pertinent mission dates are summer solstice 0.888, equinox 0.993, and 23 days before the autumnal equinox (eclipse season) 0.969.

Miscellaneous Corrections. Because most of the loads on the spacecraft may be considered constant current, the solar panel must be capable of satisfying these loads even at the lowest point in any output ripple. Ripple may arise from two areas - namely, 1) that caused by uncompensated cutouts, cell output differences, etc, or 2) that caused by nonuniform degradation resulting from micrometeoroids damage, etc. Therefore, corrections are made on current for the effect of ripple (0.98). Consideration is also given to the 0.8 volt drop across the blocking diodes and to the 0.3 volt drop in solar cell array wiring.

Radiation Effect. The methods used by Hughes to compute natural and artificial radiation effects upon solar array power output are described. Orbital flight data have verified the accuracy of the Hughes computational methods as indicated in Table 4-47. Large amounts of radiation damage data are available from cells bombarded with 1 Mev electrons. Because of this, it is a relatively simple matter to predict damage once an equivalent 1 Mev fluence has been determined.

The penetrating particles reduce the minority carrier diffusion length in a solar cell which results in reduced current output. The following relationship exist:

$$1/L^2 = 1/L_0^2 + K\phi \quad (1)$$

TABLE 4-47. HUGHES SOLAR PANEL DEGRADATION HISTORY

Program	Solar Panel	Orbit	Degradation/Time	Comments
TACSAT	0.30 mm (12 mil) coverglass full grout	Synchronous	4 to 6 percent total 3 years	Matches computations based on no significant flares and ATS-1 measurements of electrons
Intelsat IV	0.30 mm (12 mil) coverglass, zero gap cover full solder coverage on contact, no exposed silicon	Synchronous	≤3 percent total 8 months	No anomaly beyond data resolution
ATS-5	0.26 mm (30 mil) coverglass full grout	Synchronous	3 to 5 percent total 20 months	

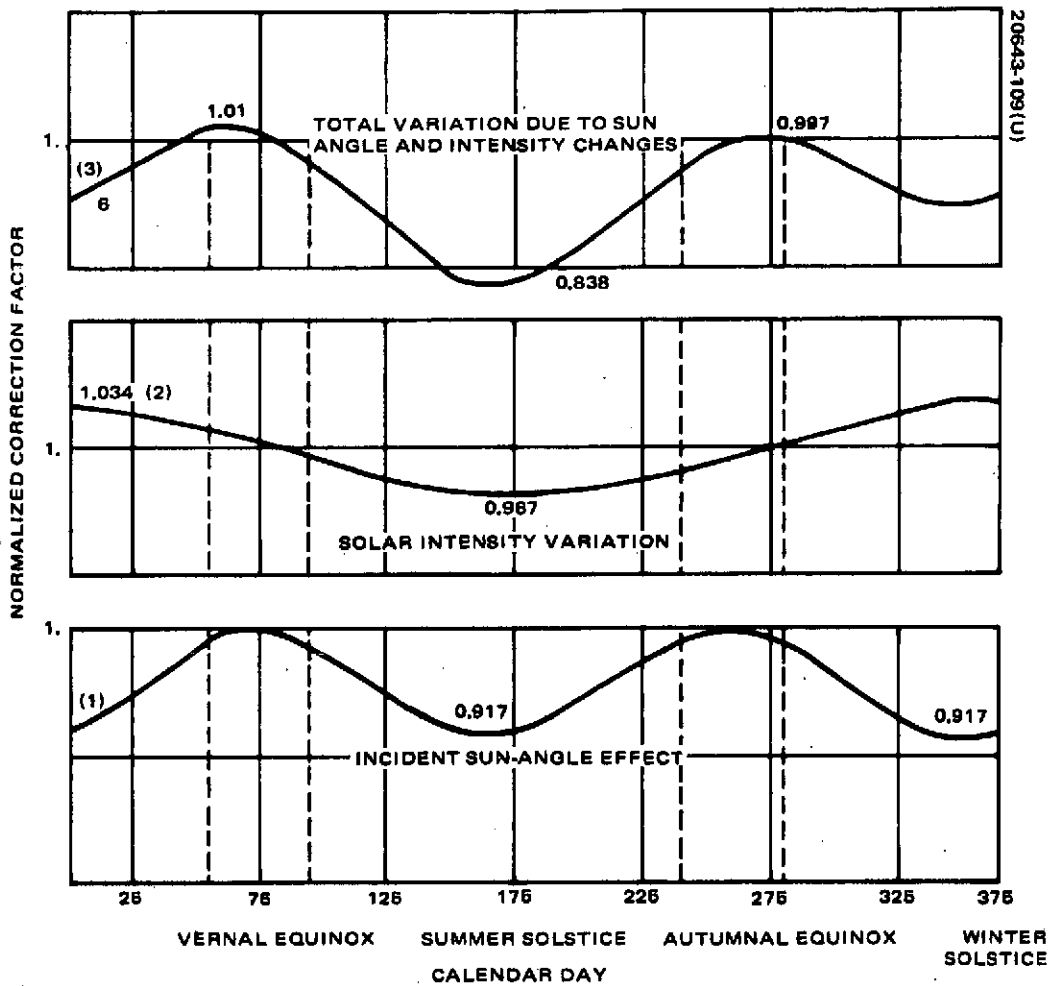


Figure 4-85. Solar Input Energy Variation for Typical Orbit

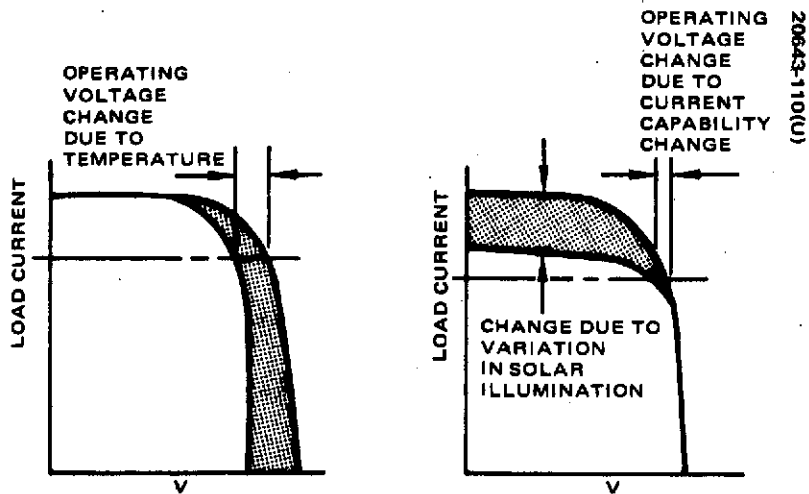


Figure 4-86. Voltage/Current Solar Panel Behavior

where

L_o = diffusion length before particle bombardment

ϕ = particle fluence

K = considered as damage/particle

From Equation 1

$$1/L^2 - 1/L_o^2 = K_1\phi_1 = K_2\phi_2 \quad (2)$$

Equation 2 is used to develop the very useful 1 Mev equivalent fluence relationship

$$\phi_e (1 \text{ Mev}) = \int_{E_c}^{\infty} \frac{\theta(E) K(E)}{K_e (1 \text{ Mev})} \left(\frac{d\phi(E)}{dE} \right) dE \quad (3)$$

where

$\theta(E)$ = shielding factor

$K(E)$ = damage coefficient

E_c = cutoff energy for selected cover

$d\phi(E)/dE$ = particle differential fluence

$K_e (1 \text{ Mev})$ = damage coefficient for 1 Mev electrons

$\phi_e (1 \text{ Mev}) \propto K(E)$ and $K(E)$, damage per particle, is dependent on:

- 1) Type of particle
- 2) Particle energy
- 3) Solar cell parameters including: a) resistivity, b) polarity, and c) thickness

That is why $\phi_e (1 \text{ Mev})$, the 1 Mev equivalent fluence, will be different not only for a different particle environment but for any change in solar cell parameters.

The effective equivalent fluence is used in Figure 4-87 as an independent variable. The damage coefficient, K, has been calculated for protons and electrons by measuring the diffusion length before and after irradiation. These damage coefficients are for bare cells on which the radiation is normally incident. Figure 4-87 represents the Hughes interpretation of the data of Martin, Statler, and Ralph from their paper titled Radiation Damage to Thin Silicon Solar Cell, dated 1967, which has been converted to a common base of the 10 ohm-cm/0.30 mm thick, N/P silicon solar cell and corrected to 25°C temperature.

The effects of covershields and the conversion of omnidirectional flux are described well with an equation of the form:

$$\theta_e(E) = 0.5 (1 - e^{-A(E-B)}) \quad (4)$$

where

θ_e = shield factor for electrons

E = incident electron energy expressed in Mev

A, B = constants to be determined.

For each coverslide type and thickness, the constants A and B in Equation 4 can be determined once the area density has been calculated.

Protons incident upon a solar cell/coverslide assembly are not scattered as easily by the material of this assembly as are electrons. Theoretical calculations have indicated that

$$\theta_p(E) = 0.5 \quad (5)$$

is a satisfactory proton shield factor for present radiation calculations for relatively thin coverslides.

The variation of solar cell maximum power at 28°C with effective 1 Mev electron fluence as shown in Figure 4-87 for 0.15, 0.25, and 0.30 mm cells (10 and 2 ohm-cm). The curves are normalized and do not represent the effect of the actual space radiation on the solar cells. The equivalent 1 Mev electron fluence is different for each cell cover, and base resistivity combination (Equation 3).

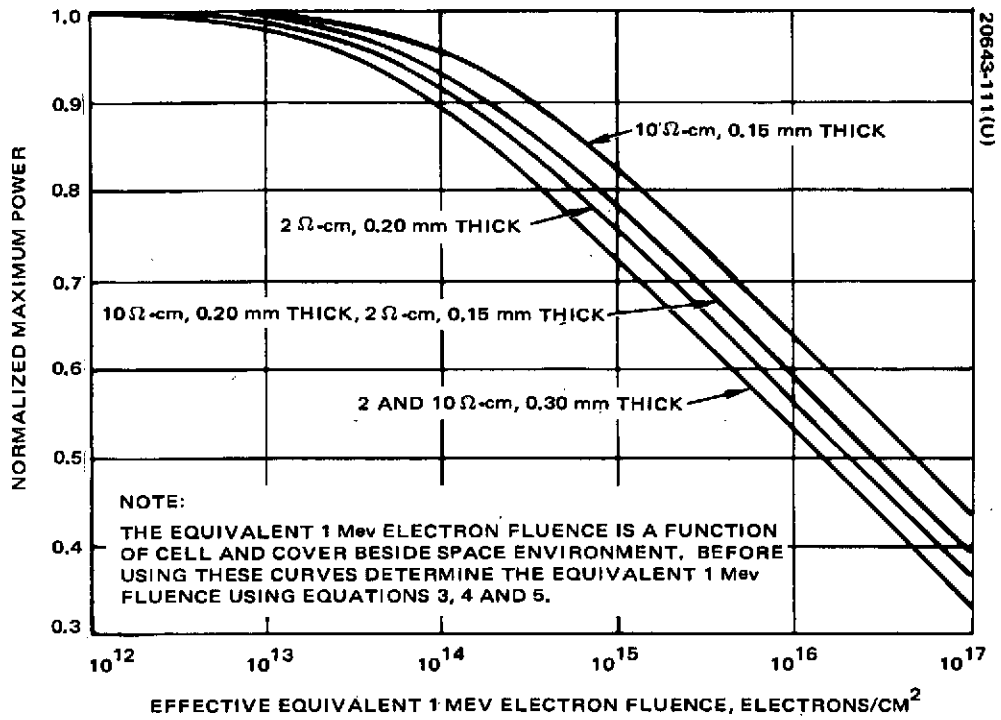


Figure 4-87. Normalized Maximum Power Versus Effective Equivalent 1 Mev Electron Fluence

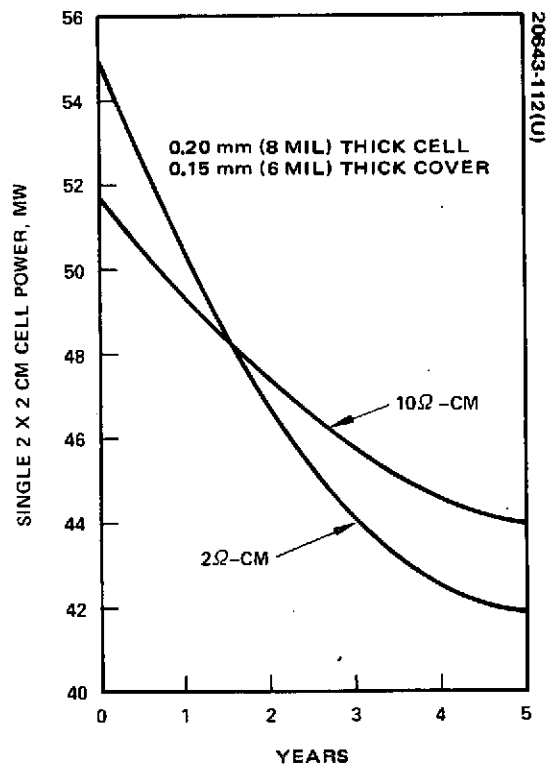


Figure 4-88. Solar Cell Output Degradation (Radiation Effects Only)

Hughes radiation environment calculation establishes for baseline a "reference" equivalent 1 MeV electron fluence for the space environment. This "reference" 1 MeV electron equivalent fluence will cause the same damage to a 12 mil (0.30 mm) thick 10 ohm-cm solar cell as the actual space environment. In a given space environment, the damage to a solar cell is dependent on cell thickness, base resistivity, and coverglass thickness. The "reference" 2.1×10^{14} "equivalent" 1 MeV electrons per cm^2 represents the effects of the 5 year synchronous environment including solar flare protons on a 0.30 mm (12 mil) thick cell with 0.030 mm (12 mil) coverslip. This environment must be converted to include the effect of coverslips and base resistivity before finding the solar cell degradation from Figure 4-87. Degradation for both 10 ohm-cm and 2 ohm-cm base resistivity 8 mil (0.20 mm) thick cells is calculated in the following steps:

Step 1 - The baseline reference 2.1×10^{14} equivalent 1 MeV electron fluence is established for a 12 mil (0.30 mm) thick 10 ohm-cm cell with 12 mil (0.30 mm) cover.

Step 2 - Effect of change in coverglass thickness is calculated. A change from 0.30 mm to 0.15 mm thick coverglass thickness on the 10 ohm-cm 0.30 mm thick cell reduces the protection and more low energy electrons and protons will cause damage. The resultant fluence is 4×10^{14} equivalent (1 MeV) electrons.

Step 3 - With this fluence the degraded power of an 8 mil (0.20 mm) thick 10 ohm-cm cell is found to be 85 percent in Figure 4-87.

Step 4 - Equivalent fluence for 2 ohm-cm cells were obtained by multiplying 10 ohm-cm equivalent by $\sqrt{10/\Omega} = \sqrt{10/2}$ as described by the data in Section IVD, Figure IV-3, Handbook of Space Environmental Effects on Solar Cell Power Systems, W. C. Cooley January 1968.

The above results in an equivalent fluence for 2 ohm-cm, solar cell with 0.15 mm thick coverglass of 8.9×10^{14} equivalent (1 MeV) electron/ cm^2 .

Using Figure 4-87, a normalized maximum degraded power for 2 ohm-cm, 0.20 mm solar cell with 0.15 mm thick coverglass is 0.76. Figure 4-88 represents the comparison of 10 ohm-cm versus 2 ohm-cm for a 0.20 mm (8 mil) thick cell and 0.15 mm (6 mil) thick coverglass. The radiation environment, including solar flare contribution, was spread evenly over the mission length.

4.6.2.2 Batteries

During a 5 year mission in synchronous equatorial orbit, there are 450 eclipse cycles when the spacecraft is powered by batteries. Battery design selection was based on laboratory cycle life test data, orbital

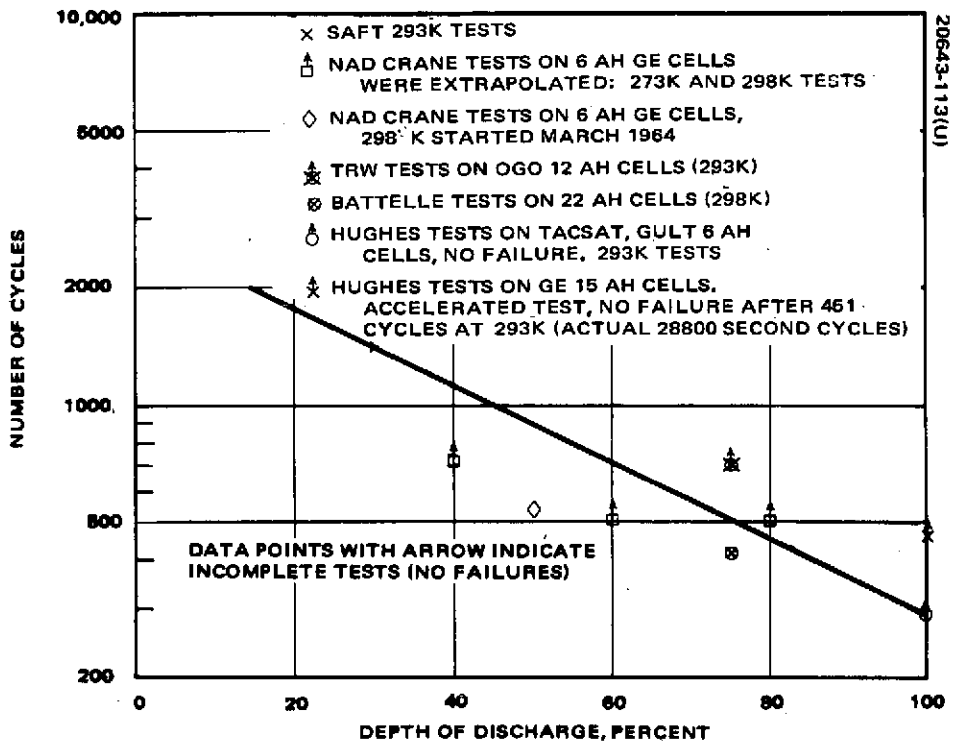


Figure 4-89. Battery Cycle Life in Simulated 24 Hour Synchronous Orbit

experience with batteries, and on careful consideration of battery temperature, depth of discharge, charge rate, limitation of overcharge, and trickle charge after completion of charging. Two parallel connected nickel-cadmium (NICAD) batteries are provided that will operate at a maximum of 60 percent depth of discharge during the maximum solar eclipse when supporting a "full-up" satellite operation. Unfortunately, there is only a limited amount of laboratory test data on battery cycle life in 24 hours synchronous orbit. Figure 4-89 shows the cycle life test data collected from different sources. These tests were conducted under varying charge-discharge regimes, and most followed a simulated in-orbit eclipse cycling. Eclipses varied from 0 to 1.2 hours over a 46 day period twice a year. Trickle charging was used during the noneclipse seasons. The depth-of-discharge in this figure indicates the maximum for each eclipse season, while the average depth of discharge is 76 percent of maximum. The points marked with an arrow indicate incomplete or continuing test. None of these batteries was reconditioned between eclipse cycles. The Battelle tests were more severe than the rest. Their failure criterion was a minimum 1.1 volt per cell end-of-discharge. Accelerated tests run by Hughes at continuous 100 percent rated depth of discharge cycling indicate a higher cycle life capability than the average shown in the figure.

The batteries in this spacecraft must provide power augmentation to the solar array during UHF voice transmission. The resulting battery discharges are very shallow, less than 4.5 percent. Power augmentation is not expected to occur more than 7000 times during the 5 year mission. The effects of these shallow discharges on battery life were assessed using low earth orbit battery cycle life data and found negligible for this application.

Each battery consists of 18 cells of 16 amp-hr capacity and is assembled in two packs. The battery design is an improved version of the Intelsat IV battery which is space-proven. Battery cell improvements considered include new metal-ceramic terminal seals and polypropylene separators.

New Metal-Ceramic Terminal Seals. The latest Hughes general procurement specification for nickel-cadmium space cells permits the use of three types of terminal seals:

- 1) A Hughes developed butt geometry, metal-ceramic terminal seal
- 2) A General Electric developed, butt geometry, metal-ceramic terminal seal
- 3) Any alternate improved seal that receives prior written approval for use from Hughes Aircraft Company.

Copper and silver usage in metal-ceramic terminal seals is undesirable. Uniform braze joint thickness is essential for acceptable space cell terminal seal assemblies. Preference will be given by Hughes to choices 1 and 2 listed above. These seals were described at the 1971 NASA/GSFC Battery Workshop.

Polypropylene versus Nylon Separators. Hughes is currently testing cells with polypropylene separators and intends to specify polypropylene in future applications only when such testing proves this material to be superior to nylon. The nylon, polyamide, separators can degrade by oxidative depolymerization and affect the cell performance while polypropylene is inert at operating conditions. The testing is concerned with ascertaining the effects of an undesirable hydrophobic surface property of polypropylene and resolving the problems involved in maintaining the surfaces hydrophilic. Available data indicate that the polypropylene separators will prove to be better than nylon.

Teflonated Negative Plates. The latest Hughes general procurement specification for hermetically sealed nickel-cadmium cells includes a requirement for high utilization negative plates and C/10, 0°C overcharge capability (overcharge capability is called out in the referenced source control drawing). Teflonated negatives have been used by Hughes in the Low Earth Orbit Battery program to retard the rate of cadmium migration. The cells used for TDRSS will include high utilization, high recombination rate negative plates.

The battery discharge voltage is stepped up by a boost discharge regulator to 25.5 volts. Each battery can operate successfully with 16 out of 18 cells operational and two cells shorted. Since open cell failures have not been experienced in flight-qualified batteries, the design provides considerable redundancy. In the event of a single battery failure, the satellite remains fully operational in sunlight operation and will provide reduced communications capability in eclipse. The battery design data are listed in Table 4-48.

In order to maximize battery life, the battery operating temperature must be kept as low as possible. This can be achieved by proper thermal control and by preventing overcharging. The battery is designed to give the best possible thermal relief, at a minimum weight, without compromising structural integrity. A similar cell and packaging design were within 3 K of the prediction. The battery temperature in the TDRSS design will be between 273 K and 298 K. Battery charging will be terminated when the temperature rises above 300 K indicating overcharge condition. The batteries will be kept on trickle charge after charging and will be also trickle charged between eclipse seasons.

Use of overtemperature control for charge termination instead of third electrode control was selected based on Hughes extensive experience with synchronous orbit battery application. It is, however, realized that recent NAD Crane tests on GE 43, 200 amp-sec (12 amp-hr) batteries in simulated synchronous orbit were using third electrode control successfully. These batteries indicated practically no degradation in 0.095 gigaseconds (3 years) of testing at 273 K and 293 K and at 60 percent and 80 percent maximum depth of discharges. The good performance of these batteries can also be attributed to the relatively high rate of charging, C/4, which is not practical for this application. A C/15 rate in Hughes experience will give similarly good results.

TABLE 4-48. BATTERIES

Type	Nickel-cadmium
Number	2
Cells	57600 amp-sec (16 amp-hr.)
Number of cells in series	18, packaged in 2 to 9 cell packs
Maximum depth of discharge	60 percent
Eclipse cycles	450
Shallow augmentation depth of discharge	4.5 percent
Shallow discharge cycles	7000
Charge rate End of Life	C/15 constant current
Trickle charge rate	C/60
Maximum temperature	300 K
Battery system mass	28.6 kg

Hughes, in every recent geosynchronous spacecraft design has included battery reconditioning capability. The cost and mass of this added electronics are insignificant compared to the added flexibility in spacecraft management. Even if battery reconditioning is not normally used, the capability to individually discharge batteries is valuable as it provides a means to check available battery capacity. It is noted that Hughes data from a continuing simulated synchronous orbit storage/reconditioning test at 25°C, now into the fourth year, indicate:

- a) No amp-hr capacity loss in conjunction with improved discharge voltage due to reconditioning
- b) Voltage divergence in reconditioned packs is less than or equal to, that in unreconditioned packs
- c) From the limited number of tests Hughes could not determine a frequency of failure increase due to reconditioning

The life expectancy of batteries, unlike electronic components, is not primarily a function of random failures. It is primarily a "wear-out" function, compounded by damage due to improper in-orbit management. The wear-out function is strongly dependent on operating temperature, and depth of discharge. This dependency is heavily dependent on cell design, i. e., overcharge margin (excess negative capacity), precharge, presence of carbonates, loss of overcharge margin due to hydrolysis of nylon separators (accelerated by high temperatures, either ambient or due to overcharge). These characteristics can be controlled by highly detailed procurement

specifications, vendor selection based on proven in-orbit performance, and laboratory life tests, electrochemical analysis before and during life tests, etc.

In-orbit battery management has two facets. The most important is battery integration such as battery thermal design, spacecraft thermal control, selection of maximum depth of discharge, charge rates, charge-termination techniques, fail-safe protection such as temperature cutoff, etc. The second is that of meticulous ground control when exercising override options on automatic battery control. The probability of successful survival of batteries for 5 years in the proposed application is in large measure based on the statistical record to date of the nickel-cadmium batteries used by Hughes in previous satellites. These data are also supplemented by extensive laboratory test data taken by Hughes, NAD-Crane, Battelle, SAFT, TRW, and others.

The capability of the battery design to meet mission requirements will be verified by a three part test program: 1) development testing of cells and cell packs, 2) qualification test of flight hardware, 3) life testing of a complete flight battery assembly. Physical, chemical, and electrochemical analyses will be performed for each section of the test program to provide a further assessment of cell performance.

Cell acceptance testing at the cell subcontractor, with additional cell flight acceptance testing at Hughes, provides ample data for grading cell characteristics. A burn-in, equivalent to approximately 5 percent of the mission cycle life requirement, provides an infant mortality screen. This is complemented at the battery assembly level by power subsystem and spacecraft preenvironmental and postenvironmental acceptance testing. Final acceptance of the battery assemblies hinges on the acceptance test results before and after mating with the launch vehicle. This is performed at the launch site, with the postmating test performed just prior to launch. Tests of a thermal model of the cell pack will be performed to verify the packaging design with emphasis on operating temperature under simulated mission conditions. Specially equipped cells will be used so that cell gas pressure and other variables can be monitored during test.

Qualification includes thermal-vacuum, shock, vibration, and acceleration tests. The accelerated cycling will include high rate overcharge (≥ 120 percent) to demonstrate the recombination capability of the negative electrode. The charge acceptance of the positive electrode at high temperature (313 K) will be demonstrated during cell acceptance testing. Every flight battery pack is subjected to flight acceptance level thermal-vacuum and vibration tests prior to delivery to the spacecraft.

Electrochemical, chemical, and physical analyses will be used at Hughes to determine a cell's predicted performance for the mission. The purpose of performing these analyses on cell components is to determine initial status as well as cycle and calendar component status of plates, separator, electrolyte, seals, etc. Cells will be pulled from various electrical performance tests to establish component status analytically. Data

from these analyses will be used to establish cycle and calendar life expectancy for the spacecraft batteries.

4. 6. 2. 3 Battery Control Electronics

Battery Charge and Recondition Control. The functions of this component include 1) automatic recharging of the batteries on exit from eclipse, 2) automatic charge termination, 3) ground control override for functions (1) and (2) on each battery separately, 4) ground control of reconditioning discharge. The automatic electronic charge circuit will connect the batteries to the battery charge arrays of the solar panel. In the event of an anomaly, it is possible to command charging for one or two batteries at a time. Solar cell strings supply a current-limited power source. When batteries are not being charged, these solar cell strings provide power to the main bus.

The batteries begin charging after emergence from an eclipse and continue charging until all batteries are fully charged. The primary method of charge cutoff is battery temperature. Four temperature set points are available for cutoff levels. The charge controller will be set to the enabled state by sensing collapse of charge string voltage.

Ground commands can be sent to override any of the charge controller functions and also to select the temperature value to be used for charge termination. Due to the pulse nature of the TT&C subsystem command outputs, the charge controller stores the command in the command buffer latches. Digital type status signals for telemetry output are obtained from these storage latches.

The battery charge circuits are essentially similar to those used on Telsat and Intelsat IV. Except here, each battery can be charged and trickle-charged from separate battery charge solar cell strings as indicated in Figure 4-90. The battery charge control electronics is designed initially redundant, any single component failure will not result in loss of battery for the mission. Figure 4-90 is a functional block diagram of the battery charge controller.

The individual temperature inputs are derived from a constant current source into a set of thermistors, one on each battery pack, which provides a mean battery temperature. Charge is terminated when individual battery temperature exceeds the common temperature reference.

Flip-flop 14 outputs determine which battery 1 or 2 or both are charging. The individual batteries are cut back from full charge to trickle charge on an individual basis by the AND gates G14 - G15. Manual charge override inputs are provided via the OR gates (G18 - G19) to allow control charging of individual batteries at the high rates, in the event of an automatic circuit malfunction. The trickle charge command enters G22 - G23 as an OR gate signal and trickle-charges both batteries at once.

The relays K1 - K2 can be used to disconnect the individual batteries from the charge control circuitry. This prevents battery failure due to switch failure which could result in long-term high rate charging.

Battery Discharge Controllers. The battery discharge controllers will be similar to those previously qualified for HS 318. The controller also functions to force equal battery current sharing within ± 5 percent. The circuit is of the boost choke type and uses pulse width modulation. It requires a minimum number of power transistors and results in lowest stress per power transistor and minimum input line filtering. To reduce power transistor stress and to minimize output filter size, each circuit is two phase, with forced current sharing between phases. In addition, each circuit is internally redundant; in effect, there are four parallel operating discharge controllers equally sharing the load during eclipse operation. Figure 4-91 is a block diagram of the discharge controller.

The battery discharge controllers maintain a regulated output voltage of 25.5 volt \pm 0.5 volt. The battery voltage can vary from 24.3 to 17.5 volts during discharge. The battery controller output is also unaffected by short circuit failure of up to two battery cells.

In case of battery controller circuit failure, the redundant battery controller circuit will automatically take over the load. The redundant circuit design also protects against complete battery failure which is most unlikely. In that case, one battery must support all the spacecraft loads and only two battery controllers out of four will operate. Since the circuits are redundant, such 100 percent overload on one battery will not result in extra stresses on the discharge controller. The four discharge controllers are packaged in one assembly with adequate heat sinking to provide for emergency mode of operation.

The function of each controller is to boost the output of the battery to hold the main bus within an allowable band, with variation in battery voltage and load. This design is electrically identical to the battery controller presently used on HS 318 program, except for reduced power rating relative to HS 318. Following is a description of the controller operation in charge and discharge modes.

Upon entering the earth's shadow during orbital eclipses, the electrical power subsystem undergoes a transitional mode from total solar panel power operation to total battery power operation with no interruption of power to the spacecraft loads. As the sun intensity decreases in the penumbra, the main bus being supplied by the solar panel will experience a corresponding reduction in voltage, and at a nominal set point of 25.5 volts dc, battery discharge control will start to function. The battery sources will then begin to share the load with the solar arrays. The power stage of the battery discharge control is variable K boost circuit that provides a regulated output voltage higher than the battery terminal voltage. This boosted output is feedback loop controlled to maintain the output voltage between 25.0 and 26.0 volts.

Page intentionally left blank

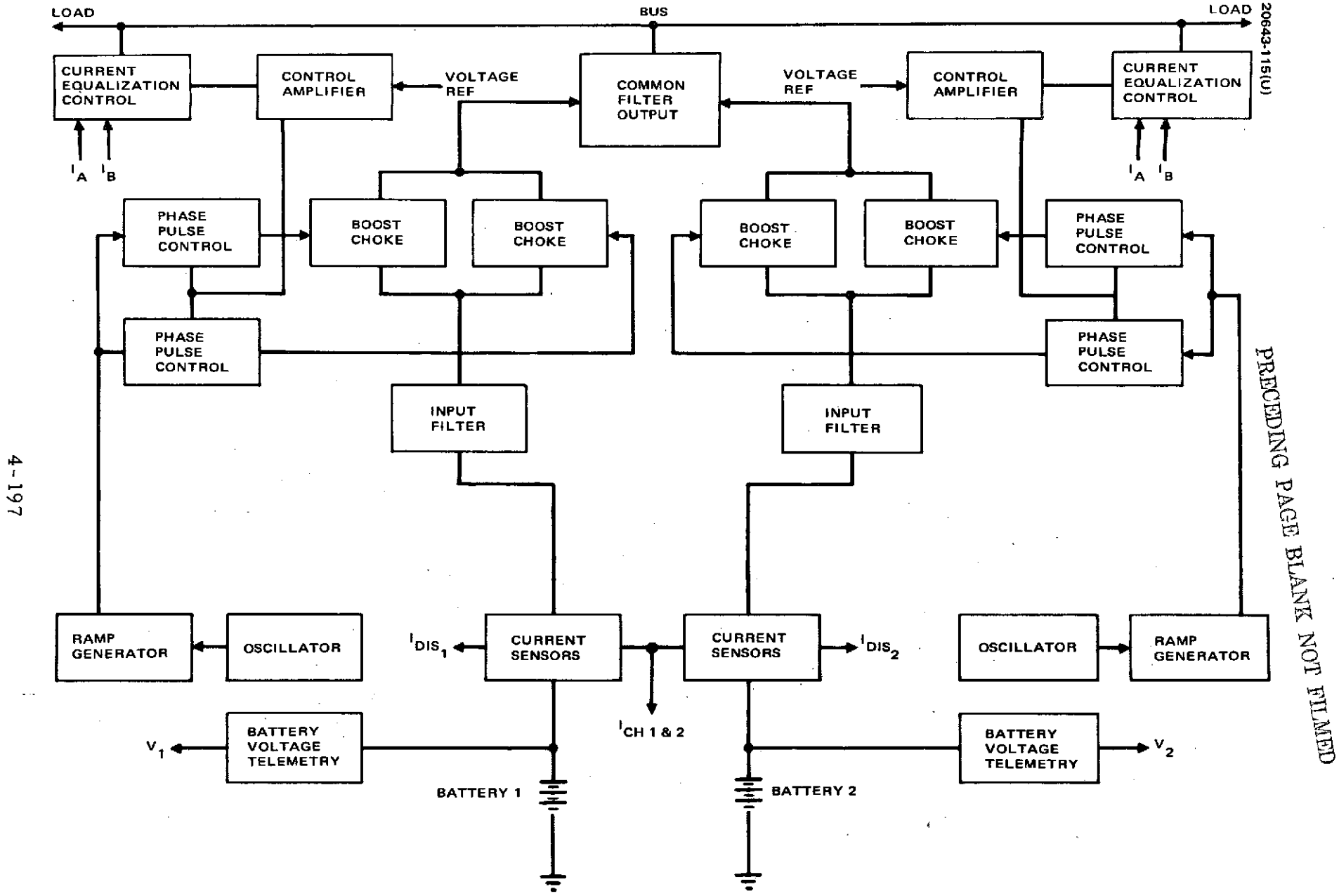


Figure 4-91. Battery Discharge Control Block Diagram

PRECEDING PAGE BLANK NOT FILMED

Thus, as the output of the solar array continues to decrease, the spacecraft batteries will continue to assume an increasingly larger portion of the load current until operation of the spacecraft is on batteries only.

As the battery terminal voltage decreases during normal discharge cycling, the voltage feedback loop continuously adjusts the K boost factor to maintain the regulated output voltage. The minimum battery control output voltage is 25.0 volts with both one cell of battery pack short and battery terminal voltage discharged to 1.05 volts per cell.

The discharge current of each battery is sensed with a magnetic current sensor and an analog output from the sensor is provided to a current comparator circuit in each battery discharge control. This circuit acts to modify voltage control in each boost-choke stage to provide current sharing between batteries to within an allowable control rating and battery depth of discharge.

The biasing effect of the current equalizing control is designed such that the output of the battery discharge control will remain within its limits in the event of one regulator circuit failure and it also will not adversely affect the performance of the three remaining batteries.

4. 6. 2. 4 Voltage Limiters

Two types of voltage limiters will be used: a shunt tap limiter and a dissipative shunt bus limiter. Both types have been qualified for other spacecraft, i. e. , tap limiter for Telesat, bus limiter for TACSAT. These limiters present no loss in series with the solar panel at EOL and full load. Additionally, they either add only a small heat load to the spacecraft when full load is on, or add a significant and desirable heat load when repeater loads are turned off.

The principal function of the tap limiter is to hold the bus voltage below 29.5 volts with full load applied, dumping surplus solar panel power at beginning of life by shunting or eliminating the current supplied by the tapped strings to the main bus. Most of the surplus power is radiated by the panel. Tap limiters also clamp the bus at 30 volts after exiting eclipse. Four tap limiters, each shunting a separate section of the array (1/8 of total array in each section) are provided. The limiters have set points separated by 0.1 volt, so that operation is incremental. As bus voltage increases, each limiter moves from open circuit to a linear control mode, and finally to a short circuit.

Bus limiters place resistive loads across the bus when the bus voltage exceed 29.5 volts. They replace some of the heat removed from the despun section during the transfer orbit, or any other time that spacecraft loads are light, to keep the temperature in the despun section above an acceptable limit and to maintain the bus voltage under 30 volts.

Tap Limiters. The function of the solar panel tap limiters is to limit the main bus voltage in the illumination period with variations in the output of the solar array caused by temperature, load, and degradation. The tap limiter group will limit the bus voltage to a value between 29. and 29.4 volts when the load is less than the array can support.

The limiter is subdivided into four units and each unit will be active over a narrow range of bus voltage. The gain of each of the limiters will be adjusted so that about 100 mV change in bus voltage will operate the power dissipating transistor output stages from cutoff to saturation. The set points for each of the units will be separated from the others by 100 mV so that only one unit is active at a time. The resultant power dissipation and operating range for each of the limiters would fit together so that individual limiter dissipation would be kept low (less than 35 watts), and the total peak dissipation would be less than 60 watts. This point is illustrated in Figure 4-92.

From the curves in Figure 4-92, it can be seen that each limiter is active over only a 100 mV bus voltage range and that this causes each regulator to go from cutoff to saturation. The amount of current carried when saturated is equal to the short circuit current of the solar array cell group that provides its input power. The power dissipation of each limiter is determined by the solar cell characteristics and by the way the cells are grouped to provide input current to the limiters.

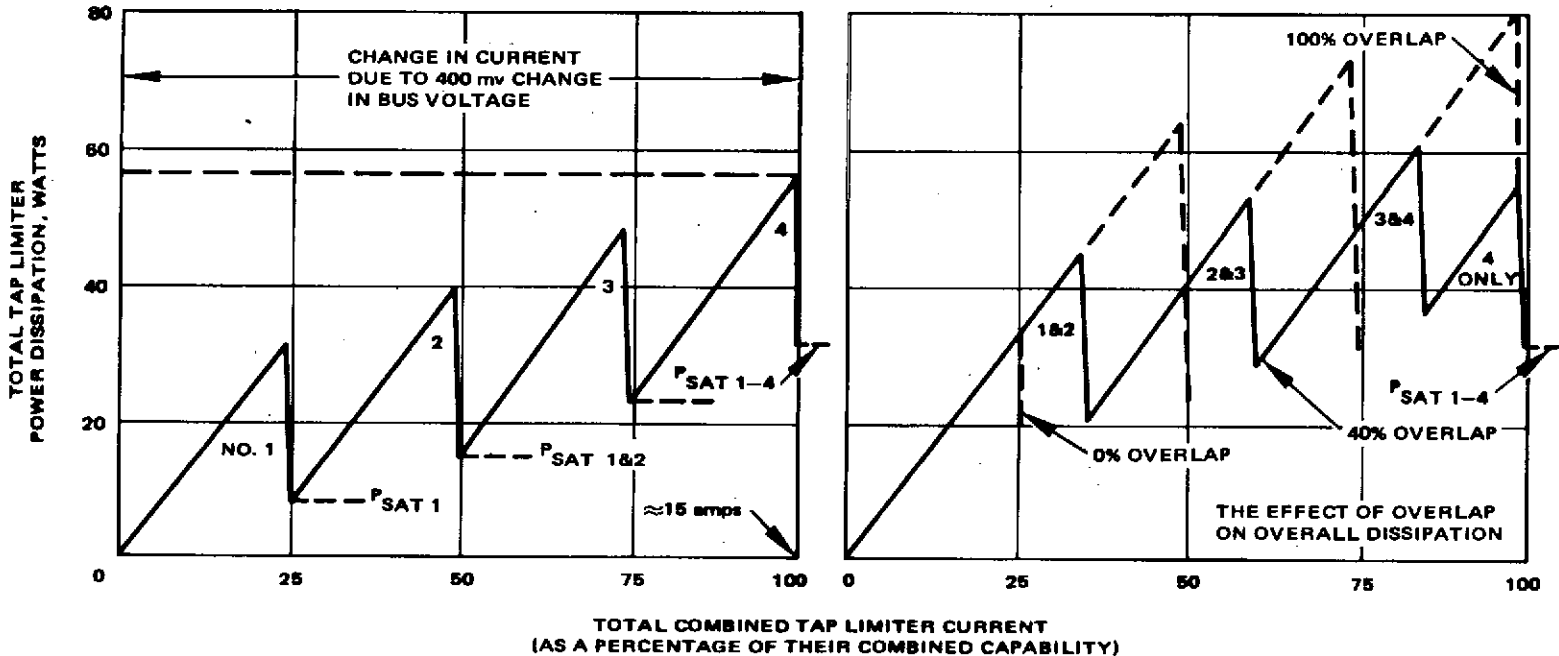
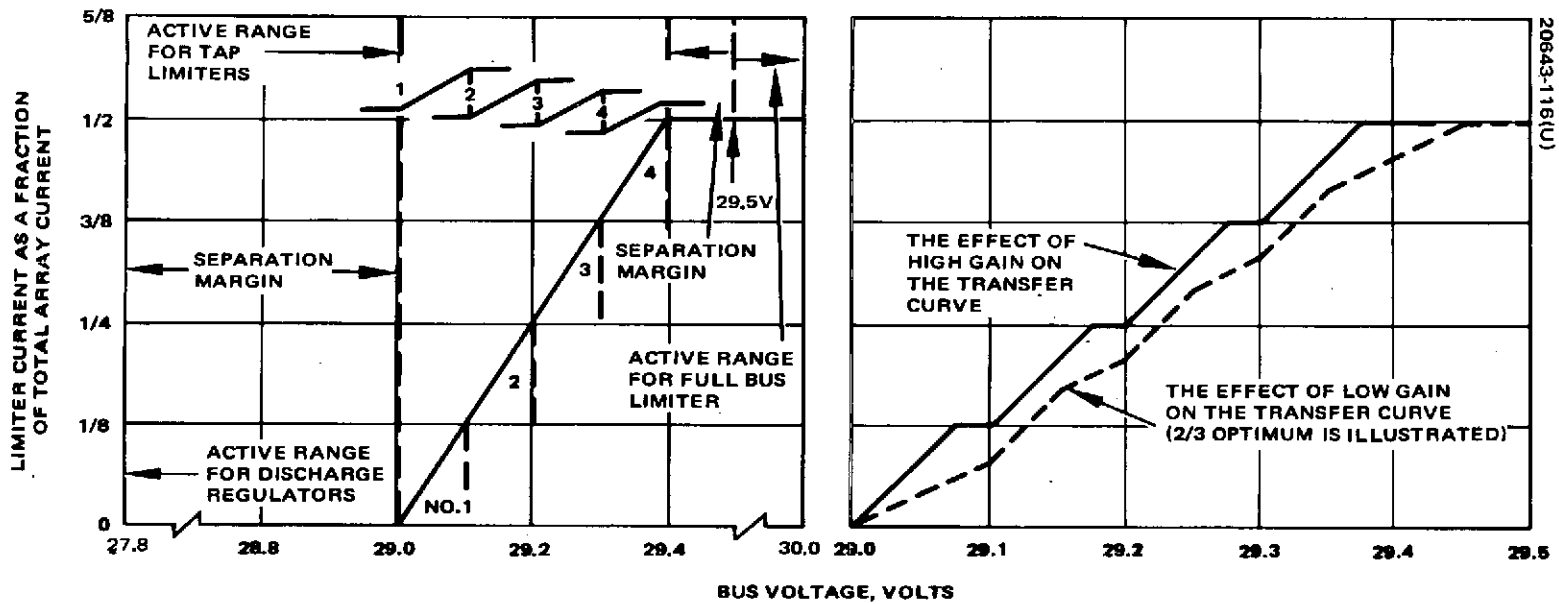


Figure 4-92. Tap Limiter Current and Dissipation Characteristics

4-200

The number of cells in series to the tap point is determined by the open circuit voltage of the cells remaining in the string after the limiter has saturated, by the saturation voltage of the limiter, and the voltage drop of the isolation diode. The open circuit voltage of the unshunted portion of the string plus the saturation voltage of the limiter and diode must be less than the desired bus voltage. This means that the tap for each limiter must be roughly at midpoint in the series string.

Upon emergence from eclipse, the tap limiters will saturate and the full bus shunt limiters may also turn on. Ground commands can be used to disable one or more tap limiters so that more bus shunt limiters will be energized and the power dissipated by the bus shunt limiters aids in warming the despun platform. As the array warms up, the bus shunt limiters turn off and control is taken wholly by the tap limiters. The total shunt current curve is a summation of the currents from each of the four units and provides a smooth transfer curve from one end of the regulation band to the other.

Bus Limiter. The bus limiter operates as a four-stage current-limited shunt regulator which when used in conjunction with other voltage limiters will prevent the solar panel bus voltage from exceeding 30.0 volts. Each voltage limiter consists of two sublimiters A and B which are adjusted to turn on at the set points. One-half of each limiter has a turn-on or set point 0.25 volt lower than the other half. Without any set point change due to commands, as the bus voltage rises, one-half of each limiter will start conducting before the other half of any limiter. This affords even distribution of heat.

Each bus limiter and its associated external load resistors dissipate a minimum of 110 watts at a bus voltage of 30.0 volts. Total dissipation for both bus limiters is 220 watts minimum at a primary bus voltage of 30.0 volts. With a primary bus voltage below 29.5 volts, the limiters are in a standby condition and dissipate a maximum of 0.58 watt.

The bus limiter will see a temperature variation at the mounting surface of 272 to 319 K during a normal orbit. A minimum mounting surface temperature of 272 K will occur in a typical eclipse orbit. Since the voltage limiter is a low dissipation device when in the standby condition, the temperature of the electronics will be very close to the mounting surface temperature. When the limiter is turned on, a maximum of 27.5 watts will be dissipated in the unit, thereby increasing the unit temperature. Heavy duty mounting webs for the high power dissipating components provide an efficient heat path to the mounting surface. The external power resistors will see a mounting surface temperature of 272 to 316 K during a normal orbit and a minimum of 255 K during a typical eclipse. Each 18 ohm power resistor will dissipate a maximum of 12.5 watts when its associated limiter is turned on.

4.6.3 Power Subsystem Performance

The power subsystem is designed to satisfy the power requirements listed in Table 4-42. A summary of the power system performance is listed in Table 4-49.

TABLE 4-49. POWER SUBSYSTEM PERFORMANCE

Solar Array Output End of Life	
Summer solstice	364 watts
23 days before equinox	399 watts
Solar array output augmented by batteries	438 watts
Maximum bus voltage	30 volts
Battery discharge turn-on voltage	25.5 volts
Minimum bus voltage, battery power	24.5 volts
Solar array maximum power voltage	26.5 volts
Solar array temperature maximum 300 K, minimum 183 K	
Battery depth of discharge maximum	60 percent
Number of eclipse cycles	450
Solar array augmentation maximum	4.5 percent
Maximum augmentation cycles	7000
Battery charging rate	C/15
Battery charge termination	Temperature signal
Battery trickle charge rate	C/60
Cell failures permitted per battery	2
Battery discharge voltage	24.3 to 17.5 volts
Battery operating temperature range	225 to 300 K
Battery discharge controller voltage	25. to 26.5 volts
Battery charge controller operation	Automatic or ground commanded
Battery discharge controller operation	Automatic
Battery reconditioning	On ground command
Tap limiters; operating voltage	29 to 29.5 volts
Bus limiters; operating voltage	29.5 to 30 volts

The power electronics selected for TDRSS includes active circuits which require power in standby mode of operation. Most power during standby is used by the battery discharge controller which includes a pre-regulator, a dc-to-dc converter, current sensor, and voltage clamp in the power stage. Standby power requirement for these circuits is 2.5 watts per regulator circuit. There are two circuits per regulator and two regulators per spacecraft requiring a total of 10 watts during standby. The standby power limiters, battery charge control, and current sensor is about 1 watt.

In eclipse when operating on battery power, the battery discharge controller losses are proportional with the load current and the battery voltage. These include losses in the switching transistors, magnetic components, filters, output rectifiers. The efficiency of these circuits is between 85 and 91 percent.

During battery charging there are losses in the battery charge circuit. A transistor switch connects the battery to the battery charge strings in the solar cell array. This switch consists of a Darlington type circuit. The forward drop in the circuit includes the collector-to-emitter voltage of the saturated drive transistor and the base-to-emitter voltage of the switching power transistor. The voltage drop in this circuit is 2 to 2.5 volts. Allowing 60 watts for battery charging at 27.5 volts, the losses in the transistors are 5.5 watts. There is an additional 1 to 1 1/2 watt loss in the relays and controls of these circuits during battery charging.

The power subsystem losses are listed in Table 4-50 according to eclipse and noneclipse seasons.

TABLE 4-50. POWER ELECTRONICS LOSSES, WATTS

Unit	Eclipse Season		Noneclipse
	Battery Charge	Battery Discharge	
Battery charge circuits	Standby		0.5
	Active	7.0	
Battery controllers	Standby	10.0	10.0
	Active	*	
Current sensor	Standby		0.5
	Active	0.5	
Tap limiters	Standby	0.1	0.1
Bus limiters	Standby	0.005	0.005
		17.65	11.15

*Battery controller losses are 8 to 15 percent of battery output.

4.6.4 Technology Status

The power subsystem design is based on 1972 state of the art. Any advancement in technology would result only in improved design margins.

Solar arrays will use a design similar to Intelsat IV and Telesat with solar cells mounted on a cylindrical substrate. The 0.18 mm (7.2 mil) thick solar cells with 0.15 mm (6 mil) cover are commercially available to date at 5 percent higher price than ordinary 0.30 to 0.35 mm (12 to 14 mil) cells. With hardware procurement starting in 1974, it is anticipated that improved solar cells will be available which could provide 5 to 10 percent more power. With these solar cells, it would be possible to reduce the need for battery augmentation during VHF/UHF voice communication without further weight increase or to provide for power growth generally.

Batteries use similar cells as an Intelsat IV and HS 318. The battery cell size is tailored on demand at a nominal cost. Therefore, the 57,600 amp-sec (16 amp-hr) rating is not unusual. The separator material can be nylon or polypropylene which promises improved performance. Battery cycle life was assessed based on batteries with nylon separators.

Electronics in the power system is space proven, similar to that used in HS 318, Telesat, and TACSAT. Components were only resized to match the solar array and battery requirements.

4.7 APOGEE MOTOR

4.7.1 Alternatives Considered

The only motor currently under development to serve as a synchronous apogee motor for a 2914 launch vehicle payload is Thiokol's TE-616, being built for the Canadian Technology Satellite. Due to concern with the CTS schedule and the lack of growth potential, preliminary designs from United Technology Center (UTC), Aerojet Solid Propellant Company (ASPC), and Hercules Incorporated (HI) were reviewed. Evaluation results are shown in Table 4-51. The only design offering a significant mass advantage was HI. For the TDRS mission, approximately 12.3 kg (27 pounds) could be saved. The mass savings are due entirely to the higher performance of the HI propellant.

4.7.2 Baseline Description

The chamber is filament wound of S-901 glass fiber and a catalized epoxy resin system, which have been successfully used for many applications, including the X-259, BE-3, and the first and second stage Poseidon chambers. The winding will be of interspersed layers of 20 degree helical and 90 degree circumferential wraps of the resin impregnated glass fiber. The chamber interior will be thermally protected from the propellant combustion gases during motor operation by asbestos filled styrene-butadiene rubber (SBR/asbestos) insulation, selected because of its demonstrated high reliability and extensive use in the X-259 motor, and its compatibility with the propellant chamber system and the motor's operating conditions. The best design features of the nozzles used on three Hercules motors are combined in the proposed design. These motors have an impressive reliability record, with over 400 successful firings. The design is regarded as state of the art technology incorporating standard, flight-proven materials.

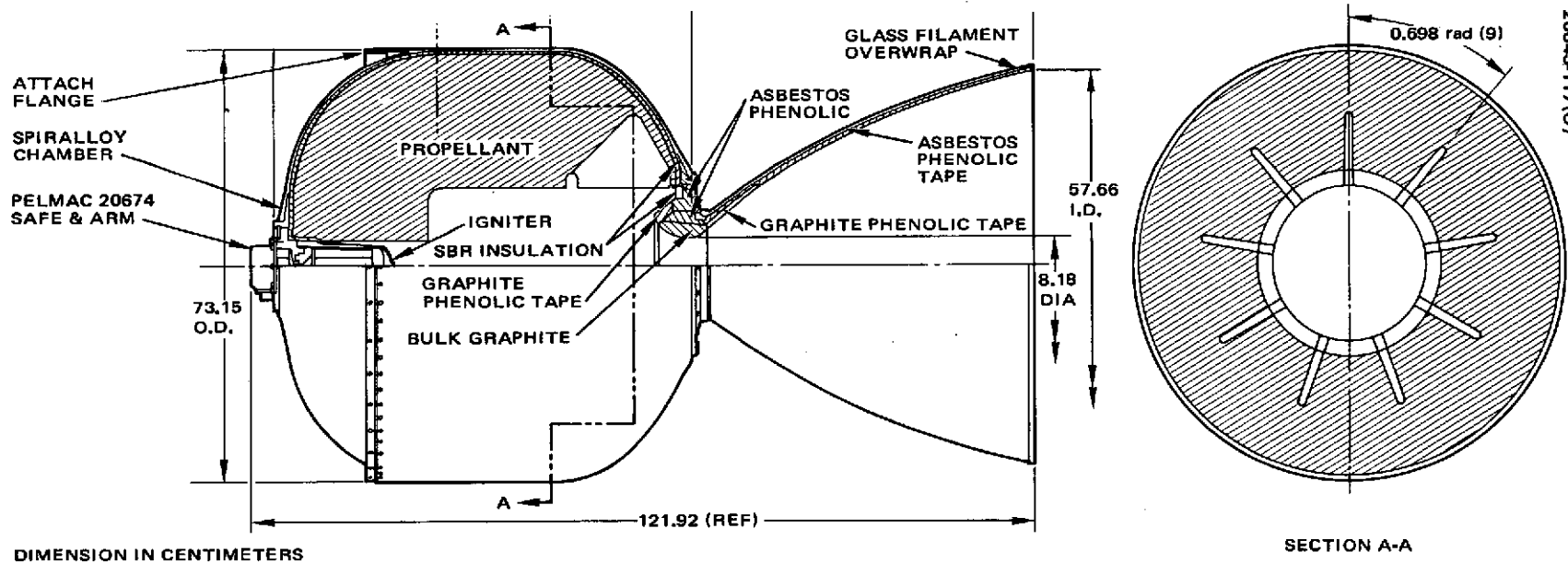
The throat and inside exit diameters are 8.19 and 57.7 cm, respectively. Internal surfaces of the nozzle are fully contoured, and efficiency losses and erosion are minimized by a hyperbolic spiral entry, which achieves a uniform and predictable heat transfer film coefficient. The expansion cone is contoured to a basic Rao parabolic geometry, modified for the propellant metal content, and provides an expansion ratio of 50:1. The motor design is shown in Figure 4-93.

The nozzle entrance and throat region is supported with an aluminum attach flange. Tapers provide an effective pressure seal and efficient method of load transmittal. The expansion cone is a composite of graphite phenolic from the throat insert aft to an expansion ratio of 7:1, and asbestos phenolic extends through the rest of the cone. The entire nozzle is overwrapped with glass filament.

TABLE 4-51. CANDIDATE MOTORS

Designation	Manufacturer	Effective ISP, seconds	Propellant Mass, kilograms	Inert Mass, kilograms	Motor Mass, kilograms	Status
TE-616	TCC	290.3	301	29.5	331	In development for CTS
-	Aerojet	291.0	300	33.1	333	New size based on SVM-5
-	UTC	281.0	306	33.1	339	New size based on FW-5
-	Hercules	302.2	291	27.7	318	New size based on X-259

4-206



20643-117(U)

Figure 4-93. Apogee Motor

The selected propellant has been used in over 850 Hercules production motors. Its performance has been well characterized in over 65 static and 190 flight tests and has remained consistent in motors fired after a period of 7 years. Because of its burn rate, high density, high delivered specific impulse, and excellent mechanical properties, this propellant is suitable for the apogee motor. It is a composite-modified, double-base (CMDB) formulation.

The grain configuration selected is patterned after the highly successful X-259 grain design and consists of a centerbore with nine aft-end wing slots. This configuration provides a relatively neutral thrust-time curve. It has the benefit of extensive use in the X-259 motor, wherein both the manufacturing technique is well established and the reliability is defined by test history.

The motor ignition system consists of the Pelmac 20674 electro-mechanical safe and arm device, used on Titan III and located at the forward end of the motor, and a pyrogen igniter mounted to the forward closure. The proposed design is an adaptation of proven design concepts and components from the Minuteman stage III M-57 motor and the X-259 motor.

4.7.3 Baseline Performance

Table 4-52 is a summary of apogee motor ballistic parameters at a nominal operating temperature of 297 K (75°F). The maximum insulator-chamber bondline temperature during burning is predicted to be 367 K (200°F). The maximum temperature under all conditions is 394 K (250°F) during burning and 533 K (500°F). Table 4-52 shows the calculated prefire weight of the motor. During firing, an estimated 2.27 kg (5 pounds) of inert mass will be expended.

The apogee motor requirements are summarized in Table 4-53. The nominal velocity increment required to circularize the spacecraft orbit at synchronous altitude from the nominal transfer orbit and to remove 20.7 degrees of inclination is 1679 m/sec (5498 fps). The variation will be held within ± 1.0 percent by requiring the motor manufacturer to verify predictions of total impulse within ± 1.0 percent of all motors tested and delivered. Maximum thrust of 40 kiloNewtons (9000 pounds) and acceleration of 113 m/sec² (11.5 g) for a 678 kg (1490 pound) spacecraft are imposed to limit the acceleration and static loads on the spacecraft. The maximum allowable case temperature of 533 K (500°F) has been established to protect the spacecraft.

The maximum allowable cg misplacement from the center of the mounting rings is set at 0.5 mm for the loaded motor and 1.0 mm for the burned out motor. (These values limit the static imbalance imposed by the spacecraft nutation requirement.) Dynamic imbalance limits have been established at 0.022 kg-m² (1200 oz-in²) for the loaded motor and 0.011 kg-m² (600 oz-in²) for the burned out motor. The allowable thrust misalignment was set at 0.5 mm displacement and 0.002 radians angular misalignment, which also limits spacecraft nutation and, in turn, velocity error during motor operation.

TABLE 4-52. APOGEE MOTOR PERFORMANCE AND MASS

<u>Parameter</u>	<u>Nominal Value</u>
Vacuum specific impulse	302.2 sec
Vacuum total impulse	861,578 Newton-sec (193,700 lbf-sec)
Average vacuum thrust	42 kn (9440 lbf)
Average chamber pressure	(621 psia) 4.28 mn/m ²
Burn time	21.2 sec
Propellant mass	290.30 kg (640 lbf)
Total motor mass	317.97 kg (701 lbf)
Burnout mass	25.40 kg (56 lbf)

The operating temperature range was established at 278 to 306 K (40° to 90°F), and 272 to 311 K for qualification. The required storage life is 3 years at any temperature between 278 to 311 K. The motor must operate in any orientation while rotating at speeds up to 10.47 rad/sec (100 rpm), and after exposure to hard vacuum for up to 10 days. The motor vibration and acceleration requirements are the same as the spacecraft requirements. These vibration levels will be applied to the apogee motor at the launch vehicle interface of the motor adapter so that the transmissibility to the apogee motor is duplicated.

4.7.4 Technology Status

The Hercules apogee motor design is a technology blend of the very successful X-259 and BE-3 motors which have had over 280 consecutive successes in space applications. Only flight proven design concepts and materials are used as shown in Table 4-54.

TABLE 4-53. APOGEE MOTOR REQUIREMENTS

Performance	
ΔV	1679 m/sec $\pm 1\%$ (5498 fps $\pm 1\%$)
Maximum thrust	40 kn (9000 LB)
Maximum acceleration	113 m/sec ² (11.5 g)
Maximum external case temperature	533 K (500°F)
Physical Characteristics	
CG: loaded	0.5mm (0.018 in.)
burned out	1.0mm (0.040 in.)
Balance: loaded	0.022 kg-m ² (1200 oz in ²)
burned out	0.011 kg-m ² (600 oz in ²)
Thrust alignment displacement	0.5mm (0.020 in.)
angular	0.002 radians (0.002 in/in)
Moment of inertia	Known within $\pm 5\%$
Environmental Conditions	
Operating temperatures	278 to 306 K (40 to 90°F)
Storage life	3 years
Spin rate	10.47 rad/sec (100 rpm)
Hard vacuum	10 days

TABLE 4-54. MOTOR DEVELOPMENT STATUS

<u>Component</u>	<u>Comment</u>
Case	New size using X259 and BE-3 materials (S-901 glass fiber) and design
Nozzle	New size using X259 and BE-3 materials and design except for contour and expansion ratio
Propellant	Composite modified double base (CMDB) fully characterized with 65 static tests and 190 flight firings over the last 7 years 318×10^6 kg (3500 tons) processed to date
Insulation	SRB/asbestos used on X259. Excellent compatibility with CMDB.
Liner	Epoxy resin standard for case bonded CMDB grains.
Igniter	Pyrogen igniter - X259 and man stage III materials and design
Safe and arm	Pelmac 20674 used on Titan III and FW5

4.8 STRUCTURE

4.8.1 Alternatives Considered

The structural design approach used on Gyrostat type spacecraft with integrated apogee injection rocket motor consists of a central conical shell that supports the apogee injection motor and the despin bearing assembly directly and that supports the solar cell array by means of arms extending from a central shell structure. The despun section is mounted on top of the despin bearing, and communication equipment is installed in this section. This central shell structure carries the principal loads encountered during launch and ascent. Studies on previous spacecraft of this type have shown that this approach results in minimum structural mass. Having selected this structural approach, then the minimum mass approach for bypassing launch loads around the despin bearing assembly is to integrate a launch load clamp into the despin bearing assembly. The alternative approach of diverting loads through the solar cell array substrate is heavier, and reliability is somewhat lower because at least three pin pullers would be required for the load release mechanism.

The TDRS is a relatively large spacecraft for the Delta 2914 launch vehicle and light structural design approaches are mandatory. Structural design approaches used on previous spacecraft which minimize structural mass have been adapted to TDRS. Beryllium structures have been employed with attendant mass savings of the order of 20 to 30 percent as compared to conventional aluminum and magnesium structures. Beryllium has been selected as the principal structural material for the primary structure.

4.8.2 Baseline Description

The TDRS for low and medium data rate user service is designed to be compatible with the Delta 2914 launch vehicle utilizing the standard 3731 spacecraft attach fitting assembly. The design requirement is to maintain the structural integrity of the spacecraft over the predicted environment for a minimum 5 year mission, including ground handling, launch, orbit injection, and on-orbit operations. A primary objective of the structural design is to satisfy the requirements with a minimum mass load carrying structure.

The primary structure of the spacecraft is made up of three basic assemblies: spun section, despun equipment section, and antenna support mast. This division results in three assemblies of roughly the same size. Manufacturing and assembly operations proceed in parallel and the spacecraft can also be checked out and shipped more conveniently.

4.8.2.1 Spun Section

The spun section consists of a central thrust cone, four ribs connected by a thin cover sheet for shear strength, and a cylindrical solar panel

substrate. The central thrust cone is an assembly of three formed conical skins and six machined rings. The formed skins are beryllium while the rings are fabricated from aluminum alloys. The lower cone has an aft ring that is machined to provide a mating surface with the launch vehicle attach fitting and a marman type separation clamp. It also includes provisions for supporting separation switch pads and separation spring pads.

The intermediate cone section and the lower cone are joined by a ring that serves a dual purpose. It provides an attachment for the lower inboard end of the spun ribs and support and alignment for the apogee motor. A ring at the juncture of the intermediate and forward cones provides the forward support for the inboard end of the spun ribs as well as the attachment of the inner perimeter of the thin magnesium sheet mounted on the rib tops. The forward ring of the cone mates with the BAPTA housing forward flange. Intermediate rings permit radial support for the BAPTA and the hydrazine propellant tank upper fitting. All primary rings are machined from aluminum alloy forgings.

The rib assembly includes four tapered beryllium ribs, intercostal ties between the tips of the ribs, and a thin magnesium cover plate that provides shear transfer in torsional loading. Four propellant tank lower fittings attach directly to each rib. In areas where equipment is mounted to the rib web, local doublers and stiffening members are provided. Support brackets for radial jets, attitude sensors, and electrical umbilicals are located on the rib intercostals. Machined fittings, mounted at the outboard end of each spun rib support the cylindrical solar panel. The cylindrical solar panel substrate is of sandwich construction with an aluminum honeycomb core, fiberglass face sheets, and edge closures. Metal inserts are bonded into the substrate for structural attachments.

4.8.2.2 Despun Equipment Section

The despun equipment section structure is composed of a central hub, six tapered radial ribs, and an equipment shelf. The hub and ribs are fabricated from beryllium sheet; the shelf is an all aluminum sandwich construction. The machined central hub supports 1) the BAPTA despun shaft and the despun shelf at its aft radial flange, 2) the antenna mast on its forward flange, and 3) the despun ribs on the cylindrical portion of the hub. The ribs are of a web and tee cup flange design, with a maximum rib depth at the central hub, and tapering in depth as they extend outboard. The aft flange supports the equipment shelf. The tee sections are constructed by bonding two angles formed from beryllium sheet back to back along the edge of the beryllium web shown in Figure 4-94.

The equipment shelf is made of aluminum honeycomb core bonded to aluminum face sheets. The despun equipment is mounted on the lower shelf surface, internal to the spacecraft spin body. The face sheet on the equipment side will have a thickness variation as required for heat transfer from the equipment while the upper face sheet will be of constant thickness.

4.8.2.3 Mast Assembly

The mast structural assembly consists of a fixed central mast and two deployable arms that are pivoted from the upper end. The assembly is fabricated from extruded beryllium tubular elements. The cylindrical central mast has a machined fitting that mates with the despun section hub. Machined fittings provide for the support of the Ku band antenna and its two axis positioner, the fixed S band order wire, and the nutation damper. The central mast is tubular in cross section, but has a chemically milled tapered wall to provide a minimum weight design.

The antenna support arms are tied to the despun platform and the central mast during spacecraft launch and provide additional structural support. After lock release in orbit, the arms pivot the S band and UHF/VHF antennas into position and provide the structural link between the central mast and the deployable antennas.

4.8.3 Performance

4.8.3.1 Dynamic Analysis

A dynamic structural model of the TDRSS using the Hughes developed MARS dynamic analysis computer program was generated for the launch configuration. The despun section was restrained against rotation by the marmon clamp within the BAPTA. A total of 43 mass stations (Table 4-55) and 64 elements was used to generate the model. The structure is fixed at the base of the adapter. Station 0.0 denotes the separation plane (Figure 4-95).

The structural elements were directly modeled using MARS type one, two, three, and five elements which are beam, shell, and plate elements, respectively. The only exceptions were the backfire and S band antennas. For modeling purposes, equivalent type two aluminum elements were formed based on a 50 Hz lateral natural frequency for pinned end supports. Structural joints for the model are assumed to be rigid, except for those noted in Table 4-56.

Table 4-57 identifies natural frequencies and mode shapes up to a frequency limit of 95 Hz. Figures 4-96 to 4-99 show the first two bending mode shapes for the X and Y system axes.

Table 4-58 denotes the static design load conditions to which the model was subjected. Dynamic loading was not investigated. Figure 4-100 presents the non-uniform lateral load distribution of Condition 2 in Table 4-58.

4.8.3.2 Preliminary Stress Analysis

A preliminary stress analysis of the primary structural elements of the spacecraft has been performed. A summary of minimum margins of safety together with the corresponding design load cases and modes of

failure are presented in Table 4-59. The analysis was performed using the three static load conditions previously described. All design loads correspond to a Delta 2914 boost vehicle using an MDAC 3731 adapter. The non-uniform lateral loading case (Case 2, Figure 4-100) proved to be critical for design of the mast and thrust cones. Case 4, Figure 4-97, which assumes a longitudinal load factor of 353 m/sec^2 (ultimate) resulting from longitudinal spacecraft vibration testing, was critical in sizing the spun and despun support ribs and the main stiffening rings.

A summary of the maximum shear, axial load, and bending moment for several spacecraft stations and corresponding math model stations is presented in Table 4-60. Figure 4-101 shows the general structural configuration. A more detailed description of spin section structure is shown in Figure 4-102. The critical spacecraft bending moment distribution for the Condition 2 (nonuniform) lateral loading is plotted in Figure 4-103.

Analysis of the thrust cones is summarized in Table 4-61. The three cones were sized for both aluminum and beryllium using the Hughes CONEA computer program which computes the minimum wall thickness and margin of safety for a given set of parameters. Beryllium conical skins result in the lighter mass structure. The antenna support mast was sized for beryllium in the interest of weight minimization. Beryllium also resulted in the lightest design for the spun and despun support ribs. The ribs are built-up sections composed of beryllium cross-rolled sheet for the webs and extruded caps.

4.8.4 Technology Status

Beryllium is proposed for fabrication of the spin cone assembly, the antenna mast, and equipment supports. The proposed components are similar to HS 318 beryllium components; i. e., the spinning cone and despun hub assembly are similar in construction to the HS 318 conical adapter, and the eight spinning ribs are similar to HS 318 spin arm assembly. The tubular mast support is however a new item.

A number of improvements have been implemented by material suppliers and by Hughes manufacturing and processes, based on HS 318 experience, which justifies the confidence to deliver on schedule at the proposed cost. Raw material is currently available from one supplier which exhibits significantly better properties than products available 3 years ago. Elongation properties in the longitudinal and transverse direction of sheet products now average in excess of 15 percent, with guaranteed minimum of 10 percent. Three years ago the minimum elongation was only 5 percent. This higher elongation means more ductility, which makes the material less susceptible to damage during fabrication. Usage of high purity beryllium powder in the initial billet is largely responsible for this improvement.

TABLE 4-55. MASS STATION DESCRIPTION

<u>Lumped Mass Station</u>	<u>Description</u>
1	Balance weight antenna support, thermal, wire harness, coaxial, and waveguide (A-T-W-C)*
2	One quarter backfire antenna, A-T-W-C
3	One quarter S band antenna, A-T-W-C
4	Nutation damper, A-T-W-C
5, 6	A-T-W-C
7	One half backfire antenna
8	One half S band antenna
9	Ku band parabolic reflector antenna, one half antenna positioner
10	One half antenna positioner, A-T-W-C
11	Ku band horns, A-T-W-C
12	A-T-W-C, thermal barrier
13	One quarter backfire antenna, A-T-W-C
14	One quarter S band antenna positioner, A-T-W-C
15	2/10 solar panel
16	5/10 solar panel
17	3/10 solar panel
18	3/9 despun shelf
19	Omitted in final model
20	Thrust cone
21	Thrust cone
22	Thrust cone
23	Thrust cone, one half adapter, thermal barrier
24	Thrust cone, one quarter BAPTA
25, 26, 27	One quarter BAPTA
28 - 31	Tanks, hydrazine propellant
32 - 35	Batteries, spinning shelf, structure, electrical equipment

*Assumed to be uniformly distributed along antenna support system.

Table 4-55 (continued)

<u>Lumped Mass Station</u>	<u>Description</u>
36	Apogee motor
37 - 42	Despun shelf structure, electrical equipment
43	Fixed base

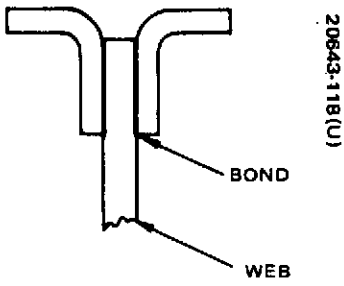


Figure 4-94. Beryllium Rib Construction

20643-118(U)

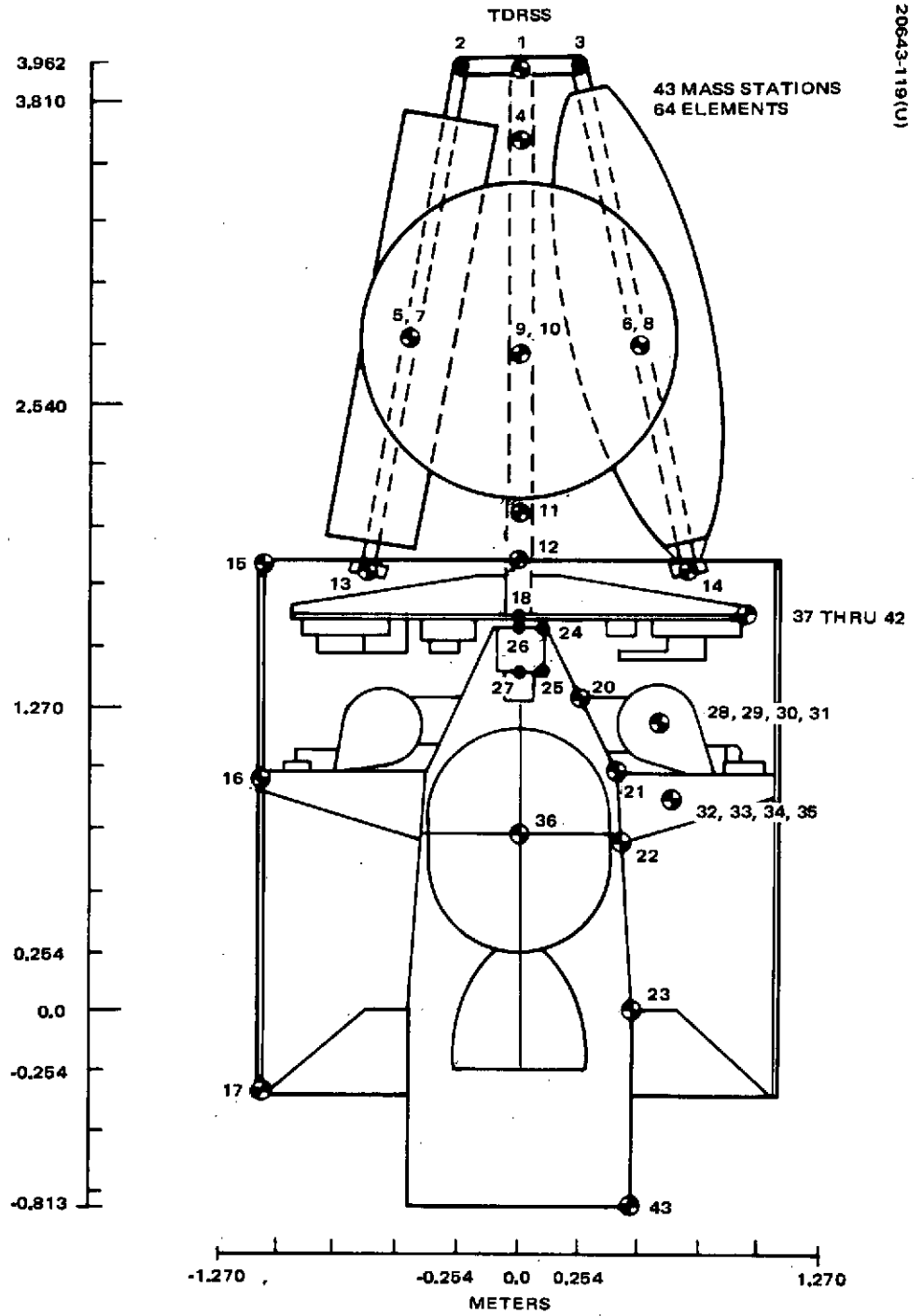


Figure 4-95. Mass Stations

TABLE 4-56. NONRIGID JOINTS

Mass Station (From - To)	End	Unrestrained Direction	Coordinate System
2 - 5	(2)	θ_x	System
2 - 7	(2)	$X, \theta_x, \theta_y, \theta_z$	Element
7 - 13	(13)	θ_x, θ_y	System
3 - 6	(3)	θ_x	System
3 - 8	(3)	$X, \theta_x, \theta_y, \theta_z$	Element
8 - 14	(14)	θ_x, θ_y	System

TABLE 4-57. MODAL CHARACTERISTICS

Mode	Frequency, cps	Type
1	11.2	X bending of mast
2	12.3	First despun torsion
3	13.6	Y bending of mast
4	23.1	Second X bending
5	24.4	Second Y bending
6	36.1	First despun shelf rocking (Y axis)
7	36.8	Second despun shelf rocking (X axis)
8	38.2	First solar panel torsion
9	41.1	Third despun shelf mode (X axis) antenna coupling
10	43.9	Antenna mode (X)
11	44.8	Fourth despun shelf rocking (Y axis)
12	44.9	Antenna mode (Y)
13	46.0	Fifth despun shelf plate mode (about X axis) (antenna coupling)
14	46.1	Sixth despun shelf plate mode
15	46.4	Antenna (X)
16	46.7	Antenna (Y)
17	53.7	Antenna, despun shelf coupled
18	55.3	K _u band parabolic reflect antenna
19	56.2	Antenna, despun shelf coupled
20	59.0	Solar panel X bending
21	59.1	Solar panel Y bending
22	72.4	Antenna mode
23	85.0	Third X bending
24	89.6	Tank mode
25	90.0	Coupled X bending (fourth) and tank mode
26	90.7	Tank mode
27	91.1	Coupled X bending (fourth) tank and apogee motor
28	92.8	Tank mode
39	149	Axial of solar panel
48	223	Axial of solar panel

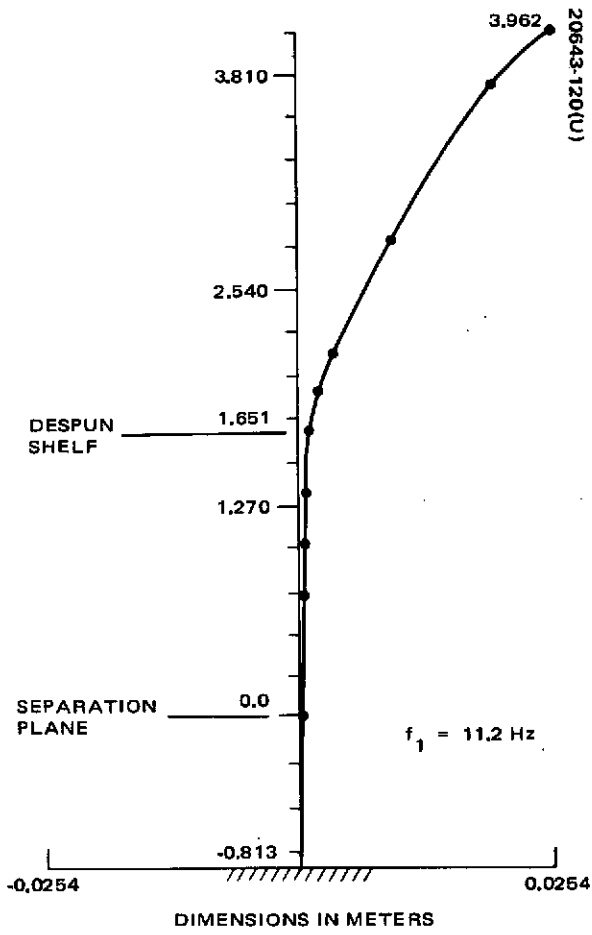


Figure 4-96. First X Bending of Mast

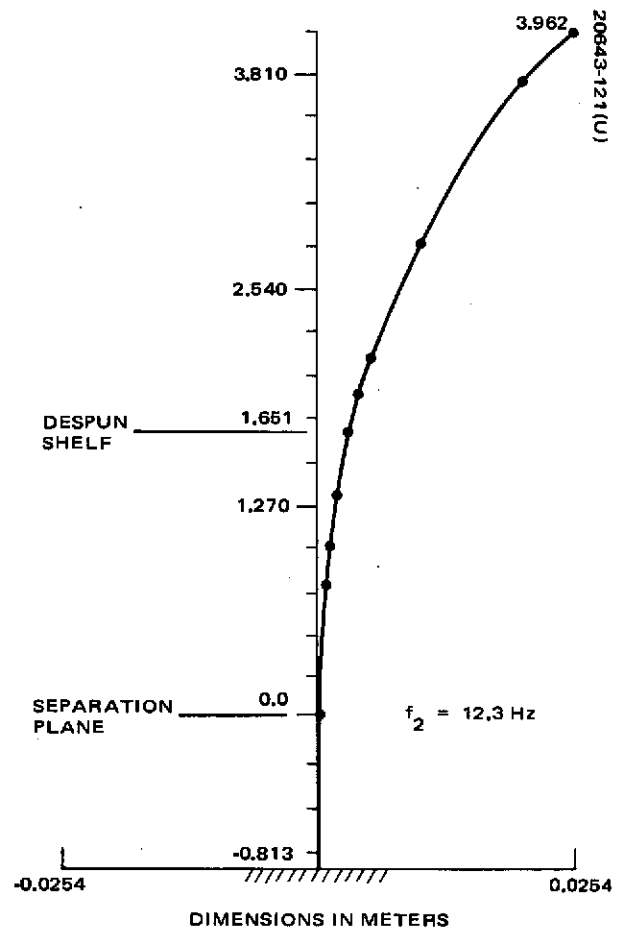


Figure 4-97. First Y Bending of Mast

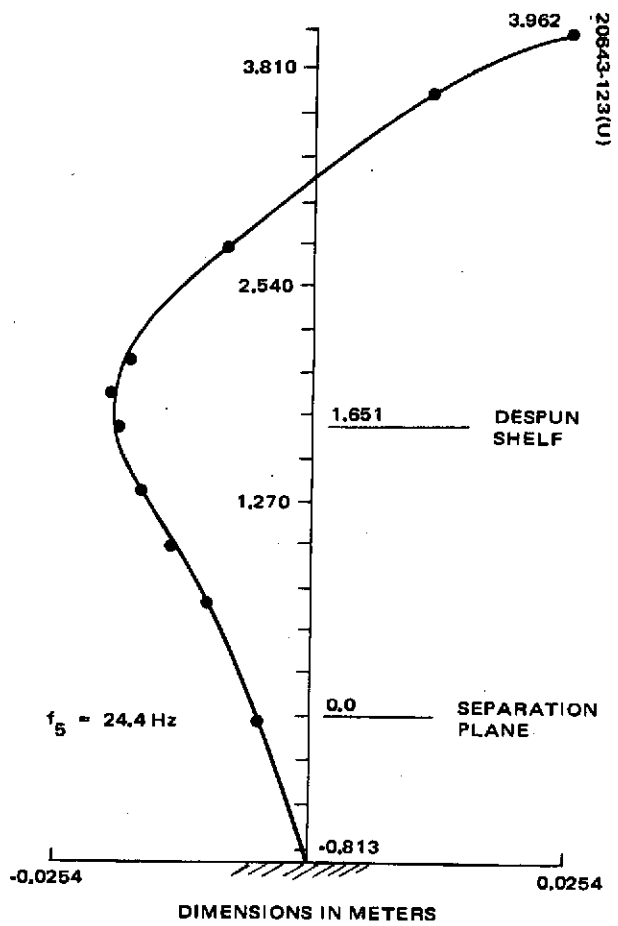
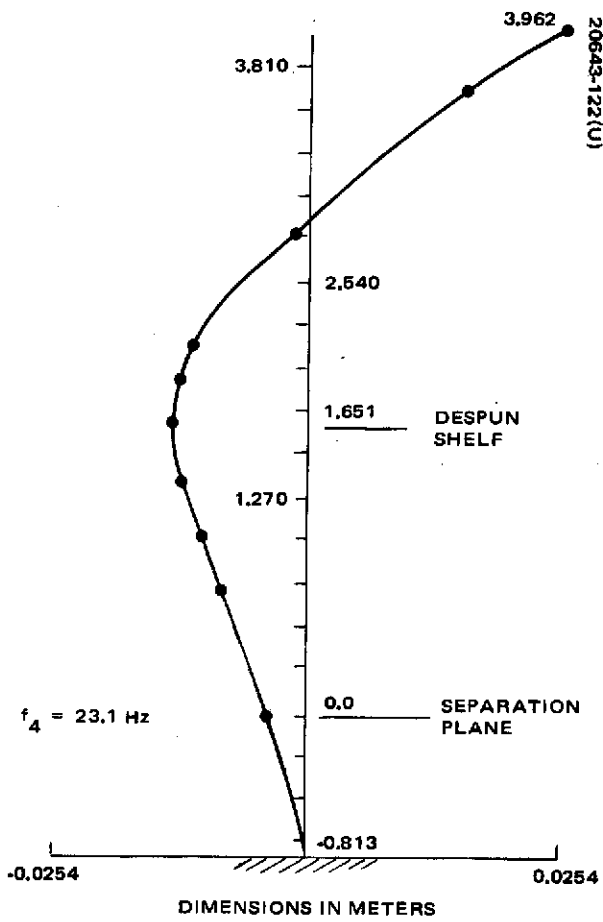


Figure 4-98. Second X Bending of Mast Figure 4-99. Second Y Bending of Mast

TABLE 4-58. CRITICAL LOAD CASES

Spacecraft Status	Axis	Acceleration, m/sec ²
Case 1, Pogo event	Thrust (Z) Lateral (X, Y)	-177. ± Uniform 9.8
Case 2, * Liftoff, Maximum αg	Thrust (Z) Lateral (X, Y)	-44., +15. ± Nonuniform load curve
Case 3, ** Third stage motor burn	Thrust (Z) Radial Lateral (X, Y)	-159. 132. R (centrifugal at R meters radius) 5. Uniform
Case 4 Estimated vibration test loads, maximum	Thrust (Z)	±353

*Loads due to MECO are encompassed by the POGO and liftoff events.
 **Case 3 also applies to apogee motor burn.

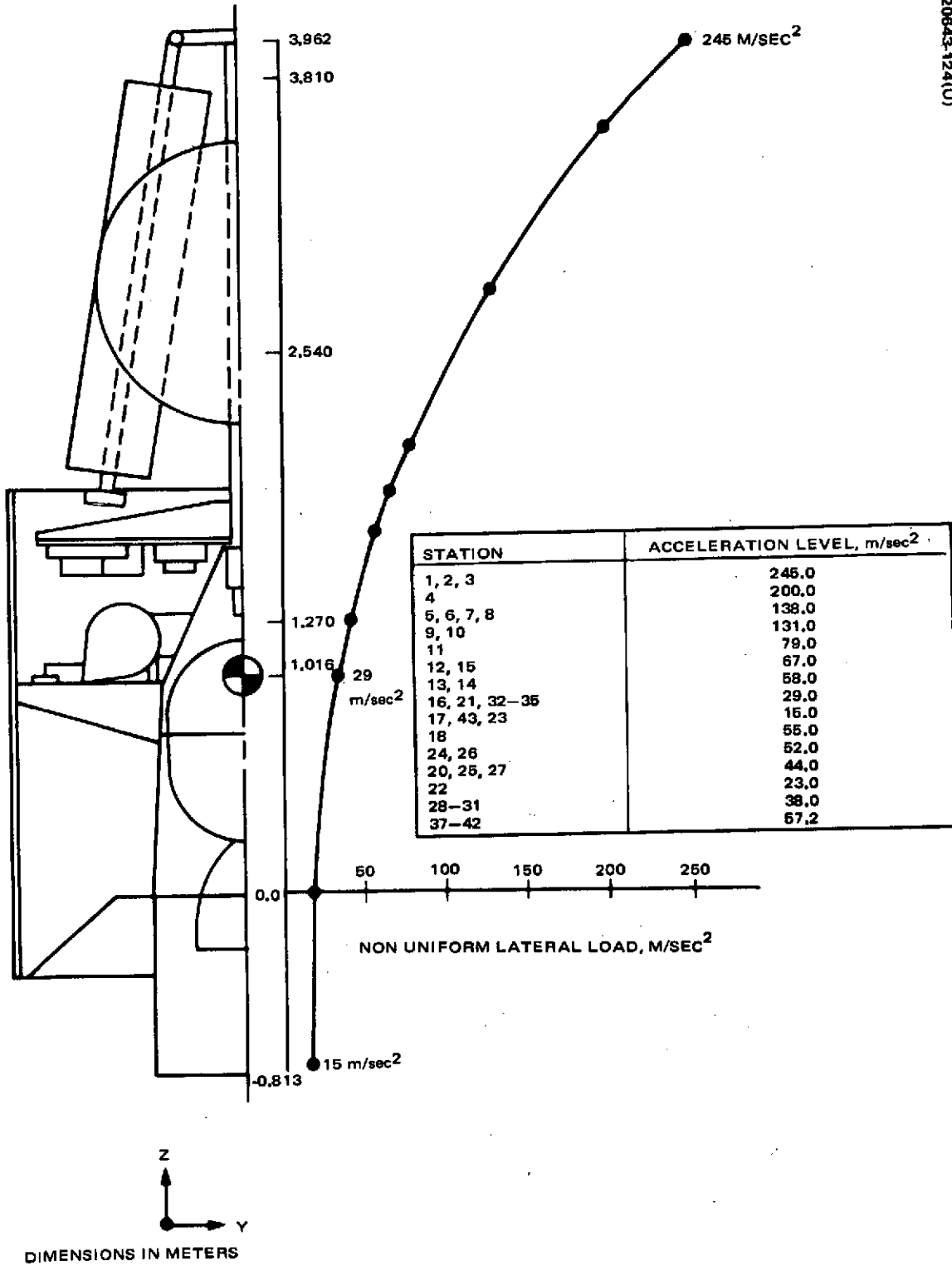


Figure 4-100. TDRSS Design Loads - Condition 2:
Lateral Loads

TABLE 4-59. SUMMARY OF MINIMUM MARGINS OF SAFETY

Part Name	Critical Condition	Type of Loading	Mode of Failure	Margins of Safety	
				MSy	MSu
Aft thrust cone	Nonuniform quasi-static loading	Bending plus shear plus compression	Buckling	-	0.17
Apogee motor run	Longitudinal vibration	Bending	Fracture	-	0.22
Intermediate thrust cone	Nonuniform quasi-static loading	Bending plus shear plus compression	Buckling	-	0.18
Forward ring - Intermediate cone	Longitudinal vibration	Bending	Fracture	-	0.51
Aft separation ring	Nonuniform quasi-static loading	Bending plus compression	Fracture	-	0.30
Forward thrust cone	Nonuniform quasi-static loading	Bending plus shear plus compression	Buckling	-	0.16
Despun ribs	Longitudinal vibration	Compression in flange	Fracture	-	0.34
Spun ribs	Longitudinal vibration	Shear in web	Shear buckling	-	0.48
Lower mast	Nonuniform quasi-static loading	Bending	Fracture	0.14	-
Middle mast	Nonuniform quasi-static loading	Bending	Fracture	0.015	-
Upper mast	Nonuniform quasi-static loading	Bending	Fracture	0.19	-

4-224

TABLE 4-60. CRITICAL DESIGN LOADS (ULTIMATE)

Spacecraft Station	Math Model Station	Condition	Axial* Load, Newtons	Shear** Load, Newtons	Moment** My or M _x (Newton-Meter)
3.962	1	IIB	1,828	1,397	247
3.556	4	IIB	1,828	1,397	(190)
	4-10	IIA	2,277	5,142	4,006
	4-10	IIB	2,042	249	1,902
2.794	10	IIA	2,691	6,370	3,908
2.096	11	IIA	2,691	6,370	8,487
1.880	12	IIA	2,807	6,579	9,908
1.651	18	IIA	3,007	6,877	11,478
1.600	24	IIA	7,108	13,474	11,320
1.270	20	IIA	7,108	13,474	17,478
1.270	20	IIB	6,512	15,288	17,420
0.991	21	IIB	6,512	15,288	19,750
0.991	21	IIB	14,728	19,233	20,596
0.737	22	IIB	14,728	19,233	25,477
0.737	22	IIB	29,852	27,192	25,680
0	23	IIB	29,852	27,192	45,711

*All axial loads are in the -Z direction (aft).

**Signs have been omitted. The most critical combination of shear and bending moment is used.

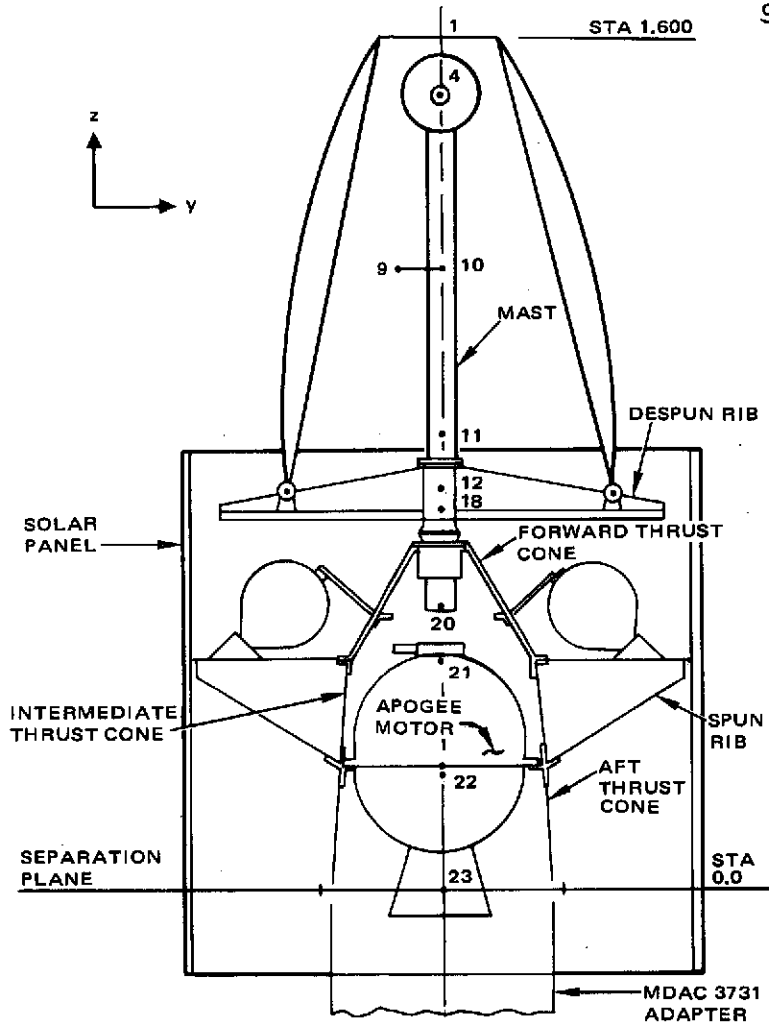


Figure 4-101. Math Model Stations

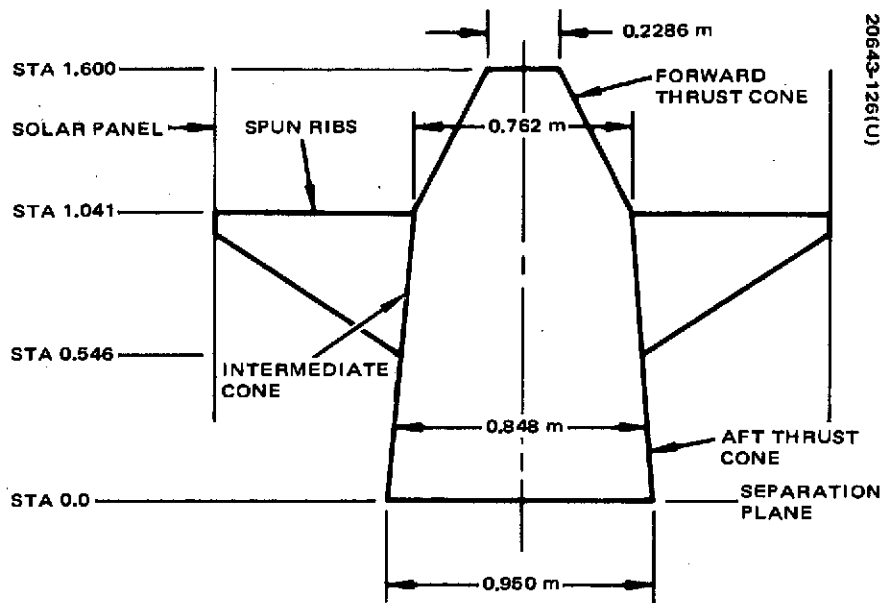


Figure 4-102. Thrust Structure Geometry

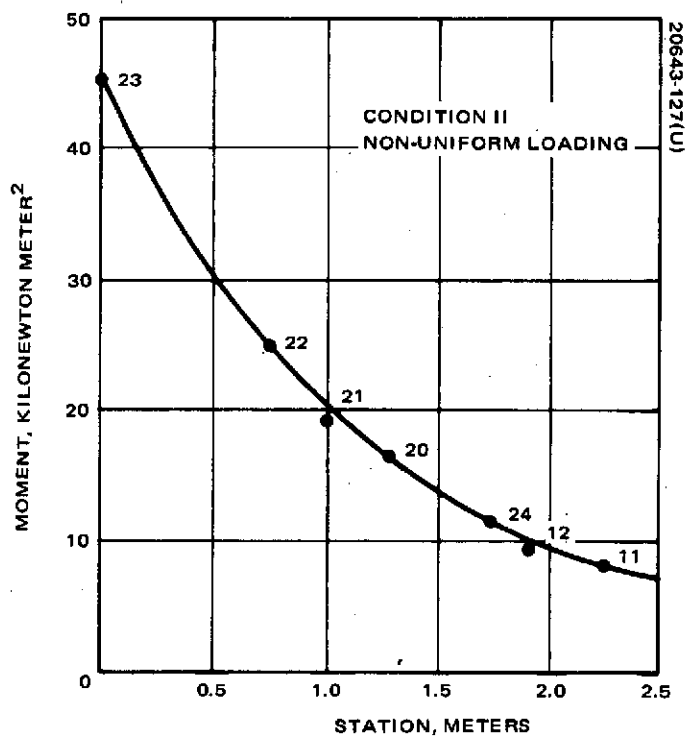


Figure 4-103. Spacecraft Moment Diagram

TABLE 4-61. SUMMARY OF DESIGN LOADS FOR THRUST CONES (ULTIMATE)

Position Name	Spacecraft Station	Condition I			Condition II		
		Axial Load, Newtons	Shear Load, Newtons	Moment Newton-meters	Axial Load, Newtons	Shear Load, Newtons	Moment, Newton-meters
Forward thrust cone	1.600	26,700		2,260.	7,108. (Be:0.035)	13,470.	11,320. (Al:0.066)
Intermediate cone	0.991	-	-	-	14,730. (Be:0.027)	19,230.	20,600. (Al:0.050)
Aft thrust cone	0.546	120,900	13,340.	6,780.	29,850. (Be:0.032)	26,870.	30,600. (Al:0.059)
Separation plane	0.0	-	-	-	29,850.	27,190.	45,720.

The use of sheet thicknesses less than 1.27mm will not be permitted for any primary structural components that require drilling and machining. A significant portion of the cost and schedule problems on HS 318 was related to the rework and scrap of the 0.89mm structural cone skin segments, which proved to be significantly more difficult to machine than sheets with thicker gages. If gages less than 0.27mm are needed, all work will be performed at 1.27mm minimum, and then chemically milled to the desired thickness after hot forming. Such an experiment was successfully demonstrated on HS-318.

Probably the most significant improvement is that Hughes has now developed an in-house capability to handle all aspects of beryllium fabrication except hot forming. Thus, many squawks and attendant rework cycles associated with improper cleaning, etching, and storage of unassembled piece parts at subcontractor's facilities will be eliminated, together with the expense of requiring quality control and engineering coverage at these locations. It is planned that all hot forming operations will be performed at Murdock, Inc., in Gardena, California, under Hughes direction. Two HS 318 cone skin assemblies have been completed using this manufacturing approach, with attendant cost savings of 40 to 50 percent per assembly.

In summary, the beryllium applications on HS 318 were very successful. Improved techniques were developed on this program which allow Hughes to commit to similar applications with high confidence regarding cost and schedule.

TABLE 4-62. SUBSYSTEM TEMPERATURE REQUIREMENTS

Equipment	Design Range, °K	Eclipse Minimum, °K	Comments
<u>Despun</u>			
Transmitters, receivers and other repeater electronics	267 to 311	261	Design limits used in the successful qualification and flight application of similar communication electronics equipment
Telemetry and command electronics	267 to 311	261	
S band antenna positioner	222 to 367	222	Identical to Intelsat IV design limits
Antenna mast and cabling	200 to 367 Mast deflection due to diametral temperature difference 0.01 rad	200	Similar to TACSAT design
VHF and S band antenna	117 to 395	117	Similar to TACSAT design
<u>Spinning</u>			
Apogee motor	278 to 306	278	Comsat UTC motor design limits
Despin bearing	273 to 311	284	
Despin electronics	267 to 323	261	Intelsat IV
Batteries	273 to 300	273	No overcharge
Solar panel	222 to 297	172	
RCS tanks	278 to 333	278	Intelsat IV design with active heating of lines and valves
lines	278 to 367	278	
valves	278 to 339	278	

4.9 THERMAL CONTROL

4.9.1 Thermal Design Requirements

The spacecraft thermal control system must provide an adequate temperature environment for all functioning subsystems for a period of at least 7 years in synchronous equatorial orbit. In particular, the design must be sufficiently flexible to accommodate significant variations in internal power dissipation that result from a combination of seasonal changes, long mission life, and optional system operating modes. The orbital design must also be compatible with survival and/or operation of all subsystems during ascent, transfer to synchronous orbit, and apogee motor burn.

Table 4-62 presents the subsystem temperature requirements that have been established for the study baseline. As indicated in the table, these design limits are all representative of values used in previous gyrostat or spin-stabilized spacecraft applications. Table 4-63 outlines the expected extremes in system power dissipation using baseline estimates of equipment power requirements, operational modes, and solar panel electrical characteristics. The maximum dissipation for the spinning equipment complement will occur when the batteries are on charge at the beginning and end of the eclipse season (short eclipse times). However, the batteries will be continuously monitored to prevent overcharge, which may cause the battery to exceed the high temperature limit.

4.9.2 Design Description

The overall concept is one of passive thermal control, which takes advantage of both the temperature averaging that results from the uniform spin rate of the vehicle solar panel and the containment of the sun within ± 0.41 radian of the orbit plane. The key features of the thermal design are identified in Figure 4-104. As a result of the large dimensions of the spacecraft, radiation is the dominant mode of heat transfer between the major elements. The temperatures of the spinning structure and low power dissipation regions are controlled by providing good radiation coupling to the solar panel in the same manner as that used for Intelsat IV. The batteries, which constitute the largest source of thermal dissipation on the spinning side, are hard mounted to the structural ribs in order to provide thermal fin capability. The lines and valves of both the axial and radial thrusters are provided with molded blanket heaters that prevent any portion of the system from reaching the freezing point of hydrazine at any time during the operational life of the spacecraft. These heater elements are wrapped with low emittance aluminum tape to minimize the heater power requirements. The hydrazine tanks can be maintained above the freezing point with multilayer insulation and do not require active heating.

The bulk of the power dissipating units are grouped on a despun platform across the forward end of the solar panel, and temperature control is achieved in the same manner as used in the TACSAT design. Platform dissipation is radiated to an intermediate radiating surface provided just forward

TABLE 4-63. THERMAL DISSIPATION LEVEL WATTS

Equipment	Solar Power 26.5 V		Solar and Battery 25 V	Battery Power 25 V		
	Operating Time					
	75	25	25	75	25	25
<u>Despun</u>						
Data transmitter, K _u band	19.0	19.0	17.9	17.9	17.9	17.9
Command transmitter, S band	11.3	62.8	10.4	10.4	59.0	10.4
Command transmitter, UHF	75.0	75.0	75.0	75.0	75.0	75.0
Voice transmitter, UHF	—	—	75.0	—	—	75.0
Command receiver, K _u band	4.7	4.7	4.5	4.5	4.5	4.5
Data receiver, S band	1.9	1.9	1.8	1.8	1.8	1.8
Data receiver, VHF	1.7	1.7	1.6	1.6	1.6	1.6
Frequency generator	8.1	8.1	7.6	7.6	7.6	7.6
Miscellaneous repeater equipment	9.5	9.5	8.9	8.9	8.9	8.9
Command decoders	4.9	4.9	4.7	4.7	4.7	4.7
Telemetry encoders	10.1	10.1	9.5	9.5	9.5	9.5
Antenna position control	<u>6.0</u>	<u>6.0</u>	<u>6.0</u>	<u>6.0</u>	<u>6.0</u>	<u>6.0</u>
Total	152.2	203.7	222.9	147.9	195.6	147.9
<u>Spinning</u>						
Telemetry transmitter, VHF	—	—	—	—	—	—
Command receiver, VHF	1.2	1.2	1.1	1.1	1.1	1.1
Despin control electronics	19.0	19.0	17.9	17.9	17.9	17.9
Power electronics	18.0	11.0	39.8	40.0	44.0	50.0
Battery charging	<u>60.0</u>	—	—	—	—	—
Total	98.2	31.2	58.8	59.0	63.0	69.0

20643-128(U)

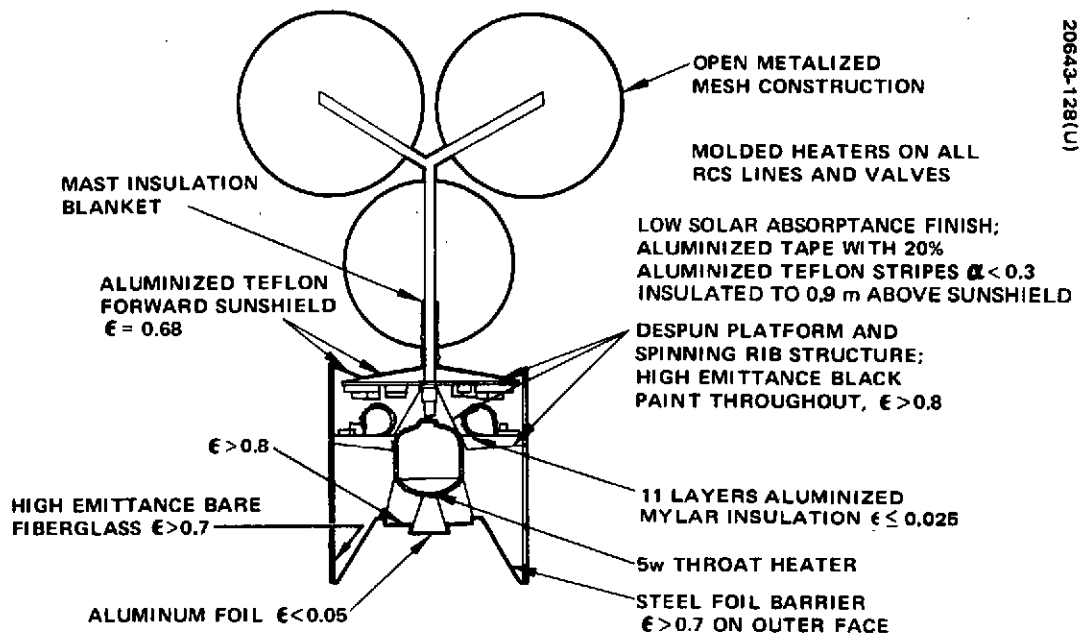


Figure 4-104. Spacecraft Thermal Control Provisions

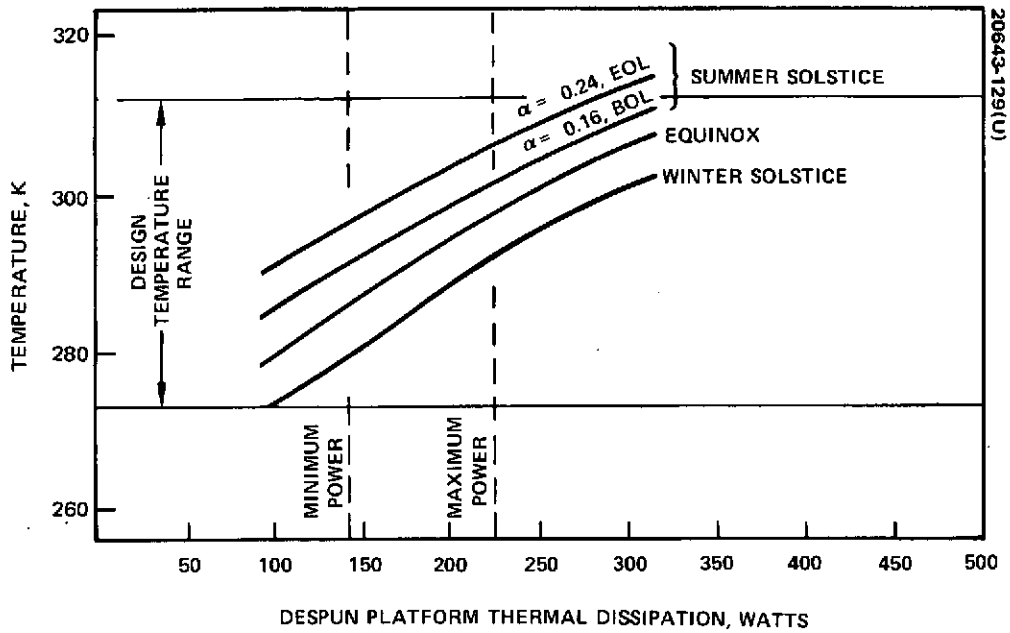


Figure 4-105. Despun Platform Power/Temperature Performance

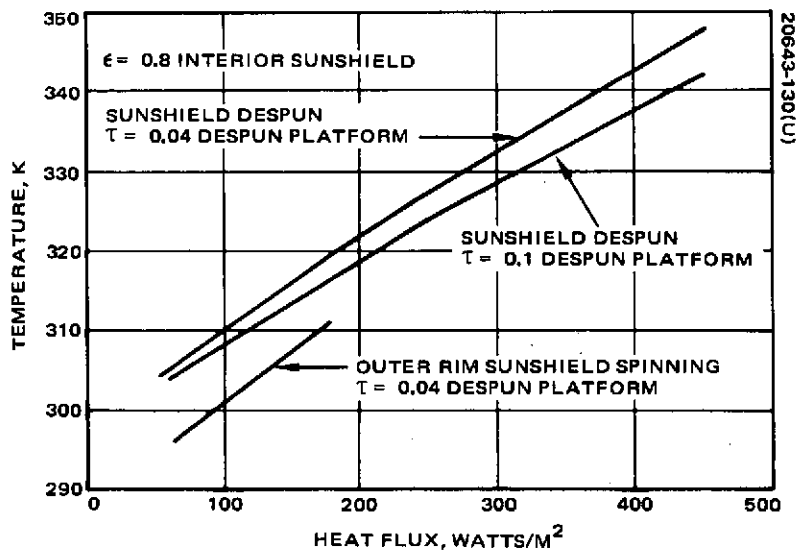


Figure 4-106. Steady State Temperature of Outer Ring of TDRSS Despun Platform Versus Heat Flux

of the platform. Most of the intermediate radiating area (inboard) is despun, while the outermost rim is spinning. The high dissipating units are located near the perimeter of the despun shelf, below the spinning cover. The use of second surface aluminized teflon as the finish on the intermediate surface serves to attenuate the temperature variation of the platform with respect to solar incidence angle. Temperature sensitivity of this platform is further attenuated by radiation coupling to the stable solar panel boundary.

The antenna mast is treated with a combination of aluminum foil and second surface aluminized teflon stripes in order to limit both the thermal bending of the mast and the peak temperature of the cabling that will be attached to the mast. The mast will be insulated for approximately 0.9 meter above the sunshield to provide the desired boundary conditions for the motor bearing assembly. The antenna element will have high emittance finishes only to the extent necessary to limit peak temperatures below 422°K in any critical areas; otherwise, these element finishes will be as dictated by functional rather than thermal requirements.

The apogee motor has an aluminized kapton multilayer insulation blanket to protect the spacecraft from post firing thermal soakback. Additional thermal isolation is provided around the aft end and around and over the nozzle to limit undesirable local temperatures near the nozzle throat during the transfer orbit. In addition to this isolation, an active heater on the nozzle throat is provided in the baseline to assure adequate temperature control of this critical element. The aft end of the spacecraft is closed and protected from apogee motor plume heating by a 0.0051 cm thick stainless steel aft barrier. This barrier has hanovia gold on the surface that faces the spacecraft interior to minimize heat inputs to the spacecraft during apogee motor firing and to minimize heat transfer at this interface during all orbital steady state conditions.

4.9.3 Thermal Performance

4.9.3.1 Despun Platform

The power temperature performance characteristics of the baseline despun platform design are shown in Figure 4-105. The temperature performance is well within the equipment design range for the extremes in both season and operating mode. Further, the end of life performance of the degraded teflon sun shield appears adequate for this mission. Thus, the aluminized teflon shield used for TACSAT is the baseline preference over the more stable, but heavier and more complex, silvered quartz mirror approach used to meet the 10 year Intelsat IV requirement.

Figure 4-106 is a plot showing the temperature of the outer ring of the despun platform-versus-heat flux input for both a totally despun and partially despun forward sun shield. With a maximum equipment flux density of 172 w/m² on the outer ring of the despun platform, the platform will stay within the temperature limits listed in Table 4-62.

20634-131(U)

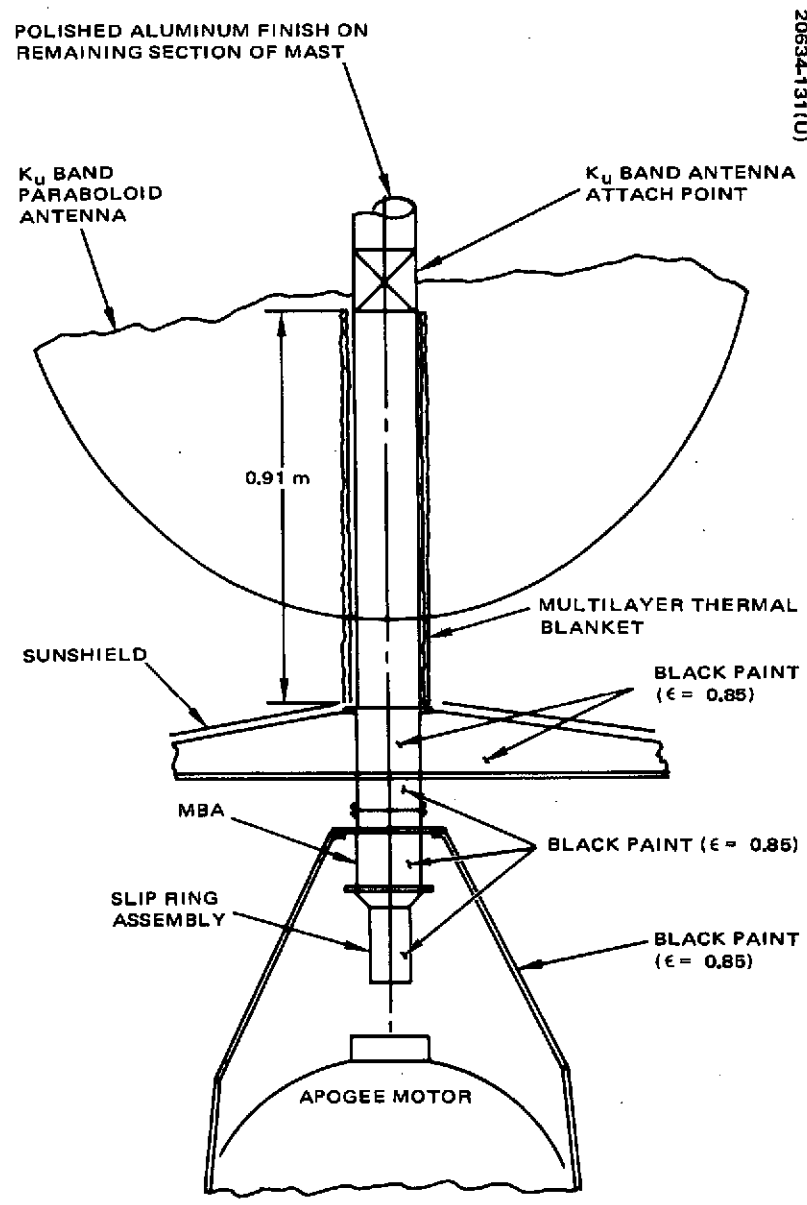


Figure 4-107. Motor Bearing Assembly/
Structure Thermal Interface

Equipment temperature drops on the order of 16.7°K to 22.2°K can be expected during eclipse. This drop will result in short term exposure of the electronic equipment to temperatures of 264° to 269°K, which satisfies the established eclipse limit of 261°K.

4.9.3.2 Motor Bearing Assembly

The motor bearing assembly (MBA) installation is shown in Figure 4-107. The bearing assembly used in this design is very similar to that used in the Canadian Domestic Satellite program. Full advantage has been taken of the detailed analysis and test data completed on the Canadian Domestic Satellite program. The only changes that are pertinent to the thermal performance are the addition of the slip ring assembly and the structural attachments, which resulted in some flange modification. The internal motor design and bearing configuration is thermally equivalent to that analyzed and tested on the Canadian Domestic Satellite program.

Thermal analysis results are presented in Table 4-64. Both warm and cold boundary condition cases were analyzed to assure that the thermal coupling between the antenna mast and the MBA does not cause any significant temperature changes on the MBA. It was verified that the antenna mast will not significantly affect MBA temperatures if the mast is insulated to a

TABLE 4-64. MBA THERMAL PERFORMANCE

Node	Location	Minimum Steady State Boundary, °K	Maximum Steady State Boundary, °K
1	Upper inner bearing race	280	304
2	Upper outer bearing race	281	305
3	Upper despun flange	281	304.5
4	Center outer spinning housing	282	304.5
5	Lower spinning flange	280.5	304
6	Lower outer bearing race	291	308
7	Lower inner bearing race	291.5	307.5
8	Lower despun flange	291.5	307.5
9	Center despun shaft	284	306
10	Spinning cone structure	279	301
11	Slip ring assembly	291.5	307.5

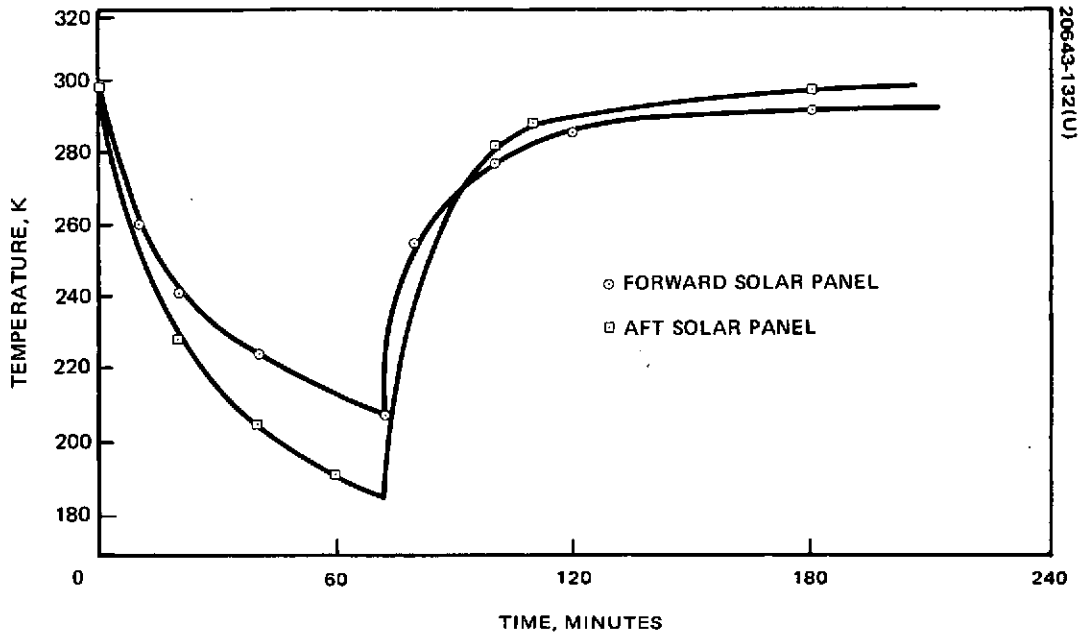


Figure 4-108. Solar Panel Eclipse Response

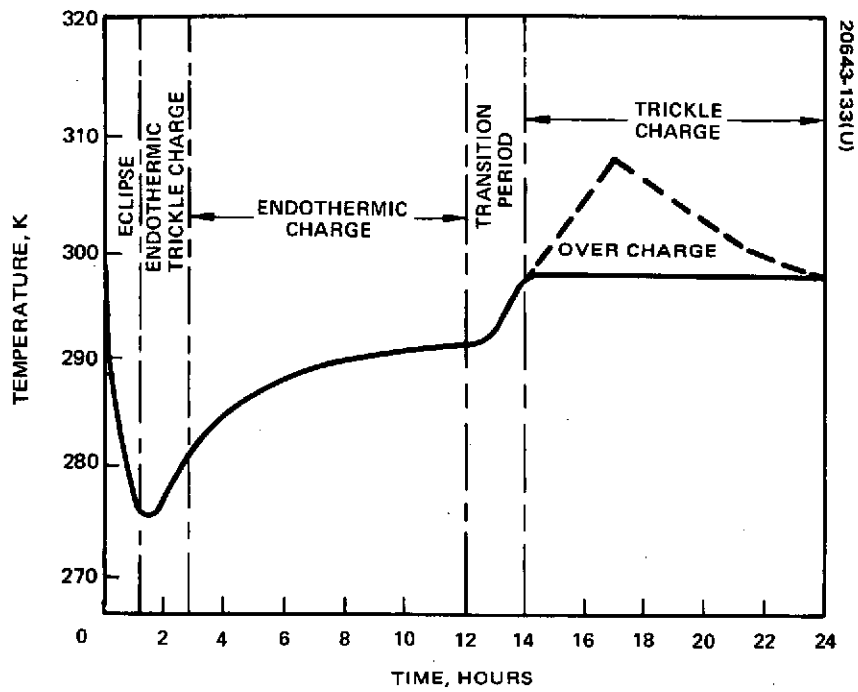


Figure 4-109. 24 Hour Battery Profile for Typical Rib Mounted Pack

point approximately 0.9 meter above the sun shield. The MBA installation shown in Figure 4-107 provides excellent boundary conditions for the MBA, since it is coupled tightly to the despun platform, which provides a stable thermal environment. The high thermal mass of the MBA results in solar eclipse bulk temperature changes of less than 11°K. During the eclipse season the steady state temperature prior to eclipse will be no less than 283°K. Therefore, the bulk temperature will be greater than 273°K at the end of a 4320 second solar eclipse.

The temperature differential across the bearings is shown to be less than 2.8°K for the worst case conditions. The 3 watt dissipation in the slip ring assembly will cause that section to run about 8.3°K warmer than the motor housing; however, it will remain well below the 323°K allowable temperature for the slip ring assembly. All motor and bearing temperatures will remain within the 273° to 311°K operational design range.

4.9.3.3 Power Subsystems

The temperature characteristics of the cylindrical spinning solar array concept are well established through correlation of predicted performance with both test and flight data. The steady state solar panel temperature for the baseline configuration will vary from a minimum of 285°K at summer solstice to a maximum of 295°K at equinox. The expected eclipse response of the panel is shown in Figure 4-108 and is based on the Intelsat IV substrate heat capacity and radiative properties.

The battery system can constitute the major thermal dissipator on the spinning side of the spacecraft. Figure 4-109 shows a typical orbital temperature cycle for an Intelsat IV battery pack where the charge rate is commanded by ground command. As indicated by the solid line, the battery temperature never exceeds 300°K. As shown in test data, the cooler the battery remains (ideally, but impossibly, 278°K) the longer lifetime it has. However, if the charge rate is not closely monitored and the battery is allowed to overcharge, the battery temperature will rise to 308°K as shown in the dashed line.

Figure 4-110 illustrates the correlation between heat dissipated per unit area of the spinning ribs and rib temperature. The effective environmental sink temperature will range from 278° to 295°K; for design purposes the higher value should be employed for equipment layout on the spinning ribs and thrust cone. With 6 watts per pack dissipated during trickle charge, the battery temperature is 300°K with a radiation environment of 295°K and the rib configuration as of 3 July 1972. The temperature penalties associated with a specific rib configuration can be established with Figure 4-110.

4.9.3.4 Reaction Control System

The heater system will require approximately 0.3 w/meter of line and 0.75 watt per thruster to ensure that no portion of the system reaches

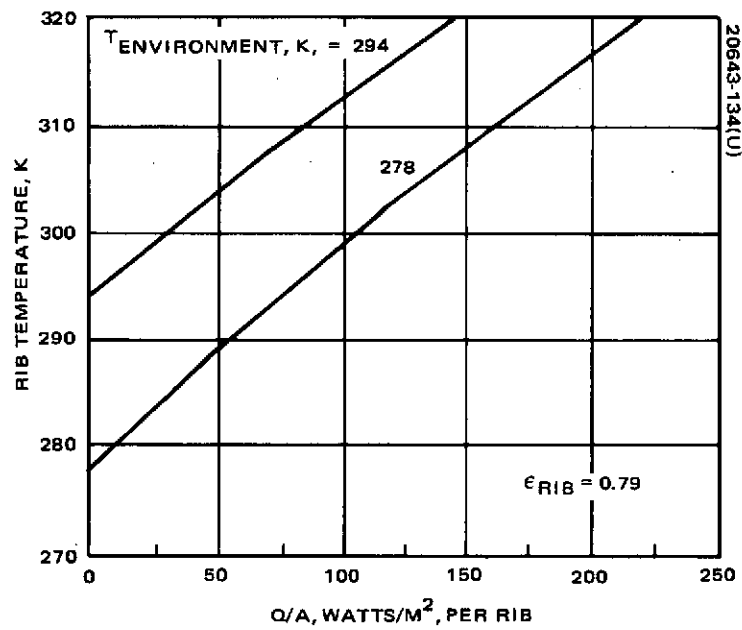


Figure 4-110. Rib Temperature Versus Input Wattage

the freezing point of hydrazine. The heater system is to be on continuously during the eclipse season and off for all other conditions.

4.9.3.5 Antenna/Mast Assembly

Mast deflection can be minimized either by using a low absorptance surface finish or, if high stability is required, by wrapping the mast with multilayer insulation. The key design parameters for the antenna tubular support structure are given in Figure 4-111. The temperature differentials across the tubes are plotted in Figure 4-112 for the chosen design parameters that are identified on the figure. The beryllium tubes will be wrapped with a combination of aluminum tape and aluminized teflon. The aluminum tape wrapping and the aluminized teflon wrapping each have the same absorptance ($\alpha = 0.17$). It can be seen in Figure 4-111 that the temperature differential across the 12.7 centimeter O.D., and 7.62 centimeter O.D. tubes are about 4 K and 1.7 K, respectively. The resulting deflection at the tip of these tubes is shown in Figure 4-113 based on the exposed tube lengths that are given in Figure 4-111. The design points indicate a deflection of about 0.15 and 0.38 mm for the 12.7 and 7.62 cm tubes, respectively. The larger deflection on the 7.62 cm tube is due primarily to the longer length of that tube since the deflection is a function of the square of the length. The deflections indicated result in an angular deflection at the tip of the tubes which is an order of magnitude less than the 0.01 radian allowable deflection.

4.3.9.6 Apogee Motor Integration

The temperature performance of the apogee motor in the transfer orbit will be very similar to that developed for the Canadian Domestic Communication Satellite motor. Figure 4-114 describes the temperature performance resulting from a detailed integration analysis of the Canadian Domestic Satellite motor, and shows that use of a 5 watt commandable heater at the throat can provide sufficient flexibility to meet the requirements for the full range of possible transfer orbit sun angles.

4.3.9.7 Aft Barrier Design

To maintain the required spacecraft heat balance a low emittance aft barrier is required. However, this barrier is subjected to transient high heating rates during the apogee motor and axial attitude thruster firings and, therefore, must sustain temperatures exceeding the limits of aluminized plastic films commonly utilized for barriers. The barrier design selected for the TDRSS is a single layer of stainless steel foil, locally stiffened and thermally isolated at its attachment points. To limit its maximum temperature the exterior surface of the foil is coated with Bo-Chem black oxide and with hanovia gold on the interior surface to provide the required thermal isolation. The design is utilized on the Canadian Domestic Satellite.

20643-135(U)

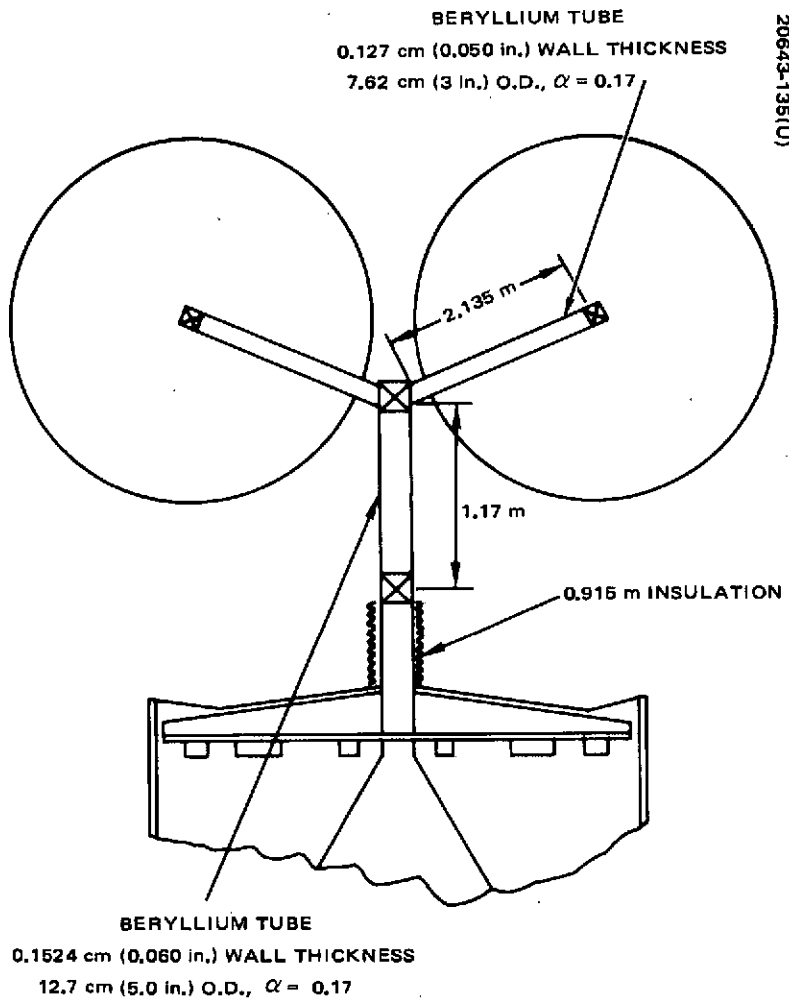


Figure 4-111. Configuration Analyzed for Thermal Distortion of Antenna Support Tubes

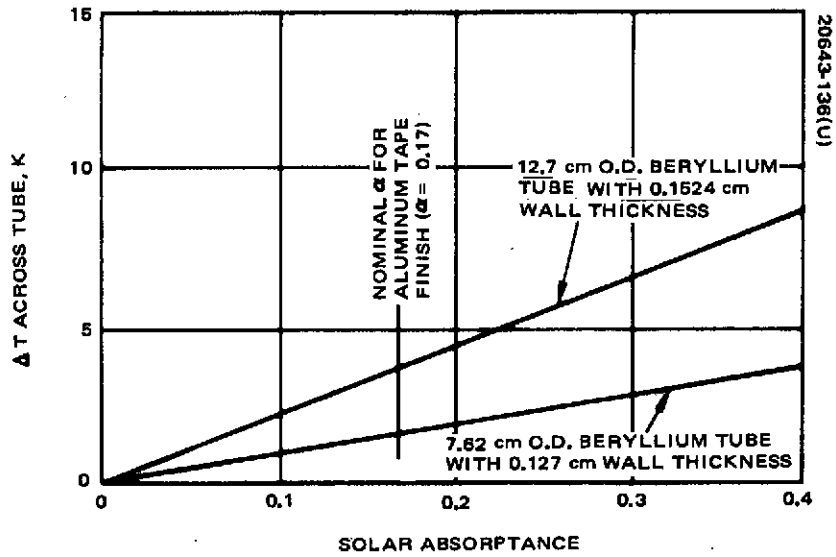


Figure 4-112. Tube ΔT Versus Solar Absorptance

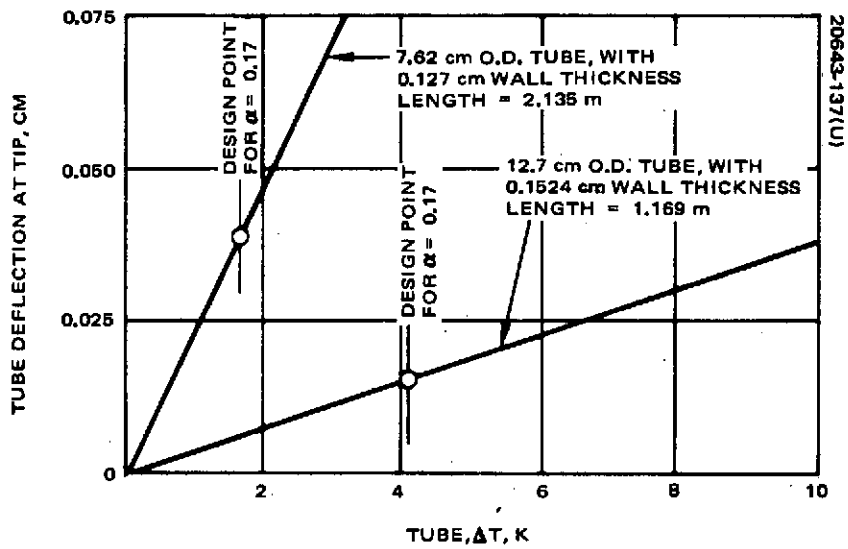


Figure 4-113. Tube Deflection Versus Tube ΔT

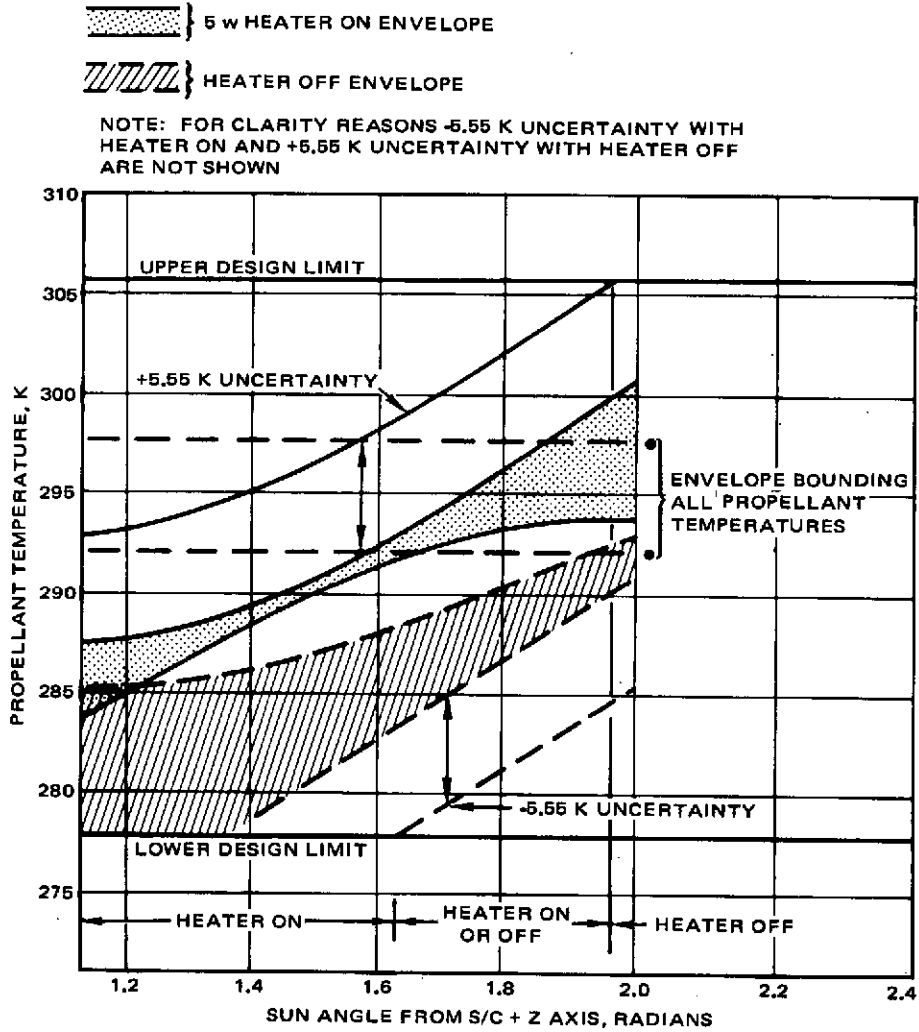


Figure 4-114. Apogee Motor Propellant Temperature Envelope

Heating Rates. Barrier design conditions are set by the apogee motor firing since higher combustion temperature and thermal radiation from the solid phase of the exhaust plume lead to higher heating rates. The arrangement of the motor nozzle, thrust tube, aft barrier, and solar panel is shown schematically in Figure 4-115. As indicated the barrier consists of an inverted truncated cone extended between the thrust tube and the aft edge of the cylindrical solar panel, and a flat annular disk closing out the region between the motor nozzle and the thrust tube.

The motor considered in the heating analysis is the Hercules, Inc. design optimized to utilize the maximum nozzle expansion ratio allowable by the TDRSS envelope. Table 4-65 summarizes the characteristics of this design. Exhaust plume characteristics were not generated for this particular motor because of time limitations. Instead an existing plume model, including boundary layer expansion generated for the Aerojet SVM-4A motor (flown on the Intelsat IV spacecraft) was used. This has a 40:1 nozzle and a similar chamber pressure. The lower expansion ratio should yield conservative local densities when used for the TDRSS analysis.

The method of characteristics solution of the SVM-4A exhaust plume into a vacuum results in the flow characteristics shown in Figure 4-116, 4-117, and 4-118. Applying these results to the TDRS system geometry leads to the definition of local density, Mach number, and flow impingement angles over the barrier. Examination of local molecular mean free path, based on local densities, indicates values on the order of an inch. Classically, the criterion for determining whether significant continuum interaction is present or free molecule flow exists is the Knudsen number, i.e., the ratio of mean free path to the "blocking" dimension of an immersed surface. However, since in this case the barrier is large relative to the exhaust flow field, the choice of a suitable characteristic length is less straightforward. If surface dimensions are considered, the flow is certainly continuum in nature. If flow field related dimensions such as shock layer

TABLE 4-65. TDRS/HERCULES BASELINE APOGEE MOTOR CHARACTERISTICS

Propellant mass	293 kg
I_{sp}	302.2 seconds
Burn time	21.2 seconds
Average chamber pressure	4.28 mn/m ²
Nozzle exit diameter	57.7 cm
Nozzle expansion (area) ratio	50:1

20643-138(U)

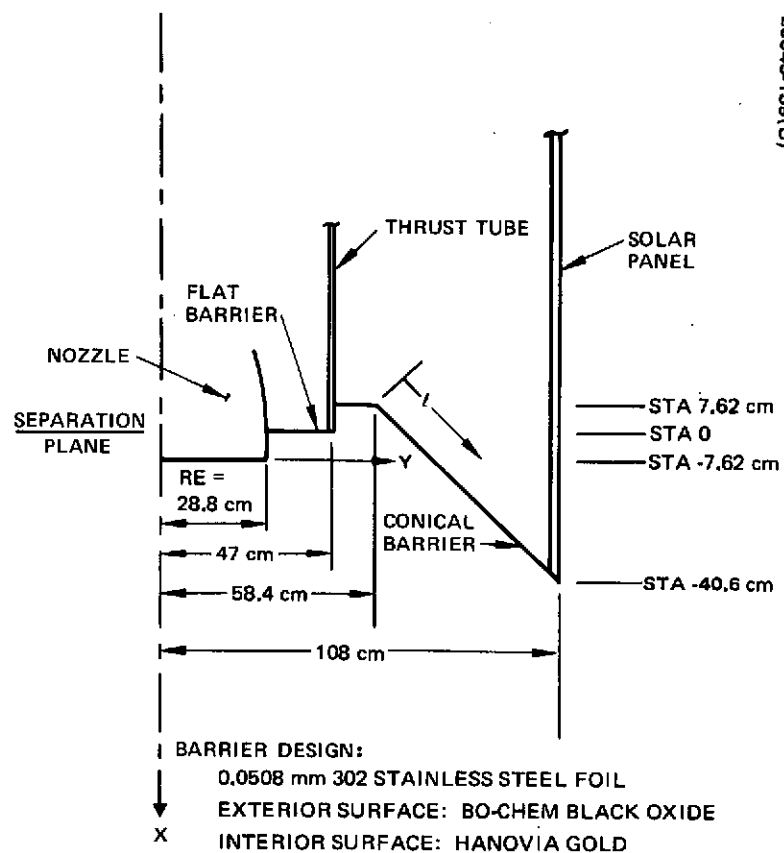


Figure 4-115. Barrier/Nozzle Geometry

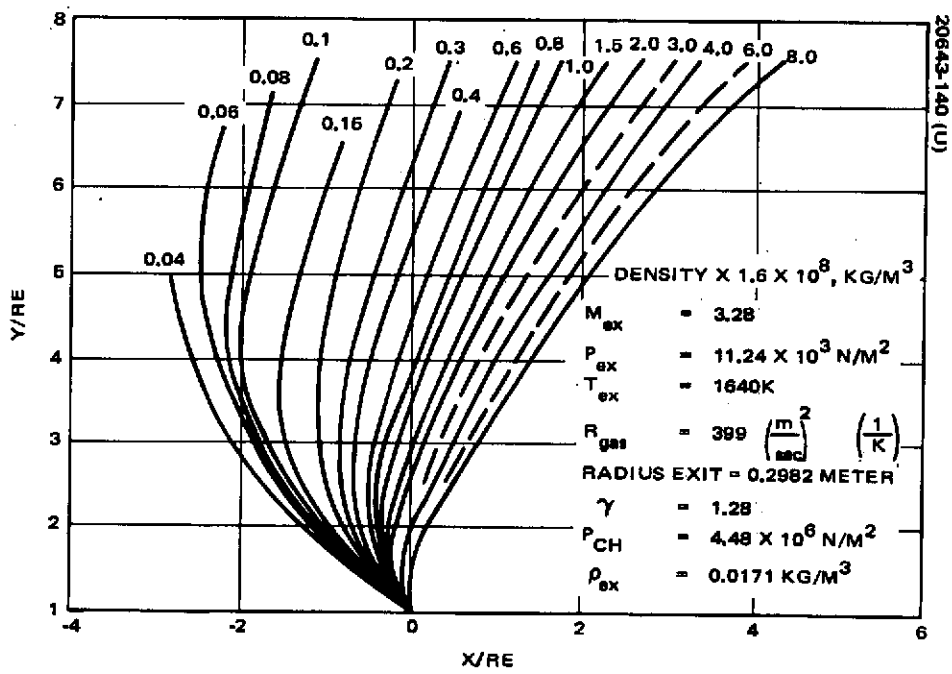


Figure 4-116. Intelsat IV Apogee Motor Plume Density With Boundary Layer

$M_{ex} = 3.28$
 $P_{ex} = 11.24 \times 10^3$
 $T_{ex} = 1640K$
 RADIUS EXIT = 0,2982 m
 $R_{gas} = 399 \left(\frac{m}{sec} \right)^2 \left(\frac{1}{K} \right)$
 $\gamma = 1.28$
 $P_{CH} = 4.48 \times 10^6 N/M^2$
 $\rho_{ex} = 0,0171 KG/M^2$

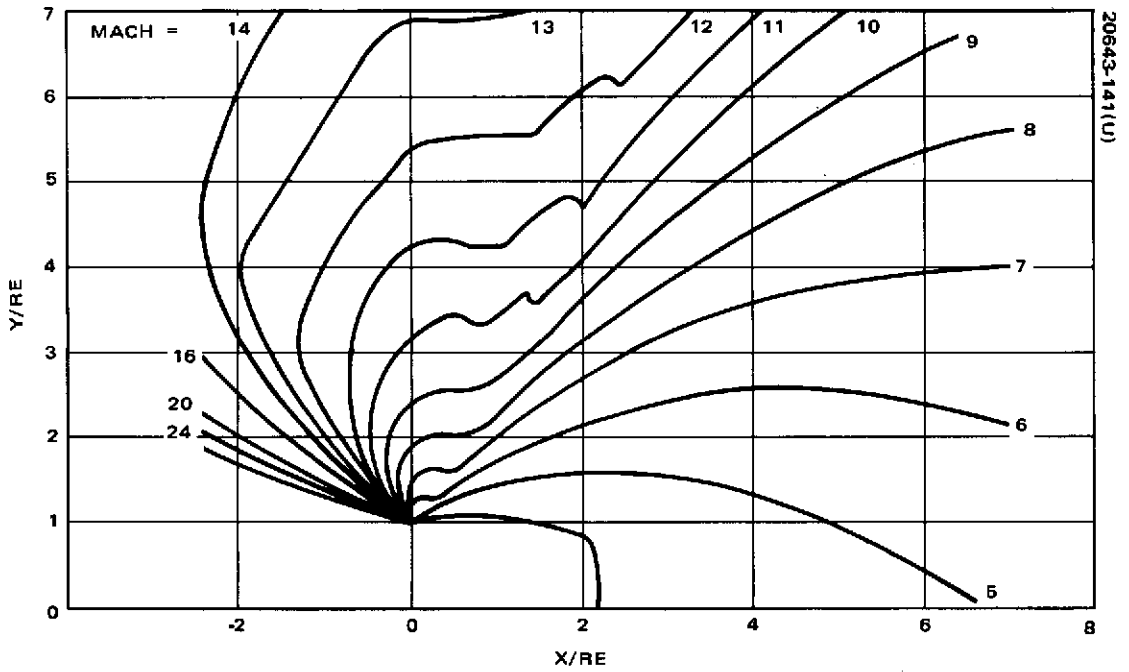


Figure 4-117. Intelsat IV Apogee Motor With Boundary Layer Constant Mach Lines

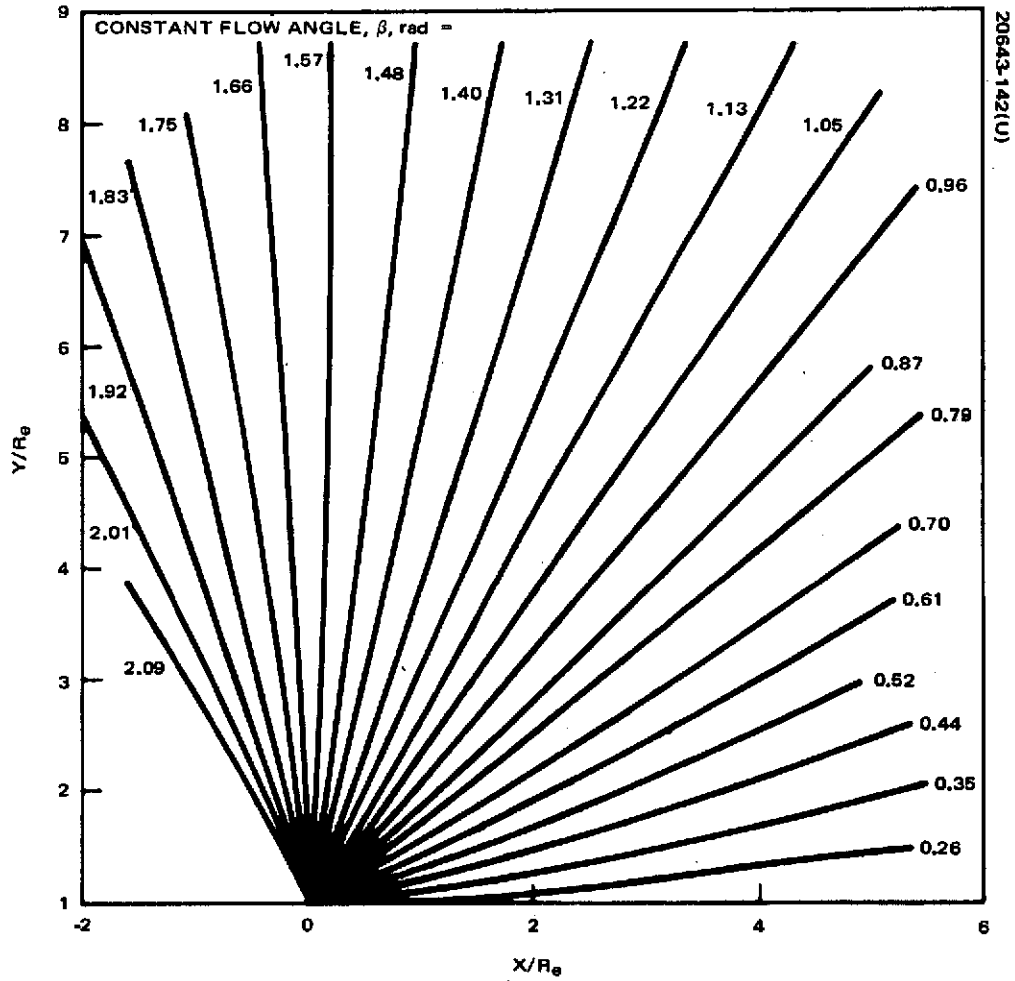


Figure 4-118. IntelSat IV Apogee Motor With Boundary Layer Constant Flow Angles

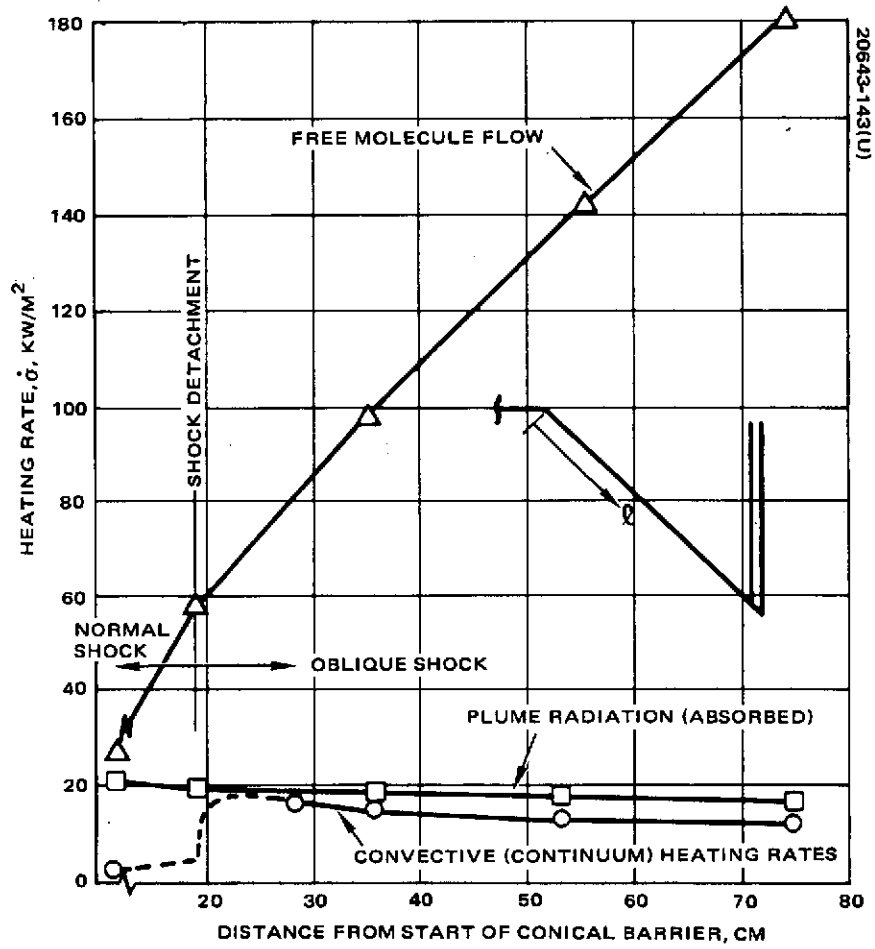


Figure 4-119. Conical Barrier Heating Rates Versus Distance Along Barrier

thickness are considered then the flow is transitional. This latter regime is difficult to describe analytically. Experimental investigation of impingement on large flatplates aligned parallel to or at moderate angles to the centerline of exhaust plumes indicate that continuum effects are present as represented by the complex system of detached and oblique shock layers observed at these plates.

Continuum heating rates along the conical barrier are shown in Figure 4-119. As indicated, there is a region over which an oblique, attached shock wave is predicted to exist. Flatplate laminar boundary layer heating rates in this region are computed using the classical oblique shock relationships to compute local conditions at the surface. Boundary layer running length is based on the distance from the point of shock attachment. Heating rates in the region of a normal shock are based on the correlation of Peisik, Koppang, and Simkin.* At the point of shock attachment, the heating rate is undefined and was estimated by fairing the heating rates from either side of this point. Also shown in Figure 4-119 are the computed free molecule flow heating rates. Based on the computed mean free paths it is felt that these much higher rates are not realistic. The radiation heating rates predicted for this plume are also included in Figure 4-119. These rates were based on the scaling of radiometric measurements obtained for the Thiokol TE 364-1 motor (Surveyor retro motor). Exit plane radiosity was determined to be $\sim 74,000 \text{ w/m}^2$.

Because of the similarity in propellant for this motor and the TDRS motor, radiosity can be scaled by propellant mass flow rate and exit plane flow velocity. This results in a scaled radiosity of $78,240 \text{ w/m}^2$ (6.9 Btu/sec ft^2). It is assumed that radiosity decays in direct proportion to the distance from the nozzle exit plane. The radiation heating rates are based on this radiosity model, the local barrier view factors to the hypothetical conical surface formed by the extension of the nozzle downstream of the exit plane, and the barrier absorptance. Heating rates were similarly derived for the annular disk portion of the barrier and shown in Figure 4-120.

Barrier Temperatures. The predicted maximum temperature distribution along the conical barrier is shown in Figure 4-121. Combined heating rates are so high that equilibrium temperatures are reached in about 10 seconds. The present sustained maximum allowable temperature for this barrier design is 923°K . As indicated the predicted temperatures exceed this limit, particularly in the region of shock attachment. However, for short exposure it is estimated that 1250°K can be withstood. Additional qualification testing will be required to verify this. Furthermore, the limiting elements are the black oxide exterior coating and the diffusion of the gold interior coating into the steel. Use of a 1590°K black coating and an increased gold layer thickness can be considered if necessary.

*"Rocket-Exhaust Impingement on a Flat Plate at High Vacuum," E. T. Piesick, R. R. Koppang, and D. J. Simkin, Paper No. 66-46, AIAA 3rd Aerospace Sciences Meeting, January 1966.

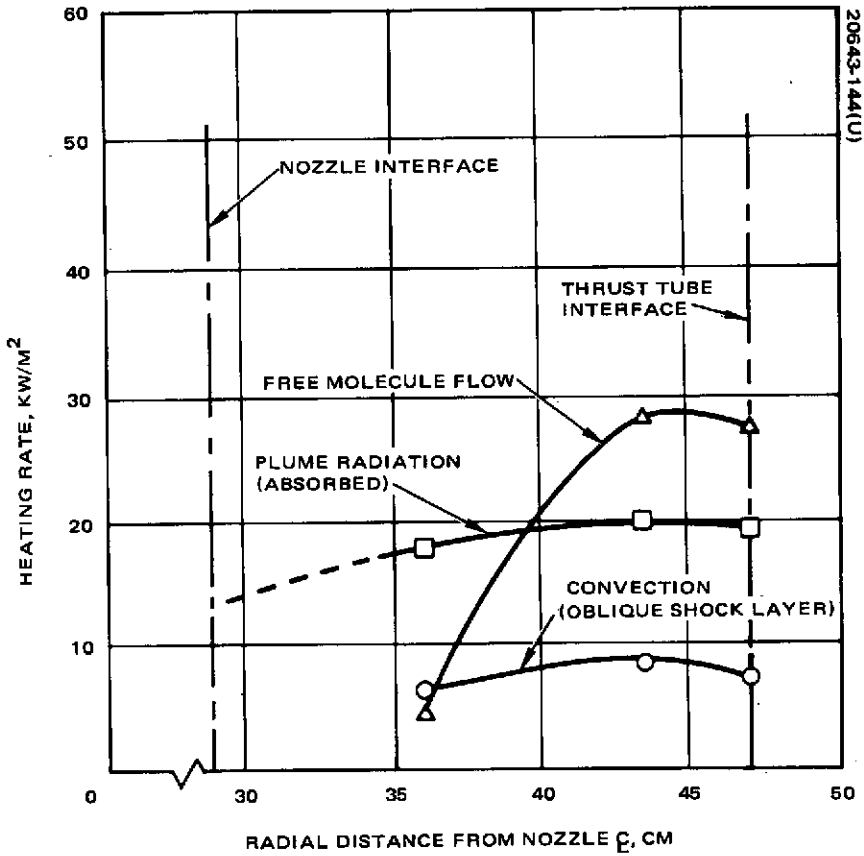


Figure 4-120. Flat Barrier Heating Rates

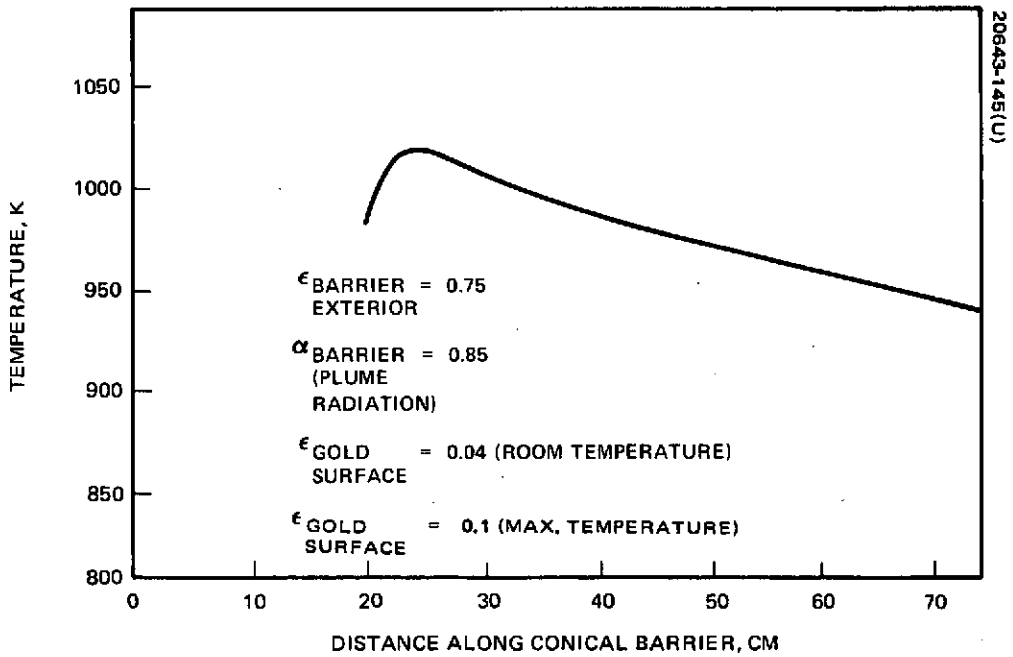


Figure 4-121. Maximum Conical Barrier Temperatures During Apogee Motor Firing

The maximum temperature of the annular disk portion of the barrier is predicted to be about 923°K. The effect of these high barrier temperatures on the solar panel temperature was briefly examined. Based on an emittance of the gold surface equal to 0.1 at maximum temperature, the solar panel temperature is predicted not to exceed 339°K locally in the worst case. This is well below the panel limit of 394°K.

APPENDIX. ATTITUDE AND DESPIN CONTROL SYSTEM

A. 1 FLAT SPIN RECOVERY PERFORMANCE

Flat Spin Dynamics

In the unlikely event of loss of despin control (e. g. battery failure during eclipse) the platform will slowly spinup due to bearing friction torque. Because of the platform cross product of inertia there will be a coning of the spin axis at the platform rotation rate. As long as the platform rotation rate is appreciably different from inertial nutation frequency, the transverse torque due to any rotating mass imbalance (represented by unequal platform transverse inertias and platform cross products of inertia) averages to zero over a nutation cycle.

For a vehicle with a roll/pitch ratio less than one, the inertial nutation rate is less than the initial rotor rate and in the same sense as platform rotation due to friction. Therefore, the platform rate will eventually coincide with the inertial nutation rate. When this happens, the transverse torques due to the rotating mass imbalance is temporarily phase-synchronized with the transverse velocity vector and thereby contributes to an increase in nutation (as illustrated in Figure A-1). For TDRS, it takes approximately 1800 seconds (30 minutes) for the platform to reach nutation rate.

If the friction is not too large relative to the effects of the cross-product, the platform inertial spin rate remains phase locked to the apparent nutation rate due to dynamic torque along the bearing axis. The moments due to the mass asymmetry then serves to continuously transfer spin momentum from the rotor to the transverse axis via bearing friction (which is the energy dissipating medium). If the bearing friction is large enough, or the effects of the cross-product is small enough, however, the dynamic bearing axis torque is overcome and the platform continues to accelerate until the relative rate between the two bodies is nulled. Then, energy dissipation due to fuel slosh would act to increase the nutation angle. The limiting relation between friction and cross-product for the phase lock condition is

$$I_{13} = \frac{T_F^{3/4} I_T^{7/4}}{H^{3/2}}$$

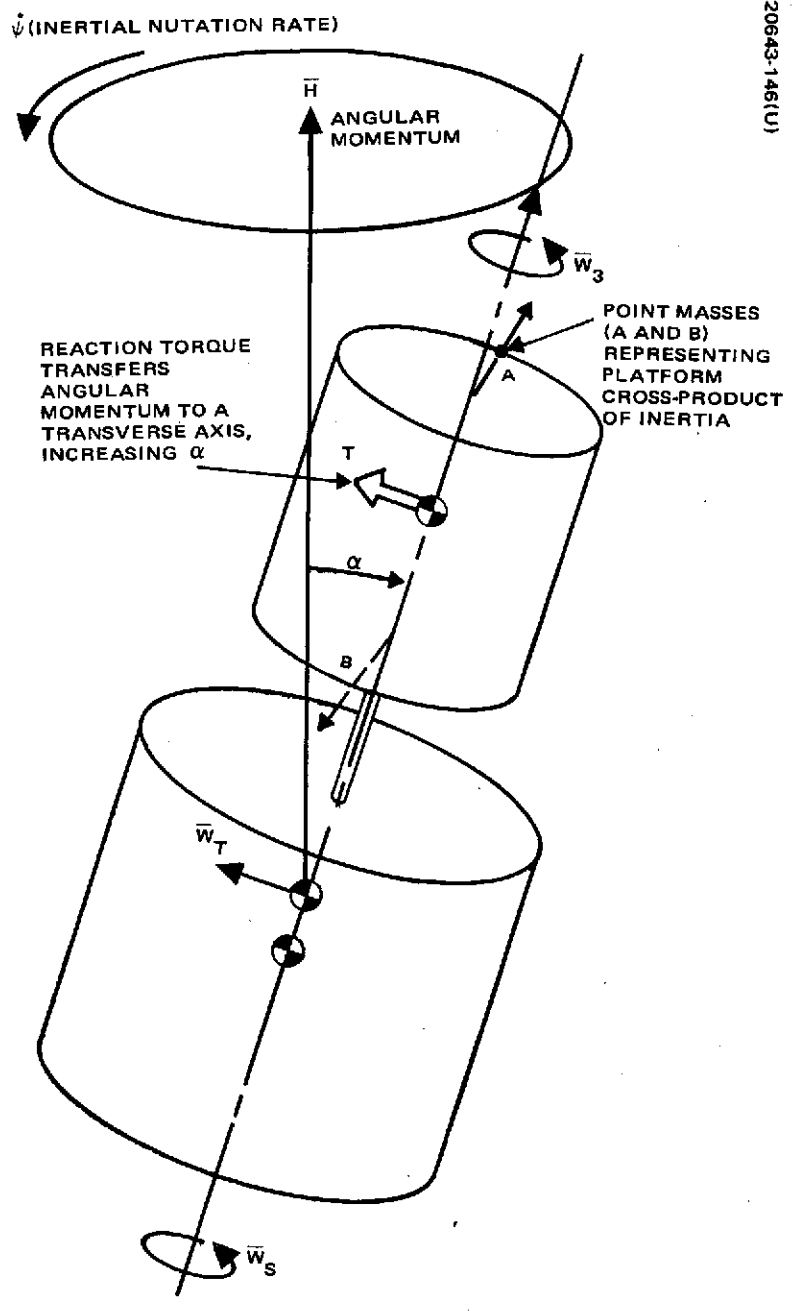


Figure A-1. Nutation Divergence Due to Spinup of Unbalanced Platform

where

I_{13} = platform cross-product of inertia

T_F = bearing friction torque

I_T = total transverse inertia

H = total angular momentum

For the TDRS this relationship shows that the phase lock condition will occur. The time required to reach the flat spin condition depends on the total energy dissipation. If bearing friction dominates, the complete divergence takes about 3600 seconds (1 hour). The divergence time decreases if other energy dissipators, such as fuel slosh, are even larger than predicted. The divergence time is not important since the despin control system must be capable of recover from a nutation angle of $\pi/2$ radians in any case.

Spacecraft Condition in Flat Spin

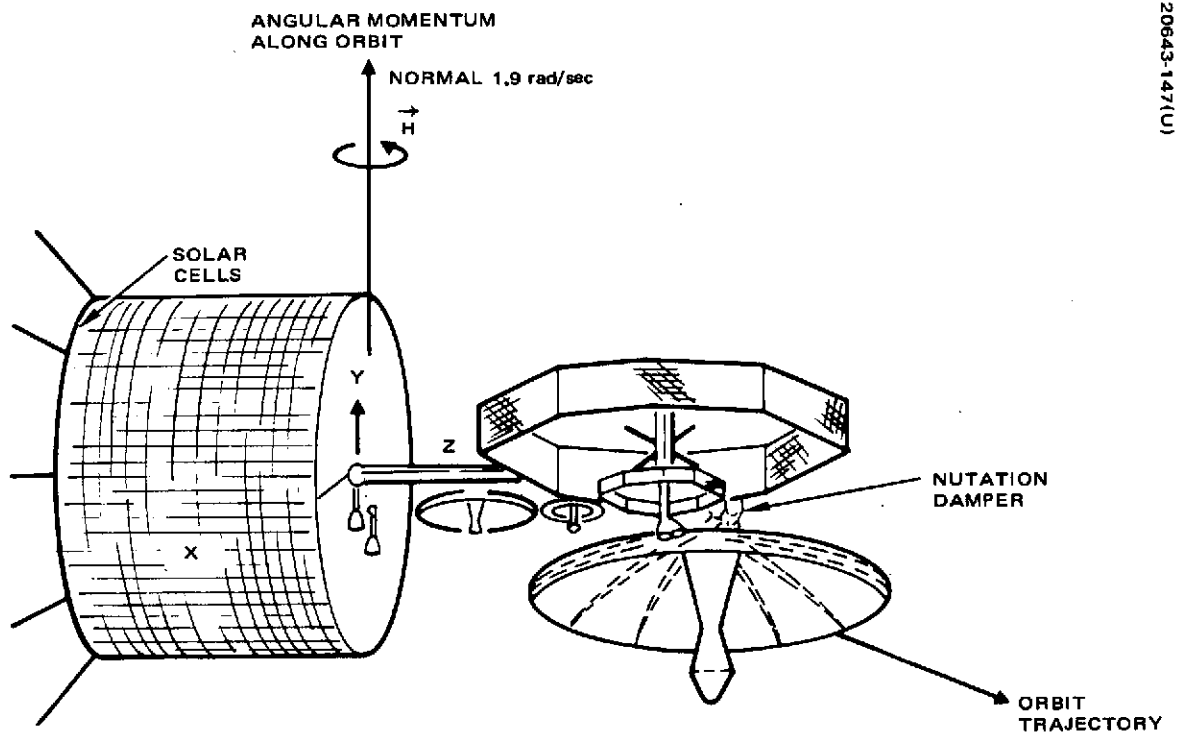
Figure A-2 illustrates the spacecraft attitude in the flat spin condition. The vehicle is rotating at 1.9 rad/sec (18 rpm) depending on inertias and nominal rotor spin rate, about its major axis of inertia (the y axis). There are small rotations in the Y-Z and X-Z planes due to small platform cross-products in these planes, but these are slight and may be neglected. The relative rate at the BAPTA interface is zero, and the inertial spin rates of both bodies about the bearing axis are zero.

The BAPTA experiences a loading in a flat spin that tends to separate the two bodies, but the bearing preload is larger than the separation force, thereby maintaining the normal single axis coupling.

The nutation damper is pinned against one of its stops due to centrifugal loading and its inverted orientation on the mast. The damper has at most a second-order effect on the system dynamics, except during the damping of residual nutation at the end of recovery to the nominal attitude.

Recovery Dynamics

In order to reorient the vehicle so that the bearing axis is coincident with the angular momentum vector, it is necessary to add energy in the form of rotor spin. Torque applied to spin up the rotor essentially plays an analogous but reverse role to that of friction in the divergence sequence. It has been shown that applied motor torque during recovery transfers momentum from the transverse axis to the spin axis through platform mass asymmetry. Recall the friction torque transferred momentum from the spin axis to the transverse axis through platform mass asymmetry.



20643-147(U)

Figure A-2. Spacecraft in Flat Spin Condition

Simplified relationships that govern the recovery process are

- 1) The minimum torque required to overcome the rotor mass asymmetries and cause it to spin up is given by

$$T (\text{min}) = \frac{\dot{\psi}^2}{2} [\Delta I_R \sin^2 \alpha]$$

where

$\dot{\psi}$ = inertial nutation frequency

α = angle between the X-axis and the angular momentum vector, measuring the precession cone

ΔI_R = rotor transverse inertia difference

- 2) The maximum allowable torque is that torque which overcomes the inertial torques and causes the platform to spin and is given by

$$T (\text{max}) = \frac{\dot{\psi}^2}{2} [\Delta I_P \sin^2 \alpha]$$

where

ΔI_P = platform transverse inertia difference

These relations are plotted in Figure A-3 for nutation angles from 0 to $\pi/2$ radians (90 degrees), along with the available motor torque.

Once the rotor asymmetries have been overcome and the recovery is proceeding, the only minimum constraint on torque is imposed by dampers such as fuel slosh. At the end of the sequence utilizing interbody torques, the despin control system despins the platform and acquires the earth. Since the angular momentum vector has not been perturbed during the entire divergence and recovery sequence, the final attitude ensures that earth sensor pulse will be received for normal DCS operation. The recovery process is complete when the platform is despun. A residual nutation angle of ≤ 0.087 radian (5 degrees) will exist. At this time both the rate and tracking loops of the despin system are providing substantial damping of nutation. The active nutation control may be activated to reduce nutation to within the linear range of the passive damper, but this is not required.

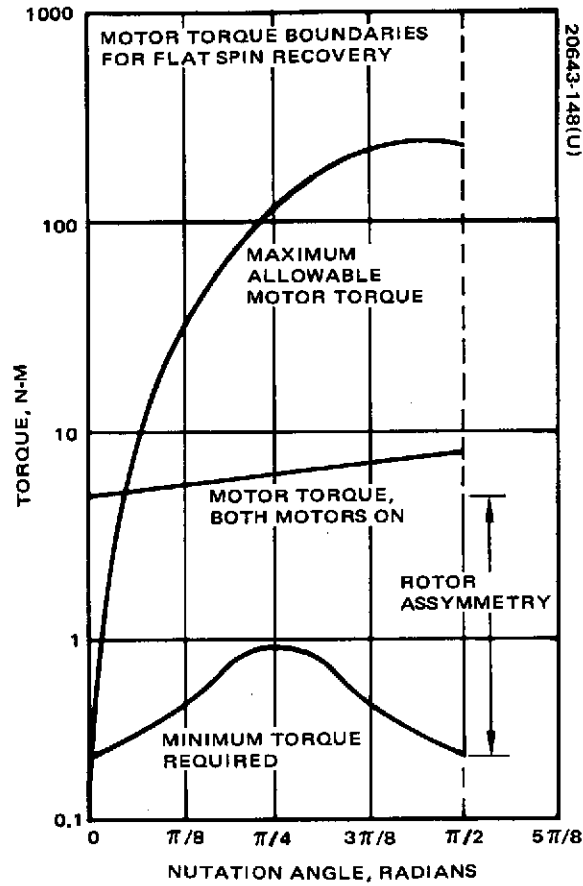


Figure A-3. Motor Torque Boundaries for Flat Spin Recovery

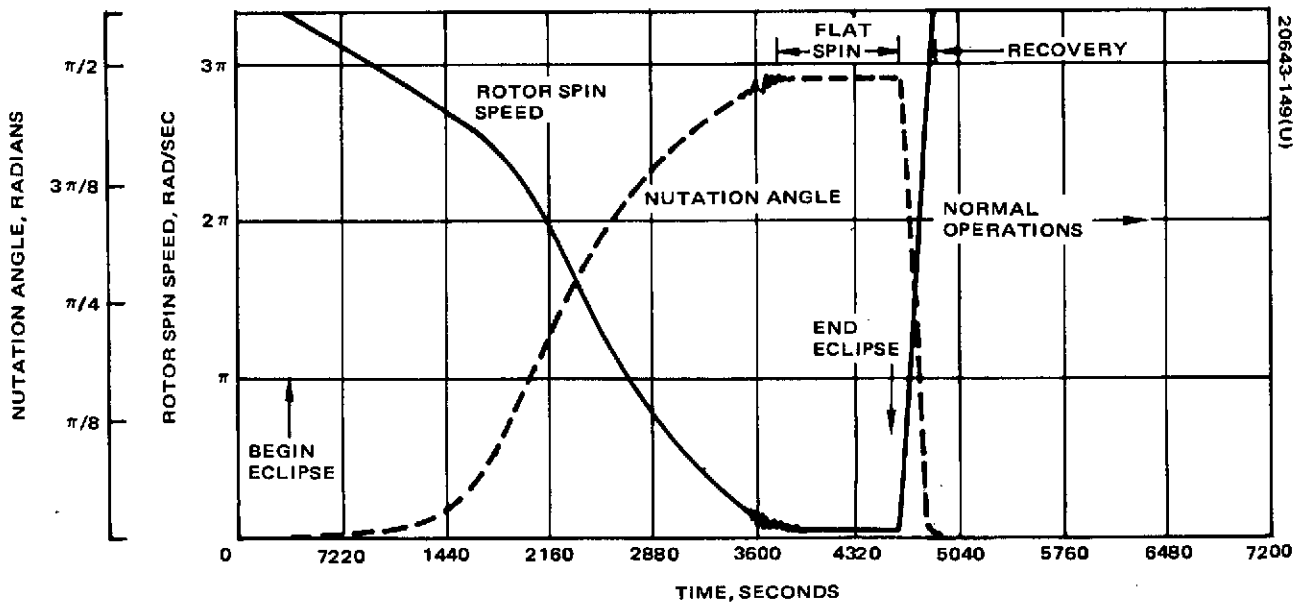


Figure A-4. Rotor Spin Rate and Nutation Angle During Flat Spin

Initialization of the despin control electronics ensures that recovery from a flat spin will occur automatically. For the condition of battery failure during eclipse resulting in a flat spin condition, the bus voltage at the end of eclipse will be similar to a rectified sine wave as the bearing axis sweeps past the sun line of sight. Thus as soon as the vehicle emerges from eclipse, full despin torque is applied in a duty cycle manner, increasing to constant torque as the cone angle decreases slightly from $\pi/2$ radians. The command for full torque is the normal logic state for the DCS when a low relative rate is sensed. The motor and drive electronics are designed to sustain the current loads at a stall condition

Flat Spin Simulation Results

A detailed simulation used to study the dynamics of flat spin was exercised for TDRS and the results are shown in Figures A-4 through A-6. They depict the spacecraft dynamic response during a maximum length eclipse of 4320 seconds (72 minutes). Figure A-4 shows the rotor spin speed (in radians per second) and the spacecraft nutation angle (in radians) over a period of time from 300 seconds before the eclipse to about 2700 seconds after the end of eclipse. Time is indicated in seconds on the curves. Figure A-5 shows the inertial body rates of the platform (in radians per second). The motor torque and the total torque opposing the motor due to energy dissipators (principally fuel slosh and bearing friction) are shown in Figure A-6.

At $t = 300$ seconds, the eclipse starts. Motor torque goes to zero, and the platform spins up due to bearing friction. When the platform rate reaches approximately 1.1 rad/sec (11 rpm), the transfer of spin momentum into transverse momentum via the cross-product of inertia begins. Approximately 600 seconds are required to reach this point.

At the nutation angle increase, the platform roll orientation changes slowly so that in the final state, the vehicle is spinning about the Y axis, which is the major principal axis of inertia. This can be seen by the response in ω_1 and ω_2 radians per second in Figure A-5. Note that both ω_3 radians per second (Figure A-5) and ω_s radians per second (Figure A-4) are decreasing as the spin axis momentum is removed.

At $t = 4620$ seconds, the spacecraft emerges from eclipse, and full despin motor torque is applied. Because of the varying angle between the sun line and the bearing axis, the despin electronics turn on and off in a pulse manner until the nutation angle is reduced enough to maintain a constant component of solar cell power. This small reduction in the net applied torque does not adversely affect the recovery, as shown in the figures. The normal initialization logic results in both motors being on, as shown in the simulation. The recovery to under 0.085 radian (5 degrees), using the despin motor, takes approximately 600 seconds after emergence from eclipse. The residual nutation is then reduced by the despin system and the passive damper. Operation thereafter is completely normal. No commands to the spacecraft are needed to perform the recovery as described. For eclipses

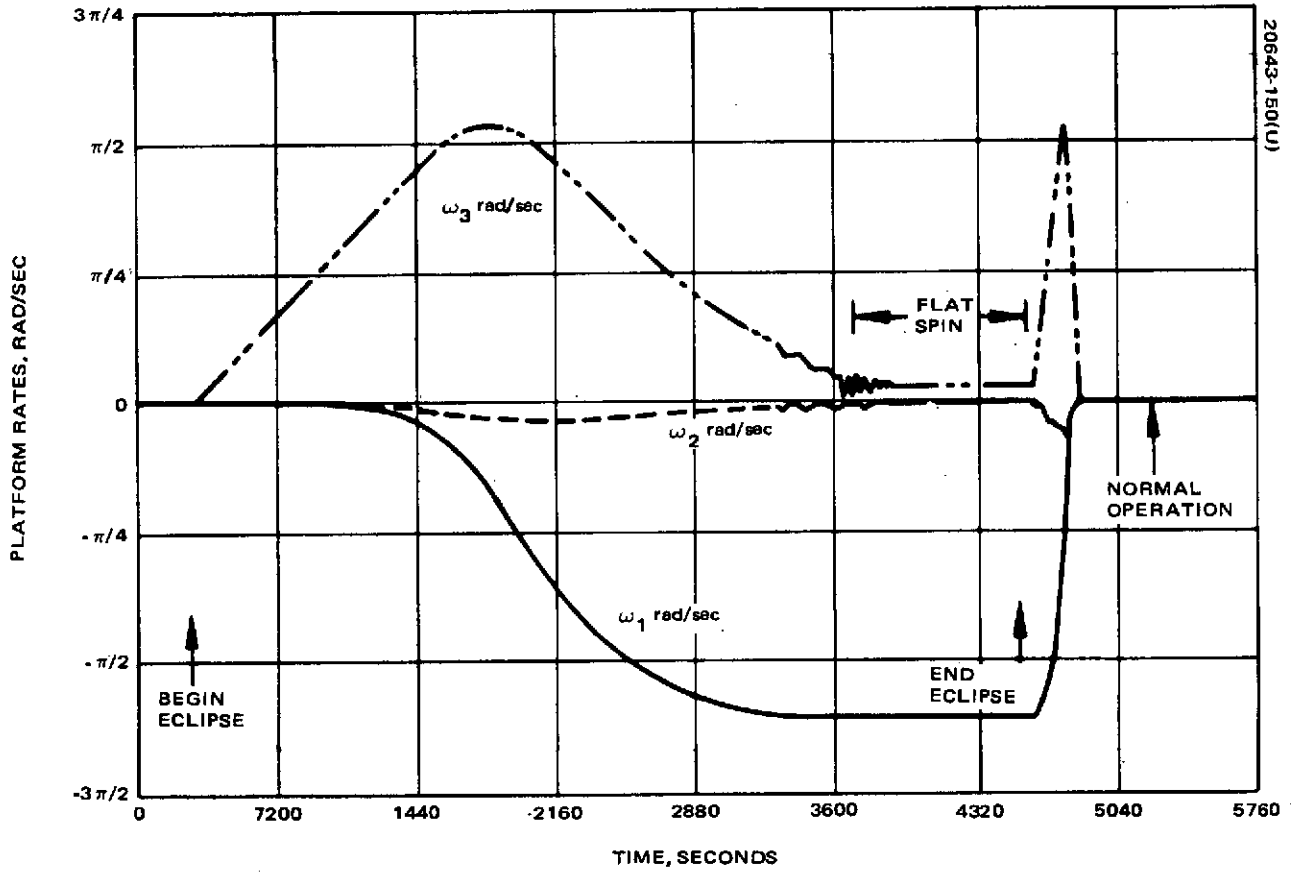


Figure A-5. Platform Rates During Flat Spin

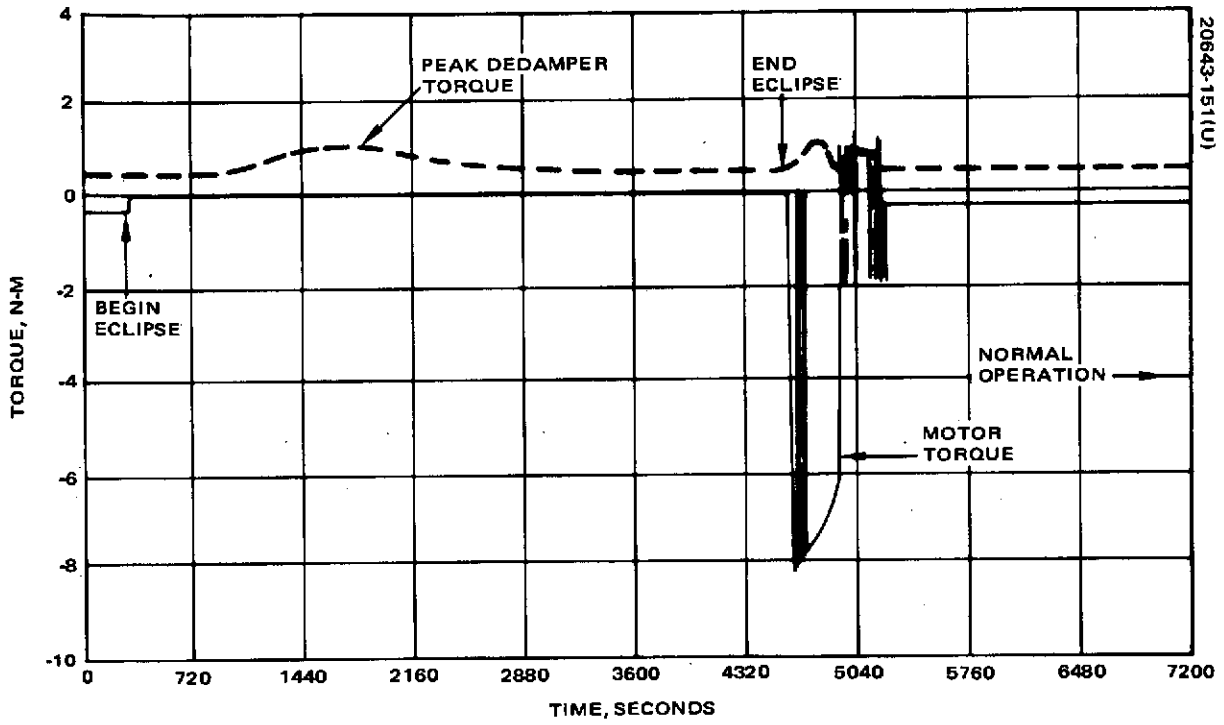


Figure A-6. Motor Torque and Dedamper Torque During Flat Spin

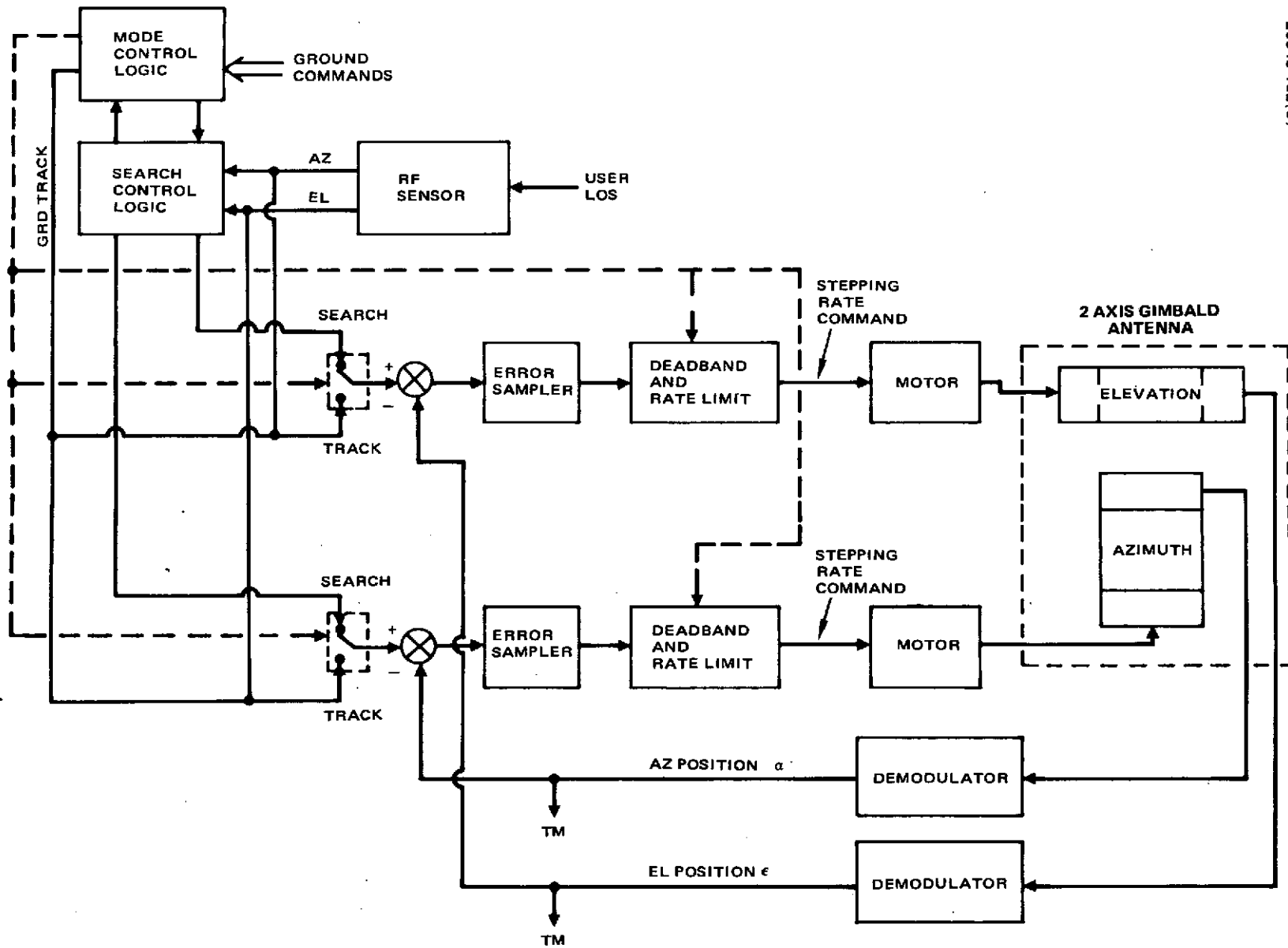


Figure A-7. S Band Gimbal Control System Block Diagram

shorter than about 2700 seconds, the maximum nutation angle is less than $\pi/2$ radians. The same recovery procedure is effective at all nutation angles, however. Simple application of despun motor torque causes the desired transfer of system momentum back into the spin axis.

A. 2 S BAND ANTENNA DYNAMICS/AUTOTRACK EVALUATION

Autotrack Trade Study

This subsection presents a preliminary tradeoff study on autotrack versus ground command of the TDRS S band antenna. The principal factors considered are:

- Cost
- Mass
- Power
- Dynamic interactions

Figure A-7 is a simple block diagram of the S band gimbal control system. The essential difference between autotrack and ground command is the addition of the RF sensor block for autotrack. The remaining elements are presently assumed identical for both systems, including the S band antenna beamwidth of 0.044 radians (2.5 degrees). The addition of autotrack (specifically the RF sensor) contributes the following penalties:

- Total cost (including six spacecraft) - \$450K
- Mass - 4.54 kg per spacecraft
- Power - 8 watts per spacecraft

A preliminary analysis (see following) indicates that the dynamic interaction effects between the spacecraft and the gimballed S band antenna are as follows:

- The antenna has for all practical purposes, zero response to a wobble (spin frequency) excitation
- The nutation amplitude developed as a result of open loop (ground command) tracking is ≤ 0.00033 radian (0.019 degree), a negligible amount.
- The S band antenna in an autotrack mode will have no effect on the vehicle nutational stability for nutation angles less than 0.0016 radian (0.09 degree) (a function of the deadband size).

For angles exceeding 0.0016 radians, a small potentially unfavorable effect is possible. An extensive study is required in this area to adequately determine the system response.

In conclusion, it appears that dynamic interaction effects are a very minor consideration in comparing autotrack to open loop ground command. The principal considerations are apparently cost, weight, and power.

Dynamic Considerations of Autotracking and Ground Command Tracking Antennas

The proposed configuration of the TDRS contains an S band parabolic reflector that is capable of tracking a radiating target. The track is accomplished either by open loop ground command or by an on-board, closed loop system, and consists of repositioning the antenna in azimuth and elevation so that its electrical boresight remains coincident (or very nearly so), with the center of the beam emanating from the target. As in all tracking systems, it is necessary to examine what impact the tracking capability will have on the overall vehicle dynamic performance. Such an examination has been carried out, the results of which are discussed in the following paragraphs.

The design of the TDRS is such that one would not expect any dynamical problems to arise because of the tracking antenna. The antenna is relatively light (its weight is less than 2.5 percent of the total vehicle in orbit weight), and therefore the reaction torque that it exerts on the platform in a tracking situation will be rather small. Also, the antenna is structurally stiff with its lowest structural frequency of 3 Hz well about the wobble and nutation excitation frequencies of 1.67 and 0.33 Hz, respectively. Hence, no adverse interaction between the vehicle structure and the control loop or nutation dynamics should result. Finally, the tracking control loops are relatively slow performing in comparison with the platform nutation period. This "slowness" in tracking loop response, which results from a maximum design slew rate of 1 step per 2 seconds (1 step = 0.00031 radians, or 0.018°), and the inclusion of a deadband of ± 5 steps will significantly reduce any coupling between the tracking performance and the vehicle nutational behavior. Hence, one would not expect the dynamics of the TDRS with tracking S band antenna to differ appreciably from an alternate version of the same vehicle in which the S band antenna is locked in its nominal position. Previous studies on the dual spin vehicle/tracking antenna interaction have indicated, however, that two areas of dynamic performance require careful scrutiny. These are vehicle/antenna wobble response and system nutational stability.

Wobble Response

Wobble is the term used to describe the coning motion of the vehicle bearing axis which results from rotor unbalance. The rotor is nominally designed so that its bearing axis is a principal axis of inertia and so that the rotor mass center lies along the bearing axis. For a variety of reasons

(i. e. , balancing machine tolerances, bearing misalignment, apogee motor propellant residuals, etc.) this design condition is never perfectly satisfied; and the resulting rotor unbalance causes the bearing axis to wobble at rotor spin frequency in a near circular motion about the system angular momentum vector (Reference 1). The wobble magnitude is inversely proportional to the difference between the rotor spin inertia and the vehicle transverse inertia. For a Gyrostat vehicle, this inertia spread is quite large and provides wobble angles of small amplitude. For example, the average measured wobble amplitude for the first three Intelsat IV vehicles is 0.00052 radians (0.03 degree).

When a tracking antenna is mounted on a dual spin vehicle, three wobble related problems can develop.

- 1) Depending on the vehicle/antenna mass geometry, a small amplitude wobble excitation can produce a large amplitude antenna oscillation.
- 2) The antenna in an autotracking mode can draw excessive power in attempting to track out the high frequency wobble motion.
- 3) In a quiescent or nontrack mode, the control loop may provide insufficient torque to hold the antenna against a wobble excitation, with excessive wear in the gimbal and motor system resulting.

For the proposed TDRS design, none of these problems arise. The amplification factor relating wobble amplitude to antenna oscillation amplitude is essentially zero; that is, the wobble oscillation excites no motion of the antenna relative to the platform. The inertia torques are simply insufficient to overcome the motor detent torque when amplified by the harmonic drive. Also, because of the ± 5 step deadband in the autotrack control loop (i. e. , ± 0.0016 radian, or 0.09 degree), no attempt is made to track out the wobble motion unless it exceed 0.0016 radian – an extremely unlikely situation. Finally, in a quiescent or hold mode, the motor detent torque applied at the antenna gimbal will never be less than (2.8 newton-meters (25 in -lb). A simple calculation (see subsection on dynamics analysis) indicates that this power off detent torque is sufficient to hold the antenna against a wobble oscillation, provided that wobble amplitude is less than 0.0028 radian (0.16 degree). Hence, one can conclude that the antenna tracking system has, for all practical purposes, zero response to a wobble excitation, and that as far as bearing wobble is concerned, the S band antenna can be treated as if it were rigidly mounted to the platform.

Nutational Stability

The nominal equilibrium condition for a dual spin vehicle consists of pure spin of the rotor about the bearing axis, with the bearing axis and system angular momentum vectors aligned. An internal or external disturbance will cause the bearing axis to nutate about the angular momentum

vector. If the nutational motion decays with time, the vehicle is said to be nutationally stable.

On a Gyrostat vehicle, nutational stability is achieved (in part or total) by means of a passive damper mounted on the platform. A nutational transient causes the damper to oscillate at platform nutation frequency. This oscillation exerts a reaction torque on the platform that is out of phase with the vehicle transverse rate vector (angular rate normal to the bearing axis). Hence, the transverse rate decays with time, and the bearing axis returns to its position of coincidence with the angular momentum vector.

An autotracking antenna behaves somewhat like a passive nutation damper in that in attempting to track out a nutation transient, the antenna oscillates relative to the platform and at platform nutation frequency. However, this oscillatory motion exerts a reaction torque on the platform that is not necessarily out of phase with the vehicle transverse rate vector. As shown in Reference 2, the autotracking motion can be stabilizing or it can be destabilizing depending, on the vehicle/antenna mass properties and the design of the autotracking control loops.

For the TDRS, the S band antenna mass properties and gimbal arrangement are such that the autotracking motion would be stabilizing if the control loops were indeed designed to track out the vehicle nutational motion. However, the control loops have not been so designed since such rapid tracking capability is not required. The ± 0.0016 radian (0.09 degree) deadband in the autotracking loops will ensure that no relative motion of the antenna occurs (and hence no effect on stability) for nutation angles less than 0.0016 radian. For nutation amplitudes exceeding 0.0016 radian, a rather sluggish motion of the antenna relative to the platform will result, with a maximum rate never more than 0.00031 radian (0.18 degree) in a 2 second period. Extensive analysis will be required to determine if this latter motion is stabilizing or destabilizing.

It is shown in the subsection on dynamic analysis that if the autotracking motion is destabilizing, the effect is easily offset by the nutation damper provided its time constant does not exceed 600 seconds. Thus the S band antenna in an autotrack mode will have no effect on vehicle stability for nutation angles less than 0.0016 radian (0.09 degree) and a small unfavorable effect for nutational angles exceeding 0.0016 radian, only if a worst case situation develops. Such a worst case situation is easily alleviated by the inclusion of shaping in the control loop design.

In addition to the autotrack mode, the antenna can track a target in open loop fashion by ground command. In this case, each ground commanded antenna step will cause a small nutation transient with a worst case situation developing if the antenna is stepped in synchronization with the platform nutation period; that is, if the target angular rate corresponds to one step each nutation period 0.00031 radian, or 0.18 degree, per 3 second interval). Under this set of circumstances, the nutation amplitude induced by any one

step will add linearly to that amplitude induced on the preceding steps, thereby producing a maximum nutation state. As shown in the dynamic analysis below, this maximum level satisfies

$$\theta_{\max} = 0.0155 \Delta \frac{\tau}{\tau_1}$$

where Δ is the step size (0.00031 radian), τ_1 is the nutation period (3 seconds), and τ is the nutation damper time constant. Using a conservative estimate of 200 seconds for τ , the largest possible nutation amplitude that can develop as a result of open loop tracking becomes

$$\theta_{\max} = 0.00033 \text{ radian (0.019 degree)}$$

Thus, no nutational problems are anticipated as a result of the open loop tracking mode.

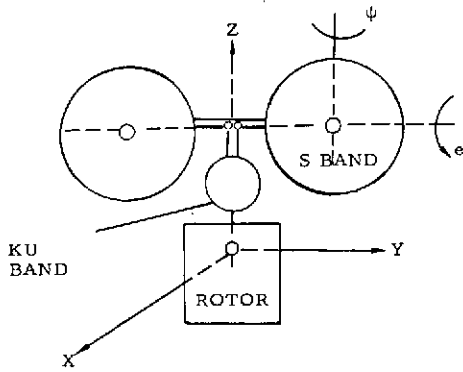
In summary, the inclusion of a tracking capability for the S band antenna will have essentially no impact on the dynamic behavior of the TDRS. The tracking control loops are too slow and the antenna structural frequencies too high to provide any appreciable interaction with the vehicle nutational or wobble motions. Hence, to develop preliminary design assessments of overall system performance, it will suffice to treat the S band antenna as if it were rigidly mounted to the vehicle platform.

Dynamic Analysis

To assess the effect of the S band antenna, the model of the system shown in Table A-1 is used. In this model the antenna is set at its nominal position with the boresight axis parallel to the platform x axis. During track, the antenna can differ as much as 0.25 radian (15 degrees) in azimuth and elevation from this position. However, the 0.25 radian change in orientation will have negligible effect on the results and is therefore neglected. Also, the two vehicle transverse inertias are equal in the model of Table A-1, but differ by about 20 percent for the proposed design. Equating the inertias simplifies the calculation without appreciably altering the results.

The system angular momentum vector \underline{h} has component representation

TABLE A-1. ANTENNA/VEHICLE MASS PROPERTIES



Nomenclature

- I_g = inertia of S band about gimbal center
 $= I_{cg} + m_s (\underline{u} \cdot \underline{u} - \underline{u}\underline{u}^T)$
- $J_1 = I_{cg} + m_s (\underline{r} \cdot \underline{r} - \underline{r}\underline{r}^T)$
- I_{cg} = inertia of S band about its mass center
- \underline{u} = vector from gimbal center to antenna mass center
- \underline{r} = vector from vehicle to antenna cg
- I = inertia of vehicle about vehicle cg
- C_1 = rotor spin inertia
- e = antenna elevation angle (zero in diagram)
- ψ = antenna azimuth angle (zero in diagram)

S band Antenna (Nominal Position)**

$m_s = 9.07 \text{ kg (20 pounds)}$

$$I_g = \begin{pmatrix} 8.8 & 0 & 0 \\ 0 & 6.8 & 0 \\ 0 & 0 & 6.8 \end{pmatrix}; \text{ kg-m}^2$$

$$J_1 = \begin{pmatrix} 9.7 & -6.3 & -8.6 \\ 0 & 6.8 & 0 \\ 0 & 0 & 6.8 \end{pmatrix}; \text{ kg-m}^2$$

$$\underline{u} = \begin{pmatrix} 0.3 \\ 0 \\ 0 \end{pmatrix}; \text{ meter}$$

$$\underline{r} = \begin{pmatrix} 0.3 \\ 2.3 \\ 3.1 \end{pmatrix}; \text{ meter}$$

Vehicle

$m = 364 \text{ kg (803 pounds)}$

$$I = \begin{pmatrix} A & & I_{xz} \\ 0 & & I_{yz} \\ I_{xz} & I_{yz} & C \end{pmatrix}$$

- I_{xz}, I_{yz} arbitrary but small
- $A = 599 \text{ kg-m}^2 \text{ (440 slug-ft}^2\text{)}$
- $C = 283 \text{ kg-m}^2 \text{ (slug-ft}^2\text{)}$

Rotor

$C_1 = 120 \text{ kg-m}^2 \text{ (88 slug-ft}^2\text{)}$

**Nominal position occurs when S band boresight is parallel to x axis of platform.

CS

$$\underline{h} = \underline{h}_o + \delta \underline{h}; \underline{h}_o = \begin{pmatrix} A\omega_x \\ A\omega_y \\ C_1\Omega \end{pmatrix}; \delta \underline{h} = \begin{pmatrix} I_{xz}\omega_z + J_1(1,2)\dot{e} + J_1(1,3)\dot{\psi} \\ I_{yz}\omega_z + J_1(2,2)\dot{e} \\ I_{xz}\omega_x + I_{yz}\omega_y + C\omega_z + J_1(3,3)\dot{\psi} \end{pmatrix} \quad (1)$$

where

$$\underline{\omega} = \begin{pmatrix} \omega_x \\ \omega_y \\ \omega_z \end{pmatrix}$$

is the platform angular rate and Ω is the rotor spin speed with nominal value

$$\Omega_o = 10.5 \text{ rad/sec (100 rpm)} \quad (2)$$

The motion of the antenna about its gimbal center is approximately described by the linearized equations (see Reference 2, Equation 28),

$$I_g(2,2)\ddot{e} + J_1(1,2)\dot{\omega}_x + J_1(2,2)\dot{\omega}_y = T_e \quad (3)$$

$$I_g(3,3)\ddot{\psi} + J_1(1,3)\dot{\omega}_x + J_1(3,3)\dot{\omega}_z = T_\psi$$

where T_e and T_ψ are the elevation and azimuth torques applied at the gimbal.

First, the wobble amplitude will be determined for which the power off detent torque minimum of 2.8 Newton-meters (25 in-lb) is just sufficient to prevent any motion of the antenna. From Reference 1, the wobble motion takes the approximate form

$$\begin{aligned} \omega_x &= \omega_o \cos \Omega t \\ \omega_y &= \omega_o \sin \Omega t \end{aligned} \quad (4)$$

$$\omega_o = \eta\Omega, \quad \eta = \text{wobble amplitude}$$

Substituting Equation 4 into the first of Equation 3 and setting \bar{e} to zero yields

$$T_e = 6.3 \omega_o \Omega \sin \Omega t + 6.8 \omega_o \Omega \cos \Omega t$$

with

$$\begin{aligned} |T_e|_{\max} &= 2.8 \text{ Newton-meters (25 in. -lb)} \\ &= \omega_o \Omega \sqrt{6.3^2 + 6.8^2} = 9.3\eta\Omega^2 \end{aligned}$$

and with

$$\eta = 0.0028 \text{ radian (0.16 degree)}$$

A similar calculation performed on the second of Equation 3 yields a slightly smaller value of η . Thus, for a wobble amplitude less than 0.0028 radian, the power off detent torque is sufficient to prevent any relative motion of the antenna.

In the autotracking mode, the effect of the antenna's motion on system nutational stability can be estimated using a modified form of Equation 9 in Reference 2, which is

$$\dot{\theta} = \frac{1}{AT} \int_0^T (\cos \lambda t \delta h_y - \sin \lambda t \delta h_x) dt \quad (5)$$

where A is the vehicle transverse inertia, T is the limit cycle period of the control system in response to a quasisteady nutational motion, and δh_x is the x component of $\delta \underline{h}$ in Equation 1. Now the ψ and ω_z motions comprising $\delta \underline{h}$ will be smaller than the evaluation motion \dot{e} . Hence, $\delta \underline{h}$ can be roughly approximated by

$$\begin{pmatrix} \delta h_x \\ \delta h_y \end{pmatrix} = \begin{pmatrix} J_1(1,2)\dot{e} \\ J_1(2,2)\dot{e} \end{pmatrix} = \begin{pmatrix} -6.3 \dot{e} \\ 6.8 \dot{e} \end{pmatrix}$$

and Equation 5 becomes

$$\dot{\theta} = \frac{9.3}{AT} \int_0^T \dot{\epsilon} \cos(\lambda t + \phi) dt; \phi = \cos^{-1} \left(\frac{6.8}{9.3} \right)$$

Note that $\dot{\epsilon}$ is zero if θ is less than 0.0016 (0.09 degree); that is, no tracking motion will occur unless the nutation amplitude exceeds the control loop deadband.

The nutation period is 3 seconds and the control system maximum response speed is one step every 2 seconds. Hence, the limit cycle period T cannot be less than 6 seconds of $4\pi/\lambda$, during which time at most three steps of the antenna can occur. Assuming these steps occur at points in time which maximize the righthand side of Equation 5 yields the worst case situation,

$$\dot{\theta} = \frac{3\lambda\Delta}{4\pi} \times \left(\frac{9.3}{599} \right) \quad (6)$$

where Δ is the step amplitude of 0.0031 radian (0.18 degree).

Observe that the right-hand side of Equation 6 is positive, and that in a worst case situation the autotracking motion will cause the nutation angle θ to increase with time. This increasing trend will be offset by the action of the passive nutation damper, which causes nutation to decay at the rate

$$\dot{\theta} + \frac{\theta}{\tau} = 0 \quad (7)$$

where τ is the damper time constant. The largest value of τ that can overcome the destabilizing effect in Equation 6 is determined by equating Equations 7 and 6 with θ set at its minimum value of 5Δ * necessary to excite the autotracking motion. This yields

$$\tau = \frac{4\pi}{3\lambda\Delta} \times \frac{599}{9.3} \times 5\Delta \cong 647 \text{ seconds} \quad (8)$$

Thus, if the damper time constant τ is less than 647 seconds, it can overcome the worst case destabilizing effect of the antenna autotracking motion.

*The control loop deadband is 5Δ .

The final calculation involves the nutation induced during open loop ground commanded track. In this case, the maximum rate of the target must be less than 0.00031 radian (0.018 deg/2 sec) for tracking to occur. Assume that the target is moving in such a direction that only elevation pulses are required to track it, and let its rate be 0.00031 radian/3 sec so that the elevation pulses occur at platform nutation frequency. This set of assumptions will provide the maximum induced nutation level.

Neglecting the z motion of the platform, which will be small, the angular momentum expression in Equation 1 becomes (in platform coordinates)

$$\vec{h} = \begin{pmatrix} h_x \\ h_y \\ h_z \end{pmatrix} = \begin{pmatrix} A\omega_x + J_1(1,2)\dot{e} \\ A\omega_y + J_1(2,2)\dot{e} \\ C_1\Omega + I_{xz}\omega_x + I_{yz}\omega_y \end{pmatrix} \quad (9)$$

But the angular momentum must be constant in inertial coordinates and equal to $C_1\Omega_0$ where Ω_0 is the speed of the rotor when the vehicle is in a non-nutating state. Thus, for small θ

$$\begin{pmatrix} h_x \\ h_y \\ h_z \end{pmatrix} \cong \begin{pmatrix} 1 & 0 & -\theta_y \\ 0 & 1 & \theta_x \\ \theta_y & -\theta_x & 1 \end{pmatrix} \begin{pmatrix} 0 \\ 0 \\ C_1\Omega_0 \end{pmatrix} \begin{matrix} \dot{\theta}_x = \omega_x \\ \dot{\theta}_y = \omega_y \end{matrix} \quad (10)$$

Combining Equations 9 and 10 yields

$$\dot{z} = \lambda iz - J\dot{e} \quad (11)$$

where

$$z = \theta_x + i\theta_y$$

$$J = J_1(1,2) + iJ_1(2,2)/A$$

But with elevation steps occurring each nutation period

$$\tau_1 = \text{nutaton period} = 2\pi/\lambda$$

$$\dot{e} = \Delta \sum_{k=1}^N \delta(t - k \tau_1) \quad (12)$$

$$\Delta = \text{step size} = 0.00031 \text{ radian} \\ (0.18 \text{ degree})$$

Substituting Equation 12 into 11 and performing the integration provides (see Reference 3)

$$\theta(N \tau_1) = \sqrt{\theta_x^2 + \theta_y^2} = |z(N \tau_1)| = N \Delta |J| = 0.0155 N \Delta \quad (13)$$

where N is the total number of pulses applied. Thus, if the antenna is stepped in elevation once each nutation period, the maximum nutation amplitude develops with $\theta_{\max} = 0.0155 N \Delta$ and where N is the total number of elevation steps. Observe that 64 steps are required to produce a nutation angle of one elevation step or 0.00031 radian, (0.018 degrees).

As indicated in Reference 3, the above result is overly conservative since it neglects the effect of the passive damper; that is, the passive damper will tend to remove the nutation so that it will not increase monotonically as the number of steps is increased. If the damper is included in the analysis, then the maximum nutation amplitude becomes

$$\theta_{\max} = 0.0155 \Delta \frac{\tau}{\tau_1}$$

where τ/τ_1 is the ratio of the damper time constant to the nutation period. Taking a conservative value of 200 seconds for τ , the above expression becomes

$$\theta_{\max} = 0.00033 \text{ radian (0.19 degree)} \quad (14)$$

Thus the ground commanded track will never produce nutation amplitudes in excess of 0.00033 radian.

A. 3 ATTITUDE STABILITY - ANALYSIS TECHNIQUES

Introduction

Analysis of the attitude stability of a dual spin spacecraft, at large, as well as small angles, has been a continuing area of study at Hughes during previous development programs. . Of most interest has been the dynamic behavior of the gyrostat system, for example, the interactions between on-board control systems and global spacecraft dynamics. The analytical modeling of large angle gyrostat dynamics has been approached from both a general, theoretical, point of view, and from the viewpoint of specific mass properties that are typical of actual vehicle designs.

During such investigations of the dynamics of a gyrostat, extensive use has been made of detailed analog and digital computer simulations, from both control system design and attitude stability viewpoints. This subsection will discuss two analytical tools that have been developed at Hughes to study spacecraft dynamic behavior, with emphasis on: 1) vehicle global attitude stability and 2) the dynamic effects of flexible elements. The success experienced in using these programs, along with other design tools, to accurately predict the dynamic behavior of Hughes' spacecraft, provides a good measure of confidence in the proposed TDRS design.

Discussion

Classically, a gyrostat is a system of bodies interconnected in such a way that the mass geometry of the system does not change when the system components move relative to each other. Such systems represent idealizations of the Hughes Gyrostat satellite; however, changes in mass geometry of these spacecraft as a result of structural flexing, nutation damper motion, and propellant slosh are small, as are the changes due to rotor spin. The classical gyrostat provides a useful idealization of the spacecraft and, depending on the smallness of the changes of mass geometry, the effects of the latter can be regarded as perturbations to the classical gyrostat equations.

This analysis provides a fundamental basis for understanding the possible motions of the Hughes Gyrostat system and for defining the design criteria relating to mass properties, despin control system performance, and nutation damper sizing. For a particular design, the analysis obtained in closed form is then supplemented by simulations taking into account a suitably exact model of the spacecraft.

At Hughes, a specific vehicle design task involves the use of two very general digital computer programs developed to handle different aspects of this simulation problem. The Satellite Attitude Dynamics (SAD) II program represents the exact nonlinear equations of motion for an arbitrary collection of connected rigid bodies, requiring only that the connectivity of the system be "treelike". The Dynamic Analysis of Spacecraft with Flexible Appendages

(DASFA) program simulates the linearized equations of motion of a dual spin spacecraft with flexible attachments to the platform and rotor. The following two sections will discuss these programs in more detail.

SAD II

The SAD II computer program is a general, nonlinear, rigid body dynamics digital simulation. Flexibility may also be incorporated through a lumped parameter model of the nonrigid elements of the spacecraft dynamics. In essence, the simulation writes the equations for the angular rates and for the angular positions of a system of interconnected rigid bodies and integrates these equations. The program is general in that the free dynamical system to be simulated is completely specified via the input data. Furthermore, the simulation handles dynamical constraints of the nonworking type, such as axle and gimbel constraints, quite readily. With the addition of special purpose subprograms, elements are made active through control system models which supply the required torques and forces, yielding a fairly detailed model of a spacecraft systems.

The viewpoint employed in writing the equations is that of a collection of nested subsystems of rigid bodies (Figure A-8). At the first, or system level of nesting, the equations for the rate of change of linear momentum of the total system and for the rate of change of angular momentum of the total system are written about a point on the platform (reference body) in terms of the contribution of each subsystem. At this level, no explicit account need be taken of the interaction forces between the bodies that comprise the system. At the next level of nesting, the equations governing the angular momentum of the subsystems attached to the platform about the corresponding attach point are written. If any of the subsystems attached to the platform consist of more than one body, the above procedure is followed at the next level of nesting, and so on, until all the bodies in the system are included.

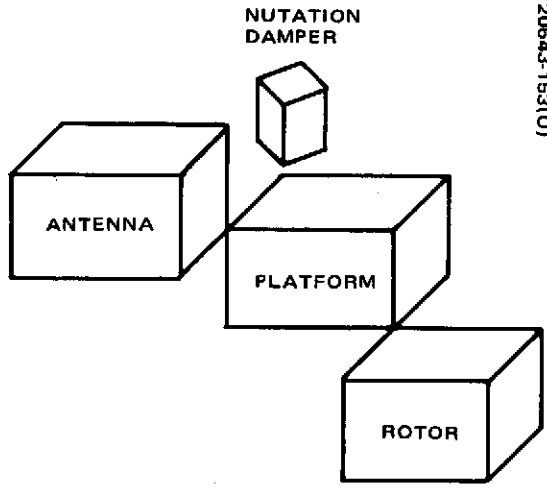
Employing matrix notation liberally, it is possible to write the equations of motion in an automatic fashion once the topology of the system is defined. The equations that result take the general form

$$T \dot{\omega} = \phi + \tau + k \quad (15)$$

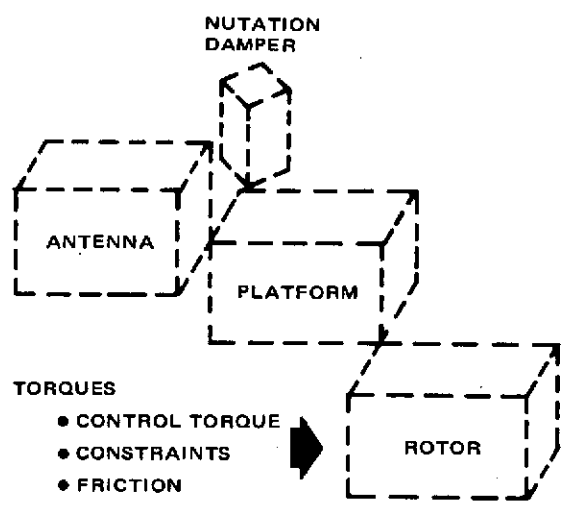
The matrix, T, is composed of blocks of three by three submatrices, and thus is of dimension 3n by 3n. The vector ω is composed of n one by three column matrices; these represent the angular rate of the platform relative to inertial space, the angular rates of the bodies of the system relative to the platform, and the linear velocity of the platform relative to an inertial reference.

A set of kinematic equations must be joined to Equation 15 to determine the quantities used to specify the position of each of the objects. An Euler parameter, or quaternion representation of the attitude of each body, is used in the program.

20643-153(U)



a) SYSTEM COMPOSED OF RIGID BODY ELEMENTS



b) ROTOR SUBSYSTEM

Figure A-8. Equation Concept - Nested Systems of Rigid Bodies

In Equation 15 the vector $\dot{\phi}$, composed of 1 by 3 column matrices, depends on the coordinates and velocities. This vector, in effect, represents apparent forces. The τ vector represents the nondynamical, or applied forces such as control torques and friction. The vector k corresponds to the forces or torques of constraints that may or may not be present, depending on the particular system.

The constraints are known in terms of their effect on the motion of the bodies rather than in terms of forces. In particular, certain components of the angular velocity vector of a given body may be constrained to be known functions of time. This can be represented algebraically by the action of a perpendicular projection operator on the velocities. Denoting the matrix of this operator by E, and the supplementary perpendicular projection matrix by F, note that

$$E \dot{\omega} = \mu(\tau)$$

and

$$E + F = I$$

where I is the identity matrix.

Furthermore, it can be shown that for nonworking constraints,

$$Fk = 0$$

In other words, the constraint forces must lie in the manifold containing the constrained components velocity. With this in mind, Equation 15 may be premultiplied by F to eliminate the forces of constraint. Algebraic manipulations of the resulting equation yield

$$\dot{\omega} = F (FTF + E)^{-1} F (\dot{\phi} + \tau - T\mu(t)) + \mu(t) \quad (16)$$

Equation 16 represents the equations of motion which are integrated by the computer program.

The key points of a typical SAD II simulation are enumerated in Table A-2. It should be emphasized that because of the generality of the program, it is possible to simulate a variety of spacecraft modes quite easily. Furthermore, it is possible to study the dynamics of distinct elements by reducing the number of degrees of freedom of the simulation; this is done through the input data.

TABLE A-2. SAD II DIGITAL SIMULATION ELEMENTS

<ul style="list-style-type: none">● Three bodies – eight degrees of freedom<ul style="list-style-type: none">Rotor (axle constraint)PlatformAntennae (axle constraint for lumped parameter model) ● Despin control loop<ul style="list-style-type: none">Earth sensor modelMaster index pulse generator modelSampled data control system ● Lumped parameter flexibility<ul style="list-style-type: none">Antenna modes of vibration simulated through hingeRigid body with equivalent damping constant and spring rate ● Reaction control jets<ul style="list-style-type: none">Two spin jets (spin speed control)Two radial jets (ΔV in plane)Two axial jets (ΔV out of plane and precession)
--

DASFA

The importance of flexibility of major spacecraft components in relation to interactions with control systems has been well appreciated by control system engineers, structural dynamicists, and system dynamicists for several years. This has led to the evolution at Hughes of an interactive approach to be followed in the design and evaluation of conceptual spacecraft.

In the initial phase of a spacecraft design, the type of despin control system to be used and its essential features are chosen based on treating the spacecraft as a rigid body or set of rigid bodies. At the same time, any especially flexible components of the conceptual design are examined and a relatively simple model of such flexible members is developed for use in a preliminary evaluation of total system interactions. This initial flexible structure study may involve comparatively small digital computer simulations of the spacecraft dynamics. Once it is determined that the basic structures and controls concepts are feasible and compatible, the structural dynamics model of the appendage is used, together with candidate control system concepts and nominal vehicle parameters, to determine overall stability as influenced by control loop compensation. This is primarily an analytical task

based on assumptions of linearity and weak coupling. The next step is to implement a simulation (using the analog computer, if possible) of the control system and the vehicle, including flexible appendages, to evaluate the stability and performance characteristics with the preliminary control system design.

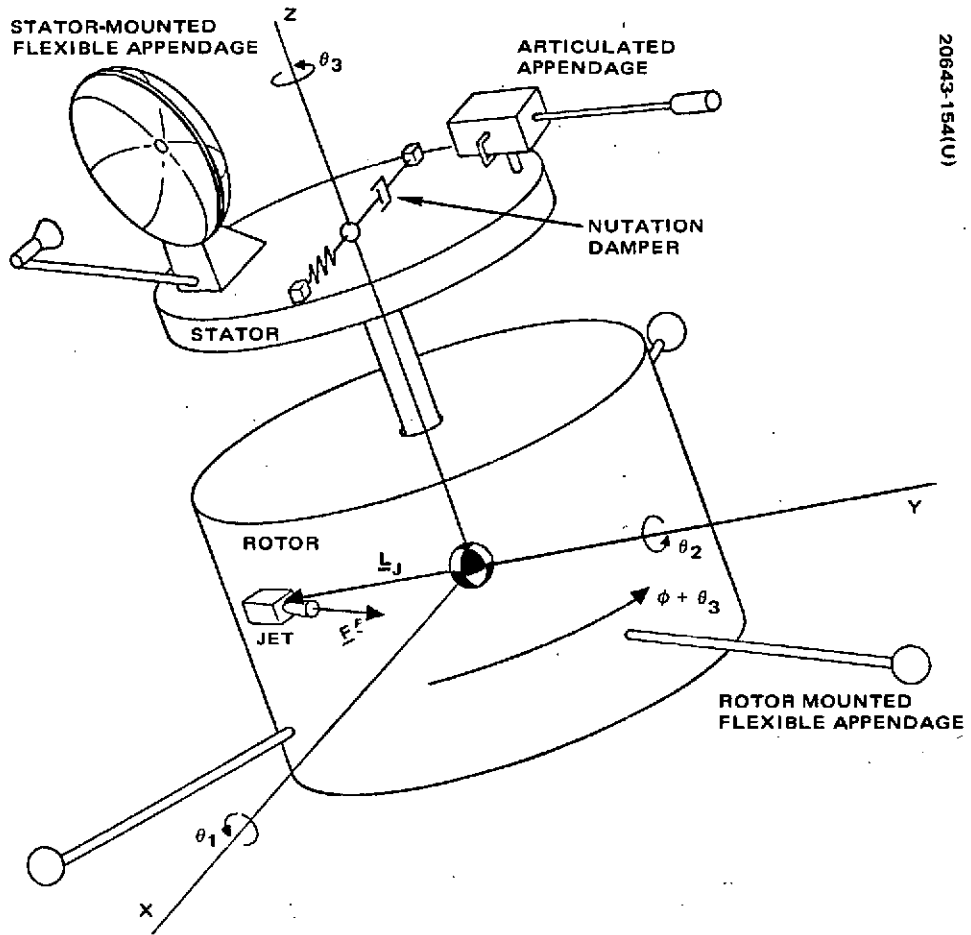
Finally, flexible structure interactions with dynamics are examined, using a much more complex and detailed representation of the flexible members, together with the spacecraft mass properties and despin control system parameters. The principal tool for such studies is the DASFA computer program. These simulations permit assessment of overall system stability, deflections of critical component, and a check on loads induced in members.

The DASFA program was generated for the purpose of studying flexible structure/attitude control system interactions on dual-spin spacecraft or three axis stabilized spacecraft (either one or two body systems). The computer program uses a linearized set of equations of motion of a coupled two body system, one of which is essentially nonspinning in inertial space and to which are attached up to four flexible appendages, the other body of the system being a rigid rotor which can also have an attached flexible appendage (Figure A-9). This rotor can possess a dynamic imbalance.

The equations describing the flexible appendages on the nonspinning platform are a normal coordinate formulation in which the equations can be truncated, i. e., higher normal vibration modes can be eliminated from the simulation. This technique of using complete, but linearized, equations of motion for the complete spacecraft, along with truncated normal coordinates representing the vibrational behavior of the flexible appendages, has been termed the "hybrid coordinate" approach. Up to six modes of each appendage may be included. Conversely, the rotor mounted appendage is modeled with up to 10 discrete masses, since standard normal mode transformations are precluded by rotational effects.

The program presently provides for several choices of interbody despin control systems, including proportional control, third order analog control and sampled data, digital control systems. There is also a single axis, appendage reorientation control system, using torque versus time tables, solar array orientation linkage control system, and reaction jet pulsing.

Standard outputs of the DASFA program are body attitudes for stability and pointing error studies, appendage deflections to monitor possible interferences and pointing errors due to flexibility, forces and moments at the appendage bases for structural requirements, damper deflections, and modal coordinates of the appendages to indicate the relative importance of the modes. Total angular momentum squared is output as an indicator of accuracy of the integration routine.



20643-154(U)

Figure A-9. General DASFA Spacecraft Configuration

The following three examples illustrate the type of results which have been obtained using the DASFA program.

Intelsat IV In-Orbit Spacecraft Interactions of Flexibility and Spacecraft Motions. One of the axial jets on the present, operational Intelsat IV was purposely pulsed on several occasions to effect attitude changes or to purposely induce a small nutation in order to measure nutation decay rates. The nutation accelerometer reading on these occasions indicate the presence of 7.5 Hz oscillation. It was strongly suspected that this represents the basic despun platform bending frequency (predicted prior to launch to be 6.5 Hz) as modulated by the accelerometer rotating at almost 1 Hz. The relative locations of the axial jet and the ANDE accelerometer on the rotor during firing are shown on Figure A-10.

To test this hypothesis, a structural dynamics model of the Intelsat IV spacecraft (already in existence since it was generated for prelaunch studies) was modified to monitor the response at the ANDE accelerometer location.

These studies were performed using the DASFA computer program, which generates time histories of spacecraft motions as influenced by a flexible despun platform. This despun platform is characterized by retaining significant normal modes of vibration of this structure, as determined by vibration analyses using the MARS (Matrix Analysis Routine for Structures) computer program. This combined spinning, rigid rotor/flexible despun platform system, as simulated in the DASFA program, was forced into motion by pulsing of an axial jet at spin frequency. The jet was fired for 0.1 seconds with a constant force amplitude of 17.8 Newtons (4 pounds), representative of the actual jet impulse.

The results of that computer run are presented on Figure A-11 which shows the resulting accelerometer response and compares it to the in-orbit data received. The qualitative agreement of the two curves is gratifying, and indeed indicates that the observed 7.5 Hz oscillation is brought about by excitation of the first bending mode of the despun platform. The rotating accelerometer is alternately in phase with this mode, then rotates until it is π radians out-of-phase, producing the "beat" phenomenon shown. The shift in phasing also produces the apparent 1 Hz addition to the frequency. The degree of quantitative agreement of the curves is almost too good to be true, considering that the response is actually the sum of a number of transients. It does lend support to extracting numerical conclusions from the simulation, however, the principal one being that the peak response was of the order of 0.049 meter/second² (0.16 ft/sec²). This is well below the threshold of the active nutation damping system (which triggers firing of the axial jet when the nutation accelerometer response exceeds certain limits); hence, this flexible structure/control system interaction should not result in spurious firings of the axial jet.

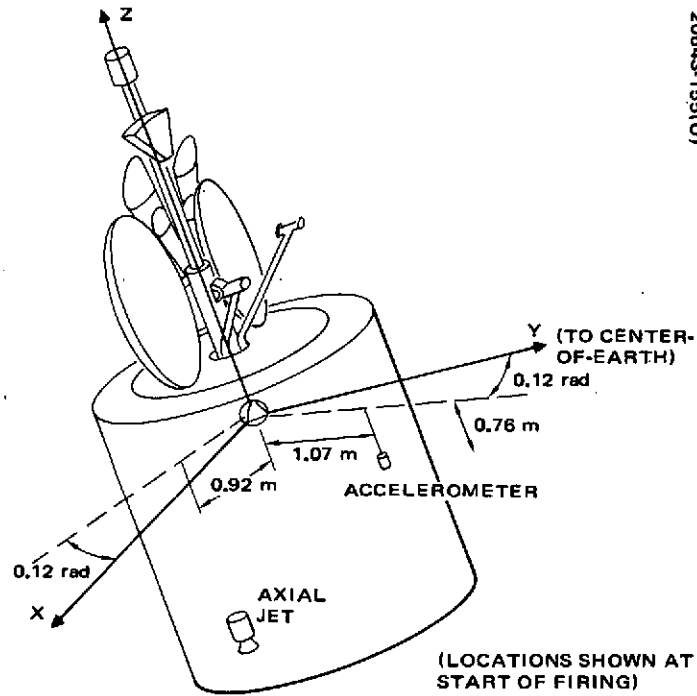


Figure A-10. Intelsat IV Spacecraft Showing Jet and Accelerometer Locations

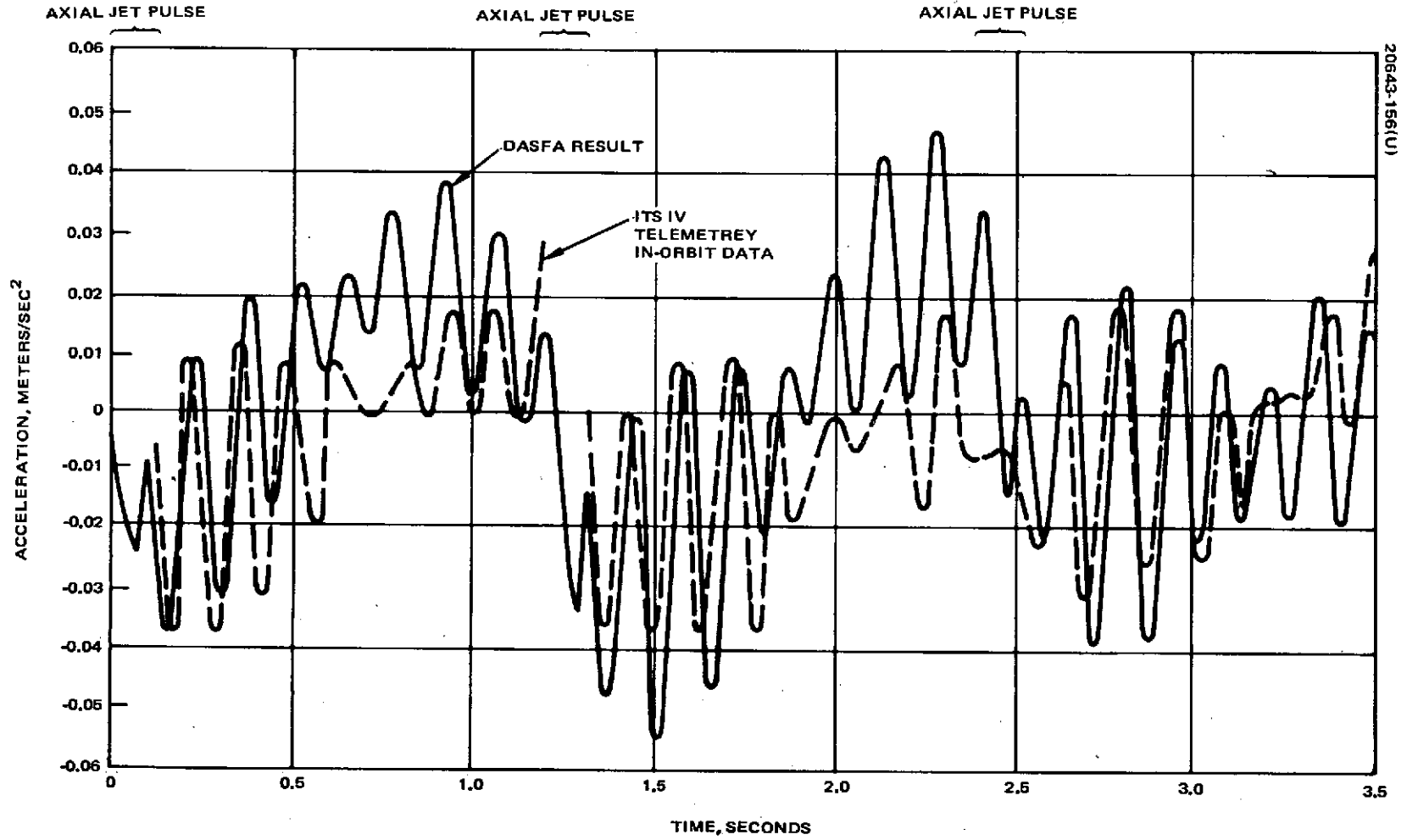
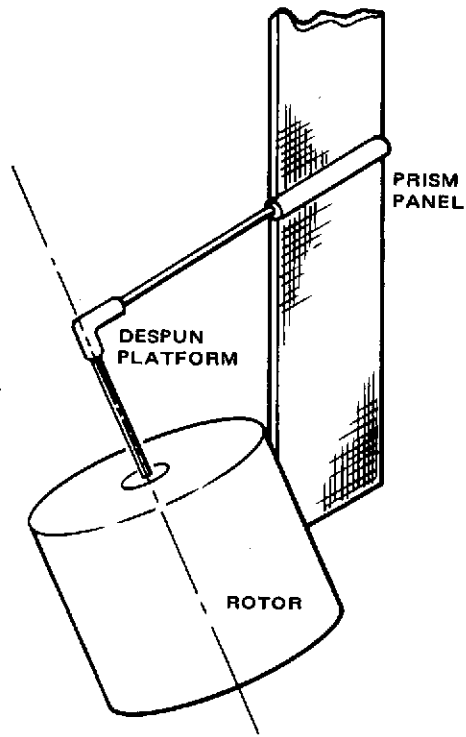


Figure A-11. Results of DASFA Simulation of IntelSat IV Dynamics



20643-157(U)

Figure A-12. Flexible
Rolled-up Solar Array
Application to Spacecraft

Dynamic Interactions to Spacecraft Using Flexible Rolled-Up Solar Arrays. To illustrate the type of analysis possible with the DASFA program and to dramatize the effects of appendage flexibility, the configuration shown in Figure A-12 was analyzed. The vibration characteristics of the Flexible Rolled-Up Solar Arrays (FRUSA) were determined using both continuum mechanics solutions and finite element computer programs. In both approaches, the important effects of preloads in this type of structure (i. e., compression in the booms, tension in the solar cell substrate) were accounted for. The lowest characteristic frequencies of these structures were retained in the DASFA computer simulation.

This system was run as a Gyrostat stabilization configuration, in which the main body is spun to provide gyroscopic stabilization, while the platform containing the solar cell arrays is essentially despun to maintain sunpointing. This situation was run with flexible arrays and also with the arrays considered to be rigid bodies. The results of these studies are shown in Figure A-13, which shows time histories of the nutation angle (i. e., the angle between the vehicle's spin axis and the angular momentum vector) for the two aforementioned situations.

For the case in which flexibility is accounted for, the transient response due to flexibility dominates the early portion of the motion. Subsequently, the motion settles down to a more or less steady decay whose characteristic time constant is somewhat longer than for the same system assuming rigid appendages. The latter aspect of the motion is probably due to the fact that the tuned nutation damper used with this system was designed for a spacecraft with rigid appendages; the actual flexibility of the solar arrays has detuned the damper frequency from the nutation frequency enough to noticeably degrade system performance.

It is evident from this example that the flexibility of the solar cell arrays had a marked effect on the dynamic behavior of the system. This will be true of any spacecraft system using flexible panels which are significant in size compared to the overall system.

Dynamic Effects of Flexibility on the Rotor of Spin-Stabilized Spacecraft. The DASFA computer program can also be used to analyze the effects of a flexible appendage on the spinning member of a spin-stabilized spacecraft. The rotor mounted appendage subroutine can handle an appendage simulated by up to 10 mass points connected by flexible elements.

In order to illustrate the capabilities of the DASFA program with this feature added to it, this subroutine was used to analyze the behavior of a spin stabilized spacecraft with a rotor mounted, two degree-of-freedom nutation damper. The system analyzed is depicted in Figure A-14. Optimum nutation damper parameters, as determined by energy sink analyses, are also shown in the figure.

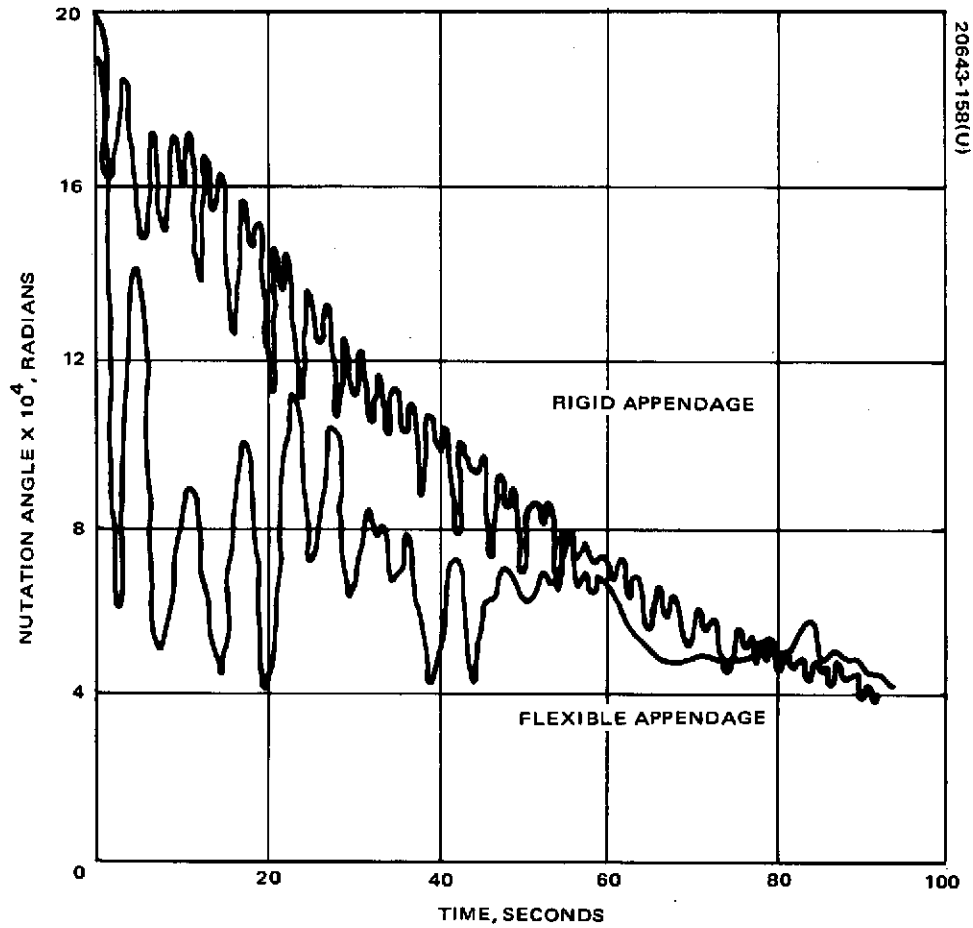


Figure A-13. Comparison Nutation Time Histories for Flexible and Rigid Solar Arrays

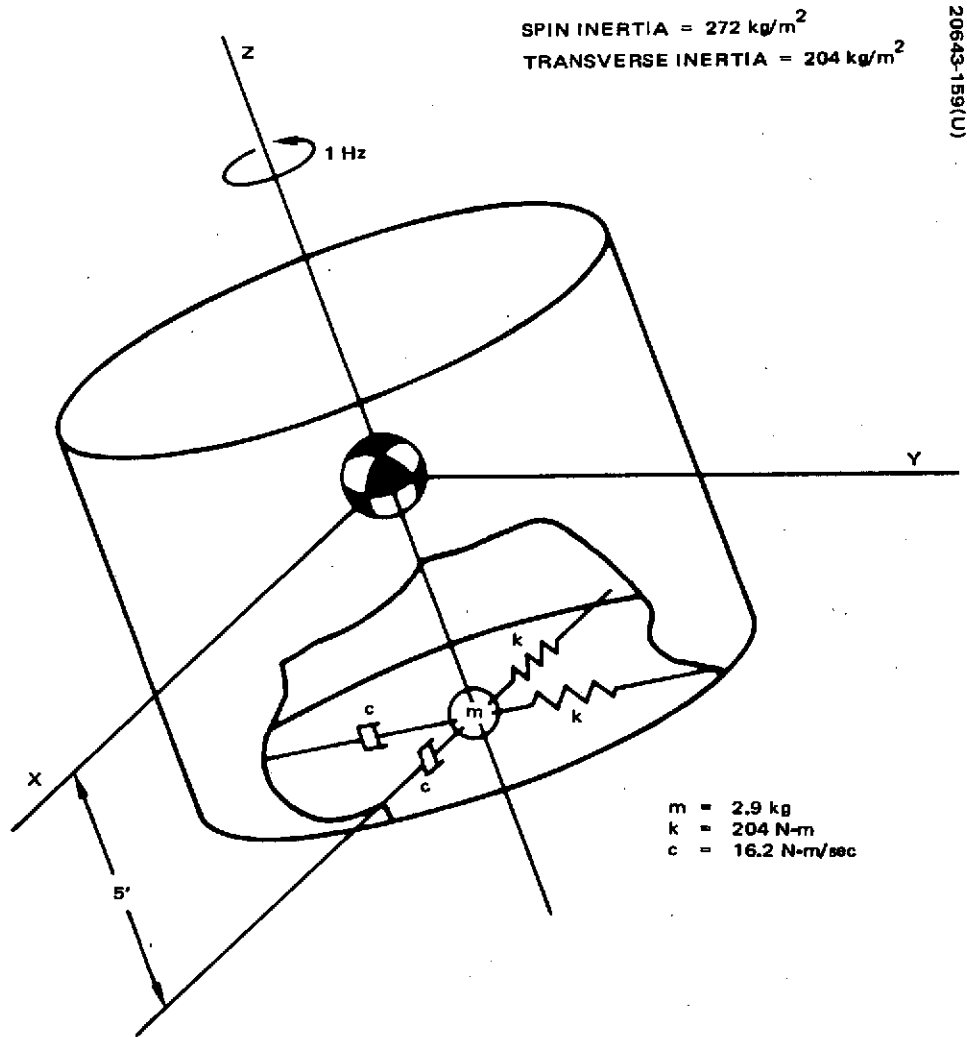


Figure A-14. Spin Stabilized Spacecraft With Rotor Mounted Nutation Damper

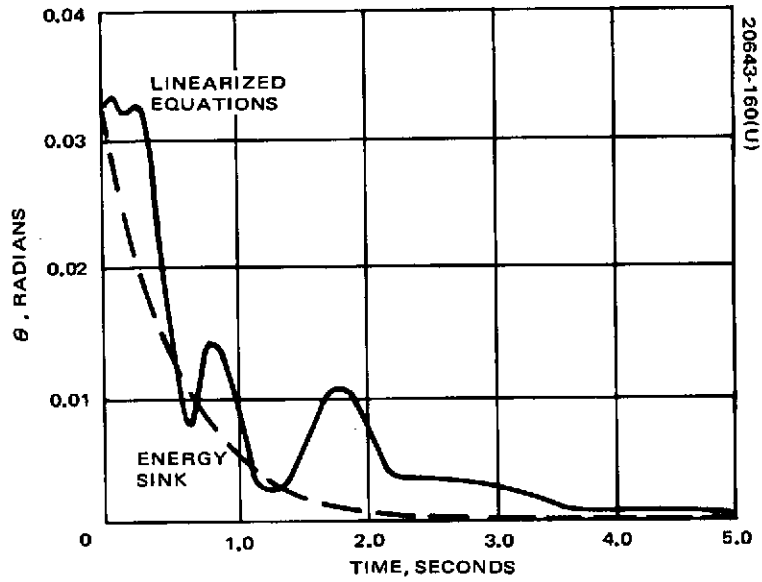


Figure A-15. Time History of Nutation Decay

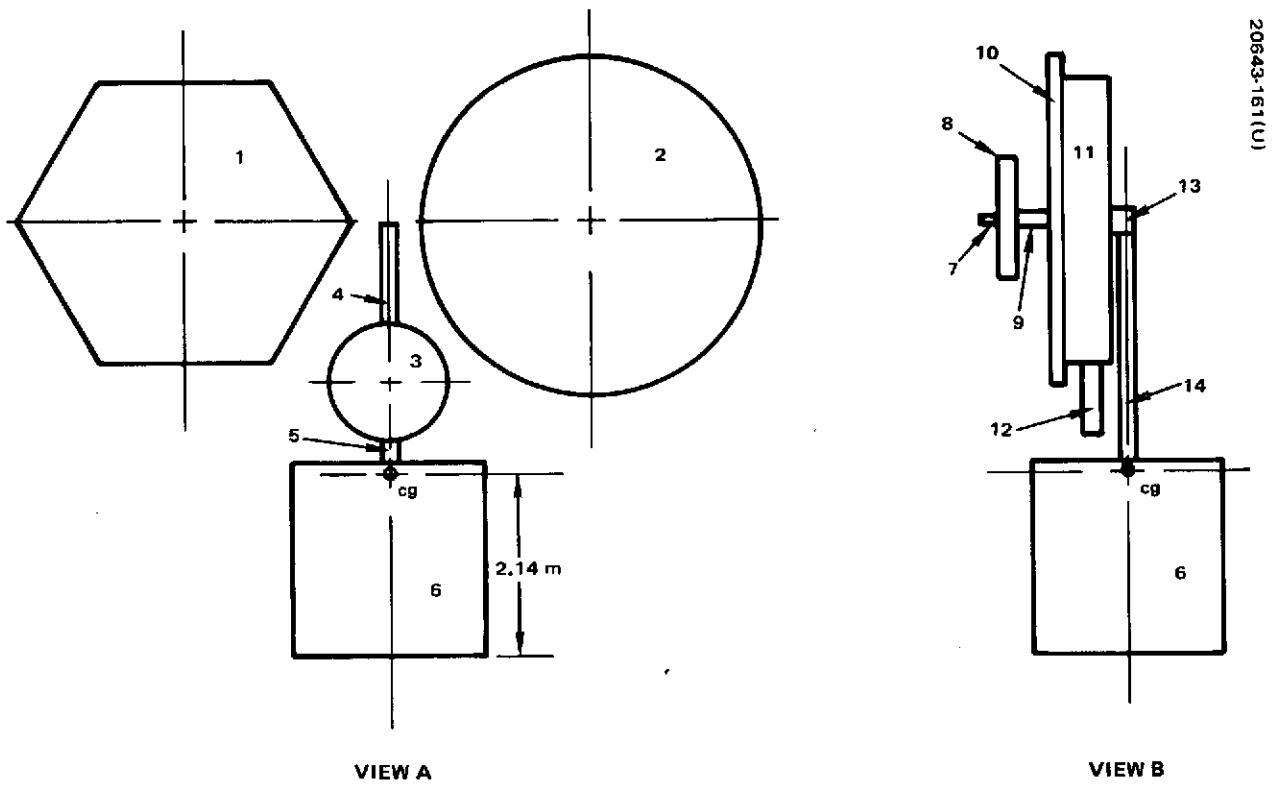


Figure A-16. TDRSS Solar Torque Model

A typical time history at the predicted resonance tuning is shown in Figure A-15, which also shows the smooth, exponential decay predicted by the energy sink approach. The complete coupled equations of motion clearly exhibit a "starting transient" in the damper motion, due to the fact that at the start of the motion, the damper was considered undeformed. The motion soon settles down to a more or less steady decay of nutation at a somewhat lesser rate than predicted by the energy sink approach. This indicates that the energy sink approach is a bit uncertain in the vicinity of damper resonances. This is due to the fact that one cannot really "tune" the damper frequency to precisely the nutation frequency. Since the two bodies actually interact, there exist two characteristic frequencies of the system, slightly separated. Hence, the "tuning" is not perfect.

The incorporation of this subroutine into the DASFA program now permits detailed studies of the interactions of flexible appendages on both the despun platform and the rotor of a dual spin satellite with the overall dynamic behavior of the satellite. This is a situation of immediate interest in attitude stability investigations since, for typical current dual spin satellites (typified by the TACSAT and Intelsat IV communication satellites), despun platform flexibility is stabilizing while rotor flexibility is destabilizing when considered singly.

A. 4 PRELIMINARY SOLAR TORQUE ANALYSIS

This subsection presents a preliminary (simplified) solar torque analysis for the current TDRS configuration. The results, based upon normal sun incidence only, indicate an average l_{cp-cg} of 1 meter (3.27 feet) producing an attitude drift of 0.0425 microradian/sec (0.21 deg/day).

Analysis

The solar torque model utilized for this analysis is illustrated in Figure A-16. This model is based upon the latest spacecraft configuration.

Table A-3 lists the pertinent spacecraft parameters utilized. The reflectances are, in part, assumptions, based upon previous analyses and the current antenna porosities, are given as 80 percent.

Assuming normal sun incidence, only the resulting torques and forces on views A and B, Figure A-16, are:

<u>View</u>	<u>Force</u>	<u>Torque</u>	<u>l_{cp-cg}</u>
A	6.31×10^{-5} Newtons	8.09×10^{-5} Newton-meters	1.26 meters
B	4.10×10^{-5} Newtons	2.40×10^{-5} Newton-meters	0.59 meters

TABLE A-3. SPACECRAFT PARAMETERS

No.	Surface Area, meters ² (feet ²)	Moment Arm, meters ² (feet ²)	Reflectance ν
1*	(20.30) 1.88	(9.33) 2.84	0.80
2	(24.54) 2.28	(9.33) 2.84	0.80
3	(14.75) 1.37	(3.42) 1.04	0
4	(1.55) 0.14	(7.40) 2.26	0.80
5	(0.42) 0.04	(0.75) 0.23	0.80
6	(51.35) 4.76	(-3.33) -1.02	0.23
7	(0.07) 0.006	(9.33) 2.84	0.80
8	(3.50) 0.32	(9.33) 2.84	0.60
9	(0.44) 0.04	(9.33) 2.84	0.80
10	(5.73) 0.53	(9.33) 2.84	0.80
11	(19.85) 1.84	(9.33) 2.84	0.60
12	(1.60) 0.15	(2.75) 0.84	0
13	(1.18) 0.11	(9.33) 2.84	0.80
14	(3.77) 0.35	(4.77) 1.45	0.80

*Antennas are assumed to have an 80 percent porosity.

The spacecraft attitude drift is a function (approximately) of the average torque on the above two views. These averages are:

<u>Average Force</u>	<u>Average Torque</u>	<u>Average cp-cg</u>
5.25×10^{-5} Newtons	5.24×10^{-5} Newton-meters	1.00 meters

resulting in an attitude drift of

$$\dot{\theta} = 0.042 \text{ microradians/sec (0.21 deg/day)}$$

If the two large antennas are assumed to have 90 percent porosities, the resulting attitude drift is given as

$$\dot{\theta} = 0.022 \text{ microradians/sec (0.11 deg/day)}$$

A. 5 BEARING AND POWER TRANSFER ASSEMBLY - DESIGN DETAILS

Spacecraft Mounting Interface

The BAPTA is centered on the spin axis of the spacecraft, between the spinning cone structure and despun platform. The spacecraft despun platform and antenna support structure are mounted to the BAPTA shaft. The spacecraft rotor cone support structure mates directly to the BAPTA housing forward flange. Additional rigidity is provided by a web between the cone and BAPTA aft housing flange. The BAPTA is electrically isolated at each of its mounting surfaces (minimum of 10,000 ohms resistance) such that stray currents cannot pass through the bearings. Both the spinning and despun interfaces are insulated for redundancy. Additional protection is provided by grounding the spinning and despun BAPTA structure through a slip ring such that static charge cannot build up and cause trickle current discharge through the bearings.

Bearings and BAPTA Structure

Bearing Loads.

The mechanical interface between spun and despun sections of the satellite during third stage burn, apogee motor burn, and orbital operation is provided by a pair of 440C stainless steel angular contact bearings, shrink fitted to a beryllium shaft and housing and 15-5 pH stainless preload spring. The bearing separation distance and divergent load lines result in a wide effective bearing separation to achieve a high bending moment capacity and stiffness for orbital operation. Bearing size and preload is based on loads applied during various phases of the mission, as summarized in Table A-4.

During first and second stage burn of launch, the mechanical interface between spun and despun sections is provided by the launch lock clamp. When the clamp is installed, the BAPTA forward bearing is demated by an axial translation of the shaft, while the aft bearing preload increases from additional deflection of the preload spring.

In this mode, all axial and shear loads, and most of the bending moment loads, are shunted past the bearings through the clamp. Due to finite structural stiffness, a small percentage of the bearing moment loads are applied to the aft bearing. Assuming 10 percent of the bending moment loads are shared by the aft bearing, 1150 Newton-meters (10,200 in-lb) bearing capacity is required. With a 0.178 meter separation distance between the clamp and the aft bearing, this results in a radial load of 6500 newtons (1460 pounds).

The axial load on the BAPTA during third stage and apogee motor burn, after clamp separation, is applied to the forward bearing only (the aft bearing is loaded axially only by the preload spring). These loads are applied while the bearing is spinning at approximately 10.5 rad/sec (100 rpm) (despun platform is partially despun to 0.2 to 0.5 rad/sec (2 to 5 rpm)).

TABLE A-4. BAPTA APPLIED LOADS, CAPACITIES

Condition	Predicted Loads Applied	Design Capacity
Locked, first and second stage maximum		
Axial, newtons	28,400 (clamp only)	44,500 clamp
Radial, newtons	26,600 (clamp only)	33,400 clamp
* Bending moment, newton-meters	11,500 total	14,400 total
	10,400 clamp (90 percent)	12,400 clamp
	1100 BAPTA (10 percent)	2000 BAPTA
Unlocked, rotation 10.5 rad/sec, third stage maximum		
Axial, newtons	25,600 (forward bearing only)	31,200**
Radial, newtons	1200	11,100***
Bending moment, newton-meters	580	1700
Apogee motor maximum		
Axial, newtons	19,800 newtons (forward bearing only)	31,200**
Radial, newtons	1200	11,100***
Bending moment, newton-meters	580	1700

*Occur simultaneously – all others non-simultaneous.

**Limit is contact ellipse containment – Hertzian stress at 31,200 newton load is only 1.73 giganewtons/m².

***Based on conservative Hertzian stress limit of 1.96 giganewtons/m².

Bearings Selected

The bearings selected for the TDRS BAPTA are 440C CEVM stainless steel angular contact bearings, 60 mm bore, extra light series (95 mm OD), with 19 balls, each 0.0103 meters (13/32 inch) diameter, with a nominal 0.436 radian (25 degree) contact angle. These bearings are of sufficient size

to withstand imposed loads with substantial margin, as indicated in Table A-4. The radial load capacity of 11,100 newtons (2500 pounds) is based on a conservative Hertzian stress level of 1.96 giganewtons/m² (285,000 psi), whereas the bearing industry advertises a 2.48 giganewtons/m² (360,000 psi) limit for brinelling the races. The axial load capacity of 31,200 newtons (7000 pounds), is based on contact ellipse containment rather than Hertzian stress limit. As the preload on the bearing increases, the contact angle increases until eventually the ball contacts the edge of the raceway at the land diameter, and the balls would become creased. In the selected TDRS bearing, the raceway limit is reached before the Hertzian stress limit. The TDRS bearing is essentially identical to the Anik I despin assembly bearings, except bearing land diameters have been modified slightly to enable 31,200 newtons axial capacity, as shown in Table A-5 and A-6. Axial capacity of the bearing could be increased further (up to 35,600 newtons or 8000 pounds maximum where Hertzian stress becomes the limit) if more detailed loads analysis results in an increase in predicted loads imposed.

The ball and race material will be 440C CEVM stainless steel, providing maximum corrosion resistance and a minimum of inclusions, thus maximizing bearing reliability. The bearings will be manufactured to AFBMA ABEC 9 class tolerances and utilize Grade 5 balls. One land of the inner race is removed, such that it can be separated from the bearing without the use of force or differential heating and cooling. The balls are captured

TABLE A-5. BEARING DIMENSIONS

Bearing Dimensions	Anik I	TDRSS Selected Design	Maximum Capacity
Axial capacity, newtons	22,200	31,200	35,600
Bore, mm	60	60	
O. D. , mm	95	95	
Number of balls	19	19	
Ball diameter, mm	10.3	10.3	
Inner race O. D. , mm	71.4	71.6	
Outer race I. D. , mm	83.9	83.4	
Retainer O. D. , mm	83.5	83.0	
Retainer I. D. , mm	72.1	72.4	

*Hertzian stress limit of 1.96 giganewtons/m²

TABLE A-6. SIGNIFICANT BEARING LUBRICATION SYSTEM TEST AND APPLICATION EXPERIENCE

Lubricant	Satellite or Vacuum Test	Pressure, Micronewtons/m ²	Temperature, °K	Speed rad/sec	Load, Newtons	Duration Gigaseconds	Bearing Size and Number of Bearings †	Remarks
Vac-Kote*	OSO V	1.33	283	π	8.9 to 22.2	0.010	3308 + R18 (1 each)	Duty cycle: on 2400 sec off 1200 sec
Vac-Kote	OSO I	1.33	283	π	8.9 to 22.2	0.047	3308 + R18 (1 each)	Operated only 0.025 gigasec during the 0.047 gigasec
Vac-Kote	OSO II	1.33	283	π	8.9 to 22.2	0.063	3308 + R18 (1 each)	Operated only 0.025 gigasec during the 0.063 gigasec interval
Vac-Kote	Vacuum test	1.33	294	π	2.2	0.048	2 at 2.54 cm outside diameter	Five other bearings in test at light load and oscillating
Vac-Kote	Vacuum test	1.33	283	2π	2.2	0.020	3308 + R18	OSO qualification test
Vac-Kote	Vacuum test	1.33	294	2π	2.2	0.017	6 bearings 3305	OSO qualification test
Vac-Kote	OSO III	1.33	283	π	8.9 to 22.2	0.068	3308 + R18 (1 each)	Duty cycle: on 2400 sec off 1200 sec
Vac-Kote	OSO IV	1.33	283	π	8.9 to 22.2	0.048	3308 + R18 (1 each)	Duty cycle: on 2400 sec off 1200 sec
Vac-Kote	TACSAT	1.33	297	2π	668	0.086	2 each 5.905 bore	In orbit since Feb 1969; still operating successfully after 0.1 gigasec
Hughes Lube (HMS 20-1727)	HS-318 BAPTA vacuum life test	1.33 to 0.133	Cycled 258 to 317	2π	668	0.045	2 each of 2 sizes (BAPTA and ECRA) 5.905 and 1.5 bore	Test presently operating successfully (started November 1970)
Hughes Lube (HMS 20-1727)	Anik I bearing vacuum life test	1.33	294	3.33π	200	0.023	2 each 2.362 bore	Test presently operating successfully
Vac-Kote	Intelsat IV BAPTA vacuum life test	1.33	Cycled 256 to 317	2π	268	0.031	2 each 3.543 bore	Test concluded - successful 0.03 gigasec
Hughes Lube (HMS 20-1727)	Various short vacuum tests	1.33	294	2π to 3.33π	268	0.023 in intervals of 0.00036 to 0.0036 each test	2 to 6 bearing per test 2.362 bore	All tests successful
Hughes Lube (HMS 20-1727)	Vacuum test	1.33	328	2π , 4π and 6π	44.5, 89.0, and 178	0.019	18 each 1.5 bore	Test concluded - successful

*Vac-Kote is a lubricant that is in the same family as the Hughes HMS 20-1727 Apiezon C lead naphthenate system. Analysis cannot distinguish between Vac-Kote and the Hughes material.

†No conversion SI units for this case.

to the outer race by the outer race riding retainer when the inner race is removed. This feature facilitates bearing installation, when each race is individually shrink-fitted to its seat, and enables 100 percent inspection of all ball and inner race surfaces after final lubrication processing without degradation of bearing cleanliness due to handling.

Preload Spring

An axial load must be applied to the angular contact bearings to maintain ball to race alignment, to prevent ball skid, and achieve the required bending stiffness during operation. A preload of 535 newtons (125 pounds) was selected for TDRSS to maintain ball to race contact and unit bending stiffness in all possible mission phases including flat spin, when centrifugal forces of up to 445 newtons (100 pounds) are applied in opposite directions on the shaft and housing, tending to separate the forward bearing. Use of an axially soft preload spring in conjunction with the angular contact bearing enables the assembly to absorb large thermal gradients and temperature excursions without significant change in bearing running torque, preload, or stress levels. For radial differential expansion (such as cold outer race, hot inner race), the races move axially, thus changing the contact angle and using up part of the bearing diametral clearance. Longitudinal (axial) differential expansion is absorbed directly by axial motion against the preload spring.

The 535 newton (120 pound) axial load is provided in the TDRS BAPTA by a Hughes developed system utilizing a shrink fit to a flexural spring on the aft bearing, combining high radial stiffness of 17.5 MN/m (100,000 lb/in.) with low axial stiffness, 1.05 MN/m (6000 lb/in.). This system avoids difficulties inherent in conventional preload spring concepts employing a wavy washer or helical coil springs against a slip fit sliding race. Radial looseness of the sliding race in the more conventional preload system can cause nutational instability and contribute to spin axis wobble. The Hughes developed system also avoids the possibility of sliding race wear, cocking, or subsequent jamming in the slip fit diameter.

The flexural spring proposed is essentially identical to the Anik I spring, except the web thickness has been increased to increase the axial spring rate, thus providing the 535 newtons (120 pounds) preload selected without excessive spring deflection.

Bearing Fits

The TDRS BAPTA bearing system radial stiffness and alignment is maintained with a slight interference fit (2.5 to 15 micrometers (0.0001 to 0.0006 inch) between all races and supporting members (two inner races to shaft, forward outer race to housing, aft outer race to preload spring, and spring to housing). During installation of these parts, the outer member is heated (351 K to 366 K or 175 to 200° F) while the inner member, at room temperature, is slipped in place and loaded against a precision shoulder. Alignment is maintained by continuous application of the load while the outer member cools and shrinks over the inner

member. Interference fits are maintained throughout the expected temperature range of 278 to 306 K (40°F to 90°F), since the beryllium, 15-5 pH stainless and 440C stainless materials are closely matched in thermal expansion coefficients.

Tolerances and Bearing Alignment

Bearing mounting interface tolerances and assembly procedures in mounting and aligning the bearings are critical for optimum bearing performance. Circularity, concentricity, parallelism, perpendicularity, surface finishes, and diametral tolerances must each be carefully controlled, measured, and utilized to advantage during assembly to assure optimum bearing alignment with resultant low torque and long life. Perhaps the most important are parallelism and perpendicularity between diameters and end faces. The specialized procedures used at Hughes to assure optimum alignment are discussed in the following paragraphs.

The high precision tolerances and finishes of the ABEC Class 9 bearings are applied to all bearing interface shoulders and diameters of the shaft, housing, and preload spring assemblies. For example, axial runout between the inner race ball track and the reference end face of a Class 9 bearing of the proposed size is 2.5 micrometers (0.0001 inch) TIR. This same tolerance is applied to shoulders on the shaft against which this reference is positioned. Corresponding tolerances are applied to all critical dimensions of the shaft, housing, and preload spring.

Obtaining these accuracies, especially between the preload spring and housing, requires specialized machining and measurement techniques. To avoid unnecessary accumulation of tolerances, the preload spring is installed and indexed to the housing prior to the final grinding of diameters and end faces. These surfaces are thus made concentric and parallel to each other with one setup eliminating tolerance accumulation through the individual parts. Each preload spring is then serialized to its mating housing.

During BAPTA assembly, prior to bearing installation, each completed shaft and housing/spring assembly is set up such that the two bearing mounting diameters are concentric. The axial runout and phase of each shoulder is then measured and recorded for use later in assembly. Similarly, the bearing axial runout and phase relationship between reference and face and raceway ball track is measured and recorded. Upon installation of each race against its appropriate shaft, housing, or preload spring shoulder, the race is rotated to the proper phase such that axial runout of the faces are compensating. The end result of these procedures is that each ball track of each race is perpendicular to the mounting diameters and parallel to the outer ball tracks, to an accuracy equal to or better than the bearing tolerances.

The importance of these procedures can be seen by considering possible accumulation of tolerances between the fixed inner races on the shaft alone. For Class 9 bearings, the ball track is parallel to the reference end face within 2.5 micrometers (0.0001 inch) TIR. The same tolerances exist for the shaft shoulder perpendicularity to the mounting diameter. If the two inner races were installed at random, a total of 10 micrometers (0.0004 inch) TIR misalignment could exist between the forward and aft inner race ball tracks. Misalignment of this magnitude between inner races alone can cause increased bearing friction, spin axis wobble, and separation of ball contact with the races as the unit rotates, resulting in ball skid and decreased wear life. Use of selective fits with the precision tolerances, however, provides a highly accurate and quiet running bearing system with maximum wear life.

Torque Noise

The bearings selected are essentially identical in size and geometry to those used in the Anik I despin assembly. Torque noise data from the Anik I program is thus directly applicable. Measurements on a completed Anik I flight unit revealed a maximum peak to peak torque fluctuation due to bearings of approximately 0.005 newton (0.004 ft-lb) (a maximum at any frequency between 0.02 and 10 Hz). This torque fluctuation is additive with to final cleaning and lubrication separately from the balls and races to prevent final cleaning residue from contaminating the bearing metal parts. Use of proper bearing retainer materials and cleaning processes, developed on Company sponsored programs, has been very effective in minimizing ball and race non-wetting.

BAPTA Torque

The predicted BAPTA friction torque at various speed and temperatures is shown in Figure A-17. The curves shown include 0.062 newton-m (0.046 ft-lb) from the slip ring assembly (assuming a conservative coefficient of friction of 0.3 for the brush/ring sliding surface) which is independent of speed and temperature, and 0.043 newton-m (0.032 ft-lb) coulomb friction from the bearings due to the 535 newton (120 pound) preload, also independent of speed and temperature. The remainder of the torque comes from viscous oil churning in the bearings, a function of both speed and temperature. A 25 percent margin above the low temperature, high speed torque prediction is allowed in the BAPTA acceptance specification; i. e., at 12.6 rad/sec (120 rpm), 278 K (40°F), BAPTA friction torque up to 0.34 newton-m (0.25 ft-lb) is acceptable. Similarly, for qualification testing at 267 K (20°F), 126 rad/sec (120 rpm), up to 0.41 newton (0.30 ft-lb) is acceptable.

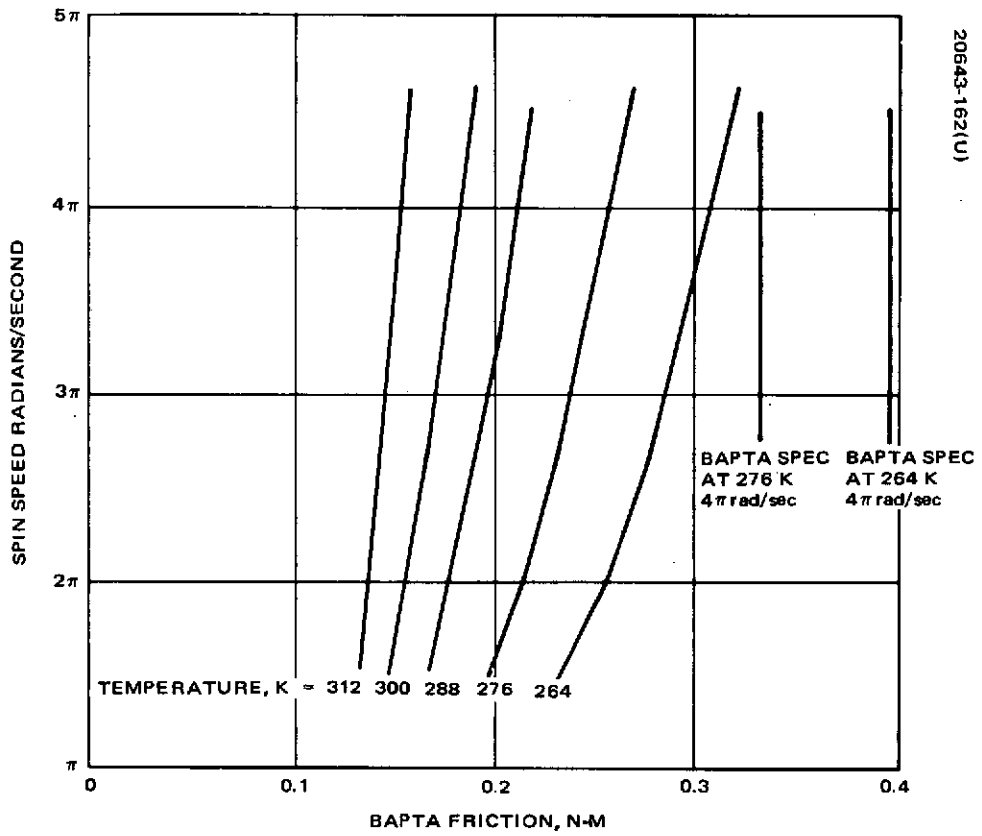


Figure A-17. Torque Versus Speed and Temperature

During third stage burn, when up to 22,500 newtons (5740 pounds) axial load is applied to the forward bearing, total BAPTA friction is predicted to be 1.285 newton-m (0.947 ft-lb) at 10.5 rad/sec (100 rpm), 288 K (60°F), as follows:

Coulomb friction, 22,500 newton bearing	1.100 newton-m
Coulomb friction, 535 newton bearing	0.022 newton-m
Coulomb friction, slip ring assembly	0.062 newton-m
Oil churning, 2 bearings, 10.5 rad/sec 288 K	<u>0.101 newton-m</u>
Total	1.285 newton-m

Bearing Life

The bearings and lubricant system proposed for TDRSS is expected to easily exceed a 0.22 gigasecond (7 year) life requirement at the expected operating conditions (8.4 to 12.6 rad/sec, 278 to 312 K) (80 to 120 rpm, 40°F to 100°F). Bearing operating speed and oil viscosity are such that an elastohydrodynamic oil film of thickness greater than ball and race asperity heights will exist throughout the speed/temperature range of operation, and metal to metal contact between ball and race is avoided, thus providing maximum wear life. Excessive bearing wear due to insufficient oil cannot be expected within the 0.22 gigasecond life requirement as the oil loss rate from the assembly ($<38 \text{ mg/gigasecond/labyrinth} \times 0.22 \text{ gigasecond} = <8.4 \text{ mg/labyrinth}$) is much less than the oil contained directly in the bearing ($>500 \text{ mg}$) and insignificant compared to the stored oil in reservoirs and internal walls (17,600 mg). All of the oil contained in the assembly cannot be considered as effective in providing proper lubrication for the bearings, however. For a conservative calculation, assuming none of the oil in the reservoirs and on internal walls is useful, and only 5 percent of the oil in the bearing retainer can be used (25 mg per bearing), lifetime to oil depletion would be slightly over 0.63 gigaseconds (20 years). Tests with phenolic retainers have shown that an oil film will quickly form on a dry bearing, with oil transfer from the retainer stopping abruptly once the balls and races become coated; the oil transfer rate from retainer to balls and races is self-regulating (with sufficient oil present on the balls and races, none flows from the retainer. With insufficient oil on the balls, oil flows until they are adequately coated.) By repeated removal of the oil on the metal parts, it has been determined that over 5 percent of the oil impregnated in the retainer will feed to the balls and races.

Bearing life reliability due to Weibull predicted fatigue for the worst case bearing (the forward bearing) is >0.9999 , considering 0.0026 gigasecond (1 month) operation at 10.5 rad/sec (100 rpm), 1870 newtons (420 pounds) preload (for ground spacecraft spin tests, preload on forward bearing is 553 newtons (120 pounds) from preload spring plus 1335 newtons (300 pounds) from despun platform), 78 seconds operation at 26,600 newtons (6000 pounds) load, 10.5 rad/sec (100 rpm) (third stage and apogee motor imposed loads are

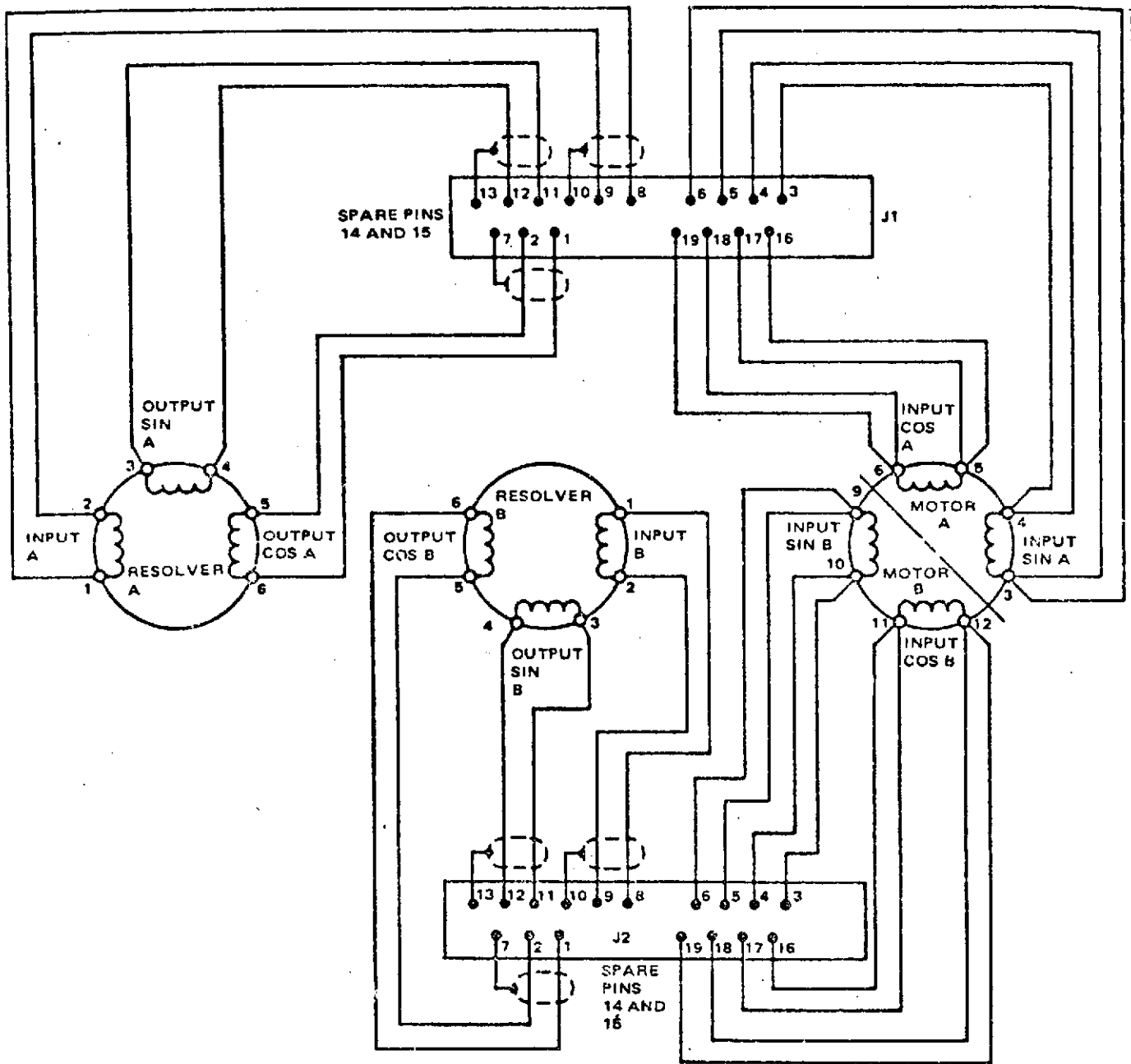


Figure A-18. Brushless Motor Assembly Schematic

less than 26,600 newtons (6000 pounds) and 0.22 gigasecond (7 years) operation at 535 newtons (120 pounds) preload, 10.5 rad/sec. Reliability to meet 0.22 gigasecond life due to random failures is 0.9957, considering both bearings.

Brushless Motor Assembly

Torquer Design and Construction

The brushless, resolver commutation dc torquer motor assembly proposed for the TDRS BAPTA is illustrated schematically in Figure A-18. The motor assembly consists of two redundant motors, segment wound on a common lamination stack, and two fully redundant resolvers. The motor is sized for a good margin of available torque above the BAPTA friction torque to enhance system reliability. This avoids the possibility of despin control loss due to unexpected bearing friction or marginal flat spin recovery capability.

Motor internal construction is essentially identical to the successful Anik I design. Features of the motor design include firmly anchored and potted lead wires, sealed protective covers over motor and resolver windings, potted laminations to provide lamination support and good heat dissipation characteristics, and a metal sleeve over the magnets to provide a smooth polished surface at the air gap. A final grinding of all critical diameters is performed after assembly of the rotor and stator. This provides a continuous smooth, highly concentric air gap, and facilitates final cleaning and inspection operations. Alnico IX permanent magnets are used for maximum field strength and high coercive force to preclude demagnetization under maximum stall torque conditions.

Motor Performance Characteristics

The performance characteristics of the despin motor selected for TDRSS are shown in Figure A-19. In selecting the major parameters shown, the prime consideration was to provide substantial margin above predicted bearing friction for nominal operation. For the nominal motor parameters selected, 1.27 newton meters (0.94 ft-lb) torque is available at 12.6 rad/sec (120 rpm) from a single motor, at minimum bus voltage (24 volt bus - 5 volt DME drop = 19 volts available to the motor), representing a margin of 4.7 to 1 over the predicted BAPTA torque of 0.27 newton meters (0.2 ft-lb) at 278 K (40°F), 126 rad/sec (120 rpm). For the worst case motor parameters (torque constant, back EMF, and winding resistance all 10 percent higher than nominal) and worst case BAPTA friction of 0.34 newton-meters (0.25 ft-lb) at 278 K (40°F), 12.6 rad/sec (120 rpm), a 3 to 1 margin exists at minimum bus voltage with one motor operating.

In the event of a flat spin, 7.6 newton-m (5.6 ft-lb) stall torque is available from both motors with 24 volts applied. Even though the probability of a flat spin is very small, consideration has been given to motor heat dissipation characteristics, when over 200 watts could be dissipated in the two motors for a short period of time during recovery. While preliminary thermal analysis indicates that temperature gradients are acceptable with the present

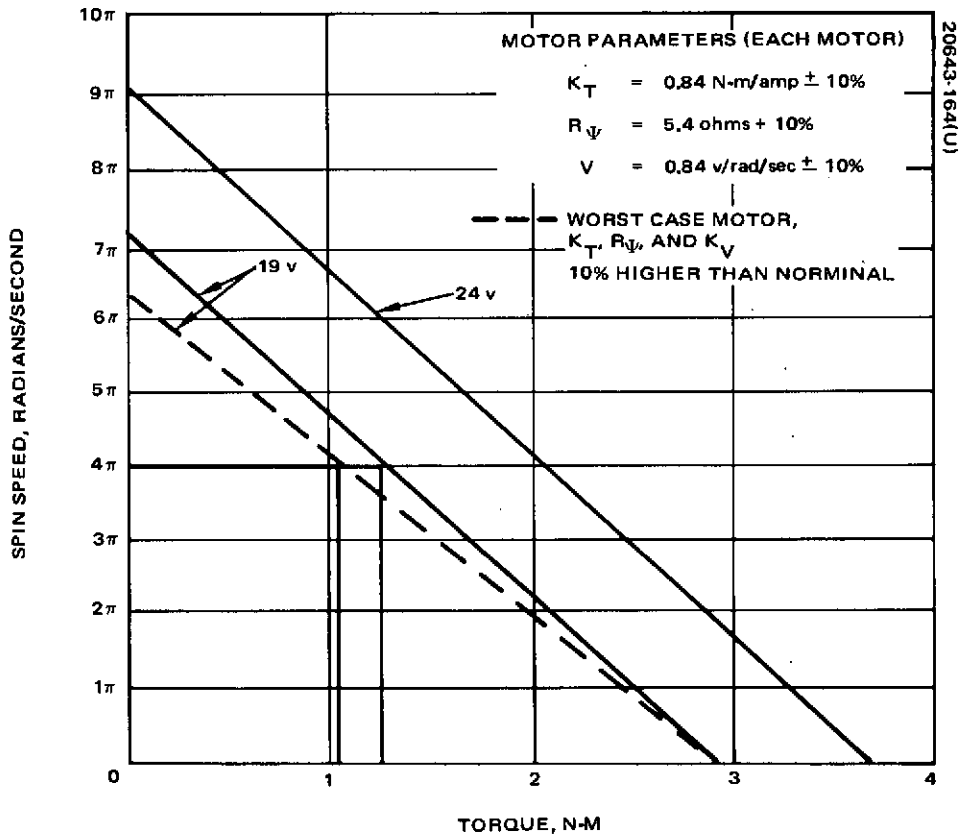


Figure A-19. Motor Characteristics

design, a more detailed analysis and development test will be performed in the motor detail design phase.

Resolvers

Commutation control of the dual wound brushless motor is provided by a redundant pair of electromagnetic resolvers, one for each set of motor windings. Each resolver consists of a stator and rotor, rigidly mounted and precisely aligned to the structures which support the motor stator and rotor, respectively. The rotor is built of high permeability iron laminations and has eight poles. The stator contains a primary (excitation) coil and a pair of secondary (sine and cosine output) windings on a laminated iron structure.

Functional operation of the resolver is shown in Figure A-20. The primary (excitation) coil is magnetically coupled to each secondary (output) coil via the air gap and the poles of the rotor. When an excitation voltage is applied to the primary windings, rotation of the rotor relative to the stator causes sinusoidal variations in the output voltage of each secondary winding as the pole pieces pass the stator coils. The angular spacing of the secondary coils relative to the spacing of the pole pieces is such that the voltage produced in the two secondary coils is $\pi/2$ radians out of phase electrically. The sine and cosine resolver outputs are demodulated and operate on the despin motor driver electronics such that current is applied to the motor sine and cosine windings in the same phase. The functional characteristics of the resolver are given in Table A-7.

Master Index Pulse Generator (MIPG)

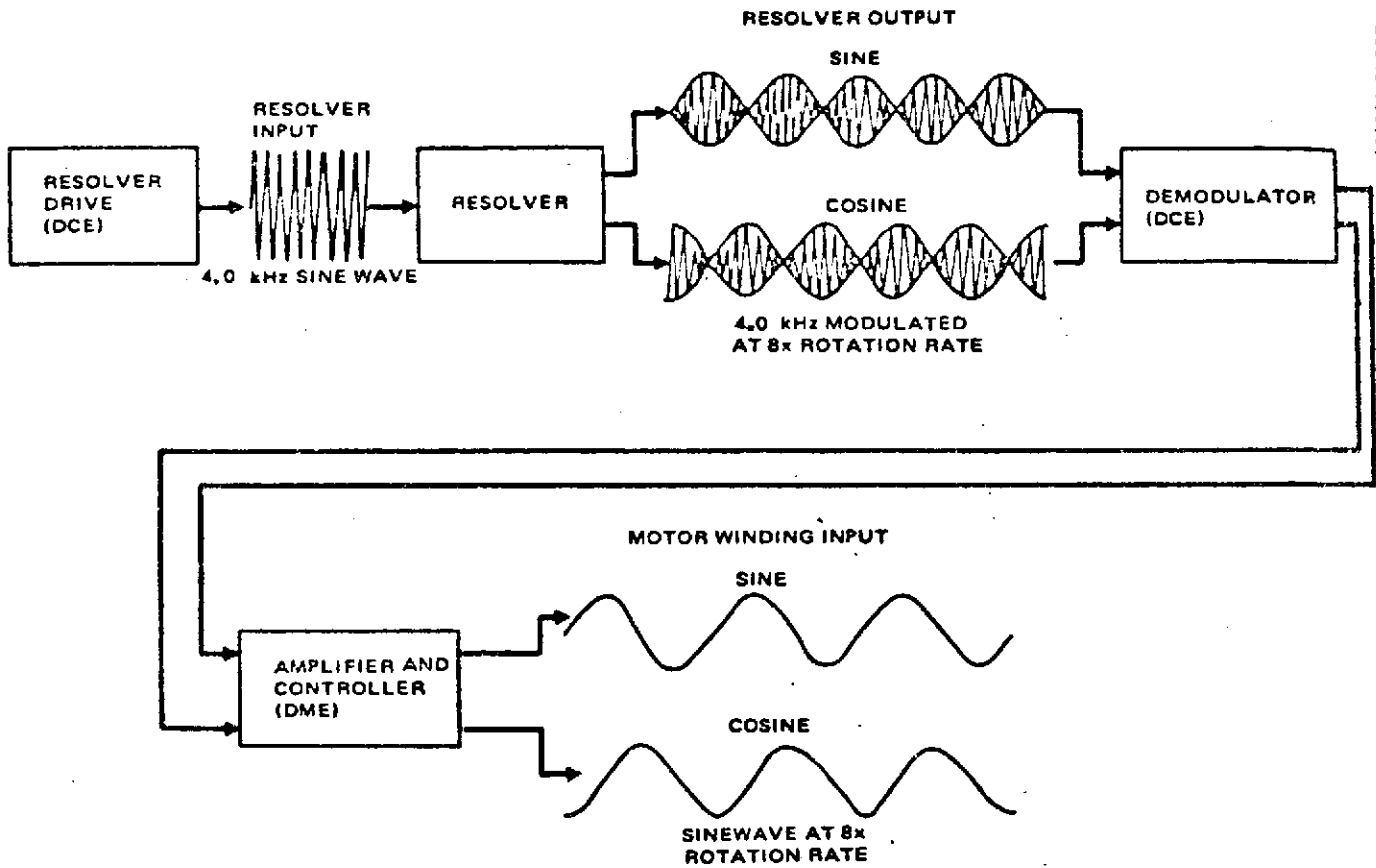
The MIPG consists of a single housing enclosing two physically separate (for redundancy) coil wound permanent magnets and is mounted on the spinning housing. Each coil provides one pulse per revolution as the magnet passes a soft iron exciter on the despun shaft. The location of the zero crossing of each pulse is calibrated with respect to the BAPTA mirrors, thus providing relative angle information between spun and despun sections.

Slip Ring Assembly (SRA)

Power and signal transfer from spun to despun sections of the satellite is accomplished with a dry lubricated slip ring assembly utilizing coin silver rings and 85 percent silver, 3 percent graphite, 12 percent molybdenum disulfide composite brushes.

The dry lubricated slip ring technology employed in the TDRSS is the result of extensive long term ground vacuum testing conducted to support the development of power transfer assemblies for previous programs, as summarized in the appendix hereto. Design details of the TDRSS SRA were borrowed directly from these programs as follows:

Brush/ring material:	Intelsat IV, TACSAT, and HS-318
Power brush design:	Intelsat IV and HS-318
Signal brush design:	HS-318



20643-166(U)

Figure A-20. Resolver Input and Output Waveforms

TABLE A-7. RESOLVER CHARACTERISTICS

<u>Input</u>	
Excitation frequency	4.0 kHz
Excitation voltage	10 volts peak
Excitation waveform	Sinusoidal
Impedance	(90 ± 9) ohms +j (350 ± 35) ohms
DC resistance	12 ± 1.2 ohms
<u>Output</u>	
Impedance	(325 ± 32) ohms +j (1450 ± 145) ohms
DC resistance	147 ± 15 ohms
Transformation ratio	0.50 ± 5 percent
Angular accuracy	± 0.0087 radian (mechanical)
Waveform	Sinusoidal
Null potential	200 mv at 10 volts excitation
Phase shift	0 ± 0.087 radian (electrical)

Wear performance of the proposed signal and power brush designs has been determined in many long term vacuum tests and is a strong function of the vacuum pressure environment near the brush/ring interface. Wear lifetime calculations are based on two models: >133 micronewtons/m² (1×10^6 Torr) internal SRA pressure and <6.6 micronewtons/m² (5×10^{-8} Torr) internal SRA pressure.

For these two cases, wear lifetime of the brushes are as follows:

Type	Conservative Worst Case (>133 micronewtons/m ²)		Conservative Best Case (<6.6 micronewtons/m ²)	
	Wear in 0.22 gigasecond, mm	Total Lifetime,* gigasec	Wear in 0.22 gigasecond, mm	Total Lifetime,* gigasec
Signal brushes	1.2	0.652	0.41	1.15
Power brushes	0.43	2.55	0.23	4.66

*Based on available wear length of 1.9 mm for signal brushes, 3.8 mm for power brushes.

Several design features have been incorporated in the TDRSS SRA design to reduce internal pressure to a minimum as follows:

- 1) All materials, coatings, insulation, etc., used in construction of the SRA will be carefully screened for selection of lowest outgassing rate.
- 2) Elevated temperature vacuum curing will be applied to certain component parts prior to installation in the SRA and to the SRA as a whole prior to final flight acceptance testing.
- 3) Venting paths are provided for each slip ring section (signal section, positive power bus, and return bus). Wear debris is prevented from leaving the SRA by cavities along the vent path which trap particles through centrifugal force, while providing low resistance to gases in the molecular flow pressure range.
- 4) Protective covers over the vents and dry nitrogen purging during ground test and handling will prevent moisture, debris, or other contamination from entering the SRA.

In addition to providing low wear, the slip ring internal design must prevent formation of low resistance paths through wear debris. In the TDRSS design, barriers between each signal ring and each signal brush, conformal coating of the signal brush springs and lead wire solder joints, and labyrinth seals isolating each power section preclude low resistance paths from circuit to circuit. The SRA anodized aluminum structural frame is completely covered with insulator brush holder materials, such that no possible path exists from circuit to ground. The wear debris itself provides some protection against formation of low resistance paths; tests have revealed that the debris is nonconductive at applied potentials of less than 50 volts.

Launch Lock Clamp

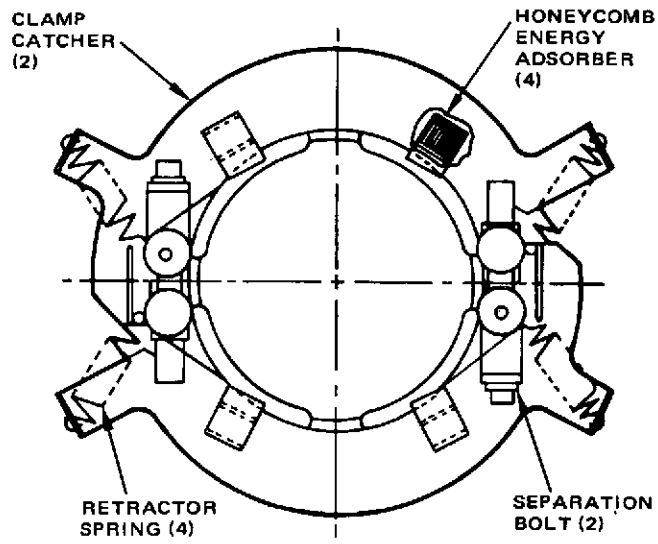
The launch lock clamp proposed for TDRSS is essentially identical to the fully developed and qualified Intelsat IV clamp, except that gage thicknesses will be increased, where appropriate (TDRSS clamp loads are smaller than Intelsat IV). The Marman type clamp shown schematically in Figure A-21 consists of four W-section shoes held in place by two pyrotechnic separation bolts and two straps in tension, a network of retraction springs, and energy absorbing shoe catchers. Upon installation of the clamp, the self-centering center section of the shoe "W" separates the BAPTA shaft and housing axially, demating the forward BAPTA bearing. Tension in the straps is applied and adjusted through the separation bolts to provide the required structural rigidity through the joint. The four retraction springs are located such that successful firing of either explosive bolt will enable retraction of the clamp shoes away from the spun/despun interface, thereby unlocking the BAPTA. The shoes are maintained in the separated position against the catcher network by the retraction springs throughout the mission. The springs operate in compression within cartridges, such that breakage of a spring coil does not cause loss of spring separation force.

The successful operation of the proposed clamp design on four Intelsat IV launches, combined with the extensive ground qualification and development program on the Intelsat IV clamp, provides high confidence in meeting the TDRSS requirements without difficulty.

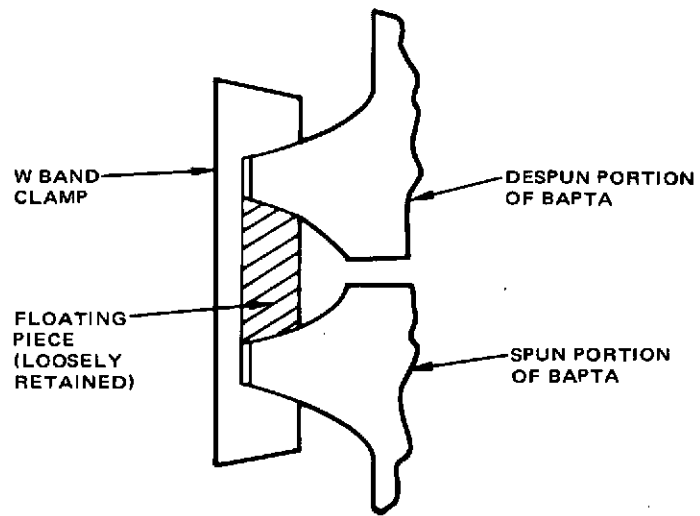
Assembly and Test

The internal geometry of the motor/bearing subassembly of the TDRSS BAPTA is essentially identical to the Anik I despin assembly. Design features and assembly procedures which were successful in providing an internally clean, readily assembleable Anik I unit are thus directly applicable to the TDRSS, as follows:

- 1) Assembly and bearing lubrication operations are performed by trained personnel with previous despin assembly experience in a Class 10,000 clean area laminar flow tunnel under the supervision of the unit engineer.
- 2) All screws and screw threads are exercised and cleaned prior to assembly.
- 3) All internal screw threads end in blind holes such that any debris generated by final installation of the screw is captured.
- 4) Careful cleaning and inspection for cleanliness is required after each assembly operation.
- 5) All assembly operations which might generate internal debris (such as screw installation and torquing, safety wiring, harness tying, adjustments, etc.) are accomplished before bearing installation (debris generated internal to assembly, if any, is removed before exposure of the bearings to the assembly).



a) Separation Clamp Assembly Schematic Diagram



b) Clamp Shoe Cross Section

Figure A-21. Marman Type Clamp

- 6) The slip ring, MIPG, and launch lock clamp subassemblies are installed after isolation of the internal motor/bearing subassembly surfaces by the labyrinth seals. These subassemblies can readily be installed or removed without disturbing the motor/bearing subassembly.

The design features and assembly precautions provide increased unit reliability by minimizing the possibility of debris entering the bearings and degrading performance.

The qualification and acceptance tests and sequence of tests planned for the TDRSS BAPTA are summarized in Table A-8.

Slip Ring Assembly Analysis, Design, and Testing

This discussion summarizes the extensive development, test, and flight history supporting the slip ring assembly design in the critical areas of lubrication and performance. The Hughes philosophy of using only those systems and design details that are well proven results in two benefits: 1) high confidence in the capability of the slip ring assembly to meet and exceed its requirements and 2) reduced design cost and minimum risk of development difficulties.

Summary of Dry Lubricated Tests

Extensive development testing of dry lubricated slip ring systems has been conducted during recent years at Hughes, as summarized in Table A-9. Two typical test fixtures are shown in Figure A-22. Over 25 different brush/ring material combinations have been evaluated in long term vacuum tests, with brush wear, brush wear rate, contact resistance, and electrical noise monitored during each test. The best material candidates were tested further to determine the effect on performance of the design variables of brush mount geometry, brush force (pressure), spring rate, contact area, number of brushes per wear track, contact angle, mold pressure orientation, current density, brush and ring surface preparation techniques, and run-in procedures. In addition, the effect on performance of ring surface speed variations was analyzed to determine the validity of accelerated speed testing. Of these parameters, the mechanical characteristic at the brush/ring interface, as provided by the brush support geometry, contact geometry, brush spring rate, and number of brushes per wear track, have the strongest effect on performance. The TDRSS design characteristics are summarized in Table A-10. Hughes has recently determined that the vacuum pressure level in the slip ring environment also has a strong effect on noise and wear performance. The effects of these parameters on performance and resulting design considerations are presented here.

TABLE A-8. BAPTA QUALIFICATION AND ACCEPTANCE TESTS

Slip Ring Run-in

- 173,000 seconds, GN₂ environment, remove wear debris, inspect

Mechanical Tests

- Runout
- Bearing preload, spring rate
- Static friction

Nonoperating Electrical

- Resistance (motor, MIPG, SRA)
- High potential (motor, SRA)
- Dielectric (motor, MIPG, SRA)

Ambient Functional

- Resolver transformation ratio
- Torque sensitivity
- Running friction
- MIPG output
- Slip ring voltage drop, noise
- Alignment

Vibration

- First unit sine and random, 3 axes, qualification level
- Subsequent units random only, 3 axes, acceptance level
- Monitor slip ring noise during vibration

Post-Vibration Tests

- Static friction
- Resistance (motor, MIPG, SRA)
- Dielectric (motor, MIPG)

Thermal Vacuum

- First unit cycled 267 to 317K
- Subsequent units cycled 278 to 306K
 - Running friction
 - MIPG output
 - Slip ring noise, voltage drop
 - Torque noise

Post-Thermal Vacuum

- Resistance (motor, MIPG, SRA)
- Remove SRA wear debris, inspection
- High potential (motor, SRA)
- Dielectric (motor, MIPG, SRA)
- Torque sensitivity
- Alignment

TABLE A-9. SLIP RING TEST SUMMARY - DRY-LUBRICATED TESTS

Test Ref. No.	Fixture	Ring Material and Number of Rings	Diameter, millimeters	Duration, giga-second	Slip Ring Environment Pressure Range, $\frac{2}{\text{newtons/m}^2}$	Rotation Rate, rad/sec	Ring Travel, $\text{m} \times 10^6$	Revolutions (10^6)	Brush Material	Brush-Type Dimensions
1	Stepped fixture Test A	Coin silver (12 total, 3 each, 4 diameters, 6.35 mm wide)	25.400 50.800 120.600 254.000	0.01080	6.65×10^{-2} to 2.66×10^{-6}	21.0	2.54 5.08 11.93 29.95	36	SM476 SM487 BAC4-53-3	Cartridge mount 4.75 x 4.75 mm tip area; 2 brushes/track, 2.6 amp/brush
2	Stepped fixture Test B	Coin silver (12 total, 3 each, 4 diameters, 6.35 mm wide)	25.400 50.800 120.600 254.000	0.00873	11.97×10^{-5} to 6.65×10^{-5}	6.3	0.635 1.422 3.048 6.350	8.7	SM476	Same as Test A, 40, 60, and 80 gram brush forces
3	Stepped fixture Test C	Coin silver (12 total, 3 each, 4 diameters, 6.35 mm wide)	25.400 50.800 120.600 254.000	0.00380	2.66×10^{-7}	6.3	2.794	3.8	SM476	Same as Test B
4	Geometry fixture Phase I	Coin silver (20 total, 12.70 mm wide)	25.400	0.00777	10.63×10^{-4} to 1.33×10^{-4}	6.3	0.608	7.8	SM476	TDRSS design; cartridge mount 5.58 x 5.58 mm; 1 and 2 per track, 3.6 amp/brush, 40, 60, 80 gram force. Cantilever spring mount - 1.27 x 3.68 mm tip area, signal brush, 50 ms/brush. Rocker arm mount - same tip as cantilever spring.
5	Material fixture	<ul style="list-style-type: none"> • Coin silver • Electro-deposited silver (two types) • Copper • Rhodium plate (20 total, 12.70 mm wide) 	25.400	0.00742	10.63×10^{-4} to 1.33×10^{-4}	6.3	0.584	7.4	SM476 SM428 SM487 SM492	TDRSS design cartridge mount 5.58 x 5.58 mm; 2 brushes/track, 3.6 amp/ brush, 80 brushes total, 4 of each of 20 material combinations.
6	OLSCA slip ring	Coin silver Pure silver	76.200	~0.00180	1.33×10^{-4}	0.105	0.0763	0.03	SM476 SM487 BAC4-53-3 BAC 046-45	Cartridge, power 17.25 x 5.58 mm, 8.2 amp/ brush; cantilever spring, signal
7	TACSAT life test (dry lube)	Coin silver (2 power 2 sec power, 20 signal)	25.400	~0.01008	Unknown 1.33×10^{-6} to 1.33×10^{-7} in chamber	5.77 52.5 105.0	3.048	38	SM476	Cantilever spring; Two types Power: 3.69 x 5.58 mm Signal: 1.14 x 3.69 mm 2 brushes/track Power: 2.5 amp/brush Signal: 50 ma/brush

A-59

Table A-9 (continued)

Test Ref. No.	Fixture	Ring Material and Number of Rings	Diameter, millimeters	Duration gigasecond	Slip Ring Environment Pressure Range newtons/m	Rotation Rate, rad/sec	Ring Travel, m x 10 ⁶	Revolutions (10 ⁶)	Brush Material	Brush-Type Dimensions
8	Modified TACSAT	Electrodeposited silver (same as above unit)	25.400	0.01260	1.33 x 10 ⁻⁴ to 1.33 x 10 ⁻⁵	5.77	0.914	11	SM476	Same as life test unit above
9	Geometry fixture Phase II	Coin silver (20 total, 12.70 mm wide)	25.400	0.02594	1.33 x 10 ⁻⁶ to 1.33 x 10 ⁻⁷	6.3 9.45	3.073	38.7	SM476	Same as Phase I
10	Signal brush fixture	Coin silver (8 total, 12.70 mm wide)	25.400	0.02594	1.33 x 10 ⁻⁶ to 1.33 x 10 ⁻⁷	6.3	1.996	25.1	SM476	TDRSS design (cantilever spring 1.52 x 6.23 mm) rocker arm 1.52 x 6.23 mm; signal, 2/track, 50 ma each
11	Accelerated life test fixture	Coin silver (electrodeposited silver 20 total, 12.70 mm wide)	25.400	0.0431	1.33 x 10 ⁻⁵ to 1.33 x 10 ⁻⁷	6.3 18.9 31.5 63.0	23.35	289.9	SM476 SM428 SM487	TDRSS design (cartridge 5.58 x 5.58 mm) 1 and 2 per track; 2.5 amp/brush
12	Intelsat IV life test - BAPTA	Coin silver (4 total)	25.400	0.03150	1.33 x 10 ⁻³ to 1.33 x 10 ⁻⁴ ECRA 1.33 x 10 ⁻⁵ to 1.33 x 10 ⁻⁷ in chamber	6.3	2.515	31.5	SM476	TDRSS design (cartridge 5.58 x 5.58 mm) 1 per track 2.5 amp/brush
13	IIS-318* BAPTA life test	Coin silver (2 power 20 signal)	28.550	0.0441	Unknown in ECRA 1.33 x 10 ⁻⁵ to 1.33 x 10 ⁻⁷ in chamber	6.3	3.935	44.0	SM476	TDRSS design (cartridge 5.58 x 5.58 mm) 1 per track, 3.6 amp/brush (cantilever spring 1.52 x 6.23 mm) 2 per track, 50 ma/brush

Brush composition:

SM476 85% Ag, 3% C, 12% MoS₂
 SM487 82.5% Ag, 2.5% Cu, 15% MoS₂
 SM428 85% Ag, 15% MoS₂
 SM492 85% Ag, 15% NbSe₂
 BAC4-53-3 16.5% Ag, 12.5% Mo, 4% Ta, 67% MoS₂
 BAC046-45 Same as 4-53-3 except without Ag

* Test still in operation.

TABLE A-10. SLIP RING ASSEMBLY DESIGN CHARACTERISTICS

Brush material	85 percent Ag, 3 percent C, 12 percent MoS ₂ per HMS 20-1652 (Stackpole Grade SM476)
Ring material	Coin silver, full hard, temper 6, per MIL-S-13282, 3.05 x 10 ⁻⁵ cm rms surface finish or better
Power brushes	
● Tip size	0.56 x 0.56 cm
● Contact area	0.31 x 10 ⁻⁴ m ²
● Brush force	80 grams
● Brush pressure	2.48 x 10 ⁴ newton/m ²
● Spring rate	39.4 gm/cm
● Steady state rating	3.6 amperes at 1.16 x 10 ⁵ (per brush)
● Impulse rating	11 amperes per brush
● Available wear length	0.382 cm
● Mount type	Cartridge
Signal brushes	
● Tip size	0.152 x 0.633 cm
● Contact area	0.904 x 10 ⁻⁴ m ²
● Brush force	25 grams
● Brush pressure	2.69 x 10 ⁴ newton/m ²
● Spring rate	77.2
● Steady state rating	1 amp at 1.16 x 10 ⁵ (per brush)
● Impulse rating	3 amperes per brush
● Available wear length	0.318 cm to zero brush force 0.191 cm to 0.10 gram brush force
● Mount type	Cantilever spring

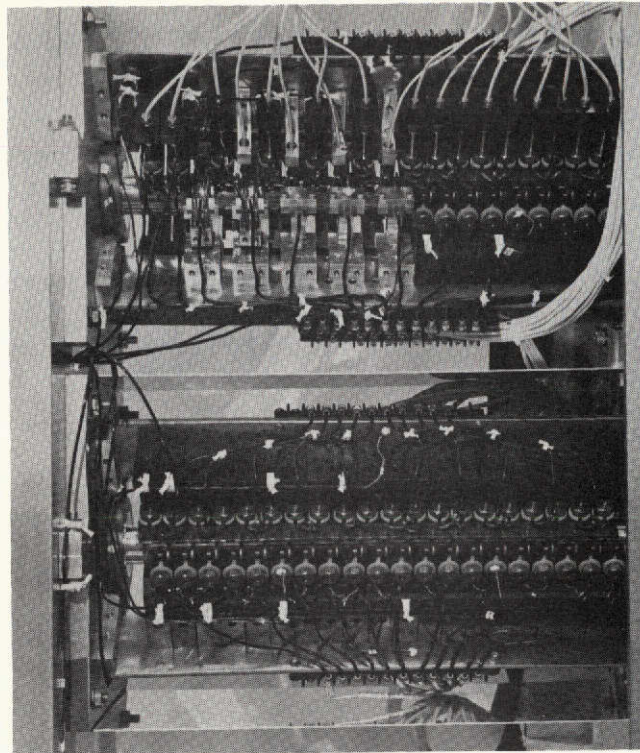


Figure A-22. Geometry Fixture (top)
and Material Fixture (bottom)
(Photo A24203-CN-A)

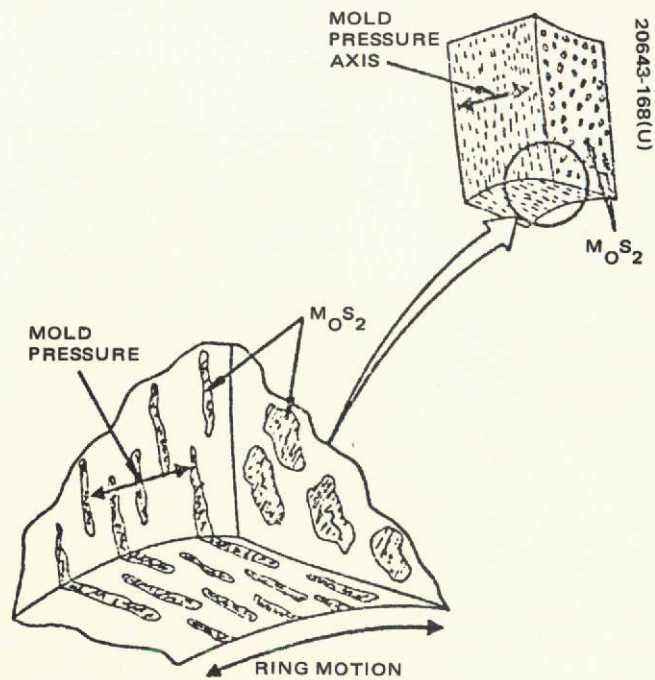


Figure A-23. Sintered Brush Grain
Structure

Lubrication Process

The brush material proposed is a sintered composite of 85 percent Ag, 3 percent C, and 12 percent MoS₂ per Hughes Aircraft Company Specification HMS 20-1652 (Stackpole Carbon Company, Grade SM476). The brushes are fabricated by mixing powders of the various materials, pressing the mixture into a mold, and maintaining pressure while sintering at a temperature near the melting point of silver. This fuses the silver particles together to provide mechanical strength of the brush, while maintaining a uniform distribution of the solid lubricant through the brush. Pore size in the brush is controlled by the applied pressure and sintering time. The resultant block of material is then cut and dry ground to the proper dimensions, with a minimum of at least 0.076 cm removed from any as-molded surface per Hughes requirements. The resultant brush has a grain pattern, as illustrated in Figure A-23. With the direction of molding pressure oriented parallel to the ring motion, the lubricant feed process and area coverage of the wear track is optimized, because no straightline wear path can be constructed across the wear face in the direction of ring motion that does not intersect several lubricant pockets.

As ring motion occurs, lubricant in the brush is fed directly to the brush/ring interface and smeared onto the ring, such that a film of lubricant is gradually burnished into the ring. Initially, when a clean metal ring exists, the brush wear rate is high. As the lubricant film becomes developed, the brush wear rate reduces, thereby reducing the rate of lubricant supply to the ring. The lubrication process is thus self-regulating, with the brush wear determined by the equilibrium between the rate of removal of lubricant from the ring and the rate of resupply as the brush wears.

Performance Versus Design Characteristics

Effect of Vacuum Pressure. The lubrication process described above is demonstrated by the performance curves of Figures A-24 and A-25, obtained from power and signal test brushes identical to the TDRSS design, where vacuum pressure in the slip ring environment was 1.33 to 0.133 micronewtons/m² throughout each test. Results from an identical test, where chamber pressure was about 1060 to 133 micronewtons/m² (8 x 10⁻⁶ to 1 x 10⁻⁶ Torr) throughout, is shown for comparison in Figure A-26. Note that the wear rate is significantly higher at the higher test pressure. Similar results have been obtained on other brush geometries and materials in several other tests. Since flight design slip rings must be isolated from their surroundings by labyrinth paths (to contain wear debris generated in orbit and to prevent contamination from entering the slip ring during ground test and handling), pressure inside the slip ring is higher than surrounding space, with the pressure level determined by equilibrium between the outgassing rate of internal materials and loss rate through the labyrinth paths. This is demonstrated by the data of Figure A-27, a plot of internal slip ring pressure and external test chamber pressure from the Intelsat IV BAPTA life test (reference test 12).

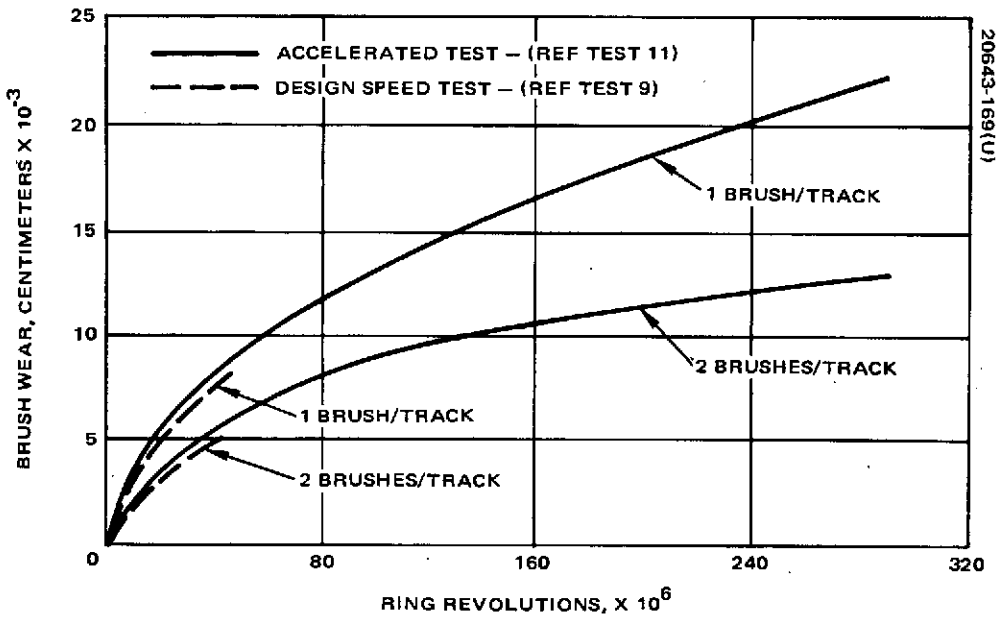


Figure A-24. Power Brush Wear Performance

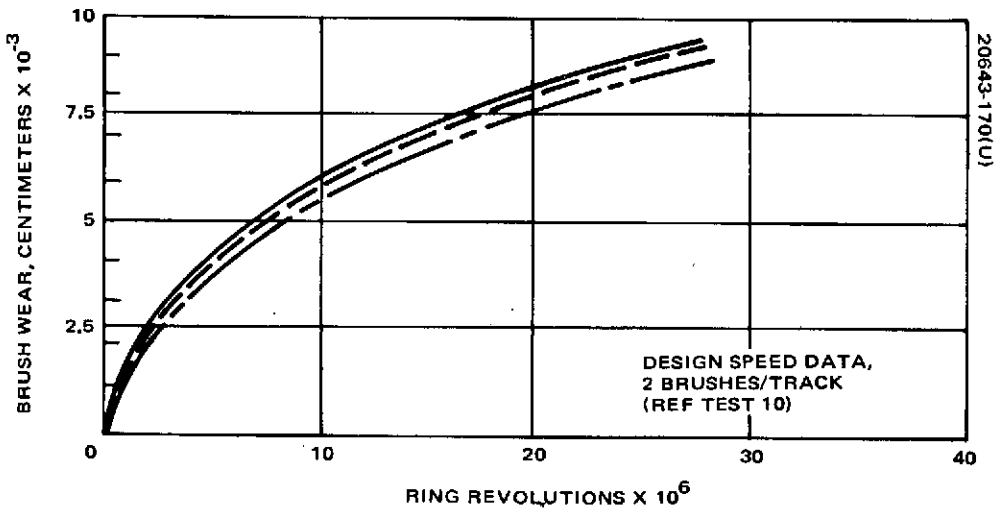


Figure A-25. Signal Brush Wear Performance

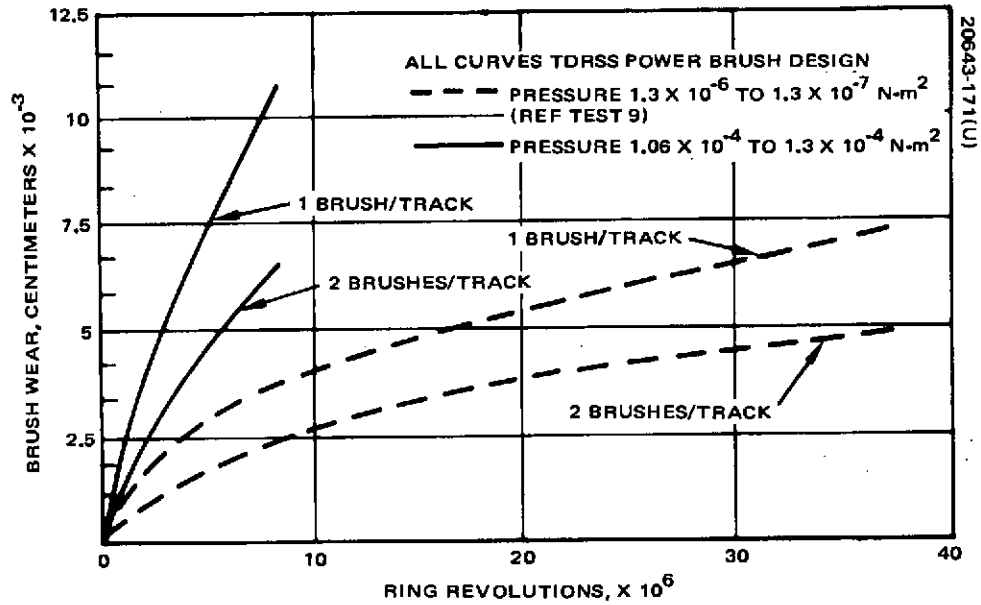


Figure A-26. Wear Performance Versus Vacuum Pressure

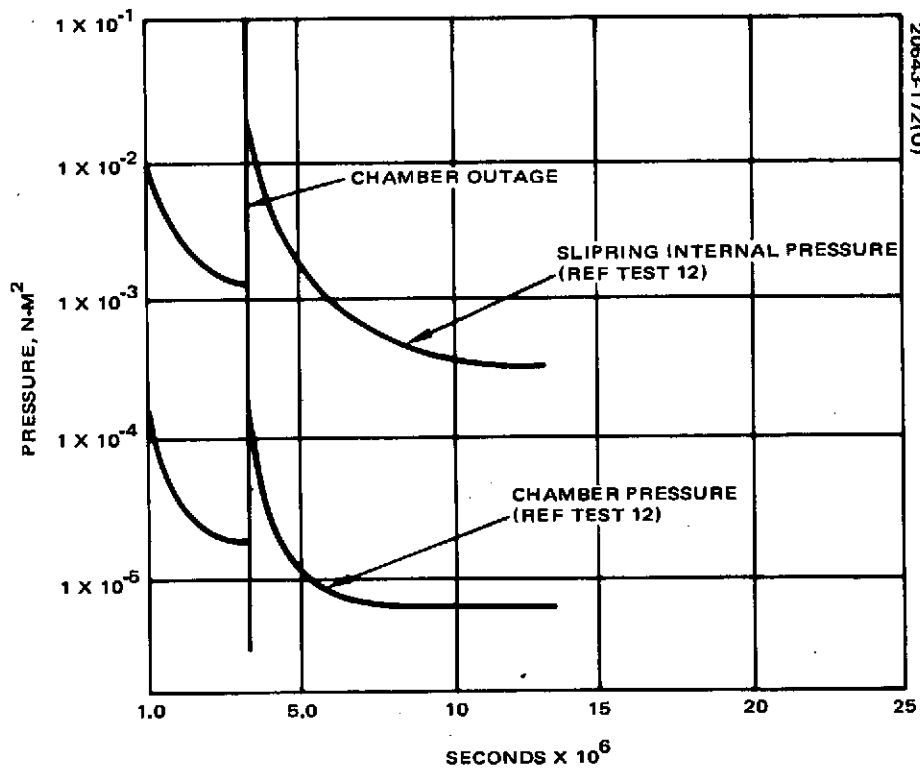


Figure A-27. Slip Ring Internal Pressure Versus Chamber Pressure

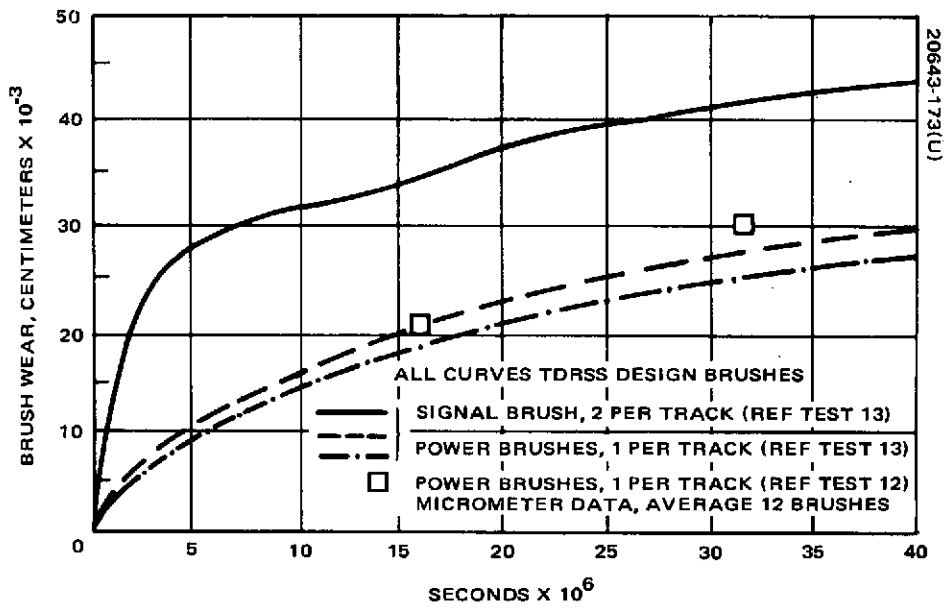


Figure A-28. Wear Data From Life Test Components

Wear data from the Intelsat IV life test is shown in Figure A-28, along with data from another BAPTA life test (test 13). Note the performance similarity between the flight type slip rings and the high pressure test of Figure A-26. Although internal pressure was not measured on the second slip ring, it is expected that the same magnitude was obtained as in the Intelsat IV, since seal geometries and internal materials are essentially identical.

Since vacuum pressure has a strong effect on brush wear rate and therefore ultimate slip ring lifetime, several design features have been incorporated in the TDRSS design to reduce internal pressure to a minimum, as follows:

- 1) All materials, coatings, insulation, etc., used in construction of the SRA will be carefully screened for selection of lowest outgassing rate.
- 2) Elevated temperature vacuum curing will be applied to certain component parts prior to installation in the SRA and to the SRA as a whole prior to final flight acceptance testing.
- 3) Venting paths are provided for each slip ring section (signal section, positive power bus, and return bus). Wear debris is prevented from leaving the SRA by cavities along the vent path which trap particles through centrifugal force, while providing low resistance to gases in the molecular flow pressure range.
- 4) Protective covers over the vents and dry nitrogen purging during ground test and handling will prevent moisture, debris, or other contamination from entering the SRA.

Since the extent to which these design features will reduce the slip ring internal pressure is unknown, brush wear lifetime calculations are made for two cases:

- 1) Worst case of high internal pressure (>133 micronewtons/m² throughout life).
- 2) Best case of low internal pressure (<6650 micronewtons/m² throughout life).

These calculations are presented later in this appendix.

Effect of Brush Force (Pressure).

- 1) Initially, brush wear rate is proportional to brush force (12,400 to 34,400 newtons/m², or 1.8 to 5.0 psi test range).

- 2) After equilibrium is reached, wear rate is independent of brush force (12,400 to 24,800 newtons/m², or 1.8 to 3.6 psi test range).
- 3) Lower brush force results in higher noise.
- 4) Noise level and contact resistance increase with time to a larger extent for low brush force than for high brush force.

Because of these results, initial brush forces during assembly will be set at 80 and 25 grams (± 10 percent), respectively. Because of the low spring rates used, the brush force remains nearly constant as the brush wears. Noise levels of less than 1 mv/amp can be expected at these values.

Effect of Brush and Ring Surface Finish. All brush contact surfaces will be contoured to match the ring diameter, using no abrasives in the cutting process. Final ring finish is achieved with a single point diamond tool. Tests have been conducted on coin silver rings, with surface finishes between 0.178 and 1.78 micrometers (7 and 70 microinch) rms roughness, with minimal effect on performance. However, the bulk of the tests and all flight units have utilized rings with 0.305 micrometer (12 microinches) rms finish or better. Processes used in obtaining this finish will be repeated for TDRS.

The effect of preburnishing the rings with MoS₂ by several processes has been tested, with no significant performance differences. This is probably because the MoS₂ was not tightly bonded to the ring and was wiped away with the first few passes of the brush. Providing a burnished film identical to that provided by the brush during the first 30 million revolutions to eliminate the transient run-in period would be extremely difficult, as evidenced by a calculation of the maximum average lubricant film thickness. From Figure A-24, total brush wear at 30 million revolutions (0.008 gigasecond, or 3 months at TDRSS design speed) is approximately 52 micrometers (0.002 inch). Assuming this wear occurred over the entire brush contact area of 0.000031 meters² (0.048 in²), total wear volume is 1.56×10^{-9} m³ (9.5×10^{-5} in³), 12 percent of which is MoS₂. If all of this MoS₂ were transferred uniformly to the ring wear track area, the average thickness would be only 0.36 micrometers (14 microinches).

Run-in Procedure. Comparison of tests on vacuum performance 1) with no previous rotation, 2) subsequent to run-in with a dry nitrogen purge, up to 1.5×10^6 revolutions, and 3) subsequent to run-in in an ambient air environment, up to 0.7×10^6 revolutions, show no significant difference. However, statistical evidence is small. From a theoretical standpoint, running in vacuum only is optimum since the lubricant (MoS₂) works best in the absence of moisture. From a practical standpoint, unit acceptance testing and running required for spacecraft testing are most readily accomplished in an ambient air environment. The 3 percent graphite contained in the brush serves as the lubricant for running in this mode. However, since statistical evidence is presently insufficient to provide that air running is not detrimental and most tests and all flight units have been run in with a dry nitrogen purge, the TDRS slip ring will be purged with dry nitrogen whenever operation is required outside a vacuum chamber.

Current Density. Current densities of 1.16×10^5 amp/m² (75 amp/in²) were used on most power brushes tested, with continuous power transfer throughout the tests. Comparison of the behavior of these brushes with those conducting no current show no significant difference. Short duration surge currents up to three times the steady state rating have shown no effect on subsequent performance.

Effect of Ring Surface Speed on Performance. Tests on cartridge mounted power brushes and cantilever spring mounted signal brushes on several brush/ring material combinations have been conducted at each of many ring surface speeds throughout the range from 0.0038 to 2.6 m/sec (9 to 6200 in/min). (TDRS design speed is 0.133 m/sec or 314 in/min at 10.5 rad/sec or 100 rpm.) Comparison of performance from each test results in the following conclusion: for properly mounted brushes, wear is a function only of distance traveled and is independent of surface speed.*

This conclusion is highly significant in demonstrating confidence in the ability of a dry-lubricated slip ring system to meet extremely long life requirements. Operation of one slip ring unit at design speeds while monitoring wear rate, contact resistance, and electrical noise will establish design speed performance. Simultaneously, operation of a second identical unit at accelerated speed to achieve the total number of revolutions required by the mission can be monitored for comparison. The wear curves generated at design speed will be essentially identical to those obtained at accelerated speed for properly mounted brushes. Extrapolation along the route traced by the accelerated test can thus be made with confidence.

TDRSS Brush Wear Calculations

Signal Brushes. For signal brushes, available wear length is determined by brush force reduction rather than brush height. With an initial force setting of 25 grams, brush spring rate of approximately 7.9 kg/m (0.2 gram/0.001 inch) (see Table A-10), and a conservative end of life brush force of 10 grams (to limit slip ring noise), brush wear length is 1.91 mm (0.075 inch) (0.127 mm/gm x 15 grams).

From Figure A-28 (worst case of high internal pressure) wear rate after 0.0315 gigasecond (1 year) of operation is 2.4 mm/gigasecond (0.003 inch/year). Wear during the first year was 0.41 mm (0.016 inch), from initial high wear rates during establishment of the lubricant track and the slow reduction of internal pressure.

* "Long Life Slip Rings for Vacuum Operation", A. C. Cunningham, IEEE Transactions on Parts, Materials and Packaging, March 1971, Vol. PMP-7, No. 1, pp. 48-61.

Assuming a continual 2.4 mm/gigasecond (0.003 inch/year) wear rate for the remainder of life, total lifetime is

$$\frac{1.91 - 0.41}{(2.4)(10^{-9})} + (0.032)(10^9) = 0.65 \text{ gigasecond.}$$

In 0.22 gigasecond, total wear would be

$$0.41 + 6(0.127) = 1.17 \text{ mm.}$$

From Figure A-24 (best case of initially low internal pressure), wear rate is 1.6 mm/gigasecond (0.002 inch/year) after 0.03 gigasecond (1 year), with total wear in the first 0.03 gigasecond of 0.10 mm (0.004 inch). Again assuming a linear wear rate (conservative), total lifetime is

$$\left[\frac{1.91 - 0.10}{(1.6)(10^{-9})} + (0.032)(10^9) \right] = 1.16 \text{ gigasecond}$$

In 0.22 gigasecond, total wear would be

$$0.10 + 6(0.05) = 0.40 \text{ mm.}$$

Power Brushes. Available wear length of power brushes is determined by brush geometry rather than force reduction. From worst case tolerances, the minimum length available will be 3.82 mm (0.150 inch). Since the power brush spring rate is only 3.94 kg/m (0.1 gram/0.001 inch), brush force reduces by only 15 grams from the original setting of 80 grams (see Table A-10). This minimum length is due to the brush pigtail bottoming in the slot in the side of the brush holder.

From Figure A-28 (worst case), brush wear rate is approximately 2.4 mm/gigasecond (0.003 inch/year), with initial wear for the first year 0.25 mm (0.010 inch). However, this data cannot be used directly since it was obtained from a one brush per wear track system. From Figures A-24 and A-26, wear per brush for two brushes/track is about 0.6 that of one brush/track.

Scaling the Figure A-28 data thus results in 1.4 mm/gigasecond wear rate and 0.15 mm wear the first 0.03 gigasecond. Again assuming a linear wear rate, total lifetime is

$$\frac{3.82 - 0.15}{(1.4)(10^{-9})} + (0.032) \times 10^9 = 2.65 \text{ gigaseconds}$$

In 0.22 gigasecond total wear would be

$$0.15 + 6(0.07) = 0.43 \text{ mm.}$$

From Figure A-24 (best case) wear rate after 0.03 gigasecond is 0.8 mm/gigasecond with total wear during the first 0.03 gigasecond of 0.06 mm. With a linear extrapolation, total lifetime is

$$\left(\frac{3.82 - 0.06}{(0.8)(10^{-9})} \right) + (0.032)(10^9) = 4.73 \text{ gigaseconds}$$

In 0.22 gigasecond, total wear would be

$$0.06 + (6)(10^9)(0.03)(0.8)(10^{-12}) = 0.22 \text{ mm.}$$

As can be seen from the accelerated test of Figure A-24, linear extrapolation results in quite a conservative answer since wear rate continues to reduce. For example, after the equivalent of 0.19 TDRS gigaseconds (6 TDRS years) operation, the power brush wear rate is only 0.24 mm/gigasecond (0.0003 inch/year), with total wear in 0.19 gigasecond (6 years) only 0.12 mm (0.005 inch). Another linear extrapolation from this point results in a phenomenal wear lifetime of

$$\left(\frac{3.82 - 0.12}{(0.24)(10^{-9})} \right) + (0.19)(10^9) = 15.4 \text{ gigaseconds.}$$

$$\approx 500 \text{ years}$$

Summary and Conclusions

A total of over 400 individual test samples of SM476/coin silver combinations have been tested at Hughes for an average duration of nearly 0.014 gigaseconds (4000 hours) each, resulting in a total of over 3.6 sample test gigaseconds (1 million sample test hours). These tests encompassed a large variety of brush geometry and mounting designs at many ring surface speeds between 0.0038 and 1.06 m/sec (9 and 2500 in/min); yet not a single test failure was observed. Fifty-two samples accumulated nearly 25 million meters (1 billion inches) of ring travel (equivalent to 0.19 gigasecond or 6 years life at TDRS design speed), while total brush wear of the worst sample was less than 0.24 mm (0.010 inch). Brush wear rates of the order of 0.8 mm brush wear per gigasecond (0.001 inch of brush wear per year) can be expected for the TDRS designs. For stable brush mounts (such as proposed for TDRS) wear rate is independent of surface speed; results from accelerated speed tests are thus applicable. The large number of successful tests, the excellent performance parameters of the proposed design, and the successful operation of TACSAT for over 0.10 gigasecond (3 years) and of three Intelsat IV spacecraft in orbit provide high confidence in the ability of the proposed system to meet the TDRSS requirements.

REFERENCES

1. McIntyre, J. E. and Gianelli, M. J., "Bearing Axis Wobble for a Dual Spin Vehicle", J. Spacecraft and Rockets, Vol. 8, No. 9, 1971.
2. McIntyre, J. E. and Gianelli, M. J., "The Effect of an Autotracking Antenna on the Nutational Stability of a Dual Spin Spacecraft", Paper No. 72-571, AIAA Fourth Communications Satellite Systems Conference, April 1972.
3. Velman, J. R., McIntyre, J. E. and Isaacs, T. M., "On the Use of a Dual Spin Vehicle for Scanning a Celestial Body", IEEE J. Aerospace Electronics, to appear.